

# REPORT DOCUMENTATION PAGE

AFRL-SR-AR-TR-02-

the  
cing  
2-  
rently

Public reporting burden for this collection of information is estimated to average 1 hour per response, including the time for reviewing data needed, and completing and reviewing this collection of information. Send comments regarding this burden estimate or any other aspect of this collection of information, including suggestions for reducing this burden, to Washington Headquarters Services, Directorate for Information Operations and Reports (0704 4302). Respondents should be aware that notwithstanding any other provision of law, no person shall be subject to any penalty for failing to comply with a collection of information if it does not have a valid OMB control number. PLEASE DO NOT RETURN YOUR FORM TO THE ABOVE ADDRESS.

1. REPORT DATE (DD-MM-YYYY)

Current Date

2. REPORT TYPE

Final

3. DATES COVERED (From - To)

12/01/98 - 02/28/02

4. TITLE AND SUBTITLE

The Role of Coating & Substrate Heterogeneities in the Long Term Performance  
Of Painted Aluminum Alloys

5a. CONTRACT NUMBER

N/A

5b. GRANT NUMBER

F49620-99-1-0060

5c. PROGRAM ELEMENT NUMBER

N/A

5d. PROJECT NUMBER

N/A

5e. TASK NUMBER

N/A

5f. WORK UNIT NUMBER

N/A

6. AUTHOR(S)

Taylor, S. R.; Kelly, R. G.; Scully, J. R.

7. PERFORMING ORGANIZATION NAME(S) AND ADDRESS(ES)

University of Virginia  
Office of Sponsored Programs  
P. O. Box 400195  
Charlottesville, Virginia 22904-4195

8. PERFORMING ORGANIZATION REPORT  
NUMBER

110762-101-GG10110-31340  
(FAS #5-25889)

9. SPONSORING / MONITORING AGENCY NAME(S) AND ADDRESS(ES)

Air Force Office of Scientific Research  
801 N. Randolph Street, Rm. 232  
Arlington, Virginia 22203-1977

10. SPONSOR/MONITOR'S ACRONYM(S)

N/A

11. SPONSOR/MONITOR'S REPORT  
NUMBER(S)

N/A

12. DISTRIBUTION / AVAILABILITY STATEMENT

Approved for public release, distribution unlimited.

Reproduced From  
Best Available Copy

13. SUPPLEMENTARY NOTES

N/A

14. ABSTRACT

This project seeks to understand the material, environmental, and interfacial factors that control the initiation and propagation of underpaint corrosion on aerospace aluminum alloys. The information needed to understand coating breakdown requires the use of local electrochemical, optical, and chemical methods. These methods have shown that intrinsic chemical heterogeneities most likely exist in the epoxy coating materials. These defects allow water and ions to the metal interface. The type and extent of subsequent underfilm corrosion is then determined by the type and possibly spacing of intermetallic compounds, as well as the ionic and material gating characteristics of the coating material.

Copies Furnished to DTIC  
Reproduced From  
Bound Original

20020719 141

15. SUBJECT TERMS

16. SECURITY CLASSIFICATION OF:

a. REPORT  
Unclassified

b. ABSTRACT  
Unclassified

c. THIS PAGE  
Unclassified

17. LIMITATION  
OF ABSTRACT

UL

18. NUMBER  
OF PAGES

1

19a. NAME OF RESPONSIBLE PERSON  
Taylor, S. R.

19b. TELEPHONE NUMBER (include area  
code)  
434-982-5788

## **Final Report**

Grant F49620-96-1-0178

Reporting Period: 8/31/00 to 2/28/02

# **The Role of Coating Defects and Substrate Heterogeneities in the Long-Term Performance of Painted Aluminum Alloys**

### **Submitted by:**

S. Ray Taylor, Robert G. Kelly, and John R. Scully

Center for Electrochemical Science and Engineering  
Department of Materials Science  
University of Virginia  
Charlottesville, VA 22904-4745

### **Submitted to:**

Lt. Col. Paul Trulove, Ph.D.  
AFOSR/NL  
801 North Randolph Street, Room 732  
Arlington, VA 22203-1977

April 2002

## SUMMARY

This project seeks to understand the material, environmental, and interfacial factors that control the initiation and propagation of underpaint corrosion on aerospace aluminum alloys. The information needed to understand coating breakdown requires the use of local electrochemical, optical, and chemical methods.

- The fidelity of local electrochemical impedance maps (LEIM) of coated substrates was examined via finite element methods and experiments employing micro-electrodes. This analysis has determined that the predominant spatial and temporal changes in the experimental data acquired via LEM is a result of chemical and physical phenomenon associated with the interface. One LEIM feature (troughing) may be a measurement artifact that results from the finite dimensions of the experimental cell.
- The local electrochemical events associated with breakdown of coated AA2024-T3 could result from either a low resistance pathway (heterogeneity) in the organic coating, or from an intense local electrochemical process on the substrate covered by a coating which is uniformly reduced in impedance by moisture and ion uptake. Initial experiments to resolve this question has used chloride sensitive fluoroprobes. These probe molecules show discrete sites of chloride uptake in the coating, and thus support the discrete pore concept.
- Confocal Scanning Laser Microscopy (CSLM) was used to examine *in situ* the early stage of corrosion. Galvanic corrosion at Al-Cu, Al-Cu-Mg, and Al-Cu-Fe-Mn intermetallic phases was investigated and compared on bare and epoxy-coated, polished surfaces of AA2024-T3. The results showed similar morphology of attack at each type of intermetallic compound on the bare surfaces in all three electrolytes investigated, as well as under coated surfaces in 0.5 M NaCl. These results suggest that the morphology and mechanism of the initial stages of local attack may be similar in all of these systems and controlled by the local galvanic coupling between the various intermetallic compounds and the matrix.
- Scanning vibrating electrode technique (SVET) demonstrated that blisters on AA1100 are entirely anodic (the cathodic current is spread over the coated surface outside the blister). For AA2024, a dynamic anode/cathode relationship is often observed within the blister. Initially, both anodic and cathodic regions exist within the blister, but as copper replating occurs, the blister becomes predominantly a cathode, driving delamination or undercutting of the coating at the periphery of the blister.

## **TABLE OF CONTENTS**

	<b>Page</b>
<b>I. PROJECT OBJECTIVES</b>	<b>3</b>
<b>II. ACCOMPLISHMENTS AND FINDINGS</b>	<b>4</b>
<b>III. PERSONNEL SUPPORTED</b>	<b>8</b>
<b>IV. PUBLICATIONS AND PRESENTATIONS</b>	<b>8</b>
<b>V. INTERACTIONS/TRANSITIONS</b>	<b>13</b>
<b>VI. DISCOVERIES, INVENTIONS, PATENT DISCLOSURES</b>	<b>17</b>
<b>VII. AWARDS AND HONORS</b>	<b>17</b>
<b>VIII. APPENDIX – SELECTED MANUSCRIPTS</b>	<b>18</b>



## I. PROJECT OBJECTIVES

The Air Force requires new coating systems with extended service lives for a diverse range of environmental conditions. The development of these coatings will require a mechanistic understanding of how the variables associated with the exterior environment, the coating, and the substrate interact to eventually lead to coating damage. A mechanistic understanding of the failure of coated aluminum will be essential for: the development of more durable coating chemistries and surface pretreatments, improved application methods, better inspection techniques, and the formulation of predictive models for coating evaluation.

This study has examined the interaction of the coating chemistry, alloy composition and microstructure, surface preparation, and environment in determining the durability of painted aluminum alloy. In order to do this, experimental techniques have been used which allow the characterization of local chemical and electrochemical events within and beneath the coating on a microscopic scale.

The specific objectives of this research are to:

- (i) Characterize the types and number density of local coating defects on aluminum alloys and examine the role of coating chemistry, alloy composition and microstructure, surface preparation, and environment on the initiation and evolution of defects.
- (ii) Examine the solution chemistry that develops beneath coating defects and determine the role of alloy composition and microstructure, coating chemistry, and environmental variables on the solution and its connection to the initiation and development of coating defects.
- (iii) Determine the role of alloy composition and microstructure, and surface pretreatment on the nature of the oxide and the subsequent impact on performance.

These objectives are being pursued via three coordinated thrusts: (A) Local Defect Mapping (Taylor), (B) Local Defect Chemistry/Electrochemistry (Kelly), and (C) Local Surface Chemistry/Electrochemistry (Scully). This interdisciplinary interaction is focused on resolving the three critical questions concerning coating defects on aluminum:

- (i) Are breakdown sites related entirely to the properties of the coating?
- (ii) What role does the chemistry of the bulk environment play in the alteration of coating properties and the life/death cycle of metastable coating defects.
- (iii) Are these defects due to the presence of a particular precipitate, alloy composition, or constituent phase at the alloy surface?

## II. ACCOMPLISHMENTS AND FINDINGS

### *(A) Local Detection and Mapping of Coatings Defects*

- This research program has allowed the construction and development of a central tool for characterizing the initial electrochemical breakdown events associated with coating degradation and underfilm corrosion, i.e., local electrochemical impedance mapping (LEIM). This method acquires the local current density by sampling the electric field at two points in solution above the electrochemical interface.
- Characteristic changes in the LEI map of initial and later stage breakdown events were observed. These features include: (1) initial admittance dips (impedance spikes) during underfilm corrosion initiation, (2) rise/decline in admittance peaks over time, and (3) admittance troughs surrounding admittance peaks. These features could have significant implications in the interpretation and correlation of local impedance data of underfilm corrosion processes if the data can be interpreted as being a result of actual physical and chemical events at the interface and not measurement artifact.
- Concern over the fidelity of the LEIM measurement launched a significant effort to mathematically model (analytically and via finite element method) the expected electric field and subsequent LEIM above an electrode in a bare and coated condition. These modeling results were verified experimentally with a gold micro-electrode array.
- The results of the mathematical analysis indicate that field sampling errors that can lead to artifacts such as reductions in admittance, are accompanied by other features that are not observed in the experimental data. This has lead to the conclusion that the local electrochemical impedance data are representative of the chemical and physical phenomenon associated with the interface.
- FEM modeling indicates that the finite size of the electrochemical cell may contribute to the trough observed at the base of admittance peaks. This result becomes less significant as the defect size,  $d$ , becomes less than ca. 2% of the total cell diameter,  $D$ .
- Experiments on electrodes fabricated using various substrate materials (gold, platinum, copper, and aluminum), coating materials (epoxy, vinyl, polyurethane), and conditions (NaCl islands,  $AlCl_3$  islands) indicate that the source of initial admittance peaks could be either: (1) a defect in the coating, or (2) a high current density from a local corrosion site (e.g., intermetallic) beneath a coating having generally reduced barrier properties (e.g. because of uniform water and ion uptake). The presence or propensity of a local admittance event on a coated substrate may be the result of an intrinsic chemical heterogeneity or it may result from subsequent coating hydrolysis via the underfilm chemistry.
- Thus, the observation of an admittance peak can not be assumed to result from an *a priori* coating defect. The precise delineation of the origins of coating breakdown (i.e., whether it is the result of an initial defect in the coating or whether coating

breakdown is the result of intermetallic compounds) will require the use of new experimental methods.

- Proof of concept experiments have been performed using chloride sensitive fluoroprobes on chloride soaked epoxy coatings spin cast on glass slides. These experiments have revealed discrete sites (ca. 10-50  $\mu\text{m}$  in diameter) of chloride concentration on coating surfaces. At this time, it is not known whether these sites penetrate through the coating.
- A new LEIM system with LabView software has been constructed. This system is operational and is presently undergoing testing.

### ***(B) Local Chemistry and Electrochemistry within Coating Defects***

- The confocal laser scanning microscope (CLSM) has been used to study the corrosion occurring on bare and coated AA2024-T3. In addition to allowing quantitative surface metrology studies after corrosion testing, microscope stages have been designed, built, and used to study bare and coated surfaces *in situ*.
- Effort has been spent on characterization of the anode/cathode separation within and outside blisters on AA1100 and AA2024 in a comparative study using the scanning vibrating electrode technique (SVET).
- Characterization of the local chemistry within blisters via microelectrode measurements of pH, electrode potential, and impedance continued as a function of bulk solution composition. In addition, the development of corrosion morphology within the blisters was investigated.
- The bulk electrolyte did not affect the concentration of species within the blisters. Active blisters showed high concentrations of chloride and the components of the alloy, except for copper. Copper replating was observed, but the concentration of copper in solution was very low.
- CLSM was used quantitatively to evaluate, *in-situ*, the corrosion topography of Al alloys both bare (with J. Scully and G. Ilievbare) and coated with a clear epoxy (with O. Schneider).
- Galvanic corrosion at Al-Cu, Al-Cu-Mg, and Al-Cu-Fe-Mn intermetallic phases was investigated (with Scully and Ilievbare) and compared on bare and epoxy-coated, polished surfaces of AA2024-T3. The results showed similar morphology of attack at each type of intermetallic compound on the bare surfaces in all three electrolytes investigated, as well as under coated surfaces in 0.5 M NaCl. These results suggest that the morphology and mechanism of the initial stages of local attack may be similar in all these systems.
- The global potential and the local potential associated with the intermetallic particles (IMCs) of the alloy combined to control blister initiation. The global potential was controlled in large part by the bulk chloride concentration and its effects on water uptake. The effect of varying chloride concentrations revealed a process that competed with potential control for blister initiation: water uptake by the coating. At low  $\text{Cl}^-$  concentrations, the degree of open circuit pitting was the controlling parameter for blister initiation whereas at high  $\text{Cl}^-$  concentrations water uptake dominated.
- In neutral solutions, underfilm corrosion in the early stages involved corrosion at intermetallic particles. Upon blister growth, trenching could be observed around

particles immediately after they became incorporated into the blister. At longer times, the particles themselves corroded. The most severe corrosion did not always take place at the initial blister site. The distribution of intermetallic particles seemed to determine where the most severe corrosion occurs. In acidic NaCl solutions, general attack on the Al-matrix seemed to be more important than intermetallic particle corrosion. In acidic sulfate solutions, the coating started to fail at many locations at the same time.

- In a study comparing the blistering behavior of AA1100 and AA2024, it was found that although the time to form blisters is longer on the lower Cu alloy (AA1100), the lateral growth of the blisters is much faster. This latter result is consistent with the lower dry adhesion strength of epoxy coatings on AA1100. The corrosion within blisters on AA2024 appears to grow in the depth direction more rapidly than the AA1100.
- The scanning vibrating electrode technique (SVET) was used to demonstrate that blisters on AA1100 are entirely anodic (the cathodic current is spread over the coated surface outside the blister). For AA2024, a dynamic anode/cathode relationship is observed within the blister. Initially, both anodic and cathodic regions exist within the blister, but as copper replating occurs, the blister becomes predominantly a cathode, driving delamination or undercutting of the coating at the periphery of the blister.

### ***(C) Role of Alloy Composition and Surface Treatment on Coating Performance***

- The primary objective was to determine the role of substrate alloy microstructure and composition on underpaint corrosion. Specifically we sought to examine and characterize the corrosion damage morphologies produced under an organic coating during the earliest stages of underpaint corrosion when microgalvanic coupling occurs between intermetallic compounds and the Al matrix. Precipitation hardened aerospace alloys such as AA 2024-T3 were the focus of the investigation.
- A secondary objective was to further our understanding of the role of microstructure in the initiation and propagation stages of underpaint corrosion. We sought to characterize the transition from micrometer scale damage events associated with micrometer scale intermetallic compounds to millimeter scale coating defects such as blisters. In collaboration with Prof. Kelly's research group, these studies were conducted in various bulk solution chemistries. Another secondary objective was to enhance our understanding of pretreatments such as chromate conversion coating on corrosion rates and damage morphologies on bare as well as organically coated AA 2024-T3.
- In order to achieve these goals, the confocal scanning laser microscopy (CSLM) method was optimized for study of underpaint corrosion on AA 2024-T3 substrates through neat resins in conjunction with R.G. Kelly and his group.
- The CSLM method was optimized for studying underpaint corrosion *in situ*. To achieve this goal exposure cells were designed and built, images of corroding AA 2024-T3 surfaces were captured illustrating the role of IMCs. CSLM images taken with both an underwater and air lens were compared to scanning electron microscope images in order to determine whether CSLM surface feature sizes and areas agreed with those seen in the scanning electron microscope using secondary electron imaging. The capabilities now exist within the UVa group to study the role of

microstructure on underpaint corrosion *in situ* on heterogeneous alloy surfaces with micrometer scale spatial resolution. Studies were conducted on bare, organic coated and chromate conversion coated AA 2024-T3.

- In order to further the study the role of microstructure on filiform corrosion in humid air, humidity chambers and specimen configurations were designed using micro- and millimeter scale engineered arrays of anodes and cathodes. Micron scale anodes and cathodes could be devised using Galium implantation and Cu deposition, respectively. Millimeter scale anodes and cathodes could be designed and used by constructing arrays of close-packed flush mounted wires.
- In order to advance the study of underpaint corrosion at the mm-scale, preliminary trial experiments were conducted on close-packed arrays of wires connected to separately addressable zero resistance ammeters. Al, Al-Cu, and Al-Cu-Mg wires were acquired for construction of model alloy surfaces.
- Progress was also made towards developing local impedance methods that would enable EIS measurements during humid air exposure. We will continue towards replacement of global EIS methods with local methods using a variety of approaches.
- The CLSM method was optimized for the investigation of corrosion processes on aluminum alloy AA2024-T3 occurring underneath a transparent organic coating. The ability of the microscope to monitor the three dimensional topography of both the alloy surface under the coating and the surface of the coating itself, was demonstrated. The resolution limits (x,y,z), when imaging through a bulk solution, coating and coating blister solution are better than 1  $\mu\text{m}$ . The technique described has potential to clarify the roles of alloy heterogeneity and corrosion damage associated with intermetallic phases at the micrometer scale on coating blister formation and growth. Optimization of the CSLM method will enable further *in situ* examinations of underpaint corrosion using a non-contact method with high resolution.
- The initial stages of underpaint corrosion were characterized in a range of environments. Galvanic corrosion at Al-Cu, Al-Cu-Mg, and Al-Cu-Fe-Mn intermetallic phases was investigated and compared on bare and epoxy-coated, polished surfaces of AA2024-T3. Exposures were conducted in 0.1 M  $\text{Na}_2\text{SO}_4$  + 0.005 M NaCl (pH 6), 0.1 M  $\text{Na}_2\text{SO}_4$  + 0.005 M NaCl + 0.0001 M NaOH (pH 10), 0.1 M  $\text{Na}_2\text{SO}_4$  + 0.005 M  $\text{Cl}^-$  (as  $\text{AlCl}_3$ ) (pH 3) and 0.5 M NaCl (pH 6). The results showed similar morphology of attack at each type of intermetallic compound on the bare surfaces in all three electrolytes investigated, as well as under coated surfaces in 0.5 M NaCl. Specifically, variations in composition were observed amongst particles with the same elemental constituents. The composition of some of the intermetallic particles were consistent with the stoichiometry of the most common intermetallics in AA 2024-T3, namely:  $\theta\text{-Al}_2\text{Cu}$ ,  $\text{S-Al}_2\text{CuMg}$  and  $\text{Al}_{20}\text{Cu}_2(\text{MnFe})_3$ .
- Scanning electron microscopy showed that some agglomerated intermetallic particles contained more than one phase. This led to different rates and morphologies of corrosion attack within one agglomerated particle. The Al-Cu-Mg particles were the most active towards corrosion in all the electrolytes investigated on the bare polished samples.
- Corrosion within some intermetallic particles was localized. All Al-Cu and Al-Cu-Mn-Fe particles do not have the same propensity to promote trenching of the Al-matrix by the mechanism of cathodic corrosion due to high cathodic reaction rates on

IMCs. This was observed in 0.1 M Na<sub>2</sub>SO<sub>4</sub> + 0.005 M NaCl (pH 6), 0.1 M Na<sub>2</sub>SO<sub>4</sub> + 0.005 M NaCl + 0.0001 M NaOH (pH 10) and 0.1 M Na<sub>2</sub>SO<sub>4</sub> + 0.005 M Cl<sup>-</sup> (as AlCl<sub>3</sub>) (pH 3). The morphology of initial stages of corrosion attack at the micro-scale at the intermetallic compounds on bare AA 2024-T3 is the same in all the electrolytes investigated.

- Preliminary indications are that pitting in either the matrix or at small matrix particles is more evident in 0.5 M NaCl than in other solutions used. In other words, high chloride content promotes pitting. Underpaint corrosion at the micrometer scale was also accelerated by high NaCl concentrations suggesting a role for pitting corrosion in addition to cathode trenching. Therefore, models of underpaint corrosion must consider a role for halide ions.
- Chromate conversion coatings inhibited any changes in surface morphological during corrosion at the micrometer scale when studied in-situ by CLSM, be it at anode (Al-Cu-Mg) or cathode (Al-Cu-Mn-Fe) sites.
- Indications of trenching of the Al-matrix due to cathodic corrosion around intermetallic compounds was observed in coating blisters formed under organic coatings in 0.5 M NaCl solutions. These results suggest that the morphology and mechanism of the initial stages of local attack may be similar in all these systems and that the initial stages of underpaint corrosion occurs initially in association with local galvanic couples.

#### IV. PERSONNEL SUPPORTED

S. Ray Taylor (PI):	25% effort
Amber Miersich (GRA):	100% effort (through 5/01)
Robert B. Leggat (GRA):	50% effort (through 9/01)
M.C. Turner (Technician):	75% effort (through 9/01)
Samual A. Taylor (Technician):	50% effort (through 8/01)
Pimsiree Moongkhamklang (GRA)	100% effort (start 9/01)
Robert G. Kelly (PI):	8.3% effort
Oliver Schneider (Senior Sci.):	50% effort
Jackie M. Williams (GRA):	100% effort
John R. Scully (P.I.):	8.3% effort
Gabrial Ilevbare (Senior Sci.):	60% effort
Daryl Little (GRA)	50% effort
Ashley Lucente (UgRA)	100% effort
Colin Quarmby (UgRA)	100% effort

#### V. PUBLICATIONS

## S.R. Taylor

### a. Refereed Journals

1. A.M. Miersich, J. Yuan, R.G. Kelly, and S.R. Taylor, "Understanding the Role of Coating and Substrate Heterogeneities in the Performance of Organic Coatings on AA2024-T3", *J. Electrochem. Soc.*, **146**(12):4449-4454 (1999).
2. A.M. Miersich and S.R. Taylor, "Characterization of the Electrochemical Events at Intrinsic Breakdown Sites on Organically Coated AA2024-T3", *J. of Corr Sci. and Engr.*, <http://www.cp.umist.ac.uk/JCSE>.
3. S.R. Taylor, "Incentives for Using Local Electrochemical Impedance Methods in the Investigation of Organic Coatings", *Progress in Organic Coatings*, **43**:141-148 (2001).
4. R. B. Leggat, N.P. Cella, C. Mastrangelo, R.G. Buchheit, and S. R. Taylor, "Development of Hydrotalcite as an Environmentally Benign Conversion Coating: Optimization by Fractional Factorial Design", *Corrosion Science*, (in review).
5. E.A. Pehovaz-Diez, R.B. Leggat, and S.R. Taylor, "Development of Hydrotalcite as an Environmentally Benign Conversion Coating: II. Effect of Bath Chemistry Evolution on Corrosion Resistance", *Corrosion Science*, (in review).
6. R.B. Leggat, S.R. Taylor, W. Zhang, and R.G. Buchheit, "Corrosion Performance of Field-Applied Chromate Conversion Coatings", *Corrosion*, **58**(3):283-291 (2002).
7. R.B. Leggat, W. Zhang, R.G. Buchheit, and S.R. Taylor, "Performance of Hydrotalcite Conversion Treatments on AA2024-T3 When Used Within a Coating System", *Corrosion*, **58**(4):322-328 (2002).
8. R.B. Leggat, S.A. Taylor, and S.R. Taylor, "Adhesion of Epoxy to Hydrotalcite Conversion Coatings: I. The Relationship to Wettability and Electrokinetic Properties", *Colloids and Surfaces A, Physicochemical and Engineering Aspects* (in press).
9. R.B. Leggat, S.A. Taylor and S.R. Taylor, "Adhesion of Epoxy to Hydrotalcite Conversion Coatings: II. Surface Modification with Ionic Surfactants", *Colloids and Surfaces A, Physicochemical and Engineering Aspects* (in press).
10. A.M. Mierisch and S.R. Taylor, "Understanding the Degradation of Organic Coatings Using Local Electrochemical Impedance Methods: I. Commonly Observed Features", *J. Electrochem. Soc.*, (in review).
11. A.M. Mierisch, S.R. Taylor, and Vittorio Celli, "Understanding the Degradation of Organic Coatings Using Local Electrochemical Impedance Methods: II. Modelling and Experimental Results of Normal Field Variations Above Disk Electrodes", *J. Electrochem. Soc.*, (in review).
12. A.M. Mierisch and S.R. Taylor, "Understanding the Degradation of Organic Coatings Using Local Electrochemical Impedance Methods: Modeling the Effect of a Dielectric Layer on the Electric Field Distribution Above a Disk Electrode", *J. Electrochem. Soc.*, (in preparation).
13. A.M. Miersich and S.R. Taylor, "Understanding the Degradation of Organic Coatings Using Local Electrochemical Impedance Methods: Experimental Verification of the Effect of a Dielectric Layer on the Electric Field Distribution Above a Disk Electrode", *J. Electrochem. Soc.*, (in preparation).
14. A.M. Mierisch and S.R. Taylor, "Underfilm Corrosion Initiates as Microscopic Spiral Pattern", *J. Electrochem. Soc. Letters*, (in preparation).

***b. Books/Book Chapters/Books Edited***

1. S.R. Taylor, "Coatings for Corrosion Protection: An Overview", Encyclopedia of Materials: Science and Technology, Ed. by K.H.J. Buschow, R.W. Cahn, M.C. Fleming, B. Ilschner, E.J. Kramer, and S. Mahajan, Pergamon, London, (3500 words).
2. S.R. Taylor, "Coatings for Corrosion Protection: Non-Metallic", Encyclopedia of Materials: Science and Technology, Ed. by K.H.J. Buschow, R.W. Cahn, M.C. Fleming, B. Ilschner, E.J. Kramer, and S. Mahajan, Pergamon, London (in press) (3500 words).
3. S.R. Taylor, "Coatings for Corrosion Protection: Metallic", Encyclopedia of Materials: Science and Technology, Ed. by K.H.J. Buschow, R.W. Cahn, M.C. Fleming, B. Ilschner, E.J. Kramer, and S. Mahajan, Pergamon, London (in press) (3500 words).
4. S.R. Taylor, "Coatings for Corrosion Protection: Organic", Encyclopedia of Materials: Science and Technology, Ed. by K.H.J. Buschow, R.W. Cahn, M.C. Fleming, B. Ilschner, E.J. Kramer, and S. Mahajan, Pergamon, London (in press) (3500 words).
5. Co-editor of Localized In-Situ Methods for Investigating Electrochemical Interfaces, **PV 99-28**, Ed. by S.R. Taylor, A.C. Hillier, and M. Seo, The Electrochemical Society, Pennington, NJ, (2000).

***c. Proceedings***

1. A.M. Mierisch and S.R. Taylor, "Interpretation of LEI Maps of Coated Substrates", in Localized In-Situ Methods for Investigating Electrochemical Interfaces, Ed. by S.R. Taylor, A.C. Hillier, M. Seo, The Electrochemical Society, **PV 99-28**, pp.229-240 (2000).
2. S.R. Taylor, "Incentives for Using Local Electrochemical Impedance Methods in the Investigation of Organic Coatings", Proceedings 26, 26<sup>th</sup> International Conference in Organic Coatings, Vouliagmeni, Greece, p.345-356, Institute of Materials Science, New Paltz, NY (2000).
3. S.R. Taylor, "Incentives for Using Local Electrochemical Impedance Methods in the Investigation of Organic Coatings", Proceedings of the 6<sup>th</sup> Biennial North American Research Conference on the Science and Technology of Organic Coatings", Institute of Materials Science, New Paltz, NY, Hilton Head, SC, pp.197-228, (2000).
4. R.B. Leggat, E.A. Pehovaz-Diez, N.P. Cella, and S.R. Taylor, "Optimization of Bath Chemistry for Hydrotalcite-Based Conversion Coatings on Aerospace Aluminum Alloys", in Corrosion and Corrosion Prevention of Low Density Metals and Alloys, Ed. by B.A. Shaw, R.G. Buchheit, and J.P. Moran, The Electrochemical Society, Pennington, NJ, **PV 2000-23**, pp.124-135 (2001).
5. S.R. Taylor and A.M. Mierisch, "Incentives for Using LEIM in the Investigation of Corrosion Initiation on Organic Coated Alloys", in Electrically Based Microstructural Characterization III, edited by R.A. Gerhardt, A.P. Washabaugh, M.A. Alim, and G.M. Choi, Materials Research Society, Pittsburgh, PA, (in press).
6. R.B. Leggat and S.R. Taylor, "Epoxy Adhesion to Hydrotalcite: Correlation Between Contact Angle and Electrokinetic Measurements", 2002 Tri-Service Conference, AFRL, San Antonio, TX (in press).
7. P. Moongkhamklang and S.R. Taylor, "The Role of Coating Heterogeneities in the Long-Term Performance of Coated Aluminum Alloys: Delineation of Ionic Pathways Using a Molecular Probe", 2002 Tri-Service Conference, AFRL, San Antonio, TX (in press).



## **R.G. Kelly**

### ***a. Refereed Journals***

1. A.M. Miersich, J. Yuan, R.G. Kelly, and S.R. Taylor, "Understanding the Role of Coating and Substrate Heterogeneities in the Performance of Organic Coatings on AA2024-T3", *J. Electrochem. Soc.*, **146**(12):4449-4454 (1999).
2. G.O. Ilevbare, J.R. Scully, J.Yuan and R.G. Kelly, "Effect of Soluble Chromate Additions vs. Chromate Conversion Coating", *Corrosion*, **56**, 227 (2000).
3. G.O. Ilevbare, J. Yuan, R.G. Kelly, J.R. Scully, "Inhibition of the Corrosion of AA 2024: Chromate Conversion Coating versus Chromate Additions," *Corrosion*, **53**(6), pp.179-193, (2000).
4. G.O. Ilevbare, J. Yuan, R.G. Kelly, J.R. Scully, "Inhibition of the Corrosion of AA 2024: Chromate Conversion Coating versus Chromate Additions," *Corrosion*, **53**(6), pp.179-193, (2000).
5. O. Schneider, G.O. Ilevbare, J.R. Scully, R.G. Kelly, "Confocal Laser Scanning Microscopy as a Tool for In Situ Monitoring of Corrosion underneath Organic Coatings," *J. Electrochem. And Solid State Letters*, **4**(12), B35-B38, (2001).

### ***b. Books/Book Chapters/Books Edited***

1. R. G. Kelly, J. R. Scully, D. W. Shoesmith, R. G. Buchheit, Electrochemical Techniques in Corrosion Science and Engineering, Marcel Dekker, 422 pgs., accepted for publication, April, 2002.
2. R. G. Kelly, "Crevice Corrosion," in Encyclopedia of Electrochemistry, M. Stratmann, ed., accepted for publication, March, 2002.
3. R. G. Kelly, "Crevice Corrosion," in ASM Handbook vol. 13 Corrosion, ASM International, accepted for publication, April, 2002.

### ***c.Proceedings***

1. G.O. Ilevbare, O. Schneider, R.G. Kelly, J.R. Scully, "In-situ Confocal Laser Microscopy Surface Metrology Studies of Corrosion on AA2024-T3, in Corrosion and Corrosion Prevention on Low Density Metals and Alloys, ECS PV 2000-23, Eds. B.A. Shaw, R.G. Buchheit, J.P. Moran, p. 87, 2001.
2. J. M. Williams, O. M. Schneider, R. G. Kelly, "Phenomenology of Localized Corrosion Failure on AA1100-H14," 2002 Tri-Services Corrosion Conference, San Antonio, TX, January, 2002.

## **J.R. Scully**

### ***a. Refereed Journals***

1. G.O. Ilevbare, J.R. Scully, J.Yuan and R.G. Kelly: "Effect of Soluble Chromate Additions vs. Chromate Conversion Coating", *Corrosion*, **56**, 227 (2000).
2. G.O. Ilevbare, and J.R. Scully: "Passivity and Localized Corrosion Mass Transport Limited Oxygen Reduction Kinetics on Chromate Conversion Coated Al-Cu, Al-Cu-Mg and Al-Cu-Mn-Fe Intermetallic Compounds", *J. Electrochem. Soc.*, **148**(5), B196-207 (2001)..

3. J.R. Scully, "Polarization Resistance Method for Determination of Instantaneous Corrosion Rates", *Corrosion*, **56**(2), 227-242, (2000).
4. G.O. Ilevbare, J. Yuan, R.G. Kelly, J.R. Scully, "Inhibition of the Corrosion of AA 2024: Chromate Conversion Coating versus Chromate Additions," *Corrosion*, **53**(6), pp.179-193, (2000).
5. G.O. Ilevbare, J.R. Scully, "Mass Transport Limited Oxygen Reduction Reaction Rates on AA 2024-T3 and Selected Intermetallic Compounds in Chromate-Containing Solutions," *Corrosion*, **57**, pp.134-152 (2001).
6. O. Schneider, G.O. Ilevbare, J.R. Scully, R.G. Kelly, "Confocal Laser Scanning Microscopy as a Tool for In Situ Monitoring of Corrosion underneath Organic Coatings," *J. Electrochem. And Solid State Letters*, **4**(12), B35-B38, (2001).
7. G.O. Ilevbare, O. Schneider, R.G. Kelly, J.R. Scully "In-Situ Confocal Laser Scanning Microscopy Surface Metrology Studies of Corrosion of AA 2024-T3: Influence of Electrolyte Compositions that Simulate Coating Blisters, *J. Electrochem. Soc.*, (in preparation), (2002).

***b. Books/Book Chapters/Books Edited***

1. R. G. Kelly, J. R. Scully, D. W. Shoesmith, R. G. Buchheit, Electrochemical Techniques in Corrosion Science and Engineering, Marcel Dekker, 422 pgs., accepted for publication, April, 2002.
2. John R. Scully, "Intergranular Corrosion of Polycrystalline Metals" in Encyclopedia of Electrochemistry, M. Stratmann, ed., accepted for publication, March, 2002.
3. John R. Scully, "Electrochemical Methods in Corrosion," in ASM Handbook vol. 13 Corrosion, ASM International, (submitted), April, 2002.
4. John R. Scully, Section Editor "Corrosion Fundamental Processes" in ASM Handbook vol. 13 Corrosion, ASM International, (submitted), April, 2002.
5. Co-editor of Localized Corrosion – NACE 2001 Topical Research Symposium, Ed. by J.R. Scully, G.S. Frankel, NACE, Houston TX, (2001).
6. John R. Scully, "Electrochemical Methods in Corrosion," in ASTM Manual 20, ASTM, West Conshohocken, PA (submitted), April, 2002.
8. John R. Scully, section editor "Test Methods for Various Types of Corrosion," in ASTM Manual 20, ASTM, West Conshohocken, PA (submitted), April, 2002

***c. Proceedings***

1. G.O. Ilevbare, O. Schneider, R.G. Kelly, J.R. Scully, "In-situ Confocal Laser Microscopy Surface Metrology Studies of Corrosion on AA2024-T3, in Corrosion and Corrosion Prevention on Low Density Metals and Alloys, ECS PV 2000-23, Eds. B.A. Shaw, R.G. Buchheit, J.P. Moran, p. 87, 2001.
2. J. M. Williams, O. M. Schneider, R. G. Kelly, "Phenomenology of Localized Corrosion Failure on AA1100-H14," 2002 Tri-Services Corrosion Conference, San Antonio, TX, January, 2002.
3. G.O. Ilevbare, O. Schneider, R.G. Kelly, J.R. Scully, "In-situ Confocal Laser Microscopy Surface Metrology Studies of Corrosion on AA2024-T3, in Corrosion and Corrosion Prevention on Low Density Metals and Alloys, ECS PV 2000-23, Eds. B.A. Shaw, R.G. Buchheit, J.P. Moran, p. 87, 2001.

4. G.O. Ilevbare, C. Jeffcoate, J.R. Scully, "Electrochemical Behavior of Selected Intermetallic Compounds in AA 2024-T3 after Chromate Conversion Coating," In the International Symposium in Honor of Prof. Norio Sato: Passivity and Localized Corrosion," The Electrochemical Society Proceedings, M. Seo, Editor, 1999.
5. G.O. Ilevbare, O. Schneider, R.G. Kelly, J.R. Scully "In-Situ Confocal Laser Scanning Microscopy Surface Metrology Studies of Corrosion of AA 2024-T3: Influence of Electrolyte Compositions that Simulate Coating Blisters, Triservices Corrosion Conf., San Antonio, TX, January, (2002).
6. D.A. Little, B.J. Connolly, and J.R. Scully, "An Electrochemical Framework to Explain the Intergranular Stress Corrosion Path of Two Al-Cu-Mg-Ag Alloys", , in Corrosion and Corrosion Protection, J.D. Sinclair, R.P. Frankenthal, E. Kalman, and W. Plieth, Editors, PV 2001-22, pp.1143-1155, The Electrochemical Society, Pennington, NJ (2001).

## VI. INTERACTIONS/TRANSITIONS

### S.R. Taylor

#### **a. Participation/presentation at meetings, conferences, seminars, etc.**

- A.M. Mierisch and S.R. Taylor, "Interpretation of LEI Maps of Coated Substrates", The Electrochemical Society Meeting, Fall 1999, Honolulu, Hawaii.
- S.R. Taylor, "Incentives for Using Local Electrochemical Impedance Methods in the Investigation of Organic Coatings", Presented at the 26<sup>th</sup> International Conference in Organic Coatings, Vouliagmeni, Greece, July 2000. (invited).
- S.R. Taylor, "An Examination of Possible Synergy Between Paired Combinations of Transition and Rare Earth Metal Salts", The Electrochemical Society Meeting, Spring 2000, Toronto, Ontario, CA
- R.B. Leggat, S.R. Taylor, R.G. Buchheit, and W. Zhang, "The Corrosion Performance of Field Applied Chromate Conversion Coatings", The Electrochemical Society Meeting, Spring 2000, Toronto, Ontario, CA
- S.R. Taylor, R.B. Leggat, R.G. Buchheit, et al., "Environmentally Compliant Corrosion Resistant and Electrically Conductive Inorganic Coatings", 2000 Corrosion Review Workshop, Hawk's Cay Resort, Duck Key, Florida, USA, January 2000
- S.R. Taylor, "The Role of Coating and Substrate Heterogeneities in the Long-Term Performance of Painted Aluminum Alloys", 2000 Corrosion Review Workshop, Hawk's Cay Resort, Duck Key, Florida, USA, January 2000.
- Co-editor of Localized In-Situ Methods for Investigating Electrochemical Interfaces, Proceedings Volume 99-28, Ed. by S.R. Taylor, A.C. Hillier, and M. Seo, The Electrochemical Society, Pennington, NJ, (2000).
- R.B. Leggat, E.A. Pehovaz-Diez, N.P. Cella, "Optimization of Bath Chemistry for Hydrotalcite-Based Conversion Coatings of Aerospace Aluminum Alloys", presented at Fall ECS Meeting, Phoenix, AZ, Oct. 2000.
- S.R. Taylor, "Incentives for Using Local Electrochemical Impedance Methods in the Investigation of Organic Coatings", presented at 3M Austin Center, Austin, TX, Aug. 2000 (invited).

- S.R. Taylor, "Incentives for Using Local Electrochemical Impedance Methods in the Investigation of Organic Coatings", 6<sup>th</sup> Biennial Conference on the Science and Technology of Organic Coatings, Hilton Head, SC, Nov. 2000 (**invited**).
- S.R. Taylor, R.B. Leggat, R.G. Buchheit, et al., "Environmentally Compliant Corrosion Resistant and Electrically Conductive Inorganic Coatings", 2001 Corrosion Review Workshop, Hawk's Cay Resort, Duck Key, Florida, USA, January 2001.
- S.R. Taylor, "The Role of Coating and Substrate Heterogeneities in the Long-Term Performance of Painted Aluminum Alloys", 2001 Corrosion Review Workshop, Hawk's Cay Resort, Duck Key, Florida, USA, January 2001.
- Attended "IR Spectroscopy: Interpretation of Infrared and Raman Spectra", Short Course at Bowdoin College, Bowdoin, ME, July 2001.
- Attended Gordon Conference on "Coatings and Thin Films", New London, NH, July 2001.
- R.B. Leggat and S.R. Taylor, "Epoxy Adhesion to Hydrotalcite: Correlation Between Contact Angle and Electrokinetic Measurements", 2002 Tri-Service Conference, AFRL, San Antonio, TX . (poster)
- P. Moongkhamklang and S.R. Taylor, "The Role of Coating Heterogeneities in the Long-Term Performance of Coated Aluminum Alloys: Delineation of Ionic Pathways Using a Molecular Probe", 2002 Tri-Service Conference, AFRL, San Antonio, TX (presentation and poster).

***b. Consultative and advisory activities***

none

***c. Transitions***

**LEIM:**

"A High Resolution Local Electrochemical Impedance Mapping and Spectroscopy System" (provisional patent filed, patent application was not pursued by the U.Va. Patent Foundation)

Bob Ross – Virginia Technology Inc., Charlottesville, VA – Has assisted in LabView software development.

Meetings/interactions with potential licencees:

Bill Eggers, Perkin Elmer (Spring 2001).

James Mason – Solartron (Summer 2001)

Martincek - Gamry Instruments (Spring 2001)

**R.G. Kelly**

***a. Participation/presentation at meetings, conferences, seminars, etc.***

- J.M. Williams, "A Comparison of the Localized Coating Failure of AA1100 and AA2024", NACE Meeting 2000, 26-31. March 2000, Orlando, Florida (student poster session).
- J.M. Williams, O. Schneider, R.G. Kelly, , "A Comparison of the Localized Coating Failure of AA1100-H19 and AA2024-T3", 197th meeting of the Electrochemical Society; 14-18 May 2000, Toronto, Ontario (poster).

- O. Schneider, R.G. Kelly, "Influence of the Bulk Solution Composition on the Blister Formation on AA2024", 197th meeting of the Electrochemical Society; 14-18 May2000, Toronto, Ontario (poster).
- J.M. Williams, O. Schneider, R.G. Kelly, "A Comparison of the Localized Coating Failure of AA1100-H19 and AA2024-T3", Gordon Research Conference on Aqueous Corrosion, 23-28July2000, New London, NH (poster).
- O. Schneider, R.G. Kelly; "Influence of the Bulk Solution Composition on the Blister Formation on AA2024", GRC conference on aqueous corrosion, 23-28July2000, New London,NH (poster).
- J. Williams, Oral presentation, 78<sup>th</sup> annual meeting of the Virginia Academy of Science, May 2000, Radford, VA, entitled "A Comparison of the Localized Coating Failure of AA1100-H14 and AA2024-T3."
- J. Williams, poster, 2001 Air Force Office of Scientific Research Corrosion Program Review, January 2001, Duck Key, FL.
- R. G. Kelly, S. R. Taylor, J. R. Scully, "The Role of Coating Defects and Substrate Heterogenieties in the Long-Term Performance of Painted Al Alloys," State Key Laboratory on Marine Corrosion and Protection, Qindao Corrosion and Protection Laboratory, Qingdao, People's Republic of China, August 14, 2001 (*invited*).

***b. Consultative and advisory activities***

Dr. Deborah Peeler  
Materials and Manufacturing Directorate  
AFRL/MLSA  
2719 12<sup>th</sup> St., Rm. 122  
Wright-Patterson AFB, OH 45433-7718  
(937) 255-4251 (phone)

I have continued to assist, in collaboration with John Scully and others, with the development and implementation of framework for corrosion management of aging aircraft, specifically the KC-135. The result is an executable corrosion prediction program for lap joint corrosion that considers current corrosion condition and future basing to predict future corrosion damage. The program will be available at the 2001 ASIP meeting in December, 2001.

***c. Transitions***

none

**J.R. Scully**

***a. Participation/presentations at meetings, conferences, seminars, etc.***

- J.R. Scully, R.G. Kelly, M. Altynova "A Model to Predict Corrosion Damage in Aging Aircraft" NACE Research in Progress Symposium – Life Prediction Session, NACE Corrosion 2001, Houston, Texas, March (2001). (*invited*)
- O. Schneider, G.O. Ilevbare, J.R. Scully, R.G. Kelly, Poster: "In-situ Confocal Scanning Laser Microscopy Studies of the Corrosion of Bare and Coated AA

2024-T3," Technical poster, 2001 Air Force Office of Scientific Research Corrosion Program Review, January 2001, Duck Key, FL.

- G.O. Ilevbare, O. Schneider, R.G. Kelly, J.R. Scully, "In-situ Confocal Laser Microscopy Surface Metrology Studies of Corrosion on AA2024-T3, in Corrosion and Corrosion Prevention on Low Density Metals and Alloys, Electrochemical Soc. Meeting, Phoenix, AZ, Fall 2000.
- G.O. Ilevbare, C. Jeffcoate, J.R. Scully, "Electrochemical Behavior of Selected Intermetallic Compounds in AA 2024-T3 after Chromate Conversion Coating," In the International Symposium in Honor of Prof. Norio Sato: Passivity and Localized Corrosion," The Electrochemical Society Meeting, Hawaii, Fall 1999.
- G.O. Ilevbare, O. Schneider, R.G. Kelly, J.R. Scully "In-Situ Confocal Laser Scanning Microscopy Surface Metrology Studies of Corrosion of AA 2024-T3: Influence of Electrolyte Compositions that Simulate Coating Blisters, Triservices Corrosion Conf., San Antonio, TX, January, (2002).
- D. Peeler, R.G. Kelly, M. Altynova, J.R. Scully, Poster: "A Model to Predict Corrosion Damage in Aging Aircraft," Triservices Corrosion Conf., San Antonio, TX, January, (2002).
- J.R. Scully, G.O. Ilevbare, "The Role of Coating and Substrate Heterogeneities in the Long-Term Performance of Painted Aluminum Alloys: Effects of Substrate Metallurgy", 2001 Corrosion Review Workshop, Hawk's Cay Resort, Duck Key, Florida, USA, January 2001.
- J.R. Scully, D.A. Little, "The Role of Coating and Substrate Heterogeneities in the Long-Term Performance of Painted Aluminum Alloys: Effects of Substrate Metallurgy", 2001 Corrosion Review Workshop, Masion Del Rio, San Antonio, TX, USA, January 2002.
- D.A. Little, B.J. Connolly, and J.R. Scully, "An Electrochemical Framework to Explain the Intergranular Stress Corrosion Path of Two Al-Cu-Mg-Ag Alloys", , in Corrosion and Corrosion Protection, The Electrochemical Society Meeting, San Francisco, CA, USA, September, (2001).

***b. Consultative and advisory activities***

- Continue to serve as a consultant to S&KT technologies in Dayton, OH on program to develop a corrosion model to anticipate and manage corrosion in KC-135 Tankers. Participated in the following technical interchange meetings:
  - Columbus, Ohio, Battelle Memorial Labs, October, 2000
  - Dayton, Ohio, UDRI, March, 2001
  - Dayton, Ohio, UDRI, June, 2001
  - Dayton, Ohio, UDRI, Nov. 2001
  - Dayton, Ohio, Dayton Marriot, April 2002
- Efforts include corrosion prediction and modeling so that the influence of corrosion damage on structural integrity may be assessed. Consulting has also involved studies of the effects of corrosion prevention compounds on local corrosion, stress corrosion and corrosion fatigue. Current scope includes fuselage and wing components.
- Interacted with the following personnel in an advisory role on this program:
  - Mr. Jim Suzel: KC-135 Corrosion Repair Task Orders,
  - Mr. John Wensit (SK&T),

Dr. Jill Ullett (SK&T),  
D. Hoeppe, (FASIDE),  
Craig Brooks (APES),  
Dr. Deb Peeler (DOD),  
Mr. Dick Kenzie (DOD),  
Mr. Nick Bellinger (NRC-Canada),  
Dr. Garry Abfalter (UDRI).

- Ongoing discussion regarding chromate inhibition issues, Dr. Martin Kendig, Rockwell International Science Center, 1049 Camino Dos Rios, Thousand Oaks, CA.

#### ***c. Transitions***

- L. Scribner of Scribner Associates has been advised on methods to construct close spaced wire arrays to simulate planar electrodes with spatially resolved electrochemical measurement

### **VII. NEW DISCOVERIES, INVENTIONS, PATENT DISCLOSURES**

- The finite element method (FEM) was used for the first time to examine the electric field about micro-electrodes within a finite dimensioned electrochemical cell. FEM revealed field alterations previously unobserved by others using conventional analytical approaches.
- The Confocal Scanning Laser Microscope was used to document corrosion morphologies around IMCs *in situ*.
- Arrays of coated electrodes simulating planar electrodes were constructed, coated, and investigated. A novel feature was that the ability to study coating degradation during atmospheric corrosion was enabled by embedding sensing electrodes within the array.

### **VII. HONORS/AWARDS**

- J. Williams was selected for a Virginia Space Grant Consortium grant to supplement her stipend and assist in her project.
- R. G. Kelly was selected as the 2001 recipient of the Robert T. Foley award of the National Capital section of the Electrochemical Society for contributions to electrochemical education and science.
- J.R. Scully was named a Society Fellow of the National Association of Corrosion Engineers (NACE) (Spring 2002).
- Ashley Lucente was elected as a finalist in the University of Virginia, SEAS Undergraduate Research and Design Symposium, (Spring 2002).

**VIII.**

**APPENDIX**  
**SELECTED MANUSCRIPTS**



## **THE ROLE OF COATING HETEROGENEITIES IN THE LONG-TERM PERFORMANCE OF COATED ALUMINUM ALLOYS: DELINEATION OF IONIC PATHWAYS USING A MOLECULAR PROBE**

**P. Moongkhamklang and S. R. Taylor**  
Center for Electrochemical Science and Engineering  
University of Virginia

### **ABSTRACT**

The mode of ion entry through thin epoxy coatings was investigated using a chloride specific chromophore in conjunction with fluorescence microscopy. 10  $\mu\text{m}$  thick epoxy coatings spin cast on glass slides were exposed to NaCl solutions at ambient and low (pH=3) pH for 1, 3, and 5 days. An additional material variable examined was the age of the material components as assessed from the date of manufacture. Following exposure to chloride solutions, the films were exposed to a chloride specific chromophore, 6-methoxy-N-ethylquinolinium iodide (MEQ). Fluorescence microscopy indicated that chloride ions were clustered in discrete sites on the surface of the coatings. The number of defect sites appeared qualitatively to increase with NaCl exposure time, but not to increase at low pH. This proof of concept experiment provides a new avenue for the characterization and quantification of coating degradation.

### **INTRODUCTION**

One of the earliest proposed and most widely accepted mechanisms by which organic coatings provide corrosion protection is that of barrier protection [1]. It is now generally agreed that conventional organic coatings function by providing a barrier to ionic species [2] as opposed to water and oxygen [3]. However, the mode by which ions enter and move through the coating, i.e., via discrete sites vs. a homogeneous front, remains unclear.

Two divergent theories have been proposed for ionic transport through contiguous organic films as presented in reference 4. One theory proposes that the flux of ions across the film is established by the presence of small imperfections or pores, which extend through the thickness of the coating and have cross-sections that are larger than the free areas typically present between the molecular chains of the matrix [5-7]. An alternate theory proposes that the ions pass through the bulk matrix of the polymer film [8], but that there are regional differences within a single coating with regards to ion selectivity [9]. These latter studies resulted in the proposed D (direct) and I (indirect) character of coating conductivity changes.

Recent research within these laboratories has examined the initial electrochemical phenomenon associated with coating breakdown on coated aluminum alloys using local electrochemical impedance spectroscopy (LEIM)[10-12]. Admittance peaks observed during early times of chloride exposure and prior to visible corrosion have been attributed to local coating sites having reduced barrier properties, i.e., pores. These LEIM results were considered as direct confirmation of the coating pore concept. However, more recent experiments using various combinations of coating materials (vinyl, epoxy, polyurethane) and substrates (Au, Pt, Al, Cu) indicate that an alternate explanation for these admittance peaks is plausible. These experiments have indicated that an LEIM admittance peak observed on a coated alloy could result from a substrate site of low interfacial impedance covered by a coating whose general

barrier properties are also intrinsically low but have been further reduced by uniform moisture and ion ingress. For example, the low interfacial impedance of the substrate could arise from an intermetallic (e.g.,  $\text{Al}_2\text{CuMg}$ ) or actively corroding site. Thus, the definitive linkage of an LEIM admittance peak to a coating pore that allows water and ion ingress, thus acting as the locus of underfilm corrosion, has not been conclusively made.

The origin of underfilm corrosion initiation and the precise interplay of the material and environmental factors that govern its evolution is unclear. If local chemical heterogeneities within the organic coating are responsible for ion entry, then their identification and elimination could provide a means for dramatically improving paint performance. A more definitive approach for the identification of chemical heterogeneities and ion transport within the organic coating is needed.

Medical and biological researchers have significantly advanced the structural characterization of cells and cell membranes in recent years through the use of moiety specific chromophores [13, 14]. This paper presents initial experiments that utilize an ion specific chromophore to identify the mode of ion entry through an epoxy coating. As mentioned, should ion channels be identified, an understanding of the material-related reasons for their existence will ultimately lead to improved resins for corrosion protection.

## EXPERIMENTAL METHODS

*Substrate:* Microscope quality-glass slides (Fisher brand) were washed with Alconox<sup>®</sup> solution, rinsed with distilled water, and blown dry with air. These glass slides were subsequently wiped with acetone, ethanol, and hexane using lint-free wipes. The slides were left to air dry under ambient conditions, and stored in a closed desiccated cabinet to shield them from dust.

*Coatings:* Cleaned glass slides were coated with a two-part epoxy solvated with butyl cellosolve. Part A consisted of bisphenol A-epichlorohydrin-based epoxy resin solution. Part B was composed of 70 wt% Epi-cure fatty acid polyethylenepolyamine-based polyamide curing agent and 30 wt% xylene. This specific epoxy resin is used as the binder resin in commercial primers for Air Force aircraft.

The coating was prepared by mixing equal amounts of part A and part B, and 8 wt% butyl cellosolve. Butyl cellosolve and xylene were used as solvents to reduce the viscosity for spin casting. Two batches of epoxy materials were used that differed in age of components. The samples in "batch 1" were made using a resin solution that was 2.5 years old and a curing agent that was 1.5 years old. The samples in "batch 2" were made from a resin solution that was, again, 2.5 years old, but the curing agent was 6.5 years old.

After mixing, the epoxy was allowed to set for 20 minutes prior to coating application. Air bubbles were removed from the resin of batch 1 using a vacuum chamber. This method was observed to leave small ( $< 5 \mu\text{m}$  diameter) air bubbles within the resin. In batch 2, a centrifuge was used to effectively remove the air from the mixed A and B materials. The coating was spin cast onto the cleaned glass slides using a spin caster to achieve a dry coating thickness of approximately  $10 \mu\text{m}$ . Samples were then cured under ambient conditions in a desiccator for at least 48 hours before exposure to test environments.

*Exposure conditions:* The coatings were exposed to 0.1 M NaCl solution at either ambient pH (ca. 5.5) or a pH adjusted to 2.5 (with HCl) using the ball-joint cell shown in Figure 1. A low pH

was selected based on observations of increased ion flux through these resins starting at pH's below 3 [15]. Samples were exposed for 1, 3 and 7 days. After exposure to NaCl solution, the samples were rinsed with distilled water and then exposed to 50  $\mu$ M MEQ solution for 20 minutes. MEQ ( $C_{12}H_{14}INO$ ) is a fluorescing molecule with a molecular weight of 315.15 grams per mole. It has absorption and emission wavelengths of 344 nm and 440 nm, respectively, and is also known to be sensitive to  $Br^-$ ,  $I^-$  and  $SCN^-$ , but insensitive to  $NO_3^-$ ,  $SO_4^{2-}$ , cations and pH [16]. The area of film exposed to MEQ was slightly larger than the region exposed to NaCl as shown in Figure 1(b). This provided a control region for comparative purposes. MEQ (6-methoxy-N-ethylquinolinium iodide) is a chloride-sensitive fluorescence indicator.

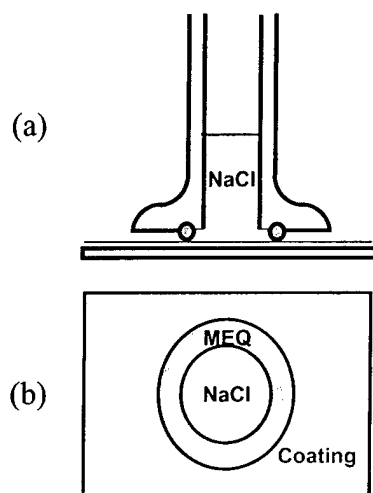


Figure 1: (a) Schematic showing exposure of a sample to NaCl solution using a ball-joint cell. (b) Schematic showing environments on surface of the sample.

**Microscopy:** Steady state fluorescence microscopy was used to visualize MEQ-tagged chloride ions within and on the surface of the coating. Images of the sample surfaces were collected in both bright and fluorescent fields. In fluorescence mode, the wavelength of the incident light was selected to be in the range of the absorption spectrum of MEQ using a 340 nm filter, and the emitted light from the sample was collected through a 420 nm-long pass filter.

## RESULTS AND DISCUSSION

Images of the coatings made from newer material components (batch 1) are shown in Figures 2, 3, 4, and 5. Images of the coating with no NaCl exposure or MEQ exposure (Figure 2) revealed no fluorescence signal in the fluorescent field, as expected. However, several dark spots were observed on the coating surface in bright field. These spots could be dust particles, but no further analysis has been performed at this time. A pattern within the epoxy was also observed, and is believed to be phase separation.

A second control experiment in which the surface of the coating was exposed to MEQ, but not to NaCl revealed results similar to those in Figure 2. Again, no features are observed in the fluorescent field indicating that there is no background chloride or other MEQ-sensitive moieties within the sample. Thus, it can be assumed that the observation of fluorescence in test experiments is solely attributable the NaCl exposure environment.

Figure 4 shows the bright and fluorescent field images of an epoxy coating that has been exposed to sodium chloride at pH 2.5 for 1 and 3 days followed by MEQ solution. Light colored

(fluorescing) spots can be seen in the fluorescent field images on the right. The fluorescing sites observed in these images strongly suggest that chloride ions enter the polymer coating through discrete pathways. Experiments to examine the penetration characteristics of the chloride are in progress. Note that there is not a one-to-one relation between dark sites observed in the bright field and the light spots observed in the fluorescent field. Determination of the chemical nature and differences of these sites will be one of the long-term goals of this research.

Figure 5 illustrates coating surfaces after exposure to sodium chloride solution at ambient pH for 1, 3, and 7 days followed by MEQ staining. It can be qualitatively observed that the number of defect sites in the coating, as observed in both bright and fluorescence fields, appears to increase with NaCl exposure time. Quantitative assessment of differences has not been performed at this time because the method of experimentation requires the sacrifice of samples by the MEQ staining procedure. Once a coating has been extracted and stained, it is not re-immersed for continual study, so the images at different times do not represent a time lapse of a single specific site.

As seen previously, it was observed that not all sites in the bright field took up MEQ and fluoresced in the fluorescence field. This could be attributable to limited access of the MEQ to chloride ions within the coating during the short MEQ soak times (20 minutes). It could also be due to the fact that there are different types of ionic pathways in the coating resin. Thus, further experiments to observe cross sections of NaCl exposed coatings in the fluorescence microscope will be performed to determine the transport depth of chloride ions and MEQ molecules in the coating. This may be a method to determine whether there are ionic pathways in the coating, and to clarify why some spots in bright field did not fluoresce.

At this time, no quantitative statement can be made about the differences in MEQ uptake between ambient pH and low pH exposures. This will be examined in subsequent experiments, and will require quantitative image analysis of numerous samples to establish distinct statistical trends.

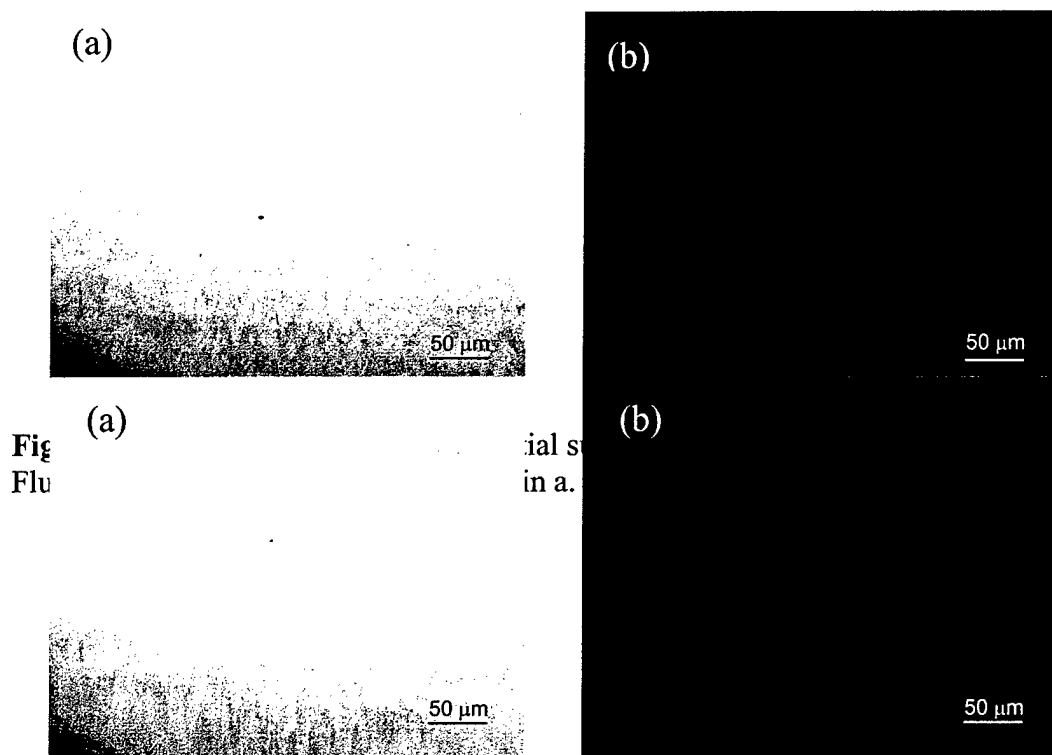


**Figure 3.** (a) A bright field image of surface of the coating (batch 1) with MEQ exposure only. (b) Fluorescence image of the same area as in a.

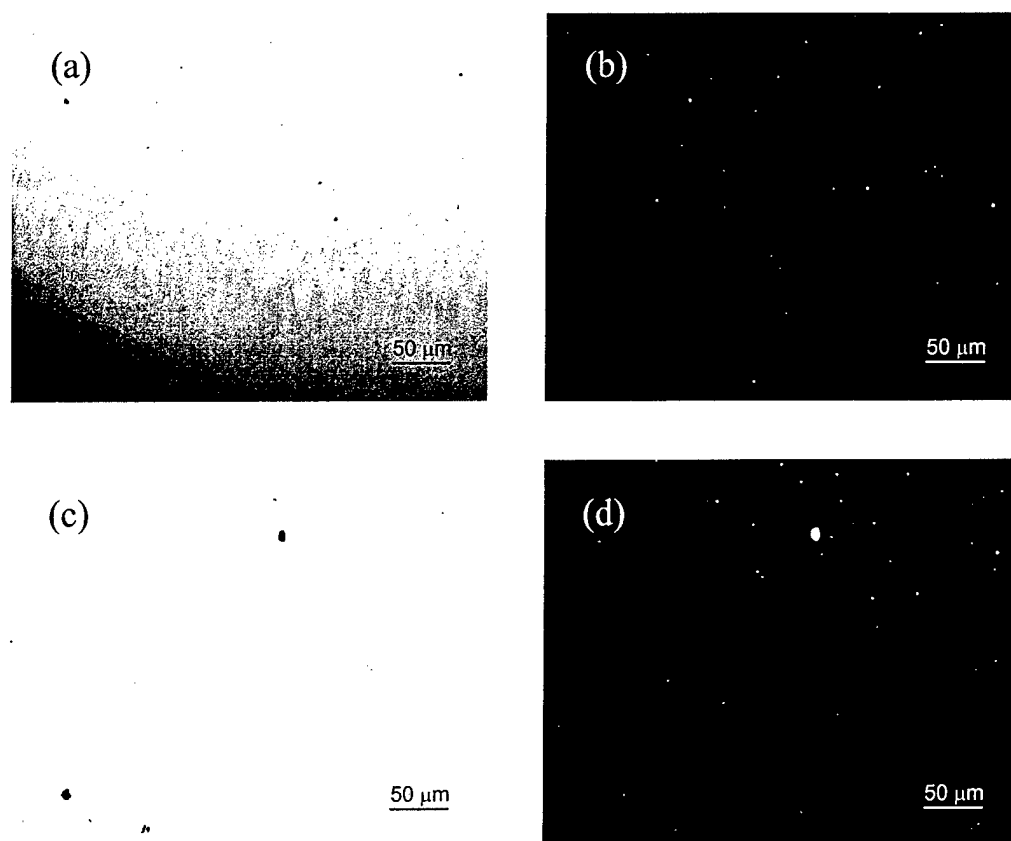


**Figure 4.** (a) A bright field image of the coating after 1 day of NaCl exposure at pH 2.5. (b) Fluorescence image of the same area as in a. (c) A bright field image of the coating after 3 days of NaCl exposure at pH 2.5. (d) Fluorescence image of the same area as in c.

Images of the coatings made with older material components (batch 2) are shown after exposure to NaCl solution at pH 2.5 and ambient pH in Figures 6 and 7, respectively. The pattern of phase separation is different and more pronounced from that of the coating made with newer materials. Though qualitative at this time, the number of defect sites and film delamination in these coatings seems to be greater than in the previous batch with the same or even shorter periods of exposure. These defects appear to increase in number with longer NaCl exposure time, as seen previously.

These proof-of-concept experiments definitively reveal discrete sites of chloride ion uptake on the surfaces of thin epoxy coatings in the early stages of immersion. It will be important to understand the depth of ion penetration as a function of time. Experiments to examine film cross-sections are planned.

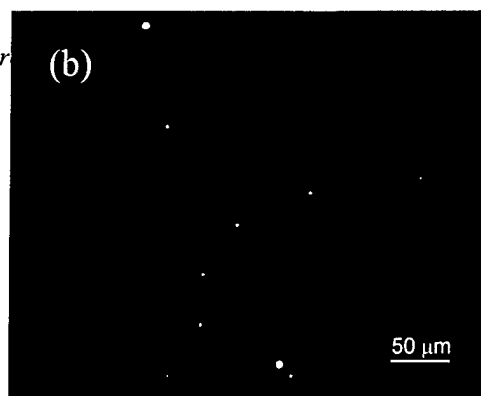
It is important to note that the present coating characterization have been performed while using a benign substrate, i.e., glass, so that the observed ion uptake is intrinsic to the coating and not a function of underfilm degradation as might occur in the blister chemistry of

active blisters on AA2024. It will therefore be important to examine the role of the alloy substrate in the evolution of these ion gates. More importantly, an understanding of the material nature of the coating regions that take-up chloride is needed. Are these local regions similar in structure and chemistry? Do specific types lead to underfilm corrosion? If these coating heterogeneities can be characterized and eliminated, the corrosion protective properties of the resin can be dramatically improved. It is believed that these molecular-probe methods will provide an important step in the approach to the characterization of coating degradation processes.

Presented (a)



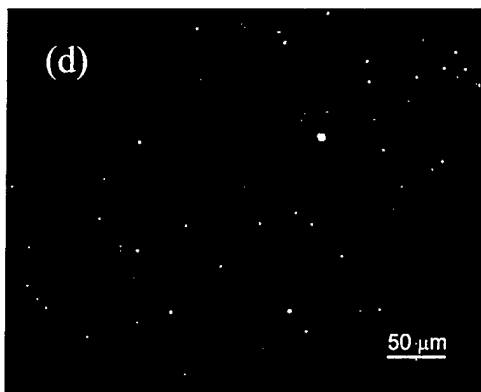
Corr (b)



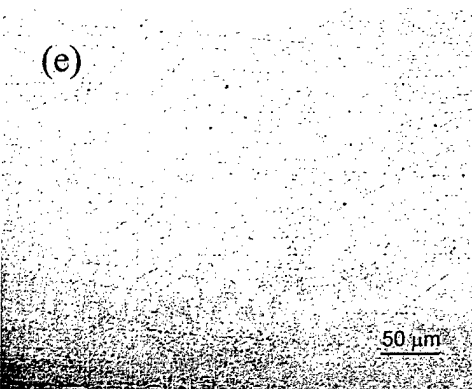
(c)



(d)



(e)



(f)

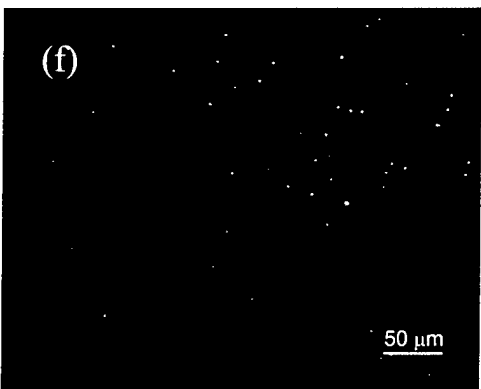


**Figure 5.** (a) A bright field image of the coating after 1 day of NaCl exposure at ambient pH. (b) Fluorescence image of the same area as in a. (c) A bright field image of the coating after 3 days of NaCl exposure at ambient pH. (d) Fluorescence image of the same area as in c. (e) A bright field image of the coating after 7 days of NaCl exposure at ambient pH. (f) Fluorescence image of the same area as in e.

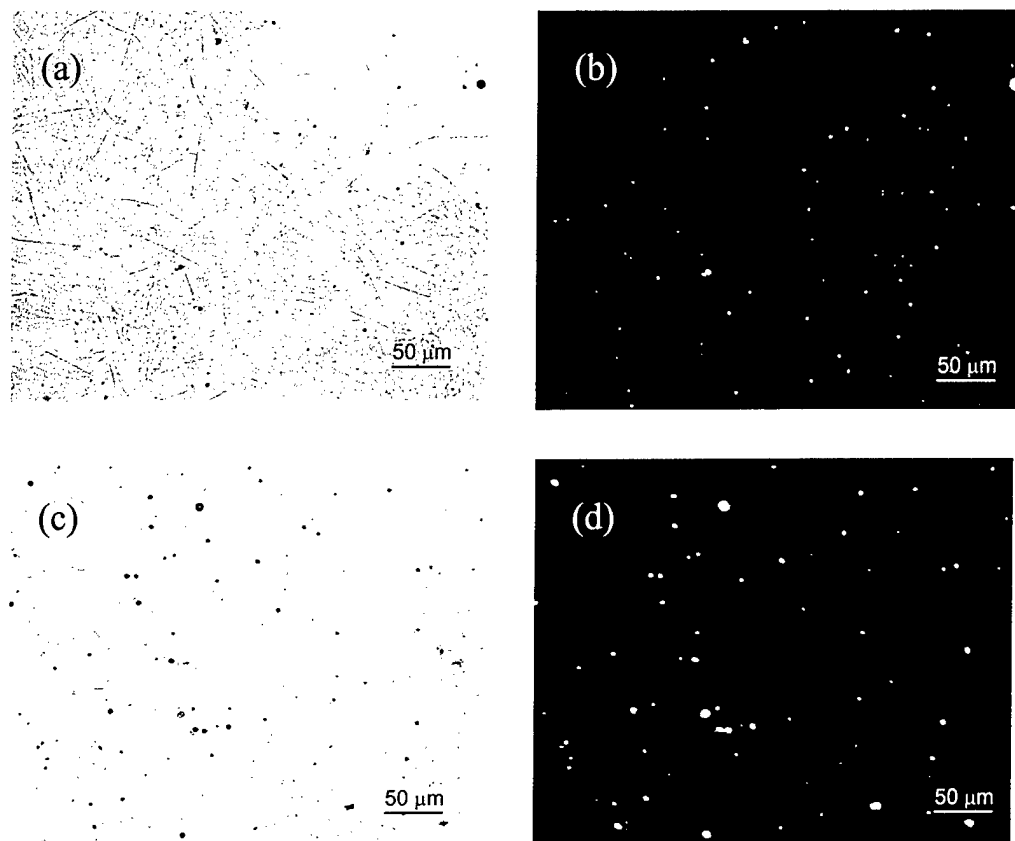


**Figure 6.** (a) A bright field image of the coating made with older materials after 1 day of NaCl exposure at pH 2.5. (b) Fluorescence image of the same area as in a. (c) A bright field image of the coating after 2 days of NaCl exposure at pH 2.5. (d) Fluorescence image of the same area as in c.

## CONCLUSIONS

These initial experiments utilize an ion specific chromophore to identify the mode of ion entry through an epoxy coating. Based on these initial experiments, the following conclusions can be made:

1. The use of MEQ has clearly indicated that following exposure to NaCl, chloride ions are clustered in discrete sites on the surface of epoxy resins. This is strongly suggestive of the discrete pore concept, however experiments to examine film penetration must be performed.
2. The number of defect sites in the coatings, as observed in both bright and fluorescent fields appears to increase with NaCl exposure time. Not all sites observed in bright field fluoresce in the fluorescent field. Whether different types of ionic pathways exist has yet to be shown.
3. The epoxy polymer phase separation morphology differs as a function of component material age. The number of spots, both in bright and fluorescence fields, appear to be greater in coatings made from older materials than those made from newer materials. Hence, the age of the resin will impact its performance, as intuitively expected.
4. At present, no quantitative distinction has been made between observation of films exposed to ambient and low pH environments. Image analysis techniques will be employed in subsequent experiments.



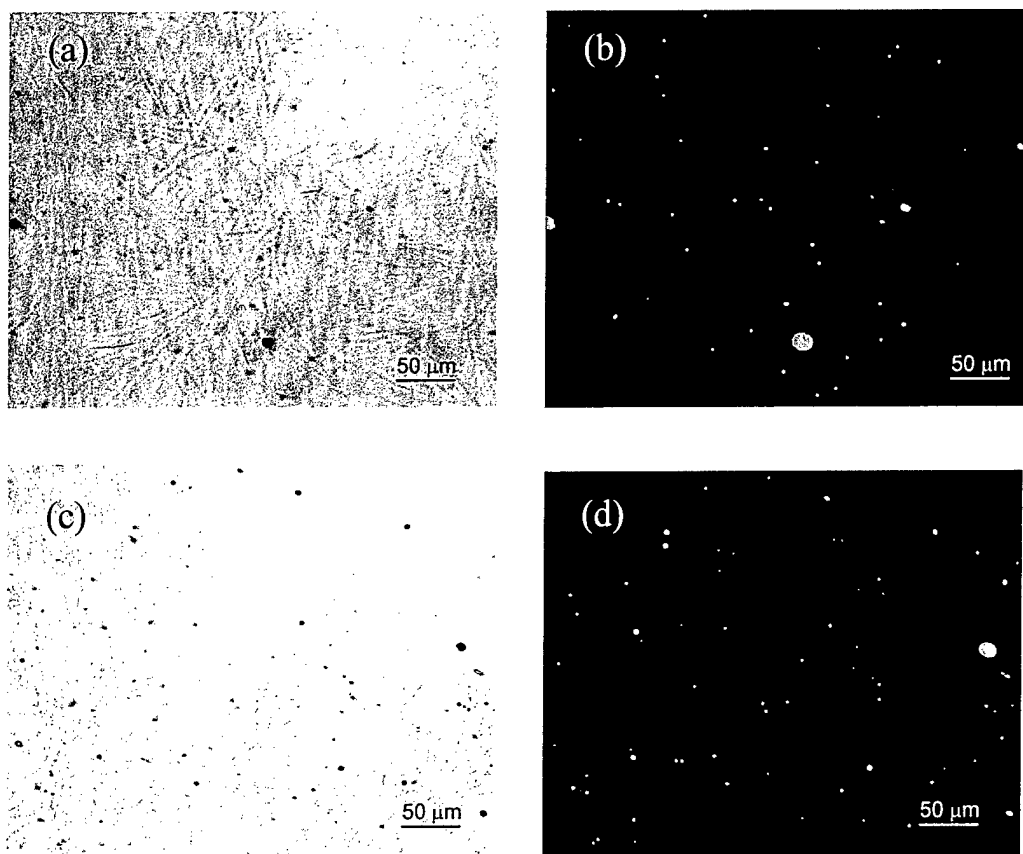


**Figure 7.** (a) A bright field image of the coating made with older materials after 1 day of NaCl exposure at ambient pH. (b) Fluorescence image of the same area as in a. (c) A bright field image of the coating after 2 days of NaCl exposure at ambient pH. (d) Fluorescence image of the same area as in c.

## ACKNOWLEDGMENTS

The authors gratefully acknowledge the financial support of this research by the Air Force of Scientific Research through contract number F49620-96-1-0178. The authors would also like to thank Dr. Ammasi Periasamy and Colten Noakes at the W.M. Keck Center for Cellular Imaging, University of Virginia, for their assistance in fluorescence microscopy.

## REFERENCES

1. C.H. Hare, *J. Protective Coatings and Linings*, Feb. 1989, pp. 59-69.
2. R.A. Dickie and A.G. Smith, *ChemTech*, Jan. 1980, pp. 31-35.
3. J.E.O. Mayne, *JOCCA*, **32**(352):481-487 (1949).
4. D. Greenfield and D. Scantlebury, *J. Corr. Sci. and Engr.*, **Vol. 3**:paper 5 (2000), <http://www.cp.umist.ac.uk/JCSE/>, ISSN
5. M.W. Kendig and H. Leidheiser, Jr., *J. Electrochem. Soc.*, **123**(7):982-989 (1976).

6. L. Beaunier, I. Epelboin, J.-C. Lestrade, and H. Takenouti, *Surface Technology*, **4**:237 (1976).
7. H. Corti, R. Fernandez-Prini, and D. Gomez, *Prog. Org. Coatings*, **10**:5-33 (1982).
8. J.E.O. Mayne, *Official Digest*, Feb. 1952, pp. 127-136.
9. E.M. Kinsella and J.E.O. Mayne, "Ionic Conduction in Polymer Films", in 3rd International Congress on Metallic Corrosion, Moscow 1966, pp. 117-120.
10. A.M. Mierisch and S.R. Taylor, *J. of Corr Sci. and Engr.*, **Vol. 2**, Paper 30 (1999), <http://www.cp.umist.ac.uk/JCSE>.
11. A.M. Mierisch, J. Yuan, R.G. Kelly, and S.R. Taylor, *J. Electrochem. Soc.*, **146**(12):4449-4454 (1999).
12. S.R. Taylor, , *Prog. Org. Coatings*, **43**:141-148 (2001).
13. R.P. Hangland and I.D. Johnson, "Intracellular Ion Indicators", in Fluorescent Probes for Biological Activity, 2nd edition, Ed. by W.T. Mason, pp.40-15 (1999).
14. A. Takahashi, P. Camacho, J.D. Lechleiter, B. Herman, *Physiol. Rev.*, **79**:1088-1125 (1999).
15. R.G. Kelly, O. Schneider, and J. Yuan, ECS Proceedings Volume 99-1, Abstract #81, Phoenix, AZ, May 1998.
16. J. Birwersi and A.S. Verkman, *Biochemistry*, **30**:7879-7883 (1991).

*Submitted to the Journal of the Electrochemistry Society (in review)*

**UNDERSTANDING THE DEGRADATION OF ORGANIC  
COATINGS USING LOCAL ELECTROCHEMICAL IMPEDANCE  
METHODS: I. COMMONLY OBSERVED FEATURES**

**Amber M. Mierisch and S. Ray Taylor**

Center for Electrochemical Science and Engineering  
Department of Materials Science and Engineering  
University of Virginia  
Charlottesville, VA 22903  
(434)982-5788  
[srt6p@virginia.edu](mailto:srt6p@virginia.edu)

## ABSTRACT

Local Electrochemical Impedance Mapping (LEIM) was used to investigate local underfilm corrosion occurring on organic coated AA2024-T3 exposed to chloride solution. Films (5-20  $\mu\text{m}$  thick) of neat epoxy, polyurethane and vinyl resins were studied. Frequently observed features in the LEI maps included: (1) an unexpected decrease in admittance in early stages of development, (2) trenching at the periphery of admittance peaks, (3) both increases and decreases in peak height over time, (4) changes in peak width over time, (5) different amplitudes in admittance over different regions of multi-lobed blisters, and (6) different admittance magnitudes for different types of defect. These LEIM features could provide significant insight into and documentation of the local breakdown processes of coated metals, if they truly represent electrochemical phenomena associated with changes at the interface. These features were observed on each of the coating chemistries studied. Proposed origins and supportive evidence of these LEIM features will be presented.

## INTRODUCTION

The corrosion protection afforded by an organic coated metal is determined by variables associated with the coating, substrate, service environment, and polymer/metal interface. In order to fully appreciate how these variables interact to control service-life, it is essential to know the origins and growth mechanisms in early stages of underfilm corrosion. For example, it is essential to know whether corrosion of a coated alloy has initiated as a result of chemical heterogeneities within the coating (e.g., regions that might facilitate ion transport), heterogeneities within the substrate (e.g., micro-galvanic couples created by intermetallic compounds), or whether corrosion initiates because of a juxtaposition of these two-types of heterogeneities. A detailed delineation of the origin and ensuing events that control corrosion breakdown of a coated metal will require a description of the local chemical and electrochemical events associated with the polymer coated metal. This paper will examine an initial library of local electrochemical events.

A wide variety of dc- and ac-based methods have been developed within different fields of science for the *in situ* examination of local electrochemical events. Some of these methods include the scanning reference electrode technique [1-5], scanning vibrating probe [6-8], scanning Kelvin probe [9-12], electrochemical microscopy [13-17], and scanning tunneling microscopy [18], among others [19]. Each of these methods is useful depending on the interface under study, the type of information desired, and the measurement resolution required. However, when considering the characterization of local electrochemical events associated with a coated metal substrate, local electrochemical impedance methods have been a logical option based on (i) the ability of an ac-based excitation to lower the impedance a dielectric interface at

higher frequencies, and (ii) the ability to more fully characterize a specific site by the application of a frequency spectra [20].

Local Electrochemical Impedance Mapping and Spectroscopy (LEIM/S) have been used in recent years to examine the local electrochemical events occurring on coated metal substrates immersed in an aqueous environment [21-30]. Improvements on original electrode designs [1,4,22,31] have allowed the local detection various types of extrinsic (i.e., man-made) defects [20,22], as well as the more recent detection of intrinsic (i.e., naturally occurring) defects occurring on organically coated steel [1] and aluminum alloy [25-30].

While it has been logical and successful to use LEIM/S for the detection of local electrochemical activity on coated metals and alloys, LEIM/S is a new measurement technique that is not fully characterized. Yet, it is being used to explore new and previously undocumented phenomenon. Therefore it is important that quantitative variations, changes in features, and temporal modulations in LEIM measurements be reliable and interpretable. Contribution from artifact or factors unrelated to local breakdown must be examined and fully accounted.

The long-term objective this research effort is to develop LEIM/S as a quantitative tool for the full characterization of local electrochemical phenomenon associated with coated metals and alloys. For example, it is of key interest to understand the origins of underfilm corrosion, i.e. to know whether the initiation of underfilm corrosion is governed by substrate heterogeneities or by coating heterogeneities. This knowledge will be directly facilitated by a more complete understanding of LEIM data.

The objective of this paper is to introduce the LEIM features that have been commonly observed throughout the early times of corrosion initiation of an organically coated aerospace aluminum alloys, and to suggest possible interpretations of their origins. These intriguing LEIM

features could provide insight into the origins and nature of coating breakdown if they are truly reflective of electrochemical activity, and not a function of outside factors such as measurement artifact. A series of subsequent papers will examine possible outside influences in detail via modeling of the electrochemical interface and subsequent comparisons to LEIM data of electrodes fabricated to an equivalent geometry.

## EXPERIMENTAL METHODS

*Materials:* Substrates consisted of 6.5 x 6.5 x 0.1 cm AA2024-T3 panels cut from 1 mm thick sheet. Neat organic resins were applied and varied in composition according to the specific study. These resins included: (a) vinyl VYHH, a copolymer of polyvinyl chloride and polyvinyl acetate, (b) polyurethane coatings which were either 100% polyether polyurethane, or a polyurethane composed of 50% polyether and 50% polyester, (both were mixed with isocyanate, a dibutyl tin dilaurate catalyst and MEK (methyl ethyl ketone) solvent, (c) an epoxy comprised of bisphenol A-epichlorohydrin-based epoxy resin solution with an Epi-cure fatty acid polyethylenepolyamine-based polyamide curing agent. Each resin was placed into solution with appropriate amount of solvent. Exact procedures used for preparation of these resins are described elsewhere [26].

*Coating procedure:* Prior to coating, AA2024-T3 samples were cleaned using a four-step procedure: scrubbed using dust-free wipes dipped in acetone, scrubbed with Alconox, cleaned ultrasonically in hexanes for 5 minutes and finally rinsed with isopropanol to remove any remaining residues. Samples were then allowed to air dry. Ultrapure water (18 M $\Omega$ ) was used for rinsing between steps. Coatings were spin cast onto the substrate to produce a uniform dried

film thickness of between 5 and 20  $\mu\text{m}$  depending on the experiment. Samples were cured in a dessicator at ambient temperature for at least 48 hours prior to use.

*Test Environment:* A 4.3 cm inner diameter glass cylinder was affixed to coated AA2024-T3 samples in order to create a reservoir. An O-ring was placed between the cylinder and the sample to create a seal. RTV silicone was used on the exterior of the cylinder and O-ring to ensure that the silicone did not contact the bulk solution and to ensure that samples could be easily removed for further study. Samples were exposed to NaCl solution ranging from 0.1 to 0.6 M. These solutions were quiescent and at ambient temperature and aeration. The glass cylinders provided a 14.5  $\text{cm}^2$  exposure area.

*Local Electrochemical Impedance Mapping (LEIM):* The LEI method employed utilizes a five-electrode configuration consisting of a conventional three-electrode arrangement (i.e., a reference electrode, a counter electrode and the substrate as the working electrode) to achieve potentiostatic control, and two additional micro-reference electrodes that are vertically separated to measure the local potential gradient in solution above the substrate surface [21-23,25-30]. The configuration used for the LEI probe employed in these experiments has been described in detail elsewhere [20]. A 15 mV rms sinusoidal voltage perturbation, with a single frequency of 700 Hz (optimized in previous experiments) was applied about the open circuit potential. The d.c. potential was maintained using a Solartron 1286 Electrochemical Interface (EI), and the a.c. excitation was generated by a Solartron 1255 HF frequency response analyzer (FRA) and input into the EI for application to the sample. Both instruments were under computer control.



## RESULTS AND DISCUSSION

### *Variable Forms of Underfilm Corrosion*

LEIM was performed on AA2024-T3 samples coated with the resins described above (either vinyl, polyurethane and epoxy) and immersed in an aqueous NaCl environment. The admittance magnitude of the coated substrates was monitored from the first hours of exposure to electrolyte in which there were no visible underfilm corrosion sites to later stages when underfilm corrosion was visible. Macroscopically, several different types of underfilm corrosion were observed on the coated panels after various times of exposure. These include red, black, white and clear blisters. Details of the initial local electrochemical and chemical characterization of these blisters has been described previously [26].

Red-colored blisters became visually apparent within 24 to 72 hours after immersion and grew rapidly (over 24 to 48 hours) to 1 – 7 mm in diameter. The blisters were bright red in color and caused aggressive pitting, as was evident by examination of the substrate after removal of the coating [26]. White and black blisters grew less rapidly (over several days) and to a diameter of only ca. 0.5 – 2 mm. Visual observation of the substrate after removal of the coating indicated that little damage to the substrate had been incurred. These defects were seen primarily on vinyl coated samples. Clear blisters were observed on all coatings, although more frequently on polyurethane coated samples immersed in low concentration electrolyte. These blisters grew over the course of several days to a final diameter of 2 – 10 mm. However, there was no sign of damage to the substrate upon examination after coating removal.

LEI maps of the regions that subsequently grew into the different types of blisters showed very different features in the admittance maps [26]. High admittance peaks were observed at early times in the coated regions that eventually grew into red blisters, while low admittances were observed in regions that became either black, white, or clear blisters. In

addition, once blisters had formed, high admittance peaks were again observed over the red blisters and low admittance peaks over the other types. The high LEIM admittance peaks associated with the red blister sites in both early and later stages of development, suggest either a high rate of electrochemical activity or a significantly decreased barrier resistance. LEIM maps are constructed using a single frequency of ac excitation (typically 700 Hz) and thus cannot fully characterize the precise nature of the interface to delineate the sources of change.

LEI spectroscopy was conducted on the specific pre-blister sites described above. These spectra confirmed the presence of a lower corrosion resistance ( $R_{\text{corr}}$ ), where  $R_{\text{corr}}$  is the magnitude of impedance at low frequency and is a combination of the pore and charge transfer resistance (33,34), in pre-red blister regions and a higher corrosion resistance above pre-black blister regions. The narrow bandwidth employed in this experiment (10 kHz – 500 mHz) and the imprecise knowledge of the electrode area accessed by the LEI probe made it difficult to extract additional detail about the local interface.

#### *LEIM Features During Underfilm Corrosion Development*

Further investigation of the red blisters yielded several interesting features in the corresponding LEI maps that could provide insight into the local breakdown process of coated alloys and metals. The interpretation of LEI maps assumes that all features are indeed representative of material and electrochemical changes of the interface under study and not due to measurement artifact. Future writings will critically examine the issue of sampling artifacts.

Common features observed in the LEIM of coated AA2024-T3 included: (1) an unexpected decrease in the admittance (increase in the impedance) in the earliest stages of underfilm corrosion, (2) trenching around the base of admittance peaks acquired over an actively corroding site, (3) temporal fluctuations (both increases and decreases) of an admittance peak

corresponding to a single defect, (4) changes in the width of an admittance peak for a single site over time, (5) the development of multiple admittance peaks of varying heights associated with different lobes of a blister, (6) different magnitudes in admittance for each different type of defect and even for a single type of defect formed under different conditions. These features were observed repeatedly for all three of the coating systems with little variation between coatings. Each of these observations is introduced below along with suggested interpretations. Some of the possible interpretations have been explored and will be discussed here, while a complete examination of the possible sources will be elucidated in a series of subsequent publications.

#### LEIM Features in Initial Stages of Exposure

The beginnings of underfilm corrosion could usually be seen visibly after approximately 24-72 hours of exposure to electrolyte. LEIM was performed on the organic coated AA2024-T3 panels at various intervals, including the time before underfilm corrosion was visible, in order to detect and monitor the earliest developmental stages. The fact that LEIM can detect the onset and location of underfilm corrosion before it is visible to the naked eye is one of the advantages of this local method over others. LEIM of these earliest stages of underfilm corrosion development showed an initial decrease in admittance (increase in impedance). This admittance depression was counterintuitive in that the beginning stages of coating breakdown would be expected to include water and ion uptake to produce an increase in admittance (decrease in impedance). An example of the temporal development of such an admittance depression on a polyurethane coated AA2024-T3 sample immersed in 0.6 M NaCl is shown in Figure 1. The underfilm corrosion was not visible until after 48 hours of exposure. It should be noted that the

time evolution of this underfilm corrosion site was typical for polyurethane coated samples, not as apparent for vinyl or epoxy coated samples.

Several possible explanations for the decrease in admittance can be suggested: (1) water nucleation, (2) accumulation of corrosion product, (3) extrinsic defects such as a small air bubble created during coating application, or (4) edge effects in the field emanating from the corrosion site. The first three of these suggestions will be addressed here, while the forth possibility will be examined in subsequent papers employing finite element models.

The first of the suggested possibilities was investigated preliminarily by examining the effect of a thin film of water on the simulated impedance of an equivalent circuit analogue. The change in admittance between the surface plane and the bottom of the trough in Figure 1 was calculated to be 18 ohms. Two equivalent circuit analogues, shown in Figure 2, were created to model a film of water beneath a coating. The first assumed that a layer of pure water in the form of a small disk existed at the interface of the alloy substrate and the polymer. Only the dielectric properties of the water were considered, and no electrochemical charge transfer at the interface was included. The second model considered that ions were present in the disk of water at the interface and assumed that interfacial polarization and charge transfer could occur. The double layer capacitance and charge transfer resistance for this model were assigned values of 25  $\mu\text{F}/\text{cm}^2$  and 1000  $\Omega\text{cm}^2$  respectively. The total impedance for the circuit analogues was then calculated using standard impedance relationships of capacitance and resistance. The results of the calculations are summarized in Table 1. The values (20 ohms) of increased impedance (reduced admittance) observed in Figure 1 could thus be duplicated through the selection of an appropriate water (or electrolyte) disk thickness. Therefore, these calculations indicate that water nucleation cannot be excluded as a possible cause of the initial admittance depression. However,

neither the presence of water nuclei nor their thickness has been confirmed by other methods. Nonetheless, presently water nucleation must be considered as a possible source of these initial LEIM changes and indicates how the results of this local electrochemical method could guide subsequent theory and research endeavor.

Equally tenable is the idea that the increased impedance is elicited by a corrosion product (e.g. thickened oxide). While the underfilm chemistry at blister sites is known to be dynamic and varied on AA2024-T3 substrates [26], there has been no interfacial characterization of these initial transient events.

Although air bubbles, either attached to the substrate or held within the bulk of the resin, are known to effect the local admittance, experiments on steel substrates have shown that they increase the admittance and not decrease it [20]. This discrepancy could be a function of time of observation, in that initially the admittance be lower because of the air and would increase as electrolyte filled the void. However, no bubble was visible and this possible source was not considered further.

#### LEIM Features in Later Stages of Development

Another interesting feature of the LEI map shown in Figure 1 and in Figure 3 was the decrease in admittance at the periphery of a an admittance peak. The trenching seen around the peak at 52 hours in Figure 1 and 28, 48 and 52 hours in Figure 3 reflects the same magnitude of admittance depression seen in early stages, however unlike the early depressions discussed above, trenching surrounding admittance peaks was often observed at all times in the LEIM of local breakdown processes on coated AA2024-T3. Trenching could be produced by several factors: the deposition of corrosion product at the periphery of the blister or sampling artifact associated with edge effects in the electric field above a local corrosion site. These two theories

will be examined in subsequent papers which theoretically examine the local electric field above a model disk electrode as a function of boundary conditions (cell size) and covering material (dielectric).

One of the most potentially informative features of LEIM of defects on organic coated AA2024-T3 was the change in height of an admittance peak over time. In some cases these peaks increase and others they decrease and essentially die. An example of this metastability can be seen in Figures 3. The increases in peak height could certainly represent an increase in electrochemical activity, hence severity of corrosion, as would be expected to occur over time. A decrease in peak height, as seen in the Figure at 48 hours, could represent either a temporary and in some cases a permanent passivation of the underfilm corrosion site or blockage of the ionic channel or pore associated with local corrosion site. Understanding the cause of such an event would have significant importance to the understanding of how the substrate, coating and environment interact to mitigate corrosion and protect the metal. In some cases, these admittance peaks reached significant heights. The peak height seen at 52 hours probably represents a physical breach in the coating as evidenced by a parallel drop in the open circuit potential.

If the changes in the admittance peak amplitude over time do actually correspond to changes in electrochemical activity, much can be learned about the local breakdown processes governing failure at these sites. However, factors such as biphasic water uptake of the coating, frequency dispersion, change in local solution conductivity, changes in electrode area, or a simple change in the height of the blister sufficient enough to necessitate a change in height of the LEI probe could also conceivably contribute to a change in peak height. In addition, instability in the LEI reference microelectrodes could also impact the measured potentials.

Since a single frequency is employed in any given LEI map sequence, inconsistencies between measurements due to use of different frequencies are not a concern in LEIM. The frequency used for excitation was optimized prior to measurement through LEIM of fabricated gold electrodes at different frequencies and through LEIM and EIS of coated AA2024-T3 at different frequencies. However, use of a single frequency of excitation does not preclude a shift in the absorbing frequency of a changing interface. Thus, while frequency dispersion may be participatory in the changing peak heights, it's mere presence is directly coupled to the precise interfacial changes that this method seeks to document.

Local concentration gradients in the bulk solution directly above a corrosion blister are not considered to be a likely artifactual source of peak amplitude changes because the current through a barrier coating on a metal is extremely low. Not only will the coating act as a buffer to ion concentration changes at the coating/solution interface, but the high concentration of the electrolyte (0.6M NaCl) is likely to overwhelm any projected difference. Thus, even though ion concentration changes will occur at the metal/solution interface beneath the coating, they will not affect the Nernst potential at the reference microelectrode of the LEI probe sitting above the coating. The micro-reference electrodes used in these studies were determined to be very stable based on extensive repeatability testing [29].

The biphasic ingress of water has been suggested as another possible source of the admittance height changes [35]. The plausibility of this explanation is reduced in light of the fact that the admittance peaks can have numerous cycles of change and can disappear in some cases or increase to very high values as discussed previously.

The probe in any given experiment was used at a fixed height above the surface in any given experiment, so this can be discounted as a cause of peak height changes. Subsequent modeling experiments will examine the effect of electrode area changes.

The admittance peaks of underfilm corrosion sites on coated AA2024-T3 panels often showed an increase in width over time. A change in the base width of an admittance peak is interpreted as an increase in the diameter of the corrosion blister. There is not a direct correlation between peak width and blister size, as will be seen, because of the differences in electrochemical activity of the substrate in the blistered region.

A feature that was observed in a growing red blisters prompted further interest in underfilm electrode activity. In most cases, red blisters began as a discrete initiation site and formed a primary lobe. Subsequently, secondary lobes formed at later times off of the initial region. An example of this is shown in the top and left images of Figure 4 which shows an optical image of a blister on an AA2024-T3 sample coated with polyester polyurethane and immersed in 0.6 M NaCl. Both the area mapped using LEIM (right) and the corresponding admittance map of the region are included in the Figure. LEIM revealed two separate admittance peaks of different magnitude for the two lobes. It was consistently observed that the peak height at the area where the underfilm corrosion initiated was significantly higher than the peak height at the area where the underfilm corrosion initiated. While the two lobes were distinguishable visibly by their tint with the aid of an optical microscope in the case shown in the figure, the lobes of smaller corrosion sites may only be distinguishable with LEIM. For this reason, it is important to determine the capability of the LEI probe to measure two distinct peaks at adjacent regions of electrochemical activity. This will addressed in a future paper. It is also important to



be able to distinguish the aggressive initiation site from secondary lobes and to determine whether this split structure is general to red blisters on organic coated AA2024-T3.

Preliminary evidence of a true correlation between LEIM of different areas of multi-lobed blisters and electrochemical activity has been found through simultaneous SEM (Scanning Electron Microscope) and EDS (Energy Dispersive Spectroscopy) of the substrate of a blister site after coating removal [26, 29]. These results showed that indeed, lower ratios of Al and Mg and a higher ratio of Cu were present at the initiation site where the admittance in LEIM was highest, both indicating a higher degree of corrosion, *i.e.*, electrochemical activity. This result has a very important implication with regards to the interpretation of LEI maps. While it was initially believed by these authors that an admittance peak represented a pore or defect in the coating, it appears equally tenable that a very high local current density due to a substrate heterogeneity beneath a hydrated coating could also provide an admittance peak.

The differences in admittance between types of defects and within multi-lobed blisters potentially reveal crucial information on the structure of underfilm corrosion sites and the evolution of electrochemical activity over time. However, it is unclear whether the differences in LEIM are due entirely to differences in electrochemical activity, or whether other factors contribute. Previous work by others [36, 37] showed that the field sampling approach is subject to measurement artifact for the case of bare electrodes. It has not yet been determined what the presence of a coating does to alter the amplitude or shape of the field emanating from electrodes and hence from underfilm corrosion. In addition, it is unclear whether local coating variations play a role in admittance measurements. It must be also determined whether salt films beneath the coating, differences in substrate material, changes in the chemistry of the underfilm solution, or other passive features contribute to LEIM.

## SUMMARY

LEIM performed on organic coated AA2024-T3 yielded different admittance responses for four types of underfilm corrosion sites (red, black, white, and clear) and for the different regions of multi-lobed blisters. In addition different features were observed that could provide insight into local breakdown processes of coated metals and alloys. These features included: (1) an unexpected decrease in admittance was seen in early stages of underfilm corrosion, (2) trenching in the admittance at the periphery of underfilm corrosion, (3) changes in the peak height of admittance plots (increases and decreases) over time evolution of corrosion sites, (4) an increase in the admittance peak width over the time evolution of underfilm corrosion sites.

Active blister sites which became red in color tended to branch into one or more secondary lobes. These secondary lobes had a lower admittance than the original lobe. It is unclear at this time whether this difference is due to the electrochemical activity of the substrate or to local sites of ionic ingress. The directionality of substrate polishing significantly impacted the nature of blisters. Directional polishing promoted filiform-type blister growth on these alloys. LEIM of these directional filiform sites indicated higher admittances at the filiform origin.

Since the potential for information on breakdown is so great and the LEIM method is relatively new, it is important to determine whether real physical events or measurement artifact unrelated to the breakdown process could contribute to measurement of these features. Accurate interpretation of these features would aid in understanding local breakdown of this coated system and of coated metals in general if the measurements truly reflect chemical and physical events corresponding to changes at the interface.

## ACKNOWLEDGEMENTS

The authors gratefully acknowledge the Air Force Office of Scientific Research for their support of this research under contract no. F49620-96-1-0178.

## REFERENCES

1. I.L. Rosenfeld and I.S. Danilov, *Corr. Sci.*, **7**, 129, (1967).
2. H.S. Isaacs and B. Vyas, in *Electrochemical Corrosion Testing ASTM STP 727*, Edited by F. Mansfeld and U. Bertocci, pp.3-33, ASTM (1981).
3. S.J. Bates, S.R. Gosden, and D.A. Sargeant, *Mater. Sci. Technol.*, **5**, 356 (1989).
4. V.S. Voruganti, H.B. Luft, D. Degeer, and S.A. Bradford, *Corrosion*, **47**, 343 (1991).
5. L.J. Gainer and G.L. Wallwork, *Corrosion*, **35**(2):61 (1979).
6. H.S. Isaacs, *Corrosion*, **43**, 595 (1987).
7. H.S. Isaacs, *Corr. Sci.*, **28**, 547 (1988).
8. L.F. Jaffe and R. Nuccitelli, *J. Cell Biol.*, **63**, 614 (1974).
9. M. Strattmann and H. Streckel, *Corr. Sci.*, **30**, 681 (1990).
10. M. Strattmann and H. Streckel, *Corr. Sci.*, **30**, 697 (1990).
11. M. Strattmann and H. Streckel, *Corr. Sci.*, **30**, 715 (1990).
12. M. Strattman and H. Streckel, *Werkstoffe Korros.*, **43**, 315 (1992).
13. A.J. Bard, F.-R. F Fan, J. Kwak and O. Lev, *Anal. Chem.*, **61**, 132 (1989).
14. J. Kwak and A.J. Bard, *Anal. Chem.*, **61**, 1794 (1989).
15. M.V. Mirkin, *Anal. Chem. News Feat.*, 177A (March 1996).
16. F.-R.F. Fan, A.J. Bard, and M. Heim, *Science*, **270**, 1849 (1995).
17. F.-R.F. Fan, A.J. Bard, D.T. Pierce, P.R. Unwin, D.O. Wipf, and F. Shou, *Science*, **254**, 68 (1991).
18. A. Gonzalez-Martin, R.C. Bhardwaj, and J.O'M. Bockris, *J. Appl. Electrochem.*, **23**, 531 (1993).
19. *Localized In-Situ Methods for Investigating Electrochemical Interfaces*, **PV 99-28**, Ed. by S.R. Taylor, A.C. Hillier, and M. Seo, The Electrochemical Society, Pennington, NJ (2000).
20. M.W. Wittmann, R.B. Leggat, and S.R. Taylor, *J. Electrochem. Soc.*, **144**, 4071 (1999).
21. R.S. Lillard, P.J. Moran, and H.S. Isaacs, *J. Electrochem. Soc.*, **139** 1007 (1992).
22. M.W. Wittmann and S.R. Taylor, in *Advances in Corrosion Protection by Organic Coatings II*, J.D. Scantlebury and M.W. Kendig, Editors, **PV 95-13**, p.158, The Electrochemical Society Proceedings Series, Pennington, NJ (1995).
23. R.S. Lillard, J. Kruger, W.S. Tait, and P.J. Moran, *Corrosion*, **51**, 251 (1995).
24. F. Zhou and D. Thierry, *Electrochimica Acta*, **42**, 3293 (1997).
25. A.M. Mierisch, S. R. Taylor, in Electrically Based Microstructural Characterization II, Vol. 500, Ed. By R.A. Gerhardt, M.A. Alim, S.R. Taylor, Materials Research Society, Warrendale, PA, p. 35 (1998).

26. A.M. Mierisch, J. Yuan, R.G. Kelly, S.R. Taylor, *J. Electrochem.Soc.*, **146**, 4449 (1999).
27. A.M. Mierisch, S.R. Taylor, *J. Corrosion Sci. and Eng.*, **2**, no. 30 (1999).
28. A.M. Mierisch, S.R. Taylor, in *Localized In-Situ Methods for Investigating Electrochemical Interfaces*, **PV 99-28**, pp. 229-240, The Electrochemical Soc., Pennington, NJ. (2000).
29. A.M. Mierisch, "Interpretation of Observations Made Using Local Electrochemical Impedance Mapping (ELIM) on Organic Coated Aluminum Alloy 2024-T3", Doctoral thesis, University of Virginia, (2001).
30. S.R. Taylor, *Progress in Organic Coatings*, **43**, 141 (2001).
31. H.S. Isaacs, M.W. Kendig, *Corrosion*, **36**, 269 (1980).
32. J.V. Standish, H. Leidheiser Jr., *Corrosion*, **36**, 390 (1980).
33. J.A. Grandle and S.R. Taylor, *Corrosion*, **50**, 792 (1994).
34. J.A. Grandle and S.R. Taylor, *Corrosion*, **53**(5): 347-355 (1997).
35. J.E. Castle, in *Corrosion Resistant Coatings*, NACE, Houston, TX, p. 165 (1997).
36. H.S. Isaacs, *Corrosion*, **46**, 677 (1990).
37. F. Zou, D. Thierry, and H.S. Isaacs, *J. Electrochem. Soc.* **144**, 1957 (1997).

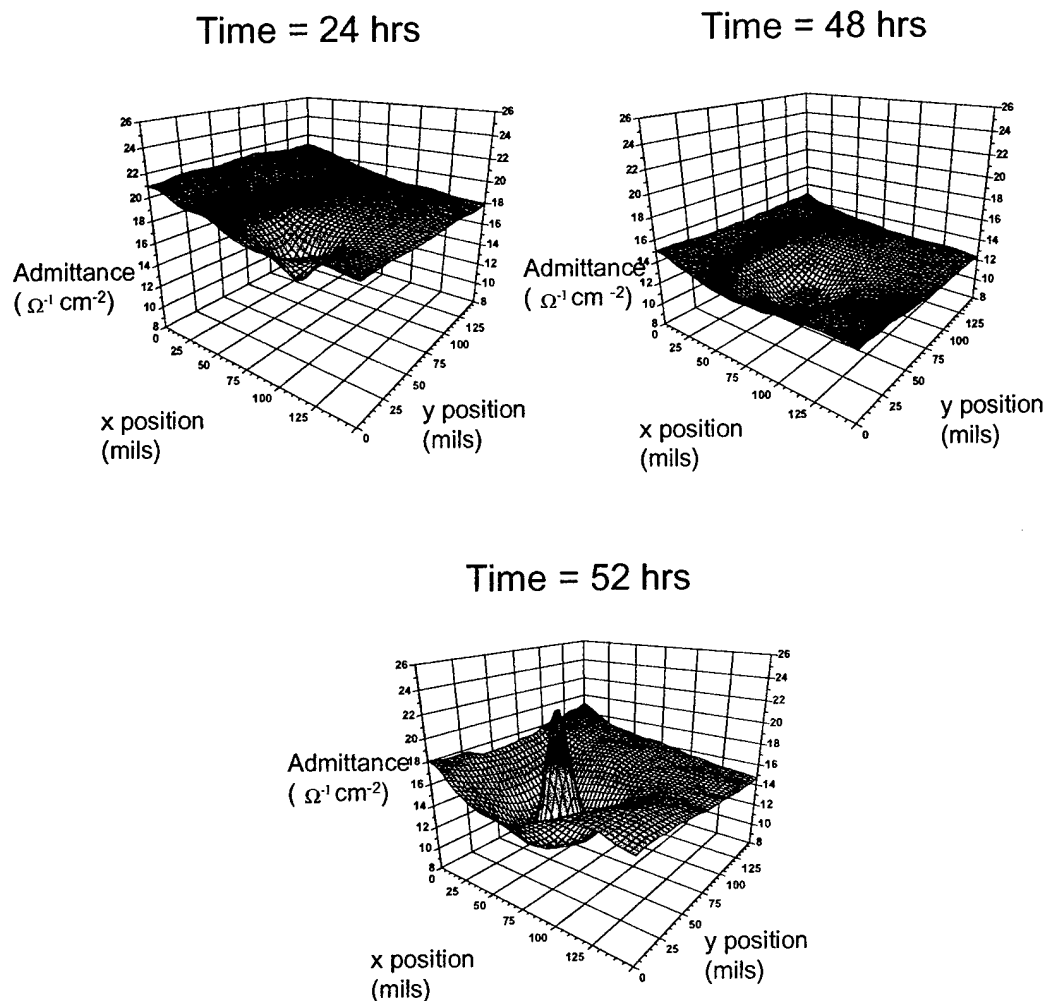


**Figure 1.** An initial decrease in the admittance is seen over a future blister site in early stages of development (24 hrs). The sample consists of 10  $\mu\text{m}$  thick 100% polyether polyurethane on AA2024-T3 immersed in 0.6 M NaCl. Trenching is observed around the peak occurring in LEIM at 52 hours.

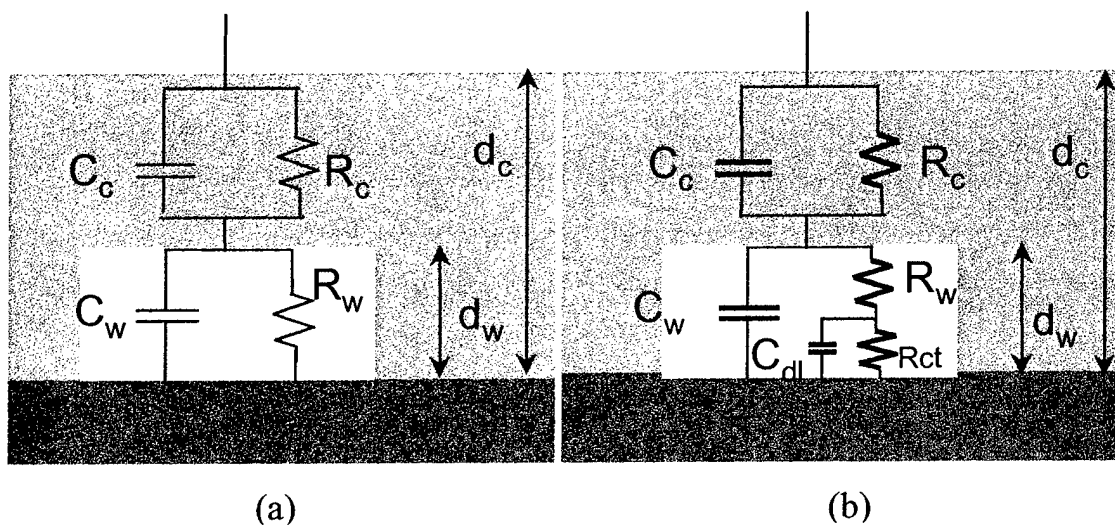


**Figure 2.** The two models used for calculation of the effect of underfilm water nucleation are shown. (a) Represents pure water in the form of a disk, and (b) represents a similar calculation with inclusion of ion transfer from the bulk electrolyte.

	$d_w$	$d_c$	$\rho_w (\Omega \text{ cm}^2)$	$\rho_c (\Omega \text{ cm}^2)$	$\kappa_w$	$\kappa_c$	$Z @ 500 \text{ Hz}$
<b>Model a</b>	0.1 $\mu\text{m}$	10 $\mu\text{m}$	$1.8 \times 10^7$	$10^{14}$	80	5	2 $\Omega \text{ cm}^2$
	1.0 $\mu\text{m}$	same	same	same	same	same	20 $\Omega \text{ cm}^2$
<b>Model b</b>	1.0 nm	same	same	same	same	same	20 $\Omega \text{ cm}^2$

**Table 1:** The values used for calculation of the increase in impedance (decrease in admittance) due to nucleation of water are shown for each model shown in Figure 2. The resulting increase in impedance is shown for each calculation using a frequency of 500 Hz.

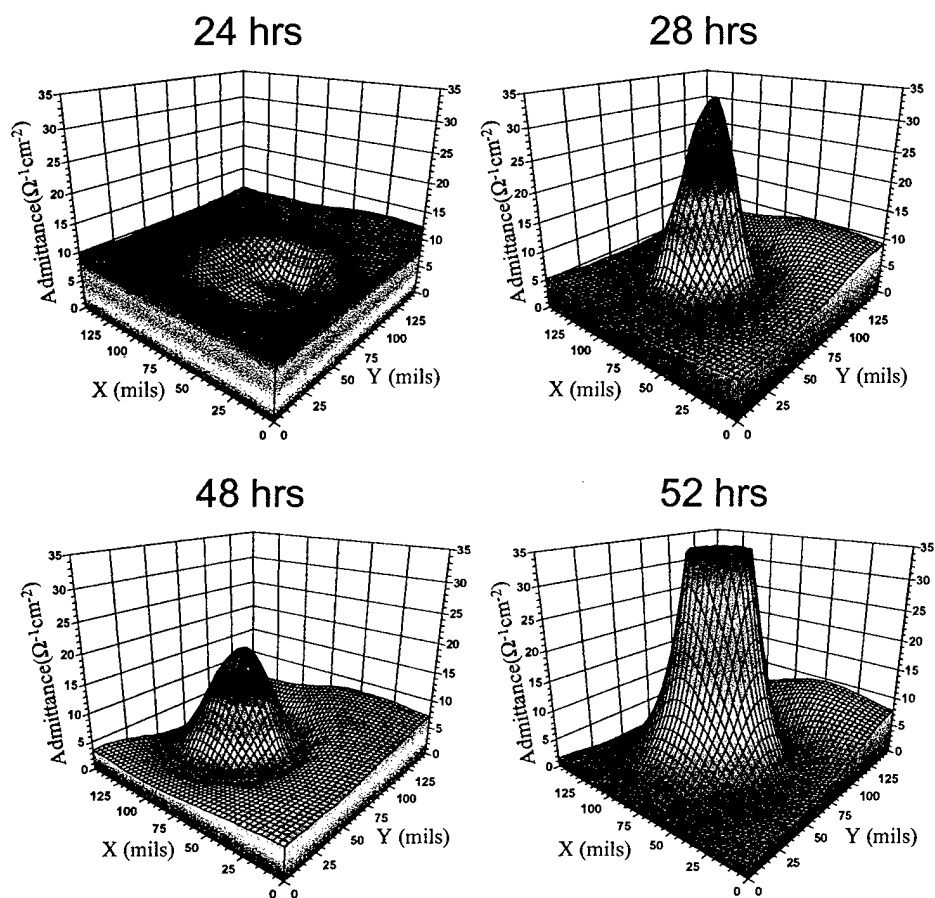
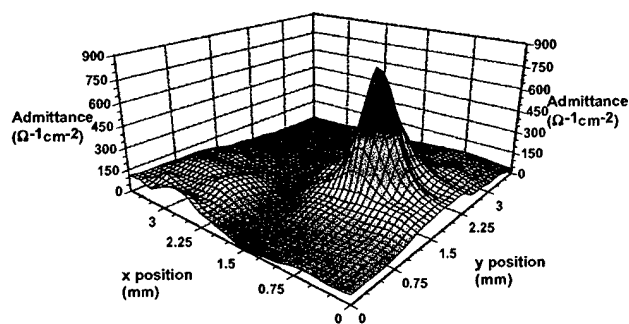
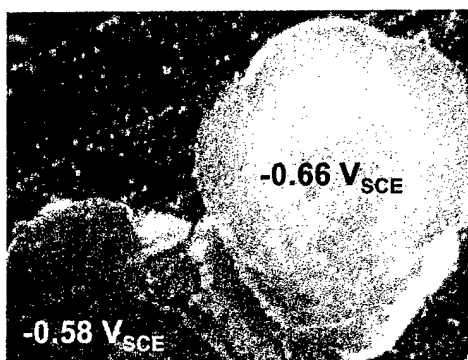


**Figure 3.** A typical time evolution of a red blister is shown. The changes in peak height are associated with possible changes in electrochemical activity. Note the decrease in peak height at 48 hours and the catastrophic increase in peak height at 52 hours. This AA2024-T3 sample was coated with polyester/polyether polyurethane and immersed in 0.6 M NaCl.





0.75 mm



## Region mapped

**Figure 4.** Red blister beneath polyester polyurethane coated AA2024-T3 in 0.6M NaCl. The optical image (top) shows an example of multi-lobed blister containing an initiation site (lighter red lobe with open circuit potential of  $-0.66 V_{SCE}$ ) and a secondary lobe (darker red lobe with open circuit potential of  $-0.58 V_{SCE}$ ). The region mapped by LEIM is shown in the image on the bottom left. Local open circuit potential values are also shown for each lobe. LEIM of the blister is shown in the plot on the bottom right. The initiation site appears to be more active (peak) than the secondary lobe.

**UNDERSTANDING THE DEGRADATION OF ORGANIC  
COATINGS THROUGH LOCAL ELECTROCHEMICAL  
IMPEDANCE METHODS:  
II. MODELING AND EXPERIMENTAL RESULTS OF NORMAL  
FIELD VARIATIONS ABOVE DISK ELECTRODES**

**Amber M. Mierisch\*, S. Ray Taylor\*, and Vittorio Celli\*\***

\*Center for Electrochemical Science and Engineering  
Department of Materials Science and Engineering  
University of Virginia  
Charlottesville, VA 22903  
(804)982-5788  
[srt6p@virginia.edu](mailto:srt6p@virginia.edu)

\*\*Department of Physics  
University of Virginia

## ABSTRACT

Local Electrochemical Impedance Mapping (LEIM) represents a potentially important tool in the characterization of discrete electrochemical phenomenon on heterogeneous surfaces, such as the degradation of a coated aluminum alloy. Since LEIM is an emerging tool, it is essential to resolve between real material and interfacial changes and possible sampling artifact to the measured LEIM response. To this end, both analytical and numerical models were developed to calculate the field above an equipotential disk to examine possible LEIM measurement artifacts. Several features in LEI maps which could be the result of artifact in the measured field above a corroding region were addressed. These included changes in the field due to the following: (1) edge effects, (2) two closely spaced corroding sites affecting spatial resolution, (3) a change in radius of a corroding site, including the ability of LEI to resolve small sites. Numerical analysis was found to more realistically model the finite dimensions and discrete change in potential that were used in actual LEIM experiments. The calculated field above the equipotential disk was then compared to experimental LEI maps of gold disk microelectrodes embedded in  $\text{SiO}_2$ . Edge effects were found to be an unlikely source for experimental observations of reduced admittance. The spatial resolution of the LEI probe was predicted through theoretical modeling and determined experimentally to be sufficient to resolve two disk separated by  $35\text{ }\mu\text{m}$ . The probe was also predicted and shown experimentally to have the capability to measure a disk of radius  $17.5\text{ }\mu\text{m}$ . The successful demonstration of this numerical model will allow the exploration of more complicated material interfaces, such as materials coated with a dielectric layer.

## INTRODUCTION

Local electrochemical impedance (LEI) is an important tool for the characterization of discrete breakdown events of coated metals and alloys [1-7]. The sensitive detection and complete characterization of these events will provide a more precise understanding of the factors that govern the initiation and propagation of underfilm corrosion. Part I of this series introduced a library of features commonly observed in the LEI mapping (LEIM) of an array of coating chemistries on an aluminum alloy (AA2024-T3) [8]. These features included: (1) a depressed admittance in the very earliest stages of underfilm corrosion, (2) the presence of an admittance trough around certain admittance peaks, and (3) temporal variations in admittance peak height, and (4) spatial variations in admittance peaks. These LEIM characteristics could provide important insight into coating failure if these features could be interpreted as originating solely from material and interfacial changes and not to measurement artifact. Because this method is relatively new and relies on subtle changes in potential or current distribution, it is crucial that results be reliably interpreted. Thus, it is of extreme interest to determine whether these features are indeed real events resulting from physical and chemical changes on or within the material, or are rather an artifact resulting from the limits of sampling subtle changes in the electric field. In order to do this, the fundamental characteristics expected in the local electric field and current distribution measurement of the corroding site must be understood. This can be accomplished by modeling the electrochemical interface and determining the field either analytically or by numerical analysis. Findings can then be compared with LEIM of electrodes fabricated to equivalent dimensions and to LEIM of organic coated AA2024-T3.

One electrode model that is well suited for the investigation of field distributions associated with localized electrodes is the equipotential disk. Previous investigators have modeled an equipotential disk electrode both analytically [9-11] and with computer simulation [9,12]. An equipotential disk is a reasonable representation of a local corrosion site undergoing uniform corrosion. A model was desired which could be used easily for such additional factors as an additional dielectric layer and other variations in geometry and parameters. The analytical and numerical models described in this paper focus on a bare equipotential disk, a system that is tractable by both approaches (i.e.,

analytical and numerical). However, since a future goal is to model the disk with the addition of a dielectric layer, which has not been previously modeled, a theoretical approach was desired that which could readily accommodate changes in materials, geometry, etc. Analytical approaches become intractable and involve severe approximations for more complex geometries. In addition, they generally do not take into consideration the finite boundaries of experimental systems. For this reason, computer modeling is a more powerful tool for consideration of additional parameters and geometries.

Verification of modeling results can be performed through LEIM of fabricated electrodes of equivalent dimensions to those employed in calculations. In this study, gold disk microelectrode arrays were created using standard semiconductor fabrication techniques. Patterns were created of disks with decreasing radius or separation distance to test LEI probe resolution capabilities. Comparison of LEIM on these electrodes with the fields above disk electrodes calculated theoretically provided conclusive prediction of probe capabilities and examined where artifact might contribute to measurements on organic coated AA2024-T3.

## EXPERIMENTAL METHODS

*Finite Element Modeling:* The finite element method was used to model an equipotential disk electrode with several variations. All models, meshes and solutions were created using ANSYS® 5.5 software on a Unix platform (AIX). An IBM RISC/6000 computer with 192 MB of RAM and at least 6 GB of free hard disk space was used. Models were meshed with 3-D tetrahedron shapes specific to electrostatic problems. Mesh density varied depending on the model. Software limitations allowed for a 128,000 node maximum. The model, shown in Figure 1, consisted of the following parts: a disk area within an insulating annulus and a series of cylindrical volumes above the disk to represent layers of different dielectric materials all confined within a cylindrical reservoir. 40 mV were applied to the disk electrode area and 0 potential was applied to all other outer boundaries.

The basic model (Figure 1) used in this study resembles the actual electrochemical cells and sample geometries used in previous LEIM experiments on

coated aluminum alloy and on the present LEIM experiments on gold microelectrodes. Experimentally, a glass reservoir is affixed to a metal or coated metal surface and filled with bulk solution. The loads are applied and the solution for the potential is found for each element and subsequently for the entire model. This model can be varied readily, with the limiting factor merely being how well it can be meshed. Small corners or curves and thin edges are more difficult to mesh than large open areas. The potential was calculated at each node and the electric field for each element. The nodal solution of the potential was used for all analyses because nodal data is more easily manipulated and because the discrete change in potential more closely represents actual LEIM data in which two discrete potential measurements are acquired above the surface. While preliminary studies of this aspect are discussed here, a detailed experimental verification will be presented in a subsequent paper in this series. Meshes were refined at two separate heights above the surface of the disk (75 and 100  $\mu\text{m}$ ) representing the positions of the two reference microelectrodes in a typical LEI experiment. Data for analysis were extracted at these two heights. The potential at the upper height was subtracted from the potential at the lower height (as is performed in LEIM) to yield a change in potential, or discrete normal field. The excitation frequency was not a parameter considered in calculations, though it was not expected to affect the general shape of the results. Because frequency was not considered, finite element calculations were not comparable in absolute amplitude to experimental measurements using LEIM. Trends, changes in amplitude and edge effects, however, are well represented by the normal field.

*LEIM:* LEIM was performed using a five-electrode system fashioned after Lillard *et al.* [13,14]. The five-electrode probe consisted of a typical three-electrode arrangement (working electrode, counter electrode, and reference electrode) used to control the dc potential and excite the interface potentiostatically with an ac signal, while two micro-reference electrodes were used to detect the local potential gradient in solution above the sample surface [3]. The dc potential and ac excitation of the samples were established with a Solartron 1286 electrochemical interface and Solartron 1255 HF frequency response analyzer all under computer control.

The probe consisted of a 250  $\mu\text{m}$  diameter Ag/AgCl wire as the main reference electrode, a ring-shaped Pt wire as the counter electrode and two micro-reference electrodes made from Teflon coated Ag/AgCl wires, each 125  $\mu\text{m}$  in diameter. The substrate served as the working electrode. The potential measured between the two micro-reference electrodes was converted to a local current density [2,3,5] and used to calculate the local impedance.

The standard excitation used for coated aluminum samples was a 15 mV (rms) sine wave oscillating at 700 Hz positioned about the open circuit value of the system. An additional +40 mV DC bias was applied to the gold disk microelectrodes in order to establish a Faradaic charge transfer. The probe was stepped across the surface in varying increments using a modified Teledyne TAC model PR-52 automatic wafer scanner with adjustable X and Y step sizes. The minimum step size, or distance between sampling points, was 10  $\mu\text{m}$ , but maps were limited to a total of 1000 data points. Step size was adjusted according to the area to be mapped. The LEI probe itself is discussed in greater detail elsewhere [3-7].

*Gold microelectrodes:* A pattern of gold disk electrodes, shown in Figure 2, was created because this electrode geometry would provide a potential distribution that would allow comparison of experimentally acquired LEI data to that acquired via FEM calculations. These electrodes would allow edge effects and questions of spatial resolution to be investigated in detail. Gold disks of decreasing radius from 500  $\mu\text{m}$  to 17.5  $\mu\text{m}$  were fabricated on 2.5 cm diameter silicon wafers. An additional pattern for determination of spatial resolution was created using disks of 100  $\mu\text{m}$  with separations distances decreasing from 1 mm to 35  $\mu\text{m}$  (measured edge-to-edge).

Gold disk electrodes were fabricated using the following procedure. An oxide was produced on the silicon wafer surfaces by heating the wafers in a wet oxidation furnace for 20 minutes at a temperature of 1160°C. This created an oxide thickness of approximately 0.3 – 0.33  $\mu\text{m}$ . Two layers of photoresist were applied to the oxide, each by spin-casting. The first layer, AZP4110, was flood exposed to UV light, and then the second layer, AZP4210, was applied. A pre-patterned mask was placed on the oxide which contained the patterns of disks or rectangles of different sizes and separation

distances. The wafer was exposed to UV light and both layers of photoresist were then developed. In this way, the pattern was transferred to the wafer. Only the portion of the oxide which was exposed was etched. The use of two layers of photoresist avoided undercutting by the etch.

Chrome was first deposited on the wafer using an evaporator to a thickness of 500 Å. This was done to enhance the adhesion of gold to the surface. Gold was then deposited to a thickness of 2500-2800 Å to achieve a surface flush with the silicon. Any extraneous metal was lifted by dissolving the photoresist in acetone. The result was a pattern of gold disk electrodes of different sizes embedded in an insulator but electrically contiguous (see Figure 2). This process has been discussed in detail elsewhere [7].

## RESULTS AND DISCUSSION

### Analytical modeling

The normal field above an equipotential disk has been calculated analytically by previous researchers [9-11]. It was thought that similar calculations may be possible for more complex cases without excessive approximation. Starting with the simpler case to establish basic equations, the normal field above a disk was calculated using rotational elliptical coordinates following a derivation by another author [10]. It should be noted that this derivation has been performed previously in both rotational elliptical coordinates [10] and cylindrical coordinates [11]. Other authors [9,12] have related the two methods by stating that the final expression in cylindrical coordinates was found by simply converting the solution expressed in elliptical coordinates to cylindrical coordinates. However, the solution can not be converted in this manner. This discrepancy is due to the fact that different boundary conditions were employed to specify an insulating plane outside the disk: either the electric field outside the disk must be 0 [10] or the current density outside the disk must be 0 [11]. While the resulting solutions for the electric potential produce similar plots, these expressions are not equivalent. The conversion of the solution for potential from elliptical coordinates to cylindrical coordinates is non-trivial and may result in an erroneous expression as seen in reference 9. The correct expression in cylindrical coordinates is derived using only cylindrical coordinates throughout the derivation [11].



The expression for the potential distribution above an equipotential disk as derived by Newman [10] in elliptical coordinates is shown in equation (1):

$$\frac{\Phi}{\Phi_0} = 1 - \frac{2}{\pi} \tan^{-1} \xi \quad (1)$$

where  $\Phi$  is the potential,  $\Phi_0$  is the constant potential within the electrolyte above the disk found for the particular geometry under consideration, and  $\xi$  is one of the elliptical coordinates ( $\eta, \xi$ ). Using the relationship between elliptical coordinates and cylindrical coordinates ( $r, z$ ) with the disk radius  $a$ , Equation (1) can be transformed to cylindrical coordinates. In order to simplify the expression, the dimensionless coordinates are defined as,

$$z = a \xi \eta \quad (2)$$

$$r = a \sqrt{(1 + \xi^2)(1 - \eta^2)} \quad (3)$$

The resulting potential in cylindrical coordinates is then given by,

$$\Phi = \Phi_0 \left[ \frac{\pi}{2} - \tan^{-1} \left( \frac{\sqrt{2}}{2} \sqrt{Z^2 + R^2 - 1 + \sqrt{1 + 4R^2 Z^2 - 2R^2 + Z^4 + R^4}} \right) \right] \quad (4)$$

The current density  $i$  was used to find the constant  $\Phi_0$ ,

$$i = -\kappa \frac{\partial \Phi}{\partial z} \Big|_{z=0} = \left( -\frac{\kappa}{a\eta} \right) \frac{\partial \Phi}{\partial \xi} \Big|_{\xi=0} = \frac{2}{\pi} \left( \frac{\kappa \Phi_0}{a\eta} \right) = \frac{2\kappa \Phi_0}{\pi \sqrt{a^2 - r^2}} \quad (5)$$

$$I = 2\pi \int_0^a i r dr = 4\kappa a \Phi_0 = 4\kappa \Phi_0 \int_0^a \frac{r}{\sqrt{a^2 - r^2}} dr = [-4\kappa \Phi_0 \sqrt{a^2 - r^2}] \Big|_0^a \quad (6)$$

$$\Rightarrow I = 4\kappa \Phi_0 a \quad \text{or} \quad \Phi_0 = \frac{I}{4\kappa a} \quad (7)$$

where  $I$  is the total current,  $\kappa$  is the solution conductivity, and  $a$  is the radius of the disk. The normal field can be found by taking the derivative of the potential with respect to  $z$ . However, because the measured impedance in LEIM experiments uses a discrete difference in potential at two points, the normal field was determined by subtracting the calculated potential at two points normal to each other and separated by  $0.25 \mu\text{m}$ . This

represents the actual separation between the microreference electrodes. The resulting plot for several heights above the surface is shown in Figure 3, using as an example

$$I = 100 \text{ } \mu\text{A}, a = 300 \text{ } \mu\text{m}, \kappa = 56.3 \text{ (m}\Omega\text{)}^{-1}, \Phi_0 = \frac{I}{4\kappa a} = 1.885 \text{ V.} \quad (8)$$

Using the methods and terminology of Zou, Thierry, and Isaacs [12], the distance between the sample surface and the lower microreference tip is considered to be the vertical height,  $z$ , of the probe from the surface. One important feature to note in Figure 3 is the reduced field over the center of the disk when the vertical height from the disk is smaller than the radius of the disk. This depression is due to the fact that the charge density on an equipotential disk is more concentrated at the edges. These edge effects are an important consideration when interpreting LEIM measurements of locally corroding sites because such depressions and other features are suggestive of edge effects as presented in Part I of this series [8]. However, the depression in admittance seen in LEI maps of early stage underfilm corrosion on organic coated AA2024-T3 do not resemble those in theoretical calculations arising from edge effects. The depression in admittance in early stages of a blister falls below the base admittance level of the surrounding region, whereas the depression in Figure 3 lies above the base field level and is only lower relative to the peaks in the normal field at the edges of the disk. In addition, it can be seen in Figure 3 that the lower the depression in the field above an equipotential disk, the higher the peaks at the edges of the disk. No raised admittance is observed at the edges of the blisters on organic coated AA2024-T3. Thus, modeling of such corrosion sites has ruled out edge effects as the cause of the experimentally observed changes in impedance amplitude. This now points to real physical or chemical changes in the materials and interface as the source for the LEI changes.

It should be noted that the normal field above an equipotential disk using the derivation in elliptical coordinates is slightly different, primarily in amplitude, from the plot using the derivation in cylindrical coordinates. A comparison of the two calculations at a dimensionless height,  $z/a = 0.25$ , is shown in Figure 4. The important features are present and similar in both plots. However, the observed differences illustrate the sensitivity of analytical calculations to boundary conditions and approximations, and

hence the impracticality of analytical modeling of a finite geometry with numerous parametric variations.

### **Numerical Modeling**

The eventual goal of analytical calculations was to model a disk electrode with the addition of a dielectric layer. It was the failure of analytical calculations to model this system in a practical and representative way which prompted the use of numerical methods instead. These calculations are shown in detail elsewhere [15]. The equipotential disk was subsequently modeled using finite element analysis.

The finite element method is a well established numerical analysis technique capable of calculating quantities such as potential distribution for complex geometries [16,17]. In the finite element method, a model is broken into many regular polygonal pieces or elements. This is referred to as meshing. Points of intersection of elements are called nodes. The desired field is interpolated within each element such that the solutions across elemental or nodal boundaries are continuous, following the concept that the sum of solutions within each element produces a solution for the entire model. The higher the density of elements and the more regular the polygonal shape (e.g. no small angles), the better the accuracy of the calculation. A great advantage of finite element method is that parameters can be modified without prohibitively complicating the solution. Current software allows for models to be created and meshed with relative ease. In addition, finite boundaries are considered, rather than unrealistic infinite planes generally considered in theoretical calculations.

The case of a bare equipotential disk was first calculated using finite element analysis, and compared to the analytical calculation for verification. The disk was 500  $\mu\text{m}$  in diameter with an outer radius of 800  $\mu\text{m}$  for the insulator and bulk solution. The heights of the two potential slices for calculation of the normal field were taken such that the lower height was consistent with the  $z/a$  heights in Figure 3. These data produced a 3-dimensional plot, comparable to LEIM data. A 2-dimensional cross section, or slice, was taken for the purpose of comparison with calculations. These results are shown in Figure 5.

The plot in Figure 5 shows not only the edge effects in the center of the disk, but also edge effects just outside the disk. An important difference between the analytical and numerical solutions that is of consequence is the reduced normal field just outside the disk seen in the finite element results but not in the analytical results. This is due to a combination of two factors. The first is that the analytical solution considers the insulating plane to be infinite, whereas the plane of zero potential surrounding the disk in the finite element model is finite. Figure 6 shows these regions of reduced field for models where all dimensions are kept the same, but the outer radius of the region of zero potential outside the disk is increased. Although an outer radius larger than the one shown was difficult to solve with accuracy because of limitations on maximum node number, it was nevertheless evident from the plot in Figure 6 that the cusp just outside the disk was reduced when the outer boundary distance was increased. The reason for the apparent oscillations in the cusp for the disk with larger outer radius is as yet unclear. The results shown in Figure 6 illustrate the importance of modeling finite boundaries for more realistic comparison with experimental data. Such cusps surrounding a peak have been observed in LEIM of coated aluminum alloy and were presented in Part I of this series [8]. However, it is unclear at this time whether these are indeed caused solely by edge effects or whether material and interfacial changes are playing a role.

The field distribution above a bare equipotential disk was calculated for different disk radii. This was done to evaluate the change in amplitude, shape and edge effects of the field using disks of smaller radius, and to predict the resolving capability of the LEI probe for a small disk. While in the former calculations, the probe height was changed relative to the radius, in these calculations the height was kept constant and the disk radius changed. The difference is that the radius of the disk is also changed relative to the outer radius of the cell (the outer cell radius is kept constant), which is representative of electrode size changes during underfilm corrosion growth within a cell of fixed size. The potential was calculated for disks of radius 500, 255, 130, 66.7, 34, and 17.5  $\mu\text{m}$ . These values were chosen to match the radii of gold micro-disk electrode arrays created for experimental verification. The two-dimensional compilation of all of the different sizes is shown in Figure 7.

From Figure 7 it is clear that while a peak would appear to be measurable over a disk of radius  $17.5\text{ }\mu\text{m}$ , both the amplitude and the width of the peak were low. The width of the peak plays a crucial role in the ability of the probe either to differentiate active and passive regions within a blister, or to detect the initiation of a breakdown site. Since the LEI probe used in this study is stepped across the surface using step sizes as low as 10 microns, the normal field must extend in the x-y plane to a large enough radius such that it will not be missed by one step of the probe. In addition, the amplitude (*i.e.* potential difference) must be within the sensitivity of the LEI system (ca. 1 nV).

It should be noted that the height of the peak in the calculated field increased as the disk approached the dimensions of a point source. As the concentration of charge became more confined within increasingly smaller disk areas, the amplitude of the field at the center of the peak increased slightly. Once the disk resembled a point source (*i.e.* no visible edge effects), a decrease in the electrode radius was accompanied by a corresponding decrease in peak amplitude. This suggests that a decrease in peak height over an established underfilm corrosion site may represent an increase in the size of the corroding area, rather than a decrease in electrochemical activity. However, this increase would also be accompanied by an increase in peak width, so that an increase in peak height due to the increase in the area of underfilm corrosion may be able to be distinguished from an increase in electrochemical activity, since the latter would have no increase in area of corrosion. An increase in peak height not accompanied by an increase in width would likely be due to an increase in electrochemical activity and not in the area of underfilm corrosion.

Spatial variations exist in the electrochemical activity across coated aluminum alloys [3-7]. For example, previous research [5-8] showed that aggressive blisters often branch into secondary lobes of reduced electrochemical activity. Therefore, it was important to address the spatial resolution of the LEI probe. It is necessary to determine whether the LEI probe can theoretically distinguish the presence of two peaks, rather than record one blended peak over the two sites. To examine this, two adjacent disks were modeled with decreasing separation distances. A diagram of the basic model used for this calculation is shown in Figure 8. The disks were located symmetrically at half the separation distance from the center of the cylindrical cell as shown.

The normal field above two 200  $\mu\text{m}$  diameter disks was calculated for several separation distances: 1 mm, 510  $\mu\text{m}$ , 260  $\mu\text{m}$ , 133  $\mu\text{m}$ , 68  $\mu\text{m}$ , and 35  $\mu\text{m}$  from edge to edge. These distances were chosen for subsequent comparison to the gold disk microelectrode arrays fabricated for experimental verification. A comparison of the cross-sections of the normal field above the disks at each separation distance is shown in Figure 9. It can be observed from the calculated field for each separation distance between disks that the field above the two disks does not begin to merge until the separation distance is approximately less than the radius of the disk. However, even with a separation distance of only 35  $\mu\text{m}$ , two separate peaks are clearly discernable.

### **LEIM of fabricated electrodes**

LEIM was first performed on a gold microelectrode with a radius of 500  $\mu\text{m}$  at several different excitation frequencies in order to optimize the frequency used for subsequent experiments. The resulting map is shown in Figure 10. Cross sections of the disk were mapped rather than the entire area, both, for improved comparison and to maximize resolution within a 1000 maximum data point limitation of the software used. From this plot it was apparent that 3000 Hz provided a map of the admittance that maximized the amplitude and correlation in shape with that predicted by theoretical calculations. This frequency was used for all subsequent LEIM of uncoated disk electrodes. It was apparent from LEIM of the disk electrode that the edge effects (*i.e.*, peak in the field at the edges of the disk and reduced field just outside the disk) seen in theoretical calculations were only somewhat apparent at the center of the disk and not visible at the periphery of the disk. This could be due to several factors. Silicon oxide, the insulator surrounding the gold microelectrodes, is not a perfect insulator and is not, therefore, held at exactly 0 potential. This factor may be enough to dampen, particularly, the outer edge effects.

LEIM was also used to measure the interfacial admittance of gold disk electrodes of decreasing radius where the lower probe microelectrode was fixed at a height of ca. 75  $\mu\text{m}$ . The dimensions of the disk were identical to those considered in the finite element models. Figure 11 shows the admittance plots for all of these disk sizes. The disk of 17.5  $\mu\text{m}$  radius is shown at a lower admittance scale for greater clarity. The change in

amplitude and in peak width correlates with that predicted by both the numerical and analytical models. However, the initial increase in amplitude calculated by numerical analysis was not observed. This is probably due to the fact that edge effects were altogether not as apparent in experimental measurements as in calculations. It is also evident that the LEI probe can easily measure the admittance of the smallest disk of 17.5  $\mu\text{m}$  radius even with a minimum step size of 10  $\mu\text{m}$ .

The spatial resolution of the probe was examined by measuring the admittance over a row of aligned disks with decreasing separation distance. The disks were each 100  $\mu\text{m}$  in radius and the separation distances from edge to edge of the disks was 1mm, 714, 510, 364, 260, 186, 133, 95, 68, 48, and 35  $\mu\text{m}$ . Because fabrication of the microelectrode arrays was both time consuming and expensive, the disks were aligned in a single row. Therefore, the admittance at the edge of one disk was affected by the field from the neighboring disk or disks. Nevertheless, LEIM of the line of disks could be compared to FEM calculations and used to predict spatial resolution. Figure 12 shows a cross-sectional plot of the first four disks (of separation 35, 48 and 68  $\mu\text{m}$ ) using LEIM. It was determined by the theoretical calculations that measurements of disks with greater separation was not necessary because the fields above the two disks were already completely separate at such distances (*i.e.* greater than the disk radius). It is evident from the figure that even at a separation of only 35  $\mu\text{m}$ , the two peaks predicted to be distinguishable in the theoretical models are experimentally distinguishable by LEIM.

This paper has demonstrated the efficacy of a FEM model in the characterization of expected results when discretely sampling the normal field above micro electrodes within cells of finite dimension. In the present study, the electrodes were left bare, so that the numerical model could be compared to analytical methods. However, the eventual goal is to examine how the presence of a dielectric layer effects the normal field. This will be examined in part III of this series.

## SUMMARY AND CONCLUSIONS

LEIM is a potentially important tool in the investigation of the degradation mechanism of coated alloys. Part I of this series has shown reoccurring features in the LEI response of coating degradation (e.g., temporal and spatial variations in admittance

peak heights, admittance depressions in early stages of breakdown, admittance troughs surrounding peaks). These features could impart significant meaning into degradation phenomenon if they could be interpreted to result solely from physical or chemical changes within the materials and interface. However, LEIM is an emerging tool, and it is unclear at present as to the contributions of artifact that could result from the discrete sampling process of the normal field.

This paper represents the first step in developing a modeling method that will allow the description of an electric field above an electrode surface covered with a dielectric layer and immersed in a cell of finite dimension. An initial analytical approach was used to validate a numerical method based on FEM. The FEM was further validated by comparison of theoretical results to experimental results of single and arrayed micro-disk electrodes.

FEM offered a much greater possibility for variation of geometry and parameters and a more realistic representation of the finite boundaries considered in experimental measurements. A negative normal field was seen in FEM results just outside the disk. This was shown to be a result of the more realistic finite boundaries used in the model. This effect was not seen in analytical calculations because of the assumption of infinite boundaries. Several conclusion could be drawn from theoretical modeling of the equipotential disk:

- The normal field above the bare disk calculated at different heights above the surface showed greater edge effects at closer distances from the disk.
- Decreasing the radius of a bare disk electrode resulted in an initial increase in the magnitude of the field but a decrease in the edge effects until the field above the disk resembled a point source. Both the magnitude and edge effects then decreased with decreasing radius. It was predicted that a disk of radius 17.5  $\mu\text{m}$  should be within the measurement capabilities of the LEI probe.
- Calculation of the field above two bare disk electrodes predicted that two distinct peaks should still be discernable even at a separation of only 35  $\mu\text{m}$ . This suggested that LEIM would be capable of discerning two separate regions of electrochemical activity located in close proximity.



- Admittance depressions observed in early stages of coating degradation were deemed real and not a result of measurement artifact. No condition within the FEM model would allow for a depression without the presence of other prominent features. These other features were not observed experimentally. However, the admittance troughs observed around admittance peaks could be a measurement artifact resulting from edge effects (charge accumulation at the edge of the electrode).
- Disks of 35 mm diameter were detected, and separations of 35  $\mu\text{m}$  were resolvable with the present LEI system. This should not be construed as the limits of the technique, but more are the limits of the system used.

## ACKNOWLEDGEMENTS

The authors would like to thank the Air Force Office of Scientific Research for financial support of this research under contract no. F49620-96-1-0178. The authors would also like to thank J. Demarest for advice, permission, and time in the use of ANSYS software and the associated computer.

## REFERENCES

1. I. Annergren, D. Thierry, F. Zou, *J. Electrochem. Soc.*, **144**, 1208 (1997).
2. S. Lillard, P.J. Moran and H.S. Isaacs, *J. Electrochem. Soc.*, **139**(4), 1007 (1992).
3. M.W. Wittman and S.R. Taylor, in Advances in Corrosion Protection by Organic Coatings II, The Electrochem. Soc., PV **95-13**:158-168 (1995).
4. A.M. Mierisch, S.R. Taylor, in Electrically Based Microstructural Characterization II, Vol. 500, Materials Research Society, Warrendale, PA, p. 35 (1998).
5. A.M. Mierisch, J. Yuan, R.G. Kelly, S.R. Taylor, *J. Electrochem. Soc.*, **146**(12), 4449 (1999).
6. A.M. Mierisch and S.R. Taylor, *J. Corrosion Sci. and Eng.*, **2**, paper 30 (1999).
7. A.M. Mierisch and S.R. Taylor, in Localized In-Situ Methods for Investigating Electrochemical Interfaces, PV **99-28**, The Electrochem. Soc., Pennington, NJ. (2000).
8. A.M. Mierisch, S.R. Taylor, and V. Celli, *J. Electrochemical Soc.* (in review).
9. H.S. Isaacs, *J. Electrochem. Soc.*, **138**(3), 722 (1991).
10. J. Newman, *J. Electrochem. Soc.*, Technical Notes, May (1966).
11. L. Nanis, W. Kesselman, *J. Electrochem. Soc.*, **118**(3), 454 (1971).
12. F. Zou, D. Thierry, H.S. Isaacs, *J. Electrochem. Soc.*, **144**(6), 1957 (1997).
13. R.S. Lillard, P.J. Moran, and H.S. Isaacs, *J. Electrochem. Soc.*, **139**, 1007 (1992).
14. R.S. Lillard, J. Kruger, W.S. Tait, and P.J. Moran, *Corrosion*, **51**, 251 (1995).

15. A.M. Mierisch, "Interpretation of Observations Made Using Local Electrochemical Impedance Mapping (LEIM) on Organic Coated Aluminum Alloy 2024-T3", Doctoral thesis, University of Virginia, (2001).
16. S. Moaveni, "Finite Element Analysis: Theory and Application with ANSYS", Prentice Hall, New Jersey, (1999).
17. O.C. Zienkiewicz, R.L. Taylor, "The Finite Element Method", McGraw-Hill Book Co., London, (1991).

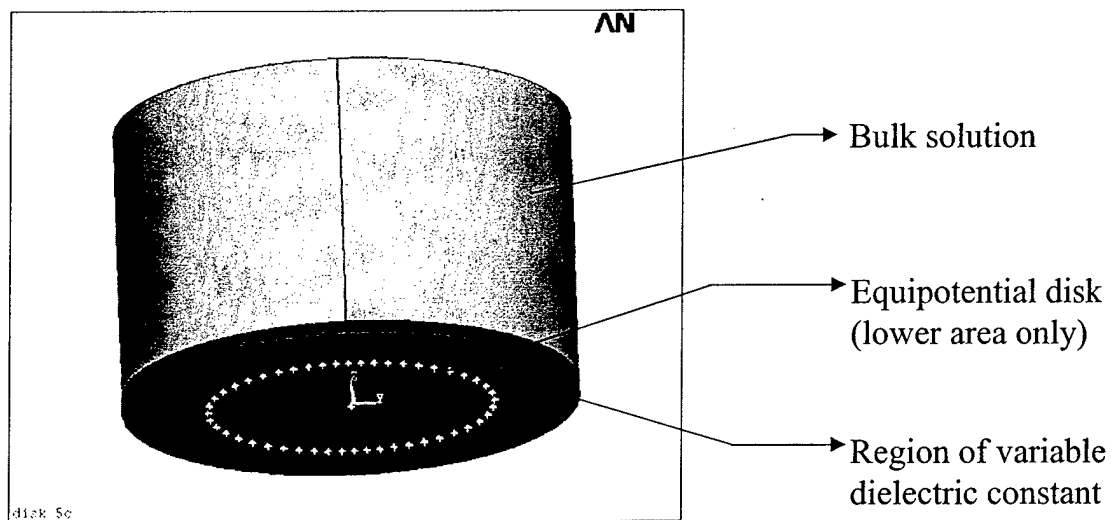


**Figure 1:** A diagram is shown of the basic model created in ANSYS to represent the different regions of dielectric constant and applied potential of the system.

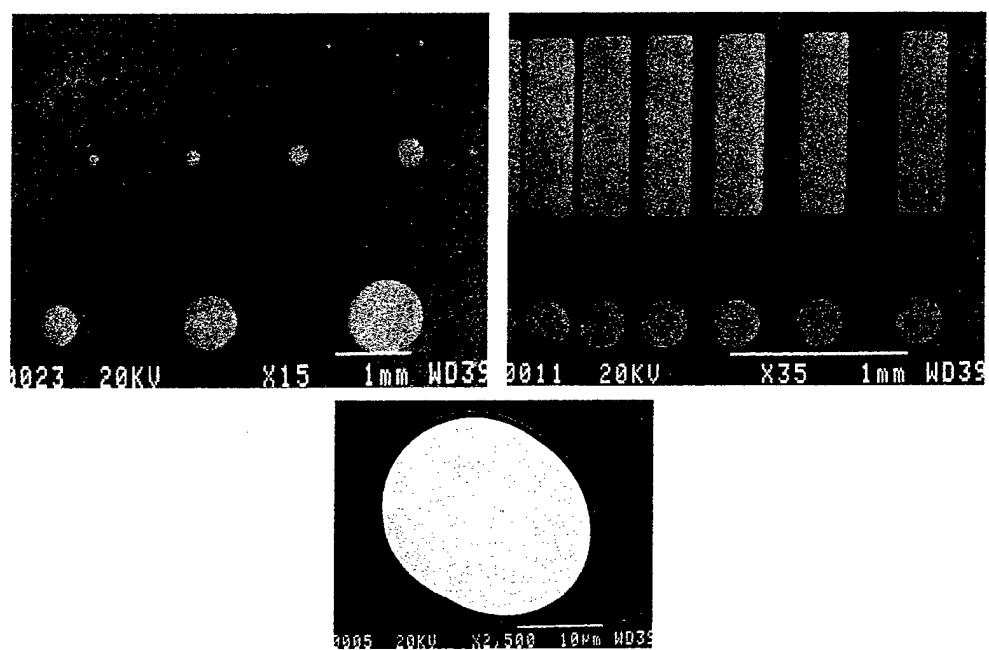


**Figure 2:** Gold disk microelectrodes were created to determine size resolution of the LEI probe and edge effects in the field emanating from a disk (upper left) and spatial resolution of the LEI probe (upper right). The pattern on the left was used for the investigations discussed in this paper. An enlarged image of the 17.5  $\mu\text{m}$  radius disk is shown below the two arrays.

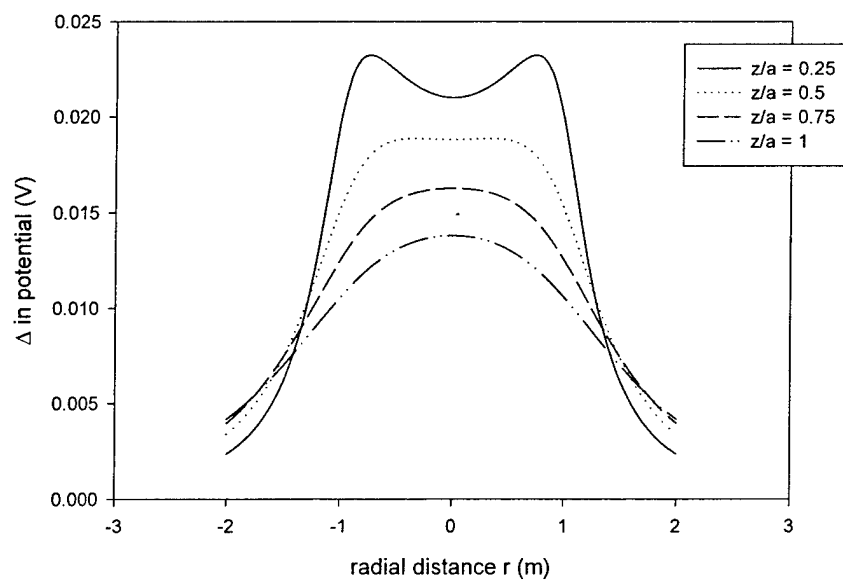


**Figure 3:** The analytically calculated normal field at varying heights,  $z$ , above the surface of an equipotential disk is shown. Both heights above the surface and radial distance are given as dimensionless quantities relative to the disk radius,  $a$ .

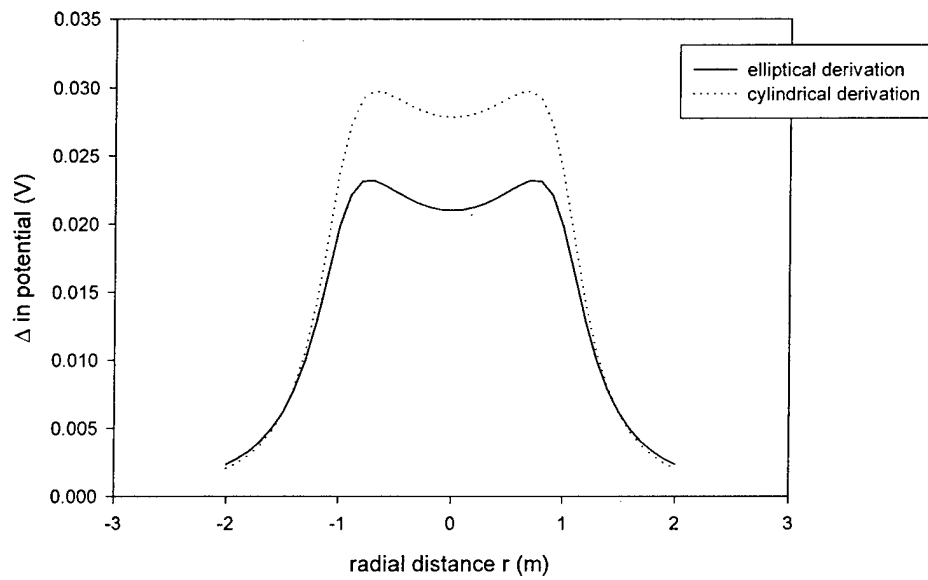


**Figure 4:** The normal field for dimensionless height  $z/a = 0.25$  above the surface of the disk is compared for the derivation of the potential in elliptical and cylindrical coordinates. While the shape is similar, the magnitudes are not equivalent between derivations.

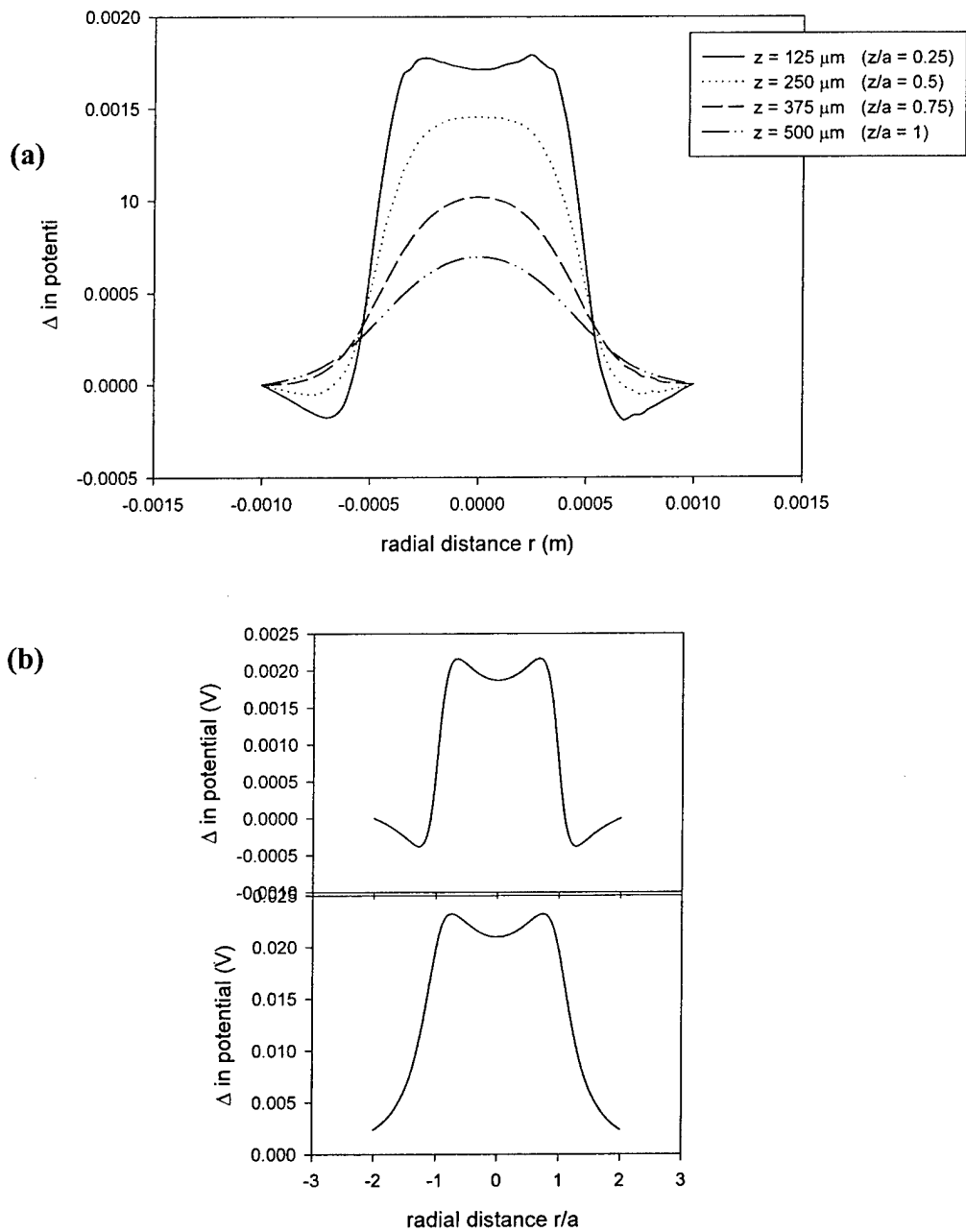


**Figure 5:** (a) The normal field is shown for different heights above the surface to represent different sampling height of the LEI probe. (b) For a height-to radius ratio of  $z/a=0.25$ , the discrete field is compared between the finite element calculation (top) and the analytical calculation (bottom). The plots in (b) are shown separately because of a difference in scale due to a difference in some parameter values. The general shape is under comparison.

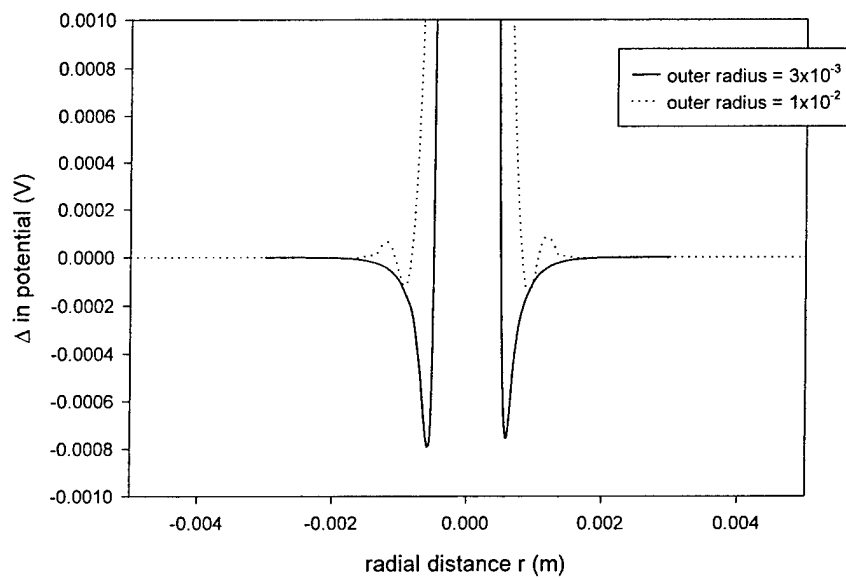


**Figure 6:** This figure demonstrates the reduction of the outer edge effects with an increase in the radius of the outer model boundary. Analytical calculations employ infinite boundaries and therefore do not show a reduced field just outside the disk.



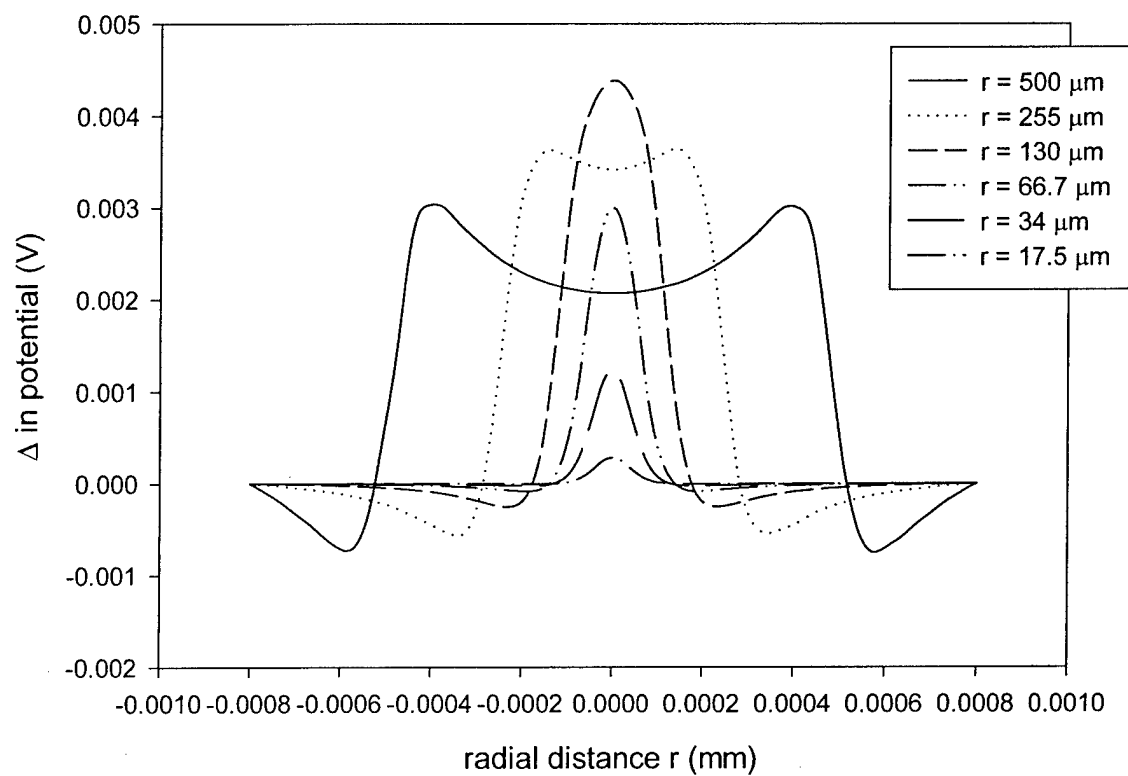


**Figure 7:** 2-dimensional cross-sections are shown for the normal field above equipotential disk of varying radius.

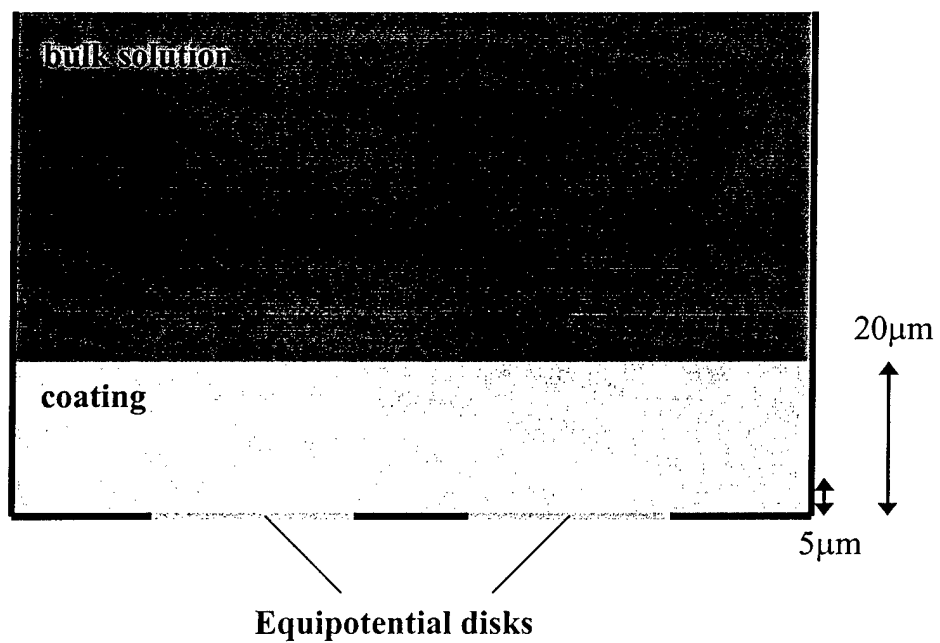


**Figure 8:** A diagram of the geometry used to model two adjacent equipotential disks.

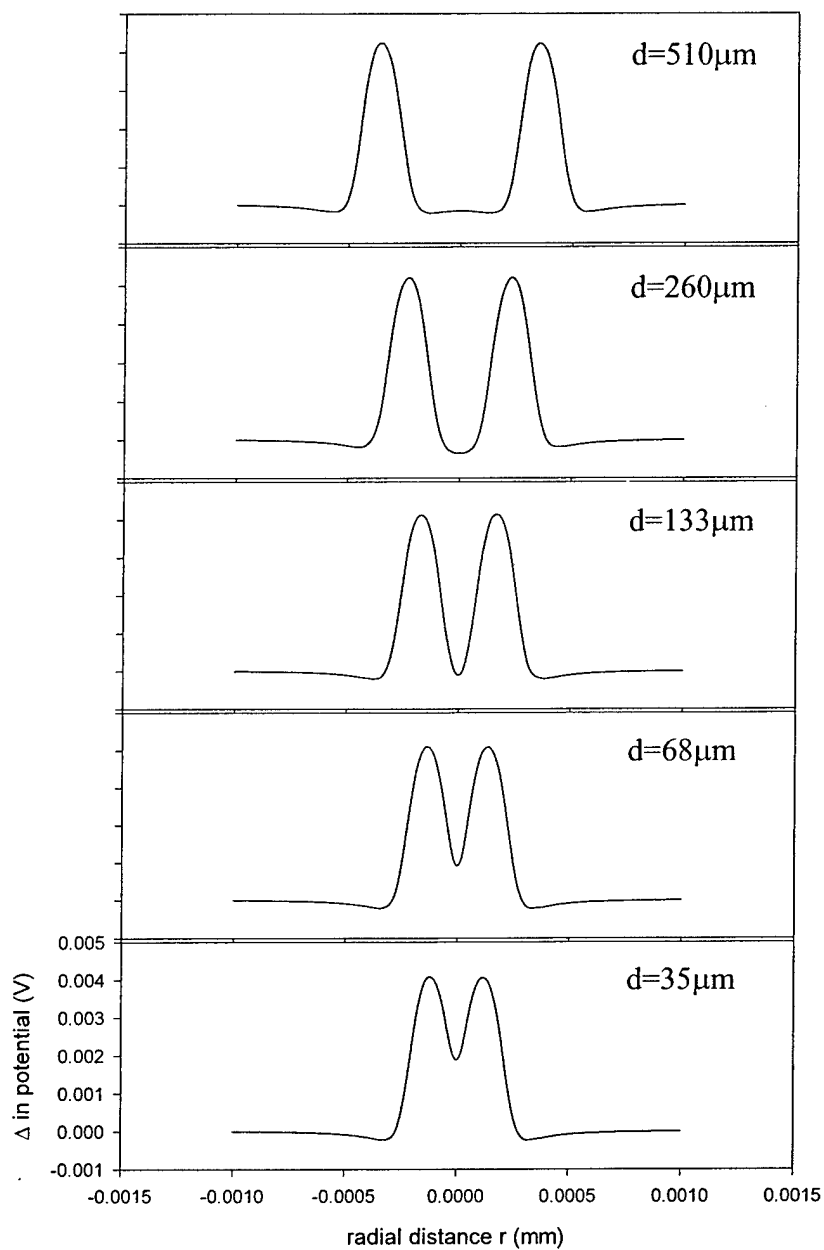


**Figure 9:** Two-dimensional cross-sections are shown of the normal field above two adjacent equipotential disk at varying separation distance. The plots have been separated for greater clarity. The change in potential axis is equivalent for each plot.

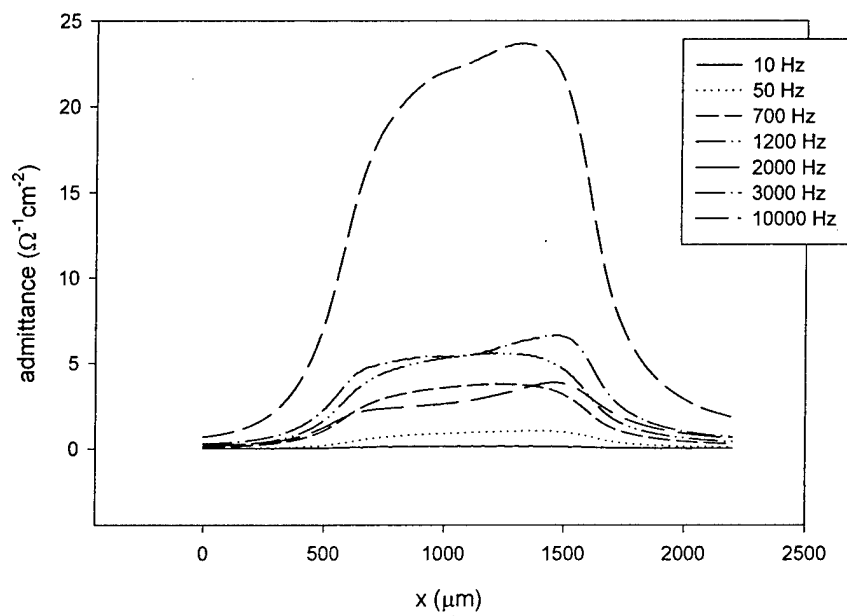


**Figure 10:** LEIM of a 1 mm diameter gold disk is shown for various frequencies. A frequency of 3000 Hz appears to be optimal.

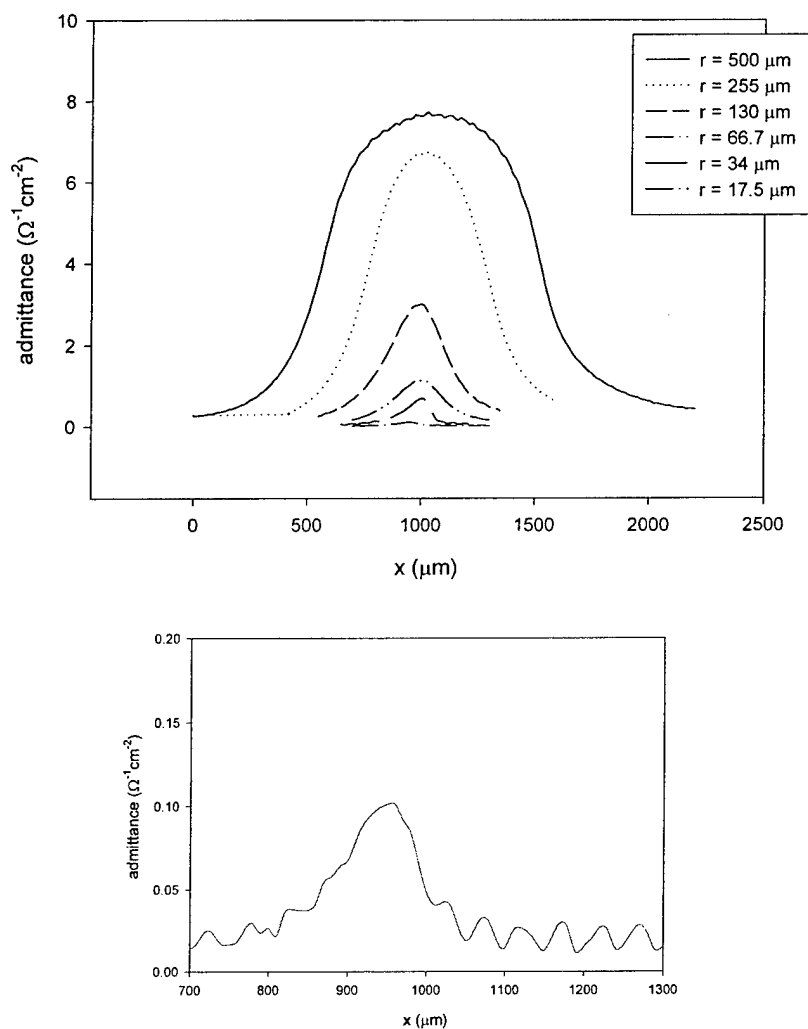


**Figure 11:** LEIM is shown for gold disk electrodes of varying radius: 500, 255, 133, 66.7, 34 and 17.5  $\mu\text{m}$  (upper). The disk of 17.5  $\mu\text{m}$  radius is shown at a lower scale (lower). Since the variations in admittance outside the disk occur within 10  $\mu\text{m}$  step intervals, these can be attributed to noise internal to the system.

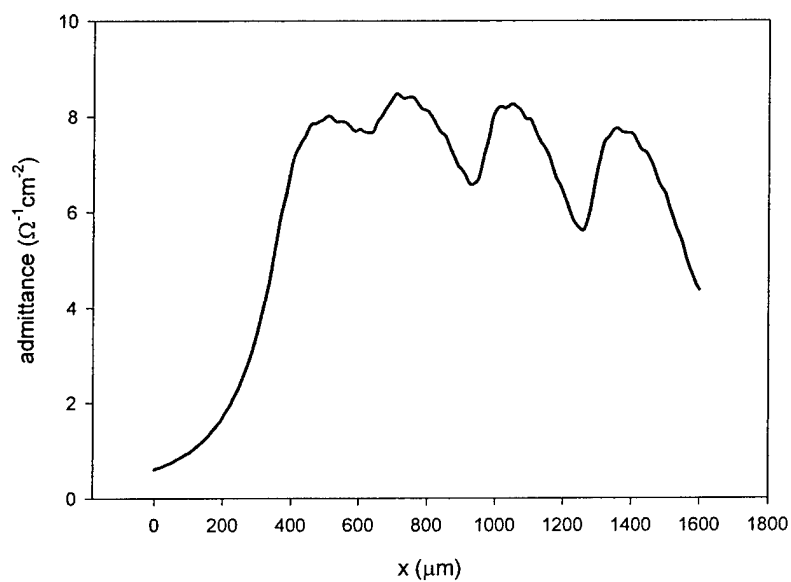


**Figure 12:** LEIM is shown for adjacent gold disk electrodes of increasing separation distance. From left to right, the separation distances are 35, 48 and 68  $\mu\text{m}$ .

# Incentives for using local electrochemical impedance methods in the investigation of organic coatings

S.R. Taylor\*

*Center for Electrochemical Science and Engineering, University of Virginia, Charlottesville, VA 22904, USA*

Received 11 September 2000; received in revised form 20 March 2001; accepted 24 April 2001

## Abstract

The assessment of changes in organic coatings in a corrosive environment has traditionally utilized global electrochemical methods, such as electrochemical impedance spectroscopy (EIS), in which a relatively large area of the sample is examined. Recently, more localized methods of impedance measurement have been developed and used to map heterogeneities across a sample surface, and the temporal changes of these regions. These localized methods are essential to further understand the breakdown process of coated alloys that inevitably occurs at discrete sites. This paper will examine the incentives for making local electrochemical impedance measurements, the advantages and limitations of this method, some of the lessons learned, and the present understanding of local breakdown processes on model-coated substrates. © 2001 Elsevier Science B.V. All rights reserved.

**Keywords:** Local electrochemical impedance spectroscopy; Local electrochemical impedance mapping; Coating defect; Heterogeneities

## 1. Introduction

Coating degradation during the course of underfilm corrosion requires ion transport and the establishment of electrochemical reactions (i.e. oxidation and reduction) at the metal interface, so it has thus been logical to approach the investigation and quantification of coating degradation with electrical and electrochemical test methods. Electrochemical impedance spectroscopy (EIS) has proven to be an extremely valuable test method for the characterization of organic coating degradation in aqueous media [1–9]. While global, i.e. surface averaged, electrochemical methods such as EIS have generally proved to be successful in delineation of the degradation kinetics of organically coated metals, mechanistic and technical questions remain as to where, why, or how the coating has failed. In spite of the volume of effort directed towards the global assessment of organic coatings using electrical and electrochemical methods, our ability to reliably predict the service-life of coatings based on these measurements is limited. This limitation is possibly linked to the statistical nature, both spatially and temporally, of the locus of failure.

Observationally, we know that the failure of organic coatings is initiated at a local site. Initial investigations of the origins of coating failure focused on electrical and electro-

chemical characterizations of dissected patches of coatings [10,11]. These investigations characterized two general types of coating behavior in epoxy materials (D- and I-type behavior) and determined that eventual coating breakdown was associated with specific-coating regions whose conductivity changed proportionally with the conductivity of the electrolyte (D-type areas). These D-type regions provided the eventual locus of failure and have been attributed to factors, such as retained solvent, high acid functionality, poor cross-linking, as well as physical holes.

Evidence for local breakdown is also seen at earlier stages of coating exposure during the time course of certain electrochemical measurements such as the open circuit potential or the pore resistance derived from global electrochemical impedance measurements. An examination of the time trajectory of these parameters frequently reveals the presence of metastable events in which the pore resistance decreases several orders of magnitude unexpectedly for a short period of time and then recovers to the original value (or higher). This suggests the formation and healing of a defect and may be one of the sources of errors when using traditional barrier property measurements as a metric for long-term coating behavior. A discrete EIS measurement of an immersed coating at a specific time could conceivably coincide with one of these metastable breakdown events and skew the general interpretation of the projected test sample properties.

Mechanistically, questions remain as to the source of these defects and the factors that control the life/death

\* Tel.: +1-804-982-5788; fax: +1-804-982-5799.  
E-mail address: srt6p@virginia.edu (S.R. Taylor).

cycle of the metastable breakdown events. It is unclear, particularly within alloy systems, whether the origins of these local breakdown sites might be associated with local heterogeneities within the substrate (e.g. intermetallics or inclusions), which are known to be responsible for the pit initiation of certain alloys (e.g. S-phase in AA2024-T3).

The local chemical and metallurgical conditions that control these discrete and transient events are poorly understood to date. From a mechanistic standpoint, further understanding of the origin and nature of organic coating failure will require localized electrochemical and chemical methods. A local electrochemical probe and mapping method that can systematically detect, locate, and characterize these defects will allow a more-detailed analysis of the factors that control these metastable events that, in turn, ultimately control the function and service-life of organic coatings.

From a technical perspective, it is important for the manufacturer of either a coating material or a coated product to determine if the failure of a coated sample is a result of: (i) the intrinsic chemistry of the coating system; (ii) intrinsic chemical heterogeneities within the resin; (iii) surface contaminants or heterogeneities associated with the substrate; or (iv) extrinsic, physical defects in the coating such as pin-holes, thinned regions, or entrapped air bubbles. Thus, from a manufacturing perspective, one would like to know why a particular coating was rejected, i.e. was the source of failure due to the surface pretreatment, method of application, level of cross-linking agent, etc. This information can conceivably be acquired via local electrochemical measurements. With this information, good coating chemistries can be delineated and corrective measures regarding application procedures, etc., can be effectively implemented if this were the limiting factor.

A wide variety of DC and AC methods have been developed in various fields of science for the *in situ* examination of local electrochemical events. Some of these methods include: scanning reference electrode techniques [12–14], scanning vibrating probes [15–17], Kelvin probes [18–20], electrochemical microscopy [21–23], among other methods [24]. Each of these methods is useful depending on the interface under study, the type of information desired, and the measurement resolution required. There are also topographic methods such as atomic force microscopy that can be used to investigate the surface morphology as opposed to the electrochemical voltage or current. This method has been applied to bare electrodes in solution [25], as well various types of organic coatings [26–28].

When considering the characterization of local electrochemical events on coated metal substrates, local electrochemical impedance techniques have been a logical option based upon: (i) the ability of an AC-based technique to lower the impedance of a dielectric-type interface (i.e. organically coated metal) by the use of higher frequencies; and (ii) the ability to more fully characterize a specific site by the application of a range of excitation frequencies to develop an impedance spectra. Local electrochemical

impedance measurements have been made extensively on uncoated (i.e. bare) substrates [29–32], however it has only been more recently that it has been applied to coated metals [33–35]. While local electrochemical impedance spectroscopy (LEIS) can be used to characterize any intrinsic or extrinsic defect that can alter the dielectric, electric, or ionic nature of the coating material/coating-substrate interface, this paper will focus on some of the key findings with regards to intrinsic defects, i.e. defects inherent within a contiguous coating. The use of LEIS to examine a range of physical heterogeneities (i.e. extrinsic defects) in organically coated alloys has been discussed previously [35].

## 2. Experimental methods

### 2.1. Local electrochemical impedance measurements

Local electrochemical impedance mapping (LEIM) and LEIS were performed using a system fashioned after Lillard and coworkers [33,34]. A five-electrode arrangement (shown in Fig. 1) was comprised of a typical three-electrode arrangement (working electrode, counter electrode, and reference electrode) used to control the DC potential and excite the interface potentiostatically with an AC signal, while two micro-reference electrodes was used to detect the local potential gradient in solution above the sample surface. The DC potential and AC excitation of the coated samples were established with a Schlumberger 1286 electrochemical interface and Schlumberger 1255 HF frequency response analyzer (FRA) which were under computer control using in-house software.

The split micro-reference electrode design used to measure the local potential gradient consisted of two Teflon-coated chloridized silver wires (0.125 mm diameter) having a vertical separation between the tips of 1.5 mm

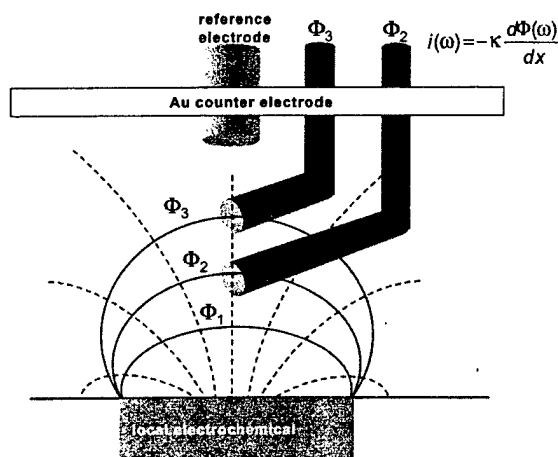


Fig. 1. Schematic of five-electrode configuration used to acquire LEIS data. Current (dashed) and potential (solid) lines associated with a local defect are shown.



(center-to-center). This design differs from the methods used by others [36,37] in which a vibrating platinum electrode is used to acquire the local potential and current data. The vibrating platinum electrode approach may have advantages from the standpoint of spatial resolution and minimum corruption by dispersion effects [37]. However, this approach is limited in sampling frequency by the electrode vibration frequency selected, suffers from the inherent "reference" electrode instability characteristic of a non-reference electrode material (i.e. platinum), and introduces solution convection by the vibration of the electrode.

At any given location, the potential difference between the probes was increased by a factor of 100 through the use of a high input impedance instrumentation amplifier ( $10^{10} \Omega$ ,  $G = 100$ ). The amplified probe voltage was then input into the current channel of the FRA for subsequent impedance analysis. The probe potential difference was converted to a current density using the relationship

$$i = \frac{\Delta V \kappa}{\Delta x G} \quad (1)$$

where  $\Delta V$  is the potential difference measured between the probes,  $\kappa$  the solution conductivity,  $\Delta x$  the vertical separation distance between the two micro-reference electrodes and  $G$  the gain of the preamplifier used to amplify the "current" signal obtained by the voltage-drop method.

The local impedance was mapped by fixing the probes approximately 25  $\mu\text{m}$  above the sample surface and then moving the sample. The sample sat on a positioning table comprised of a modified Teledyne TAC model PR-52 automatic wafer probe with adjustable  $X$  and  $Y$  step sizes ranging from 25 to 10,000  $\mu\text{m}$ . The local impedance measurement could consist of either a frequency spectrum taken at a single location (LEIS) or a single-frequency measurement taken at discrete points and mapped over an area (LEIM). The excitation frequency was selected to optimize the difference between a defective and non-defective region in the coating or to optimize the signal-to-noise ratio in the measurement. This criterion was satisfied at different frequencies depending on the particular experiment and ranged between 100 and 1000 Hz. A typical LEI map consisted of plotting the magnitude of the admittance, rather than impedance, simply for the aesthetic ease of observing defect sites as peaks rather than valleys.

## 2.2. Materials

Samples of AA2024-T3 were cut from 1 mm thick sheet into 6.5 cm  $\times$  6.5 cm panels. The samples were cleaned in a four-step procedure: Alconox<sup>®</sup> scrub, ultrasonically cleaned in hexane for 10 min, acetone rinse, followed by an isopropanol rinse. The samples were left to air dry under ambient conditions.

Cleaned aluminum samples were coated with various neat resins. No surface pretreatment (e.g. conversion coating) was used. Initial experiments were performed on samples coated

with vinyl VYHH, a copolymer of polyvinyl chloride and polyvinyl acetate. Polyurethanes of different soft segment chemistry, i.e. varied ratios of polyether and polyester, were also examined. These coatings consisted of a polyurethane composed of 100% polyether and a polyurethane composed of 50% polyether and 50% polyester. Each resin formulation was mixed with isocyanate (3.2 g ether/4 g isocyanate), a dibutyl tin dilaurate catalyst and methyl ethyl ketone solvent (1 cm<sup>3</sup>). A third polyurethane was also examined and consisted of a two-part polyester polyurethane mixed with butyl cellulose, and represents the resin used in commercial polyurethane primers.

All coatings were spin cast onto the cleaned samples to a dry coating thickness of 5–10  $\mu\text{m}$ . Samples were dried in a dessicator for at least 36 h after coating application, before exposure to corrosive environments.

Glass cylinders with an inner diameter of 4.3 cm were fixed to the coated substrate using silicone rubber adhesive sealant (GC Electronics, Rockford, IL) to create a reservoir for test electrolyte. This provided a 14.5 cm<sup>2</sup> exposure area. Most experiments were made using 0.6 M NaCl solution, although 0.1 M, or more dilute solutions of NaCl, KCl, NaSO<sub>4</sub> and K<sub>2</sub>SO<sub>4</sub> were also used in specific cases. All chemicals were reagent grade. All solutions were quiescent and at ambient temperature.

## 3. Results and discussion

### 3.1. Different types of failure sites are observed [38]

Several types of corrosion sites on the coated aluminum alloy substrates were observed. These sites differed in both electrochemical behavior and physical attributes.

One striking difference between these defects as seen in later stages of development was their visual color. For reasons of convenience, the defects will be referred to by their color, even though in the early stages of development the color may not be observable. When using VYHH resin, two later-stage defect types, having either a reddish or black color, were commonly observed. The black blister sites were essentially round with diameters of ca. 1–2 mm attained within 2–7 days of exposure. The red blister sites were irregularly shaped with a size of 1–7 mm attained within 1–2 days of exposure.

LEIM was performed on examples of both of these defect types at early stages of development prior to the development of a visible colored blister. The results are shown in Fig. 2. It is evident from the admittance surface plots that the sites that eventually evolve into red blisters show a significantly higher admittance peak than the site that eventually becomes the black blister. This suggests that higher currents are emanating from the red blister. The electrochemical character was confirmed with LEIS. Fig. 3 reveals that the red pre-defect site has a lower polarization resistance, again, indicating higher electrochemical

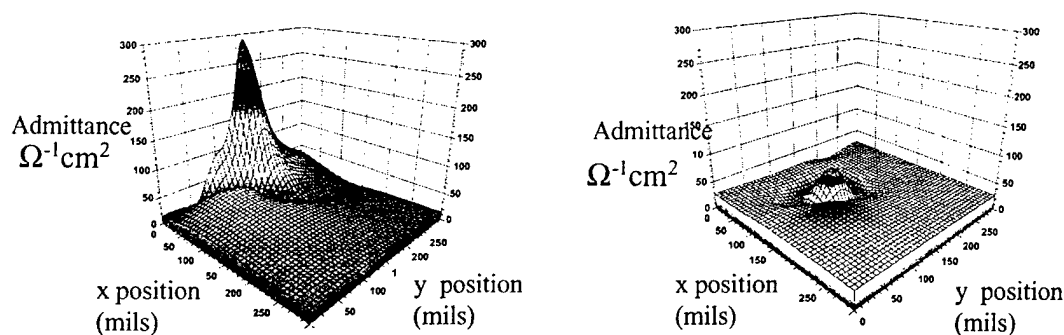


Fig. 2. Comparison of LEI maps for red (left) and black (right) defects beneath a vinyl coating on AA2024-T3 after 35 h exposure to 0.6 M NaCl.

activity. The site that eventually becomes the black blister defect was lower in admittance and had a higher polarization resistance (as shown in Fig. 3) as intuitively expected.

Subsequent chemical analysis of the solutions that developed inside of the red and black blisters revealed that the pH within the red sites was very low (pH = 3–5), while the pH inside of the black blisters was significantly higher (pH = 8–11). Upon ionic analysis via capillary electrophoresis (CE) [38], the red blister solution contained significant amounts of  $\text{Cu}^{2+}$ ,  $\text{Al}^{3+}$  and  $\text{Mg}^{2+}$ , acetate and formate. The cations present, along with the reddish color, suggest the involvement of the S-phase [39] ( $\text{Al}_2\text{CuMg}$ ) which interestingly has the same elemental content, although not the same stoichiometry as the blister solution. Rigorous analysis of the carrier solutions used in CE analysis did not reveal the presence of acetate or formate ions. Thus, the acetate and formate are believed to have originated from the polyurethane coating itself. Acetate was also observed in low pH solutions contacting freestanding polyurethane films. Similar analyses of solutions beneath vinyl coatings did not reveal the pres-

ence of these organics. These results are consistent with the possibility that ester linkages within the polyurethane coating have undergone hydrolysis, while the saturated bonds of the vinyl resin remain stable. Hydrolysis of the polyurethane above the red blister sites could be catalyzed by the low pH as well as the ionic content of this blister solution. This observation raises the possibility that the underfilm solution chemistry, which has a composition determined initially by the exterior environment and substrate electrochemistry, further degrades the organic coating, thus creating a potential feedback effect. It is also possible that a chemical heterogeneity present in the initial unexposed coating provided the original initiation site and allowed the ingress of specific ions (e.g. chlorides) to initiate the corrosion process. It is important to note that red blisters contained high chloride levels, while black blisters contained low chloride levels.

### 3.2. Different regions of activity within a single defect [38]

Continuous observation of a single red blister revealed an interesting trend. Generally, one or more lobes grew from the original blister area during long-term exposure. These secondary lobes appeared to have a darker color than the initiation site. The electrochemical activity of the different regions was measured using LEIM. The region mapped is shown along with the LEIM plot in Fig. 4. Interestingly, the initial blister site contained a high-admittance site within it, possibly representing the site of initial electrolyte ingress. The secondary lobes had much lower admittances, and were thus less active. Correspondingly, local open circuit potential values acquired via the use of micro-electrodes inserted beneath the coating revealed that the initial lobe had a more active potential. The open circuit potential at the site of initiation was  $-0.66V_{\text{SCE}}$ , whereas the open circuit potential within the secondary lobe was  $-0.58V_{\text{SCE}}$ . Subsequent autopsy of this sample revealed that significant pitting occurred beneath the active region (initial lobe — higher admittance), while the less active region was the segment representing the advancing front of the filiform. This is in contrast to the classic thinking of advancement of filiform by anodic processes.

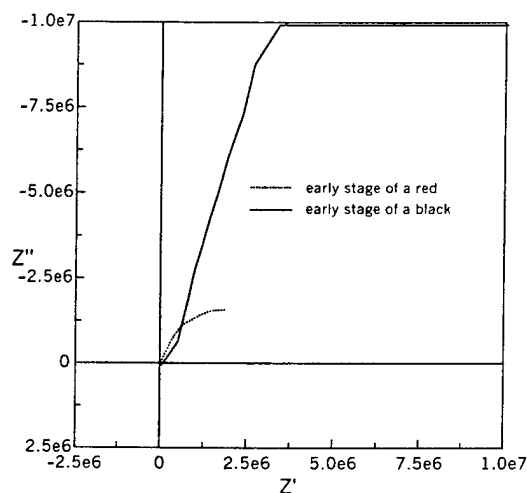


Fig. 3. Comparison of red and black defects in the complex impedance plane during early stages of development using LEIS. Note the lower polarization resistance for the red site than for the black site.

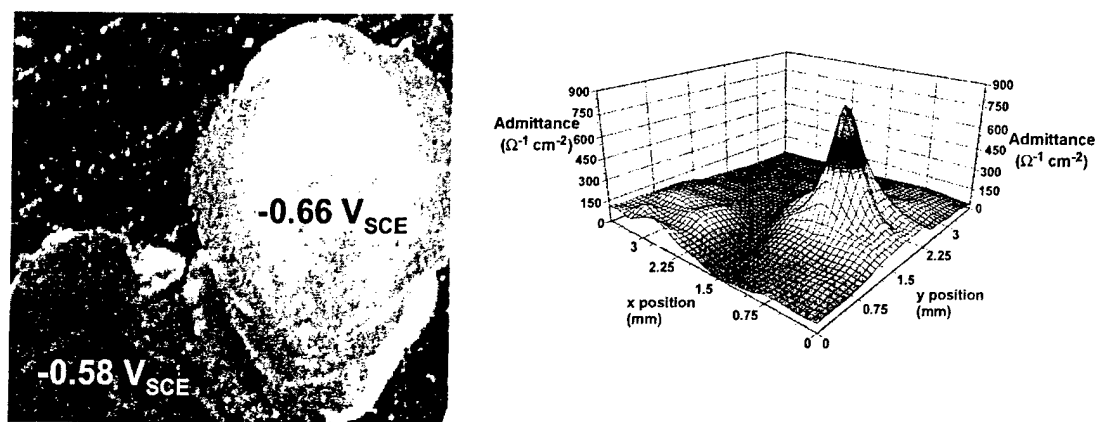


Fig. 4. Optical micrograph of the actual region mapped by LEIM (left) and the corresponding LEI map (right). Note higher admittance at the initiation site.

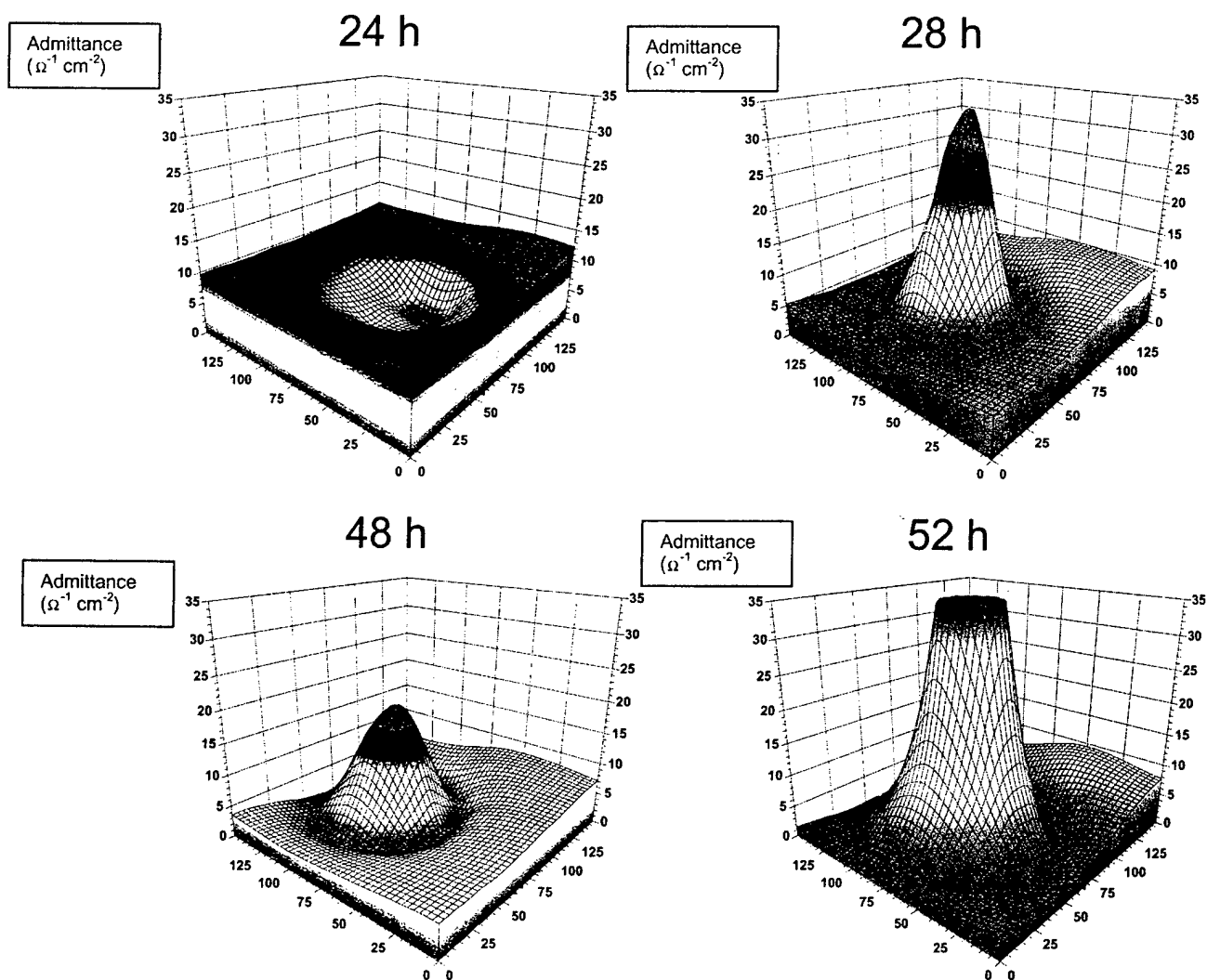


Fig. 5. LEIM of a local defect as a function of time. Note the low admittance (high impedance) at initial stages, as well as fluctuations in peak height as a function of time. Sample is a 50/50 polyether–polyester polyurethane on AA2024-T3 in 0.6 M NaCl.

### 3.3. Confirmation of a growth/death cycle in an intrinsic defect [40]

In addition to locating defects in early stages of development and identifying different types of defects, LEIM has been used to monitor the time evolution of an intrinsic defect in a 50/50 polyether–polyester polyurethane-coated AA2024-T3 sample. Fig. 5 shows the time course of a blister on polyurethane-coated AA2024-T3 from an early non-visible stage (24 h) to later actively corroding stages. Several interesting features are observed: (1) the initial decrease in admittance in the earliest stage of observation (to 24 h); (2) a decrease in admittance of the blister seen by the lower peak at 48 h; (3) the rapid rise in peak height at 52 h. These features represent significant insight into the evolution of underfilm corrosion events assuming that the data is not corrupted by measurement artifact. Possible contributors to artifact include instability of the reference electrode and frequency dispersion. Frequency dispersion is a term that refers to deviations from ideal results due to non-uniform current distribution. These factors have been ruled out [40], hence

the present wisdom is to interpret the observed changes LEIM data as legitimate changes.

The changes in local pH of the underfilm solution in this blister correspond to LEIM peak height and thus discounts the hypothesis that biphasic water uptake of the coating causes the variation in the peak height. Preliminary EIS studies performed on free-polymer films of neat resins revealed that the majority of water uptake occurs within the first 1–2 h of immersion. It is evident from Fig. 5 that the changes in peak height occur after this point in time. It should be noted, however, that changes in peak height during the first 1–2 h of immersion could very likely be affected by the changes in the coating due to water uptake and plasticizing of the resin. It is thus believed that changes in peak height of admittance maps in Fig. 5 result from actual metastable electrochemical events associated with the blister defect.

Several theories have been proposed to explain the admittance dip in early stages [40], a phenomenon observed numerous times. Assuming that the high initial impedance (lower admittance) is indeed reflective of physical events (and not artifact), three possible explanations are proposed.

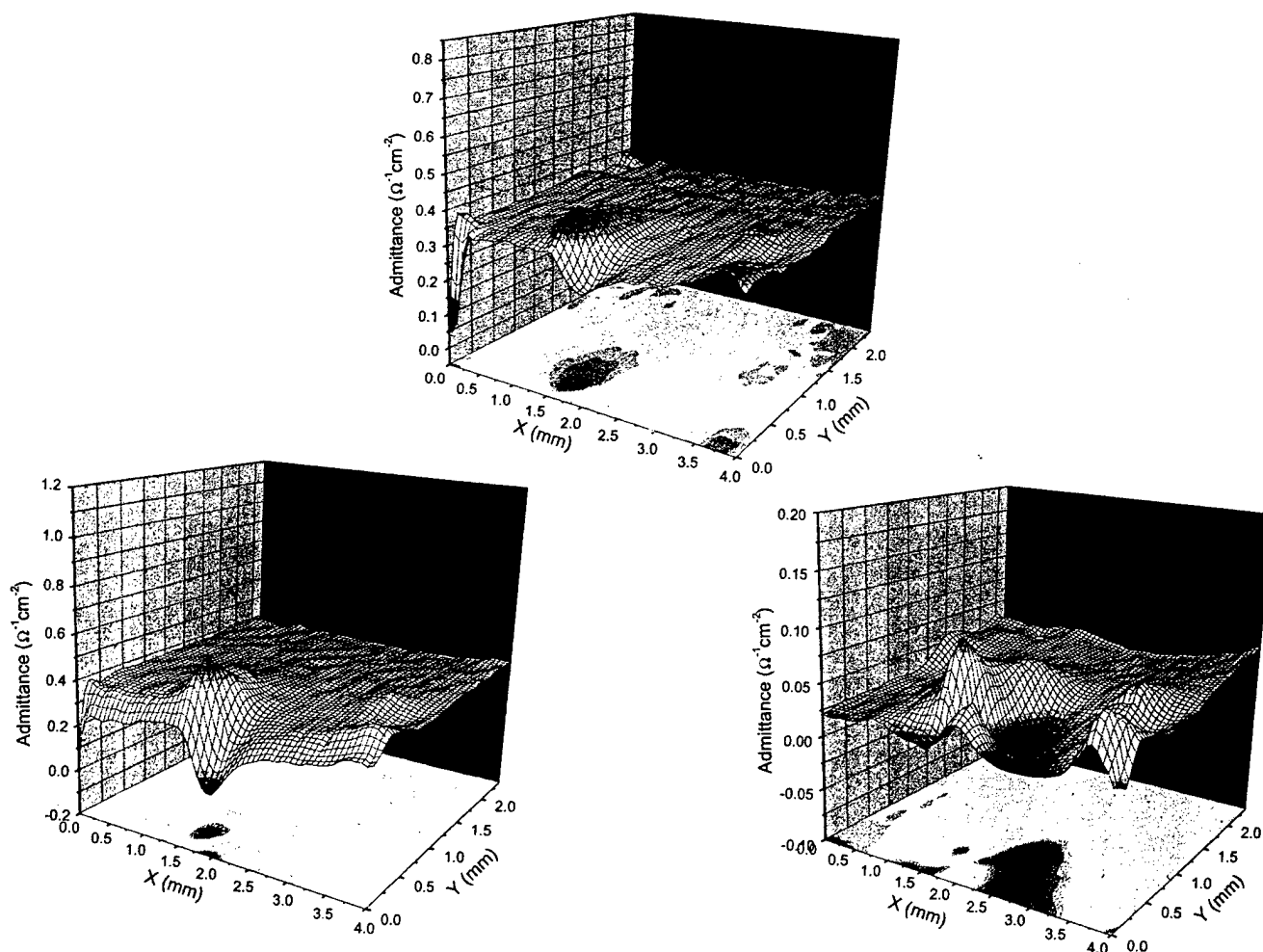


Fig. 6. LEI maps of an intrinsic defect within an epoxy coating on a 99.999% gold substrate in 0.6 M NaCl. Note the metastable time evolution of this defect.

A heterogeneity in the coating that exhibits a higher impedance than the film in general could be a site where a blister initiates. While the initiation of blisters at coating heterogeneities has been observed, this explanation is not considered plausible in this particular case because uneventful “flat” admittance maps preceded the dips. An admittance dip due to an extrinsic coating heterogeneity resulting from application or handling would likely be present in the LEIM before a blister had initiated. It was hypothesized that water nucleation occurring at the initiation site could cause a local decrease in the admittance. Impedance values were calculated for two possible equivalent circuit representations of the water layer [40], and it was concluded by the results that water nucleation could indeed cause the 20  $\Omega$  increase in impedance. The accumulation of corrosion product could also be the origin for the decreased admittance. At this time, the accumulation of a resistive product is considered the most-plausible explanation of the admittance dips.

#### 3.4. Is the origin of corrosion within the coating or within the substrate

One of the principle reasons for performing localized chemical and electrochemical measurements is to determine the origin of coating failure. In order to de-couple the effects of the substrate from the measurement, one should theoretically perform LEIM on a free film. Due to the complexity of producing a free film without the introduction of extrinsic defects, the author chose to examine a neat resin (epoxy) cast on a 99.999% gold substrate. Fig. 6 reveals not only that an intrinsic defect appears to exist within the coating, but also it demonstrates metastable behavior similar to the coated aluminum alloy. This further confirms the need to rule out all possible source of artifact to provide the highest confidence in data. Studies are in progress to model the electric field and current distribution associated with a disk electrode possessing a dielectric layer.

#### 4. Summary and conclusions

Local electrochemical impedance mapping and spectroscopy provides an invaluable tool for the investigation of local electrochemical events. The AC-based nature of impedance makes it particularly suited for the examination of local events associated with organically coated substrates. This method has been shown to easily observe extrinsic-type defects associated with processing and manufacture. LEIM/S has also been used to observe for the first time, evidence for individual intrinsic-coating defects. These defects show a non-intuitive admittance dip in the early stages of development which may be attributable to water nucleation at the metal/coating interface or to the development of a resistive corrosion product. In addition, some observed defects demonstrate metastability which is supportive of previous findings of metastability within

global EIS measurements of coated alloys. Initial LEIM studies of coated gold indicate that the origin of these defects may be within the coating, however the importance of the substrate and underfilm chemistry that develops cannot be overstated. Evidence for the underfilm attack of the coating by acidic blister solutions has been shown.

#### Acknowledgements

The author wishes to express his sincere appreciation to M.W. Wittmann, R.B. Leggat, A.M. Mierisch, J. Yuan, and R.G. Kelly for their technical contributions to this endeavor, as well as to the Air Force Office of Scientific Research for their financial support of this research. The author would also like to thank Ball Corporation, American National Can/Pechiney, Reynolds Metals Corporation, and Metal Container/Anheuser Busch for their prior support in the development of the LEIM/S equipment used in these experiments.

#### References

- [1] M.W. Kendig, H. Leidheiser Jr., *J. Electrochem. Soc.* 123 (7) (1976) 982.
- [2] L.M. Callow, J.D. Scantlebury, *J. Oil Colour Chem. Assoc.* 64 (2) (1981) 83.
- [3] M. Piens, R. Verbist, in: H. Leidheiser Jr. (Ed.), *Corrosion Control by Organic Coatings*, NACE, Houston, TX, 1981, pp. 103–110.
- [4] T. Szauer, *Prog. Org. Coat.* 10 (1982) 171.
- [5] J. Hubrecht, J. Vereeken, *J. Electrochem. Soc.* 132 (2) (1985) 2886.
- [6] M.W. Kendig, F. Mansfeld, S. Tsai, *Corr. Sci.* 23 (4) (1983) 317.
- [7] S.R. Taylor, *IEEE Trans. Electron. Insul.* 24 (1989) 787.
- [8] F. Mansfeld, C.H. Tsai, *Corrosion* 47 (1991) 958.
- [9] R. Hirayama, S. Haruyama, *Corrosion* 47 (1991) 953.
- [10] D.J. Mills, J.E.O. Mayne, in: H. Leidheiser Jr. (Ed.), *Corrosion Control by Organic Coatings*, NACE, Houston, TX, 1981, pp. 12–17.
- [11] J.E.O. Mayne, J.D. Scantlebury, *Br. Polym. J.* 2 (5) (1970) 240.
- [12] H.S. Isaacs, B. Vyas, in: F. Mansfeld, U. Bertocci (Eds.), *Electrochemical Corrosion Testing*, ASTM STP 727, ASTM, 1981, pp. 3–33.
- [13] S.J. Bates, S.R. Gsoden, D.A. Sargent, *Mater. Sci. Technol.* 5 (1989) 356.
- [14] V.S. Voruganti, H.B. Luft, D. Degeer, S.A. Bradford, *Corrosion* 47 (1991) 343.
- [15] H.S. Isaacs, *Corrosion* 43 (1987) 594.
- [16] H.S. Isaacs, *Corr. Sci.* 28 (1988) 547.
- [17] L.F. Jaffe, R. Nuccitelli, *J. Cell Biol.* 64 (1974) 614.
- [18] M. Stratmann, H. Streckel, *Corr. Sci.* 30 (1990) 681.
- [19] M. Stratmann, H. Streckel, *Corr. Sci.* 30 (1990) 697.
- [20] M. Stratmann, H. Streckel, *Corr. Sci.* 30 (1990) 715.
- [21] A.J. Bard, F.R.F. Fan, J. Kwak, O. Lev, *Anal. Chem.* 61 (1989) 132.
- [22] J. Kwak, A.J. Bard, *Anal. Chem.* 61 (1989) 1794.
- [23] M.V. Mirkin, *Anal. Chem. News Feat. A* 177 (1996).
- [24] S.R. Taylor, A.C. Hillier, M. Seo (Eds.), *Localized In-situ Methods for Investigating Electrochemical Interfaces*, ECS Proceedings PV99-28, The Electrochemical Society, Pennington, NJ, 2000.
- [25] H.J. Butt, M. Jaschke, W. Ducker, *Bioelectrochem. Bioenergy* 38 (1995) 191.
- [26] T. Gesang, R. Hoper, S. Dieckhoff, V. Schlett, W. Possart, O.D. Hennemann, *Thin Solid Films* 264 (1995) 194.
- [27] J. Frommer, *Angew. Chem. Int. Ed. Engl.* 3 (1992) 1298.

- [28] G.P. Bierwagen, R. Twite, G. Chen, D.E. Tallman, *Prog. Org. Coat.* 32 (1997) 25.
- [29] H.S. Isaacs, M.W. Kendig, *Corrosion* 36 (1980) 269.
- [30] R.S. Lillard, P.J. Moran, H.S. Isaacs, *J. Electrochem. Soc.* 139 (1992) 1007.
- [31] F. Zhou, D. Thierry, H.S. Isaacs, *J. Electrochem. Soc.* 144 (1997) 1208.
- [32] I. Annergren, D. Thierry, F. Zhou, *J. Electrochem. Soc.* 144 (1997) 1957.
- [33] R. Lillard, J. Kruger, W.S. Tait, P.J. Moran, *Corrosion* 51 (1995) 251.
- [34] M.W. Wittmann, S.R. Taylor, in: J.D. Scantlebury, M.W. Kendig (Eds.), *Advances in Corrosion Protection by Organic Coatings II*, PV95-13, The Electrochemical Society, Pennington, NJ, 1995, p. 158.
- [35] M.W. Wittmann, R.B. Leggat, S.R. Taylor, *J. Electrochem. Soc.* 146 (11) (1999) 4076.
- [36] E. Bayet, F. Huet, M. Keddam, K. Ogle, H. Takenouti, *J. Electrochem. Soc.* 144 (1997) L87.
- [37] E. Bayet, L. Garrigues, F. Huet, M. Keddam, K. Ogle, N. Stein, H. Takenouti, in: S.R. Taylor, A.C. Hillier, M. Seo (Eds.), *Localized In-situ Methods for Investigating Electrochemical Interfaces*, ECS Proceedings PV99-28, The Electrochemical Society, Pennington, NJ, 2000, pp. 200–211.
- [38] A.M. Miersich, J. Yuan, R.G. Kelly, S.R. Taylor, *J. Electrochem. Soc.* 146 (12) (1999) 4449.
- [39] R.G. Buchheit, R.P. Grant, P.F. Hlava, B. McKenzie, G.L. Zender, *J. Electrochem. Soc.* 144 (1997) 2621.
- [40] A.M. Miersich, S.R. Taylor, in: S.R. Taylor, A.C. Hillier, M. Seo (Eds.), *Localized In-situ Methods for Investigating Electrochemical Interfaces*, ECS Proceedings PV99-28, The Electrochemical Society, Pennington, NJ, 2000, pp. 229–240.

Amber M. Mierisch and S. Ray Taylor  
Center for Electrochemical Science and Engineering  
University of Virginia, Charlottesville, VA 22903  
[amu5u@virginia.edu](mailto:amu5u@virginia.edu), [srt6p@virginia.edu](mailto:srt6p@virginia.edu)

## ABSTRACT

Interpretation of impedance measurements on coated alloys requires consideration of all possible contributions, including the suspected chemical, electrochemical, and physical processes as well as artifact. Observations in Local Electrochemical Impedance Maps (LEIM) of organic coated AA2024-T3 using the split Ag/AgCl (SSSC) electrode LEI probe were investigated for the possibility of artifact and the contribution of causes other than electrochemical breakdown processes. An admittance dip observed in early stages of blister development, and the metastability of blisters over time were explored in detail. The effect of the coating as a dielectric layer over a corroding region on the electric field was calculated to first order by the method of images for an equipotential disk electrode. Gold disk electrodes were subsequently used to experimentally validate the effect of a dielectric layer on the impedance.

## INTRODUCTION

Local electrochemical impedance (LEI) has been an effective in situ tool for measuring local electrochemical activity of coated metal substrates in aqueous environments [1-5]. Recent LEI maps [2] of coated aluminum alloys have revealed unexpected impedance changes during the initial stages of blister defect formation, as well as fluctuation of the impedance magnitude suggesting growth/death cycles of local breakdown sites [2,3]. These data represent new insight into the breakdown phenomena of organic coated alloys, provided the data is interpreted as being entirely attributable to interfacial changes associated with the interface. However, any associations between experimental measurements and actual changes involving the material and interface must first rule out the possibility of artifact. Conceivable deviations of the measured impedance from the actual interfacial impedance have been proposed to arise from several possible sources: frequency dispersion [6], edge effects of the local electric field [7], and measurement artifact associated with interfacial concentration gradients [8]. The effect of a dielectric layer of organic coating over an electrochemical site on the measured impedance must also be considered.

The objective of this study was to determine the validity of the proposed theories of artifact as they pertain to the study of organic coated metals. In addition, several different physical hypotheses for the unexpected impedance values of early stage blisters

were examined assuming that the data were factual. These included water nucleation and the accumulation of corrosion product. Physical explanations are also given for changes in peak height over the time evolution of a blister. The effect of an organic layer over a disk electrode was quantified both theoretically and experimentally. These assessments were restricted to results obtained with the split Ag/AgCl micro-reference electrode (SSSC).

## EXPERIMENTAL

The LEI probe used in this investigation consists of a five-electrode configuration employing the split Ag/AgCl micro-reference electrode or SSSC [1-4]. Two 125  $\mu\text{m}$  diameter teflon coated Ag/AgCl micro-reference electrodes, chloridized on the end in NaCl solution, are used to measure the local potential gradient. A 250  $\mu\text{m}$  diameter Ag/AgCl reference electrode is positioned on the probe assembly so that the center of the reference electrode is at the same height as the upper micro-reference electrode but removed 800  $\mu\text{m}$  horizontally. A single, small amplitude (ca. 15 mV) sine wave perturbation at a single frequency (generally 700 Hz) was applied to a DC potential set at the global open circuit potential of the substrate. The local current density is determined by measuring the potential gradient in solution above the substrate between the two micro-reference electrodes and then converting this potential difference through Ohm's law to a local current density. The local impedance was determined by comparing the global voltage to the local current density. An LEI map is generated by stepping the probe across the sample and plotting the magnitude of the local admittance as a function of x,y position. The voltage signal from the split micro-reference electrode was amplified in order to both minimize the required excitation signal and maintain a nondestructive character.

Substrates consisted of 6.5 x 6.5 x 0.1 cm AA2024-T3 panels coated primarily with vinyl or polyurethane. Both the compositions of these coatings and pre-coating cleaning methods have been discussed elsewhere [3]. All coatings were spin cast to a uniform dry coating thickness of 5-20  $\mu\text{m}$  depending on the experiment.

Reference standard electrodes were created to provide consistent geometry and fields with which to differentiate between factual and artificial measurements and to evaluate size and spatial resolution of the probe. The standards were made from 1 inch diameter silicon wafers. The wafers were cleaned according to the standard RCA procedure [9]. An oxide layer was grown in a wet oxidation furnace (to 1160°C for 20 min.) to a thickness of approximately 0.3 - 0.33  $\mu\text{m}$ . A layer of AZP4110 photoresist was applied by spin-casting. This layer was flood-exposed with UV light and then a second layer of AZP4210 photoresist was applied. A pre-patterned mask was placed on the wafer during exposure and then both layers were developed. The oxide was etched only in the exposed areas in order to transfer the pattern. Chrome was deposited using an evaporator onto the surface of the wafer to a thickness of 500 Å for adhesion purposes. Gold was then deposited onto the wafer to a 2500-2800 Å thickness with the net deposit flush with the oxide surface. The photoresist was dissolved with acetone and the extraneous metal

lifted. The result was a pattern of gold disk electrodes of different sizes embedded in an insulator but electrically contiguous.

## RESULTS AND DISCUSSION

### Interpretation of LEIM

LEIM provides a nondestructive, in situ method of locating microscopic defects in early stages, characterizing different types of defects, and monitoring changes in electrochemical activity over the time evolution of a corroding region. Figure 1 shows an example of a time course of a blister on polyurethane coated AA2024-T3 from an early non-visible stage (24 hrs) to later actively corroding stages.

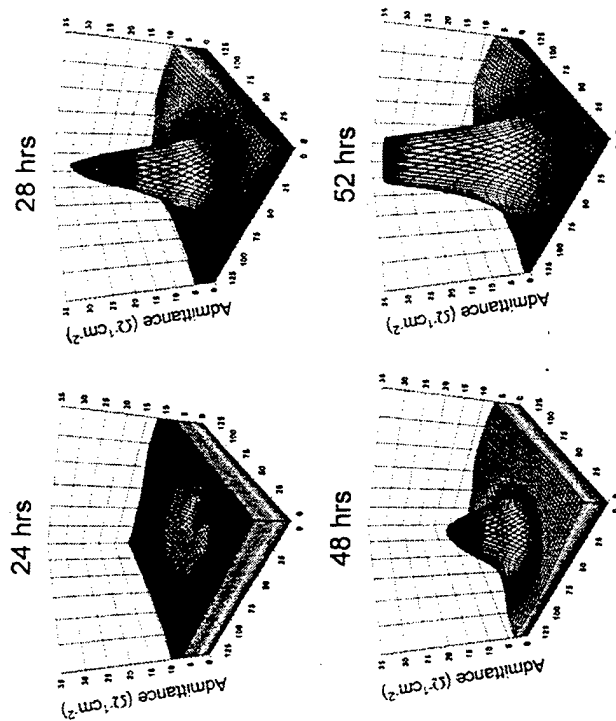


Figure 1: LEIM of a blister on 50/50 polyether-polyester polyurethane coated AA2024-T3 at different stages in blister development. Note admittance dip in early stages, metastable behavior over time, and rapid rise in peak height at 52 hrs. The x and y positions are shown in 0.1  $\mu\text{m}$  units.

Several interesting features are observed: (1) the initial decrease in admittance in the earliest stage (to 24 hrs), (2) a decrease in admittance of the blister seen by the lower peak at 48 hrs, and (3) the rapid rise in peak height at 52 hrs. While these features could



represent significant insight into the evolution of underfilm corrosion events, measurement artifact must not be overlooked.

Metastable behavior of breakdown sites has been noted on organic coated substrates [2,10]. It is, however, unclear from the maps in Figure 1 alone whether the fluctuations in peak height represents metastable behavior of the system under study or are evidence of measurement artifact. Artifact could result from instability of the Ag/AgCl reference electrodes of the LEI probe over time. However, this was deemed unlikely by way of LEI measurements on gold wire electrodes embedded in epoxy. Maps of the wires were generated repeatedly over time and the peak heights were found to be consistent between maps. If the chloridization of the electrodes were unstable, this would cause a change in the overall base value of the map rather than just the peak itself. It is particularly evident in the 52 hr map of Figure 1 that the change in peak height does not correspond to a change in base values of admittance.

Frequency dispersion [6] and concentration gradients of ions in the bulk solution [8] have also been suggested as possible causes for changes in peak height or deviations in peak properties from expected values. A change in peak height over time due to frequency dispersion is unlikely because LEIM employs a constant single frequency consistent for all maps of a given area. The conductivity of 0.6 M NaCl is also considered high enough for frequency dispersion not to pose a problem. However, it is possible for the electrochemical character of the interface (e.g. time constant, current distribution) to change over time such that phenomena observed at different characteristic frequencies dominate at different times. While this change is expected to be minor, the possible effect on peak height cannot be fully discounted. Concentration gradients in bulk solution are not likely to be a significant factor when studying coated substrates because of the lower levels of local ion transfer at a corroding area to the bulk solution on a coated metal as opposed to bare metal.

For these reasons, the apparent metastability of the blister found in LEIM has not thus far been attributed to measurement artifact. This claim is supported by the fact that local pH values have been found to change in accordance with peak height changes [3]. An active blister contains an underfilm solution of 3-4, whereas a blister shown by LEIM to have partially repassivated contains an underfilm solution of pH 6-8. Visual observation of the growth in diameter of blisters over time as documented using a digital microscope camera also revealed that growth of the blister occurred in spurts. Future experiments will attempt to correlate these growth spurts with rising peak heights in LEIM.

The change in local pH of the underfilm solution in blisters corresponding to LEIM peak height also discounts the hypothesis that biphasic water uptake of the coating [11], causes the variations in peak height of Figure 1. Preliminary studies of global EIS performed on free polymer films of neat resins used in experimentation revealed by observation of the coating capacitance over time that the majority of water uptake occurred within the first 1-2 hours of immersion. It is evident in Figure 1 that the changes in peak height occur after this point in time. It should be noted, however, that changes in peak height during the first 1-2 hours of immersion could very likely be

affected by the changes in the coating due to water uptake and plasticizing of the resin, and this possibility should not be discounted in very early stages. For the reasons given above it is suspected that the changes in peak height of LEIM in Figure 1 result from actual electrochemical metastability of the blister.

Several theories are proposed to explain the admittance dip in early stages, a phenomenon observed on several occasions. Assuming that the raised initial impedance is physical in nature, three possible explanations are proposed. A heterogeneity in the coating exhibiting a higher impedance than the film in general could be a site where a blister initiates. While the initiation of blisters at coating heterogeneities has been observed [3,12], this explanation is not considered plausible because of the fact that the LEIM of admittance dips were often preceded by maps revealing no changes in the impedance over the surface of the substrate just after the addition of solution. An admittance dip due to a coating heterogeneity from coating application would likely be present in LEIM even before a blister had initiated. It was hypothesized that water nucleation occurring at the initiation site could cause a locally decreased admittance. Impedance values were calculated for two possible equivalent circuit representations of the water layer [2] and it was concluded by the results that water nucleation could in fact cause the ca. 20 Ohm increase in impedance. The accumulation of corrosion product could also originate a decreased admittance. At this stage, the accumulation of a resistive product is considered the most likely explanation for the admittance dips.

It was suggested that the decreased admittance could be artifact due to the shape of the field emanating from a blister geometry [7]. This possibility was examined by theoretically generating the field of an equipotential disk electrode. Rotational elliptical coordinates were used following Newman [13], where the rotational elliptical coordinates  $\xi$  and  $\eta$  are related to the cylindrical coordinates  $z$  and  $r$  with the radius of the disk  $a$ .

$$z = a \xi \eta \quad (1)$$

$$r = a \sqrt{(1 + \xi^2)(1 - \eta^2)} \quad (2)$$

$$\frac{\partial}{\partial \xi} \left[ (1 + \xi^2) \frac{\partial \Phi}{\partial \xi} \right] + \frac{\partial}{\partial \eta} \left[ (1 - \eta^2) \frac{\partial \Phi}{\partial \eta} \right] = 0. \quad (3)$$

The resulting expression for the potential above the disk is found through the standard separation of variables procedure to be

$$\frac{\Phi}{\Phi_0} = 1 - \frac{2}{\pi} \tan^{-1} \xi \quad (4)$$

Equation 4 was transformed directly to cylindrical coordinates for graphing and interpretation purposes. The normal field, which is proportional to the admittance, was calculated by taking the derivative with respect to the cylindrical height coordinate  $z$ . Similar calculations for an equipotential disk have been made in other studies [7,14]. The normal field used for this study was calculated directly without the use of approximations. The results are graphed as a function of radial distance normalized to the disk radius  $a$  for various heights relative to the radius of the disk in Figure 2.

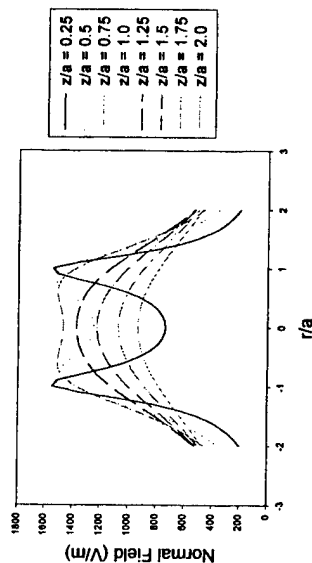


**Figure 2:** Plots of the normal field of a 300  $\mu\text{m}$  equipotential disk are shown for different heights above the surface. Dimensionless heights are given as related to the radius of the disk. Note that at  $z/a < 1$  a dip in the field can be observed, although the base value of the field is also significantly higher and a ridge at  $r/a = 1$  is present..

The coefficient  $\Phi_0$  was calculated in this case for a 300  $\mu\text{m}$  disk with a current of  $I = 100 \mu\text{A}$  and solution conductivity of  $\kappa = 56.3 (\text{Qm})^{-1}$ . It is clear from the plot that because of the preferential distribution of charge at the edge of the disk, a ridge is seen in the field at the boundary of the disk ( $r/a = 1$ ) for  $z/a < 1$ . This ridge is not observed in the LEIM of admittance dips. At values of  $z/a < 1$  a dip in the field is also seen toward the center of the disk. However, the dip does not drop below the base level of the field (i.e.  $|r/a| > 2$ ). The admittance dips in LEIM of Figure 1 begin a decrease in value from the base level of the field. For these reasons, artifact in these LEIM due to edge effects of the field are not considered to be a possible cause of the admittance dip. It should be cautioned, however, that blister geometries are generally more complex than a simple disk and artifact due to field properties should not be excluded in other cases.

#### The Effect of a Dielectric Layer on Measurement and Calculation of Fields

While the theoretical potential distributions surrounding bare electrodes of several geometries have been discussed [7,13,15], the effect of an added dielectric layer on the impedance and field measurements has not been closely examined. Free film measurements quantify general changes in coating properties but do not address measurement accuracy and interpretation using local electrochemical techniques on coated substrates. In order to address this, the field emanating from a disk electrode with the addition of a dielectric layer was considered theoretically. Gold disk electrodes with and without coating were used to obtain experimental results for comparison. Current studies are focused on solving this geometry analytically and will be published in a future paper. For the present paper, a first order approximation was calculated for the field as affected by the dielectric layer. This approximation is found by using the method of

images [16]. This method uses the fact that if a point charge  $q$  in a region of one dielectric constant (region A) is separated by a plane from a region of differing dielectric constant (region B), the resulting electric field in region A is the same as a field would be if an "image charge"  $q'$  were present in region B. This would have the effect of producing a dipole. The field in region B can be calculated as a field emanating from a new charge  $q''$  in air of different value in the position of  $q$  in region A. The diagram in Figure 3 illustrates this concept.

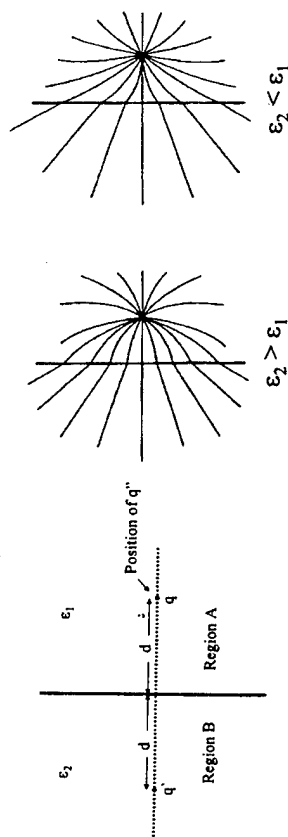


**Figure 3:** The illustration on the left shows two regions of differing dielectric constant with a charge  $q$  in region A. The image charge would be located in region B where shown. The new field in region B can be represented by considering a charge  $q''$  in air located where charge  $q$  was in region A. The schematics to the right, taken from Jackson [16], show the change in field due to the dielectric boundary.

The result is that the field in region B is the same shape as it would be from the original point charge but increased or decreased in amplitude depending on which region has the higher dielectric constant  $\epsilon$ . This method is precise for a point charge but not exact for a disk because the dielectric actually changes the distribution of charge on the disk itself. However, to first order, it can be approximated that the field from the disk electrode will also be the same as it would be without the dielectric layer but lessened by the same factor as for the point charge. This approximation becomes more valid as the thickness of the coating increases relative to the diameter of the disk. The factor by which the field is lessened is derived in Jackson [16] and the result is given below.

$$q' = -\left(\frac{\epsilon_2 - \epsilon_1}{\epsilon_2 + \epsilon_1}\right)q \quad q'' = \left(\frac{2\epsilon_2}{\epsilon_2 + \epsilon_1}\right)q \quad (5)$$

$\therefore$  the field is reduced by the factor  $2\epsilon_2/(\epsilon_2 + \epsilon_1)$ .

In this case region A is approximated to be a thin layer of associated water. The dielectric constant of associated water (80) is used in the assumption that the underfilm solution is generally water with ions, the ions contributing primarily to the conductivity. The dielectric constant of vinyl VYHH (polyvinyl chloride with polyvinyl acetate) is ca. 3. Therefore, the field is reduced by,

$$h \cdot \left( \frac{2\epsilon_2}{\epsilon_2 + \epsilon_1} \right) - 0.019 \left[ h \cdot \left( \frac{2\epsilon_2}{\epsilon_2 + \epsilon_1} \right) \right] \quad (6)$$

where  $h$  represents the height of the peak. It is important to note only the amplitude of the field is reduced, while the shape of the field remains unchanged. The equation of the field from an equipotential disk provided previously for the uncoated case is used as the original field. The percentage of decrease in the field due to the thickness of the coating is then obtained by calculating the difference in the field at different heights corresponding to the thickness. The peak values of the field at the different heights are subtracted with an original value taken at a height  $z/a=1.25$ , where  $z$  is the vertical distance from the surface and  $a$  is the radius of the disk, so that a peak value is easily discernable. In all, this provides only a rough approximation of the change in the field due to the coating but a useful one for the purposes of this paper.

Experimental measurements of the effect of a dielectric layer were performed on the reference standard electrodes described in the experimental section. Figure 4 shows an electron micrograph of the standard created.

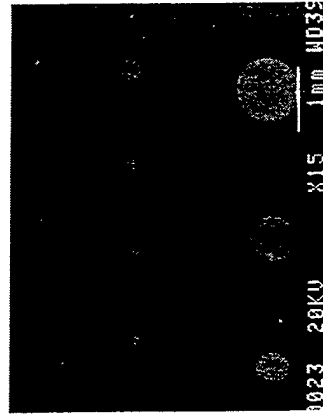


**Figure 4:** An electron micrograph is shown of the reference standard pattern. The pattern is used to test for size limitation and shape recognition of the probe and to compare theoretical calculations for a disk electrode with experiment.

The standard was created for testing detection limits and shape recognition of the LEI probe and for the purposes of comparing fields calculated for disk electrodes with actual fields. The disk electrodes decrease in diameter from 1 mm to 35  $\mu\text{m}$ . The 510  $\mu\text{m}$  disk (bottom left corner of figure) was used for comparison of theory and experiment. An LEI map was first generated for the disk with no coating. An AC amplitude of 30 mV and a frequency of 700 Hz were used. The result is shown in Figure 5. The peak value of the admittance is ca.  $2.8 \Omega^{-1}\text{cm}^{-2}$ . The reference standard was then coated by spin casting solvated vinyl VYHH to produce a thin film of 4  $\mu\text{m}$  thickness. In this case, the starting height of the field used in the percent change of peak height due to the thickness of the coating (change in height of the probe from the disk) was ( $z/a = 1.25$ )  $z = 318.75 \mu\text{m}$  with the final height being 322.75  $\mu\text{m}$ .

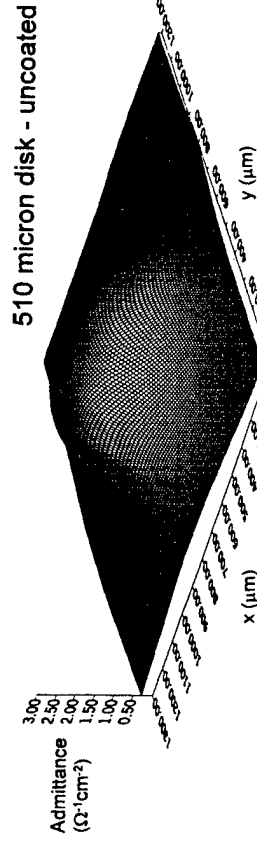


**Figure 5:** LEIM of a 510 micron diameter gold disk ( $a=255$ ) yields a peak height of ca.  $2.8 \Omega^{-1}\text{cm}^{-2}$ . This plot was taken before the disk was coated. The reference standard electrodes were immersed in 0.6 M NaCl.

The percentage change in the field was calculated to be 1.9%. The field is further reduced by the factor 0.0723 due to the dielectric nature of the coating. Therefore, the amplitude of the admittance, which is directly related to the field, should theoretically be reduced to a peak value in  $(\Omega^{-1}\text{cm}^{-2})$  given below.

$$h \cdot \left( \frac{2\epsilon_2}{\epsilon_2 + \epsilon_1} \right) - 0.019 \left[ h \cdot \left( \frac{2\epsilon_2}{\epsilon_2 + \epsilon_1} \right) \right] = 2.8(0.0723) - 0.019(0.2024) = 0.1986 \quad (7)$$

This formula does not take into account the settings of the system itself i.e. amplification, frequency, current measuring resistors, etc. This makes a direct comparison between theoretical and experimental results difficult. In fact, no peak was seen in the LEIM generated for the coated disk. Even with an 80 mV AC perturbation applied around the open circuit potential of the cell, no evidence could be found of the disk beneath the coating. Under open circuit conditions, a coated gold microelectrode did not have a sufficient current to establish a measurable voltage drop at the micro-reference electrode. However, the use of a 40 mV DC bias, with 1 minute of bias applied before measurement as pretreatment, and an AC perturbation of 30 mV did allow the establishment of such a voltage drop. The resulting LEIM of the disk in the case of no DC bias and in the case of 40mV DC bias are shown in Figure 6. The fluctuations in admittance are due to coating which was not completely uniform.

This observation illustrates that underfilm corrosion sites on coated alloys cannot be well represented by assuming a simple disk electrode geometry. The ionic exchange and local current flows of these regions must be considered as well. It is known from cyclic voltammetry of gold that even significant perturbations to the potential will not necessarily induce a faradaic current flow. However, the noble nature of gold makes it the most stable choice for reference standards for the purpose of quantifying probe capabilities and bare surface impedance measurements. New methods will need to be devised to experimentally quantify the effect of the coating on the measured field.

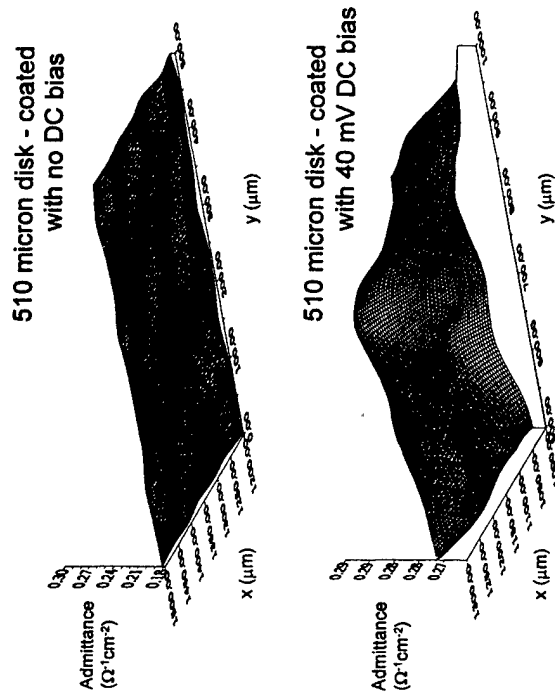


**Figure 6:** LEIM of the 510 µm disk after it has been coated with a 4 µm vinyl film is shown above. The lower figure is LEIM of the same disk with an applied DC bias of 40 mV and pretreatment of 60 s.

However, present theoretical calculations do confirm that any impedance or potential measurements taken above the surface of a coated substrate must consider the effect the coating and changes in coating properties. Calculations also provide an approximate change in the field of actual corroding areas of a coated metal due to the effect of the coating.

## CONCLUSIONS

The use of LEIM as a function of time can provide insight into the breakdown processes on coated alloys. The technique is nondestructive and can be used *in situ*. However, it is important that upon interpretation of measurements, possible contributions from artifact are considered. Artifact must be ruled out in a given instance, in order to attribute results to various electrochemical, chemical, or physical causes. Several possible sources for artifact were explored regarding measurements made using LEIM on coated AA2024-T3.

1. The observance of metastability in LEIM peak height of a blister during its evolution was examined. The change in height was not likely to be caused by instability of the micro-reference electrodes, frequency dispersion, or concentration gradients. It was

suspected that the metastability is electrochemical in nature. This conclusion was supported by visual observation of growth spurts and by changes in local pH corresponding to the electrochemical activity found in LEIM.

2. An initial dip in admittance was found in early stages of blister development. Artifact due to edge effects of the field from the corroding region was shown through theoretical calculations of the shape of the field as measured at different heights above the surface to be an improbable cause of the dip. Water nucleation and accumulation of corrosion products were offered as possible explanations.
3. The effect of the coating as a dielectric layer on measurement of impedance was considered. A first order approximation by the method of images was used to calculate the theoretical change in the field above a disk electrode due to the presence of a coating. The shape of the field was not expected to change, however, the amplitude of the field was expected to decrease. This effect becomes more significant as the coating thickness increases.
4. Coated gold electrodes showed no peak in LEIM unless a DC bias was applied. This suggested the necessity of a significant current through the coating in order to establish a measurable potential in solution. It was concluded that representation of an underfilm corroding region by a disk electrode alone is insufficient. Calculations do provide an estimate of the effect of the coating for experimental situations on coated metals.

## ACKNOWLEDGMENTS

The authors would like to thank the Air Force Office of Scientific Research for their funding of this project, Dr. Vittorio Celli for consultation in theoretical calculations, and Lisa DeLong for assistance in reference standard production.

## REFERENCES

1. R.S. Lillard, P.J. Moran, H.S. Isaacs, *J. Electrochem. Soc.*, **139**(4):1007 (1992).
2. A.M. Mierisch, S.R. Taylor, in *Electrically Based Microstructural Characterization II*, Vol. 500, Materials Research Society, Warrendale, PA, p. 35 (1998).
3. A.M. Mierisch, J. Yuan, R.G. Kelly, S.R. Taylor, "Probing Coating Degradation on AA2024-T3 Using Local Electrochemical and Chemical Techniques" *J. Electrochem. Soc.* In press.
4. M.W. Wittman, S.R. Taylor, in *Advances in Corrosion Protection by Organic Coatings II*, The Electrochem. Soc., PV **95-13**:158-168 (1995).
5. F. Zou, D. Thierry, *Electrochimica Acta*, **42**(20-22):3293 (1997).
6. E. Bayet, F. Huet, M. Keddam, K. Ogle, H. Takenouti, in *Materials Science Forum*, V289-282 (1997).
7. H.S. Isaacs, *J. Electrochem. Soc.*, **138**(3):722 (1991).
8. E. Bayet, F. Huet, M. Keddam, K. Ogle, H. Takenouti, in *Proceedings of the 4<sup>th</sup> International Symposium on Electrochemical Impedance Spectroscopy*, Angra dos Reis, Brazil (1998).

9. S. Wolf, R.N. Tauber, in *Silicon Processing for the VLSI Era* Vol. 1 1986, Sunset Beach, California: Lattice Press.
10. J.A. Grandle, S.R. Taylor, *Corrosion*, **50**(10):792 (1994).
11. J.E. Castle, in *Advanced Monitoring and Analytical Techniques*, Ed. By F. Mansfeld, W.H. Smyrl, *Proceeding of Corrosion*, (1997).
12. J.E.O. Mayne, D.J. Mills, *J. Oil Col Chem Assoc.*, **58**:155 (1975).
13. J. Newman, *J. Electrochem Soc.*, Technical Notes, May 1996.
14. F. Zou, D. Thierry, H.S. Isaacs, *J. Electrochem Soc.*, **144**(6):1957 (1997).
15. M.W. Verbrugge, D.R. Baker, J. Newman, *J. Electrochem. Soc.*, **140**(9):2530 (1993).
16. J.D. Jackson, *Classical Electrodynamics*, p148, John Wiley & Sons, New York (1975).

# UNDERSTANDING COATING AND SUBSTRATE HETEROGENEITIES USING ELECTROCHEMICAL IMPEDANCE METHODS

A. M. MIERISCH, S.R. TAYLOR

Center for Electrochemical Science and Engineering, Dept. of Materials Science,  
University of Virginia, Charlottesville, VA 22903, sr6p@s1.mail.virginia.edu

## ABSTRACT

This study examines natural breakdown events on organic coated AA 2024-T3 coated using Local Electrochemical Impedance (LEI) mapping (M) and spectroscopy (S). LEIM was able to identify not only different types of defects on this system, but also provided information about the kinetics and stages of development of these defects. Supportive evidence regarding the impedance characteristics of these defects was provided by Capillary Electrophoresis (CE). Data from early stages of defect development indicate that an increased impedance develops at the site. This is related to either the development of aggregated water or electrolyte, as well as corrosion product development. Direct evidence of defect healing is also provided.

## INTRODUCTION

The corrosion protection provided by organic coatings on metals has traditionally been investigated with electrical or electrochemical methods (e.g. open circuit potential, electrochemical impedance spectroscopy, electrochemical noise) which provide surface averaged data [1-6]. Frequently, the time course of these measurement clearly indicate breakdown events which are often metastable [7], and believed to occur at discrete sites on the surface [8,9]. While it is logical to think of breakdown events on organic coated alloys as occurring at local sites, particularly on multi-phase engineering alloys, clear demonstration of these events on contiguous coatings has been forthcoming. A method which could locate and evaluate these breakdown sites *in situ* could also be invaluable in understanding the mechanistic issues which control the life/death cycle of these defects, as well as the source of these defects. Questions remain as to whether the defects originate in the coating, the substrate, or whether they exist in both coating and substrate and must be juxtapositioned. Knowledge of the events at these sites will be important to understanding the parameters which control the performance of coated metal substrate.

A method for mapping the local impedance of coated metal substrates was introduced by Lillard, Moran, and Isaacs [10] and later expanded upon in the investigation of a variety of intentional chemical and physical defects [11,12]. Although numerous electrochemical methods are available for the mapping of local electrochemical phenomenon [13-18], Local Electrochemical Impedance Spectroscopy (LEIS) is particularly well suited for the investigation of organic coated substrates due to the AC nature of the excitation which lowers the impedance of the dielectric interface.

As mentioned above, this technique has been used thus far to investigate simulated chemical and physical defects on organic coated steels. The objective of the present research is to locate and characterize local electrochemical breakdown events that

occur naturally on a coated aluminum alloy when exposed to an aqueous chloride environment. An understanding of the nature of these defects will eventually lead to an understanding of the factors which limit the service life of coated engineered products, and thus to ways for improvement.

## EXPERIMENTAL METHODS

Local electrochemical impedance measurements were made with a five electrode arrangement shown in Figure 1 and discussed elsewhere [11,12]. The interface is excited potentiostatically using a conventional three electrode technique, however the local current is assessed by two vertically displaced micro-reference electrodes. The potential difference between these two electrodes is amplified, then converted into a local current density knowing the solution conductivity and using Ohm's law (see Figure 1), and compared to the excitation voltage via a Frequency Response Analyzer (FRA) to generate the local impedance. A 15 mV sine wave excitation at a fixed frequency (500 to 700 Hz) was used in the case of LEIM, and a swept frequency (from 1 Hz to 10 kHz) in the case of LEIS. The DC potential and AC excitation of the coated samples were established with a Solartron 1286 Electrochemical Interface and Solartron 1255 HF FRA all under computer control.

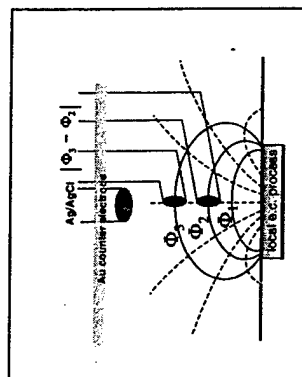


**Figure 1.** Schematic of five electrode configuration used to acquire LEIS data. Note current lines (dashed) and local field lines (solid) associated with local defect.

The local impedance system can be used in two operational modes. In one mode, the probe and sample substrate can be fixed at a single position while the excitation frequency is swept through a range. These authors prefer to call this mode Local Electrochemical Impedance Spectroscopy (LEIS). In the second mode, the excitation frequency can be fixed as the local admittance magnitude is mapped over the surface. This mode is called Local Electrochemical Impedance Mapping (LEIM). The local admittance is mapped for convenience, so that local breakdown events appear as peaks rather than valleys. In the present system, the mapping is accomplished by holding the electrodes fixed and moving the substrate with a positioning table. The positioning table used in this study consisted of a modified Teledyne TAC model PR-52 automatic wafer probe with adjustable X and Y step sizes ranging from 25 to 25,000  $\mu\text{m}$ .

The substrate material used in all experiments was AA 2024-T3 in the form of 1 mm thick sheet. Samples were cleaned in high purity water ( $18 \text{ M}\Omega \text{ cm}^2$ ), then ultrasonically cleaned in hexane for 5-10 minutes and left to air dry at room temperature.

Model coated substrate systems were made with two coating chemistries, a vinyl (Vinyl VYHH) and polyurethane. The vinyl was a copolymer of polyvinyl chloride and polyvinyl acetate. The polyurethane coatings were either a 100% polyether polyurethane, or a polyurethane composed of 50% polyether and 50% polyester. Both the 100% and 50/50 polyurethanes were mixed with isocyanate, a dibutyl tin dilaurate catalyst and methyl ethyl ketone solvent. All coatings were spin cast onto the cleaned aluminum samples with a resulting dry coating thickness of ca. 10  $\mu\text{m}$ . The application of neat resin chemistries directly to an untreated substrate (i.e. no conversion coating or primer) is a model system and is not meant to represent a commercial system. The long-term goal of this project will be to eventually examine the effects of the various components within a commercial coating, as well as the effects of various surface treatments (e.g. chromates, alternate conversion coatings, primers, etc.).

Electrochemical test cells were established on the coated samples by attaching glass cylinders to the coating. The test electrolyte consisted of room temperature 0.6M NaCl with ambient aeration.

## RESULTS AND DISCUSSION

Initial characterizations of "inherent" defects that develop naturally on coated AA 2024-T3 substrates focused on barely visible spots. After making LEI maps as a function of time on several of these spots, it became apparent that two types of defects were evolving. The distinction between these two types of defects can be seen electrochemically in the LEI maps shown in Figures 2 and 3. Differences also became visually apparent with time as one type was more active, growing to a bright red colored blister site 2 to 5 mm in diameter within several days. While the other type of defects were more passive, either black or white, and were smaller in size (1 to 2 mm diameter). For convenience, the active blisters will be referred to as "red" blisters, and the other type

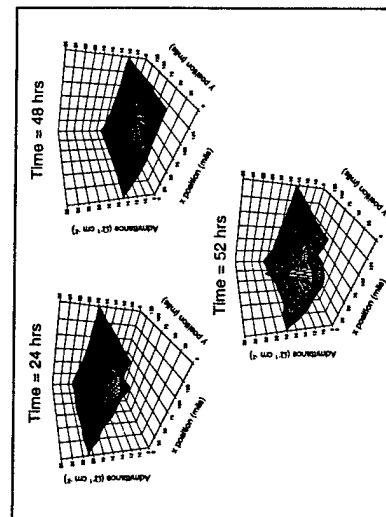


**Figure 2.** LEI maps of red colored blister at various times. Sample consisted of 10  $\mu\text{m}$  thick Vinyl VYHH on AA 2024-T3. The electrolyte was 0.6 M NaCl.

as "black" blisters. The distinctive active and passive character of the red and black defects respectively is shown in the LEIMs and local impedance spectra in Figure 4. Although the data shown in Figures 2, 3, and 4 are from samples with different coating chemistries, the statements made concerning their characteristic development, was consistent regardless of the coating material.

Further testing of these defects was performed through the analysis of the solution chemistry beneath the coating using Capillary Electrophoresis (CE). CE is a technique which can identify and determine the concentration of the anions and cations within very small quantities of solution (10 nl) at very low levels of ion concentration (e.g. ppb to ppm). The electropherograms for the black and red blister solutions using two different carrier solutions (UVCat I and UVCat II) are shown in Figure 5. The two background carriers were needed to highlight specific ions.

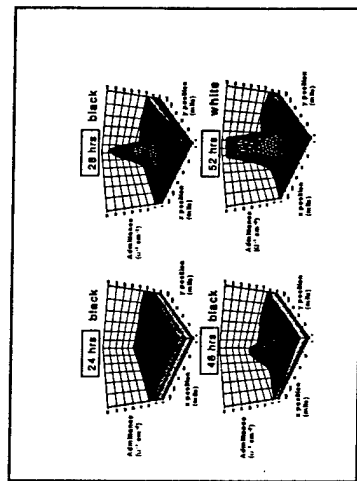


**Figure 3.** LEIM of black colored blister at various times. Sample consisted of 10  $\mu\text{m}$  thick polyurethane (50/50) film on AA 2024-T3. The electrolyte was 0.6 M NaCl.

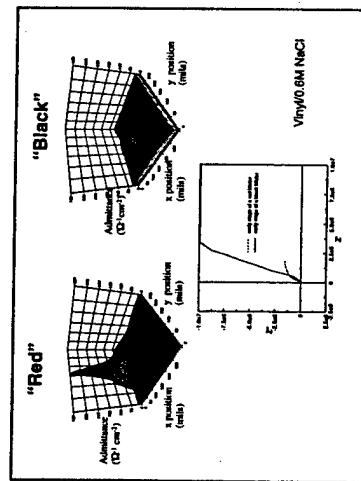


**Figure 4.** Comparison of LEIM and LEIS (below) of red and black defects beneath a vinyl coating at 35 hours. Notes higher admittance in map and lower polarization resistance in spectra for the red site, and converse for black.

It is clear from this data, that the red blisters contain significant concentrations of  $\text{Cu}^{2+}$ ,  $\text{Al}^{3+}$ , and  $\text{Mg}^{2+}$  ions, whereas the black blister solution contained essentially no Cu or Al ions, but did contain  $\text{Mg}^{2+}$  and  $\text{Zn}^{2+}$ . Although future experiments will utilize other surface analysis techniques (e.g. Scanning Auger Microscopy) to investigate the origins of these defects, it is speculated at this point that the behavior of these defects is related to specific precipitates within the substrate such as  $\text{Al}_2\text{CuMg}$  (S phase)[19] in the case of red spots, and perhaps a magnesium bearing precipitate for the black/white spot. It should be noted that the red spots formed in the presence of various electrolytes including NaCl, KCl, and  $\text{Na}_2\text{SO}_4$ .

The "black" spot had the character of changing from black to white. The time sequence of LEIMs shown in Figure 3 indicate that the color changes along with the individual maps. This color change may be related to the conversion of a magnesium oxide as the chemistry within the blister changes. It is also interesting to note that the

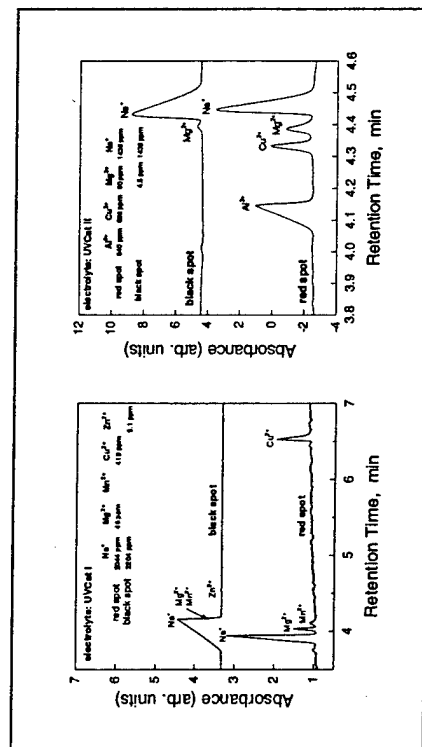


**Figure 5.** Electropherograms of underfilm solution from red and black defects of Figures 4.

open circuit potential of the sample became significantly more negative at the time of the color change. Further studies will hopefully explore the origins of these changes.

Also of note, is the time sequence of the admittance peaks in the LEIMs for the black defect. It can be seen that at early times the admittance grows, then gets smaller, and then grows catastrophically. This is strongly suggestive of a metastable type defect that "heals" itself with time. It has been postulated by others that "healing" of films can occur through the sealing effects of corrosion products precipitated at the defect site [8]. In this case the defect eventually re-establishes itself.

Another interesting and unexpected result from LEIM studies of early stages of defect development was that the earliest observations of initial defects began with a decrease in the admittance magnitude relative to the background. An example of this is



seen in Figure 6. This behavior is counterintuitive. Intuitively, one would expect that the admittance would increase (impedance would decrease) as electrolyte penetrates the film and initiates corrosion.

In Figure 6, the difference between the lowest point in the trough and median point in the background plane is ca.  $10 \text{ ohm}^{-1}$ . This difference converts to an increase of 20 ohms. It has been suggested by some that this decrease may be artefactual in nature due to nonuniform current distribution. Since the microreference electrodes only sense the vertical component of the local current, a shift of cathodic current from the counter electrode to local surrounding cathodes would alter the measurement. While it is extremely important to consider current distribution issues in the

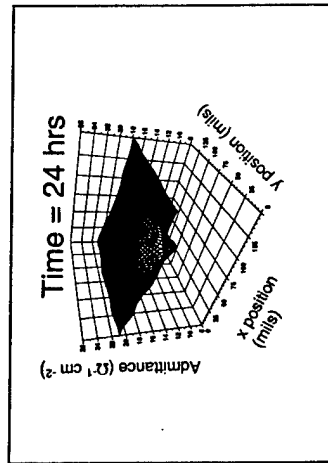


**Figure 6.** Decrease in admittance observed during early stages of defect development. Sample is 10 mm thick polyurethane (100%) on AA 2024-T3 in 0.6 M NaCl.

measurement of these local events, it is unlikely that it is the source of the observed dip. The redistribution of current as described would increase the apparent impedance of the local site, but the defect impedance would not be above the background value (admittance would not be below the background value). Even if the current reversed direction (anode became cathode), it would not change the LEI map since we are plotting magnitudes.

Another possibility proposed by others is that this dip in the admittance may be the result of nucleated water (or hydroxide)[20]. To examine the efficacy of this theory, calculations based on two models were considered. In the first model, it was assumed that a "nucleus" of pure water in the form of a disk was placed at the metal/polymer interface and only the dielectric properties of the materials were considered, i.e. no ions or charge transfer were considered. In the second model, it was assumed that ions were present in solution and interfacial polarization could occur. The physical representation of the models and values assumed for the calculation are shown in Figure 6 and Table 1 respectively. In Model 2 the assumed double layer capacitance and charge transfer resistance were  $25 \mu\text{F}/\text{cm}^2$  and  $1000 \Omega \text{ cm}^2$  respectively. Based on these calculations, it is conceivable that either the collection of associated pure water of sufficient thickness or the inclusion of electrochemical processes could cause the observed dip in the admittance.

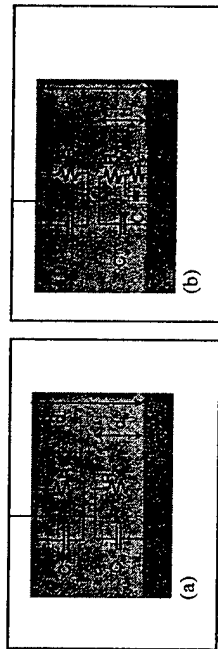


**Figure 6.** Circuit models used to calculate the local impedance associated with the collection of a small mass of pure water (Model I) or the development of an electrochemical interface in ionic solution (Model II).

	$d_w$	$d_c$	$\rho_w (\Omega \text{ cm}^2)$	$\rho_c (\Omega \text{ cm}^2)$	$K_w$	$K_c$	$Z @ 500 \text{ Hz}$
<b>Model 1</b>	$0.1 \mu\text{m}$	$10 \mu\text{m}$	$1.8 \times 10^7$	$10^{14}$	80	5	$2 \Omega \text{ cm}^2$
<b>Model 2</b>	$1.0 \mu\text{m}$	same	same	same	same	same	$20 \Omega \text{ cm}^2$
	$1.0 \text{ nm}$	same	same	same	same	same	$20 \Omega \text{ cm}^2$

**Table 1.** Values of constants and dimensions used in the calculation of local impedance.

Another consideration for the decreased admittance in the initial stages of defect development is that a resistive oxide or corrosion product forms. As stated previously, the eventual goal of this project will be to try to examine the aluminum surfaces of autopsied specimens to characterize the surface chemistry at these early stage defects.

The effect of corrosion product on the LEI map is possibly seen in Figure 7. In this map, the admittance peak is surrounded by an admittance trough. This peak to trough behavior might be explained by the recent proposed mechanism for filiform corrosion on aluminum [21]. In this mechanism, the underfilm corrosion of aluminum is established by an active anode at the periphery of the site. This region is of low pH. The cathode is established more to the center of the site, and becomes alkaline. The low and high pH regions can be established by the development of a precipitated corrosion product which acts as a separator of these two regions.

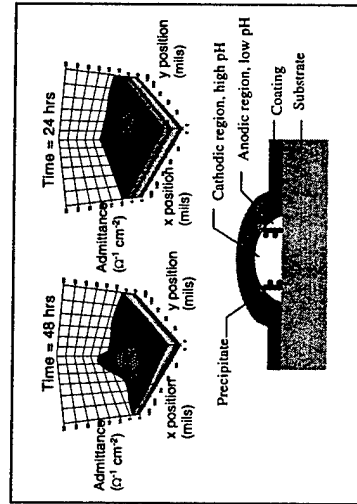


**Figure 7.** LEI map of 50/50 polyurethane on AA 2024-T3 in 0.6 M NaCl at 24 and 48 hours. Note the trough at the base of the peak. This might be explainable by the development of corrosion product which separates the anodic and cathodic regions of the corrosion process.

## CONCLUSIONS

Local Electrochemical Impedance Mapping (LEIM) and Spectroscopy (LEIS) has been successful at locating and characterizing natural electrochemical defects on model coated substrates using vinyl and polyurethane coatings on AA2024-T3. Several types of natural defects have been observed, differing in rate of development, admittance magnitude (severity), and underfilm chemistry suggesting different precipitates as sites of origin. In the development of defects in this coating/alloy system, several important stages of defect development have been documented. Early development starts as a decrease in the admittance (increase in the impedance). This could be explained by the development of an underfilm water or electrolyte layer, or the development of an oxide or corrosion product. It has also been observed that defects can heal and re-grow, possibly from the development of an expansive corrosion product.

## ACKNOWLEDGEMENTS

The authors gratefully acknowledge the Air Force Office of Scientific Research for financial support of this research, and J. Yuan and Prof. R.G. Kelly for their contribution of Capillary Electrophoresis data and analysis.

## REFERENCES

1. H. Leidheiser, Jr., Corrosion, 39(5):189 (1983).
2. F. Mansfield, M.W. Kendig, S. Tasi, *Corros. Sci.*, 23(4):317 (1983).
3. S.R. Taylor, *IEEE Trans. Elec. Insul.*, 24(5):787 (1989).
4. S. Haruyama, M. Asari, Tsuru, "Corrosion Protection by Organic Coatings", The Electrochemical Society, Proc. 87-2 (1987), p.197.
5. S. Hirayama, S. Haruyama, *Corrosion*, 47(12):953 (1991).
6. C.T. Chen and B.S. Skerry, *Corrosion*, 47(8):598 (1991).
7. J.A. Grandle, S.R. Taylor, *Corrosion*, 50(10):792 (1994).
8. J.E.O. Mayne, D.J. Mills, *J. Oil Col Chem Assoc.*, 58:155 (1975).
9. R.C. Bacon, J.J. Smith, F.M. Rigg, *Ind. Engr. Chem.*, 40(1):161 (1948).
10. R.S. Lillard, P.J. Moran, H.S. Isaacs, *J. Electrochem. Soc.*, 139(4):1007 (1992).
11. M.W. Wittmann, S.R. Taylor, in Advances in Corrosion Protection by Organic Coatings II, Ed. by J.D. Scantlebury and M.W. Kendig, The Electrochem Soc., PV 95-13:158-168 (1995).
12. S.R. Taylor, M.W. Wittmann, in Electrically Based Microstructural Characterization, Ed. by R.A. Gerhardt, S.R. Taylor, and E.J. Garboczi, Vol. 411, MRS (1996), p.31.
13. H.S. Isaacs, B. Vyas, in Electrochemical Corrosion Testing ASTM STP 727, Ed. by F. Mansfeld, U. Betocchi, ASTM 1981, p. 3.
14. I.L. Rosenfeld, I.S. Danilov, *Corros. Sci.*, 7:129 (1967).
15. H.S. Isaacs, *Corros. Sci.*, 28(6):547 (1988).
16. M. Stratman, H. Streckel, *Werkstoffe und Korrosion*, 43:316 (1992).
17. J.V. Standish, H. Leidheiser, Jr., *Corrosion*, 36(8):390 (1980).
18. H.S. Isaacs, M.W. Kendig, *Corrosion*, 36(6):269 (1980).
19. R.G. Buchheit, R.P. Grant, P.F. Hlava, B. McKenzie, G.L. Zender, *J. Electrochem. Soc.*, 144(8):2621 (1997).
20. J.E. Castle, in Corrosion Resistant Coatings, NACE, p.165 (1997).
21. J.H.W. deWit, D.H. van der Weijde, H.J.W. Lenderink, paper no. 102, 13<sup>th</sup> International Corrosion Congress, 1997.

## Probing Coating Degradation on AA2024-T3 Using Local Electrochemical and Chemical Techniques

A. M. Mierisch,\* J. Yuan, R. G. Kelly,\*\* and S. R. Taylor\*\*\*,z

Center for Electrochemical Science and Engineering, Department of Materials Science and Engineering, University of Virginia, Charlottesville, Virginia 22903, USA

The local electrochemical and chemical characteristics of intrinsic breakdown sites on organically coated aerospace alloys were investigated. Local electrochemical impedance spectroscopy and mapping were used in conjunction with capillary electrophoresis, local pH, and local open-circuit potential measurements to classify the electrochemical activity and chemical properties of individual failure sites on organic coated AA 2024-T3 exposed to an aqueous environment. Panels coated with vinyl or polyurethane and exposed to chloride solutions were examined. Several different types of blister sites, both active and passive, were observed and characterized. A strong correlation was observed between the underfilm chemical characteristics, the electrochemical impedance, and the visual appearance of the blisters. Evidence suggestive of hydrolysis of the polyurethane coating was found during the propagation of coating defects.

© 1999 The Electrochemical Society. S0013-4651(99)01-051-4. All rights reserved.

Manuscript submitted January 13, 1999; revised manuscript received June 30, 1999.

The service life of an organic coating on a metal substrate is determined by variables associated with the environment, the coating, the substrate, and the interphasial chemistry that develops between the substrate and the coating. Although our basic understanding of the corrosion and materials issues within each of these regions is increasing, our understanding of the interactions among them and how these interactions lead to failure is limited. This gap in understanding is, in part, associated with the need to understand the origins of failure. Because corrosion failures on coated alloys initiate and grow from a local site, it is essential to know whether heterogeneities within the coating material, substrate alloy, or both are controlling the initiation of corrosion events. An understanding of the localized breakdown events of a coated alloy substrate will require a description of the local chemical and electrochemical events that take place within the coating and at the polymer/metal interface.

Whereas the characterization of local electrochemical events on bare metal surfaces has been widely investigated,<sup>1-7</sup> the examination of local events on coated alloys has been less extensive.<sup>8-12</sup> It has been only recently that investigations of local defects of coated alloys has moved from the characterization of extrinsic (*i.e.*, man-made) defects to the characterization of intrinsic<sup>10</sup> (*i.e.*, naturally occurring) heterogeneities. The use of local electrochemical impedance methods has enabled the identification and monitoring of local breakdown processes of coatings on certain alloys. However, a more detailed understanding of defect origins and growth characteristics requires information on substrate microstructure and surface chemistry, as well as the underfilm solution chemistry that develops at a local site.

Prior research on the analysis of underfilm chemistry has been limited to either pH determinations<sup>13-15</sup> or to more detailed chemical analyses of blisters on coated steel under cathodic conditions.<sup>16-20</sup> Acquiring information on the chemistry within these late stage defects represents an important step in the evolution of coatings research. Nonetheless, it would be of greater benefit to be able to sample the solution chemistry of an underfilm corrosion site in its early stages of development. Capillary electrophoresis (CE) is a technique that has shown feasibility of sampling and analyzing extremely small volumes of solutions (*e.g.*, *ca.* 30 nL) from occluded corrosion sites to speciate and quantify the ions present.<sup>21-23</sup> Its potential application to analyzing the underfilm chemistry beneath early stage blisters has been explored in the present study.

This investigation was an initial venture into understanding the breakdown of organic coatings on an aerospace alloy, AA2024-T3,

through the characterization of the local electrochemical and chemical changes at the local sites. Information on the location and electrochemical nature of these defects along with the interfacial chemistry that develops beneath the coating is an essential step in understanding the events which lead to the deterioration of organic coatings on alloy substrates.

### Experimental

**Materials.**—Samples of AA 2024-T3 were cut from 1 mm thick sheet into 6.5 × 6.5 cm panels. The samples were cleaned in a four-step procedure. First they were scrubbed with Alconox® in high purity water (18 MΩ cm), then ultrasonically cleaned in hexane for 5-10 min. Any inks used for identification purposes were then removed with acetone, and finally, any residues were removed with isopropanol. The samples were left to air dry under ambient conditions.

Cleaned aluminum samples were coated with various neat resins. No surface pretreatment was performed (*e.g.*, conversion coated). Initial experiments were performed on samples coated with Vinyl VYHH, a copolymer of polyvinyl chloride and polyvinyl acetate. Polyurethanes of different soft segment chemistry, *i.e.*, varied ratios of polyether and polyester, were also examined. These coatings consisted of a polyurethane composed of 100% polyether and a polyurethane composed of 50% polyether and 50% polyester. Each resin formulation was mixed with isocyanate (3.2 g ether/4 g isocyanate), a dibutyl tin dilaurate catalyst and methyl ethyl ketone solvent (1 cm<sup>3</sup>). A third polyurethane was also examined, consisting of a two-part polyester polyurethane mixed with butyl cellosolve, and represents the resin used in commercial polyurethane primers.

All coatings were spin cast onto the cleaned samples to a dry coating thickness of 5-10 μm. Samples were dried in a dessicator for at least 36 h after coating application before exposure to corrosive environments.

Glass cylinders with an inner diameter of 4.3 cm were fixed to the substrate using silicone rubber adhesive sealant (GC Electronics, Rockford, IL), creating a reservoir for test electrolyte. This provided a 14.5 cm<sup>2</sup> exposure area. Most experiments were made using 0.6 M NaCl solution, although 0.1 M or more dilute solutions of NaCl, KCl, NaSO<sub>4</sub>, and K<sub>2</sub>SO<sub>4</sub> were also used in specific cases. All chemicals were reagent grade. All solutions were quiescent and at ambient temperature.

**Electrochemical test methods.**—Local electrochemical impedance (LEI) measurements were made using a LEI probe developed in-house after the original design of Lillard *et al.*<sup>8</sup> and enhanced for investigating various physical and chemical coating defects.<sup>9,24-26</sup> The method uses a five-electrode configuration. A diagram of the probe configuration is shown in Fig. 1. Potentiostatic polarization was achieved with a

\* Electrochemical Society Student Member.

\*\* Electrochemical Society Active Member.

<sup>z</sup> E-mail: srt6p@Virginia.edu

standard three-electrode configuration, and the local potential was measured between two vertically displaced Ag/AgCl microreference electrodes each 125  $\mu\text{m}$  in diam. This local potential was amplified and scaled to the local current density using Ohm's law and the known solution conductivity. A frequency response analyzer (FRA) compared this local current density to the excitation voltage and the resulting local impedance was calculated. Although the local current density was compared to a global voltage, the 250  $\mu\text{m}$  diam Ag/AgCl reference electrode used to obtain the global voltage was typically less than 1 mm horizontally and 100  $\mu\text{m}$  from the site under study. The potential and excitation frequencies were established with a Solartron 1286 electrochemical interface and a Solartron 1255 HF FRA, respectively, both under computer control. A 10 mV sine wave excitation was typically applied with frequency depending on the specific experiment. The most invaluable asset to this technique is that nondestructive assessment of the local interfacial impedance could be made *in situ*.

The LEI probe was operated in two modes. In the first mode, referred to as local electrochemical impedance mapping (LEIM), the excitation frequency was fixed as the probe was stepped across a designated area of the sample surface. Prior testing had determined 700 Hz to be an optimum frequency for mapping. The local current density was measured at each position and the calculated local admittance magnitude (inverse of impedance magnitude) was plotted as a function of  $x, y$  position. Admittance was plotted rather than impedance so that areas of increased electrochemical activity generally appeared as peaks. The positioning stage consisted of a Tele-dyne TAC model PR-52 automatic wafer probe with adjustable  $x$  and  $y$  direction stepping motors, which moved the substrate in controlled steps while holding the probe fixed. Step size was adjustable from 25 to 25,000  $\mu\text{m}$ .

In the second mode, local electrochemical impedance spectroscopy (LEIS), the substrate is fixed in position so that the electrodes are suspended directly above the electrochemical region of interest, and the excitation frequency is swept through a spectrum, usually ranging from 1 Hz to 3 kHz. The upper range is limited to ca. 2–3 kHz, most likely as a result of the instrumentation amplifier used to boost the signal from the microreference electrodes. Results are generally plotted in the standard Nyquist and/or Bode formats.

Capillary electrophoresis, which speciates ions based on their differing mobilities in an applied electric field,<sup>27–30</sup> was used to examine the ionic content of underfilm solution. Analysis of ionic content can be made using nanoliter volumes of solution. Bulk solution was removed briefly from the cell and solution from inside the blister was drawn using a World Precision Instruments model UMP microinjection syringe system. The microsyringe can extract volumes as small

as 52 pL. Generally between 300 and 1500 nL of solution were drawn and then diluted for use in CE analysis. In this way, even very small blisters still in early stages could be analyzed. However, it should be noted that because the syringe breached the film, this technique did not allow for further *in situ* testing. Analyses were made using several electrolytes in order to detect all species of possible interest. Details of the CE analysis methods can be found elsewhere.<sup>30</sup>

The local pH and open-circuit potential were also measured inside blister sites. A calibrated Ir/IrO<sub>2</sub> electrode was used to measure the local pH inside the blisters, and a Ag/AgCl electrode was used in conjunction with a standard reference electrode to measure the local open-circuit potential (OCP) inside. Each electrode had a 250  $\mu\text{m}$  diam tip and both measurements can be made in blisters as small as 1 mm. To make the measurements, the combination Ir/IrO<sub>2</sub> and Ag/AgCl microelectrode was used to pierce a blister on a sample from which the bulk electrolyte had been removed.

Scanning electron microscopy (SEM) was used in conjunction with energy dispersive spectroscopy (EDS) to examine the surface features of substrate corrosion and to analyze the elemental content of different regions of the corroded area. An accelerating potential of 20 kV and a probe current ranging from  $3 \times 10^{-11}$  to  $1 \times 10^{-10}$  A were used.

## Results and Discussion

**Classification and comparison of failure sites.**—Several types of corrosion sites on the coated substrate system were observed which differed in both electrochemical behavior and physical attributes. One striking difference between many of the defects at later stages of development was their color. For this reason defects will, for convenience, often be referred to throughout this paper by their color. When using VYHH resin, two later-stage defect types, having either a reddish or black color, were commonly observed. The black blister sites were essentially round with diameters of ca. 1–2 mm, attained within 2–7 days of exposure. The red blister sites were irregularly shaped with a size of 1–7 mm, attained within 1–2 days of exposure.

LEIM was performed on examples of both of these blisters and the results are shown in Fig. 2. It is evident from the surface plots that the red blister showed a significantly higher admittance peak than the black, suggesting that higher currents were emanating from the red blister. The electrochemical character was confirmed with LEIS, performed on similar defect sites when they were in an earlier (microscopic) stage of development. Figure 3 shows a lower polarization resistance for the "red" site, again indicating higher electrochemical activity at the future red blister site. It is also interesting to note the lower admittance surrounding the peak in the LEI map of the black blister.

Observation of both blisters before and after coating removal under a stereomicroscope indicated that more severe corrosion had taken place at the red sites. This attack was accompanied by active hydrogen evolution, observed within the blister prior to coating removal and by markedly deeper pits, observed after the coating was removed. Figure 4 shows an SEM micrograph with an example of a pit formation at a red blister site where the coating has been removed. These findings prompted the use of supporting techniques to further investigate the more active red blister in particular.

The ionic content of the solution inside blister sites from a vinyl-coated sample was analyzed using capillary electrophoresis. The red blister solution typically contained Cu<sup>+2</sup> (0.05 M), Al<sup>+3</sup> (0.58 M), and Mg<sup>+2</sup> (0.03 M) ions, whereas the black blister solution contained only a small amount of Mg<sup>+2</sup> (0.0004 M) ions. The red color was a result of replated copper. The copper was likely dissolved from second-phase particles that had been physically displaced by the force of hydrogen evolution and then oxidized. Aluminum and magnesium dissolve preferentially from the S phase (Al<sub>2</sub>CuMg),<sup>31–35</sup> which, interestingly has the same elemental content, although not the stoichiometry as the eventual blister solution. The origin of the black color in the black blisters is as yet unknown.

Previous investigations support the idea that corrosion of bare<sup>31–34</sup> and coated<sup>35</sup> AA 2024 initiates at intermetallics containing Al, Cu,

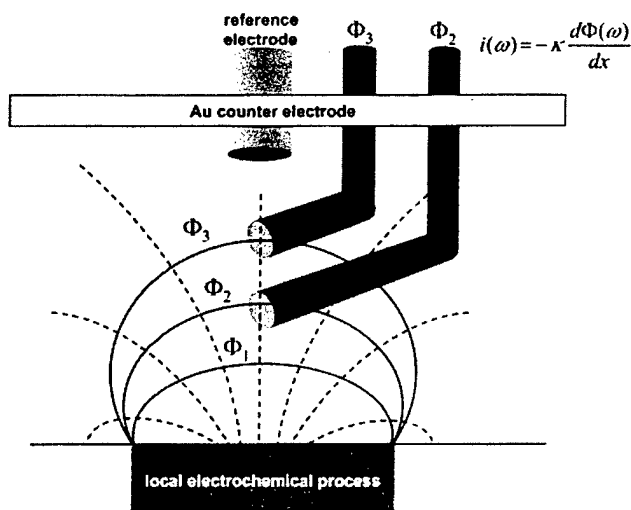


Figure 1. Schematic of five-electrode configuration used to acquire LEIS data. Note current lines (dashed) and local field lines (solid) associated with local defect

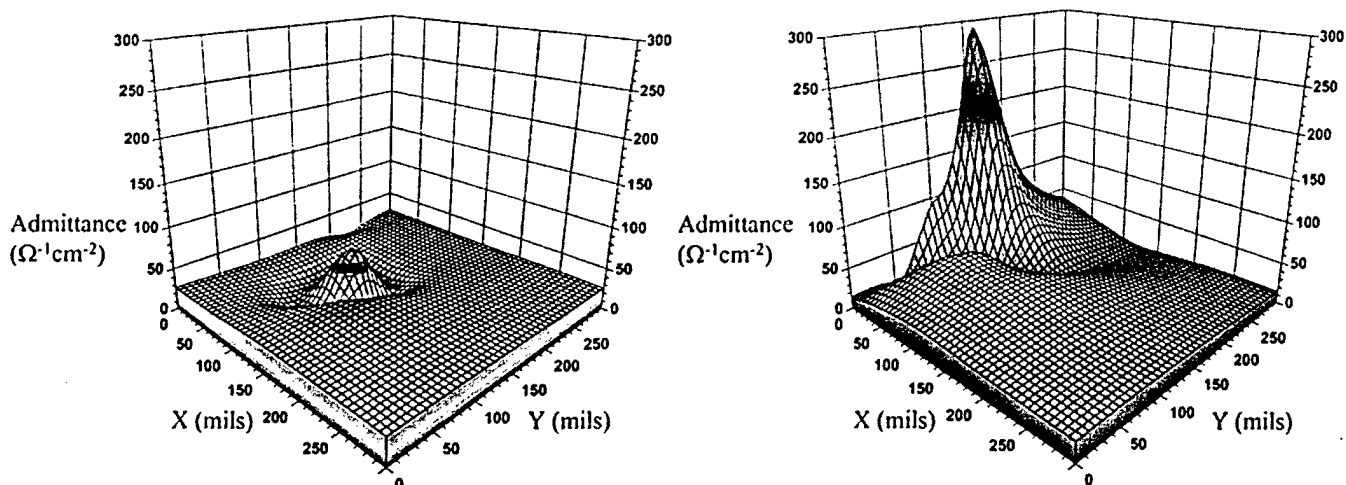


Figure 2. Comparison of LEI maps for red right and black left defects beneath a vinyl coating on AA 2024-T3 after 35 h exposure to 0.6 M NaCl. Note higher admittance in map for the red site than for the black.

and Mg and intermetallics containing Al, Cu, Mn, and Fe. Each type of intermetallic displays different corrosion behavior.<sup>32,33</sup> Al, Cu, Mg, and Al, Cu, Mn, Fe intermetallics are typically 5-20  $\mu\text{m}$  in diameter and randomly distributed with variable separation distance averaging 20-50  $\mu\text{m}$ .<sup>33</sup> The role of individual intermetallics is unclear, due in part to two apparent inconsistencies. First, the coated samples in this study developed only one or two red (active) blisters per exposure field (14.5  $\text{cm}^2$ ), indicating that only a small minority of intermetallic particles would have influenced the onset of the severe pitting sites. Open-circuit potential (OCP) measurements have revealed that the formation of a red blister site accompanied by a drop in the OCP precludes the formation of additional red blister sites. It is proposed that large protective cathodic regions form around these more severe corrosion sites, protecting the nonblistered areas of the sample. Second, a blister generally grew large enough (>1 mm) to encompass both types of intermetallics. Initiation may still have occurred at one single particle site, but the continued growth would have to take into account the effect of additional particles. While cop-

per and magnesium ions are found consistently within red-colored blisters, it is unclear how they participate in subsequent substrate electrochemistry and blister growth.

*The influence of bulk solution on defect formation polyurethane coating.*—Other experiments sought to determine how the solution inside and outside the blister influenced electrochemical activity and growth. The first of these considerations was a preliminary investigation of the bulk solution, i.e., the chloride concentration of the immersion solution. For this and all subsequent experiments, only polyurethane-coated samples were explored. The shift from the VYHH resin was made to more closely examine a coating material that would be used in aircraft. Black blisters were not observed with polyurethane coatings as they were with the vinyl coatings. However, the general corrosion performance of the coatings, as assessed by visual observation of the rate and number of red site formation, was found to be comparable. All pertinent experiments performed on vinyl-coated panels were repeated on polyurethane-coated panels. Although several different polyurethane chemistries were examined in this study, delineation in performance between these chemistries is not discussed at this time.

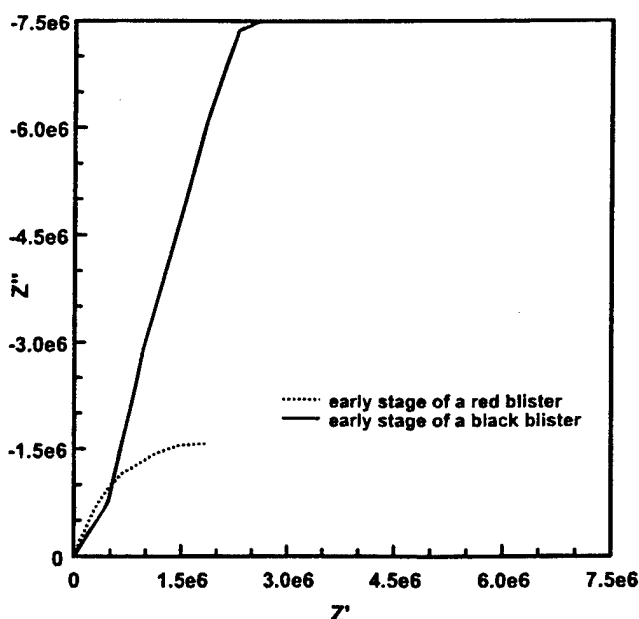


Figure 3. Comparison of red and black defects during early stages using LEIS. Note lower polarization resistance for the red site than for the black.

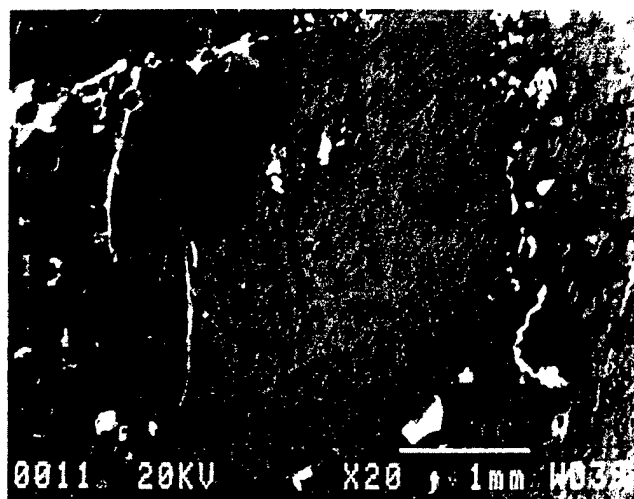


Figure 4. An SEM micrograph showing a red blister site after coating removal. Note the large pit area in the upper left hand corner. This appears shiny metallic, while the surrounding area is red in color.

Samples were exposed to varying concentrations of NaCl. It should be noted that, although samples were tested in NaCl, red blisters were occasionally observed in other electrolytes, *e.g.*, KCl, Na<sub>2</sub>SO<sub>4</sub>. Table I summarizes the observations in the different chloride concentrations. The results indicate that at higher chloride concentrations, attack was limited to several (1-3) isolated red blisters that grew faster and larger compared to more dilute solutions. In solutions of lower chloride concentration, attack was typified by small [*ca.* 20  $\mu$ m] white corrosion patches over the entire sample with a red blister forming only occasionally. Interestingly, the samples which were exposed to low chloride concentrations also developed large clear blisters 2-8 mm in diam.

As a result of these observations, attention was returned to the environment inside the blisters. The local pH and OCP values were measured in the solution inside each type of blister using the Ir/IrO<sub>2</sub> and Ag/AgCl electrodes described previously. Figure 5 shows a plot of the OCP inside the various blisters vs. their internal pH. The more active sites had lower OCPs and acidic pHs, whereas the more passive sites (black and clear) had more positive OCPs and pHs that were either neutral or alkaline. Interestingly, the red blisters had an OCP similar to that of Al<sub>2</sub>CuMg on 0.1 M KCl.<sup>34</sup> Whereas LEI maps of red blister sites showed increased electrochemical activity, preliminary maps of clear blister sites did not, *i.e.*, the LEI map was flat across the surface on which clear blisters were present, indicating that current was not passing from these blister sites to the counter electrode.

Further CE testing was performed on polyurethane-coated panels in order to ensure that results for this system corresponded with those from the vinyl-coated panels. The clear blisters, now identified as an additional kind of defect, were considered in these tests as well. These samples were immersed in KCl because the Na<sup>+</sup> peak tends to overshadow any Mg<sup>+2</sup> peak during CE testing. The red blister again contained Cu<sup>+2</sup> (0.01 M), Al<sup>+3</sup> (0.075 M), and Mg<sup>+2</sup> (0.007 M) ions, but this time also contained acetate (0.006 M) and formate (0.015 M). The clear blisters contained a notably low concentration of chloride ions (0.005 M) and also contained acetate (0.013 M).

Rigorous analysis of the carrier solutions used in CE analysis did not reveal the presence of acetate or formate ions. Thus, the acetate and formate originated from the polyurethane coating itself. Although suggestions have been made that acetone as a cleaning agent could account for the presence of acetate in various situations,<sup>36</sup> this is not a concern for the experiments described in this paper. Acetate was observed in the underfilm solution in cases when no acetone was used in the cleaning process. In addition, acetate has been observed in low pH solutions contacting freestanding polyurethane films in which no substrate was present. Similar analyses did not reveal the presence of these organic moieties within the solution beneath vinyl coatings. These results are consistent with the possibility that ester

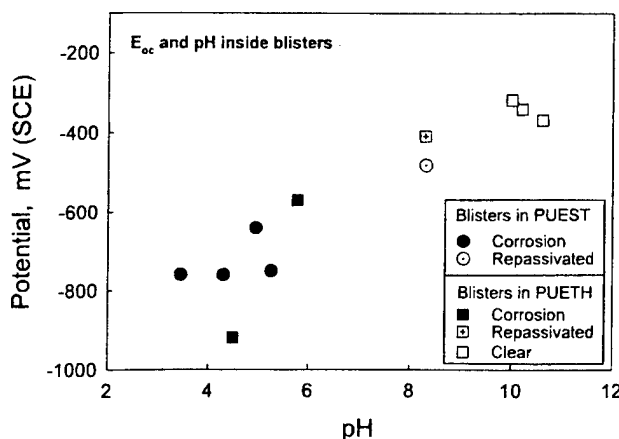


Figure 5. Open-circuit potential and occluded region pH of AA2024-T3 inside different blisters. The red blister solution had a low pH and an active OCP, while the clear blister solution has a high pH and a passive OCP. Note: PUEST represents a polyester based polyurethane coating and PUETH a polyether urethane.

linkages within the polyurethane coating have undergone hydrolysis,<sup>27,28</sup> while the saturated bonds of the vinyl resin remain stable. Further, hydrolysis of the polyurethane above red blister sites could be catalyzed by the low pH as well as the ionic content of this blister solution.<sup>32</sup> This observation raises the possibility that the underfilm solution chemistry, which has a composition determined at a minimum by the exterior environment and substrate electrochemistry, further degrades the organic coating, thus creating a potential feedback effect. To date, this solution chemistry has not been quantitatively investigated in early stages of underfilm corrosion except for macroscopic blisters on steel.<sup>13,26</sup> It is also possible that a chemical heterogeneity present in the unexposed coating provided the original initiation site and allowed the ingress of specific ions (*e.g.*, chlorides) to initiate the corrosion process.

**The importance of underfilm chemistry.**—Observation of red blister growth revealed an interesting trend. Generally, one or more lobes grew from the original blister area during long-term exposure. These secondary lobes appeared to have a darker red color than the initiation site. An example of this can be seen in Fig. 6. The electrochemical activity of the different regions was measured using LEIM. The region mapped is shown along with the LEIM plot in Fig. 7.

Table I. Summary of the effects of different chloride concentration in the exterior bulk solution on blister formation and growth. All results were obtained through visual observation. Growth rates were variable and not necessarily continuous. Rapid growth is estimated by 1 mm increase in diameter over the course of 2-18 h. Slow growth indicates days of exposure before a 1 mm increase in diameter is observed.

Red blisters	Growth rate	Number per sample area, red blisters (40.1 cm <sup>2</sup> )	Size (mm)
0.6 M NaCl Ether and ester polyurethanes	Rapid and sudden growth	1-2	1-4
0.1 M NaCl Ether and ester polyurethanes	Slower growth	0-2	0.5-2
0.01 M NaCl Ether polyurethane	If grows at all, grows very slowly	~0	0.2-1

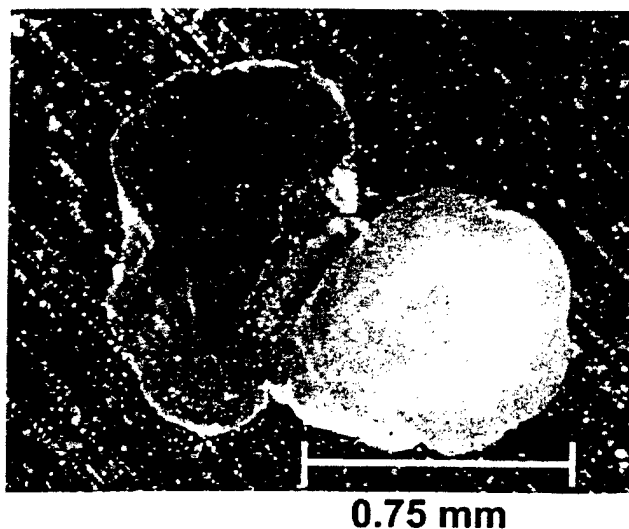


Figure 6. Optical micrograph of a red blister site which exhibits an initiation site and a secondary lobe. The lighter region to the right was the initiation site and the darker lobe to the left was a secondary lobe.

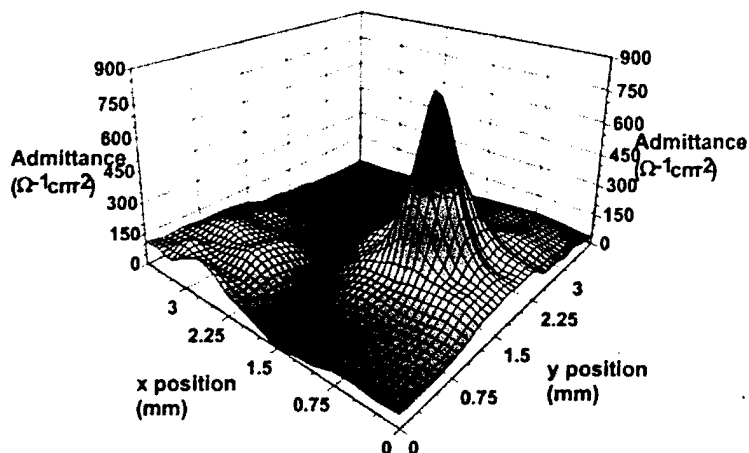
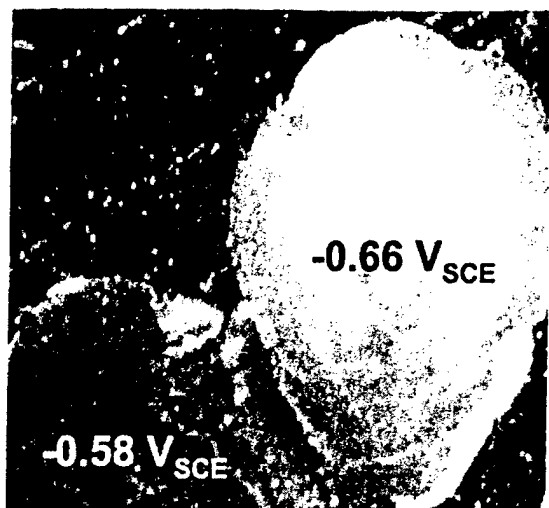


Figure 7. Optical micrograph of the actual region mapped by LEIM (left) and the corresponding LEI map (right). Note higher admittance at the initiation site.

Interestingly, the initial blister site contained a high admittance site within it, possibly representing the site of initial electrolyte ingress. The secondary lobes had much lower admittances, and were thus less active. Correspondingly, local OCP values were measured beneath the coating and also revealed the initial lobe to be more active. The OCP value at the initiation site was  $-0.66 \text{ V}_{\text{SCE}}$  whereas the value at the secondary lobe was  $-0.58 \text{ V}_{\text{SCE}}$ .

A similar defect was examined using SEM and EDS. EDS spot analysis of the substrate was performed on three regions shown in Fig. 8: (a) a site on the substrate with no visible corrosion, (b) the initiation site, and (c) a secondary lobe. The figure shows an electron micrograph of the regions targeted by EDS and the accompanying ratios of the compositional elements Al, Cu, and Mg of the S phase found in the analysis. It is important to note that this analysis is not quantitative. However, ratios of elemental content are consistent for

each spot analysis. For the sake of accuracy, each target region was analyzed more than once and several different areas were analyzed both on this particular sample and on other similar samples. The ratios shown in Table II typify the results found in the combined experiments.

The substrate within the region of the secondary lobe did not show significant differences in composition compared to the substrate region beneath the intact coating. However, the initiation site revealed a higher amount of Cu and a lower amount of Mg and Al, which is consistent with the dissolution theories suggested for copper-bearing intermetallics.<sup>31-33</sup>

EDS analysis was performed on the blister site previously shown in Fig. 4 to further examine substrate surface composition. Spot analysis was performed in several regions both inside the pit and in the blister region just outside of the pit. Representative spectra are shown in Fig. 9. A higher ratio of copper to aluminum is clearly visible in the region directly adjacent to the pit ( $>1:2$ ) compared to the pit itself ( $<1:4$ ), suggesting that the initiation area itself can be partitioned further into regions with differing electrochemical behavior. Major dissolution takes place within the pit itself, while redeposition occurs proximally to the pit site. This result would appear to support theories made by Buchheit *et al.*<sup>31</sup> for bare 2024 alloy that following dealloying of Al and Mg, copper is removed from the pit region by hydrogen and then redeposited directly outside of the pit.

The local OCP, underfilm chemistry, and elemental content of the surface strongly suggest that copper bearing intermetallics (e.g.,  $\text{Al}_2\text{CuMg}$ ) play a role in the initiation of severe underfilm corrosion sites. LEIM of blister sites support the idea that once initiated, subsequent growth of these blister sites is a strong function of the underfilm solution chemistry that evolves. This blister chemistry is an interactive function of the substrate electrochemistry, the exterior environment, and film chemistry, although the latter variable has not been elucidated in the present study. While this investigation has examined corrosion processes associated with neat resins on bare

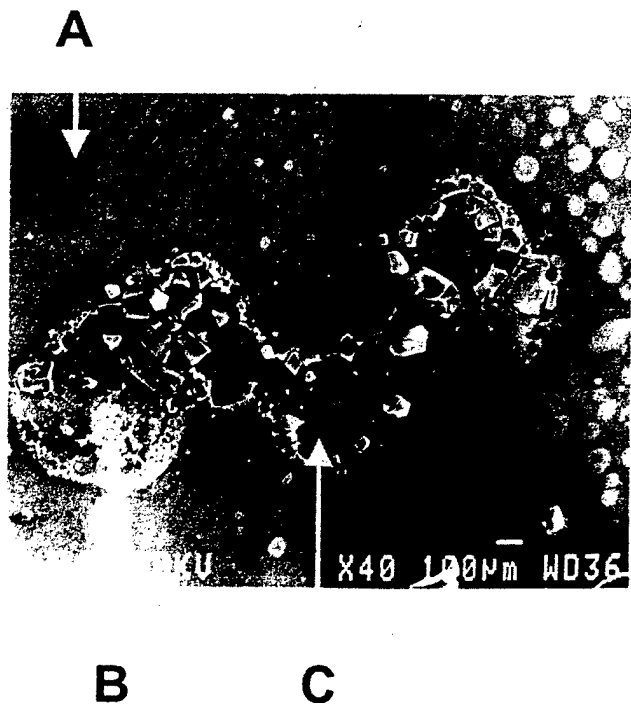


Figure 8. SEM image of a red blister site, after coating removal, where secondary lobes had formed. The regions targeted by EDS are labeled where A was an area of the substrate which was not affected, B was the initiation site, and C was a region inside a secondary lobe.

Table II. Ratios of the elements Al, Cu, and Mg (S phase =  $\text{Al}_2\text{CuMg}$ ) found using EDS analysis of the regions denoted in Fig. 8. Note the higher relative amount of Cu in the region of initiation (B).

Area sampled	Cu:Al	Mg:Al	Cu:Mg
A	1:32	1:33	11:10
B	1:7	1:43	6:1
C	1:35	1:43	12:10



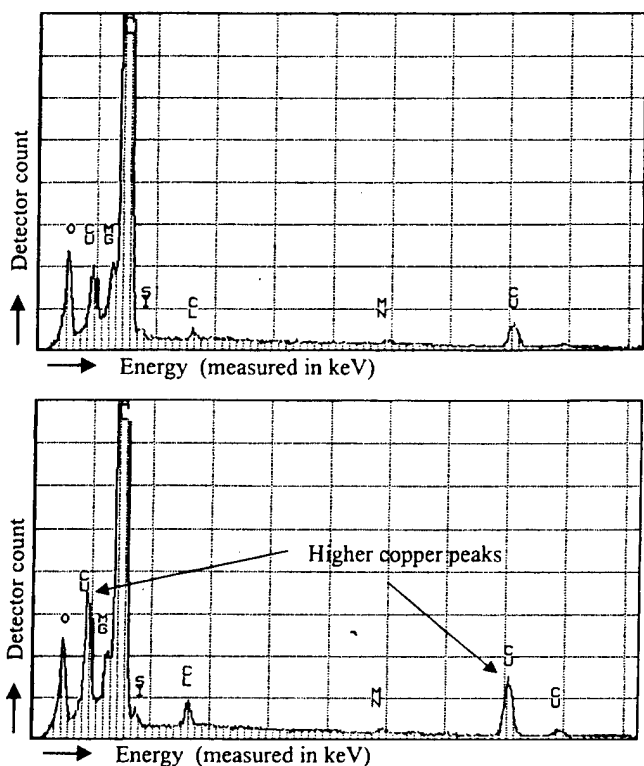


Figure 9. EDS spot analysis spectra for a region within the pit of Fig. 4 (top) and just outside the pit (bottom). Note the markedly higher amount of copper just outside the pit region.

(i.e., nonconversion coated) aluminum alloys, it has initiated a more detailed approach to the understanding of coating degradation processes through the use of local chemical and electrochemical methods.

The effect of pH on microconstituent pitting has also been discussed in the literature.<sup>33</sup> Pitting was found to occur in solutions with a pH ranging from 3 to 5.8 or in alkaline solutions up to pH 11. These results reinforce the significant role of the underfilm chemistry in coating degradation and support the results found in this paper. Once initiated, subsequent progression of the underfilm corrosion requires the development of an aggressive chemistry in the underfilm region.

### Conclusions

Several different types of defects were identified which can be classified according to their visual appearance: red, black, and clear. The present work focused primarily on characterization of the red active blisters.

1. Red blisters were shown through LEIM, LEIS, and local OCP measurements to be more electrochemically active than other defects.

2. The solution inside the red blisters was found via CE and local pH measurements to be the most aggressive of all the blister solutions, having a low pH and an active open-circuit potential. Significant concentrations of  $\text{Cu}^{+2}$ ,  $\text{Al}^{+3}$ , and  $\text{Mg}^{+2}$  ions were found in the underfilm solution of the red blisters. Acetate and formate were also present in the solutions extracted from polyurethane-coated samples, suggesting coating degradation had occurred via hydrolysis.

3. The concentration of chloride in the bulk solution influenced the growth and frequency of the active blister formation. A higher bulk chloride concentration yielded an earlier initiation time, higher occurrence, a higher growth rate, and a larger final size of the blisters. Low concentrations introduced the appearance of clear blisters. CE analysis showed a notably low chloride concentration inside

these clear blisters. Little corrosion attack was observed in these clear blisters.

4. Red blisters exhibited a trend of an initiation site followed by the growth of secondary lobes. LEIM and local OCP measurements found the initiation site to be more electrochemically active. EDS of the substrate found that the initiation site contained more Cu and less Mg and Al than in intact regions. The substrate at the secondary lobes showed no significant difference in composition to unaffected regions.

### Acknowledgments

The authors gratefully acknowledge the financial support of this research by the Air Force Office of Scientific Research through contract no. F49620-96-1-0178. The authors would also like to thank Dr. Gabriel Ilievbare and Professor John Scully at the University of Virginia for information regarding the electrochemistry of intermetallics.

The University of Virginia assisted in meeting the publication costs of this article.

### References

1. I. Annergren, D. Thierry, and F. Zou, *J. Electrochem. Soc.*, **144**, 1208 (1997).
2. H. S. Isaacs and B. Vyas, *Electrochemical Corrosion Testing*, F. Mansfeld and U. Bertocci, Editors, p. 3, ASTM, Philadelphia, PA (1981).
3. H. S. Isaacs, *Corrosion*, **43**, 594 (1987).
4. A. J. Bard, F.-R. F. Fan, J. Kwak, and O. Lev, *Anal. Chem.*, **61**, 132 (1989).
5. E. Bayet, F. Huet, M. Keddad, K. Ogle, and H. Takenouti, *J. Electrochem. Soc.*, **144**, L87 (1997).
6. I. L. Rosenfeld and I. S. Danilov, *Corros. Sci.*, **7**, 129 (1967).
7. J. Zhao, G. Frankel, and R. L. McCreery, *J. Electrochem. Soc.*, **145**, 2258 (1998).
8. R. S. Lillard, P. J. Moran, and H. S. Isaacs, *J. Electrochem. Soc.*, **139**, 1007 (1992).
9. M. W. Wittman and S. R. Taylor, in *Advances in Corrosion Protection by Organic Coatings II*, J. D. Scantlebury and M. W. Kendig, Editors, PV 95-13, p. 158, The Electrochemical Society Proceedings Series, Pennington, NJ (1995).
10. A. M. Mierisch and S. R. Taylor, in *Electrically Based Microstructural Characterization II*, R. A. Gerhardt, M. A. Alim, and S. R. Taylor, Vol. 500, p. 35, Materials Research Society, Warrendale, PA (1998).
11. R. S. Lillard, J. Kruger, W. S. Tait, and P. J. Moran, *Corrosion*, **51**, 251 (1995).
12. F. Zou and D. Thierry, *Electrochim. Acta*, **42**, 3293 (1997).
13. J. J. Ritter and J. Kruger, in *Corrosion Control by Organic Coatings*, H. Leidheiser, Editor, p. 28, NACE, Houston, TX (1981).
14. G. M. Hoch, in *Localized Corrosion*, R. W. Staehle, B. F. Brown, J. Kruger, and A. Agrawal, Editors, p. 134, NACE, Houston, TX (1974).
15. W. H. Slabaugh, W. DeJager, S. E. Hoover, and L. L. Hutchinson, *J. Paint Technol.*, **44**(566), 76 (1972).
16. S. Haruyama, M. Asari, and T. Tsuru, in *Proceedings of the Symposium on Corrosion Protection by Organic Coatings*, M. W. Kendig and H. Leidheiser, Editors, PV 87-2, p. 11, The Electrochemical Society Proceedings Series, Pennington, NJ, (1987).
17. J. Parks and H. Leidheiser, *Ind. Eng. Chem. Prod. Res. Dev.*, **25**, 1 (1986).
18. J. F. Watts and J. E. Castle, in *Proceedings of the Symposium on Corrosion Protection by Organic Coatings*, M. W. Kendig and H. Leidheiser, Editors, PV 87-2, p. 68, The Electrochemical Society Proceedings Series, Pennington, NJ (1987).
19. H. Leidheiser and W. Wang, and L. Igetoft, *Prog. Org. Coat.*, **11**, 19 (1983).
20. A. G. Smith and R. A. Dickie, *Ind. Eng. Chem. Prod. Res. Dev.*, **17**, 42 (1978).
21. H. S. Scully, L. Brumback, and R. G. Kelly, *J. Chromatography*, **640**, 345 (1993).
22. B. K. Nash and R. G. Kelly, *J. Electrochem. Soc.*, **139**, L48 (1992).
23. G. Salamat, G. A. Juhl, and R. G. Kelly, *Corrosion*, **51**, 826 (1995).
24. H. S. Isaacs and B. Vyas, in *Electrochemical Corrosion Testing*, ASTM STP 727, F. Mansfeld and U. Bertocci, Editors, p. 3, ASTM, Philadelphia PA (1981).
25. S. R. Taylor and M. W. Wittman, in *Electrochemically Based Microstructural Characterization*, R. A. Gerhardt, S. R. Taylor, and E. J. Garboczi, Editors, Vol. 411, p. 31, MRS, Pittsburgh, PA (1996).
26. S. Haruyama, M. Asari, and Tsuru, in *Proceedings of the Symposium on Corrosion Protection by Organic Coatings*, M. W. Kendig and H. Leidheiser, Editors, PV 87-2, p. 197, The Electrochemical Society Proceedings Series, Pennington, NJ (1987).
27. P. Blais, *J. Appl. Biomater.*, **1**, 197 (1990).
28. M. Szycher and A. Siciliano, *J. Biomater. Appl.*, **5**, 323 (1991).
29. G. E. Zaikov, *JMS-Rev. Macromol. Chem. Phys.*, **C25**, 551 (1985).
30. R. G. Kelly, J. Yuan, C. M. Weyant, and K. S. Lewis, *J. Chromatog.*, In press.
31. R. G. Buchheit, R. P. Grant, P. F. Hlava, B. McKenzie, and G. L. Zender, *J. Electrochem. Soc.*, **144**, 2621 (1997).
32. P. Schmutz and G. S. Frankel, *J. Electrochem. Soc.*, **145**, 2295 (1998).
33. G. S. Chen, M. Gao, and R. P. Wei, *Corrosion*, **52**, 8 (1996).
34. G. O. Ilievbare, J. Yuan, R. G. Kelly, and J. R. Scully, Abstract 111, The Electrochemical Society Meeting Abstracts, Vol. 98-1, San Diego, CA, May 3-8, 1998.
35. K. Nisancioglu, *J. Electrochem. Soc.*, **137**, 69 (1990).
36. S. V. Kagwade, C. R. Clayton, M. L. Du, and F. P. Chiang, in *Proceedings of the Symposium on Surface Oxide Films*, J. A. Bardwell, Editor, PV 96-18, p. , The Electrochemical Society Proceedings Series, Pennington, NJ (1996).



# Corrosion Performance of Field-Applied Chromate Conversion Coatings

R.B. Leggat, S.R. Taylor,\* W. Zhang, and R.G. Buchheit\*\*

## ABSTRACT

Alternative conversion coatings designed to replace chromate conversion coatings (CCC) are typically compared to laboratory-prepared CCC with regard to stand-alone corrosion performance. This study seeks to determine the stand-alone corrosion resistance of field-applied CCC to establish a more realistic benchmark for new nonchromate conversion coatings. Salt spray exposure, wet tape adhesion tests, and measurement of electrical contact resistance were performed according to the military specifications that govern what conversion coatings are accepted for use by the U.S. Department of Defense (DOD) facilities. In addition, other analytical techniques such as electrochemical impedance spectroscopy and Auger electron spectroscopy depth profiling were used. In an initial study, all of the field-applied coatings on AA2024 (UNS A92024), AA6061 (UNS A96061), and AA7075 (UNS A97075) displayed significant pitting after 168 h salt spray exposure. Additionally, attention to pre-cleaning the surface prior to coating was found to increase CCC corrosion resistance. Based on the results of the field-applied coatings, a second phase of investigation was initiated to examine the effects of coating time and application method (spray vs immersion) on the corrosion resistance and paint adhesion. This study was conducted using facilities designed to simulate conditions in an aircraft maintenance depot. It was found that spray and immersion application produced coatings with equivalent performance. Regardless of application method, 5 min of continuous exposure to solution was required to obtain adequate coating weight. The results of this study suggest that a re-

view of the relevant military specifications is merited so that emerging, environmentally benign conversion coatings can be evaluated against an appropriate metric.

**KEY WORDS:** adhesion, aluminum aerospace alloys, chromate conversion coating, corrosion resistance, electrical contact resistance, military specifications, salt spray

## INTRODUCTION

Conversion coatings are applied to metals in order to increase corrosion resistance and increase adhesion of subsequently applied organic coatings. A conversion coating is the result of two chemical reactions: dissolution of the native surface oxide and formation of a more corrosion-resistant, inorganic compound of the original metal.<sup>1</sup>

Chromate conversion coatings (CCC) are the most common conversion coatings applied to aluminum aerospace alloys. Although CCC provide excellent corrosion resistance and adhesion, many of the chemicals used in the processing are under strict regulation because of their toxicity. Epidemiological studies have established the carcinogenicity of hexavalent chromium.<sup>2-3</sup> The worker's health and safety risks of using chromate-based conversion coatings are compounded by effluent disposal costs.<sup>4</sup> Thus, the health risks and cost of producing CCC has driven the development of nontoxic, environmentally benign alternatives, which have recently been reviewed by Nylund.<sup>5</sup>

Presently, CCC remain an essential component in effective corrosion protection systems on aluminum alloys for military applications. In order for

Submitted for publication March 2001; in revised form, August 2001.

\* Center for Electrochemical Science and Engineering, University of Virginia, Charlottesville, VA 22903.

\*\* Fontana Corrosion Center, The Ohio State University, Columbus, OH 43210.

# Corrosion Performance of Field-Applied Chromate Conversion Coatings

R.B. Leggat, S.R. Taylor,\* W. Zhang, and R.G. Buchheit\*\*

## ABSTRACT

Alternative conversion coatings designed to replace chromate conversion coatings (CCC) are typically compared to laboratory-prepared CCC with regard to stand-alone corrosion performance. This study seeks to determine the stand-alone corrosion resistance of field-applied CCC to establish a more realistic benchmark for new nonchromate conversion coatings. Salt spray exposure, wet tape adhesion tests, and measurement of electrical contact resistance were performed according to the military specifications that govern what conversion coatings are accepted for use by the U.S. Department of Defense (DOD) facilities. In addition, other analytical techniques such as electrochemical impedance spectroscopy and Auger electron spectroscopy depth profiling were used. In an initial study, all of the field-applied coatings on AA2024 (UNS A92024), AA6061 (UNS A96061), and AA7075 (UNS A97075) displayed significant pitting after 168 h salt spray exposure. Additionally, attention to pre-cleaning the surface prior to coating was found to increase CCC corrosion resistance. Based on the results of the field-applied coatings, a second phase of investigation was initiated to examine the effects of coating time and application method (spray vs immersion) on the corrosion resistance and paint adhesion. This study was conducted using facilities designed to simulate conditions in an aircraft maintenance depot. It was found that spray and immersion application produced coatings with equivalent performance. Regardless of application method, 5 min of continuous exposure to solution was required to obtain adequate coating weight. The results of this study suggest that a re-

view of the relevant military specifications is merited so that emerging, environmentally benign conversion coatings can be evaluated against an appropriate metric.

**KEY WORDS:** adhesion, aluminum aerospace alloys, chromate conversion coating, corrosion resistance, electrical contact resistance, military specifications, salt spray

## INTRODUCTION

Conversion coatings are applied to metals in order to increase corrosion resistance and increase adhesion of subsequently applied organic coatings. A conversion coating is the result of two chemical reactions: dissolution of the native surface oxide and formation of a more corrosion-resistant, inorganic compound of the original metal.<sup>1</sup>

Chromate conversion coatings (CCC) are the most common conversion coatings applied to aluminum aerospace alloys. Although CCC provide excellent corrosion resistance and adhesion, many of the chemicals used in the processing are under strict regulation because of their toxicity. Epidemiological studies have established the carcinogenicity of hexavalent chromium.<sup>2-3</sup> The worker's health and safety risks of using chromate-based conversion coatings are compounded by effluent disposal costs.<sup>4</sup> Thus, the health risks and cost of producing CCC has driven the development of nontoxic, environmentally benign alternatives, which have recently been reviewed by Nylund.<sup>5</sup>

Presently, CCC remain an essential component in effective corrosion protection systems on aluminum alloys for military applications. In order for

Submitted for publication March 2001; in revised form, August 2001.

\* Center for Electrochemical Science and Engineering, University of Virginia, Charlottesville, VA 22903.

\*\* Fontana Corrosion Center, The Ohio State University, Columbus, OH 43210.

**TABLE 1**  
*Corrosion-Resistance Requirements of MIL-C-81706*

Corrosion-Resistance Properties	Treatment Class	Aluminum Alloys Treated with Film-Forming Materials	Exposure to 5% Salt Spray (h)
For qualification	1A <sup>(A)</sup>	2024-T3, 7075-T6	336
	3 <sup>(B)</sup>	6061-T6	168
For quality	1A	2024-T3	168
conformance inspection	3	6061-T6	168

<sup>(A)</sup> Class 1A coatings are used for maximum protection against corrosion.

<sup>(B)</sup> Class 3 coatings are used for protection against corrosion where low electrical (contact) resistance is needed.

candidate nonchromate conversion coatings to gain attention as viable candidates for use by the U.S. Department of Defense, they must meet the requirements of two military specifications: MIL-C-81706, "Chemical Conversion Coatings for Coating Aluminum and Aluminum Alloys," and MIL-C-5541, "Chemical Conversion Coatings on Aluminum and Aluminum Alloys."

The two aforementioned specifications both govern the same systems (i.e., chromate conversion coatings on aluminum) but have important differences with regard to whether it is the process or the end product that is monitored. MIL-C-81706 is a "materials" specification and defines the characteristics of the conversion coating chemistry including appearance and properties of the applied coating. This specification differentiates two classes of coatings, 1A and 3, depending on the intended purpose of the coating. Class 1A coatings are used when maximum corrosion protection is needed, while Class 3 coatings are used when corrosion protection and low electrical contact resistance are needed. In addition, MIL-C-81706 specifies two levels of performance for qualification and quality conformance. To be placed on the Qualified Products List (QPL) associated with MIL-C-81706 (QPL-81706), a product must perform at the qualification level. The quality conformance requirements are used mainly for quality control and lot inspection. On the other hand, MIL-C-5541 is a "process" specification and defines the characteristics of a coating applied in a production environment. This specification defines the requirements for monitoring the processes used in coating production and is independent of the materials that are used. A "process" specification is typically used when the properties of the end product are not easily measured. The process is controlled assuming that the product will be within specification as long as the process is within its parameters.

Under the military specifications, corrosion performance of conversion-coated aluminum is assessed by exposure to 5% salt spray according to ASTM B 117.<sup>6</sup> The corrosion-resistance requirements are more rigorous for MIL-C-81706 than MIL-C-5541. To meet MIL-C-81706 requirements, no evidence of corrosion with the exception of 1/4 in. of the edge is

allowed after exposure of five panels for a specified time. The required exposure time varies depending on the alloy and coating class as shown in Table 1. Under MIL-C-5541, a single panel can have no more than five pits and no more than a total of 15 pits for five panels to meet the requirement.

In addition to corrosion resistance, these two military specifications also mandate adhesion performance, electrical contact resistance, and coating weight. Adhesion of an epoxy primer and topcoat to the conversion coating is satisfactory for both military specifications when no intercoat separation is observed after wet tape testing per Method 6301 of Federal Test Method Standard no. 141.<sup>7</sup> Electrical contact resistance of  $<5 \text{ m}\Omega\text{-cm}^2$  for as-coated surfaces and  $<10 \text{ m}\Omega\text{-cm}^2$  post salt spray exposure are required by MIL-C-81706. A coating weight of at least 40 mg/ft<sup>2</sup> is required by MIL-C-81706 for Class 1 coatings.

These stringent military specifications, although initially developed for CCC, are presently used as the benchmark for new nonchromate conversion coatings. The corrosion resistance, paint adhesion, and electrical contact resistance of 29 chromate-free conversion coatings on test panels of five aluminum alloys were evaluated using military specifications in a study by the National Center for Manufacturing Sciences.<sup>8</sup> In this study, the coatings were applied by immersion in each of the respective manufacturer's laboratories. In a similar study on vendor-prepared, spray-applied coatings by the Air Force Research Laboratory, 10 conversion coating systems were evaluated.<sup>9</sup> These studies indicate that while progress has been made in the area of alternative conversion coatings, they do not compare well to CCC when tested according to these military specifications.

The common understanding of the structure, chemistry, and performance of CCC has been developed through examination of coatings applied by immersion processing normally under ideal or near-ideal conditions. However, it is likely that coatings applied during normal aircraft depot maintenance are considerably different. These coatings are applied by spraying using contact times that are relatively short. Thus, the goal of this study was to character-

ize coatings formed using flightline (or field) application methods.

This study consisted of two related investigations. The first was conducted at an Air Logistic Center (ALC), which are the actual facilities used when a plane is brought in for scheduled maintenance. Results from the initial investigation prompted a second investigation, in which samples were prepared by the Coatings Technology Integration Office (CTIO) of the Air Force Research Labs using specially designed laboratories to simulate the environmental conditions of the different ALC that support the fleet. The follow-up study was conducted at this facility in an attempt to reproduce the conditions of initial study at the ALC depot.

## EXPERIMENTAL PROCEDURES

### ALC-Applied Coatings

CCC were formed on 4-in.-by-5-in. (102-mm-by-127-mm) coupons of three different alloys: AA2024-T3 (UNS A92024, Al-4.4Cu-1.5Mg-0.6Mn), AA6061-T6 (UNS A96061, Al-1.0Mg-0.6Si), and AA7075-T6 (UNS A97075, Al-5.6Zn-2.5Mg-1.6Cu). The as-received samples were initially subjected to a deoxidizing pretreatment using a phosphoric acid ( $\text{H}_3\text{PO}_4$ )/nitric acid ( $\text{HNO}_3$ ) solution. The deoxidizing solution was spray-applied and permitted to contact the samples for a total of 5 min prior to rinsing with tap water. The samples were then conversion-coated by spray application using Turco Alumigold B<sup>†</sup>, which is a MIL-C-81706 qualified product. The conversion coating solution was in contact with the panels for 5 min, then the samples were rinsed and allowed to dry.

A second batch of panels was then prepared using the same general procedures as just described. However, these panels were manually abraded with nonmetallic scouring pads while in contact with the deoxidizing solution for 12 min.

After drying overnight, selected panels were primed and topcoated, again using standard ALC procedures and materials. The spray-applied primer was a two-part, high-solids epoxy with a maximum of 340 g/L volatile organic content. After drying, a high-solids polyurethane topcoat was spray-applied.

The panels were subsequently tested as stand-alone CCC, and as candidate coating systems (CCC + primer + topcoat). In addition to the testing required by the military specifications, other analytical methods were used. The weight of the CCC was measured according to MIL-C-81706. The panels were weighed, stripped in  $\text{HNO}_3$ , and re-weighed to determine coating weight. Powder scraped from the CCC panels was analyzed by x-ray diffraction (XRD). The surface of the CCC panels were inspected by scanning electron

microscopy (SEM). The electric contact resistance was measured using a 1-in.<sup>2</sup> (6.5-cm<sup>2</sup>) copper-contacting electrode under a load of 200 lb per MIL-C-81706. Compositional depth analysis was performed using Auger electron spectroscopy (AES). A 3-keV Ar<sup>+</sup> ion beam was used for sputtering. The 66-, 210-, and 229-eV peaks were monitored for aluminum, oxygen, and chromium.

Corrosion resistance of the panels receiving the CCC treatment alone was assessed by electrochemical impedance spectroscopy (EIS) and salt spray. EIS was performed after 24 h exposure to 0.5 M sodium chloride (NaCl). A metric indicative of corrosion resistance,  $R_{\text{corr}}$ , was fit from the spectra using a nonlinear least-squares program. The  $R_{\text{corr}}$  is the polarization resistance minus diffusional impedance and has previously been used in the analysis of conversion-coated aluminum alloys.<sup>10</sup> Salt spray exposure was done according to ASTM method B 117. The coatings were ranked by time-to-failure. Visual detection of five or more pits per panel constituted a failure.

Testing of primed samples was done according to MIL-PRF-85285, "Performance Specification Primer Coatings: Epoxy, High-Solids," because any conversion coating would be expected to eventually perform as part of a coating system that would include a primer coat. Adhesion was tested by the wet tape test according to ASTM D3359, Test B.<sup>11</sup> This method conforms to the military specifications with the exception of a crosshatch cut of the paint rather than an X-cut. This modification was used because it is more quantitative. The coated sample was exposed to distilled water for 24 h prior to introduction of the lattice cuts through the film to the substrate. Pressure-sensitive tape was laid across the lattice and then removed. The samples were ranked from 0 to 5 by comparison with descriptions and images. A ranking of 5 was given for a sample displaying no paint removal and a ranking of 0 was given for  $\geq 65\%$  paint removal as seen in Table 2.

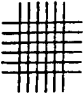
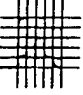
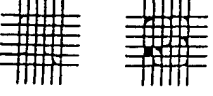
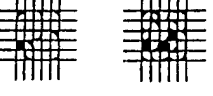
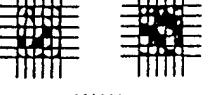

### Lab-Simulated Coatings

Based on the results of the ALC-prepared samples, a follow-up study was designed to examine the effect of chromate conversion coating time and the effect of application method. The study was limited to AA2024-T3. The panels were manually abraded prior to degreasing for 20 min at 100°F. Panels were then deoxidized for 2 min in 18%  $\text{H}_3\text{PO}_4$  at room temperature. Both immersion and constant overflow spray of the coating solution were used for application of the CCC. Exposure times of 2, 5, and 9 min were used. The coating solution had been made 3 days prior. The coating times were chosen to assure that a coating weight of 40 mg/ft<sup>2</sup> was achieved based on calibration experiments made at the time of the solution preparation. During spray application, the panels were held in racks at 45°

<sup>†</sup> Trade name.

TABLE 2

Ranking of Tape Test Samples According to ASTM D3359<sup>(A)</sup>

Rank	% Removed	Example
5B	0	
4B	<5	
3B	5 to 15	
2B	15 to 35	
1B	35 to 65	
0B	>65	

<sup>(A)</sup> Reprinted with permission. Copyright ASTM.

TABLE 3

Testing Done on Lab-Simulated Coatings<sup>(A)</sup>

	2 min	5 min	9 min
<b>CCC alone</b>			
Coating weight	X	X	X
EIS			X
Salt spray exposure	X	X	X
<b>CCC + primer</b>			
Pull-off tensile strength	X	X	X
Wet tape test	X	X	X
<b>CCC + primer + topcoat</b>			
Salt spray exposure			X

<sup>(A)</sup> Matrix identical for spray- and immersion-applied coatings.

TABLE 4

EIS Results for ALC-Applied Coatings  
on AA2024, AA6061, and AA7075

	$R_{\text{corr}}$ ( $\text{k}\Omega\text{-cm}^2$ ) <sup>(A)</sup>
<b>Pretreatment 1 (As-received)</b>	
AA2024	11.1 $\pm$ 1.7
AA6061	323.8 $\pm$ 316.5
AA7075	18.3 $\pm$ 3.6
<b>Pretreatment 2 (Abraded)</b>	
AA2024	25.7 $\pm$ 19.5
AA6061	1,997.5 $\pm$ 1,657.9
AA7075	4,863.2 $\pm$ 2,357.4

<sup>(A)</sup>  $R_{\text{corr}}$  fit from spectra for both pretreatments.

with a constant overflow of solution. After drying overnight, selected panels were primed using a two-part, high-solids epoxy. In addition, a fraction of the primed panels were topcoated with high-solids polyurethane.

Testing was similar to that done for the initial study. Some of the testing performed in the initial study was limited to the samples with 9-min exposure times as seen in Table 3. In addition to the wet tape test, the pull-off tensile strength of the epoxy primer was tested according to ASTM method D4541 using a Type IV self-alignment adhesion tester.<sup>12</sup>

Panels receiving the CCC, primer, and topcoat were scribed and exposed to salt spray according to ASTM B 117. The exposure time was 2,000 h. MIL-PRF-85285 requires that "the primer coating, with and without a topcoat, shall not exhibit blistering, lifting of either coating, nor substrate corrosion." Filiform testing, also required by MIL-PRF-85285, was not performed.

## RESULTS AND DISCUSSION

### ALC-Applied Coatings

As can be seen in the EIS test results shown in Table 4, the samples that were abraded prior to conversion coating had higher average  $R_{\text{corr}}$  values for all three alloys. Previous studies of conversion-coated aluminum alloys have proposed a correlation between the  $R_{\text{corr}}$  parameter and salt spray performance.<sup>10</sup> Based on the results of this earlier study, conversion coatings on AA2024 and AA6061 with  $R_{\text{corr}}$  values  $>2 \times 10^6 \Omega\text{-cm}^2$  are expected to pass 168 h of salt spray exposure, while an  $R_{\text{corr}}$  value of at least  $1.5 \times 10^7 \Omega\text{-cm}^2$  is required for coatings on AA7075. Using these proposed threshold values, only the abraded AA6061 coatings were expected to pass 168 h salt spray.

Regardless of pretreatment, little or no weight change was detected after stripping the CCC, indicating that the coatings were very thin. On the basis of coating weight, these coatings would qualify as Class 3 because their weight was  $<40 \text{ mg/ft}^2$ . Class 1A films, used for maximum corrosion resistance, require  $40 \text{ mg/ft}^2$ . Therefore, based on film weight alone, these coatings were not expected to survive 168 h salt spray. Even though the weights of the ALC-applied CCC were very low, the contact resistance of the films was higher than that specified for a Class 3 coating. The electrical contact resistance for the coatings on AA2024, AA6061, and AA7075 were 9, 12, and 12  $\text{m}\Omega\text{-in.}^{-2}$ , respectively. The military specifications require an electrical contact resistance of no more than  $5 \text{ m}\Omega\text{-in.}^{-2}$ .

The salt spray performance is shown as fraction failed per observation time in Table 5. Only the abraded AA6061 coatings passed the 168-h salt spray exposure required for quality conformance by

**TABLE 5**  
Fraction of ALC Coatings that Failed  
Per Observation Time in Salt Spray<sup>(A)</sup>

	24 h	48 h	66 h	168 h
<b>Pretreatment 1 (As-received)</b>				
AA2024	5/5			
AA6061	3/5	4/5	5/5	
AA7075	0/5	1/5	5/5	
<b>Pretreatment 2 (Abraded)</b>				
AA2024	5/5			
AA6061	0/5	0/5	0/5	0/5
AA7075	5/5			

<sup>(A)</sup> MIL-C-81706 requires 168 h for quality conformance on alloys.

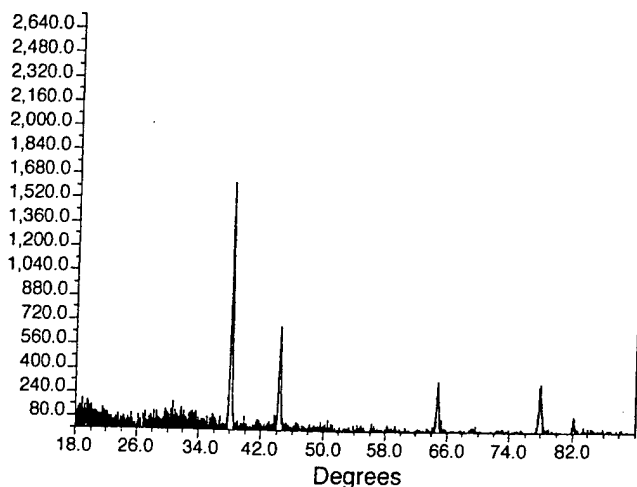


**FIGURE 1.** XRD spectrum for CCC scraped from ALC-applied coatings. Peaks in the spectrum are a result of aluminum removed from the panel during scraping.

MIL-C-81706. This was predicted by the  $R_{\text{corr}}$  values obtained from the EIS testing. As previously mentioned, the  $R_{\text{corr}}$  threshold proposed for predicting salt spray performance of AA7075 is higher, therefore the AA7075 coating was not expected to pass.

Rankings from the wet tape test are shown in Table 6. MIL-C-5541 specifies no separation. Coatings receiving a rank of 4 or 5 were considered to have passed. It can be seen that the ALC-applied CCC were able to provide passing adhesion results for the majority of samples. Pretreatment (i.e., abraded vs nonabraded) or alloy type did not effect adhesion results.

XRD indicated that the CCC was amorphous regardless of alloy or pretreatment. No other compounds were detected. The peaks seen in the XRD spectrum are from aluminum metal that was removed with the conversion coating by the scraping process (Figure 1). The SEM image shown in Figure 2 reveals that the surface of the coating is rough and apparently inhomogeneous. This appearance is typi-

**TABLE 6**  
Adhesion Testing of Primed and Topcoated  
ALC-Applied Coatings by Wet Tape Testing<sup>(A)</sup>

	D3359 Ranks	MIL-Spec
<b>Pretreatment 1 (As-received)</b>		
AA2024	3B, 4B, 5B	2/3 pass <sup>(B)</sup>
AA6061	2B, 4B, 5B	2/3 pass
AA7075	4B, 5B, 5B	3/3 pass
<b>Pretreatment 2 (Abraded)</b>		
AA2024	4B, 4B, 5B	3/3 pass
AA6061	4B, 4B, 4B	3/3 pass
AA7075	3B, 5B, 5B	2/3 pass

<sup>(A)</sup> Ranked according to ASTM D3359 on a scale of 5 to 0, with 5 being the best and 0 being the worst.

<sup>(B)</sup> Pass or fail according to MIL-C-5541, based on a ranking of 4 or 5 considered passing.

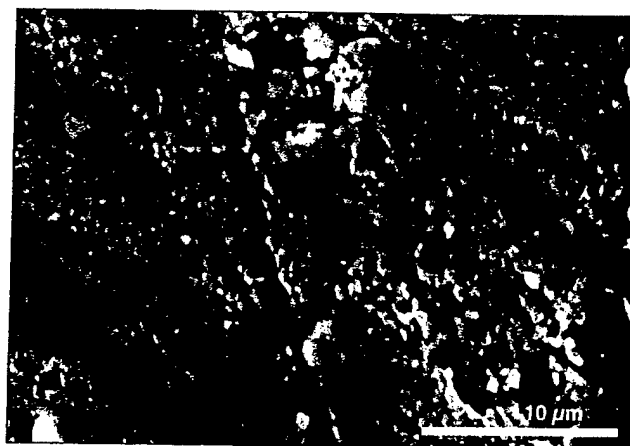


**FIGURE 2.** SEM image of ALC-applied CCC. Sample abraded prior to coating.

cal of CCC whether they are applied in the field or in the lab.<sup>13-14</sup>

The AES depth profiles shown in Figure 3 varied considerably among the different alloys for the panels receiving no pretreatment. On the other hand, the depth profiles of the conversion coating on abraded panels were much more consistent for the different alloys. The coating nonuniformity on the panels that received no pretreatment is evident in the photograph shown in Figure 4.

Based upon the results of this study, none of the field-applied (ALC-applied) coatings would have qualified as a Class 1A coating. For these coatings, it can be seen that pretreatment by abrasion during the deoxidation process made a significant improvement in the conversion coating performance. The difference between abraded and nonabraded samples is likely a result of the tenacious rolling oils present on as-received sheet stock. It should be noted that MIL-C-5541 does require that the base metal be cleaned such that a "water break-free surface" is obtained.

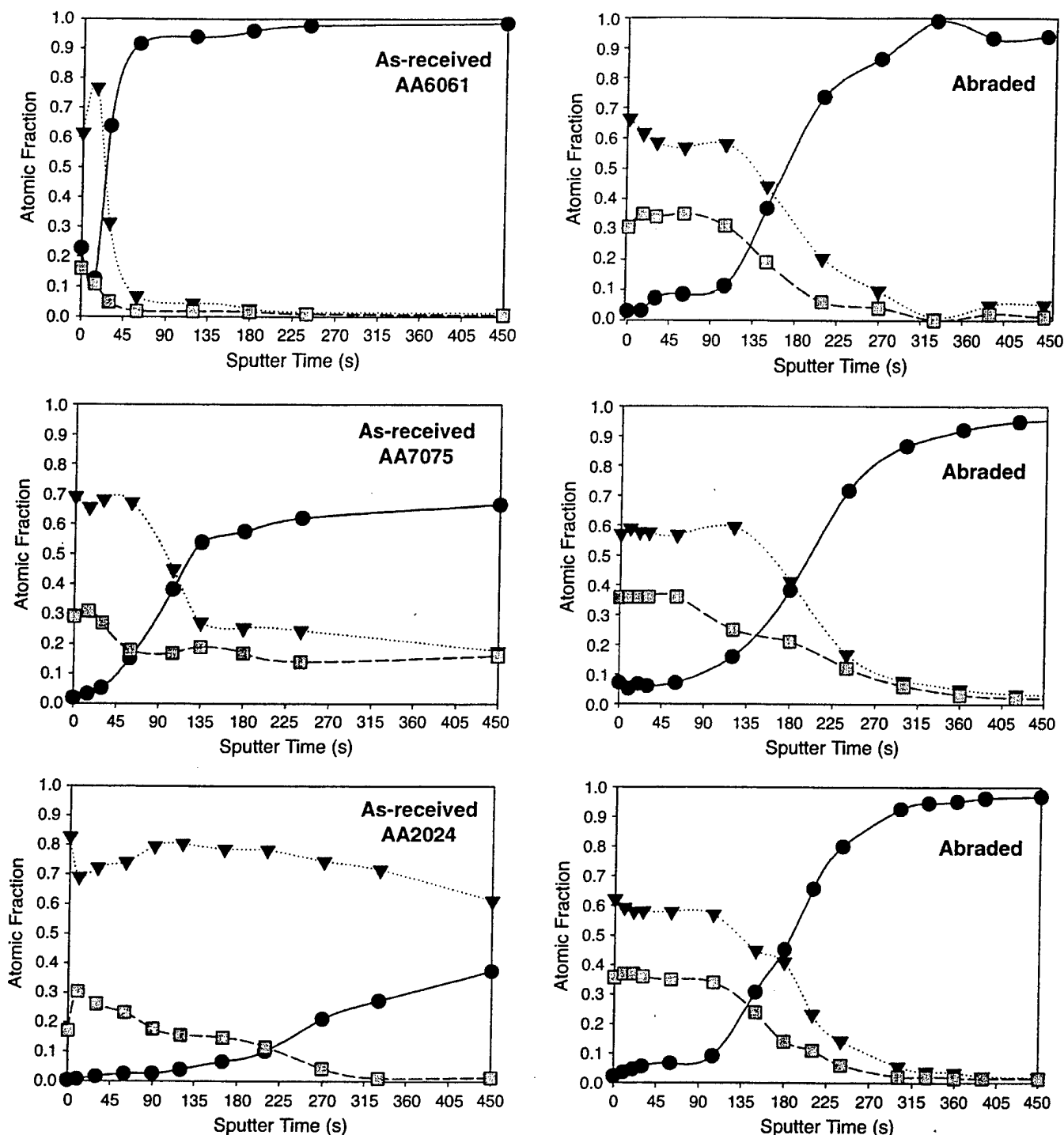


FIGURE 3. AES depth profiles for ALC-applied coatings. Spectra for coatings on AA2024, AA6061, and AA7075 with both pretreatments shown. Concentrations of (▼) oxygen, (●) aluminum, and (■) chromium plotted as atomic fraction.

### Lab-Simulated Coatings

A follow-up study was designed to address issues raised by the ALC study. A study by the Air Force Research Laboratory had suggested that 2 min of constant overflow during spray application was necessary to obtain sufficient coating weight.<sup>9</sup> In addition, the effect of the application method (spray vs immersion) was of interest.

Coating weight measurements were made for all coating times (2, 5, and 9 min) and for both application methods (spray and immersion). Based on the coating weights shown in Table 7, the required 40 mg/ft<sup>2</sup> was achievable only for the 5-min and 9-min exposure times for both application methods. The values listed for the spray application are based on a coating area of 0.28 ft<sup>2</sup> (2 sides by 4 in. by

5 in. by 0.007 ft<sup>2</sup>/in.<sup>2</sup>). This area is artificially high because only one side was directly sprayed, although both sides were in contact with the solution to some degree. Therefore, the calculated weights for the spray-applied coatings are believed to be artificially low. Based on the requirement of 40 mg/ft<sup>2</sup> for Class 1A coatings, the coatings with 5- and 9-min exposure times are expected to pass 168 h salt spray.

$R_{\text{corr}}$  values fit from the EIS measurements were  $3.3 \times 10^6 \pm 2.5 \times 10^6 \Omega\text{-cm}^2$  and  $2.9 \times 10^6 \pm 2.8 \times 10^6 \Omega\text{-cm}^2$  for the 9-min exposure times of the immersion and spray-applied coatings, respectively. Based on the previously discussed threshold  $R_{\text{corr}}$  value of  $2 \times 10^6 \Omega\text{-cm}^2$  for coatings on AA2024, these coatings were expected to pass the 168-h salt spray exposure. It should be noted that while the range of  $R_{\text{corr}}$  values observed for the immersion and spray-applied coatings was large ( $8.8 \times 10^5$  to  $8.4 \times 10^6 \Omega\text{-cm}^2$  and  $2.8 \times 10^5$  to  $1.1 \times 10^7 \Omega\text{-cm}^2$  for the immersion and spray-applied coatings, respectively), it is typical of the scatter observed for barrier property measurements of inorganic or organic coatings. The arithmetic mean of eight samples per treatment was used in this study for comparison with a previously determined  $R_{\text{corr}}$  critical threshold value, which had been determined by Buchheit, et al.,<sup>10</sup> using the mean rank method for an 80% cumulative passing frequency. As previously stated, the EIS testing was limited to the 9-min application times to minimize the size of the experimental matrix.

Salt spray results are reported in Table 8 as fraction failed per observation time. The samples were left in the salt spray chamber for 1,000 h. Only 168 h is required for quality conformance and 336 h for qualification of coatings on AA2024. A majority of the 5-min and 9-min coatings survived 336 h. The spray-applied coating performed better than immersion-applied coatings. At each observation time, a greater fraction of the spray-applied coatings survived than the immersion-applied coatings for the same coating time. Note that none of the 2-min immersed samples passed 168 h of salt spray, while none of the 2-min spray-applied coatings could survive 336 h of salt spray.

Adhesion was measured by the wet tape test and by measuring the pull-off tensile strength. Results of the adhesion testing, shown in Table 9, indicate that the adhesion measured by the wet tape test was comparable regardless of coating time or application method. Additional adhesion tests (pull-off tensile strength) verified that the adhesion was statistically equivalent for all treatments.

The scribed, primed, and topcoated panels were evaluated after 2,000 h exposure to salt spray. No blistering or lifting of the topcoat or primer was observed for any of the 9-min spray or immersion-applied panels. However, corrosion was observed on two of the four immersion-applied panels. Therefore,

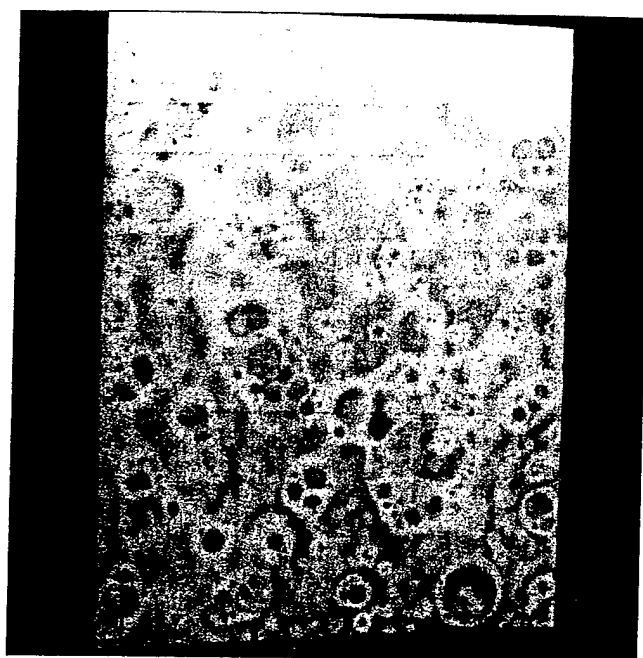


FIGURE 4. Photograph showing nonuniformity of CCC on samples receiving no pretreatment.

TABLE 7  
Coating Weights for All Times  
of Spray and Immersion Application<sup>(A)</sup>

	Coating Weight (mg/ft <sup>2</sup> )
<b>Immersion</b>	
2 min	23.9 ± 5.4
5 min	41.2 ± 4.5
9 min	48.8 ± 3.6
<b>Spray</b>	
2 min	N/A
5 min	36.3 ± 1.5 <sup>(B)</sup>
9 min	37.5 ± 12.8 <sup>(B)</sup>

<sup>(A)</sup> Samples produced in lab-simulating depot conditions.

<sup>(B)</sup> Coating on both sides of 4-in.-by-5-in. panel assumed.

two of the four 9-min immersion-applied panels failed the salt spray exposure, but all of the spray-applied panels passed.

The better salt spray performance of the spray-applied coatings (both stand-alone and painted) was unexpected. This may be attributable to bath chemistry changes with time for the immersion coatings. Spray-applied coatings are formed by a constant chemistry that is continually refreshed, while immersion techniques form coatings in a bath that will change with time. The effect of bath chemistry evolution on the corrosion performance of a nonchromate conversion coating has recently been reported in which coating quality was found to decrease with bath age.<sup>15</sup> Another factor is that the immersion coatings were at a constant elevated temperature, while no temperature control was provided for the spray



**TABLE 8**  
*Fraction of Coatings that Failed  
 per Observation Time in Salt Spray<sup>(A)</sup>*

	168 h	336 h	504 h	672 h	1,000+ h
<b>Immersion Application</b>					
2 min	4/4				
5 min	0/4	1/4	3/4	3/4	4/4
9 min	0/4	0/4	2/4	3/4	4/4
<b>Spray Application</b>					
2 min	1/4	4/4			
5 min	0/4	0/4	0/4	1/4	4/4
9 min	0/4	0/4	1/4	1/4	4/4

<sup>(A)</sup> MIL-C-81706 requires 168 h for quality conformance and 336 h for qualification on AA2024. Samples produced in lab-simulating depot conditions.

**TABLE 9**  
*Adhesion Testing of Primed Coatings  
 Produced in Lab-Simulated Depot Conditions  
 by Wet Tape Test and Pull-Off Tensile Strength*

	POTS (psi)	Tape Test	MIL- Spec
<b>Immersion</b>			
2 min	995 ± 142	4B, 5B	2/2 pass <sup>(A)</sup>
5 min	1,046 ± 182	5B, 5B	2/2 pass
9 min	964 ± 166	5B, 5B	2/2 pass
<b>Spray</b>			
2 min	973 ± 139	4B, 5B	2/2 pass
5 min	1,036 ± 143	4B, 5B	2/2 pass
9 min	900 ± 154	4B, 5B	2/2 pass

<sup>(A)</sup> Pass or fail according to MIL-C-5541, based on a ranking of 4 or 5 considered passing.

application. It should be stated that the sprayed solution was at an elevated temperature but cooling certainly occurred once in contact with the panels. The effect of cooling during spraying has not been investigated.

In light of this, coating systems should be viewed as an interdependent entity in which the performance of the whole is more than the simple sum of its individual components (i.e., conversion coating, primer coat, and topcoat). A case in point is the present investigation of CCC. Although the field-applied CCC did not pass the military specifications for stand-alone corrosion protection, these same CCC perform quite well when used in the field within a complete coating system. The antithesis may also be true, in that a new alternative conversion coating may perform well as a stand-alone corrosion protection material, but not possess the requisite interfacial chemistry to function within a complete coating system. This has been observed in testing within these laboratories and will be reported in a subsequent paper. Results of this study strongly suggest the need to use a total system test approach to

qualify alternative conversion coatings when incorporated into a complete coating system. The ideas presented here will possibly make pre-screening of conversion coatings a more cumbersome process, but additional research is being conducted to better understand the interfacial properties that control substrate coating interactions.

## CONCLUSIONS

❖ There were several significant results in this study of field-applied and lab-applied coatings. The salt spray performance was predicted by EIS and coating weight. The prediction of salt spray performance based on threshold  $R_{corr}$  values was supported by these results. The adhesion required by military specification was obtained regardless of alloy type, pretreatment, application method (spray or immersion), or coating time. At least 5 min of continuous exposure during coating was needed to obtain adequate coating weight for both application methods. In the lab-simulated study, the spray-applied coatings were slightly better than the immersion-applied.

❖ Present military specifications for conversion coatings require a level of performance that not even field-applied CCC can meet. Yet we know from experience, that field-applied CCC provide an excellent substrate for coating, and that the coatings on these same field-applied CCC do pass military specifications for a coating system (i.e., conversion coating, primer, and topcoat). Thus, present military specifications may set unreasonable requirements for emerging environmentally benign conversion coatings that would eventually be used within a coating system, and may screen out very adequate conversion coating materials.

## ACKNOWLEDGMENTS

This work was sponsored by the Defense Advanced Research Projects Agency (DARPA) (contract no. F49620-1-0305) under the direction of S. Wax and P. Trulove (Air Force Office of Scientific Research [AFOSR]). The assistance of B. Ghim and S. Finely of CTIO are greatly appreciated. Discussions with S. Susta of Science Applications International Council (SAIC) were helpful in conducting this study.

## REFERENCES

1. J.W. Davis, J.I. Maurer, L.E. Steinbrecher, "Surface Cleaning, Finishing, and Coating," in *Metals Handbook*, vol. 5, 9th ed. (Materials Park, OH: ASM International, 1982), p. 457.
2. "Rankings of Pollutants with Respect to Hazard to Human Health," in *Environmental Protection Agency Report no. EPA/4503-92/010* (Springfield, VA: National Technical Information Service, 1994).
3. H.J. Gibb, *Plat. Surf. Fin.* 86 (1999): p. 19.
4. C.J. Carpenter, *Plat. Surf. Fin.* 77 (1990): p. 35.
5. A. Nylund, *Alum. Trans.* 2 (2000): p. 121.
6. ASTM Method B 117, "Standard Test Method of Salt Spray (Fog) Testing" (West Conshohocken, PA: ASTM, 1999).

7. Federal Test Standard no. 141, Method 6301.1, "Adhesion (Wet) Tape Test" (Springfield, VA: National Technical Information Service, 1965).
8. "Alternatives to Chromium for Metal Finishing," Report no. 0273RE95 (Ann Arbor, MI: National Center for Manufacturing Sciences, 1995).
9. S. Susta, Science Applications International Corp., correspondence with R.B. Leggat, May 10, 2000.
10. R.G. Buchheit, M. Cunningham, H. Jensen, M.W. Kendig, M.A. Martinez, Corrosion 54 (1998): p. 61.
11. ASTM Method D3359, "Standard Test Methods for Measuring Adhesion by Tape Test" (West Conshohocken, PA: ASTM, 1995).
12. ASTM Method D4541, "Standard Test Method for Pull-Off Strength of Coatings Using Portable Adhesion Testers" (West Conshohocken, PA: ASTM, 1995).
13. J.A. Treverton, M.P. Amor, A. Bosland, Corros. Sci. 33 (1992): p. 1411.
14. A.E. Hughes, R.J. Taylor, B.R.W. Hinton, Surf. Interf. Anal. 25 (1997): p. 223.
15. R.B. Leggat, E.A. Pehovaz-Diez, N.P. Cella, S.R. Taylor, "Optimization of Bath Chemistry for Hydrotalcite-Based Conversion Coatings of Aerospace Aluminum Alloys," in Corrosion and Corrosion Prevention of Low-Density Metals and Alloys, ed. B.A. Shaw, R.G. Buchheit, J.P. Moran (Pennington, NJ: Electrochemical Society, 2001), p. 124.

**Don't miss out on this Golden Opportunity**

Do you need help in planning your week at the NACE Annual Conference? Visit the CORROSION/2002 section of the NACE Web site at [www.nace.org](http://www.nace.org) to find targeted information on the technical committee meetings, symposia, courses, tutorials and seminars.

**CORROSION/2002**

# Performance of Hydrotalcite Conversion Treatments on AA2024-T3 When Used in a Coating System

R.B. Leggat,\* W. Zhang, R.G. Buchheit,\*\* and S.R. Taylor\*

## ABSTRACT

Hydrotalcite (HT) conversion coatings are a possible alternative to chromate conversion coatings (CCC) for the pretreatment of aluminum aerospace alloys, but they must meet several criteria for acceptance. Relevant to acceptance are the abilities of these coatings to provide stand-alone corrosion protection, suitable adhesion with subsequent organic layers, and overall corrosion protection when used within a coating system. This study examines the salt spray performance of nine different HT treatments on AA2024 (UNS 92024) as stand-alone conversion coatings and as a substrate for an epoxy primer. In addition, the adhesion of epoxy to the HT and the corrosion characteristics of HT coatings as assessed by electrochemical impedance spectroscopy (EIS) were determined. Salt spray testing was performed under pertinent military specifications, and CCC was used as the benchmark. Two epoxy primers were evaluated: one with a chromate inhibitor (Class-C) and one with a nonchromate inhibitor (Class-N). The stand-alone HT treatments did not perform as well as the CCC but showed favorable performance relative to bare AA2024. In the primed samples, the CCC and bare AA2024 performed better than the HT-coated samples. Current HT coating chemistries have been optimized for stand-alone corrosion resistance. A correlation between stand-alone salt spray performance and EIS response was observed. The stand-alone corrosion resistance or epoxy adhesion could not explain the salt spray performance of the

epoxy-primed samples, supporting the need for a total system testing approach in coatings development.

**KEY WORDS:** AA2024, adhesion, conversion coatings, electrochemical impedance spectroscopy, salt spray testing

## INTRODUCTION

Conversion coatings are commonly applied to aluminum alloys to increase corrosion resistance and to provide increased adhesion of subsequent organic layers.<sup>1</sup> Currently, chromate-based conversion coatings (CCC) are used and are a key component in the performance of aerospace coating systems. Although they provide excellent adhesion and corrosion performance, chromates are hazardous materials that require significant expenditure in waste processing.<sup>2</sup>

Conversion coatings based on a naturally occurring compound, hydrotalcite (HT), are being developed as an alternative to CCC.<sup>3</sup> HT is formed on aluminum alloys by exposure to alkaline lithium salt solutions. The compound formed consists of aluminum/lithium-hydroxide layers intercalated by anions from the lithium salt. The physical and chemical properties of HT-based coatings can be controlled by selection of this interlayer anion, as well as by numerous post-coating treatments,<sup>4-5</sup> thus providing a large array of treatment options in the discovery of an optimal conversion coating procedure.

Previous research has focused on optimizing stand-alone corrosion resistance of HT-based coatings on an aerospace alloy (AA2024-T3 [UNS 92024]<sup>(1)</sup>).<sup>6</sup> However, in order for candidate conversion coating chemistries to be used ultimately by cer-

Submitted for publication June 2001; in revised form, November 2001.

\* Department of Materials Science and Engineering, University of Virginia, Charlottesville, VA 22904.

\*\* Department of Materials Science and Engineering, The Ohio State University, Columbus, OH 43210.

<sup>(1)</sup> UNS numbers are listed in *Metals and Alloys in the Unified Numbering System*, published by the Society of Automotive Engineers (SAE) and cosponsored by ASTM.

tain customers (e.g., department of defense [DOD] facilities), they must conform to military specifications. One such specification is MIL-C-81706, "Chemical Conversion Materials for Coating Aluminum and Aluminum Alloys."<sup>7</sup> This is a materials specification that defines the characteristics of the conversion coating chemistry, including appearance and properties of the applied coating. Another specification that also covers conversion coatings on aluminum alloys, MIL-C-5541E, "Chemical Conversion Coatings on Aluminum and Aluminum Alloys,"<sup>8</sup> is a process specification that defines the characteristics of a coating applied in a production environment. MIL-C-5541E controls the qualification of candidate systems and is therefore the specification relevant to the present study.

Given that a conversion coating will be used as part of a coating system consisting of a conversion coating, a primer, and one or more topcoats, testing of candidate conversion coatings should also include samples coated with at least a primer coat. The military specification that controls epoxy primers is MIL-PRF-23377G, "Performance Specification Primer Coatings: Epoxy, High Solids."<sup>9</sup> Any conversion coating that causes a previously qualified primer to fail the tests specified by MIL-PRF-23377G should not be used, even if the conversion coating itself qualifies under MIL-C-5541E.

Salt spray exposure is the method specified for assessing corrosion resistance by both MIL-C-81706 and MIL-PRF-23377G. Although there is considerable criticism of the method's reliability and relevance to service performance, salt spray testing is recognized as the standard in many industries as well as in the military.<sup>10</sup>

In the current study, the salt spray performance of HT-coated, epoxy-primed AA2024-T3 was investigated. The primary goal was to determine the optimal treatment for service performance. The selection of treatments for evaluation was based on a number of considerations. During the coating step, bath chemistries including different lithium salts were used to incorporate various oxoanions (e.g., carbonate, nitrate, and persulfate) into the HT structure. Some of the coated samples also received additional post-coating treatments such as a transition metal seal, hydrothermal reversion, or adsorption of a hydration inhibitor. Practicality was another factor in determining what treatments were analyzed. Eliminating potentially unnecessary processing steps (e.g., degreasing and/or deoxidizing) and energy-intensive parameters (e.g., elevated temperature) would be beneficial to producing these coatings on an industrial scale.

The flexibility of numerous treatment options available for HT processing is coupled with questions

of product variation. Treatment variables that could be relevant include the following:

- the degreasing and deoxidizing steps
- different anions in the HT interlayer
- different temperature/time combinations during processing
- post-coating treatments such as hydrothermal reversion or adsorption of a hydration inhibitor
- incorporation of active corrosion protection

Additional testing included electrochemical impedance spectroscopy (EIS) and adhesion testing. These tests were performed to determine the relative importance of stand alone corrosion resistance and coating adhesion in salt spray performance. Although the importance of adhesion in the corrosion resistance of painted substrates is debated,<sup>11-12</sup> it is generally recognized that some degree of wet adhesion is necessary for adequate corrosion protection.<sup>13</sup>

## EXPERIMENTAL PROCEDURES

### *Application of Coatings*

Various HT coating chemistries were applied to 4-in.-by-5-in. (102-mm-by-127-mm) AA2024-T3 panels. Prior to processing, the panels were scrubbed with nonmetallic scouring pads in detergent solution, then rinsed in deionized water and air-dried. Most of the HT coatings were applied using a conventional three-bath process consisting of degreasing, deoxidizing, and coating. Bare AA2024-T3 was included as a blank, while CCC, applied by an Alodine<sup>†</sup> process per manufacturer's instructions, were used as a control. A total of nine different HT coatings were evaluated. These treatments and their designations used in this study are listed in Table 1.

A total of 15 panels were made for each treatment evaluated. Five of the panels were set aside for stand-alone salt spray testing. Three days after the conversion coatings were applied, the remaining panels were coated with a two-part, high-solids epoxy primer. Half of the primed samples were coated with a chromated primer (Type 1, Class C per MIL-P-23377G), while the others received a primer with nonchromate inhibitors (Type 1, Class N). After drying, a high-solids polyurethane topcoat was applied. The top-coated and primed samples were allowed to dry for 3 weeks prior to salt spray exposure. (The primed and top-coated samples are hereafter referred to as "primed.")

### *Salt Spray Exposure*

The samples were exposed to 5 wt% sodium chloride (NaCl) salt spray in accordance with ASTM B117.<sup>(2)</sup> Salt spray exposure was initiated 10 days after the conversion coatings were applied. The stand-alone (unprimed) samples were exposed for 336 h per MIL-C-81706 and visually inspected for signs of corrosion after 168 h and 336 h of exposure.

<sup>†</sup> Trade name.

<sup>(2)</sup> ASTM, 100 Barr Harbor Drive, West Conshohocken, PA 19428.

**TABLE 1**  
*HT Conversion Coating Chemistries Evaluated<sup>(A)</sup>*

Coating Designation	Time (min)	Temperature (°C)	Recipe
AlO <sub>2</sub>	5	95	NO <sub>3</sub> -5-95 coating followed by 15 min immersion in boiling 0.1 M Al <sub>2</sub> O <sub>3</sub> ·Na <sub>2</sub> O
Bare	—	—	Bare AA2024-T3 as blank
CCC	—	—	Alodine process used as a control
CO <sub>3</sub>	5	95	0.07 M Na <sub>2</sub> CO <sub>3</sub> , 0.015 M Li <sub>2</sub> CO <sub>3</sub> , 0.1 M LiOH·H <sub>2</sub> O, 600 ppm Al <sub>2</sub> O <sub>3</sub> ·Na <sub>2</sub> O
Hydro	5	95	NO <sub>3</sub> -5-95 coating followed by 15 min immersion in boiling deionized H <sub>2</sub> O
MnO <sub>4</sub>	5	95	NO <sub>3</sub> -5-95 coating followed by 5 min immersion in NO <sub>3</sub> recipe + 0.01 M MnO <sub>4</sub> at 95°C
NO <sub>3</sub> -PPA	5	95	NO <sub>3</sub> -5-95 coating followed by dip in 10 wt% PPA at RT
NO <sub>3</sub> -30-RT	30	RT	0.3 M KNO <sub>3</sub> , 0.03 LiNO <sub>3</sub> , 0.1 M LiOH·H <sub>2</sub> O, 600 ppm Al <sub>2</sub> O <sub>3</sub> ·Na <sub>2</sub> O (NO <sub>3</sub> recipe)
NO <sub>3</sub> -5-95	5	95	NO <sub>3</sub> recipe
NO <sub>3</sub> -nopre	5	95	NO <sub>3</sub> recipe without degreasing or deoxidizing steps
S <sub>2</sub> O <sub>8</sub>	5	95	NO <sub>3</sub> recipe + 0.01 M K <sub>2</sub> S <sub>2</sub> O <sub>8</sub>

<sup>(A)</sup> Immersion time, temperature, and components of coating bath listed in addition to other processing variations.

The panels were removed and washed before the final evaluation was made. MIL-C-81706 specifies that no corrosion whatsoever should be visible. For comparison, specimens were rated on a scale of 0 to 5, where 0 indicates no corrosion and 5 severe corrosion. Ranking was based on the appearance of all five replicates in aggregate.

The primed samples were exposed for 2,000 h per MIL-PRF-23377G. According to the military specification, the primer "shall exhibit no blistering, lifting of the coating system, or substrate corrosion after exposure." Again, a qualitative ranking was used for comparison. Three parameters were evaluated for each replicate: corrosion at the scribe, undercutting, and blistering. For corrosion, 0 indicates a bright, clean scribe; 1 indicates staining and possible minor corrosion spots but no buildup of corrosion product; and 2 through 5 indicate the relative severity of corrosion product buildup, with 2 and 3 typically being limited to the scribe and 4 and 5 showing migration from the scribe. Undercutting indicates lifting, or loss of adhesion of the coating system at the scribe caused by corrosion. Blistering indicates attack at the scribe only. The rankings for undercutting and blistering were also on a scale of 0 to 5 (0 = no change, 1 = minor, 2 = minor to moderate, 3 = moderate, 4 = major, and 5 = severe).

### EIS

AA2024-T3 panels were treated with selected coating chemistries listed in Table 1, including AlO<sub>2</sub>, CO<sub>3</sub>, Hydro, MnO<sub>4</sub>, NO<sub>3</sub>-5-95, NO<sub>3</sub>-PPA, and S<sub>2</sub>O<sub>8</sub>.

Bare AA2024-T3 was also tested as a blank. EIS data for the samples were collected after 24 h exposure to 0.5 M NaCl at room temperature and ambient aeration. A parameter indicating the corrosion resistance of the coating,  $R_{corr}$ , was fit from the spectra using a complex nonlinear least-squares fitting program.  $R_{corr}$  is the polarization resistance minus the diffusional impedance and has been used successfully in previous studies of conversion-coated aluminum alloys.<sup>14</sup>

### Adhesion Testing

Epoxy coatings were applied to panels treated with selected coating chemistries, listed in Table 1 (AlO<sub>2</sub>, CO<sub>3</sub>, Hydro, MnO<sub>4</sub>, NO<sub>3</sub>-5-95, and S<sub>2</sub>O<sub>8</sub>). Bare AA2024-T3 and CCC were also coated as a blank and control, respectively. The epoxy consisted of a bisphenol A(BPA)-epichlorohydrin resin with a polyamide hardener and is representative of the epoxy chemistry used in epoxy primers for aerospace applications. Spin casting was used to apply epoxy coatings 25  $\mu$ m to 75  $\mu$ m thick.

The practical adhesion was measured by the pull-off tensile strength (POTS) of the epoxy, which was taken from the samples using a pneumatic adhesion tensile testing instrument (PATTI). The POTS tests were performed in accordance with ASTM Method D4541, "Standard Test Method for Pull-Off Strength of Coatings Using Portable Adhesion Testers," using a Type IV self-alignment adhesion tester.

In addition to the dry adhesion, the wet state adhesion was measured after 24 h exposure to deion-

TABLE 2

Stand-Alone Corrosion-Resistance Results of Salt Spray and EIS Testing for Unprimed Treatments<sup>(A)</sup>

Specimen	Ranking <sup>(B)</sup>	$R_{corr}$ ( $k\Omega\text{-cm}^2$ )
AlO <sub>2</sub>	3	26 ± 7
Bare	5	7 ± 1
CCC	0	944 ± 568
CO <sub>3</sub>	5	16 ± 2
Hydro	2	285 ± 142
MnO <sub>4</sub>	2	250 ± 130
NO <sub>3</sub> -PPA	5	11 ± 2
NO <sub>3</sub> -30-RT	4	—
NO <sub>3</sub> -5-95	4	26 ± 6
NO <sub>3</sub> -nopre	5	—
S <sub>2</sub> O <sub>8</sub>	3	96 ± 26

<sup>(A)</sup> Reported values are the average of five replicates.  $R_{corr}$  values fit from EIS data after 24 h exposure to 0.5 M NaCl.

<sup>(B)</sup> Rankings after 336 h salt spray exposure. "0" indicates no corrosion, and "5" indicates the greatest severity of corrosion.

ized water. After aqueous exposure, the samples were wiped dry and the pull-off stubs were attached with cyanoacrylate adhesive. The adhesive was allowed to cure for 30 min prior to testing.

## RESULTS AND DISCUSSION

The salt spray ranking of the unprimed and primed samples are listed in Tables 2 and 3, respectively. Rankings of the damage parameters (corrosion, undercutting, and blistering) for the Class-N (nonchromated) and Class-C (chromated) primer-coated samples are graphically depicted in Figures 1 and 2, respectively.

### Stand-Alone Corrosion Protection

The most apparent result from the salt spray is that the CCC performed better than the HT treatments for both the stand-alone and primer-coated samples. In the present study, the laboratory-applied CCC was the only unprimed treatment to pass the 336-h requirement of MIL-C-81706. However, it should be pointed out that, in a previous study of field-applied CCC,<sup>15</sup> the salt spray performance of the CCC did not conform to the military specification, despite the proven service history of CCC.

Six of the HT treatments ranked better than the bare AA2024-T3. Two of the treatments, MnO<sub>4</sub> and Hydro, received a ranking of 2, followed by S<sub>2</sub>O<sub>8</sub> and AlO<sub>2</sub> (ranking of 3) and NO<sub>3</sub>-5-95 and NO<sub>3</sub>-30-RT (ranking of 4). Based on prior studies, the MnO<sub>4</sub> and Hydro coatings would have been expected to display good stand-alone corrosion resistance. MnO<sub>4</sub> coatings have been shown to provide active corrosion protection.<sup>16</sup> Hydrothermal treatment of HT coatings has been shown to revert the HT to a bayerite layer with a thickness comparable to that of anodized coatings.<sup>4</sup>

TABLE 3

Rankings of Primed Treatments after 2,000 h of Salt Spray Exposure<sup>(A)</sup>

Specimen	Class-N Primer	Class-C Primer
AlO <sub>2</sub> (1)	2-4-2	1-1-0
AlO <sub>2</sub> (2)	2-5-2	1-1-0
AlO <sub>2</sub> (3)	2-5-0	1-2-0
AlO <sub>2</sub> (4)	2-4-2	1-1-0
AlO <sub>2</sub> (5)	2-4-2	2-1-0
Bare (1)	2-2-2	0-0-0
Bare (2)	2-1-3	1-0-0
Bare (3)	2-1-1	1-0-0
Bare (4)	2-1-1	1-0-0
Bare (5)	2-1-2	0-0-0
CCC (1)	1-0-0	0-0-0
CCC (2)	1-0-0	0-0-0
CCC (3)	1-0-0	1-0-0
CCC (4)	1-0-0	1-0-0
CCC (5)	1-0-0	0-0-0
CO <sub>3</sub> (1)	3-1-5	2-3-0
CO <sub>3</sub> (2)	3-0-5	2-2-0
CO <sub>3</sub> (3)	3-0-5	2-2-0
CO <sub>3</sub> (4)	3-0-5	2-3-0
CO <sub>3</sub> (5)	3-1-5	2-3-0
Hydro (1)	3-1-2	1-2-0
Hydro (2)	3-1-1	1-2-0
Hydro (3)	3-2-2	1-2-0
Hydro (4)	3-3-1	1-2-0
Hydro (5)	3-2-3	1-3-0
MnO <sub>4</sub> (1)	3-1-1	1-3-0
MnO <sub>4</sub> (2)	3-2-1	1-3-0
MnO <sub>4</sub> (3)	4-2-0	1-3-0
MnO <sub>4</sub> (4)	4-1-1	1-3-0
MnO <sub>4</sub> (5)	3-1-0	1-4-0
NO <sub>3</sub> -PPA (1)	3-2-2	2-5-0
NO <sub>3</sub> -PPA (2)	3-1-1	2-5-0
NO <sub>3</sub> -PPA (3)	3-1-0	2-5-0
NO <sub>3</sub> -PPA (4)	3-1-1	2-5-0
NO <sub>3</sub> -PPA (5)	3-1-1	2-5-0
NO <sub>3</sub> -30-RT (1)	3-1-3	1-0-0
NO <sub>3</sub> -30-RT (2)	3-0-4	2-0-0
NO <sub>3</sub> -30-RT (3)	3-1-5	2-0-0
NO <sub>3</sub> -30-RT (4)	3-1-5	1-0-0
NO <sub>3</sub> -30-RT (5)	3-0-4	1-0-0
NO <sub>3</sub> -5-95 (1)	3-1-1	1-1-0
NO <sub>3</sub> -5-95 (2)	3-1-1	1-4-0
NO <sub>3</sub> -5-95 (3)	3-1-0	2-3-0
NO <sub>3</sub> -5-95 (4)	3-2-1	1-3-0
NO <sub>3</sub> -5-95 (5)	3-2-1	2-4-0
NO <sub>3</sub> -nopre (1)	3-1-3	2-0-0
NO <sub>3</sub> -nopre (2)	3-0-2	1-0-0
NO <sub>3</sub> -nopre (3)	3-0-3	1-0-0
NO <sub>3</sub> -nopre (4)	3-0-3	1-0-0
NO <sub>3</sub> -nopre (5)	3-0-3	2-0-0
S <sub>2</sub> O <sub>8</sub> (1)	3-1-0	1-4-0
S <sub>2</sub> O <sub>8</sub> (2)	3-1-0	1-4-0
S <sub>2</sub> O <sub>8</sub> (3)	3-1-1	1-4-0
S <sub>2</sub> O <sub>8</sub> (4)	3-1-1	1-3-0
S <sub>2</sub> O <sub>8</sub> (5)	3-1-0	1-3-0

<sup>(A)</sup> Three parameters evaluated for each replicate: corrosion, undercutting, and blistering (left to right). 0 to 5 indicates lowest to highest degree of severity. Class-N primer contains a nonchromate inhibitor, and Class-C is a chromated primer.

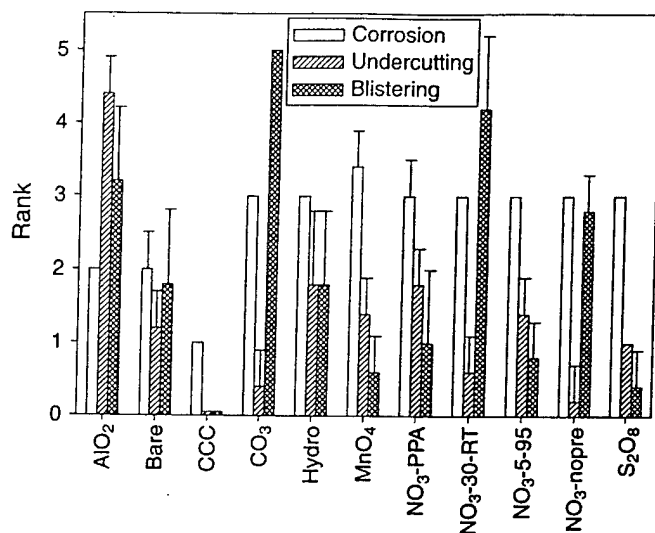


FIGURE 1. Rankings of the degree of corrosion, undercutting, and blistering for treatments with nonchromated primer (Class-N). The bar indicates the average value for five replicates.

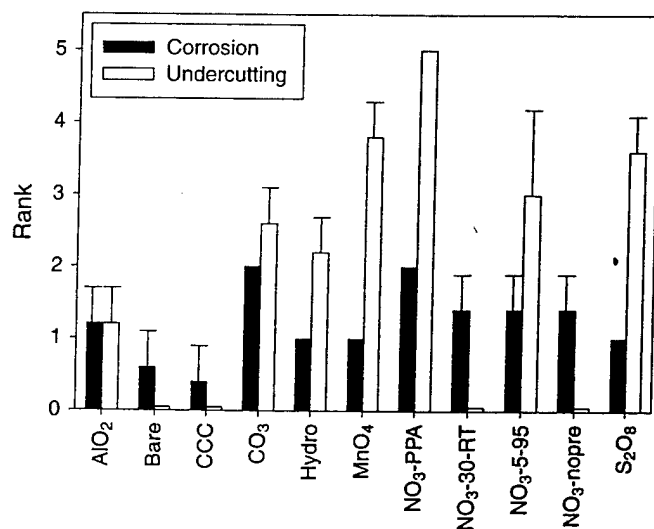


FIGURE 2. Rankings of the degree of corrosion and undercutting for treatments with chromated primer (Class-C). The bar indicates the average value for five replicates. No blistering was observed for any treatment.

The  $R_{\text{corr}}$  values fit from the EIS data for each treatment are included in Table 2. Threshold  $R_{\text{corr}}$  values have been proposed as indicators of the salt spray performance of conversion-coated aluminum alloys.<sup>14</sup> Conversion coatings on AA2024-T3 with a  $R_{\text{corr}}$  value  $> 2 \times 10^6$  to  $5 \times 10^6 \Omega\text{-cm}^2$  would be expected to have  $\leq 5$  visible pits after 168 h of salt spray. The exposure time in the present study was greater (336 h), and ranking was based on an ordinal scale rather than pass/fail. Nonetheless, the  $R_{\text{corr}}$  values can be used as a qualitative indicator of salt spray performance. In fact, the stand-alone salt spray performance correlated reasonably well with the  $R_{\text{corr}}$  values. For the chromated control samples,

values from the previously mentioned study were included for reference.<sup>14</sup>

### Primed Samples

When Class-C (chromated) primers were used, the conversion coating seemed to be unnecessary in terms of corrosion resistance. However, this was not the case for nonchromated primers. In the presence of the Class-N primer (nonchromated), the bare AA2024-T3 samples performed only slightly worse than the CCC, and only one HT treatment ( $\text{AlO}_2$ ) performed as well as the blank. Thus, eight of the nine HT conversion coatings tested decreased the corrosion resistance when used within a coating system.

It should also be pointed out that chromate in both the conversion coating and primer greatly reduced the amount of blistering. However, the Class-N primer showed better undercutting resistance in 6 of the 11 treatments.

Looking at the results for the stand-alone conversion coatings and the primer-coated samples, the effects of the different treatments can be compared. The degreasing and deoxidizing steps decreased the corrosion resistance of the nonprimed  $\text{NO}_3$ -HT conversion coating. However, in the primer-coated samples, an equivalent corrosion resistance was seen regardless of the pretreatment steps. In addition, when the pretreatment was included, the two time-temperature combinations had the same corrosion resistance whether tested as stand-alone or with primer coats. Varying the time and temperature of the coating step altered the coating thickness and morphology. The fact that the two time-temperature combinations produced coatings with similar corrosion resistance suggests that the coating morphology is not the determining factor in corrosion resistance. It is difficult to delineate the separate effects of time and temperature because neither was independently controlled. Practically, these results indicate that the cost associated with elevated temperature is not justified by improved corrosion resistance.

Several post-coating treatments for HT were evaluated in the present study. The results of the unprimed  $\text{MnO}_4$  and Hydro coatings have already been discussed. In general, none of post-treated HT conversion coatings performed well when used within a coating system. It was believed that the use of a hydration inhibitor, phenylphosphinic acid (PPA), as a post-coating would increase the environmental durability of the conversion coating/primer interface. Not only did it decrease the performance of the primed samples, but it also decreased the corrosion resistance of the unprimed samples. In addition to adsorption, the PPA might have reacted with the HT by intercalation, causing the observed decrease in corrosion resistance. Other researchers have reported intercalation of PPA in HT-like compounds by anion exchange.<sup>17</sup>



TABLE 4  
Dry and Wet POTS of Epoxy from Treated Substrates

Specimen	Dry POTS (MPa)			Wet POTS (MPa)		
	Mean	Std. Dev. <sup>(A)</sup>	Median	Mean	Std. Dev.	Median
AlO <sub>2</sub>	3.21	1.03	3.19	1.43	0.37	1.4
Bare	4.04	1.66	3.79	1.28	0.59	1.22
CCC	6.8	1.08	6.72	3.66	1.18	3.69
CO <sub>3</sub>	5.35	1.34	5.31	2.47	0.99	2.4
Hydro	4.53	1.51	4.85	1.41	0.37	1.47
MnO <sub>4</sub>	4.72	1.02	4.64	1.88	0.49	1.96
NO <sub>3</sub> -5-95	4.98	1.39	4.85	2.2	0.65	2.25
S <sub>2</sub> O <sub>8</sub>	3.91	1.92	4.29	2.32	0.38	2.39

<sup>(A)</sup> Standard deviation.

As a means of comparing the overall performance of the primed treatments, the corrosion, undercutting, and blistering parameters were summed for all five replicates. For the Class-N primer, the ranking is as follows:

$$\text{CCC} > \text{S}_2\text{O}_8 \geq \text{bare AA2024} \geq \text{NO}_3\text{-5-95} = \text{NO}_3\text{-PPA} > \text{other treatments} \quad (1)$$

For the Class-C primer:

$$\text{CCC} > \text{bare AA2024} > \text{NO}_3\text{-nopre} = \text{NO}_3\text{-30-RT} > \text{AlO}_2 > \text{other treatments} \quad (2)$$

This is intended not as a rigorous analysis but merely as a method to compare the treatments.

### Adhesion

The dry- and wet-state POTS results are shown in Table 4. Cumulative probability plots are useful for visualizing the POTS distributions and rankings for different treatments, as seen in Figures 3 and 4 for the dry and wet states, respectively.

A one-way analysis of variance (ANOVA) was used to test for differences among the average POTS values. Tukey's method was used to compare each treatment with the others to see which were significantly different at a 95% confidence.<sup>18</sup> The fact that the population sizes and standard deviations were different among the treatments decreases the rigidity of the test, but a reasonable approximation was obtained. The comparison from Tukey's method can be interpreted by looking at which treatments significantly differ from one another. The CCC POTS is significantly greater than that of all other treatments. Comparing the bare AA2024-T3 POTS with that of the other treatments, the CO<sub>3</sub>, NO<sub>3</sub>, and MnO<sub>4</sub> POTS are all higher than the POTS of the degreased AA2024-T3. The POTS of the Hydro and S<sub>2</sub>O<sub>8</sub> HT are equivalent to that of the bare AA2024-T3 while the POTS of the AlO<sub>2</sub> HT is worse than that of the bare AA2024. The rankings are as follows:

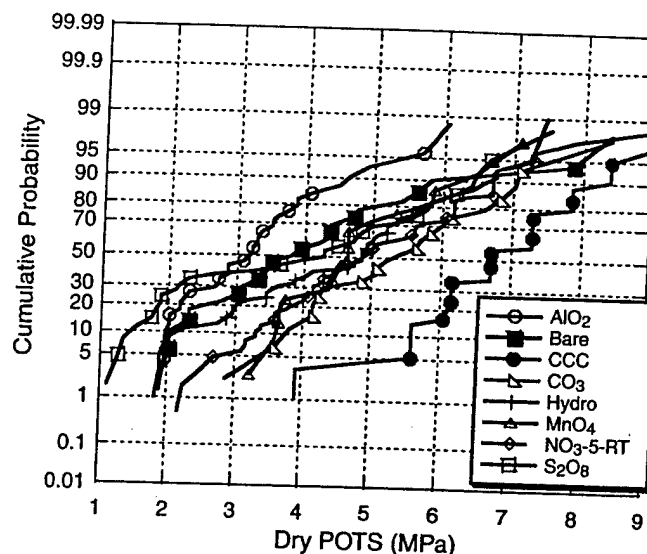


FIGURE 3. Dry POTS cumulative probability curves.

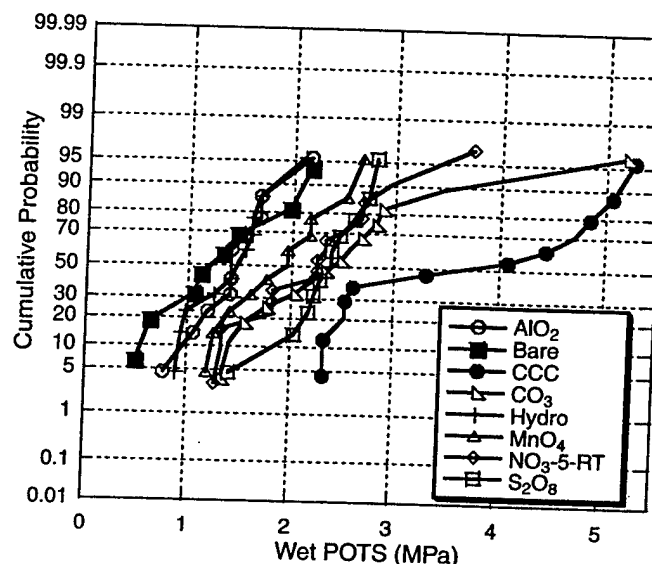


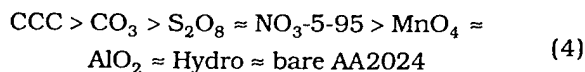
FIGURE 4. Wet POTS cumulative probability curves.

$$\text{CCC} > \text{CO}_3 \approx \text{NO}_3 \approx \text{MnO}_4 > \text{Hydro} \approx \text{bare AA2024} \approx \text{S}_2\text{O}_8 > \text{AlO}_2 \quad (3)$$

Similar analysis was used for the wet POTS results. The most significant result is the large decrease in the wet-state POTS relative to the dry state. This was true for all treatments. Fischer's LSD Multiple Comparison Test indicated that the POTS for CCC and CO<sub>3</sub> are significantly larger than for all other treatments. Most likely, the POTS for CO<sub>3</sub> is not equivalent to that of CCC, as evidenced by the difference in the median values shown in Figure 4. Comparing the bare AA2024-T3 with the other treatments, the POTS for S<sub>2</sub>O<sub>8</sub> and NO<sub>3</sub> are higher than the bare AA2024. The POTS for MnO<sub>4</sub>, AlO<sub>2</sub>, and Hydro HT are all equivalent to that of the bare AA2024.



The rankings are as follows:



There is a factor not accounted for in the EIS or adhesion tests that could account for the difference in the corrosion performance observed for the stand-alone and primed samples. The intercalation reaction by which the HT is formed is reversible. As previously mentioned, the HT will de-intercalate. This is not problematic in the absence of a primer. However, in the presence of a primer, the release of ions beneath the primer provides an osmotic gradient that further promotes water ingress. This mechanism can be viewed as an asset or a liability. If the HT were engineered such that the interlayer oxoanion were a slowly leaching inhibitor, de-intercalation could provide a reservoir for active corrosion protection at the onset of water ingress.

## SUMMARY

No correlation was observed between the wet and dry POTS rankings and the salt spray performance of the primer-coated samples. Adhesion issues will be examined in future publications. In addition, no correlation was observed between the primer-coated salt spray performance and the stand-alone corrosion resistance, whether gauged by EIS or salt spray.

This study has determined that the salt spray performance of the nine HT conversion coatings tested is not as good as that of CCC when implemented within a full coating system (i.e., conversion coating with a primer and a topcoat). In some cases, HT performs worse than a nonconversion-coated but primed sample. Thus, present HT coating chemistries are better optimized for stand-alone corrosion resistance than for resistance within a coating system. The salt spray performance of a coating system cannot be predicted by simple addition of the independent performance of each component, which points to the need to test the coating component under development within a total coating system. Individual components of a coating system may perform well in isolation, yet their composite may behave in an unexpected manner.

## CONCLUSIONS

- ❖ Present HT coating chemistries are optimized for stand-alone corrosion resistance.
- ❖ The HT coating chemistries tested in the present study do not perform as well as CCC as a coating pretreatment (i.e., within a coating system).

- ❖ Neither the pretreatment, incorporation of active corrosion protection, reversion, nor hydration inhibitor improved the salt spray performance of the primed samples.
- ❖ The salt spray performance of primed and conversion-coated AA2024 does not correlate with the epoxy adhesion or stand-alone corrosion resistance of the conversion coating.
- ❖ The need for an integrated approach in coatings development is reinforced.

## ACKNOWLEDGMENTS

This work was sponsored by the Defense Advanced Research Project (DARPA Contract no. F49620-1-0305) under the direction of S. Wax and P. Trulove of the Air Force Office of Scientific Research (AFOSR). The assistance of D. Peeler (Air Force Research Laboratory [AFRL]), K. Chitwood, K. Clendenon, D. Huff, S. Lanter, A. Logue, and D. Tocci of the University of Dayton Research Institute (UDRI) in paint application and salt spray testing is acknowledged.

## REFERENCES

1. J.W. Davis, J.I. Maurer, L.E. Steinbrecher, "Surface Cleaning, Finishing, and Coating," in *Metals Handbook*, vol. 5 (Materials Park, OH: ASM International, 1982), p. 597.
2. C.J. Carpenter, *Plat. Surf. Fin.* 77, 4 (1990): p. 35.
3. R.G. Buchheit, M.D. Bode, G.E. Stoner, *Corrosion* 50, 3 (1994): p. 205.
4. R.G. Buchheit, M.A. Martinez, L.P. Montes, N.P. Cella, S.R. Taylor, G.E. Stoner, "Non-Electrolytic Formation of Al-Oxide Surface Layers by Reversion of Hydrotalcite," *CORROSION/98*, paper no. 216 (Houston, TX: NACE International, 1998).
5. R.G. Buchheit, M.A. Martinez, L.P. Montes, N.P. Cella, S.R. Taylor, G.E. Stoner, "Inorganic Cr-Free Conversion Coatings for High Corrosion Resistance and Low Electrical Contact Resistance," *CORROSION/98*, paper no. 212 (Houston, TX: NACE, 1998).
6. R.B. Leggat, E.A. Pehovaz-Diez, N.P. Cella, S.R. Taylor, "Optimization of Bath Chemistry for Hydrotalcite-Based Conversion Coatings of Aerospace Aluminum Alloys," in *Corrosion and Corrosion Prevention of Low-Density Metals and Alloys*, eds. B.A. Shaw, R.G. Buchheit, J.P. Moran (Pennington, NJ: Electrochemical Society [ECS], 2001), p. 124.
7. MIL-C-81706, "Military Specification Chemical Conversion Materials for Coating Aluminum and Aluminum Alloys" (Warminster, PA: U.S. Naval Air Development Center, 1979).
8. MIL-C-5541E, "Military Specification Chemical Conversion Coatings on Aluminum and Aluminum Alloys" (Lakehurst, NJ: Naval Air Engineering Center, 1990).
9. MIL-PRF-23377G, "Primer Coatings: Epoxy, High-Solids" (Lakehurst, NJ: Naval Air Engineering Center, 1989).
10. B.R. Appleman, *J. Coat. Technol.* 62, 787 (1990): p. 57.
11. P. Walker, *J. OCCA* 68, 12 (1985): p. 319.
12. W. Funke, *J. OCCA* 69, 3 (1986): p. 78.
13. R.A. Dickie, "Adhesion of Organic Coatings and Its Loss Due to Corrosion," in *Adhesion Aspects of Polymer Coatings*, ed. K.L. Mittal (New York, NY: Plenum Press, 1983), p. 391.
14. R.G. Buchheit, M. Cunningham, H. Jensen, M.W. Kendig, M.A. Martinez, *Corrosion* 54, 1 (1998): p. 61.
15. R.B. Leggat, S.R. Taylor, W. Zhang, R.G. Buchheit, *Corrosion* 58, 3 (2002): p. 283.
16. R.G. Buchheit, S.B. Mamidipally, P. Schmutz, H. Guan, *Corrosion* 58, 1 (2002): p. 3.
17. F.M. Vichi, O.L. Alves, *J. Mater. Chem.* 7, 8 (1997): p. 1,631.
18. J.L. Devore, *Probability and Statistics for Engineering and the Sciences* (Pacific Grove, CA: Duxbury, 2000), p. 141.

## IN-SITU CONFOCAL LASER SCANNING MICROSCOPY SURFACE METROLOGY STUDIES OF CORROSION ON AA 2024-T3:

### Influence of electrolyte composition on the corrosion morphology of bare AA2024-T3

G. O. Ilevbare, O. Schneider, R.G. Kelly, J.R. Scully

Center for Electrochemical Science and Engineering, Department of Materials Science and Engineering, University of Virginia, Charlottesville, VA 22904-4745

### ABSTRACT

The electrochemical behavior of bulk synthesized Al-Cu, Al-Cu-Mg, and Al-Cu-Fe-Mn intermetallic compounds as well as that of AA 2024-T3 have been studied and correlated with the morphology of attack at and around the intermetallic compounds present on the bare polished surface of AA 2024-T3. Exposures were conducted in four solutions: 0.1 M Na<sub>2</sub>SO<sub>4</sub> + 0.005 M NaCl (pH 6), 0.1 M Na<sub>2</sub>SO<sub>4</sub> + 0.005 M NaCl + 0.0001 M NaOH (pH 10), 0.1 M Na<sub>2</sub>SO<sub>4</sub> + 0.005 M Cl<sup>-</sup> (as AlCl<sub>3</sub>) (pH 3) and 0.5 M NaCl (pH 6). Similar morphology of attack was observed at each type of Intermetallic regardless of electrolyte composition. However, the rates of attack differed. These results suggest that the mechanism of the initial stages of local attack may be similar in all these electrolytes.

**KEYWORDS:** AA 2024-T3, intermetallics, localized corrosion, *in-situ* microscopy

### INTRODUCTION

Aluminum-based precipitation age hardened alloys containing Cu and Fe are prone to localized corrosion such as pitting induced by galvanic interactions between Cu-rich intermetallics compounds (IMC) and the Al-alloy matrix. These local galvanic cells, which induce pitting and alkaline attack, are often formed by Cu- and Fe-containing intermetallics or replated Cu [1-13]. In AA 2024-T3, pit initiation sites include Al-Cu-Mg particles [1, 2, 7, 11-13], the periphery of Cu-enriched Al-Cu-Mg particles that have been dealloyed of Al and Mg [2], and the matrix adjacent to Al-Cu and Al-Cu-Fe-Mn particles [1, 8, 11, 10]. Of these intermetallics, the Al-Cu-Mg type is the most active. It is anodic to the Al-matrix and generally dissolves leaving a fine Cu-sponge (resulting from the de-alloying of both Al and Mg). Thus, with time it now becomes cathodic to the matrix [1, 2, 12, 13]. Under certain conditions, some authors have observed rings of redeposited Cu around these Al-Cu-Mg precipitates [14]. As much as 60% of the intermetallics on the surface of an AA 2024-T3 sample could be of the Al-Cu-Mg type [2, 15]. The Al-Cu, and Al-Cu-Mn-Fe types of intermetallic compounds are positive (serve as cathodic sites) relative to the Al-matrix [16]. As a result, Cu<sup>2+</sup> ions dissolved in solution can be reduced readily on these particles [1]. The generation of OH<sup>-</sup> ions at these particles due to the reduction of oxygen leads to alkaline attack of the Al adjacent to these particles, resulting in a trench-like attack morphology (trenching), which often forms a perimeter around the particle [8, 11, 17, 18]. In addition, pitting can occur in the matrix in halide containing solutions [16].

This work focuses on the comparison of the attack morphology of localized corrosion on AA 2024-T3 at these IMC studied in-situ in various electrolytes that simulate blister solutions under painted AA 2024-T3 [19], and the correlation of these observations to electrochemical data from AA 2024-T3 and the bulk synthesized analogues of the different types of IMC in the various solutions. Of interest is the effect of bulk solution pH and chloride concentration on the attack morphologies at IMC particles on bare polished AA 2024-T3 surfaces. In a subsequent paper,

these results shall be compared to the corrosion processes observed in underpaint corrosion [20, 21].

The method applied for in-situ studies was Confocal Laser Scanning Microscopy (CLSM). CLSM significantly surpasses the capabilities of common optical microscopy to measure and quantify surface metrology [8, 22-24]. A laser beam scans the surface of the sample in the x-y direction. A small pinhole is located in front of the detector at a position that is optically conjugate to the focal point in the sample plane. The intensity of the light reflected from the sample on the focal plane is measured by the detector for each x-y-position. Most of the light scattered from out-of-focus planes is focused outside the pinhole and, therefore, does not reach the detector. This effect allows sharp imaging of a single sample plane known as a slice. By moving the sample surface stepwise through the focal plane (upwards and downwards) with a z-scanning stage, the three-dimensional surface topography can be calculated from assembly of the slices recorded at each z-step. This assembly is known as a stack. Data for surface roughness, surface profiles and pit depths can thus be obtained. In addition, a 2-dimensional (2D) microscopic image with extended depth-of-focus can be calculated. This process assigns a grey level to each image pixel, which corresponds to the brightest level at this x-y-position in all slices.

CLSM is a contact-free method [8, 22]. CLSM has found extensive use in biology because it allows the three-dimensional (3D) *in-vivo* monitoring of transparent biological entities such as cells [22]. In materials science it has been used, for example, to study defects in thermal spray coatings [23]. The method has recently been applied to corrosion studies on bare aluminum alloy 2024-T3 (AA 2024-T3) [8, 9, 24]. It was also shown to be a powerful tool for the in-situ study of underfilm corrosion [20].

## EXPERIMENTAL PROCEDURES

CLSM was carried out using a Zeiss model LSM 510 microscope. Imaging was performed with an argon laser (488 nm wavelength). The studies were conducted on 1.5 mm thick AA 2024-T3 sheets (from Kaiser) with the composition (major elements): Cu 4.5%, Mg 1.30%, Mn 0.62%, Fe 0.18%, Zn 0.10%, Si 0.093%, (in wt. %), balance Al. AA 2024-T3 coupons were cut from 90 by 120 cm sheets to squares of about 2.5 by 2.5 cm. One face of the coupons was abraded with SiC paper (from 180 up to 1200 grit), and then polished with 1  $\mu$ m diamond suspension. A thickness of about 0.1-0.3 mm of the sample was removed during the grinding and polishing processes.

SEM-EDS (Scanning Electron Microscopy-Energy Dispersive X-Ray Spectroscopy) studies were conducted on some samples to identify and analyze the intermetallic particles on the surface with a Jeol 840 SEM coupled to a Kevex EDS system at a voltage of 20 KV. Secondary Electron Images (SEI) were generated in all cases. In order to monitor the topography changes in-situ, a specially constructed flat electrochemical cell was mounted on the x-y-z-stage of the CLSM. A detailed description of the cell can be found elsewhere [20]. The electrolytes were not stirred, and there were several mm of electrolyte on the substrate in the flat cell. Prior to the introduction of any electrolyte, areas of interest for study were then selected with the 100x immersion objective lens of the CLSM. In some cases, some of the surface features that were studied were first chosen with the aid of the SEM. Imaging of the areas of interest commenced after the introduction of electrolyte into the flat cell, and any changes in surface morphology were monitored with time. 0.5 M NaCl (pH 6) was chosen as an example of a very corrosive environment. A solution containing 0.005 M NaCl + 0.1 M Na<sub>2</sub>SO<sub>4</sub> (pH 6)<sup>a</sup> was chosen for its lower corrosivity. This composition has been used in previous studies [16, 25, 26]. It produces differences between OCP and the pitting potential ( $E_{pit}$ ) in AA 2024-T3 [16]. However, some galvanically induced pitting corrosion is still observed in this electrolyte because of the close

<sup>a</sup> This is referred to as the 'standard solution'.

proximity of OCP to pitting potential associated with the Al-matrix [16]. To examine the influence of the pH such as seen under blisters on painted Al [19] 0.1 M  $\text{Na}_2\text{SO}_4$  + 0.005 M NaCl + 0.0001 M NaOH (pH 10, "alkaline solution"), and 0.1 M  $\text{Na}_2\text{SO}_4$  + 0.005 M  $\text{Cl}^-$  (as 0.00167 M  $\text{AlCl}_3$ ) adjusted to pH 3 with  $\text{H}_2\text{SO}_4$  ("acidic solution") were also used.

Electrochemical studies were performed on high purity Al (99.998%), Cu (99.999%), AA 2024-T3 and bulk synthesized intermetallic castings:  $\text{Al}_2\text{Cu}$  (Al-Cu),  $\text{Al}_2\text{CuMg}$  (Al-Cu-Mg), and  $\text{Al}_{20}\text{Cu}_2(\text{MnFe})_3$  (Al-Cu-Mn-Fe). Open circuit potential (OCP) exposures followed by potentiodynamic polarization experiments were performed in the sulfates based electrolytes given above, at ambient temperature in a 3-electrode cell that was open to lab air. Details are discussed elsewhere [16, 27]. The reference used was the saturated calomel electrode (SCE).

## RESULTS

### a) SEM-EDS

SEM-EDS results from bare polished surfaces of AA 2024-T3 samples indicated the presence of Al-Cu, Al-Cu-Mg and Al-Cu-Mn-Fe type intermetallic compounds. Al-Cu-Mg intermetallic particles were usually spherical while Al-Cu and Al-Cu-Mn-Fe intermetallics had blocky angular features (Figures 1a and 1b). Clustering of distinct Al-Cu and Al-Cu-Mn-Fe particles was especially observed.

Results from EDS analyses of the intermetallics particles on AA 2024-T3 prior to electrolyte exposure are presented in Table 1. Differences in apparent composition were observed amongst particles with the same elemental constituents. The compositions of some of the intermetallic particles were consistent with the stoichiometry of the most common intermetallics in AA 2024-T3, namely:  $\theta\text{-Al}_2\text{Cu}$ ,  $\text{S-Al}_2\text{CuMg}$  and  $\text{Al}_{20}\text{Cu}_2(\text{MnFe})_3$ . Others were not. Other intermetallic particles contained distinct regions with differing composition. In some cases, regions containing an Al-Cu-Mg composition occurred next to regions, which predominantly contained an Al-Cu composition (Particles 5 in Table 1, and Figures 1a and 1b). Si was detected in some of the spectra. Apart from the Si present in the alloy, another possible source of Si observed in the spectra might be from the SiC paper used in the grinding process.

### b) Electrochemical Studies

Figure 2 compares the OCP values obtained after two hours of immersion for the different synthesized IMC and AA 2024-T3 in acidic (pH 3), near neutral (standard solution-pH 6), and alkaline (pH 10) solutions. All data points are the averages from at least four runs. These plots present comparisons in OCP in the pH 3 (Figure 2a) and pH 10 (Figure 2b) solutions with the standard pH 6 solution as departures from the diagonal line. Measurements close to the diagonal line indicate little or no difference in OCP. In acidic solution AA 2024-T3 showed a drop in potential compared with the alkaline and near neutral solutions within two hours of immersion. The OCP of AA 2024-T3 was much higher in the alkaline solution compared with the standard solution probably due to Cu replating (Figure 2b). The S-phase showed no significant dependence on pH. The OCP of  $\text{Al}_{20}\text{Cu}_2(\text{FeMn})_3$  was generally slightly more positive than that of  $\text{Al}_2\text{Cu}$  in the electrolytes. In the acidic solution, the values both intermetallics registered were much lower when compared with those recorded in the near neutral and alkaline solutions. The OCP of Al was lower at high pH. Notably, a galvanic potential driving force existed in each solution.

Figures 3a to 3f illustrate the overall E-log i behavior on AA 2024-T3, Al, Cu, and the Al-Cu, Al-Cu-Mg, and Al-Cu-Mn-Fe IMC in 0.1 M  $\text{Na}_2\text{SO}_4$  + 0.005 M NaCl (pH6), 0.1 M  $\text{Na}_2\text{SO}_4$  + 0.005

M NaCl + 0.0001 M NaOH (pH 10), and 0.1 M Na<sub>2</sub>SO<sub>4</sub> + 0.005 M Cl<sup>-</sup> (pH 3) after a 2 hour exposure at OCP. The horizontal lines shown in Figures 3a to 3d represent the mean OCP values of AA 2024-T3 in the respective environments (the lines are not shown in multiple pH plots, Figures 3e and 3f). In the pH 6 solution (Figures 3a and 3b), the OCP of Cu, the Al-Cu, and the Al-Cu-Mn-Fe intermetallics are more positive than that of AA 2024-T3 (horizontal line) and far more positive than those of the Al-Cu-Mg intermetallic compound and Al. The Al-Cu-Mg intermetallic is not passive at OCP and exhibits a high dissolution rate upon anodic polarization. Figure 3b shows that the Al-Cu-Mn-Fe intermetallic is passive near the OCP of AA 2024-T3 but undergoes pitting at potentials above it. AA 2024-T3 pits at its OCP and large pits have been observed that extend into its matrix beyond any IMCs that might serve as initiation sites [28]. Cathodic kinetics were enhanced on all Cu-containing materials and AA 2024-T3 compared to high purity Al (Figure 3a) as noted by Prior and Kier for Al containing Fe and Cu [5]. The pH of the electrolyte (between 3 and 10) does not alter the enhancement of cathodic kinetics exhibited by the Cu-containing intermetallics, nor the relative position of the OCP values when compared with the behavior in the pH 6 electrolyte. The Al-Cu-Mg IMC shows a passive region in the pH 10 electrolytes (possibly due to Mg and Cu content) but none at pH 3 (Figures 3d and 3e). AA 2024-T3 showed the presence of a passive region in both the pH 3 and 10 electrolytes (Figure 3e). No such passive region is seen in the pH 6 electrolyte. However, it should be noted that the OCP of AA 2024-T3 in the pH 3 electrolyte is much lower than in the pH 6 electrolyte (Figure 2). Anodic dissolution on the Al-Cu-Mg IMC and AA 2024-T3 proceeds at a faster rate in the pH 3 electrolyte compared with the pH 10 electrolyte (Figure 3e). Cathodic kinetics also proceeds at a faster rate on the Al-Cu and Al-Cu-Mn-Fe IMC in the pH 3 compared with the pH 10 electrolytes (Figure 3f). Compared with the pH 6 solution, the pitting potential on AA 2024-T3 is lower at pH 3, and higher at pH 10 possibly due to Cl<sup>-</sup>/OH<sup>-</sup> ratio (Figure 3g). It is now commonly accepted that the conventional pitting potential is a measure of stabilization of micropits that may have formed at potentials below the pitting potential [29, 30]. Nevertheless, pitting potentials were determined using the criterion that pitting would have occurred by the time the anodic current density of the specimen reached  $3 \times 10^{-5} \text{ Acm}^{-2}$  and, hence, this apparent current density criterion was taken to be the pitting threshold for our various systems [15, 29, 31-33]. It was used purely as a basis for comparison for the susceptibility of pitting, and bears no other significance. Nonetheless, at this current density, enough anodic charge would have been passed so that pitting potentials reflected pit stabilization of pits large enough to include the matrix and not solely dissolution of a small region of S phase or metastable pitting. The cumulative probability plots (Figure 3g) were constructed using procedures reported elsewhere [34]. Of all the materials tested, AA 2024-T3 showed the most drastic changes in OCP and pitting potential as a function of pH. The mean OCP for AA2024-T3 was  $-0.665 \pm 0.023 \text{ V(SCE)}$ , at pH 3,  $-0.466 \pm 0.010 \text{ V(SCE)}$  at pH 6, and  $-0.352 \pm 0.079 \text{ V(SCE)}$  pH 10, with all error values at a 95% confidence level (Figures 2a, 2b and 3g). Figure 3g also shows bands (depicted with vertical lines) for regions where the minimum and maximum OCP values for pure Cu, and the IMC fall in relation to AA 2024-T3 in the pH 3, 6 and 10.

### c) *In-situ CLSM Studies*

Corrosion studies on bare, untreated AA 2024-T3 in the four different solutions described above were performed with CLSM. The observed galvanic corrosion morphological features associated with micron scale constituent particles could be divided into four different categories: (i) particles which corroded, (ii) particles which caused trenching in the adjacent matrix, (iii) particles which did not corrode at all during the time of immersion, (iv) pitting near intermetallic compounds. In addition matrix etching was observed in acidic solution.

Particles identified with EDX as Al-Cu-Mg particles started to corrode within ten minutes after exposure to standard solution. The corrosion behavior of the particle in Figure 1a composed of regions of Al-Cu-Mg and Al-Cu is shown in Figure 4a after 2 h immersion. The Al-Cu-Mg phase corroded, whereas the Al-Cu-phase did not. Figures 4b to 4d show the corrosion of the particle

from Figure 1b at selected times. After 13 minutes, the Al-Mg-Cu phase already showed corrosion at the surface. After 40 minutes, corrosion attack had occurred on the entire Al-Cu-Mg surface and had expanded into the matrix. The other sections of the constituent particle remained with slight indications of trenching in the matrix. After 110 minutes, other sites had developed corrosion pits within the matrix.

Different types of localized corrosion attack on large intermetallic particles were observed as well in the standard solution as in 0.5 M NaCl. In the standard solution, one hexagonally shaped particle started corroding at its center, leaving behind a great deal of corrosion product (Figure 5). The corroded area increased and covered the entire particle within a few hours. After the entire particle was involved, attack of the surrounding matrix occurred. Figure 6a shows a rectangular-shaped IMC on the AA 20204-T3 surface. The attack on this particle started with the formation of many tiny pits close to one edge (Figure 6b). In the early stages, the depth changes were too small to be resolved (Figure 6b), and the corrosion could only be made visible by the black spot in the extended depth-of-focus image. Later on, pit depths of  $>4\text{ }\mu\text{m}$  could be verified. The dissolution progressed through the rest of the particle (Figure 6c), and the attack of the matrix started before the particle was completely corroded. Precipitated corrosion products were observed around and on the particle (Figure 6d).

Figures 7a-7c show the formation of four larger pits on an IMC exposed to 0.5 M NaCl, of which three merged together. Two of these pits initiated at or close to the interface with the matrix, and the other two on the particle itself. The surrounding matrix exhibited pit formation, as well.

Figures 7d-7f show corrosion of a large IMC starting at several locations along the interface with the matrix. The total area (particle + corroded) remained fairly constant during the exposure time. This means that the IMC particle corroded, whereas the matrix itself was only slightly attacked, if at all in the vicinity of this large IMC particle. Otherwise, the total area would have increased with time. In the upper left area, pit formation was observed, which initiated at a small particle and grew to a size much larger than the original particle.

Individual IMC particles were attacked much earlier in 0.5 M NaCl solution compared with the standard (pH 6) solution. Figure 8 demonstrates this difference by comparing the attacked areas for the IMC from Figure 7 and Figure 5. Once corrosion has started also in standard (pH 6) solution significant corrosion rates (slope of Figure 8) can be achieved.

Trench formation occurred around particles in all electrolytes. An example from standard solution (pH 6) is given in Figures 9a and 9b. Both images show the same particle surrounded by a trench  $2.5\text{ }\mu\text{m}$  wide. The particle itself had not been affected by corrosion at all after 1 day of exposure, still showing the polishing lines. The depth of the trench was about  $3\text{ }\mu\text{m}$ . It was observed that in standard solution (pH 6), severe corrosion took place in large-sized indentations<sup>b</sup> made on a sample ( $\sim 30\text{ }\mu\text{m}$  diameter). This prevented trenching at all nearby particles. These nearby particles were both of the Al-Cu and Al-Cu-Mn-Fe types. The particles that showed trenching had rather high Cu-concentrations (Table 2), with virtually no Mn or Fe suggesting they were Al-Cu. Indeed, several particles where no trenching occurred were identified by EDX as Al-Cu-Fe-Mn. In some cases, the matrix around some Al-Cu particles remained unattacked even though these were close to others, which trenched. In the alkaline solutions (pH 10), trenching appeared to be the most common form of corrosion, and sometimes involved more than a single IMC. Examples are given in Figures 9c to 9e. Deposition of corrosion products could be observed around all these trenched areas.

---

<sup>b</sup> Micro-hole put onto the metal surface that acted as an identification marker for surface features during microscopy.

In acidic solution, trenching was observed as well. An example is given in Figure 9f. Even after 18 hours of exposure, the width of the trench was only about 0.5 to 1  $\mu\text{m}$ , and the depth (in so far as not obscured by corrosion products) only 1.3 to 2.3  $\mu\text{m}$ . Figure 9g shows an area originally containing 2 large IMC and a small one in-between, separated by a thin strip of matrix material. After 72 min of immersion in 0.5 M NaCl, one trench surrounding all three particles had formed, and the matrix between the IMC particles had corroded. In both alkaline and acidic solutions there were particles, which did not corrode and showed no trenching within the duration of the experiment (~1 day).

In several cases, a combination of cathodic trenching and anodic dissolution was observed in the same IMC particle cluster. This is shown in Figures 10a and 10b for the acidic solution. Within two hours, corrosion ended on some parts of the particle agglomerate (black areas), whereas other parts formed narrow trenches with time.

Figure 11 plots differences in corrosion rate in the different electrolytes when expressed by area attacked. For this plot, the localized corrosion occurring on larger sample areas (130 by 130  $\mu\text{m}$ ) was monitored with time (instead of monitoring individual intermetallic particles like in Figure 8), and related to the total IMC areas present at the beginning of the experiment. Again, it is obvious that the corrosion in concentrated chloride solution occurred much more rapidly than in standard solution (pH 6). However, the influence of the pH could not be clarified. Even for different areas on the same sample (pH 10-data) very different corrosion rates were sometimes observed. Sometimes entire clusters of IMC showing similar behavior (trenching or no attack at all) were observed in these studies.

## DISCUSSION

The shapes of the intermetallic phases found by SEM are consistent with the findings of other authors [7-9, 13, 15, 35-37]. The variations in the chemical compositions of the different phases (Table 1) could be due to a number of reasons: (i) the interaction volume of the SEM-EDS beam may possibly be greater than the volume of the IMC, resulting in signals also being collected from the Al-matrix; (ii) selective dissolution during wet grinding; or (iii) an indication of more than one phase (transitional phases) of these IMC being present on the metal surface<sup>c</sup>. The increased Cu-content found after corrosion might be due to Cu replating or dealloying of other constituents.

The SEM-EDX observation of Al-Cu-Mg and Al-Cu phases adjacent to one another is confirmed by the findings of other authors who reported the occurrence of different intermetallic phases in very close proximity to one another [38]. This proximity may have promoted the selective dissolution of the Al-Cu-Mg phase, whereas the Al-Cu phase remained unattacked for a long time (Figure 1, 4). This is in agreement with the differences in OCP and E-log  $i$  behavior of the pure phases (Figures 2 and 3), which suggest that upon galvanic coupling the Al-Cu-Mg phase should undergo active dissolution, whereas Al-Cu phases should serve as a cathode. It is also possible that the proximity of the cathodic site even accelerates the corrosion of the Al-Cu-Mg. The corrosion of the matrix in the vicinity of this particle can be explained by the formation of sufficiently aggressive pit solution to promote attack of the Al-matrix. The reason for the initiation of corrosion (filiform-like) several  $\mu\text{m}$  below the original site of Al-Cu-Mg dissolution is unknown at this point (Figure 4d). One possibility is that it might have initiated at another defect(s) in the matrix, which was not previously identified by the imaging analyses carried out prior to exposure to electrolyte.

---

<sup>c</sup> It is possible that formation of one constituent particle can serve as a nucleation site for the next one.

Compositional analyses of large-sized intermetallic particles (Figure 5 and 6) showing localized corrosion attacks were not performed. Based on the SEM/EDX analyses of other samples and a correlation between shape and composition, the IMC in Figure 5 was probably of the Al-Cu-Fe-Mn type, whereas the IMC in Figure 6 could be Al-Cu. Several factors might contribute to the localized attacks on these particles. The observed differences in local composition within the same particle (which have also been observed by other authors [36]) might be one reason. This compositional variation might lead to a galvanic couple within a particle (compare OCP differences in Figure 2), and initiate pitting within the particle (Figure 5, 7a and 7c), or dissolution beginning at the interface to the matrix (Figures 7d and 7f). The pitting of the particle as well as the matrix in Figure 7b might suggest the presence of small defects with a size close to the resolution of the microscope ( $< 500$  nm), which serve as initiation sites. These may be Al-Cu-Mg particles. Based on the OCP of the Al-Cu and Al-Cu-Fe-Mn phases (Figure 2) alone, pitting would not be expected at the OCP of AA 2024-T3 for those particles. However corrosion attack on Al-Cu-Fe-Mn phases has been seen before in 0.1 M NaCl [10].

The Al-Cu-Mg intermetallic would still dissolve in a galvanic couple with the other IMC, Cu or AA 2024-T3 at the pH values of 3 and 10 as shown based on the OCP data relative to the anodic behavior of Al-Cu-Mg (Figure 2). However, it should dissolve faster at pH 3 than at pH 10 (Figure 3e). The Al-Cu and Al-Cu-Fe-Mn particles will still serve as cathodic sites. The close proximity of the two different types of particles can explain the corrosion features shown in Figure 10, where corrosion of some particles and formation of narrow trenches at the interfaces to matrix material can be observed next to each other.

Cathodic trenching has been extensively discussed in the literature [1, 3, 8, 10, 11, 17, 18]. It is thought that the local increase in pH at the cathodic Al-Cu and Al-Cu-Fe-Mn particles attacks the oxide film at the interface to the alloy matrix. In the present work, it was found that the susceptibility to trenching is not the same for all particles (Table 2). The data in Table 2 suggested that Al-Cu particles trench faster than Al-Cu-Mn-Fe in standard solution. This could be due to differences in the cathodic current densities on Al-Cu, and Al-Cu-Mn-Fe IMC (Figure 3a). However, present experimental data did not show any significant differences that could explain the differences in trenching behavior. Differences in susceptibility to trenching at particles cathodic to the Al-matrix were also observed in the alkaline and acidic solutions. It was not confirmed by EDX whether the particles more susceptible to trenching in these solutions were Al-Cu. Clearly, further investigation is still required in this area as selective trenching of particles may have been limited to only the specific conditions under which the tests were carried out. Trenching might depend not only on the exact particle composition, and the intermetallic compound crystal plane exposed, but also on the microstructural and compositional details of the corrosion processes in the matrix close to each type of intermetallic. For instance, extensive recrystallization of small grains next to the constituent particles could change the corrosion properties of the matrix. It is possible that acidic concentration fields oppose alkaline trenching. However, observations of trenching in the acidic electrolyte argue against this. The effect of the lower bulk pH is probably partially compensated by the larger cathodic currents occurring under acidic conditions, which in turn increases the local pH at the IMC site.

On the bulk synthesized IMC, a lower OCP was observed in acidic solutions, and the cathodic current densities were higher. Based on mixed potential theory an increase in cathodic current densities alone would result in a more positive OCP compared to neutral solutions. If the anodic partial currents are larger in acidic solution too, a more negative OCP is possible. The passive layer on the compounds is probably thinner in a pH 3 environment, because Al-oxides are not stable under these conditions [39]. The same is true for the passive layer on the matrix of AA 2024-T3. That is why matrix etching was observed in the acidic STD-electrolyte, which contributes to the faster rate of anodic dissolution observed in the electrochemical experiments (Figure 3e).



As a result of the lower OCP registered by AA 2024-T3 in the pH 3 solution (-0.665 V(SCE)) compared with the OCP in the pH 6 solution (-0.466 V(SCE)), an increase in the possibilities of trenching of the AA 2024-T3 matrix around the Al-Cu and Al-Cu-Mn-Fe IMC particles embedded in the AA 2024-T3 matrix is predicated from Figure 3g. Following this line of reasoning, this relative risk should reduce in the pH 10 solution (-0.352 V(SCE)) due to the higher OCP registered by AA 2024-T3. However, the galvanic couples, which exist on AA 2024-T3, are far more complicated. For instance, the data in Figure 3g also predicts that with regard to these galvanic couples, at pH 3, a slower rate of dissolution of an Al-Cu-Mg IMC particle on the surface of AA 2024-T3 should result, while at pH 10, the rate of dissolution should be faster. However, data in Figure 3e show that the rate of dissolution is much faster at pH 3 compared with at pH 10 thus, the smaller difference in potential between the Al-Cu-Mg IMC and the AA 2024-T3 matrix in the galvanic couple is offset by its faster rate of dissolution. In addition, the Al-Cu-Mg IMC exhibits some degree of passivity at pH 10, which also counterbalances the effect of the larger potential difference that exists between the Al-Cu-Mg IMC and AA 2024-T3 at this pH. This might be a contributing factor to the higher pitting potential exhibited in the pH 10 solution by AA 2024-T3. The high rate of dissolution of the Al-Cu-Mg IMC might result in the faster formation of a dealloyed porous Cu-rich sponge and islands, which in turn could promote trenching. The lower pitting potential (in spite of the passive region exhibited) of AA 2024-T3, and the higher anodic and cathodic current densities exhibited by the IMC suggests that the pH 3 solution is the most aggressive of the three environments with the same  $[Cl^-]$  concentration.

Figure 11 shows that at high chloride concentration the overall corrosion rate as observed by CLSM is much larger than for 0.1 M  $Na_2SO_4$  + 0.005 M NaCl in the entire pH range investigated. The differences for the sulfate-based electrolyte are more subtle and show very low reproducibility. Agglomerates of certain IMC compounds can sometimes be found on AA 2024-T3. This is responsible for the low reproducibility of the data especially for the pH 10 electrolyte (Figure 11): One area had many particles supporting trenching and therefore showed a high corrosion rate. Other areas on the same substrate (probably clusters of Al-Cu-Fe-Mn phases) showed a low corrosion rate. A window of 130 x 130  $\mu m$  is statistically insufficient to represent the behavior of the entire substrate and to analyze the influence of subtle changes in the environment. Larger areas must be analyzed, or, alternatively, more areas on one sample in combination with several samples would have to be analyzed to strengthen this statement. However, the increase in corrosion rate at high chloride concentrations is so significant that it is clearly visible in the Figure.

Based on electrochemical measurements, corrosion should be the fastest in the pH 3 electrolyte, where matrix etching could be observed in CLSM. This could explain why low pH blisters exhibit rapid attack in underpaint corrosion studies on coated AA 2024-T3.

## CONCLUSIONS

1. Variations in composition were observed amongst particles with the same elemental constituents.
2. The composition of some of the intermetallic particles were consistent with the stoichiometry of the most common intermetallics in AA 2024-T3, namely:  $-Al_2Cu$ ,  $S-Al_2CuMg$  and  $Al_{20}Cu_2(MnFe)_3$ .
3. EDS showed that some agglomerated intermetallic particles contained more than one phase. This led to different rates and morphologies of corrosion attack within one agglomerated particle.
4. The Al-Cu-Mg particles were the most active in all the electrolytes investigated on the bare polished samples and corroded rapidly.
5. Corrosion within some intermetallic particles was localized.

6. All Al-Cu and Al-Cu-Mn-Fe particles do not have the same propensity to promote trenching of the Al-matrix. Electrochemical studies of synthesized IMC suggest, that differences in the cathodic reaction rates on each IMC contribute to this behavior.
7. The morphology of initial stages of corrosion attack at the micro-scale at the intermetallic compounds on bare AA 2024-T3 is similar in all the electrolytes investigated. The influence of the bulk pH on effects caused by a local pH increase can be partially compensated by a change in cathodic reaction rate. Based on electrochemical measurements, corrosion should be the fastest in the pH 3 electrolyte, where matrix etching could be observed in CLSM.
8. Preliminary indications are that pitting in the matrix or at small matrix particles is more evident in 0.5 M NaCl than in other solutions used, particularly the pH 10 solution, which is supported by electrochemistry on Al-Cu-Mg and 2024-T3.

## ACKNOWLEDGEMENTS

The authors gratefully acknowledge the AFOSR for the financial support of the project under contract number F49620-96-1-0178, with Lt. Col. Paul Trulove, Ph.D., as program director. Perkin Elmer Instruments and Scribner Associates, Inc. are thanked for continuing support of electrochemical instrumentation and software in CESE.

## REFERENCES

1. G.S. Chen, M. Gao, R.P. Wei, *Corrosion*, **52**, 8 (1996).
2. R.G. Buchheit, R.P. Grant, P.F. Hlava, B. McKenzie, G.L. Zender, *J. Electrochem. Soc.*, **144**, 2621 (1997).
3. G.S. Chen, C.-M. Liao, K.-C. Wan, M. Gao, R.P. Wei, ASTM STP 1298, W.A. Van Der Sluys, R.S. Piascik, R. Zawierucha, Eds., p.18, ASTM (1997).
4. J.R. Scully, T.O. Knight, R.G. Buchheit, D.E. Peebles, *Corros. Sci.*, **35**, 185 (1993).
5. M.J. Pryor, D.S. Keir, *J. Electrochem. Soc.*, **102**, 241C (1955).
6. R.G. Buchheit, *J. Electrochem. Soc.*, **142**, 3994 (1995).
7. M. Büchler, J. Kerimo, F. Guillaume and W.H. Smyrl, *J. Electrochem. Soc.*, **147**, 3691 (2000).
8. M.A. Alodan and W.H. Smyrl, *J. Electrochem. Soc.*, **144**, L282 (1997).
9. M.A. Alodan and W.H. Smyrl, *J. Electrochem. Soc.*, **145**, 1571 (1998).
10. P. Schmutz and G.S. Frankel, *J. Electrochem. Soc.*, **145**, 2295 (1998).
11. T. Suter and R.C. Alkire, in *Critical factors in Localized Corrosion III*, Electrochemical Society Proceedings **98-17** p.118 (1999).
12. R.G. Buchheit, L.P. Montez, M.A. Martinez, J. Micheal and P.F. Hlava, *J. Electrochem. Soc.*, **146**, 4424 (1999).
13. V. Guillaumin and G. Mankowski, *Corros. Sci.*, **41**, 421 (1999).
14. N. Dimitrov, J.A. Mann and K. Sieradski, *J. Electrochem. Soc.*, **146**, 98 (1999).
15. C. Blanc, B. Lavelle and G. Mankowski, *Corros. Sci.*, **39**, 495 (1997).
16. G.O. Ilevbare, J.R. Scully, J. Yuan and R.G. Kelly, *Corrosion*, **56**, 227 (2000).
17. M. Büchler, T. Watari and W.H. Smyrl, *Corros. Sci.*, **42**, 1661 (2000).
18. J.O. Park, C.H. Paik, Y.H. Huang and R.C. Alkire, *J. Electrochem. Soc.*, **146**, 517 (1999).
19. A.M. Mierisch, J. Yuan, R.G. Kelly and S.R. Taylor, *J. Electrochem. Soc.*, **146**, 4449 (1999).
20. O. Schneider, G.O. Ilevbare, J.R. Scully, R.G. Kelly, *Electrochemical and Solid State Science Letters*, **4**, B35 (2001).
21. O. Schneider, G.O. Ilevbare, J.R. Scully, R.G. Kelly, in preparation for *J. Electrochem. Soc.*
22. J. B. Pawley, Editor, *Handbook of Biological confocal Microscopy*, 2nd ed., Plenum Press, New York and London (1995).
23. N. Llorca-Isern, M. Puig, M. Español, *J. Therm. Spray Technol.*, **8**, 73 (1999).
24. F. Guillaume, L.F. Darfias-Mesias, M. Buchler and W.H. Smyrl, in *Critical factors in Localized Corrosion III*, Electrochemical Society Proceedings **98-17** p.155 (1999).

25. M. E. Inman, R. G. Kelly, S. A. Willard, and R. S. Piascik, "Coordinated Metallographic, Chemical and Electrochemical Analyses of Fuselage Lap Splice Corrosion", Proc. of the ASIP Conference, Atlanta, November 1996.
26. R.G. Kelly, O. Schneider and J. Yuan, ECS Meeting Abstract Vol. 99-1, Abstract #81, May, (1998).
27. G.O. Ilevbare and J.R. Scully, Corrosion, **57**, 134 (2001).
28. H. H. Strehblow, C. M. Melliar-Smith, and W. M. Augustyniak, J. Electrochem. Soc., **125**, 915 (1978).
29. S.T. Pride, J.R. Scully and J.L Hudson J. Electrochem. Soc., 141 (1994): p. 3028.
30. P. C. Pistorius P.C and G. T. Burstein, Phil. Trans. R. Soc. Lond., A 341 (1992): p. 531.
31. A. Broli and H. Holtan, Corros. Sci., 13, (1973): p. 237.
32. W. Zhang, S. Smialowska and G. S. Frankel, "Influence of  $\text{Cr}^{6+}$  Concentration and pH on Polarization Curves of AA 2024-T3", MURI report by G. S. Frankel, The Ohio State University, September 1998 p. 51.
33. M. Kendig, M. Cunningham, S. Jeanjaquet, and D. Hardwick, J. Electrochem. Soc., 144 (1997) p. 3721.
34. T. Shibata and T. Takeyama, Corrosion, 33 (1977) p. 243.
35. G.P. Halada, C.R. Clayton, M.J. Vasquez, J.R. Kearns, M.W. Kendig, S. L. Jeanjaquet, G.G. Peterson, G.S. McCarthy and G.L. Carr, in Critical factors in Localized Corrosion III, Electrochemical Society Proceedings **98-17** p.139 (1999).
36. T.J.R. Leclère, A.J. Davenport, J. Deakin, D. Raikes and R.C. Newman, in Critical factors in Localized Corrosion III, Electrochemical Society Proceedings **98-17** p.130 (1999).
37. P. Schmutz and G.S. Frankel, J. Electrochem. Soc., **145**, 2285 (1998).
38. P Campestrini, E.P.M. van Westing, H.W. van Rooijen and J.H.W. de Wit, Corrosion Science, **42**, 1853 (2000).
39. M. Pourbaix, "Atlas of electrochemical equilibria in aqueous solutions", 2<sup>nd</sup> edition, National Association of Corrosion Engineers, Houston, Texas 1974.

**Table 1.** EDS analyses (in At. %) of intermetallic particles before exposure to electrolyte.

**Table 2.** EDS analyses (in At. %) of intermetallic particles after exposure to electrolyte.

Particle	Al	Cu	Mg	Mn	Fe
1	64.0	26.5	9.5	0.0	0.0
2	96.7	2.0	1.0	0.1	0.2
3	73.6	26.2	0.0	0.2	0.0
4	80.32	19.1	0.3	0.14	0.14
5-1	62.48	20.8	16.5	0.14	0.08
5-2	81.0	17.9	0.7	0.1	0.3
6	74.7	12.4	0.0	3.7	9.2
7	85.1	8.7	6.1	0.1	0.0
8	85.8	5.2	0.2	3.5	5.3
9	88.3	3.7	0.3	3.0	4.7
10	97.1	2.4	0.3	0.2	0.0

Particle	Al	Cu	Mg	Mn	Fe	Corrosion
A	51.4	48.3	0.0	0.2	0.1	Trenched
B	64.8	34.8	0.0	0.2	0.2	Trenched
C	86.7	12.9	0.0	0.3	0.1	Trenched
D	77.6	8.7	0.0	5.1	8.6	No trench
E	80.2	7.3	0.0	5.2	7.3	No trench
F	76.1	8.6	0.0	5.5	9.8	No trench
G	71.5	28.0	0.0	0.0	0.5	No trench
H	77.4	21.8	0.0	0.3	0.5	Trenched
I	84.9	4.4	0.0	6.3	4.4	No trench
J	72.1	25.2	2.4	0.2	0.1	Trenched
K	75.9	7.6	0.0	6.4	10.1	No trench
L	95.6	3.1	0.5	0.4	0.4	Trenched
M	32.7	66.5	0.0	0.5	0.3	Trenched
N	65.4	34.6	0.0	0.0	0.0	Trenched
O	95.9	2.7	0.7	0.7	0.0	Dark part Close to N
P	85.3	14.7	0.0	0.0	0.0	Trenched

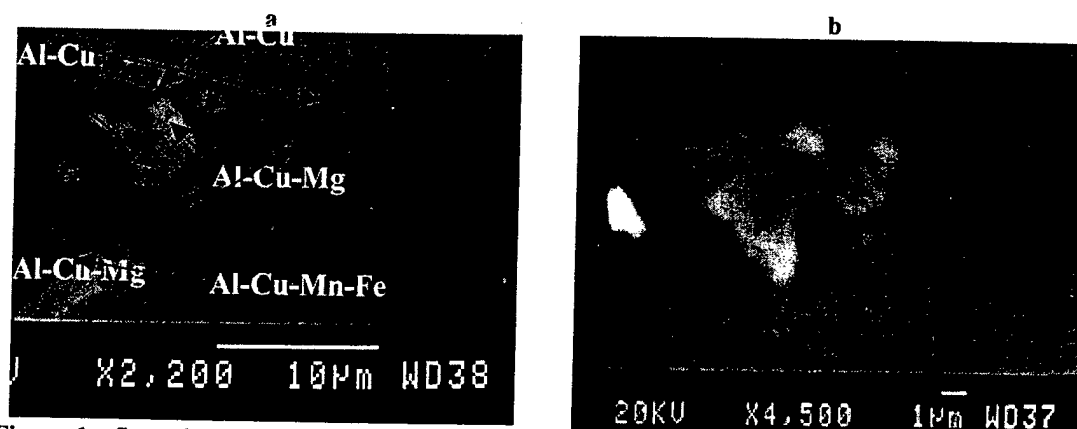


**Figure 1.** Secondary electron SEM images of intermetallic particles on AA 2024-T3. The three major types of IMC as identified by EDX are shown.

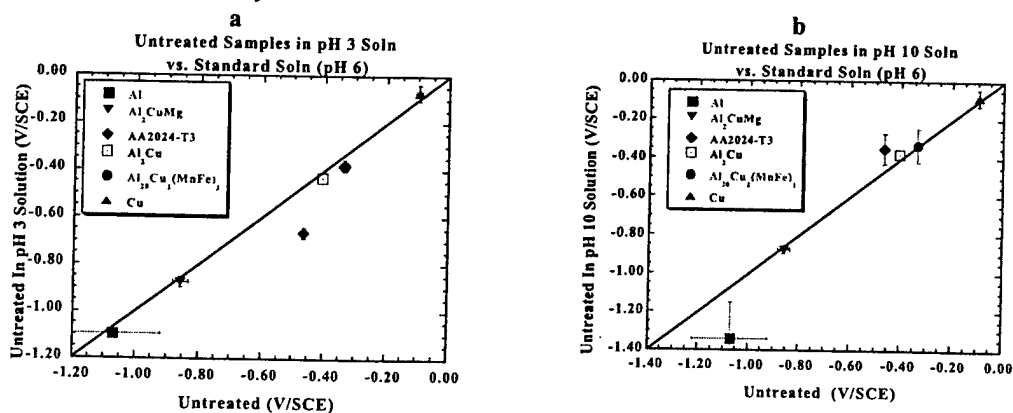
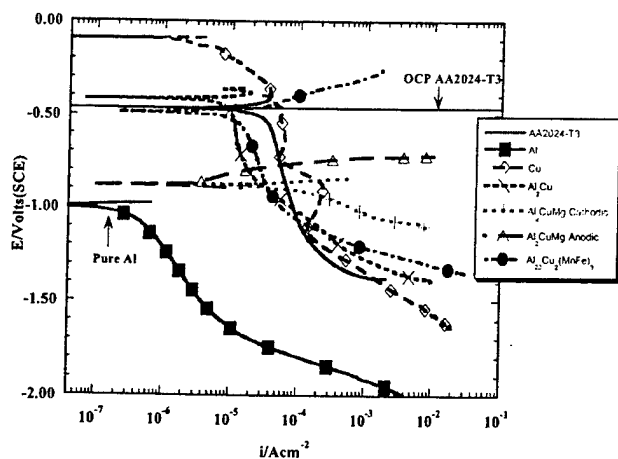
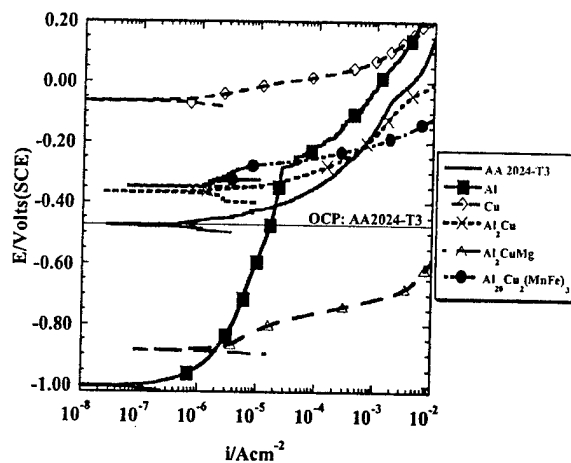


**Figure 2.** Open circuit potentials of untreated 99.998% Al, Al<sub>2</sub>CuMg, AA 2024-T3, Al<sub>2</sub>Cu, Al<sub>20</sub>Cu<sub>1</sub>(MnFe)<sub>3</sub>, and 99.999% Cu in 0.1 M Na<sub>2</sub>SO<sub>4</sub> + 0.005 M NaCl (pH 6) after 2 hours compared with those of their counterparts in (a) 0.1 M Na<sub>2</sub>SO<sub>4</sub> + 0.005 M Cl<sup>-</sup> (as 0.00167 M AlCl<sub>3</sub>) adjusted to pH 3 with H<sub>2</sub>SO<sub>4</sub>, and in (b) 0.1 M Na<sub>2</sub>SO<sub>4</sub> + 0.005 M NaCl + 0.0001 M NaOH, pH 10.

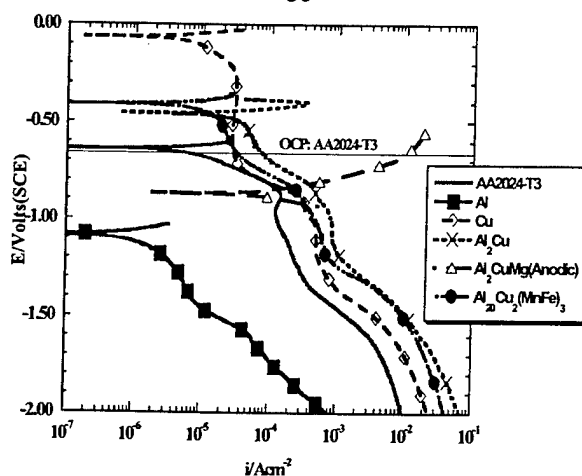
3a



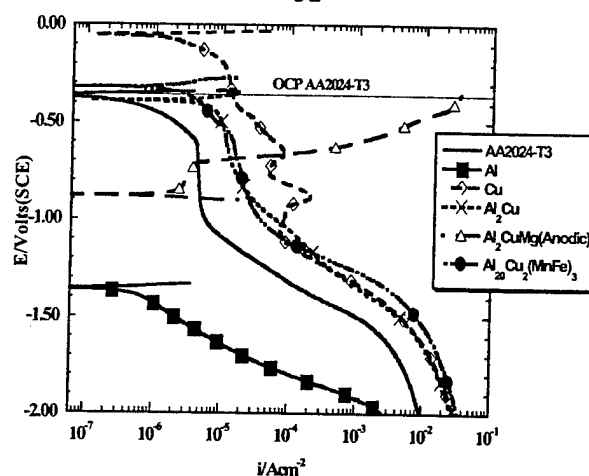
3b



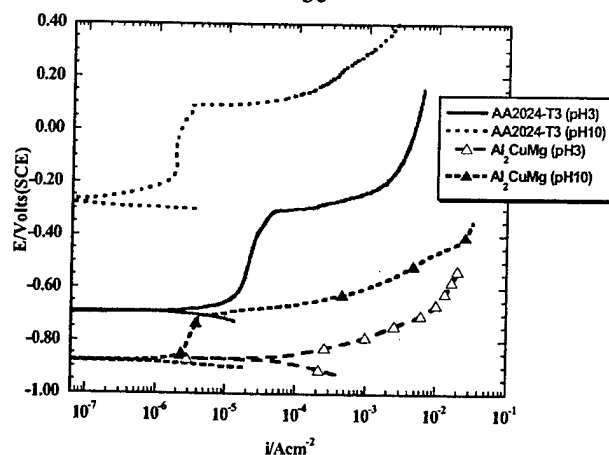
3c



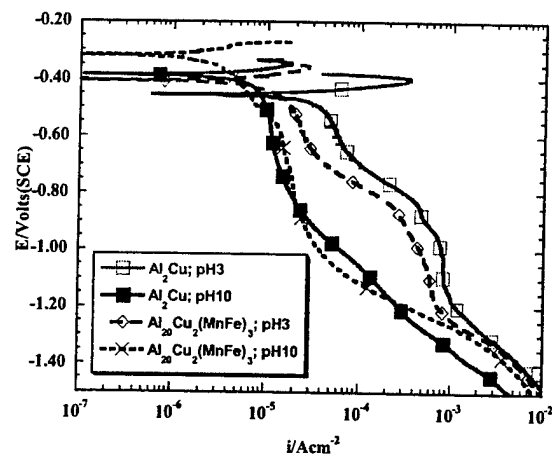
3d

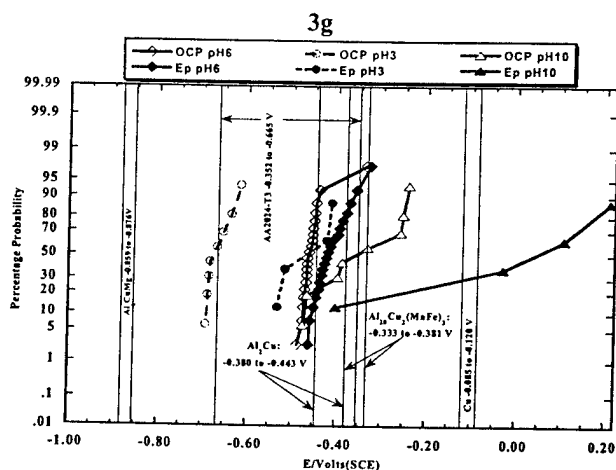


3e



3f





(3g) . Cumulative probability of the OCP and the pitting potential of bare untreated AA 2024-T3 in 0.1 M Na<sub>2</sub>SO<sub>4</sub> + 0.005 M NaCl (pH 6), 0.1 M Na<sub>2</sub>SO<sub>4</sub> + 0.005 M Cl<sup>-</sup> (pH 3), and 0.1 M Na<sub>2</sub>SO<sub>4</sub> + 0.005 M NaCl + 0.0001 M NaOH (pH 10) under ambient aeration. There was a 2 h wait at OCP in all experiments. The vertical lines are the OCP indicated at the mean values attained amongst the 3 electrolytes listed above for each of the IMC, AA 2024-T3 and Cu.

**Figure 3.** The E-logi behavior of stationary electrodes of AA 2024-T3, Al, Cu,  $\theta$ -Al<sub>2</sub>Cu S-Al<sub>2</sub>CuMg, and Al<sub>20</sub>Cu<sub>2</sub>(MnFe)<sub>3</sub> at ambient aeration, (3a) Cathodic, (including anodic Al<sub>2</sub>CuMg curve), and (3b) anodic, in 0.1 M Na<sub>2</sub>SO<sub>4</sub> + 0.005 M NaCl; (3c) cathodic, (including anodic Al<sub>2</sub>CuMg curve) in 0.1 M Na<sub>2</sub>SO<sub>4</sub> + 0.005 M Cl<sup>-</sup> (as 0.00167 M AlCl<sub>3</sub>) adjusted to pH 3 with H<sub>2</sub>SO<sub>4</sub>; (3d) cathodic, (including anodic Al<sub>2</sub>CuMg curve) in 0.1 M Na<sub>2</sub>SO<sub>4</sub> + 0.005 M NaCl + 0.0001 M NaOH (pH 10); (3e) anodic, AA 2024-T3 and S-Al<sub>2</sub>CuMg) in 0.1 M Na<sub>2</sub>SO<sub>4</sub> + 0.005 M Cl<sup>-</sup> (as 0.00167 M AlCl<sub>3</sub>) adjusted to pH 3 with H<sub>2</sub>SO<sub>4</sub> and 0.1 M Na<sub>2</sub>SO<sub>4</sub> + 0.005 M NaCl + 0.0001 M NaOH (pH 10); (3f) Cathodic,  $\theta$ -Al<sub>2</sub>Cu and Al<sub>20</sub>Cu<sub>2</sub>(MnFe)<sub>3</sub> in 0.1 M Na<sub>2</sub>SO<sub>4</sub> + 0.005 M Cl<sup>-</sup> (as 0.00167 M AlCl<sub>3</sub>) adjusted to pH 3 with H<sub>2</sub>SO<sub>4</sub> and 0.1 M Na<sub>2</sub>SO<sub>4</sub> + 0.005 M NaCl + 0.0001 M NaOH (pH 10);

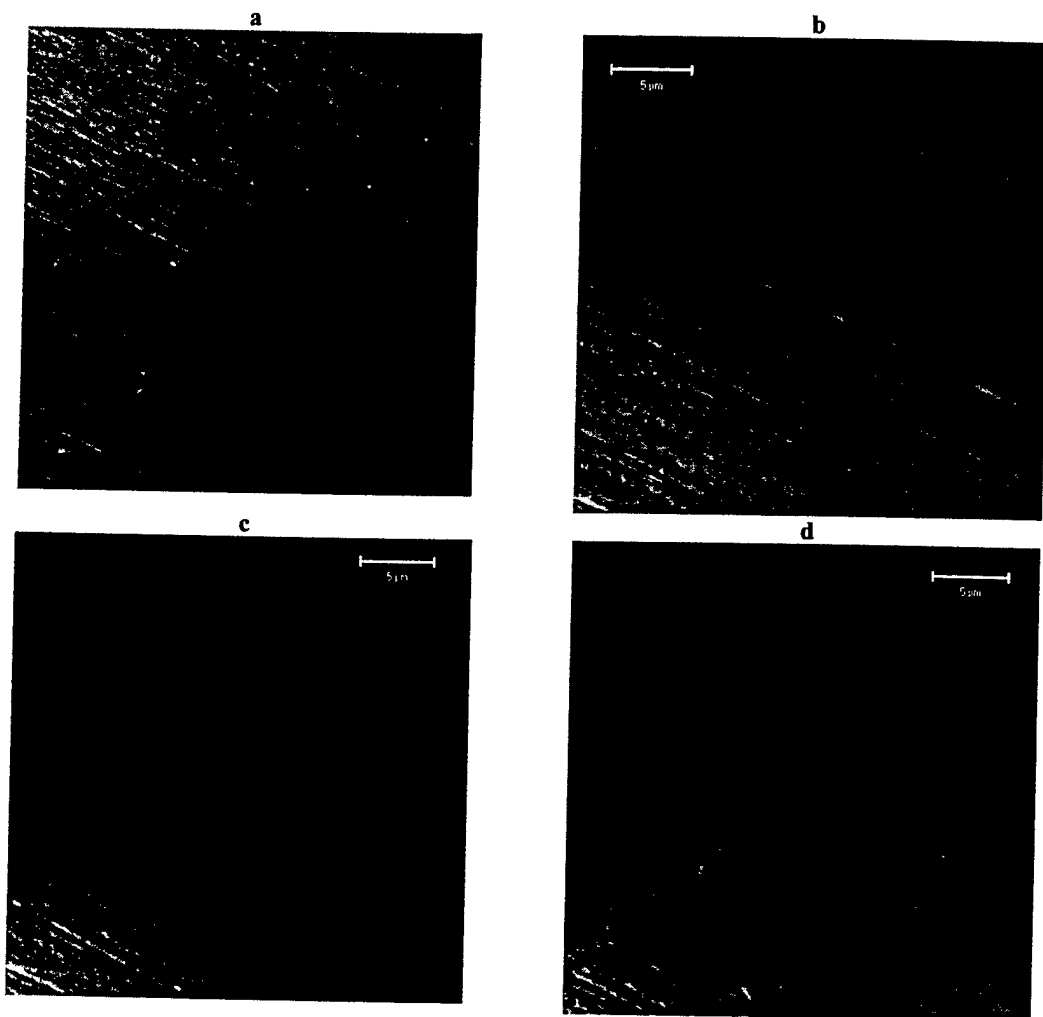


**Figure 4.** Selective Al-Cu-Mg corrosion on bare AA2024-T3: (a) CLSM image of the particle shown in Figure 1a after 2 h immersion in standard solution. (b-d) CLSM of the particle from Figure 1b during immersion in standard solution (immersion times: 13 minutes (b), 40 minutes (c), and 110 minutes (d)).

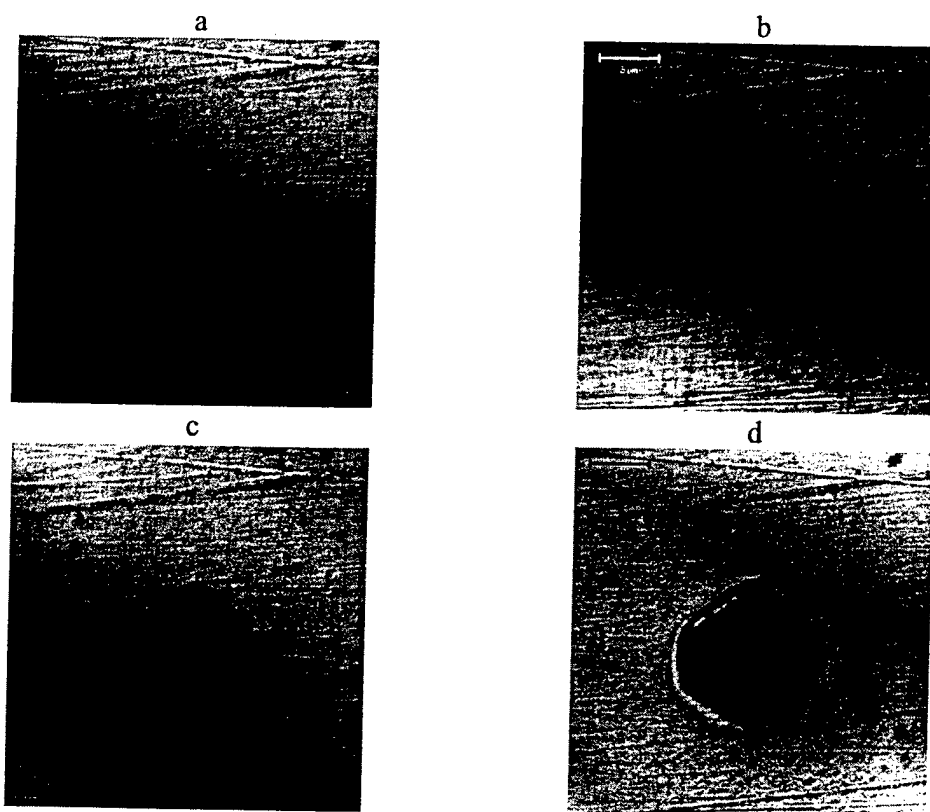


**Figure 5.** Intermetallic particle corroding on bare AA2024-T3 in 0.1 M  $\text{Na}_2\text{SO}_4$  + 0.005 M NaCl. Immersion times: (a) 17 min (b) 83 min (c) 139 min and (d) 280 min.

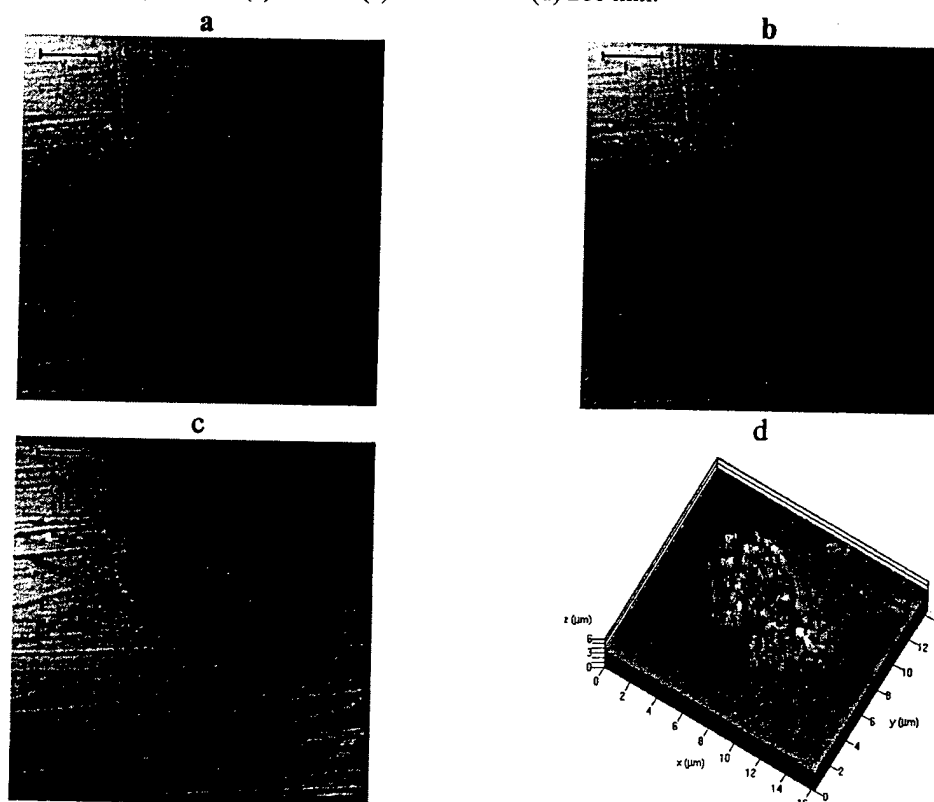


**Figure 6.** Corrosion attack on an intermetallic particle in 0.1 M  $\text{Na}_2\text{SO}_4$  + 0.005 M NaCl (pH 6) after (a) 45 minutes (b) 147 minutes (c and d) 366 minutes.

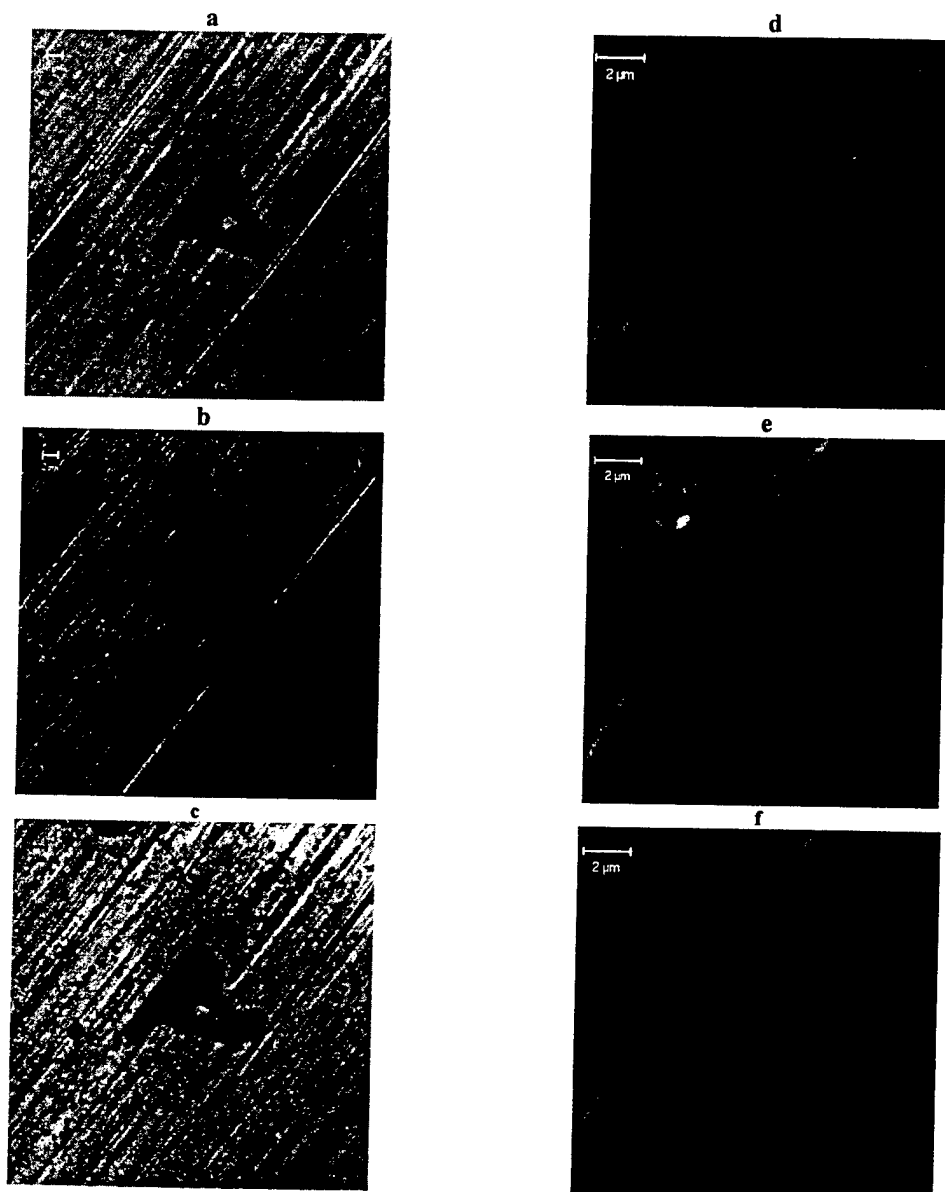


**Figure 7.** (a to c) Localized attack on IMC particle in 0.5 M NaCl (bar: 2  $\mu\text{m}$ , immersion time (i.t.): (a) 0, (b) 50, and (c) 97 min); (d to f) dissolution of IMC particle in 0.5 M NaCl starting at the interface to the matrix (bar: 2  $\mu\text{m}$ , i.t: (d) 0, (e) 22, and (f) 65 min). Pit growth at small particles in the matrix is also seen.

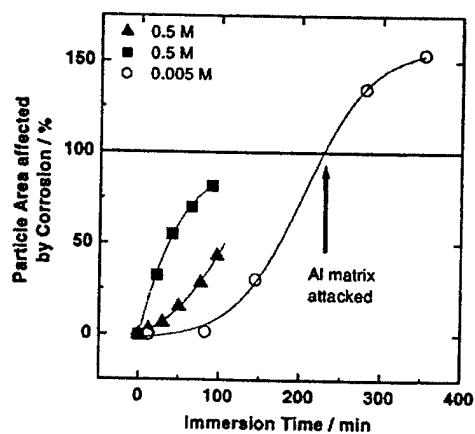


**Figure 8.** Comparison of the corrosion rate (based on the area affected by corrosion) of selected intermetallic particles on AA2024-T3 in 0.5 M NaCl (triangles, squares, particles from Figure 7) and 0.1 M Na<sub>2</sub>SO<sub>4</sub> + 0.005 M NaCl (circles, particle from Figure 5). All areas are given relative to the particle size before corrosion. A value of more than 100% indicated that matrix material around the particle has corroded as well.



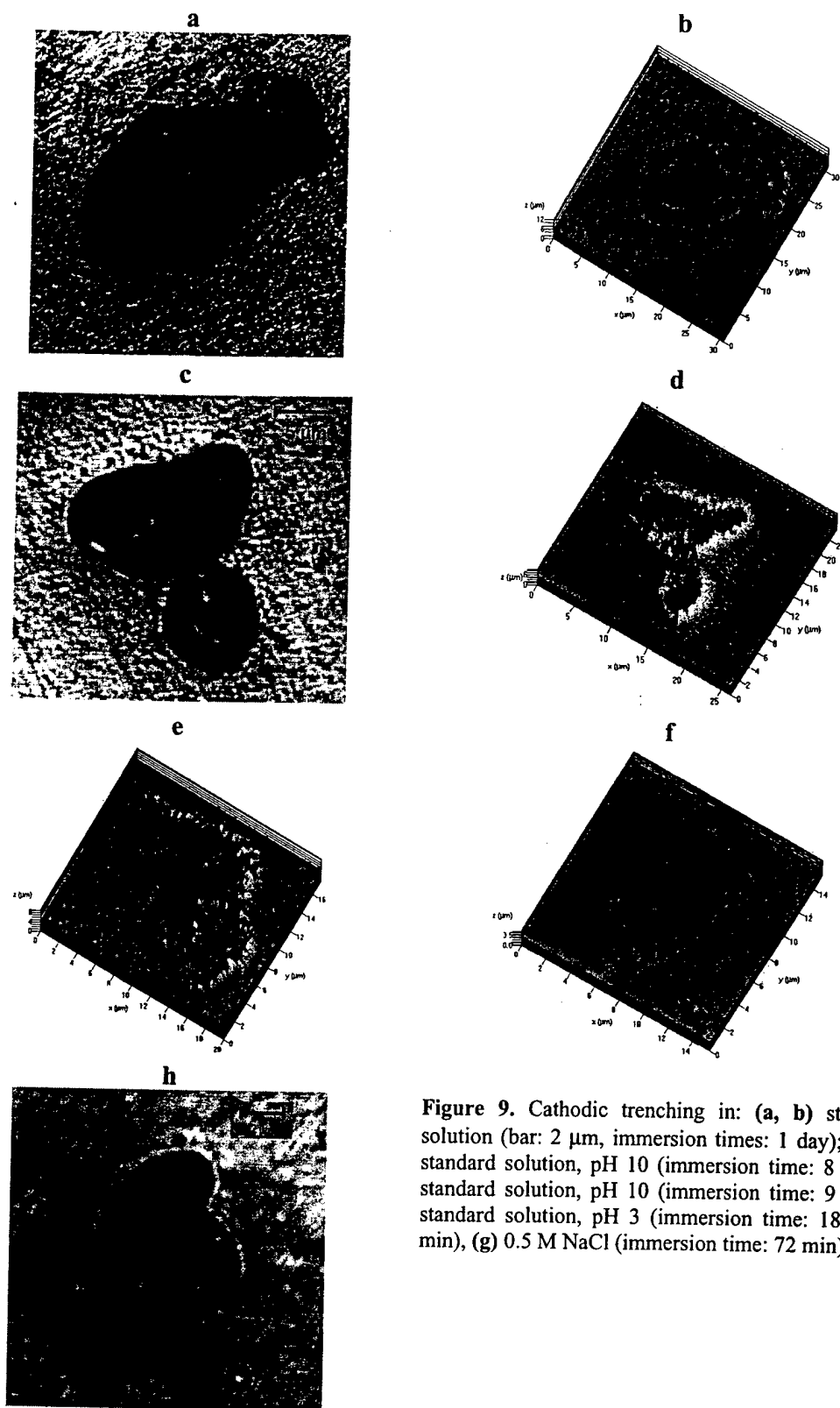
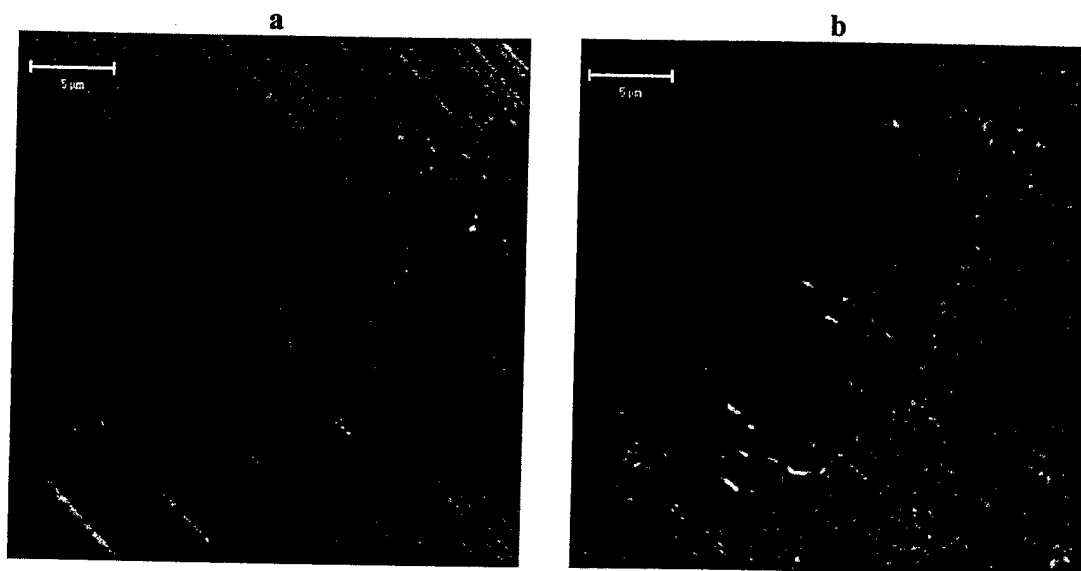
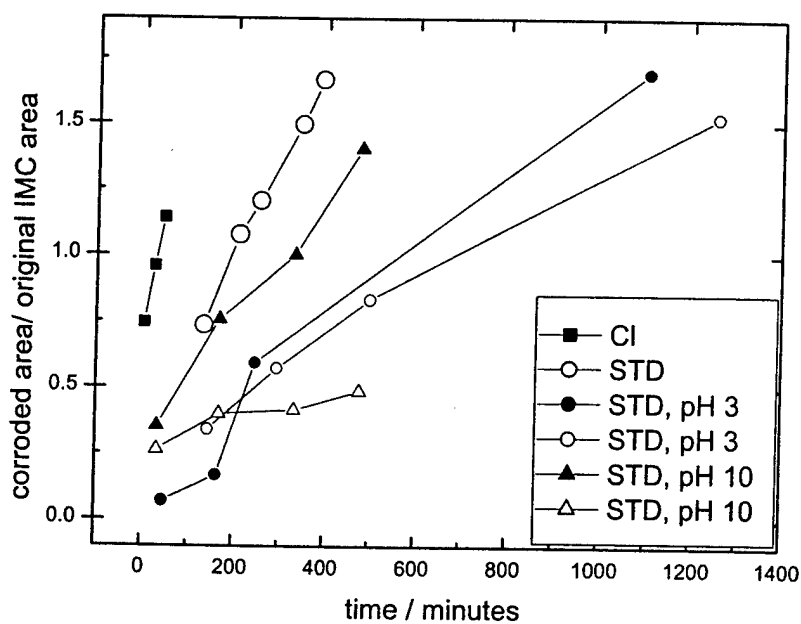


Figure 9. Cathodic trenching in: (a, b) standard solution (bar: 2  $\mu\text{m}$ , immersion times: 1 day); (c, d) standard solution, pH 10 (immersion time: 8 h), (e) standard solution, pH 10 (immersion time: 9 h), (f) standard solution, pH 3 (immersion time: 18 h, 20 min), (g) 0.5 M NaCl (immersion time: 72 min).



**Figure 10.** Cluster of intermetallic particles on bare AA 2024-T3, exposed to pH 3 0.1 M  $\text{Na}_2\text{SO}_4 + 0.005 \text{ I}^-$ : (bar: 5  $\mu\text{m}$ , immersion times: (a) 110, (b) 280 min).



**Figure 11.** Increase of corroded area with time in different electrolytes: 0.5 M chloride (squares) and 0.1 M  $\text{Na}_2\text{SO}_4 + 0.005 \text{ M NaCl}$  of pH 6 (large circles), 3 (small circles), and 10 (triangles). The areas analyzed were 130 by 130  $\mu\text{m}$ , and the area affected by corrosion is given relative to the total area of IMC visible in the CLSM pictures before the onset of corrosion. Open and filled symbols are data from different regions on the same sample.



## Confocal Laser Scanning Microscopy as a Tool for *In Situ* Monitoring of Corrosion Underneath Organic Coatings

O. Schneider,\* G. O. Ilevbare,\* J. R. Scully,\* and R. G. Kelly\*<sup>‡</sup>

Department of Materials Science and Engineering, Center for Electrochemical Science and Engineering,  
University of Virginia, Charlottesville, Virginia 22904-4745, USA

This paper discusses the application of confocal laser scanning microscopy for the investigation of corrosion processes on aluminum alloy AA2024-T3 occurring beneath a transparent organic coating. The ability of the microscope to monitor the topography of both the alloy surface under the coating and the surface of the coating, itself, in three dimensions, is demonstrated. The resolution limits ( $x$ ,  $y$ ,  $z$ ), when imaging through a bulk solution, coating, and coating blister solution are better than 1  $\mu\text{m}$ . The technique described has potential to clarify the roles of alloy heterogeneity and corrosion damage associated with intermetallic phases at the micrometer scale on the underpaint corrosion process and coating blister formation and growth.  
© 2001 The Electrochemical Society. [DOI: 10.1149/1.1413703] All rights reserved.

Manuscript submitted May 21, 2001; revised manuscript received July 20, 2001. Available electronically October 10, 2001.

Confocal laser scanning microscopy (CLSM) significantly surpasses the capabilities of common optical microscopy to measure and quantify surface metrology.<sup>1-4</sup> In a typical CLSM configuration, a laser beam scans the surface of the sample in  $x$ ,  $y$  direction. A small pinhole is located in front of the detector at a position that is optically conjugate to the focal point in the sample plane. The intensity of the light reflected from the sample on the focal plane is measured by the detector for each  $x$ ,  $y$  position. Most of the light scattered from out-of-focus planes is focused outside the pinhole and, therefore, does not reach the detector. This effect allows sharp imaging of a single sample plane, called a slice. By moving the sample surface stepwise through the focal plane with a  $z$ -scanning stage, the three-dimensional surface topography can be calculated from assembly of the slices recorded at each  $z$ -step. This assembly is called a stack. Data for surface roughness, surface profiles, and pit depths can thus be obtained. In addition, a 2D microscopic image with extended depth-of-focus can be calculated. This process assigns a gray level to each image pixel, which corresponds to the brightest level at this  $x$ ,  $y$  position in all slices. The CLSM is a contact-free method,<sup>1,3</sup> with working distances between sample and lens of 1 mm or more.

CLSM has found extensive use in biology because it allows the three-dimensional *in vivo* monitoring of transparent biological entities such as cells.<sup>1</sup> In materials science it has been used, for example, to study defects in thermal spray coatings.<sup>2</sup> The method has recently been applied to corrosion studies on bare aluminum alloy 2024-T3 (AA2024-T3).<sup>3,4</sup>

One advantage of CLSM for corrosion studies over traditional methods like scanning electron microscopy (SEM) is that measurements can be made on the surface *in situ* as corrosion damage develops over time, without serial removal and dry analysis under vacuum. Removal and drying virtually eliminates the chance to observe the evolution of corrosion damage at the same surface heterogeneities. Other common techniques for studying surface topographies in corrosion like atomic force microscopy (AFM), profilometry, and scanning near-field optical microscopy (SNOM) can be done *in situ* but require contact or at least close proximity (tens of nanometers) to the surface to be studied, or are based on force interactions with the surface to be studied.<sup>4-6</sup> Therefore, they cannot be applied to the study of corrosion processes taking place underneath a several micrometer thick organic coating.

This study shows that CLSM is able to monitor the changes taking place during corrosion on an alloy substrate underneath a transparent organic coating with three-dimensional information (*i.e.*, in a plane parallel to the surface as well as vertically). Heterogeneous alloys like AA2024-T3 suffer from corrosion induced by mi-

crogalvanic coupling of the Al-rich matrix and Al-Cu, Al-Cu-Mg, as well as Al-Cu-Mn-Fe(Si) intermetallic compound (IMC) phases.<sup>7-10</sup> The measurements can be performed *in situ*. Therefore, a detailed quantitative evolution of coating failure and localized corrosion beneath organic coatings can be obtained without removing the coating to look at the underlying metal surface.

### Experimental

Studies were conducted on 1.5 mm thick AA2024-T3 panels (Kaiser Corp.) cut to squares of about  $2.5 \times 2.5$  cm. One face of each panel was wet abraded with SiC paper (from 180 to 1200 grit), and then polished with 1  $\mu\text{m}$  diamond suspension (Buehler). The polished surface of some panels was spin coated with an epoxy polyamide coating typical of aircraft primers. It was prepared by mixing equal weights of Epon resin 1001-CX-75 (Shell) with Epi-Cure 3115 X73 curing agent (fatty acid-polyethylenepolyamine based polyamide mixture, Shell), and adding 5 wt % Butylcellosolve. The samples were cured in a desiccator over anhydrous  $\text{CaSO}_4$  at ambient temperature for at least 2 weeks. The coating thickness was determined by a coating thickness gauge based on eddy current measurements (DeFelsko 6000-2) to be approximately 10  $\mu\text{m}$ . The entire surface of the coated AA2024-T3 panels except a  $2 \times 2$  mm window was masked off with a Micro XP2000 lacquer (Pyramid Plastics).

CLSM was carried out on a Zeiss LSM 510 microscope with a 100 times magnification water immersion objective (Achromplan, numerical aperture 1.0). Imaging was performed with an argon laser (488 nm wavelength). The  $z$ -step height was 0.6  $\mu\text{m}$ . The samples were connected to a specially constructed flat electrochemical cell made from poly-methylacrylate, and fastened onto the CLSM stage (Fig. 1). The cell allowed for immersion of the objective lens into

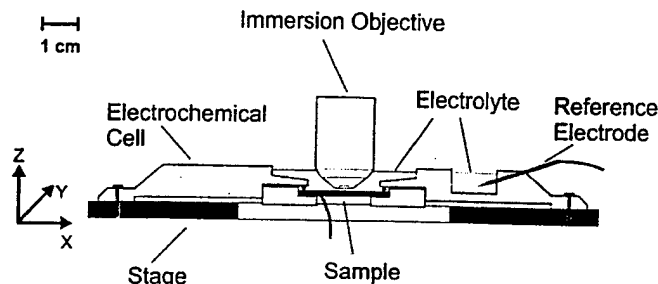


Figure 1. CLSM setup. A 100 times magnification immersion objective is immersed in the electrolyte solution of the electrochemical cell holding the epoxy-coated AA2024-T3 specimen in the configuration of a flat sheet. The cell is mounted on the microscope stage. The open-circuit potential can be measured with an Ag/AgCl microreference electrode.

\* Electrochemical Society Active Member.

<sup>‡</sup> E-mail: rgkelly@virginia.edu

Table I. Areas of four intermetallic particles ( $\mu\text{m}^2$ ) as determined by CLSM in air and aqueous solution using the 100x immersion lens and SEM. The errors indicate the range of values measured.

Particle	CLSM (air)	CLSM (solution)	SEM
1	$17.5 \pm 1.7$	$24.2 \pm 2.2$	$26.1 \pm 3.5$
2	$14.8 \pm 1.7$	$20.5 \pm 1.2$	$17.9 \pm 2.4$
3	$14.4 \pm 1.9$	$18.8 \pm 1.3$	$16.5 \pm 1.4$
4	$8.7 \pm 0.5$	$11.0 \pm 1.2$	$11.8 \pm 1$

the electrolyte and for its approach to the sample surface. The samples were immersed in either 0.5 M NaCl or 0.5 M NaCl + 0.0032 M HCl (pH 2.5). During measurements, these bulk cell solutions were refreshed every few hours. Overnight, the cell was covered with laboratory film to minimize evaporation. Stepwise scans of the entire surface (referred to as tile scans, at constant  $z$ ) were performed periodically to detect the onset of corrosion. Because the field of view for a single image (tile) is limited to  $130 \times 130 \mu\text{m}$  with the 100 times magnification objective, the stage was moved stepwise in the  $x$ - or  $y$ -direction after recording a tile. The software assembled the rows and columns of tiles into an image of the entire area. Once indication of corrosion was found at a specific surface position, the stage was moved to that position and the three-dimensional surface topography was monitored with time (*i.e.*, with no  $x$ ,  $y$  movement of the stage). After the end of the experiments, the coating was removed from some samples, the surface treated with 50% nitric acid to remove corrosion products,<sup>11</sup> and the sample imaged with a 50 times magnification air objective (Epiplan-Neofluar) to examine the final surface morphology.

Intermetallic particles on uncoated AA2024-T3 panels were studied with CLSM in air, under immersion in 0.1 M  $\text{Na}_2\text{SO}_4$  + 0.005 M NaCl and with SEM (using secondary electron imaging). The areas of these particles were determined in the CLSM software by approximating the interface particle/matrix with a polyline (a connected series of straight line segments) until the entire area was enclosed. The software then displayed the area within the polyline. From several trials for the assignment of this polyline the error in the area measurement could be obtained. The procedure was applied to SEM images by scanning the actual photographs, importing the files into the CLSM software and calibrating the obtained area by the apparent length of the micrometer bar in the SEM image.

### Results

The optical properties of the water immersion lens used are tailored for application in a medium with a refractive index of 1.33 (water). IMCs on AA2024-T3 could be monitored because they had slightly different reflected light intensities compared to the matrix. No height difference between matrix and IMCs could be detected before onset of corrosion (*i.e.*, less than  $0.6 \mu\text{m}$  if any). Before quantitative investigations of the corrosion processes underneath organic coatings could be performed, the accuracy of the dimensions obtained with CLSM had to be verified.

For uncoated AA2024-T3 panels comparison of the surface areas of the same intermetallic particles measured with CLSM under immersion in 0.1 M  $\text{Na}_2\text{SO}_4$  + 0.005 M NaCl and with SEM (Table I) showed that the dimensions obtained with CLSM under immersion are in agreement with actual values determined by SEM (using secondary electron imaging) within 7-15%. It was usually difficult to locate the interface between matrix and particle exactly even in the SEM. This led to the errors of about  $\pm 10\%$  in the individual values given in Table I.

Before immersing uncoated AA2024-T3 panels into an electrolyte solution, selected areas of the sample surfaces were examined in air with CLSM to study the topography before any corrosion could occur. These studies had to be performed with the water immersion

Table II. Areas of eight intermetallic particles ( $\mu\text{m}^2$ ) as determined by CLSM with the water immersion lens in air and in aqueous solution.

Particle	Air	Solution	Particle	Air	Solution
1	15.4	20.1	5	48.2	64.5
2	18.0	23.6	6	15.0	18.9
3	7.4	11.1	7	56.4	78.0
4	7.8	10.3	8	13.8	19.0

lens because the lenses of the microscope suitable for monitoring in air are too large to be used with the electrochemical cell. Comparison of the same IMCs before and immediately after immersion showed, that the areas found in air were  $74\% \pm 3\%$  of the real values (Table I and II). A similar comparison of pit depths showed that dimensions in the  $z$ -direction were overestimated by a factor of  $\sim 3$  when imaged in air using a water immersion lens. In air, the contrast and the resolution ( $\sim 0.5 \mu\text{m}$ ) were worse than in solution and the images were slightly blurred.

IMCs could be monitored with high resolution through a thin layer of epoxy, and even through the occluded solution in a coating blister. The dimensions obtained under these conditions were not distorted. This was demonstrated by monitoring some IMCs in a coating blister on an AA2024-T3 panel immersed in 0.5 M NaCl (pH 2.5) with the water immersion lens. After the end of the experiments, the specimen was removed from the cell, the organic coating was stripped and corrosion products were cleaned off. The same IMCs were imaged in air, using a 50 times magnification objective optimized for use in air. For a selected IMC, the areas found under both immersed and air conditions were identical within 2% ( $80 \mu\text{m}^2$ ).

All images shown in Fig. 2, 3, and 4 were recorded under immersion of the sample in 0.5 M NaCl. Figure 2 shows a part of the AA2024-T3 surface seen through a  $10 \mu\text{m}$  thick epoxy coating after 14 d 3 h of (continuous) immersion in 0.5 M NaCl. Besides some corrosion damage from the wet polishing process (A, B, C), no corrosion was visible. Surface details of a size of  $\sim 300 \text{ nm}$  could

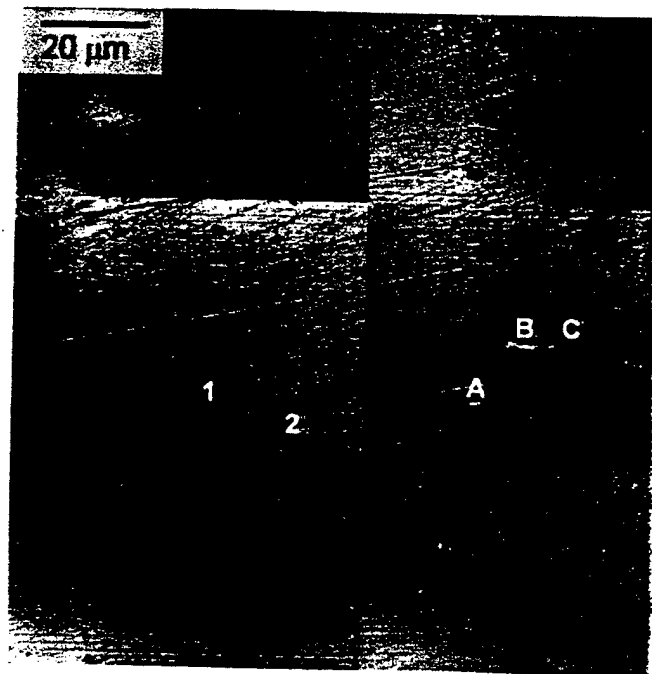
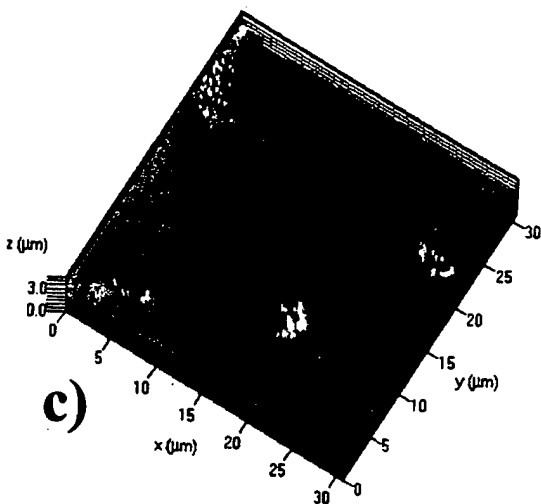
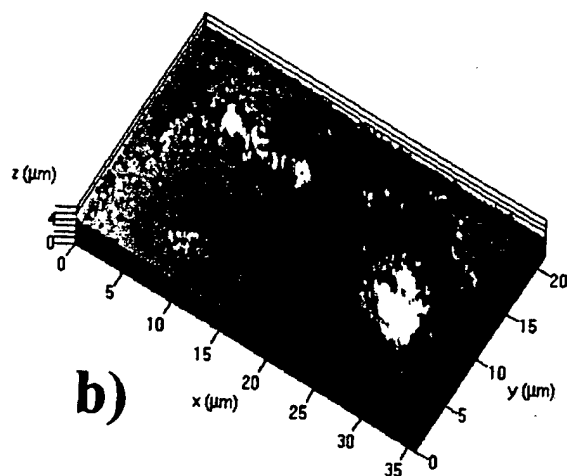
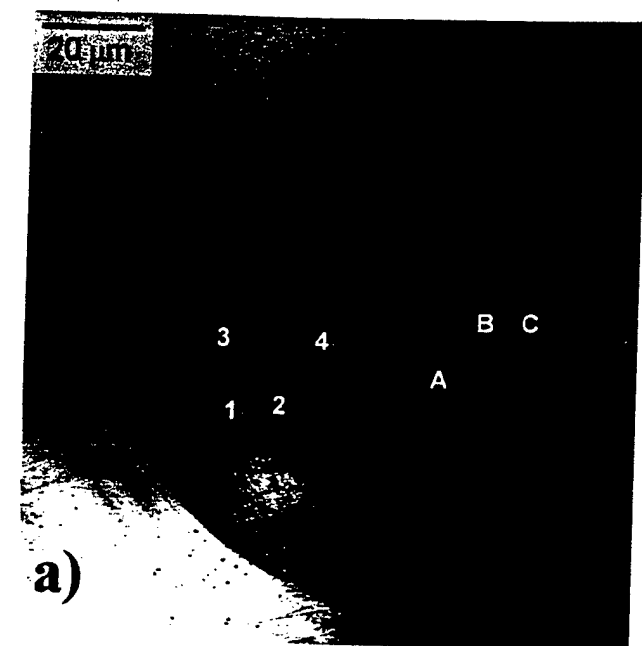
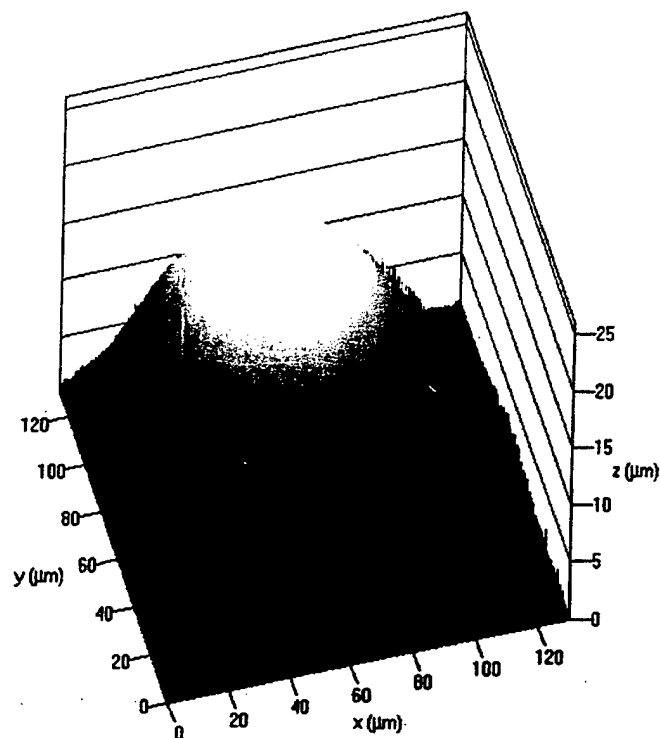


Figure 2. Selected area of epoxy-coated AA2024-T3 after 14 days, 3 h immersion in 0.5 M NaCl. The image contains information from one sample plane only. The numbers indicate spots where later (cmp. Fig. 3) pits form.



**Figure 3.** (a) Extended depth-of-focus image of epoxy-coated AA2024-T3 after blister formation. The area shown is the same as that in Fig. 2. Immersion time in 0.5 M NaCl was 16 days, 7 h. (b) Topographic image of the left area marked in a with a box ( $35 \times 20 \mu\text{m}$ ). (c) Topographic image of the right area marked in a with a box ( $30 \times 30 \mu\text{m}$ ).



**Figure 4.** Three-dimensional image of the coating dome over a blister on epoxy-coated AA2024-T3 after 16 days, 21 h of immersion in 0.5 M NaCl.

be distinguished. Figure 3 shows an extended depth-of-focus presentation of the same area as well as three-dimensional representations of parts of the area after two additional days of immersion. The coating had now failed locally, and a blister had formed in the coating over the site where changes could be seen in the alloy substrate. Several pits on the metal surface, partially filled with corrosion product, were visible within the blister (Fig. 3b,c). They appeared dark in the extended depth-of-focus representation. Some of the pits had originated at IMC particles (noted as 1, 2 in Fig. 3a). Other pits (3, 4) initiated in the alloy matrix or at very small IMCs (diameter close to or smaller than the CLSM resolution of *ca.* 300 nm).

The edge of the blister in the coating could be identified by the fringe-like lines in Fig. 3a, which originated from light reflected from the top of the coating. By increasing the detector gain and selecting the *z*-range in a way that the alloy surface was not scanned, it was possible to monitor the surface topography of the coating itself. The coating "dome" of the blister is clearly visible in the 3D-representation of Fig. 4.

### Discussion

The maximum resolution which can be achieved with a given microscope objective depends on its numerical aperture and the wavelength of the light used, not on the magnification.<sup>1</sup> Any high-quality immersion lens in laser microscopy is designed to be operated in a medium of a specific refractive index, *n*. Any substantial deviation from this refractive index decreases the resolution in the *x*-, *y*-, and especially *z*-directions, introduces imaging errors such as spherical aberration,<sup>1</sup> and changes the area scanned by the laser beam. In addition, the focal length on the sample side changes, and the confocal principle no longer works well. The role of lenses in CLSM is discussed in detail in Ref. 1. The water immersion lens is optimized for *n* = 1.33. Use in air (*n* = 1.0) causes the systematic error shown in Table I and II (compare columns 1 and 3). Imaging in air was, therefore, done mainly to select areas of interest and to get preliminary information about the sample prior to exposure. The refractive indices for 0.5 M NaCl and 0.1 M Na<sub>2</sub>SO<sub>4</sub> is very close

to that of water.<sup>12</sup> Consequently, all dimensions obtained in these solutions are accurate (Table I). The differences seen between the particle areas as determined in solution by CLSM and in SEM are caused by uncertainties in determination of the exact location of the interface between the particle and the matrix for the individual particles, and not by an actual difference in the imaged object size. Also, a clear organic coating does not disturb the measurements as long as it is only a few micrometers thick (and as long as the coating blister does not become too large and no gas accumulation takes place within the blister).

Although intermetallic particles are known to be critical in the initiation and growth of pits on uncoated AA2024-T3,<sup>5-10</sup> their role in blister initiation and growth on coated material is unclear. Quantitative, *in situ* investigations of coating defect evolution at the micrometer scale have been difficult due to a lack of appropriate tools, but are needed to answer questions concerning the role of IMCs in underpaint corrosion. This work shows that CLSM represents a tool amenable to such studies with an *x, y*-resolution close to the theoretical limit of 300 nm for a wavelength of 488 nm.<sup>1</sup> The *z*-resolution was given by the 0.6  $\mu\text{m}$  steps, associated with movement of the *z*-stage during image acquisition. The acquisition time for a single stack ranged between 1 and 4 min and was, therefore, short enough to prevent large changes in the topography during image acquisition.

CLSM allows the surface of the alloy under a transparent coating to be imaged quantitatively, as shown in Fig. 2 and 3. The difference in reflectivity of the intermetallics relative to the matrix of the AA2024-T3 made it possible to detect them under the intact coating that allowed transmission of reflected light from the opaque metallic surface beneath the coating. The different reflectivity of IMCs could result from the differences in composition compared to the Al-rich matrix. Once a blister developed, the ability of CLSM to probe inside the blister allowed the corrosion damage associated with the intermetallics to be followed, as clearly visible from the 3D images in Fig. 3b and c. Subsequently, these capabilities enabled the study of the corrosion of IMC with time once they were incorporated into the blister during its growth. Several factors can contribute to the low reflectivity of the surface close to the pits: the increase in roughness due to the corrosion reaction and dealloying (*e.g.*, Fig. 3, pit 4), the replating of copper, and, in part, intensity loss by light scattering through corrosion products. The last effect enables imaging of cor-

rosion products accumulated at the edge of pits (*e.g.*, Fig. 3, pit 3) or within pits (*e.g.*, Fig. 3, pit 2). Thin layers of corrosion product (<2  $\mu\text{m}$ ) are probably transparent to light in the wavelength used.

By changing the imaging conditions, the height of the coating delamination and the shape of the blister could be monitored.

### Conclusions

Confocal laser scanning microscopy can be used for noncontact, *in situ* study of corrosion processes underneath transparent organic coatings. Three-dimensional information on alloy surface morphology underneath a transparent organic layer with submicrometer resolution in *x, y*, and *z* is obtained. CLSM thus provides a tool for studying the submicrometer scale processes associated with blister initiation and growth on a heterogeneous alloy surface such as AA2024-T3 in real time.

### Acknowledgments

The financial funding of this project and acquisition of the CLSM by the Air Force Office of Scientific Research (AFOSR) under contract no. F49620-96-1-0178 is gratefully acknowledged.

The University of Virginia assisted in meeting the publication costs of this article.

### References

1. *Handbook of Biological Confocal Microscopy*, 2nd ed., J. B. Pawley, Editor, Plenum Press, New York (1995).
2. N. Llorca-Isern, M. Puig, and M. Español, *J. Therm. Spray Technol.*, **8**, 73 (1999).
3. M. A. Alodan and W. H. Smyrl, *J. Electrochem. Soc.*, **144**, L282 (1997).
4. F. Guillaume, L. F. Garfias-Mesias, M. Büchler, and W. H. Smyrl, in *Critical Factors in Localized Corrosion III*, R. G. Kelly, G. S. Frankel, P. M. Natishan, and R. C. Newman, Editors, PV 98-17, p. 155, The Electrochemical Society Proceedings Series, Pennington, NJ (1999).
5. P. Schmutz and G. S. Frankel, *J. Electrochem. Soc.*, **145**, 2295 (1998).
6. R. M. Rynders, C.-H. Paik, R. Ke, and R. C. Alkire, *J. Electrochem. Soc.*, **141**, 1439 (1994).
7. G. O. Ilevbare, J. R. Scully, J. Yuan, and R. G. Kelly, *Corrosion (Houston)*, **56**, 227 (2000).
8. G. O. Ilevbare, C. S. Jeffcoat, and J. R. Scully, in *Passivity and Localized Corrosion*, M. Seo, B. MacDougall, H. Takahashi, and R. G. Kelly, Editors, PV 99-27, p. 269, The Electrochemical Society Proceedings Series, Pennington, NJ (1999).
9. G. O. Ilevbare and J. R. Scully, *J. Electrochem. Soc.*, **148**, B196 (2001).
10. G. O. Ilevbare and J. R. Scully, *Corrosion (Houston)*, **57**, 134 (2001).
11. K. S. Ferrer and R. G. Kelly, *Corrosion (Houston)*, **57**, 110 (2001).
12. *Handbook of Chemistry and Physics*, 79th ed., D. R. Lide, Editor, p. 8, CRC Press, Boca Raton, FL (1998).

# Polarization Resistance Method for Determination of Instantaneous Corrosion Rates

J.R. Scully\*

## ABSTRACT

The polarization resistance method for the determination of instantaneous corrosion rates of metals were reviewed. The assumptions in electrode kinetics that govern the connection between the slope of steady-state applied electrochemical potential-applied current density ( $E_{app}$ - $i_{app}$ ) measurements (i.e., the polarization resistance) and the corrosion rate were restated. Electrochemical impedance, as well as statistical and spectral electrochemical noise methods for obtaining polarization resistance, also were discussed. Traditional sources of error such as high excitation voltage amplitudes, insufficiently slow voltage ramp rates, high alternating current (AC) frequencies, inadequate polarization hold periods, high solution resistance, presence of parallel reduction-oxidation reactions, and nonuniform current and potential distributions were examined with the goal of defining some of the conditions and circumstances where these complicating factors are important. Other complicating factors such as diffusion-controlled reactions, potential-dependent film coverages, and adsorption pseudo-capacitance that affect electrochemical reaction rates were discussed. Their influence on measured interfacial resistance values and subsequent determination of corrosion rates was discussed.

**KEY WORDS:** current-step method, impedance method, instantaneous corrosion rate, linear polarization resistance, noise resistance, polarization resistance, potential-step method, potentiodynamic method, power spectral density, solution resistance, spectral noise resistance

## INTRODUCTION

A variety of methods such as electrical resistance, gravimetric-based mass loss, quartz crystal microbalance-based mass loss, electrochemical, and solution analysis methods enable the determination of corrosion rates of metals. The polarization resistance method, based on electrochemical concepts, enables determination of instantaneous interfacial reaction rates such as corrosion rates and exchange current densities from a single experiment. There are a variety of methods capable of experimentally determining instantaneous polarization resistances such as potential step or sweep, current step or sweep, impedance spectroscopy, as well as statistical and spectral noise methods. All of these methods utilize either two-, three-, or four-electrode electrochemical cells. Instantaneous corrosion rate information can be obtained from such relatively rapid electrochemical measurements in short time periods. Other methods such as the electrical resistance change of the solid electronic conducting phase, gravimetric and quartz crystal microbalance measurements of mass loss, and solution analysis to detect metallic cations released into the ionic conducting phase all provide historical or integrated information on the instantaneous corrosion rates that have occurred over some period of time. Therefore, the derivative of multiple measurements over exposure time must be used to obtain rate information. Therefore, instantaneous rates can not be determined by a single measurement of these types and electrochemical methods, for instantaneous rate determination remain extremely

Submitted for publication February 1998. Presented as paper no. 304 at CORROSION/98, March 1998, San Diego, CA.

\* Center for Electrochemical Sciences and Engineering, Department of Materials Science and Engineering, Thornton Hall, University of Virginia, Charlottesville, VA 22903-2442.

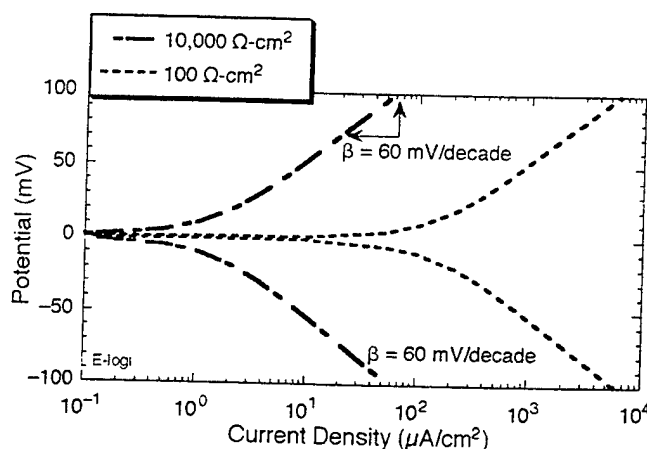


**FIGURE 1.**  $E\text{-}\log(i_{app})$  data for hypothetical corroding interfaces with  $R_p = 100 \Omega\text{-cm}^2$  and  $10,000 \Omega\text{-cm}^2$  (assumed  $1\text{-cm}^2 A$ ) and  $\beta_a = \beta_c = 60 \text{ mV/decade}$ . The two cases produced corrosion current densities,  $i_{corr}$ , of  $130.4 \mu\text{A/cm}^2$  and  $1.3 \mu\text{A/cm}^2$ , respectively. The Tafel slopes were obtained from  $\partial E/\partial \log(i_{app})$  data at high overpotential where  $E\text{-}\log(i_{app})$  is linear. The OCP was arbitrarily selected to be  $0 \text{ mV}$ .

attractive. However, numerous issues can make the task of extracting a polarization resistance value (that is inversely proportional to the instantaneous corrosion rate) from electrochemical data a complex one whether the experiment is conducted in the frequency or time domains. The goal of the present study was to review some of these issues.

### Governing Electrode Kinetics in Corrosion Processes

The following relationship is observed experimentally between applied electrochemical current density and potential for a corroding electrode in the absence of parallel reduction-oxidation reactions.<sup>1,2</sup> The applicability of this simple relationship relies on the presence of a single charge-transfer-controlled cathodic reaction and a single charge-transfer-controlled anodic reaction:

$$i_{app} = i_{corr} \left( \exp \left| \frac{2.3(E - E_{corr})}{\beta_a} \right| - \exp \left| \frac{2.3(E - E_{corr})}{\beta_c} \right| \right) \quad (1)$$

where  $\beta_a$  and  $\beta_c$  are the anodic and cathodic Tafel parameters given by the slopes of the polarization

<sup>1,2</sup> This review focuses on corroding systems. However, the concept of polarization resistance applies equally well to reduction-oxidation systems. Here, the exchange current density ( $i_0$ ) may be calculated from the  $R_p$ , as defined below, where  $R$  is the ideal gas constant,  $T$  is the temperature, and  $\alpha_a$  and  $\alpha_c$  are the anodic and cathodic multi-step electron transfer coefficients, respectively, for the reduction-oxidation process.

$$R_p(\Omega\text{-cm}^2) = \left| \frac{\Delta E}{\Delta i} \right|_{E=E_{rev}} \rightarrow 0 = \left( \frac{RT}{i_0(\alpha_a + \alpha_c)} \right)$$

curves ( $\partial E/\partial \log i_{app}$ ) in the anodic and cathodic Tafel regimes, respectively.  $E\text{-}\log(i_{app})$  data that is governed by such kinetics are shown in Figure 1.  $E_{corr}$  is the corrosion potential.  $E$  is an applied potential such that  $E - E_{corr}$  is  $\Delta E$ , and  $i_{corr}$  is the corrosion current density. This relationship provides the basis for the electrochemical polarization technique as applied to a corroding electrode at its corrosion potential.

### Derivation of the Polarization Resistance

Many investigators have experimentally observed that  $i_{app}$  is approximately linearly related to applied potential within a few millivolts of polarization from  $E_{corr}$ .<sup>3</sup> Stern and Geary simplified the kinetic expression to provide an approximation to the charge-transfer-controlled reaction kinetics given by Equation (1) for the case of small overpotentials with respect to  $E_{corr}$ .<sup>4-6</sup> Equation (1) can be linearized mathematically by taking its series expansion (e.g.,  $e^x = 1 + x + x^2/2! + x^3/3! + x^4/4! \dots$ ) and by neglecting higher terms when  $\Delta E/\beta < 0.1$ . This simplified relationship has the following form:

$$R_p(\Omega\text{-cm}^2) = \left| \frac{\Delta E}{\Delta i_{app}} \right|_{E=E_{corr}} \rightarrow 0 = \left( \frac{\beta_a \beta_c}{2.3 i_{corr} (\beta_a + \beta_c)} \right) \quad (2)$$

rearranging:

$$i_{corr} = \frac{1}{(2.3 R_p)} \left( \frac{\beta_a \beta_c}{\beta_a + \beta_c} \right) = \frac{B}{R_p} \quad (3)$$

where  $R_p$  is the polarization resistance given by  $(\partial E/\partial i_{app})_{E=E_{corr}, \Delta E=0}$  ( $\Omega\text{-cm}^2$ ), and  $B$  is a proportionality constant. Since charge transfer is assumed in Equation (3),  $R_p$  is equal to a charge-transfer resistance ( $R_{ct}$ ). The units for  $R_p$  are ohms as obtained from  $E\text{-}I_{app}$  data (where  $I_{app}$  is the applied current) when the applied current is not normalized by electrode area. Such data must be multiplied by electrode area to yield  $R_p$  ( $\Omega\text{-cm}^2$ ). If electrode area is doubled, then the measured  $R_p$  value in ohms is halved, but the intrinsic polarization resistance value  $R_p$  ( $\Omega\text{-cm}^2$ ) would be the same since the electrode area is doubled. This gives the result that corrosion rate per unit area is independent of electrode area. However, the working electrode area must be known to calculate corrosion rate.

The  $B$  factor is dominated by the smaller of the two anodic and cathodic Tafel slopes ( $b_a$ ,  $b_c$ ), if unequal. Therefore, cathodic mass transport control, such that  $b_c \rightarrow \infty$ , results in  $B = b_a/2.3$ . Similarly, anodic mass transport control results in  $B = b_c/2.3$ .<sup>7</sup> Knowledge of  $R_p$ ,  $b_a$ , and  $b_c$  enables direct determination of the corrosion rate at any instant in time using



Equation (3).<sup>4-9</sup>  $i_{app}$  often is approximately linear with potential within  $\pm 5$  mV to 10 mV of  $E_{corr}$  (Figure 2). The slope of this plot is  $\Delta E/\Delta i_{app}$ . When determined from a tangent to the  $E-i_{app}$  curve at  $E_{corr}$ , as shown in Figures 2(a) and (b), it defines the polarization resistance. Consequently, this method often is called the linear polarization method (LPR). The slope at  $E_{corr}$  is independent of the degree of linearity,<sup>3</sup> although the extent of the approximately linear  $E-i_{app}$  region can vary considerably among corroding systems.

The fact that the corrosion rate is inversely proportional to the  $R_p$  is seen clearly in Equation (3). Taking the logarithm of this equation, it is seen that  $\log i_{corr}$  vs  $\log R_p$  is linear with a slope of  $-1$  and has the intercept  $\log B$ .<sup>3</sup>

$$\log(R_p) = \log B - \log(i_{corr}) \quad (4)$$

Stern and Wiesert confirmed such a relationship over a nearly 6 orders-of-magnitude change in corrosion current density for many corroding systems and for exchange current density for many reduction-oxidation systems.<sup>8,11</sup>

### Time Domain Methods for Determining Polarization Resistance

ASTM standards D-2776<sup>9</sup> and G-59<sup>10</sup> describe standard procedures for conducting polarization resistance measurements. Potentiodynamic,<sup>11</sup> potential step, and current-step methods<sup>12-13</sup> all have been described to determine the linear  $E-i_{app}$  behavior of an electrode near  $E_{corr}$ . Regardless of the method utilized, independent determination of  $\beta_a$  and  $\beta_c$  still is required.

Alternative techniques exploit nonlinearity at larger overpotentials. Nonlinearity invalidates Equation (3). However, the nonlinearity, if treated properly, can enable determination of  $\beta_a$  and  $\beta_c$  without excessive polarization. The Oldham-Mansfeld method calculates  $i_{corr}$  from nonlinear  $E$  vs  $i_{app}$  data obtained within  $\pm 30$  mV of  $E_{corr}$ , without the need for high overpotential determination of  $\beta_a$  and  $\beta_c$ .<sup>14</sup> Computerized curve fitting can exploit nonlinearity to calculate  $\beta_a$  and  $\beta_c$  from low-overpotential data, avoiding the destructive nature of large overpotentials.<sup>15</sup> The Mansfeld technique substitutes Equation (3) into Equation (1) eliminating  $i_{corr}$ .<sup>15</sup>  $\beta_a$  and  $\beta_c$  are determined from the best fit of the resulting expression containing  $\beta_a$  and  $\beta_c$  as unknowns to a nonlinear plot of  $\Delta E$  vs  $2.3i_{app}R_p$ .  $R_p$  is determined in the usual way from the slope of a linear tangent to the  $E$  vs  $i_{app}$  data at  $E_{corr}$ .  $i_{corr}$  is determined subsequently from Equation (3) for known values of  $R_p$ ,  $\beta_a$ , and  $\beta_c$ . In this technique, elimination of  $i_{corr}$  enables determination of only two unknowns by fitting. Advancements in computerization enable a direct fit of  $E-i_{app}$  data to Equation (1), but this requires simultaneous determi-

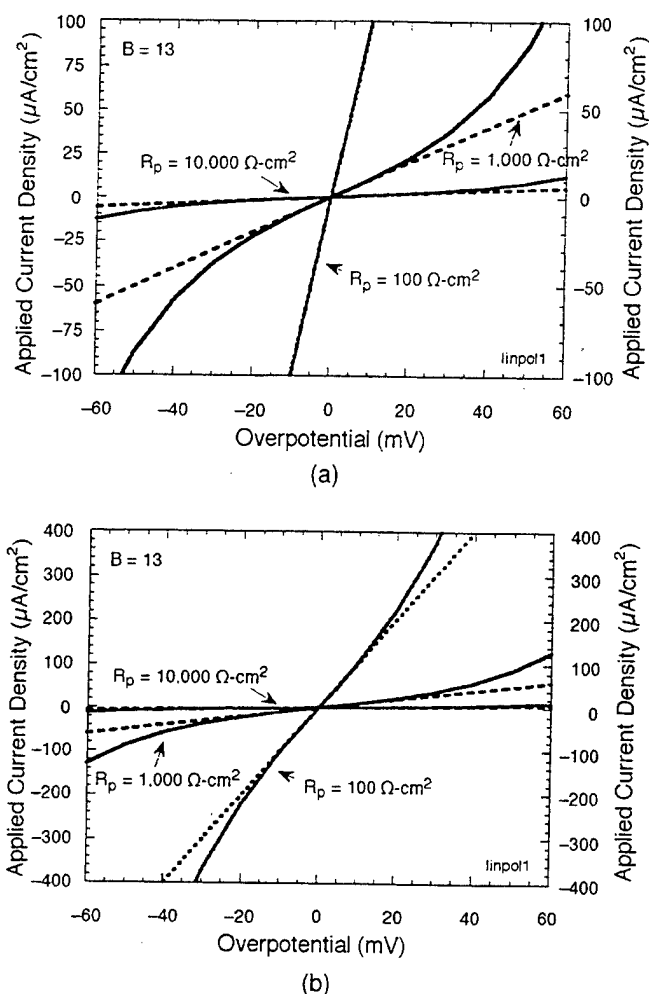
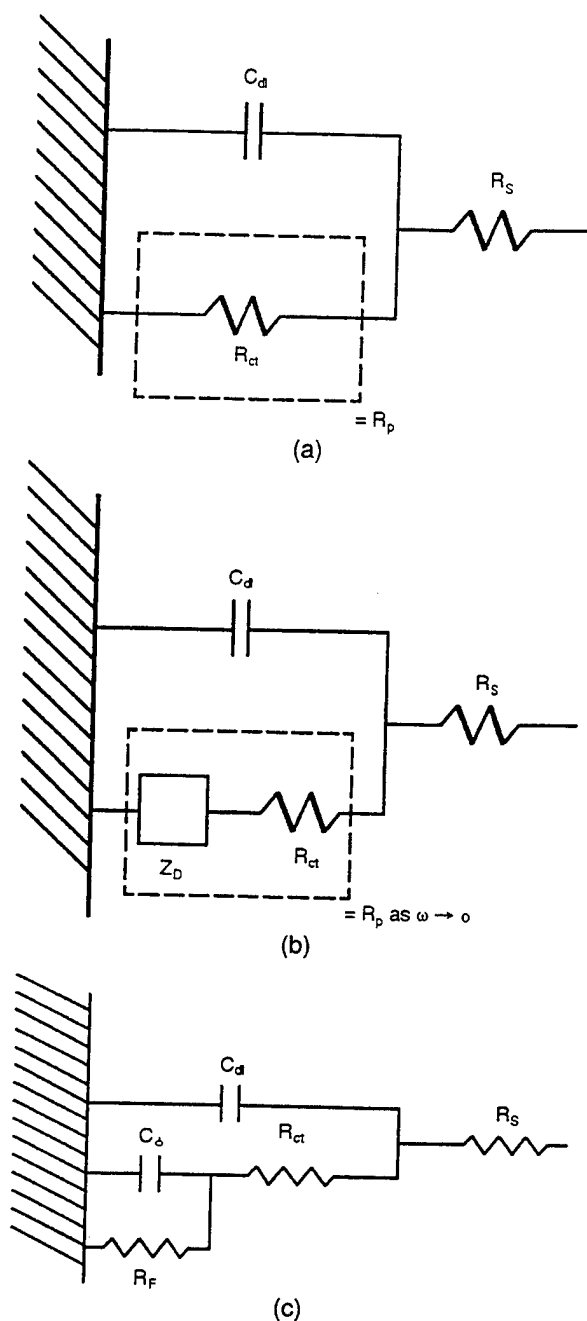


FIGURE 2.  $E-i_{app}$  data according to Equation (1) for hypothetical corroding interfaces with  $R_p = 100, 1,000$ , and  $10,000 \Omega \cdot cm^2$  (assumed  $1 \cdot cm^2 A$ ) and  $\beta_a = \beta_c = 60$  mV/decade. The three cases produced corrosion current densities of 130.4, 13.0, and 1.3  $\mu A/cm^2$ , respectively. Plots a and b of the same data provide different current scales to indicate the extent of nonlinearity in each case.

nation of three unknowns. Consequently, extremely high-quality  $E-\log(i_{app})$  data that is corrected for ohmic voltage error and does not contain other sources of overpotential (i.e., mass transport overpotentials) are required.

### Electrochemical Impedance Methods for Determination of Polarization Resistance

Some of the complications and sources of error associated with the polarization resistance method, such as a high solution resistance and fast scan rate, are explained more readily after introducing electrical equivalent circuit parameters to represent and simulate the corroding electrochemical interface.<sup>1,16-20</sup> The impedance method is a straightforward approach for analyzing such electrical circuits and extracting the values of the circuit parameters. The simplest form of such a model pertinent to a corroding interface is



**FIGURE 3.** Electrical equivalent circuit models commonly used to represent an electrochemical interface undergoing corrosion.  $R_p$ ,  $C_d$ ,  $C_a$ ,  $R_{ct}$ , and  $R_F$  are all potential dependent. (a) Randles-type circuit where  $R_p = R_{ct}$  when there are no mass transport limitations; electrochemical reactions involve no adsorbed intermediates and instantaneous charge-transfer control prevails. (b) Electrical equivalent circuit for a corroding metal containing a diffusional impedance parameter representing presence of a finite diffusional impedance.  $R_p = R_D + R_{ct}$  at the DC limit in the case of a finite mass transport limitation to the reaction rate. (c) Electrical equivalent circuit for a corroding metal containing an adsorption  $C_a$  associated with an adsorbed intermediate. In the example, the charge-transfer reaction rate is inversely proportional to  $R_{ct}$  for a transient period until the adsorbed intermediate coverage was formed. This situation is described by a resistor in series with a capacitor. Once the coverage is formed creating an interphase that slows the reaction, the overall reaction rate is given by  $R_p = R_{ct} + R_F$  at the DC limit.

shown in Figure 3(a). The three circuit parameters ( $R_p$ , solution resistance [ $R_s$ ], and double-layer capacitance [ $C_d$ ]) that approximate a corroding electrochemical interface are shown.  $C_d$  arises whenever an electrochemical interface exists between electronic and ionic phases. The circuit models described in Figures 3(b) and (c) describe cases where diffusional impedances and adsorption pseudo-capacitances occur, respectively.

ASTM standard G 106 provides a standard practice for verification of algorithm and equipment for electrochemical impedance measurements.<sup>20</sup> The standard also contains an appendix reviewing the technique. The electrochemical impedance method is conducted over a range of alternating current (AC) frequencies. Typically, a small-amplitude sinusoidal potential perturbation is applied to the working electrode at a number of discrete frequencies ( $\omega$ ). At each one of these frequencies, the resulting current waveform will exhibit a sinusoidal response that is out of phase with the applied potential signal by an amount depending upon the circuit parameters of the corroding interface and will have a current amplitude that is inversely proportional to the impedance of interface. This electrochemical impedance ( $Z(\omega)$ ) is the frequency-dependent proportionality factor that acts as a transfer function by establishing a relationship between the excitation voltage signal and the current response of the electrochemical system:

$$Z(\omega) = \frac{E(\omega)}{i(\omega)} \quad (5)$$

where  $E$  is the time varying voltage across the circuit,  $E = E_0 \sin(\omega t)$ ;  $i$  is the time varying current density through the circuit,  $i = i_0 \sin(\omega t + \phi)$ ;  $Z(\omega)$  is the impedance ( $\Omega\text{-cm}^2$ ); and  $t$  is time (s).  $Z(\omega)$  is a complex-valued vector quantity with real and imaginary components whose values are frequency dependent:

$$Z(\omega) = Z'(\omega) + jZ''(\omega) \quad (6)$$

where  $Z'(\omega)$  is the real component of impedance, where  $Z'(\omega) = |Z(\omega)| \cos(\phi)$ ;  $Z''(\omega)$  is the imaginary component of impedance, where  $Z''(\omega) = |Z(\omega)| \sin(\phi)$ ;  $j^2$  is the square of the imaginary number, or  $-1$ ;  $|Z(\omega)|$  is the impedance magnitude or modulus, where  $|Z(\omega)| = (Z'(\omega)^2 + Z''(\omega)^2)^{1/2}$ ; and the phase angle ( $\phi$ ) =  $\tan^{-1} Z''(\omega)/Z'(\omega)$ . An example of an impedance  $Z(\omega)$  vector with real and imaginary (capacitive) components is shown elsewhere.<sup>20</sup>

$Z(\omega)$  is a fundamental characteristic of the electrochemical system it describes. A knowledge of the frequency dependence of impedance for a corroding system enables a determination of an appropriate equivalent electrical circuit describing that system. Such a circuit typically is constructed from resistors

and capacitors. Table 1 shows the transfer functions for resistors, capacitors, and inductors. The capacitor can be a  $C_{dl}$  or a  $C_{dl}$  and a pseudo-capacitance ( $C_s$ ) associated with an adsorbed intermediate. Figure 3(a) illustrates a simple equivalent electrical circuit model commonly used to represent an actively corroding metal in an aqueous solution under charge-transfer control. The following expression describes the impedance for the simple circuit described in Figure 3(a):

$$Z(\omega) = R_s + \frac{R_p}{1 + \omega^2 R_p^2 C_{dl}^2} - \frac{j\omega C R_p^2}{1 + \omega^2 R_p^2 C_{dl}^2} \quad (7)$$

where  $\omega = 2\pi f$  is the frequency of the applied signal (rad/s),  $f$  is the frequency of the applied signal (Hz), and  $C_{dl}$  is the interfacial capacitance (F/cm<sup>2</sup>). The complex plane, Bode magnitude, and phase plots resulting from a circuit such as shown in Figure 3(a) and described by Equation 7 are shown for three different values of  $R_p$  in Figure 4. At very low frequencies:

$$Z_{\omega \rightarrow 0}(\omega) = R_s + R_p \quad (8)$$

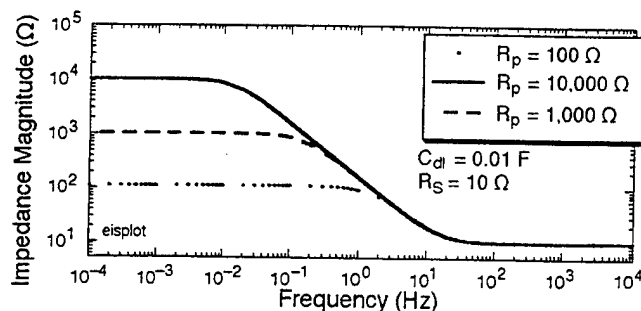
This is because the impedance associated with a capacitor approaches infinity as frequency approaches zero, and parallel electrical circuit elements are dominated by the element with the smallest impedance. Therefore, the sum of  $R_s$  and  $R_p$  is measured at zero frequency; while at very high frequencies:

$$Z_{\omega \rightarrow \infty}(\omega) = R_s \quad (9)$$

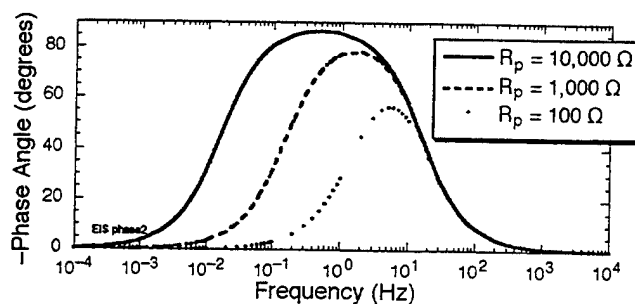
Since the algebraic sum of  $R_s$  and  $R_p$  is measured when a direct current (DC) measurement is performed (e.g., zero AC frequency, long hold time during potential or current step, or slow scan rate approaching zero), the true corrosion rate will be underestimated by  $|Z(\omega)|$  at the zero frequency limit when  $R_s$  is appreciable (Figure 5). However,  $R_p$  can be determined in media of high resistivity when  $R_p$  is separated mathematically from  $R_s$  by taking the difference between  $Z(\omega)$  obtained at low and high  $\omega$  ( $R_p = |Z(\omega \rightarrow 0)| - |Z(\omega \rightarrow \infty)|$ ). In other words, determination of  $R_p$  can be achieved by subtracting the results of Equation (9) from the results of Equation (8). This is a particularly useful approach if  $R_s$  is nearly the same value as  $R_p$  (Figure 5 for  $R_s = 100 \Omega$ ). The need for this subtraction may result from either low conductivity environments or placement of the reference electrode far away from the working electrode; in either case,  $R_s$  may become large. Conversely, any experiment conducted at too fast a

**TABLE 1**  
*Linear Circuit Elements*  
*Commonly Used in Electrochemical Impedance*

Circuit Component	Impedance
Resistor (R)	$Z(\omega) = R$
Capacitor (C)	$Z(\omega) = -1/j\omega C$
Inductor (L)	$Z(\omega) = j\omega L$



(a)

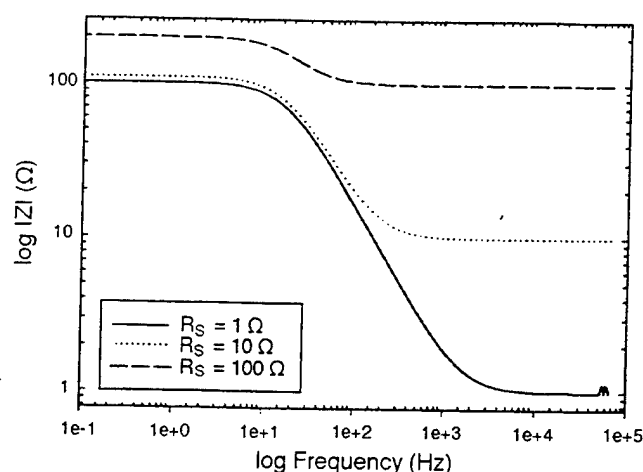


(b)

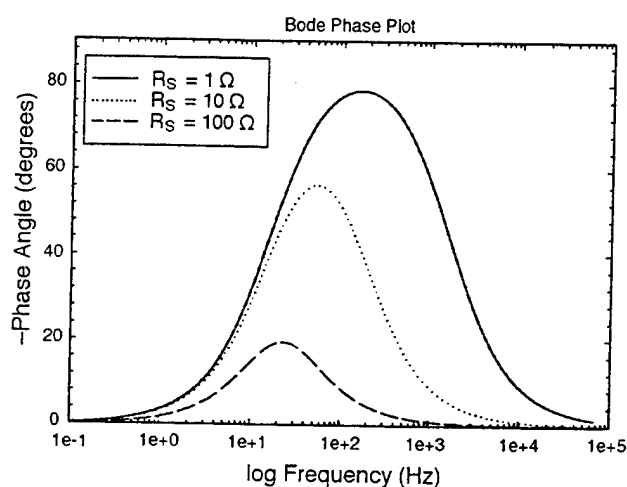
**FIGURE 4.** (a) Bode magnitude and (b) Bode phase angle plots for a hypothetical corroding interface using the electrical equivalent circuit model given by Figure 3(a) with  $R_p = 10, 100, \text{ or } 1,000 \Omega$ ,  $C_{dl} = 1,000 \mu\text{F}$ , and  $R_s = 10 \Omega$ .

voltage scan rate (short time or too high of an AC frequency) causes the algebraic sum of the ohmic resistance and the resultant frequency dependent parallel impedance of the parallel resistive-capacitive network to be measured. This value will be lower than the sum of  $R_p$  and  $R_s$  determined at an infinitely slow scan rate or frequency because current leaks through the parallel capacitive element at a higher scan rate because of its low impedance at high frequency. This usually will result in an overestimation of the true corrosion rate. These complications in scan rate or current-step hold time can be overcome, or at least detected more easily, by using the electrochemical impedance method.<sup>1,16,20</sup> Corrosion rate determination in Equation (3) still requires knowledge of  $\beta_a$  and  $\beta_c$ .

Either the anodic or cathodic half-cell reaction can become mass-transport limited and restrict the rate of corrosion at  $E_{corr}$ . The presence of diffusion-



(a)



(b)

**FIGURE 5.** (a) Bode magnitude and (b) Bode phase angle plots for hypothetical corroding interfaces with  $R_p = 100 \Omega$ ,  $C_{dl} = 100 \mu F$ , and  $R_s = 1, 10$ , or  $100 \Omega$  using the electrical equivalent circuit model of Figure 3(a).

controlled corrosion processes does not invalidate the electrochemical impedance spectroscopy (EIS) method but does require extra precaution and a modification to the circuit model of Figure 3(a). In this case, the finite diffusional impedance is added in series with the usual charge-transfer parallel resistance shown in Figure 3(b). The transfer function for the frequency dependent finite diffusional impedance ( $Z_D$ ) has been described by:<sup>21</sup>

$$Z_D(\omega) = R_D \left[ \frac{\tanh \sqrt{j\omega s}}{\sqrt{j\omega s}} \right] \quad (10)$$

Here,  $s = l_{eff}^2/D$ , where  $l_{eff}$  is the actual finite diffusion length and  $D$  is the diffusion coefficient of the diffusing species that limits the interfacial reaction. The

value of  $Z_D(\omega)$  approaches the real component of the diffusional impedance,  $R_D$ , as  $\omega \rightarrow 0$ . The maximum frequency required to obtain  $R_D$  depends upon the value of  $s$ . The larger the value of  $s$ , such as when  $l_{eff}$  is large or  $D$  is small, the lower the frequency required as illustrated in Figure 6.  $R_p$ , defined as  $[\Delta E/\Delta i_{app}]$  as  $\omega \rightarrow 0$ , is the sum of  $R_{ct}$  and  $R_D$  contributions to the polarization resistance, assuming that  $R_D + R_{ct} \gg R_s$ :

$$R_p = R_{ct} + R_D \quad (11)$$

A very low frequency or scan rate may be required to obtain  $R_p$  defined by Equation (11) under certain circumstances (Figure 6). Here, a  $l_{eff}$  of 0.1 cm and  $D = 10^{-5} \text{ cm}^2/\text{s}$  requires that a frequency  $< 0.1 \text{ mHz}$  be implemented to obtain  $R_p$  from  $|Z(\omega)|$  at the zero frequency limit. Hence, a common experimental problem for diffusion-controlled electrochemical reactions is that extremely low frequency (or scan rates) are required to complete the measurement of  $R_p$ . When  $R_p$  is defined by Equation (11), the Stern approximation of Equations (2) and (3) must be modified to account for the Tafel slope for the anodic or cathodic reactions under diffusion-controlled conditions (i.e.,  $\beta \rightarrow \infty$ ). In fact, Equation (1) becomes invalid. Moreover, it has been argued that the use of  $R_p$  in the Stern equation breaks down in the case of mixed or partial diffusion control.

Another relevant situation to corrosion rate determination occurs when an adsorbed intermediate participates in the overall reaction process (Figure 3(c)).<sup>22</sup> Here,  $R_{ct}$  is a faradaic resistance proportional to a charge-transfer process that occurs instantaneously given a certain adsorbed intermediate coverage.  $R_s$  and  $C_{dl}$  have their usual meanings.  $C_a$  is a new capacitance term that depends upon the change in the charge stored in the adsorbed intermediate film resulting from a gradual change in the film coverage with potential.<sup>2</sup> The adsorbed film has a charge associated with it in this case because it is formed by a charge-transfer process. Recall that the source of any fixed capacitance is a charge that is proportional to potential. Hence, the rate of change of surface charge is proportional to the rate of change in interfacial potential. The capacitance ( $C$ ) is the proportionality factor that is independent of the rate of change in charge or potential assuming a fixed capacitance:<sup>2</sup>

$$C = \left( \frac{dq}{dE} \right) = \left( \frac{dt}{dE} \right) \left( \frac{dq_T}{dt} \right) \quad (12)$$

In the case of a double-layer capacitance,  $C_{dl} = dq_{dl}/dE$ . For  $C_a = dq_F/dE$ . Here,  $q_F$  is the charge to form the surface film of an adsorbed intermediate, for ex-

ample.  $q_F = q_M \theta$ , where  $\theta$  describes the fractional surface coverage by the film (assumed to be one monolayer thick), and  $q_M$  describes the charge required to form one monolayer:

$$C_o = \left( \frac{dq_F}{dE} \right) = q_M \left( \frac{d\theta}{dE} \right) = q_M \left( \frac{dt}{dE} \right) \left( \frac{d\theta}{dt} \right) \quad (13)$$

Hence,  $C_o$  differs from  $C_{dl}$  since the former involves charge transfer to create the change in surface charge. The latter involves a charge balance across an electrochemical interface brought about by rearrangement of ions in solution in response to a change in excess charge in the metal.<sup>2</sup> Therefore,  $C_{dl}$  requires no charge transfer. The adsorption  $C_o$  appears in the circuit model as a physically justified capacitance that behaves just like a capacitor should: it allows passage of an AC signal but provides an infinite resistance to a DC signal. The physical significance of this, when placed in series with a resistor, is that it allows a transient current flow when the potential is shifted until the coverage reaches the equilibrium value defined by the new potential. If the reaction still proceeds at a new steady-state rate after the coverage has formed, this can be described by placing a second resistor in parallel with  $C_o$ . In this example, the charge-transfer reaction rate and coverage are assumed to increase with potential, with increasing coverage acting against the overall reaction rate. In this case, the interphase acts as an added resistor such that  $|Z(\omega)|$  at the zero frequency limit is equal to  $R_s + R_F + R_{ct}$ . Therefore,  $R_F$  and  $R_{ct}$  are both potential dependent, and  $R_F + R_{ct}$  yields  $R_p$  if  $R_s$  is minimal. As the frequency of an AC signal increases, the coverage can no longer change with potential, and  $C_o$  approaches zero. Since the coverage is frozen,  $d\theta/dE$  approaches zero and the interface can be represented by a simplified Randles' circuit where  $C_{dl}$  is parallel to  $R_{ct}$ .  $R_{ct}$  is therefore a charge-transfer resistance inversely proportional to the charge-transfer reaction rate at zero or frozen coverage.

### Electrochemical Noise Resistance

Electrochemical noise analysis can provide a parameter called the electrochemical noise resistance ( $R_n$ ).<sup>23-29</sup> It is desirable to utilize this parameter in an analogous fashion as the polarization resistance. One electrode configuration that enables such a measurement involves connecting a zero resistance ammeter between two nominally identical corroding electrodes immersed in the same solution. A third, nominally identical electrode can be immersed in solution and connected to the first two using a high impedance voltmeter. This electrode serves as a "noisy" pseudo-reference electrode. This approach is attractive in field applications because of the more rugged nature

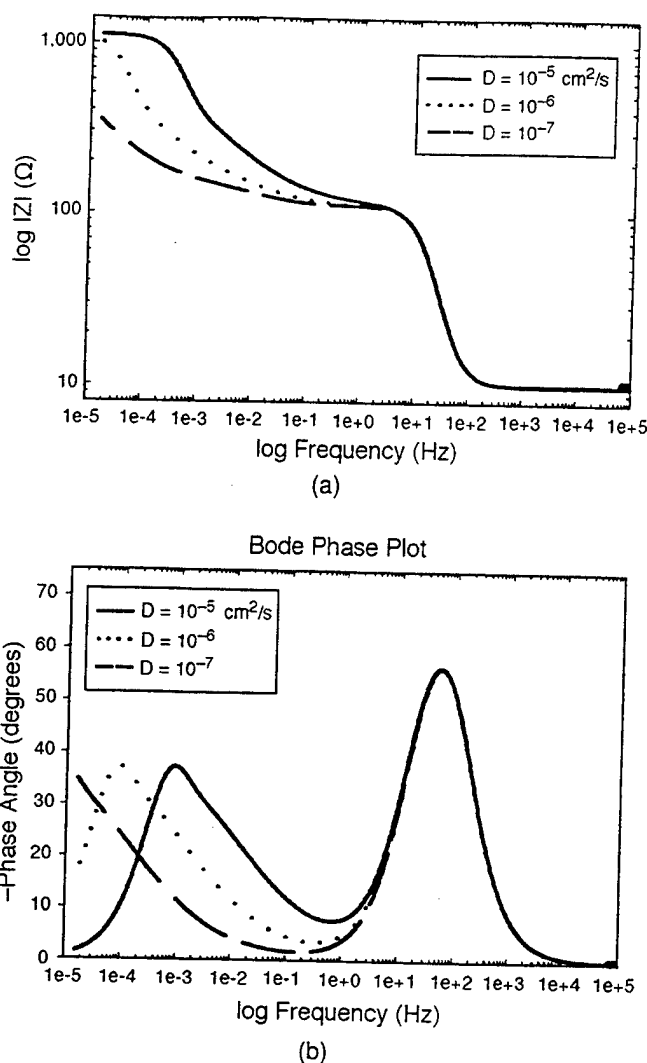


FIGURE 6. (a) Bode magnitude and (b) Bode phase angle plots for hypothetical corroding interfaces with  $R_{ct} = 100 \Omega$ ,  $R_D = 1,000 \Omega$ ,  $C_{dl} = 100 \mu F$ ,  $R_s = 10 \Omega$ ,  $l_{eff} = 0.1 \text{ cm}$ , and  $D = 10^{-5}$ ,  $10^{-6}$ , and  $10^{-7} \text{ cm}^2/\text{s}$  using the electrical equivalent circuit model of Figure 3(b).

of the metallic electrode compared to laboratory reference electrodes but complicates the analysis because two uncorrelated potential sources (i.e., from the couple and the pseudo-reference) are measured in the collection of potential noise ( $V_n$ ). Since  $V_{n(\text{meas})} = (V_{n(\text{couple})} + V_{n(\text{pseudo-ref})})^{1/2}$ ,  $V_{n(\text{meas})}$  must be divided by  $\sqrt{2}$ <sup>30</sup> to yield  $V_{n(\text{couple})}$ . Another alternative is a four-electrode arrangement where the first pair is coupled through a zero resistance ammeter to monitor current and the second pair is connected with a high-impedance voltmeter to sample an uncorrelated  $V_{n(\text{couple})}$ . Alternatively, a less noisy, conventional reference electrode may be utilized in the three-electrode arrangement. In this case,  $V_{n(\text{meas})}$  and  $I_{n(\text{meas})}$  are correlated, where  $I_n$  is the electrochemical current noise. The reference electrode noise can be defined separately as the electrochemical voltage noise between two nominally identical reference electrodes.<sup>31</sup> If the

reference electrode noise is low, then the  $\sqrt{2}$  correction factor is not needed. In either case, the third electrode (reference electrode) is connected to the first two via a high-impedance voltmeter. These arrangements enable simultaneous recording of the galvanic current with time and the galvanic couple potential versus time. The standard deviation of the voltage noise divided by the standard deviation of the current noise has been proposed to yield a statistical parameter called the noise resistance ( $R_n$ ).<sup>23-30,32</sup> Further analysis of simulated noise data has led to the conclusion that the ratio of the standard deviations of the current and voltage noises measured between two identical electrodes can be normalized by surface area by multiplying by  $\sqrt{A_v A_i}$ :<sup>29</sup>

$$R_n = \frac{\sigma_{V(\text{meas})}}{\sigma_{I(\text{meas})}} \sqrt{A_v A_i} \quad (14)$$

where  $\sigma_{V(\text{meas})}$  is the standard deviation of the voltage noise,  $\sigma_{I(\text{meas})}$  is the standard deviation of the current noise, and  $A_v$  and  $A_i$  are the surface areas of the electrodes used for voltage and current measurement, respectively. Correlations between this parameter and conventionally determined  $R_p$  and mass-loss-based corrosion rates have been obtained.<sup>24,30</sup> Unfortunately, experimental confirmation of the area normalization factor has not been performed extensively. Recall that in the case of a  $R_p$  determined from  $E-i_{\text{app}}$  data or EIS data at the zero frequency limit, measured resistance can be multiplied by electrode area and will yield the same area normalized  $R_p$  over a broad range of electrode areas.

Moreover, the correlation has lacked a rigorous fundamental foundation for correlating  $R_n$  with corrosion rate, despite the intuitive connection between  $\sigma_v$  and  $\sigma_i$  given by the proportionality factor  $R_n$ . It is clear that the surface of one freely corroding electrode could be divided into areas that experience fluctuations in interfacial resistance that produce changes in anodic and cathodic half-cell reaction rates in any one patch. The electrode potential must change then in each patch to drive the half-cell reactions such that the sum of all the anodic half-cell currents from all patches equals the sum of all cathodic half-cell currents, regardless of whether the source of cathodic half-cell current is from capacitive discharge or electrochemical reaction.<sup>28</sup> Some global change in potential also occurs on the electrode. If the first electrode is now connected to a second electrode whose interfacial properties and global electrode potential do not change on their own at the same instant in time and by the same degree as on the first electrode, then a galvanic cell is created momentarily, which induces a further difference in anodic and cathodic half-cell currents on the first electrode. Current now flows between the first and

second electrodes such that the sum of anodic and cathodic half-cell currents over all patches on both electrodes is equal. When the interfacial resistances return to normal values over all patches, the potential difference between the two electrodes is eliminated and so is the measurable current between the two electrodes. Bertocci argued that the external current fluctuation measured between two identical electrodes is identical to the fluctuation in one electrode.<sup>28-29</sup> Others have argued using concepts of mixed potential theory that, at worst, the current sampled is only one half of the total for equal-sized electrodes.

Theoretical relationships establishing the connection between  $R_n$  and  $R_p$  have been sought by several researchers,<sup>29,33-36</sup> but their validity has been questioned. A great concern has been that the largest current peaks would occur during the most rapid voltage fluctuations since the electrode interface contains a capacitance through which current can be shorted.<sup>28-29</sup> Thus, when voltage fluctuations are rapid, the measured noise current will be shorted through the interfacial capacitance assuming a simple electrical equivalent circuit model consisting of a two-parallel resistor-capacitor network describing the interface for each electrode connected in series through  $R_e$ . This situation would lead to the lowest impedance between the two electrodes during the most rapid voltage fluctuations that, in turn, produce the greatest current fluctuations. The theoretical maximum measured current would be given by the voltage fluctuation divided by  $R_e$ . The outcome would be a statistical  $R_n$  parameter that is proportional to, or heavily influenced by higher frequency data. Indeed,  $R_n$  is found to equal an absolute impedance at some frequency that depends on the frequency of the voltage fluctuations and the resistive-capacitive (RC) time constant of the electrode interface in one study of simulated noise.<sup>28</sup> Unfortunately, a  $R_n$  value obtained at high frequency would be smaller in magnitude than the  $R_p$  obtained at the zero frequency limit. Hence, it would not represent the desired zero frequency limit interfacial resistance,  $R_p$ . Indeed, such underestimations in the true value of  $R_p$  have been observed experimentally.<sup>30,32</sup>

Recently, a more rigorous theoretical and experimental analysis has been made comparing the spectral noise resistance ( $R_{sn}(\omega)$ ) obtained at each frequency with the  $R_p$  obtained from the zero frequency limit of impedance data  $|Z(\omega = 0)|$ , as well as the frequency dependent impedance of two electrodes.<sup>37-41</sup> The spectral noise resistance ( $R_{sn}(\omega)$ ) is determined by taking the square root of power spectral density of the voltage noise,  $V_{PSD}$ , ( $V^2/\text{Hz}$ )<sup>1/2</sup> and dividing it by the square root of power spectral density of the current noise,  $I_{PSD}$ , ( $A^2/\text{Hz}$ )<sup>1/2</sup> at each frequency using the same two electrode arrangement as discussed above.<sup>40-41</sup>

$$R_{sn}(\omega) = \frac{\sqrt{V_{PSD}}}{\sqrt{I_{PSD}}} \quad (15)$$

$R_{sn}(\omega)$  is proportional to the magnitude of the cell impedance,  $|Z(\omega)|$ , in the two-electrode arrangement.<sup>40-41</sup> The proportionality factor is unity in the case of identically sized electrodes in a two-electrode cell with identical impedances and a noiseless reference electrode.<sup>40-41</sup> Therefore, the  $R_{sn}(\omega)$  at the zero frequency limit could equal the interfacial impedance at the zero frequency limit  $|Z(\omega = 0)|$  in the theoretical case of identical electrode impedances with negligible  $R_s$ . Figure 7 illustrates data for identical iron electrodes in 1 M sodium sulfate ( $\text{Na}_2\text{SO}_4$ ) with an iron reference electrode. Here,  $R_{sn}(\omega) = \sqrt{3} |Z(\omega)|$  resulting from the noisy reference electrode (RE). Thus,  $2 |Z(\omega)|$  and  $R_{sn}(\omega)$  appear to be similar. It is well known that in many instances  $|Z(\omega = 0)|$  equals  $R_p$ . Even  $R_n$  may equal  $R_{sn}(\omega = 0) = |Z(\omega = 0)| = R_p$  if  $|Z(\omega)|$  equals  $R_p$  in the frequency regime dominating the  $R_n$  value. The frequency range dominating the  $R_n$  value is determined by several factors, but this statement is more likely to be true if  $|Z(\omega)|$  and  $R_{sn}(\omega)$  exhibit long low-frequency plateaus over a broad frequency range that encompasses the  $f_{min}$  and  $f_s$  utilized in the  $R_n$  measurement. Here,  $f_{min}$  is given by the total sampling time ( $T$ ), where  $f_{min} = 1/T$  and  $f_s$  equals the data sampling rate.  $R_n$  typically varies with  $f_s$  and underestimates  $|Z(\omega = 0)|$ . Unfortunately,  $R_{sn}(\omega \rightarrow 0)$  does not equal  $R_p$  in the zero frequency limit under many other conditions, such as when  $\log(R_s/R_p) > 0$  or in the case of very noisy reference electrodes.<sup>40-41</sup> Moreover,  $R_{sn}(\omega)$  can be dominated by the properties of the high-impedance electrode in the case of dissimilar electrode impedances that are equally noisy, but this is not always the case. For instance, the low-impedance electrode in a two-electrode cell with a third reference electrode can be sensed by  $R_{sn}(\omega)$  if the higher impedance electrode is much noisier than the low-impedance electrode.<sup>40-41</sup> Recent attempts have been made to address circumstances where  $R_{sn}(\omega)$  lies between  $|Z(\omega)|_1$  and  $|Z(\omega)|_2$  representing the impedance values of the high- and low-impedance electrodes. Methods have been suggested for sensing the current fluctuations on both electrodes.<sup>42</sup>

### Complications With Polarization Resistance Measurements

Error-producing complications related to the polarization resistance method and possible remedies are reported in the literature.<sup>14-15,43-48</sup> The most common errors involve invalidation of the results through oxidation of some other electroactive species besides the corroding metal in question; a change in the open-circuit or corrosion potential during the time

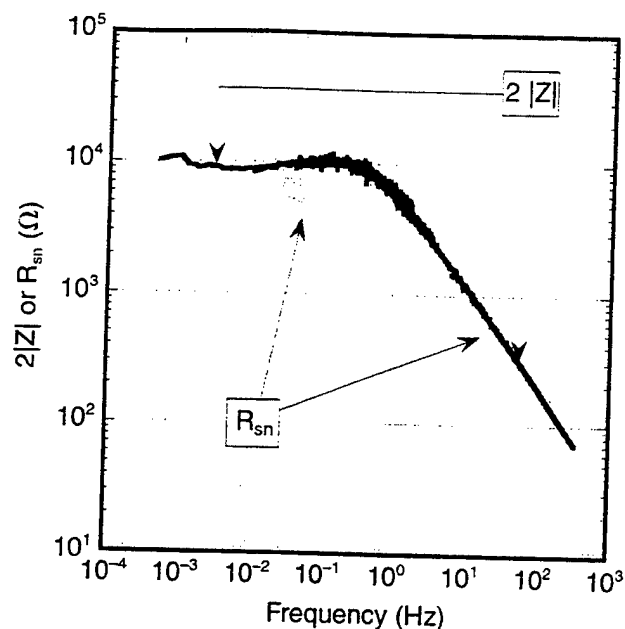


FIGURE 7.  $R_{sn}(\omega)$  vs frequency compared to two times the impedance  $|Z(\omega)|$  vs frequency for two iron electrodes in 1 M  $\text{Na}_2\text{SO}_4$  at pH 4 with a "noisy" iron reference electrode. Impedance measurements performed in a two-electrode cell yielded  $2|Z(\omega)|$ .  $R_{sn}(\omega) = \sqrt{3}|Z(\omega)|$  for the case of three "noisy" electrodes.<sup>41</sup> (Reproduced by permission of The Electrochemical Society, Inc.)

taken to perform the measurement; use of  $\Delta E$  that is too large, invalidating the assumption of a linear relationship between  $i_{app}$  and  $E$  required by Equation (2) (i.e.,  $\Delta E/\beta < 1$ ); too fast of a voltage scan rate or insufficient potential hold time; ohmic solution resistance; and current and potential distributions.

### Oxidation or Reduction of Some Other Electroactive Species

If the  $E_{corr}$  of the corroding system is close the reversible electrode potential of the anodic or cathodic reactions or near the reversible electrode potential of any other redox process, then the corrosion rate likely will be overestimated because electrochemical reactions occur in parallel to metal dissolution. This situation can be ascertained experimentally with the use of any noncorroding, readily polarizable electrode such as platinum, gold, or high-density graphite. These materials have a low corrosion rate in most aqueous solutions and will assume a redox potential that is governed by the dominant parallel reduction-oxidation processes occurring in the system. If the corrosion potential of the corroding metal is very close to the redox potential of such an electrode, then  $E_{corr}$  may be close to a reversible electrode potential. The error in estimation of the corrosion rate depends upon the exchange current density for the redox process,  $i_{corr}$ ,  $\beta_a$ ,  $\beta_c$ , and the difference in potentials between  $E_{corr}$  and the reversible electrode potential in question.<sup>48</sup> A cyclic voltammogram on the platinum

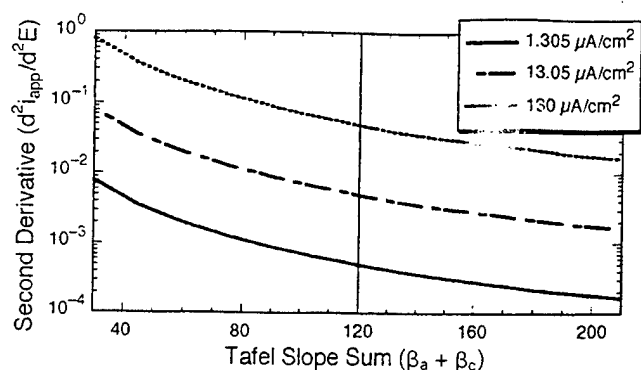


FIGURE 8. Second derivative of  $E-i_{app}$  data ( $d^2i_{app}/d^2E$ ) vs the sum ( $\beta_a + \beta_c$ ) for  $i_{corr} = 1.305, 13.05$ , and  $130.5 \mu A/cm^2$ , indicating that curvature of  $E-i_{app}$  data is a function of corrosion rate and Tafel parameters.

electrode may reveal the approximate reaction rate of any parallel redox process over the potential range of interest.

### Deviations from Linearity Near the Open-Circuit Potential

Deviations from linearity have been discussed in the literature.<sup>48-50</sup> At issue is the question of when the range of  $\Delta E$  is small enough such that the higher terms in the series expansion of Equation (1) reasonably can be neglected. This requires that  $\Delta E/\beta \ll 1$ . Clearly, the extent of the  $E-i$  region where Equation (2) is a good approximation of Equation (1) depends on the values of  $\beta_a$  and  $\beta_c$ . An approximately linear region can be restricted to  $\pm 2$  mV for low values of  $\beta_a$  and  $\beta_c$  and can be  $> 60$  mV for high values. This curvature has been described mathematically as:<sup>48</sup>

$$\left( \frac{\partial^2 i_{app}}{\partial^2 E} \right) = i_{corr} \left( \frac{1}{(\beta_a/2.3)^2} + \frac{1}{(\beta_c/2.3)^2} \right) \quad (16)$$

Therefore, the extent of the curvature will depend upon  $i_{corr}$ , which itself depends on  $B/R_p$  and is inversely proportional to the squares of  $\beta_a$  and  $\beta_c$ . Hence, the curvature will be greater for smaller  $R_p$  (Figures 2 and 8), and smaller values of  $\beta_a$  and  $\beta_c$ . Obviously, the linear regions will differ for anodic versus cathodic polarization if differing values of  $\beta_a$  and  $\beta_c$  exist. Of course, the  $R_p$  always is obtained properly from the tangent of the  $E-i_{app}$  data in the vicinity of  $E_{corr}$ . Stated another way, there always will be finite curvature associated with the true governing electrode kinetic expression given by Equation (1) when plotted as  $E$  vs  $i_{app}$  (Figure 2). Since the  $E-i_{app}$  behavior of the corroding electrode will have a finite, albeit small curvature, the presence of persistent linearity over a significant potential range may be a clue that ohmic voltage-controlled  $E-i$  behavior exists.<sup>48</sup>

A second related issue is the asymmetry in the  $E-i$  response near  $E_{corr}$  for different values of  $\beta_a$  and  $\beta_c$ . Corrosion involves a cathodic electron transfer reaction that is different from the metal oxidation reaction. Therefore, there is no fundamental reason why  $\beta_a$  and  $\beta_c$  should be equal and they should be expected to differ. The extent of their difference defines the degree of asymmetry. Asymmetry matters because the extent of the region where Equation (2) is a good approximation of Equation (1) then differs for anodic compared to cathodic polarization.<sup>50</sup> The errors in assuming  $\pm 10$  mV linearity using the tangent to the  $E-i_{app}$  data at  $E_{corr}$  and for 10 mV or  $-10$  mV potentiostatic polarizations has been defined for different Tafel slopes.<sup>51</sup>

### Voltage Scan Rate, AC Frequency, or Hold Time During Potential or Current Step

Capacitive current can result in hysteresis in small amplitude cyclic voltammogram  $E-i_{app}$  plots.<sup>16,51-55</sup> Hysteresis in the current density-applied potential plot is brought about by combinations of high-voltage scan rate, large interfacial capacitances, and large polarization resistances. High capacitance, multiplied by a rapid voltage scan rate, causes a high capacitive current that results in hysteresis in cyclic  $E-i_{app}$  data. Attempting to determine  $R_p$  at too fast of a scan rate can underestimate the true value inversely proportional to corrosion rate as shown by Macdonald,<sup>52</sup> leading to an overestimation of corrosion rate. This error can be minimized by determining the polarization resistance at a slow scan rate or extrapolating the results at several different slow scan rates to zero scan rate.<sup>52</sup> Alternatively, one may take two or more current density measurements from potentiostatic data after long time periods near  $E_{corr}$  to minimize scan rate effects. However, since cyclic voltammograms, potential steps, and current steps all represent the Fourier synthesis of sine waves, they all equally require adequate hold time, a low enough scan rate, or a low  $f_{max}$  to perform each measurement. This required time period depends on the  $R_p C_{dl}$  time constant of the electrochemical interface (Figure 3[a]) for an electrode that does not involve mass-transport-controlled reactions or  $C_s$  associated with adsorbed intermediates.

The maximum scan rate allowed to obtain accurate measurements of the  $R_p$  has been addressed in the literature.<sup>56</sup> The governing principles are best understood through the concepts of impedance and the Bode magnitude plot for the simplified Randles' circuit (Figures 4[a] and [b]). Here, the maximum applied frequency allowed to obtain  $R_s + R_p$  from the low-frequency plateau can be approximated by:

$$f_{max} < f_{bp} \approx \frac{1}{2\pi C(R_s + R_p)} \quad (17)$$



where  $f_{bp}$  is an approximation of the lower breakpoint frequency (Hz) and  $f_{max}$  is the maximum test frequency (Hz). Thus, it can be seen from Equation (17) that increasing values of  $C$ ,  $R_s$ , or  $R_p$  dictate that a lower  $f_{max}$  is required to accurately obtain  $R_p + R_s$  on the low-frequency plateau as  $Z_{\omega \rightarrow 0}$  (Figure 4). Capacitances may become larger than that expected for the  $C_{dl}$  when adsorption  $C_a$  are present. Such a  $C_a$  may be caused by an adsorbed intermediate with some fractional monolayer coverage. Corrosion of steel in concrete can complicate LPR measurements owing to very large apparent capacitances that actually may represent the finite diffusional impedance associated with mass transport control of the oxygen reduction reaction.<sup>57</sup> One way that  $R_p$  may be increased is by passivity. Another is by diffusion-controlled corrosion such that  $R_p = R_{ct} + R_D$ . A 1-mHz frequency typically is chosen as a reasonable initial choice of  $f_{max}$ , but it is obvious from Equation (17) that either lower or higher frequencies may be required depending upon the exact values of  $R_s$ ,  $R_p$ , and  $C$ . Since the magnitudes of  $C$ ,  $R_s$ , and  $R_p$  are not known explicitly, a priori prudence dictates that  $f_{max}$  be selected as one tenth of the estimated  $f_{bp}$ . Mansfeld and Kendig proposed that  $f_{max}$  determined from the impedance method defines the maximum voltage scan rate ( $v_{max}$ ) for the potentiodynamic method.<sup>43</sup> This derivation is based on the assumption that the  $v_{max}$  should not exceed the maximum rate of change of voltage with time during the sinusoidal voltage excitation at  $f_{max}$ .

$$v_{max} = \frac{\pi \Delta E_{pp} f_{max}}{10} \quad (18)$$

Here,  $\Delta E_{pp}$  is the peak-to-peak voltage excitation. Therefore,  $v_{max}$  is 0.16 mV/s assuming a 10-mV peak-to-peak amplitude for the equivalent circuit shown in Figure 3 with  $R_p = 1,000 \Omega$ ,  $R_s = 10 \Omega$ , and  $C = 1,000 \mu F$ . If  $\Delta E$  is  $\pm 5$  mV, then the time required for one complete cyclic voltammogram at such a potential sweep rate is 125 s. However, for a slowly corroding electrode with the  $R_s + R_p = 10,010 \Omega$ ,  $v_{max}$  becomes 0.0157 mV/s and the time required is 1.250 s. Similarly, a frequency above the high-frequency breakpoint ( $f_{hf}$ ) must be applied to obtain  $R_s$ . Typically,  $f_{app}$  must be in the KHz range to determine accurately  $R_s$ :

$$f_{hf} \geq \frac{1}{2\pi C R_s} \quad (19)$$

In separate but parallel efforts, Gabrielli,<sup>53</sup> Macdonald,<sup>52</sup> and Townley<sup>54</sup> each discussed the appropriate choice of voltage scan rates for accurate  $R_p$  determination from small amplitude cyclic voltammograms. Each investigator considered a

simple equivalent circuit (Figure 3[a]). Macdonald and Townley derived the current response of the standard three-element electrical equivalent circuit to describe an electrochemical interface (Figure 3[a]) to a small amplitude triangular voltage excitation (e.g., a potential sweep at fixed scan rate with a reverse sweep at some peak potential). The  $E-i_{app}$  response of this circuit to the triangular voltage excitation was shown to be a complex function of circuit elements,  $\Delta E_{pp}$ , and the voltage sweep rate. The relationships between the various  $\Delta E/\Delta i_{app}$  slopes ( $R$ ) and scan rate were determined. Macdonald characterized the  $E-i_{app}$  response by the diagonal resistance associated with  $i_{app}$  at the peak potentials,  $R_d$ . The apparent resistance ( $R_{app}$ ) determined from the tangent to the  $E-i_{app}$  curve at the end of the upward sweep before the downward sweep (and vice versa),  $R_{app}$ , and the hysteresis current. Townley obtained  $R_{meas}$ , which is similar to the tangent resistance,  $R_{app}$ :

$$\frac{1}{R_d} = \frac{1}{R_s + R_p} + \left( \frac{2R_p^2 C}{\Delta E (R_s + R_p)} \right) \left( \frac{e^{a\Delta E_{pp}/vb} - 1}{e^{a\Delta E_{pp}/vb} + 1} \right) \quad (20)$$

$$\frac{1}{R_{app}} = \frac{1}{R_s + R_p} + \left( \frac{2R_p}{R_s(R_s + R_p)} \right) \left( \frac{1}{1 + e^{a\Delta E_{pp}/vb}} \right) \quad (21)$$

$$\frac{1}{R_{meas}} = \frac{1}{R_s + R_p} + \left( \frac{R_p}{R_s(R_s + R_p)} \right) e^{-t/\tau} \quad (22)$$

In these equations,  $a = R_s + R_p$ ,  $b = R_s R_p C$ ,  $t$  is time,  $v$  is sweep rate, and  $\tau = 1/R_s C + 1/R_p C$ . Time ( $t$ ) in Equation (22) can be equated to the sweep rate since  $t = \Delta E_{pp}/v$ . Therefore, all three equations include a term that is independent of the voltage scan rate and a second transient term that depends on voltage scan rate or time relative to the RC time constant of the equivalent circuit representing the electrochemical interface. The scan rate dependent term becomes negligible at low scan rates. These analyses predict an increase in current hysteresis and deviation of  $R_d$  and  $R_{meas}$  from  $R_p + R_s$  at high scan rates, as shown in the theoretical cyclic  $E-i_{app}$  data of Figure 9(a). Figure 9(b) shows actual experimental results from a Cu-Ni alloy in flowing seawater. A plot of experimental  $1/R_d$  and  $1/R_{app}$  data vs scan rate is shown in Figure 9(c) for the Cu-Ni system. Macdonald and Townley deduced (Equations [21] and [22]) that it is theoretically possible in the ideal case to determine  $R_p + R_s$  from the tangent to the  $E-i_{app}$  curve at the end of the forward and reverse sweeps at much higher scan rates than predicted by Equations (17) and (18). The ideal

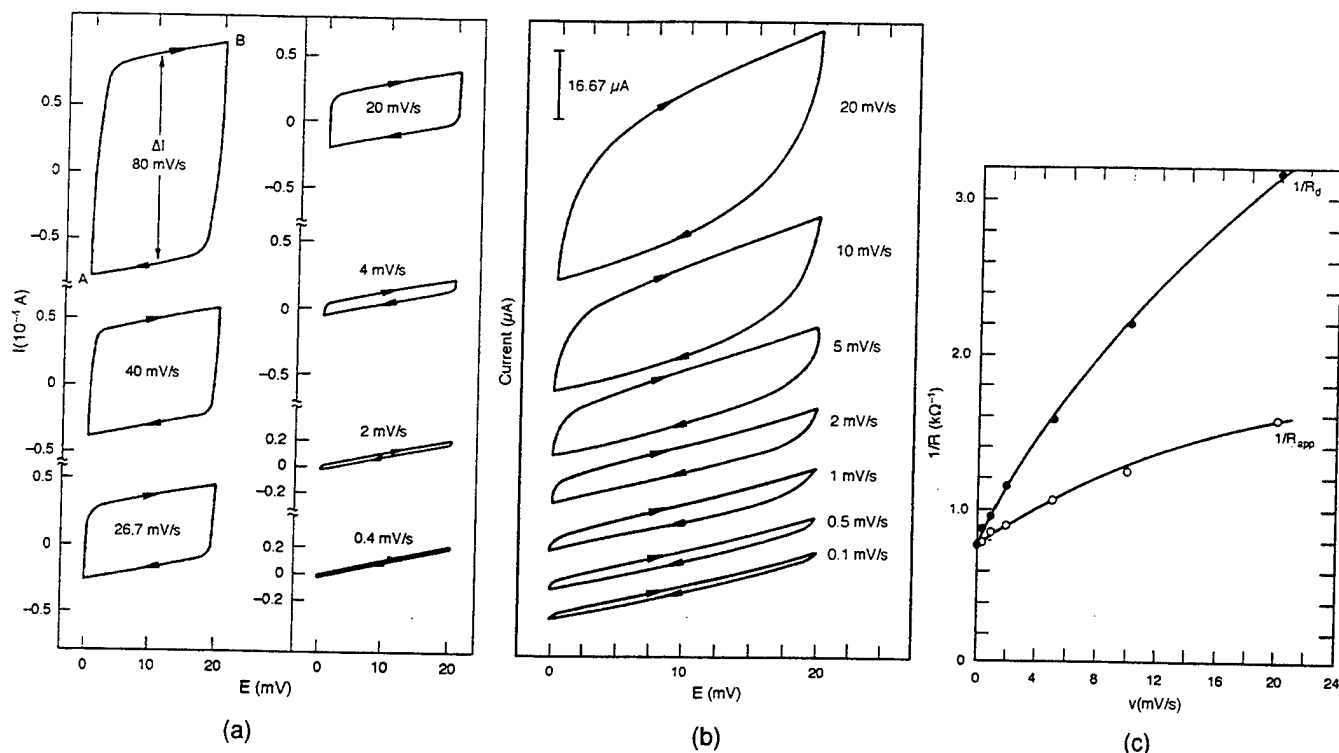


**FIGURE 9.** (a) Small amplitude cyclic voltammograms depicting the theoretical  $E-i_{app}$  response for the electrical equivalent circuit of Figure 3(a) with  $R_p = 1,000 \Omega$ ,  $C_{dl} = 1,000 \mu F$ , and  $R_s = 10 \Omega$  when triangle voltage excitation waveform is applied to a corroding interface at the various scan rates indicated. All results are for the circuit parameters listed above. (b) Experimental small amplitude cyclic voltammograms for 90:10 Cu-Ni in flowing seawater showing effect of voltage scan rate. (c) Reciprocal values of  $R_d$  and  $R_{app}$  vs scan rate obtained from experimental  $E-i_{app}$  data for 90:10 Cu-Ni in seawater. (D.D. Macdonald, *J. Electrochem. Soc.* 125 (1978): p. 1,443. Reproduced by permission of The Electrochemical Society, Inc.)

scan rate maxima can be seen in Figures 10(a) and (b) for the same circuit parameters as examined above (i.e.,  $R_s = 10 \Omega$ ,  $R_p = 1,000 \Omega$ , and  $C = 10^{-3} F$ ). Specifically, it is shown that  $1/R_{meas}$  and  $1/R_{app}$  approach the values  $1/(R_s + R_p)$  at scan rates as high as 100 mV/s when the slope of the  $E-i_{app}$  plot is carefully taken at the very end of the forward or reverse voltage scan just before reversal. However, accurate determination of  $1/(R_s + R_p)$  from experimental  $1/R_d$  values still requires a scan rate  $< 1$  mV/s, which is in agreement with the predictions from Equations (17) and (18).

The equivalence of  $R_{app}$  to  $(R_s + R_p)$  at fast scan rate must be treated with precaution in real corroding systems. Such an equivalence is only true for ideal, fast charge-transfer-controlled corrosion processes and ideal finite  $C_{dl}$  (e.g., when  $R_p = R_{ct}$ ). The presence of mass transport control or an adsorption  $C_s$  caused by formation of an adsorbed intermediate that participates in the corrosion process may complicate the results and the ability to use faster scan rates. Roles of adsorbed intermediates and mass transport in corrosion may not be accounted for properly at very fast scan rates because the surface coverage and diffusional boundary layer does not have time to react fully and adjust to a very fast

change in voltage.  $R_{ct}$  may be determined instead of  $R_p$  at the DC limit if the scan rate is so fast so as to freeze in the coverage (Figure 3[c]). Unfortunately, a sufficiently fast scan rate that "freezes-in" an intermediate coverage also may result in large capacitive currents that could result in  $R_d$  values far below  $R_p$ . Moreover, as the scan rate or frequency is lowered, the effects of an adsorbed intermediate that gives rise to an adsorption  $C_s$  and dependency of  $R_p$  on the sum of  $R_{ct}$  and the parallel impedance of  $C_s || R_f$  become factors in the resistance measured (Figure 3[c]). Indeed, Macdonald observed that an accurate value of  $R_s + R_p$  was, in fact, not obtained from  $R_{app}$  or  $R_d$  determined at fast scan rates for a corroding Cu-Ni alloy in flowing seawater (Figures 9[b] and [c]).<sup>52</sup> The experimental case of Cu-Ni in seawater shows that a much lower scan rate is required despite the more optimistic predictions of Equations (20) through (22) (Figures 10[a] and [b]). In contrast, a model like that of Figure 3(a) for an ideal  $R_p C$  interface, where  $R_p = R_{ct}$ , suggests that 4 mV/s to 20 mV/s scan rates would be more than slow enough to obtain an  $R_{app}$  value that approaches  $R_p$ . Experimentally, this is not the case in the Cu-Ni system since corrosion rate would be overestimated from such an assumption. In this system, the  $O_2$  reduction reaction is likely at

least partially mass-transport controlled at the  $E_{\text{corr}}$  of the Cu-Ni alloy and adsorbed oxidized Cu intermediate species also control the overall dissolution process.

Regarding measurement speed, Jones and Greene proposed that a current step method was attractive because of measurement speed and ability to contend with  $E_{\text{corr}}$  drift during the time taken to conduct the measurement.<sup>58</sup> For negligible  $R_s$ , it has been shown the potential transient during a current step is given by:

$$E_{\text{app}} = E_{\text{corr}} + i_{\text{app}} R_p \left( 1 - \exp^{-t/R_p C} \right) \quad (23)$$

When  $t \geq 4 R_p C$ ,  $E_{\text{app}}$  reaches 98% of the value achieved at infinite time. Therefore, the polarization resistance condition is reached when  $t \geq 4 R_p C$ , and Equation (23) reduces to  $\Delta E / i_{\text{app}} = R_p$ . The time required to reach this condition is  $\sim 4$  s for  $R_p = 1,000 \Omega$ ,  $R_s = 10 \Omega$ , and  $C = 1,000 \mu\text{F}$ . However, the time required for a slowly corroding electrode with  $R_p = 10,000 \Omega$  is  $\sim 40$  s. Thus, in comparison to polarization scans using the voltage scan rates predicted from Equation (18), the time required for a single current step to approach steady state is much less than the time required to complete a low-amplitude cyclic voltammogram given exactly the same electrical equivalent circuit parameters. It also has been argued that the measurement of overvoltages at selected times after a series of small current steps produces  $\Delta E$  vs  $i_{\text{app}}$  plots that develop linear slopes approximating the steady-state conditions after incomplete, short periods of decay.<sup>58</sup>

Finally, short time, fast scan rate, or high  $f_{\text{max}}$  concerns equally plague time as well as frequency domain methods for obtaining  $R_p$ , since in the time domain measurement, the triangle waveform is simply the Fourier synthesis of a series of sinusoidal signal functions. However, voltage sweep, potential step, and impedance methods should all yield the same value of  $R_p$  when all the scan rate and AC frequency precautions discussed above are taken into consideration such that the low-frequency plateau in  $|Z(\omega)|$  data is obtained and this data represents  $R_p + R_s$ . This has been demonstrated by Syrett in a study that produced  $R_p$  values that were independent of voltage excitation waveform.<sup>59</sup>

#### Use of $R_{\text{ct}}$ vs $R_p$ When the Adsorbed Intermediate Surface Coverages Affect Anodic and/or Cathodic Reaction Rates

Some complexities remain concerning whether to use  $R_{\text{ct}}$  at intermediate frequencies instead of  $R_p$  at the DC limit when attempting to conduct corrosion rate determinations in the presence of adsorbed intermediate surface coverages that affect anodic and/or cathodic reaction rates. To address this issue, it is

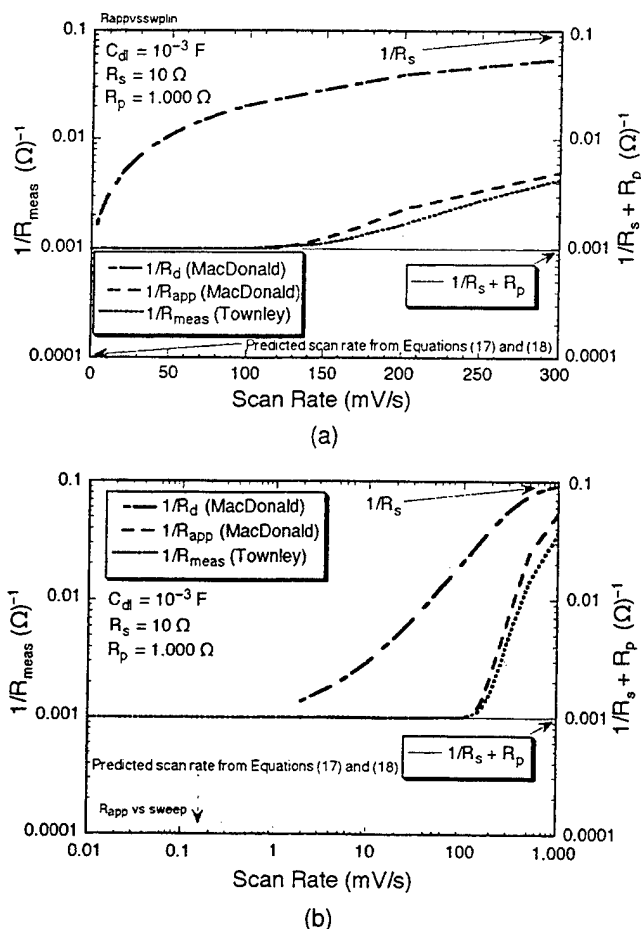


**FIGURE 10.** Relationship between measured  $R_{\text{app}}$ ,  $R_d$ , and  $R_{\text{meas}}$  and scan rate using Equations (20) through (22) for the circuit model of Figure 3(a) with  $R_p = 1,000 \Omega$ ,  $C_d = 1,000 \mu\text{F}$ , and  $R_s = 10 \Omega$ . The impedance of the system at the limit of zero scan rate is  $R_s + R_p$ . The impedance of the system at infinite scan rate is  $R_s$ . Measured  $R_{\text{app}}$ ,  $R_d$ , and  $R_{\text{meas}}$  values lie in between these limits depending on scan rate: (a) linear scale and (b) semilogarithmic scale. The predicted  $v_{\text{max}}$  from Equations (17) and (18) is indicated.

necessary to clarify the difference between  $R_{\text{ct}}$  and  $R_p$ . Recall the definition of  $R_p$  given by  $(\partial E / \partial i_{\text{app}})_{t=\infty, \Delta E=0}$ . To define  $R_{\text{ct}}$ , consider a derivation of the slope of the  $E$ - $i_{\text{app}}$  data from a cyclic voltammogram conducted near  $E_{\text{corr}}$  following the derivation of Epelboin.<sup>60-61</sup>  $i_{\text{app}}$  is the difference between the anodic and cathodic half-cell currents:

$$i_{\text{app}} = i_a - i_c \quad (24)$$

where the subscripts a and c represent the anodic and cathodic half-cell reaction rates.  $R_p (\Omega)$  is given in terms of  $i_a$  and  $i_c$  as:

$$\frac{1}{R_p} = \left( \frac{\partial i_{\text{app}}}{\partial E} \right)_{t=\infty, \Delta E=0} = \frac{\partial i_a}{\partial E} - \frac{\partial i_c}{\partial E} \quad (25)$$

When the low-overpotential linear approximation is valid at small values of  $\Delta E$ ,  $\partial I_a/\partial E$ , and  $\partial I_c/\partial E = 2.3I_{(a)corr}/\beta_a$  and  $-2.3I_{(c)corr}/\beta_c$ , respectively. Here,  $I_{(a)corr}$  and  $I_{(c)corr}$  describe the anodic and cathodic currents at the corrosion potential. At  $E_{corr}$ , these equal  $I_{corr}$ , and  $\beta_a$  and  $\beta_c$  are Tafel slopes for the anodic and cathodic reactions.

$$\frac{1}{R_p} = \frac{1}{R_{ct}} = \frac{\partial I_{app}}{\partial E} = 2.3I_{corr} \left( \frac{1}{\beta_a} + \frac{1}{\beta_c} \right) \quad (26)$$

A complexity arises in taking the derivatives  $\partial I_a/\partial E$  and  $\partial I_c/\partial E$  if a corrosion reaction is considered that depends upon the surface coverage ( $\theta$ ) of an intermediate that participates in the anodic dissolution or cathodic reduction reactions. Here, either the overall anodic or cathodic reaction or both occur on only a fraction  $\theta$  of the total electrode surface area ( $A$ ). An oxidized intermediate is typical of corrosion processes that involve multiple oxidation or electrochemical reaction steps that must be completed sequentially to describe the overall reaction rate. The reaction only can proceed on the fraction of surface area containing the required intermediate. Example of intermediates during active metallic dissolution include  $Fe/Fe(OH)/Fe(OH)^+/Fe^{2+}$  and  $Ti(OH)^-/Ti(OH)/Ti(OH)^+/Ti(OH)^{2+}/Ti(OH)^{3+}/Ti^{3+}$ ,<sup>62-63</sup> although no Tafel  $E\text{-}\log(i_a)$  region is observed in the case of the latter. In these cases, the overall corrosion rate may depend upon the coverage of the anodic intermediate  $\theta_a$ , depending upon the exact rate-determining step. Similarly, a cathodic reaction such hydrogen evolution (HER) may depend upon the coverage of bare sites, special sites, or for the electrochemical desorption HER mechanism by sites already covered with adsorbed hydrogen ( $\theta_h$ ). Depending on the HER mechanism, the rate may increase or decrease with coverage. Often, these coverages are potential dependent. The reaction rate per fractional area is then  $i_a = I_a/\theta_a$  and  $i_c = I_c/\theta_c$  assuming unity electrode area ( $A$ ).  $R_p$  will depend on two terms that yield the overall slope  $\partial I_{app}/\partial E$  at fixed coverage and two terms that are dependent on the variation in the coverages with potential:

$$\frac{1}{R_p} = \frac{\partial I_{app}}{\partial E} = \theta_a \left( \frac{\partial i_a}{\partial E} \right) - \theta_c \left( \frac{\partial i_c}{\partial E} \right) + i_a \left( \frac{\partial \theta_a}{\partial E} \right) - i_c \left( \frac{\partial \theta_c}{\partial E} \right) \quad (27)$$

The first two right-hand terms equal  $R_{ct}$  in this simple analysis where charge transfer describes simple interface charge-transfer control occurring quickly (subject to charging of the  $C_{dl}$ ) at fixed coverages  $\theta_a$  and  $\theta_c$ . The dependency of  $R_p$  on reaction intermediate coverage occurs when the third and fourth terms apply. The third and fourth terms can be ignored under two conditions. In either case,  $R_p$

then equals  $R_{ct}$  given by the first two terms. The first condition is the simple ideal case where the coverages are fixed at a value equal to the coverage present at  $E_{corr}$  or there is no coverage involved and reactions proceed over the total bare area of the electrode. The second case is at some high voltage scan rate or AC frequency, where the applied potential ( $E$ ) changes too quickly to allow the coverage to be modified during the potential sweep or sinusoidal voltage excitation (the potential sweep must not be so fast so as to produce appreciable  $C_{dl}$  currents). At fast scan rate, the coverages present at  $E_{corr}$  are effectively "frozen in" and the third and fourth terms equal zero. The current shorts through the  $C_{dl}$  created by such a coverage (Figure 3[c]).<sup>22</sup> If ideal charge-transfer control is assumed at fixed coverages,  $i_a$  and  $i_c$  respond almost instantaneously to an applied potential through the following relationships:

$$i_a = i_{(a)corr} \exp \left( \frac{2.3(E - E_{corr})}{\beta_{a\theta(a)corr}} \right) \quad (28)$$

$$i_c = i_{(c)corr} \exp \left( \frac{-2.3(E - E_{corr})}{\beta_{c\theta(c)corr}} \right) \quad (29)$$

where  $\beta_{a\theta(a)corr}$  and  $\beta_{c\theta(c)corr}$  give the Tafel slopes at a fixed coverage equal to the coverages present at  $E_{corr}$ . Taking the derivatives  $\partial i_a/\partial E$  and  $\partial i_c/\partial E$  using the small overpotential approximation yields  $i_a = 2.3i_{(a)corr}/\beta_{a\theta(a)corr}$  and  $i_c = -2.3i_{(c)corr}/\beta_{c\theta(c)corr}$ . Making these substitutions, recognizing that  $i_{corr} = i_{a(corr)} = i_{c(corr)}$ , and rearranging yields the Stern-Geary equation in a slightly different form:

$$\frac{1}{R_p} = \frac{\partial I_{app}}{\partial E} = \theta_{(a)corr} \left( \frac{2.3i_{(a)corr}}{\beta_a} \right) + \theta_{(c)corr} \left( \frac{2.3i_{(c)corr}}{\beta_c} \right) \quad (30)$$

Recognizing that  $i_{(a)corr} = I_{a(corr)}/\theta_{a(corr)}$ ,  $i_{(c)corr} = I_{c(corr)}/\theta_{c(corr)}$ ,  $I_{corr} = I_{a(corr)} = I_{c(corr)}$ , and by making these substitutions, a familiar linear relation is obtained with the simple distinction that  $\beta_{a\theta(a)corr}$  and  $\beta_{c\theta(c)corr}$  define the Tafel slopes for the coverages present at the  $E_{corr}$ :

$$\frac{\partial I_{app}}{\partial E} = \frac{1}{R_p} = 2.3I_{corr} \left( \frac{1}{\beta_{a\theta(a)corr}} + \frac{1}{\beta_{c\theta(c)corr}} \right) \quad (31)$$

Thus,  $R_{ct} = R_p$  in the simple cases where ideally fast charge transfer occurs and the coverage is fixed or when there is no coverage dependency.

A more complicated result is obtained at slow scan rate or low AC frequency when the coverage can

change with potential. Again, the linear approximation is enabled as  $\Delta E$  becomes small:

$$\frac{\partial i_{app}}{\partial E} = \frac{1}{R_p} = 2.3I_{corr} \left( \frac{1}{\beta_{a\theta(a)corr}} + \frac{1}{\beta_{c\theta(c)corr}} \right) + I_{corr} \left( \frac{1}{\theta_a} \frac{\partial \theta_a}{\partial E} - \frac{1}{\theta_c} \frac{\partial \theta_c}{\partial E} \right) \quad (32)$$

The first right-hand term is  $1/R_{ct}$  (e.g., the instantaneous portion related to the faradaic current) and the whole right-hand expression gives  $1/R_p$ .<sup>60-61</sup> The  $1/(\theta \partial \theta / \partial E)$  terms are typical nonzero contributions at  $E_{corr}$  when there are potential dependent coverages that are nonzero near  $E_{corr}$ . There is absolutely no reason that the coverages should be zero at  $E_{corr}$  since the corrosion potential is an "open-circuit" potential established at a specific potential somewhere between the respective reversible electrode potentials of the cathodic and anodic half-cell reactions. Specifically,  $E_{corr}$  is established at the potential where  $i_a \theta_a = i_c \theta_c$ . Therefore, it is clear that  $R_p$  may be  $>$  or  $<$   $R_{ct}$ , depending whether the partial derivatives  $\partial \theta_a / \partial E$  and  $\partial \theta_c / \partial E$  are positive or negative quantities as the applied potential is swept in forward and reverse directions. This can account for the common observation that  $R_p > R_{ct}$  in the case of so-called pseudo-capacitive behavior,<sup>22</sup> as shown in the circuit model of Figure 3(c) containing an adsorption pseudo-capacitance. Moreover, it is possible that  $R_p < R_{ct}$ ,<sup>64</sup> as in the case of so-called pseudo-inductive behavior where an inductance is observed at low frequency (Figure 6[b]<sup>63</sup>). The condition,  $R_p > R_{ct}$ , has been seen by subtracting the  $C_{dl}$  from the faraday impedance data.<sup>65</sup> Thus, Equation (32) supports the view that  $R_p$  at the zero frequency limit can be  $<$  or  $>$   $R_{ct}$ , depending on how the coverages that factor into the anodic and cathodic reaction rates change with potential. The differences between  $R_p$  and  $R_{ct}$  are observed sometime to decrease when the magnitude of the voltage perturbation is reduced such that the coverage is negligibly altered.<sup>64</sup> An alternative view of the effect of voltage perturbation in the case of inhibitors is that the inhibitor is desorbed irreversibly by potential scanning above  $E_{corr}$  such that the corrosion rate is increased.<sup>64</sup> However, such phenomena also might be understood using Equation (32) since  $R_p$  would be expected to be similar to  $R_{ct}$  when the voltage perturbation is smaller. Also, physically unrealistic parameters such as the electrical inductor do not have to be invoked. It is tempting to eliminate the right-hand second term by conducting experiments at fast scan rate to freeze-in or fix the coverages.<sup>66</sup> However, the lower impedance of the  $C_{dl}$  and adsorption  $C_a$  at high frequency may complicate measurements by switching capacitive currents into

the  $i_{app}$  measurement. Furthermore, it also must be recognized that the Tafel slopes presented in the first right-hand term of Equation (32) still would need to be the "iso-coverage" Tafel slopes, ideally obtained by experiments where the coverages were fixed at their values present at  $E_{corr}$ . Unfortunately,  $\beta_a$  and  $\beta_c$  rarely are obtained under iso-coverage conditions in practical corrosion situations.<sup>67-71</sup> Iso-coverage Tafel parameters have been produced by correction of HER reaction rate data by exploiting hydrogen absorption and permeation through iron foils to control coverage.<sup>67</sup> Here, foil thickness decreased as current density is increased to change permeation flux such that surface coverage is held constant over a range of reaction rates. Consequently, determination of corrosion rates in the presence of adsorbed intermediates is not a simple matter of obtaining  $R_{ct}$  at high frequency or scan rate, where  $\partial \theta_a / \partial E$  equals zero because  $\theta$  might be frozen during such rapid potential changes. As shown here, another source of errors is the values of  $\beta_a$  and  $\beta_c$  obtained in slow scans at high overpotential because this mixes  $\Delta E$ - $i_{app}$  data where the coverage is frozen-in (e.g.,  $R_{ct}$ ) with  $E$ - $\log(i_{app})$  Tafel data (e.g.,  $\beta_a$  and  $\beta_c$ ) where potential dependent coverages may differ from those at  $E_{corr}$ . An additional problem is that there is now another reason why  $\partial i / \partial E$  should not be linear even as  $\Delta E$  approaches zero if the coverage changes significantly with potential over the same potential range. Moreover, there is no reason why  $E$ - $\log(i_{app})$  data obtained over a large potential range should be linear on a semi-log plot when the coverage changes with potential. Nonstraight Tafel data often are observed.<sup>68,71</sup> Theoretical  $E$ - $\log i_{app}$  data with changing intermediate coverage are shown in Figure 11. The data is presented for charge-transfer-controlled oxidation kinetics over a fraction of the surface area given by coverage  $\theta_a$ . The  $E$ - $\log(i_{app})$  curve was created under the following conditions. Anodic coverage ( $\theta_a$ ) is commonly an exponential function of potential as governed by the following expression assuming a Langmuir isotherm. This expression yields a nonzero coverage at  $E = E_{corr}$ :

$$\left( \frac{\theta_a}{1 + \theta_a} \right) = k \exp \left( \frac{F(E - E_{rev})}{RT} \right) \quad (33)$$

As an example, a hypothetical  $E$ - $i_{app}$  relationship is considered for corrosion involving an overall oxidation half-cell reaction ( $M + OH^- \rightarrow MOH^+ + 2e^-$ ) that depends on the coverage  $\theta_a$  as described in Equation (33) for the adsorbed intermediate  $MOH$  that participates in a series of single electron transfer reactions. The cathodic reaction in this example is assumed to be the fast-discharge slow electrochemical desorption hydrogen evolution reaction. This HER reaction rate

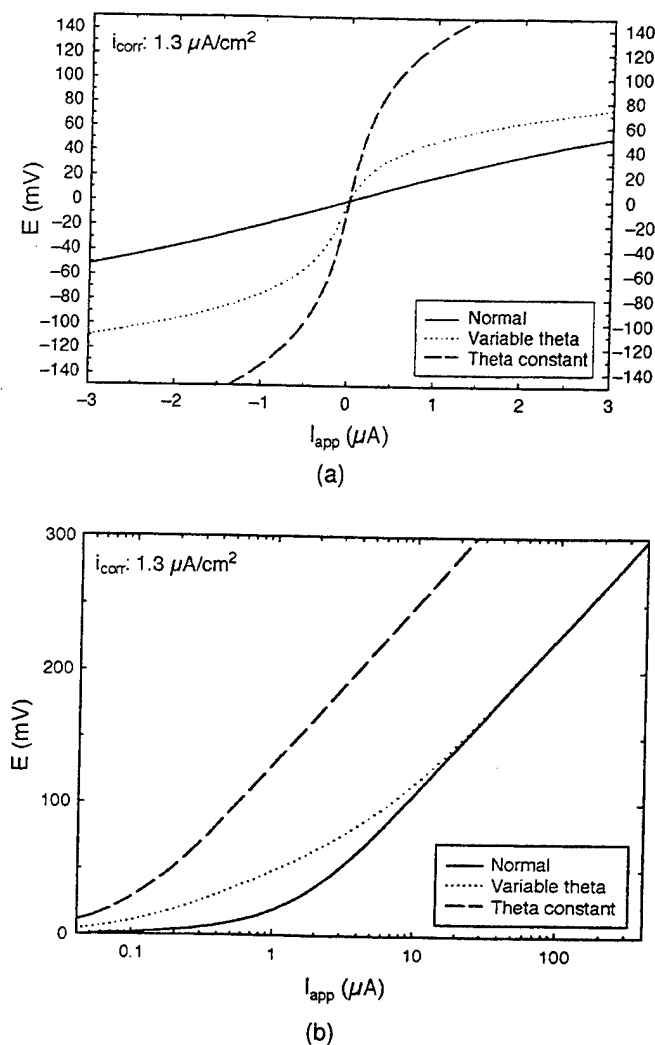


**FIGURE 11.** (a) Theoretical  $E\text{-}\log(i_{app})$  plot and (b) corresponding  $E\text{-}i_{app}$  plot for reactions rates that depend upon film coverage based on Equation (34). The anodic coverage is an exponential function of potential according to Equation (33) with  $k = 0.01$  in the case of the dotted curve. The dashed curve is constructed at fixed coverages ( $\theta_a [E = E_{corr}] = 0.068$ ,  $\theta_{HER} [E = E_{corr}] = 0.06$ ) equal to the coverages present at OCP (0 V). The solid curve assumes no role of coverage such that the reaction proceeds over the entire electrode area of  $1 \text{ cm}^2$ . The open-circuit potential was selected arbitrarily to be 0 mV, and the corrosion rate is  $1.3 \mu A/cm^2$  per unit area covered with the intermediate film MOH.  $\beta_a = \beta_c = 120 \text{ mV}$  in all calculations.

depends on the coverage of adsorbed hydrogen. This situation is similar to the corrosion mechanism of iron in acid where either the catalyzed mechanism of Huesler<sup>72-73</sup> or the intermediate mechanism of Bockris<sup>62</sup> involves an anodic half-cell reaction whose rate depends on the coverage of the adsorbed complex  $FeOH_{ads}$ . In the present example, the coverage of the hypothetical activated complex  $MOH_{ads}$  is a factor determining the overall anodic half-cell reaction rate. Consider the case where the coverage changes from near zero to near one in the vicinity of  $E_{corr}$ , such that the assumption of a fixed Tafel slope is unrealistic.

even though it often is assumed to be constant in the literature. In conventional textbook examples, the coverage is assumed to either remain near zero or near unity and a fixed Tafel slope can be developed and used as a reaction diagnostic. For instance, the Tafel slope often is taken to be constant at  $\beta_a = 2.3RT/[(1 + 2\alpha_a)F]$ , assuming a low coverage ( $\theta_a$ ) at all potentials when the  $FeOH_{ads}$  coverage is an exponential function of potential. In this case, the Tafel slope approaches 0.029 V when the symmetry factor ( $\alpha_a$ ) is 0.5 in agreement with experimental data. However, the assumption has been made that  $\theta_a$  remains low over the entire potential range of the experiment. This is not the case in the hypothetical example used here. If coverages change considerably in the potential range studied, the more general expression should be used where  $\theta_a$  is determined from Equation (33):

$$I_{app} = i_{corr} A \left( \theta_a \exp\left(\frac{\alpha_a F (E - E_{corr})}{RT}\right) - \theta_c \exp\left(\frac{-\alpha_c F (E - E_{corr})}{RT}\right) \right) \quad (34)$$

Here, the anodic and cathodic reactions increase with the coverages of adsorbed MOH and H species, the coverages change from near zero to near unity over the potential range near  $E_{corr}$ , and the Langmuir isotherm is assumed. In this case, the condition of equality at  $E_{corr}$  is that  $i_{a(corr)} A \theta_{a(corr)} = i_{c(corr)} A \theta_{c(corr)}$ , where  $A$  is the total electrode area. Under these simple assumptions, the resulting  $E\text{-}\log(i_{app})$  data exhibits a continuously varying slope  $\partial E / \partial \log(i_{app})$  that does not yield a single value for  $\beta_a$  until  $\theta_a$  reaches one (Figure 11). Therefore, to determine the corrosion rate in a rigorously correct manner in the case of adsorbed intermediate coverages that change near  $E_{corr}$ ,  $R_{ct}$  obtained from suitably fast scans only can be used only if  $\beta_a$  and  $\beta_c$  values also are representative of the iso-coverage conditions existing at  $E_{corr}$ . In other words, Tafel slopes need to be determined at a relevant frozen-in or fixed coverage. This could be achieved by obtaining  $\beta_a$  and  $\beta_c$  from fitting  $E\text{-}i_{app}$  data near  $E_{corr}$  under the premise that coverage changes only slightly at low  $\Delta E$ ; producing iso-coverage Tafel data from  $E\text{-}\log(i_{app})$  data fixed at the coverage present at  $E_{corr}$ ; or determining Tafel slopes from  $E\text{-}\log(i_{app})$  data at fast scan rate to freeze-in  $\theta_a$  and  $\theta_c$ , assuming negligible capacitive current. Unfortunately, the merits of these various methods toward producing accurate results compared to one another remain relatively untested. Obviously, numerous other situations can be envisioned that have not been covered here, such as inhibiting species desorbing as a function of potential, coverage governed by Frumkin or Temkin isotherms, reaction mechanisms that change near  $E_{corr}$ , or multiple-step, single-

electron-transfer reactions that have other coverage dependencies, etc. The purpose of the present example was only to illustrate the role of changing coverage in creating a difference between  $R_{ct}$  and  $R_p$  and in adding complexities to the determination of Tafel slopes.

$R_p$  still is often estimated from slow scans approaching the DC limit by taking a tangent to the nonlinear  $E-i_{app}$  data near  $E_{corr}$ . The Stern-Geary approximation still is utilized to estimate  $i_{corr}$  using an apparent B factor involving apparent Tafel slopes that are imprecise. Such data still often agrees with gravimetric mass loss and solution analysis data. Two reasons emerge. Although the terms  $1/\theta(\partial\theta/dE)$  in Equation (32) are often nonzero at  $E_{corr}$ , they often are small. Moreover, the weak dependence of corrosion rate on the parameter B in the Stern approximation permits imprecise estimates of Tafel slope to be tolerated in many cases. Of course,  $R_p$  values obtained at extremely low-frequency or scan rates should be used in the modified Stern equation in the case of total mass transport control of either the anodic or cathodic reaction (with an infinite Tafel slope for the mass-transport-controlled reaction) as well as in the case of passive dissolution. Use of the  $R_{ct}$  obtained at higher frequency or scan rate yields the value of corrosion rate that would be pertinent if both anodic and cathodic reactions were under instantaneous charge-transfer control.  $R_{ct}$  should be used in the Stern approximation if Tafel slopes under charge-transfer-controlled conditions are utilized.<sup>66</sup> In some cases, effects of inhibitor concentration on iron corrosion rate were best assessed using  $R_{ct}$  as opposed to  $R_p$ .<sup>66</sup>

### Effect of Solution Resistance

Another frequently encountered complication is the need to correct polarization data for errors that arise from the contribution of  $R_s$ .  $R_s$  contributes to a voltage error as well as a scan rate error.<sup>2</sup> Since the applied potential is increased by an ohmic voltage component, an apparent value of  $R_p$  is obtained, which overestimates  $R_p$  by an amount equal to  $R_s$ . Consequently, the corrosion rate is underestimated.

### Nonuniform Current and Potential Distributions to Polarization Resistance Probes

A dimensionless parameter known as the Wagner number is useful for qualitatively predicting whether a current distribution will be uniform or nonuniform.<sup>2,74-75</sup> This parameter helps to answer the question of which current distribution applies to the electrochemical cell: primary, secondary, or tertiary?

The Wagner parameter ( $W$ ) is the ratio of the kinetic resistance to the ohmic resistance. The  $W$  is the ratio of the true polarization slope given by the partial derivative,  $\partial E_{true}/\partial i_{app}$ , (evaluated at the overpotential of interest at constant pressure, tem-

perature, and concentration) divided by the characteristic length and the  $R_s$ .<sup>2,74</sup>

$$W = \left( \frac{\kappa}{L} \right) \left( \frac{\partial E}{\partial i} \right) \quad (35)$$

where  $\kappa$  (or  $1/\rho$ ) is the specific solution conductivity ( $\Omega\text{-cm}$ )<sup>-1</sup> and  $L$  is a characteristic length (cm), or the dimension of "irregularity." Its value marks the transition from the primary to the secondary current distribution. When the Wagner number is much less than 1, the ohmic component dominates and current and potential distributions are governed primarily by cell geometry. When it is much larger than 1, the kinetic component dominates and the resistance of the interface primarily governs the current flow from counter electrode to working electrode. In practice, the primary current distribution is said to exist when  $W < 0.1$ , and the secondary current distribution exists if  $W > 10^2$ . The partial derivative,  $\partial E/\partial i$ , can be taken from any expression describing the interfacial potential ( $E_{true}$ ) as a function of  $i_{app}$  or obtained as a  $R_p$  from experimental  $E$  vs  $i_{app}$  data. The partial derivative,  $\partial E/\partial i$ , has the units of  $\Omega\text{-cm}^2$ . The  $R_s$  expressed in the same units is given by  $(\kappa/L)$ . The resulting Wagner number in the low-overpotential region where the linear  $E-i$  approximation can be applied is:

$$W = \frac{R_p}{R_s} \quad (36)$$

Thus, the experimenter interested in estimating the current distribution "regime" pertinent to their polarization cell can estimate whether the primary or secondary current distribution applies from knowledge of  $R_p$  and  $R_s$ . The corrosion engineer can use this information in the following way. If the primary current distribution applies ( $W < 0.1$ ), then current distributions are likely to be very nonuniform unless an ideal cell geometry leading to a uniform primary current distribution is used. Otherwise, errors in polarization resistance and other kinetic parameters are then likely because the electrode area actually undergoing polarization differs from the total area. Low scan rate data at the zero frequency limit may yield the same apparent value of  $R_p + R_s$ , but the area required to compute a true  $R_p$  value is uncertain.

Errors in  $R_p$  from nonuniform primary or secondary current distributions have been documented.<sup>76</sup> Data presented in the literature (Figure 12) show examples of the extent of such errors.<sup>77</sup> Positioning of the reference electrode at the center, edge, and at infinity with respect to the disk-shaped working electrode altered the apparent polarization resistance value ( $R_{eff}$ ) by some amount relative to the true value

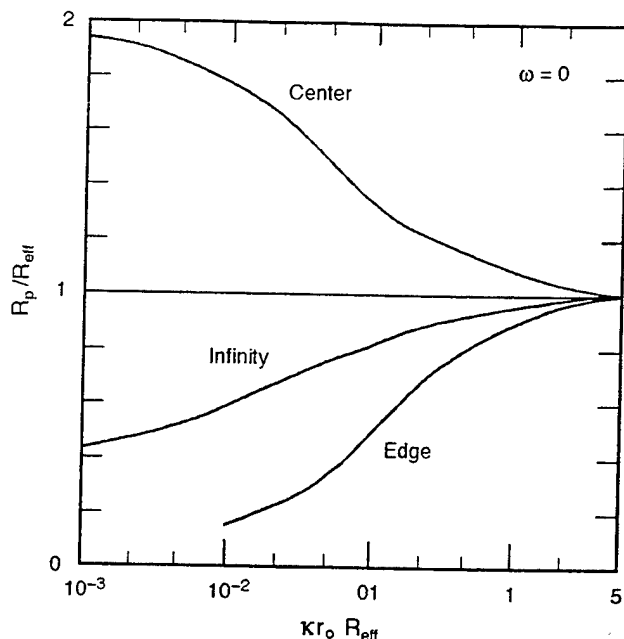


FIGURE 12. Relationship between the measured  $R_{eff}$  value and true  $R_p$  value at  $\omega = 0$  for nonuniform current distributions to a flush-mounted electrode. The error decreases with increasing Wagner number, which is equivalent to a decreasing error as  $R_{eff}$  and solution conductivity increase.<sup>77</sup>

given by  $R_p$ . Placement at the edge is typical of flush-mounted probes. The source of difference between  $R_p$  and  $R_{eff}$  with position lies in the fact that no single  $R_s$  value applies for all electrode positions. In other words, there is a nonuniform ohmic potential drop over the disk. There can be large errors depending on reference electrode position (center, infinity, edge), solution conductivity geometry, and  $R_p$ .<sup>73</sup> When solution conductivity ( $\kappa$ ) and  $R_{eff}$  are increased, the Wagner number becomes larger, indicating a more uniform current distribution and minimization of this source of error. Similarly, counter and reference electrode placement in low conductivity environments can alter  $R_s$  values and apparent  $R_{eff}$  values.<sup>78</sup>

## SUMMARY

The polarization resistance method, when performed properly, enables reliable determinations of instantaneous corrosion rates. Modern methods for obtaining  $R_p$  data such as the electrochemical impedance as well as statistical and spectral noise methods are now available. The  $R_{sn}(\omega)$  has been shown in the literature to be equivalent to the electrochemical impedance over the same frequency range for identical electrodes in a two-electrode cell. The  $R_{sn}(\omega)$  near the zero frequency limit is proportional to  $R_p$  if the impedance yields  $R_p$  over the same range of frequency. The statistical noise resistance taken from E-t and  $i_{app}$ -t data is typically equivalent to the cell impedance

at some frequency above zero. Traditional sources of error such as high excitation voltage amplitude, insufficiently slow scan rate, high AC frequency, inadequate polarization hold period, high solution resistance, presence of parallel reduction-oxidation reactions, and nonuniform current and potential distributions can confound accurate determination of corrosion rate. Lastly, the affects of potential-dependent adsorbed intermediate films that regulate the overall reaction rate and adsorption  $C_d$  on electrochemical reaction rates are discussed with emphasis on how they influence the measured interfacial resistance. The  $R_{ct}$  can be obtained if the coverage is unchanged by excitation voltage but it may be larger or smaller than  $R_p$ .

## ACKNOWLEDGMENTS

Financial support from the Air Force Office of Scientific Research (Major H.D. Long) and The Office of Naval Research (A.J. Sedriks) is acknowledged. Electrochemical Instrumentation and Software in the Center for Electrochemical Science and Engineering are supported by EG&G Instruments and Scribner Associates, Inc. C. Quarmby and R. Leggat assisted in manuscript preparation.

## REFERENCES

1. J.O'M. Bockris, A.K.N. Reddy, *Modern Electrochemistry 2* (New York, NY: Plenum Press, 1970).
2. E. Gileadi, *Electrode Kinetics for Chemists, Chemical Engineers, and Materials Scientists* (New York, NY: VCH Publishers, 1993).
3. D.A. Jones, *Principles and Prevention of Corrosion* (New York, NY: Macmillan Publishing, 1992).
4. M. Stern, R.M. Roth, *J. Electrochem. Soc.* 104 (1957): p. 390.
5. M. Stern, A.L. Geary, *J. Electrochem. Soc.* 105 (1958): p. 638.
6. M. Stern, A.L. Geary, *J. Electrochem. Soc.* 104 (1957): p. 56.
7. I. Epelboin, C. Gabrielli, M. Keddam, H. Takenouti, *Electrochemical Corrosion Testing*, STP 727, eds. F. Mansfeld, U. Bertocci (West Conshohocken, PA: ASTM, 1981), p. 150.
8. M. Stern, E.D. Weisert, "Experimental Observations on the Relation Between Polarization Resistance and Corrosion Rate," in *ASTM Proceedings*, vol. 59 (West Conshohocken, PA: ASTM, 1959), p. 1,280.
9. D 2776-79, 03.02, "Test Methods for Corrosivity of Water in the Absence of Heat Transfer (Electrical Methods)," *Annual Book of ASTM Standards* (West Conshohocken, PA: ASTM).
10. ASTM Standard G-59, "Standard Practice for Conducting Potentiodynamic Polarization Resistance Measurements," *Annual Book of Standards* (West Conshohocken, PA: ASTM).
11. F. Mansfeld, *Electrochemical Techniques for Corrosion*, ed. R. Baboian (Houston, TX: NACE, 1977), p. 18.
12. D.A. Jones, N.D. Greene, *Corrosion* 22 (1966): p. 198.
13. D.A. Jones, *Corrosion* 39 (1983): p. 444.
14. K.B. Oldham, F. Mansfeld, *Corros. Sci.* 13 (1973): p. 813.
15. F. Mansfeld, *J. Electrochem. Soc.* 120 (1973): p. 515.
16. D.D. MacDonald, M.C.H. McKubre, *Electrochemical Corrosion Testing*, STP 727, eds. F. Mansfeld, U. Bertocci (West Conshohocken, PA: ASTM, 1981), p. 110.
17. A.J. Bard, L.R. Faulkner, *Electrochemical Methods: Fundamentals and Applications* (New York, NY: John Wiley and Sons, 1980).
18. F. Mansfeld, *Corrosion* 36, 5 (1981): p. 301.
19. F. Mansfeld, M.W. Kendig, S. Tsai, *Corrosion* 38 (1982): p. 570.
20. ASTM G 106, vol. 03.02, "Practice for Verification of Algorithm and Equipment for Electrochemical Impedance Measurements," *Annual Book of ASTM Standards* (West Conshohocken, PA: ASTM).



21. D.R. Franceschetti, J.R. Macdonald, *Electroanal. Chem.* 101 (1979): p. 307.
22. S.R. Taylor, E. Gileadi, *Corrosion* 51 (1995): p. 664.
23. D.A. Eden, A.N. Rothwell, J.L. Dawson, "Electrochemical Noise for Detection of Susceptibility to Stress Corrosion Cracking," *CORROSION/91*, paper no. 444 (Houston, TX: NACE, 1991).
24. J.L. Dawson, ASTM STP 1277, "Electrochemical Noise Measurement for Corrosion Applications," eds. J. Kearns, J.R. Scully, P.R. Roberge, D.L. Reichert, J.L. Dawson (West Conshohocken, PA: ASTM, 1996), p. 3-35.
25. D.A. Eden, K. Hladky, D.G. John, J.L. Dawson, "Electrochemical Noise — Simultaneous Monitoring of Potential and Current Noise Signals from Corroding Electrodes," *CORROSION/86*, paper no. 274 (Houston, TX: NACE, 1986).
26. D.A. Eden, A.N. Rothwell, "Electrochemical Noise Data: Analysis Interpretation Presentation," *CORROSION/92*, paper no. 292 (Houston, TX: NACE, 1992).
27. A.N. Rothwell, D.A. Eden, "Electrochemical Noise Techniques for Determining Corrosion Rates and Mechanisms," *CORROSION/92*, paper no. 223 (Houston, TX: NACE, 1992).
28. U. Bertocci, ASTM STP 1277, "Electrochemical Noise Measurement for Corrosion Applications," eds. J. Kearns, J.R. Scully, P.R. Roberge, D.L. Reichert, J.L. Dawson (West Conshohocken, PA: ASTM, 1996), p. 39-58.
29. U. Bertocci, F. Huet, *Corrosion* 51 (1995): p. 131.
30. D.L. Reichert, ASTM STP 1277, "Electrochemical Noise Measurement for Corrosion Applications," eds. J. Kearns, J.R. Scully, P.R. Roberge, D.L. Reichert, J.L. Dawson (West Conshohocken, PA: ASTM, 1996), p. 79-89.
31. P.C. Searson, J.L. Dawson, *J. Electrochem. Soc.* 135, 8 (1988): p. 1908.
32. F. Mansfeld, H. Xiao, ASTM STP 1277, "Electrochemical Noise Measurement for Corrosion Applications," eds. J. Kearns, J.R. Scully, P.R. Roberge, D.L. Reichert, J.L. Dawson (West Conshohocken, PA: ASTM, 1996), p. 59-78.
33. G.P. Bierwagen, *J. Electrochem. Soc.* 141 (1994): p. L155.
34. F. Mansfeld, H. Xiao, *J. Electrochem. Soc.* 141 (1994): p. 1.402.
35. F. Huet, *J. Electrochem. Soc.* 142 (1995): p. 2.861.
36. J.F. Chen, W.F. Bogaerts, *Corros. Sci.* 37 (1995): p. 1.839.
37. H. Xiao, F. Mansfeld, *J. Electrochem. Soc.* 141 (1994): p. 2.332.
38. F. Mansfeld, H. Xiao, *J. Electrochem. Soc.* 140 (1993): p. 2.205.
39. F. Mansfeld, L.T. Han, C.C. Lee, *J. Electrochem. Soc.* 143 (1996): p. L286.
40. U. Bertocci, C. Gabrielli, F. Huet, M. Keddam, *J. Electrochem. Soc.* 144 (1997): p. 31.
41. U. Bertocci, C. Gabrielli, F. Huet, M. Keddam, *J. Electrochem. Soc.* 144 (1997): p. 37.
42. A. Bautista, F. Huet, *J. Electrochem. Soc.* 146 (1999): p. 1.730-1.736.
43. F. Mansfeld, M. Kendig, *Corrosion* 37, 9 (1981): p. 556.
44. R. Bandy, D.A. Jones, *Corrosion* 32 (1976): p. 126.
45. M.J. Danielson, *Corrosion* 36, 4 (1980): p. 174.
46. J.C. Reeve, G. Bech-Nielsen, *Corros. Sci.* 13 (1973): p. 351.
47. L.M. Callow, J.A. Richardson, J.L. Dawson, *Brit. Corros. J.* 11 (1976): p. 132.
48. F. Mansfeld, K.B. Oldham, *Corros. Sci.* 27 (1971): p. 434.
49. S. Barnartt, *Corros. Sci.* 9 (1969): p. 148.
50. R.L. Leroy, *Corrosion* 29 (1973): p. 272.
51. F. Mansfeld, *Corrosion* 29 (1973): p. 397.
52. D.D. MacDonald, *J. Electrochem. Soc.* 125 (1978): p. 1.443.
53. C. Gabrielli, M. Keddam, H. Takenouti, V. Kirk, F. Bourelle, *Electrochem. Acta* 24 (1979): p. 61.
54. D.W. Townley, *Corrosion* 47 (1991): p. 737.
55. D.D. MacDonald, *J. Electrochem. Soc.* 125 (1979): p. 1.977.
56. F. Mansfeld, M. Kendig, *Corrosion* 37 (1981): p. 545.
57. K. Videm, R. Myrdal, *Corrosion* 53 (1997): p. 734.
58. D.A. Jones, N.D. Greene, *Corrosion* 22 (1966): p. 198.
59. B. Syrett, D.D. MacDonald, *Corrosion* 35 (1979): p. 505.
60. I. Epelboin, M. Keddam, *J. Electrochem. Soc.* 117 (1970): p. 1.052-1.056.
61. I. Epelboin, M. Keddam, H. Takenouti, *J. Appl. Electrochem.* 2 (1972): p. 71-79.
62. J.O'M. Bockris, D. Drazic, A.R. Despic, *Electrochim. Acta* 4 (1961): p. 315.
63. E.J. Kelly, *J. Electrochem. Soc.* 126, 12 (1979): p. 2.064-2.075.
64. W.J. Lorenz, F. Mansfeld, *Corros. Sci.* 21, 9 (1981): p. 647-672.
65. H. Schweikert, W.J. Lorenz, H. Friedburg, *J. Electrochem. Soc.* 127 (1980): p. 1.693.
66. I. Epelboin, C. Gabrielli, M. Keddam, H. Takenouti, ASTM STP 727, "Electrochemical Corrosion Testing," eds. F. Mansfeld, U. Bertocci, (West Conshohocken, PA: ASTM, 1981), p. 150-166.
67. R.N. Iyer, H.W. Pickering, *J. Electrochem. Soc.* 137, 11 (1990): p. 3.512-3.514.
68. C. Cato, H.J. Grabke, B. Egert, G. Panzer, *Corros. Sci.* 24 (1984): p. 591.
69. E.G. Daff, K. Bohnenkamp, H.J. Engell, *Corros. Sci.* 19 (1979): p. 591.
70. R.N. Iyer, I. Takekeuchi, M. Zamanzadeh, H.W. Pickering, *Corrosion* 46 (1990): p. 460.
71. R.S. Lillard, J.R. Scully, *Corrosion* 52 (1996): p. 125.
72. K.E. Heusler, Habilitation Thesis, Univ. Of Stuttgart, 1966.
73. K.F. Bonhoeffer, K.E. Heusler, *Z. Phys., Chem., N.F.*, 8 (1956): p. 390.
74. J. Newman, *Electrochemical Systems* (Englewood Cliffs, NJ: Prentice Hall, Inc., 1973).
75. C. Wagner, *J. Electrochem. Soc.* 101 (1959): p. 225.
76. W.C. Ehrhardt, ASTM STP 1056, "The Measurement and Correction of Electrolyte Resistance in Electrochemical Cells," eds. Scribner, Taylor (West Conshohocken, PA: ASTM, 1990), p. 5-26.
77. K. Nisancioglu, *Corrosion* 43 (1987): p. 258.
78. M.A. Pech-Canul, A.A. Sagues, P. Castro, *Corrosion* 54, 8 (1998): p. 663.

## LIST OF SYMBOLS

A	= electrode area (cm <sup>2</sup> )
B	= proportionality constant used in Stern-Geary Equation
C	= capacitance (farad-cm <sup>-2</sup> )
C <sub>dl</sub>	= double layer capacitance (farad-cm <sup>-2</sup> )
C <sub>φ</sub>	= adsorption pseudo-capacitance (farad-cm <sup>-2</sup> )
E	= electrochemical potential (volts)
E <sub>corr</sub>	= corrosion potential (volts)
E <sub>rev</sub>	= reversible electrode potential (volts)
F	= Faraday's constant (96,485 coul/equivalent)
f	= frequency (s <sup>-1</sup> )
f <sub>max</sub>	= maximum frequency (s <sup>-1</sup> )
i <sub>app</sub>	= applied current density (amp-cm <sup>-2</sup> )
i <sub>corr</sub>	= corrosion current density (amp-cm <sup>-2</sup> )
I <sub>a</sub>	= anodic half-cell current (amp)
I <sub>c</sub>	= cathodic half-cell current (amp)
I <sub>PSD</sub>	= power spectral density of current noise (amp <sup>2</sup> -Hz <sup>-1</sup> )
j	= √-1
k	= pre-exponential term defining Langmuir coverage
q	= charge (farads)
q <sub>F</sub>	= charge in adsorbed film (farads)
q <sub>M</sub>	= charge associated with one monolayer of film (farads)
R	= ideal gas constant (8.31441 J-mol <sup>-1</sup> -K <sup>-1</sup> )
R <sub>s</sub>	= solution resistance (Ω-cm <sup>2</sup> )
R <sub>ct</sub>	= charge-transfer reaction resistance (Ω-cm <sup>2</sup> )
R <sub>eff</sub>	= measured resistance at DC limit in case of nonuniform current distribution (Ω-cm <sup>2</sup> )
R <sub>F</sub>	= additional reaction resistance in the presence of an adsorbed intermediate that creates additional resistance to charge transfer at the interphase (Ω-cm <sup>2</sup> )
R <sub>p</sub>	= polarization resistance (Ω-cm <sup>2</sup> )
R <sub>D</sub>	= reaction resistance under mass transport control (Ω-cm <sup>2</sup> )

$R_d$	= diagonal resistance from $E-i_{app}$ plot ( $\Omega\text{-cm}^2$ )	$Z(\omega)$	= complex impedance ( $\Omega\text{-cm}^2$ )
$R_{app}$	= tangent resistance from $E-i_{app}$ plot ( $\Omega\text{-cm}^2$ )	$ Z(\omega) $	= impedance modulus ( $\Omega\text{-cm}^2$ )
$R_n$	= noise resistance ( $\Omega\text{-cm}^2$ )	$\alpha_a$	= symmetry factor for anodic reaction (-)
$R_{sn}(\omega)$	= spectral noise resistance ( $\Omega$ )	$\alpha_c$	= symmetry factor for anodic reaction (-)
$s$	= diffusional impedance time factor, $l_{eff}^2/D$ (s)	$\beta_a$	= anodic Tafel slope (V/decade)
$t$	= time (s)	$\beta_c$	= cathodic Tafel slope (V/decade)
$T$	= total time of measurement (s)	$\theta$	= surface coverage of adsorbed intermediate (-)
$T$	= temperature (K)	$\phi$	= impedance phase angle (degrees)
$V_n$	= potential noise	$\eta$	= overpotential (volts)
$V_{PDS}$	= power spectral density of voltage noise ( $V^2\text{-Hz}^{-1}$ )	$\sigma_v$	= standard deviation of $V_n$ - time record
$W$	= Wagner number (-)	$\sigma_I$	= standard deviation of current - time record
$Z'(\omega)$	= real component of impedance ( $\Omega\text{-cm}^2$ )	$\omega$	= frequency ( $\text{rad}\cdot\text{s}^{-1}$ )
$Z''(\omega)$	= imaginary component of impedance ( $\Omega\text{-cm}^2$ )		

---



# Oxygen Reduction Reaction Kinetics on Chromate Conversion Coated Al-Cu, Al-Cu-Mg, and Al-Cu-Mn-Fe Intermetallic Compounds

G. O. Ilevbare<sup>\*,z</sup> and J. R. Scully<sup>\*</sup>

Center for Electrochemical Science and Engineering, Department of Materials Science and Engineering,  
University of Virginia, Charlottesville, Virginia 22904-4745, USA

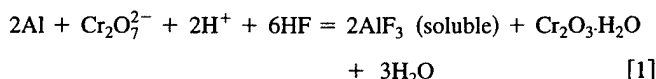
Oxygen reduction reaction (ORR) kinetics were investigated on bulk synthesized analogues of Al-Cu, Al-Cu-Mg, and Al-Cu-Fe-Mn intermetallic phases with and without chromate conversion coating (CCC) in 0.1 M Na<sub>2</sub>SO<sub>4</sub> + 0.005 M NaCl (pH 6) with minimal levels of total dissolved chromate. The results were compared to AA 2024-T3 and high purity Al, Cu, Cr, and Au. Net cathodic ORR mass transport-limiting current densities of Al-based materials, lacking large quantities of Fe, Mn, or Cu were lower than the theoretically predicted rates in the mass transport controlled regime of ideal electronic conductors. This suggests a second rate-limiting factor in the case of these Al-based materials that was deduced to be related to Al-rich surface oxides. A second rate-limiting effect was also seen for pure Cr, implying that Cr<sub>2</sub>O<sub>3</sub> inhibits ORR kinetics. CCC inhibited open circuit corrosion, via reduced ORR kinetics. It also serves as a diffusive barrier to O<sub>2</sub> transport. The role(s) of CCC as an enhanced electronic barrier to electron transfer or barrier to O<sub>2</sub> chemisorption remains unclear.

© 2001 The Electrochemical Society. [DOI: 10.1149/1.1360206] All rights reserved.

Manuscript submitted August 8, 2000; revised manuscript received December 21, 2000.

Aluminum-based precipitation age hardened alloys containing Cu and Fe are prone to localized corrosion such as pitting. Pitting and alkaline attack are often induced by local galvanic cells formed by Cu- and Fe-containing intermetallics or replated Cu.<sup>1-6</sup> In AA 2024-T3, pit initiation sites include Al-Cu-Mg particles,<sup>1</sup> the periphery of Cu-enriched Al-Cu-Mg particles that have been dealloyed of Al and Mg,<sup>2</sup> and the matrix adjacent to Al-Cu-Fe-Mn particles.<sup>1</sup> Both chromate conversion coating (CCC) and anodization of these alloys improve localized corrosion resistance, particularly in chloride salt spray testing.<sup>1,2,7,8</sup> This suggests that either one or more of the four stages of localized corrosion at the anodic site (*i.e.*, nucleation, stabilization, growth, and repassivation) or the properties of sites that support fast cathodic reactions (*e.g.*, cathodic intermetallic phases and replated Cu) are altered by the presence of the CCC.

The CCC process on Al in a dichromate solution containing NaF involves the following overall electrochemical reaction



Al<sub>2</sub>O<sub>3</sub> is dissolved by fluoride. This is generally regarded as desirable since it facilitates the formation of CCC.<sup>9,10</sup> CCCs consist predominantly of Cr(OH)<sub>3</sub> from the reduction of Cr<sup>6+</sup> species along with some Al<sub>2</sub>O<sub>3</sub> which could vary from about 0.4 to over 8.0% in content.<sup>5,10-14</sup> Al oxidation is required to form CCCs. It is expected that Al oxidation is also thermodynamically possible on Cu-containing intermetallic phases that include a significant concentration of Al, and that the reaction described by Eq. 1 will occur spontaneously in a chromate conversion coating bath. It has generally been observed that the formation of CCC over intermetallic compounds proceeds at a slower rate than the surrounding Al matrix<sup>9,15</sup> and as a result, thinner films with lower Cr content tend to be formed over the intermetallics. However, it has even been suggested that the initial rate of conversion coating formation is faster on some intermetallics than on the Al matrix.<sup>15,16</sup> X-ray adsorption near edge spectroscopy (XANES) data collected on the CCC formed on the Al-Cu-Mg intermetallic was found to contain less Cr<sup>6+</sup> than the Al matrix.<sup>15</sup> Nevertheless, some workers have observed that the thickness of the CCC over the Al matrix and intermetallics becomes approximately the same after 5 min of immersion in a conversion coating solution.<sup>9</sup> It is not yet fully understood why intermetallic

compounds resist CCC, nor why the rate of conversion coating on the various intermetallics vary. It is generally accepted that K<sub>3</sub>Fe(CN)<sub>6</sub> (ferricyanide) plays the role of an accelerator in the formation of CCC.<sup>11,17</sup> However, understanding is still limited about the exact mechanism by which it accelerates the CCC process and CN<sup>-</sup> may complex with Cu making conversion coating on intermetallics more difficult.<sup>9,18</sup> Cr<sup>6+</sup> and Cr<sup>3+</sup> may exist within the CCC in several specific forms.<sup>12,19,20</sup> The reduction of Cr<sup>6+</sup> to Cr<sup>3+</sup> in the form of hydrated chromium oxide is often incomplete and CCCs typically contain 9-60% Cr<sup>6+</sup> chromate.<sup>9,21-23</sup> Aging of the coatings affects the amount of Cr<sup>6+</sup> present and, hence, the amount available to be leached out.<sup>21,24</sup>

Chromate is an extremely effective solution phase corrosion inhibitor for localized corrosion.<sup>22,25-27</sup> The mechanism(s) by which chromate or its reaction products inhibit metallic corrosion of Al may differ in solutions of different halide/anion ratios, temperatures<sup>28-30</sup> and pit sizes.<sup>31-33</sup> The role of the CCC as an inhibitor to anodic dissolution, and its effects on the electrochemistry of intermetallics that create galvanic cells in Al-based precipitation age hardened alloys are not entirely certain. For instance, deposited layers have been found to contain pores.<sup>34,35</sup> Apparent cathodic inhibition of oxygen reduction reaction (ORR) on intermetallics has been reported in chromate solution but is subject to further investigation.<sup>33,36</sup> One reason this is necessary is that anode sites were not separated from cathode sites in these studies, and open circuit corrosion may have led to extensive Cu replating. Anodic inhibition would have minimized creation of a new cathode area by Cu replating mechanisms along with altered surface roughness and reduction of pH. These make the study of cathodic kinetics very difficult, and make it imperative that any alterations in surface conditions, especially when corrosion [*e.g.*, at open circuit potential (OCP)] is a factor be accounted for in the estimation of cathodic kinetics. In several studies where cathodic inhibition was observed by chromate-containing solution, the issue of cathode area alterations due to the occurrence of surface corrosion (before measurements were taken) was not considered.<sup>37,38</sup> It is known that chromate passivates Al<sub>2</sub>CuMg.<sup>39</sup> A recent investigation suggests that CrO<sub>4</sub><sup>2-</sup> may block O<sub>2</sub> adsorption sites when chemisorbed onto Cu surfaces that prevented the creation of a new cathode area during testing.<sup>39</sup> Both CCC and soluble Cr<sup>6+</sup> may alter the cathodic electrochemistry of the relevant intermetallic phases. ORR as well as hydrogen evolution reaction (HER) proceed at enhanced rates on intermetallic compounds relative to high purity Al.<sup>39</sup> At issue is whether any reaction products from CCC along with the physical presence of the CCC alter net cathodic kinetics. This paper provides

<sup>\*</sup> Electrochemical Society Active Member.

<sup>z</sup> E-mail: goi6c@virginia.edu

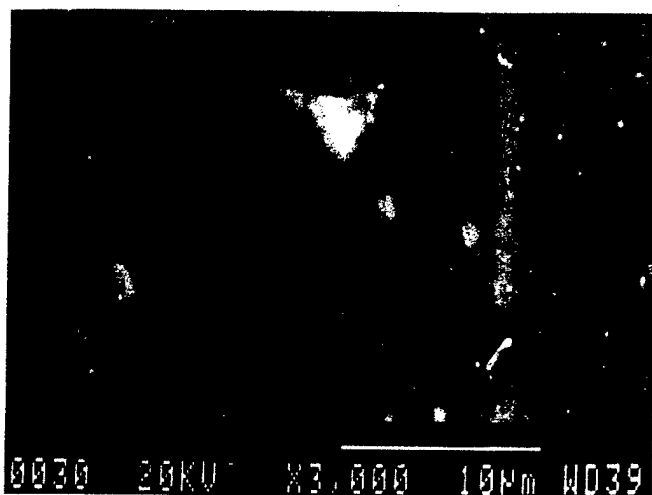


**Figure 1.** SEM photo of a mirror finished surface of AA 2024-T3 showing intermetallic particles, which measure from less than 1  $\mu\text{m}$  to about 2.5  $\mu\text{m}$  across. Particle a is of the type Al-Cu and particle b is of the type Al-Cu-Mn-Fe.

preliminary insight into the role of chromium conversion coatings (CCC) as inhibitors of cathodic ORR kinetics when acting as a reservoir for  $\text{Cr}^{6+}$  ions.<sup>9,21,22,25</sup> We also address whether chromate conversion coatings can minimize the ability of local heterogeneities to form potent galvanic couples on AA 2024-T3 by intrinsically altering cathodic ORR rates.

### Experimental

Studies were conducted on 1.5 mm thick AA 2024-T3 sheets with the composition (major elements, by wt. %): Cu 4.5, Mg 1.30, Mn 0.62, Fe 0.18, Zn 0.10, and Si 0.093 with the balance Al. Scanning electron microscope-energy dispersive spectroscopy (SEM-EDS) studies indicate the presence of coarse Al-Cu-Mg and Al-Cu-Mn-Fe constituents on the surface (Fig. 1). In other SEM-EDS studies on AA 2024-T3 of similar composition, it was found that the predominant micrometer-sized intermetallic phases were of the Al-Cu-Mg and Al-Cu-Fe-Mn type<sup>1-3,40,41</sup> with lesser amounts of the Al-Fe-Cu.<sup>2</sup> The intermetallics studied here were multiphase Al-Cu, Al-Cu-Mg, and Al-Cu-Mn-Fe. X-ray diffraction (XRD) showed that the intermetallic castings consisted of large amounts of  $\text{Al}_2\text{Cu}$ ,  $\text{Al}_2\text{CuMg}$ , and  $\text{Al}_{20}\text{Cu}_2(\text{MnFe})_3$ , respectively, for the intermetallic compound types listed above. Other materials studied were polycrystalline 99.998% Al, 99.999% Cu, 99.9985% Au, and 99.7% Cr.

Auger electron spectroscopy (AES) was used to carry out surface composition analyses with a Perkin-Elmer 560 ESCA/SAM system at a chamber pressure of about  $10^{-10}$  Torr. The AES system was equipped with an electron multiplier detector and a cylindrical mirror analyzer. AES spectra were taken with an electron gun voltage of 3 keV at a resolution of 0.6%. Depth profiles were generated with Ar sputtering at a beam voltage of 3 kV, in the raster mode, at a pressure (in the ion gun) of between 10 and 20 mPa. Confocal laser scanning microscopy (CLSM) was carried out on a Zeiss model LSM 510 microscope. Imaging was carried out with an argon laser with a wavelength of 488 nm. Surface topographical maps of the bare (uncoated) and CCC surfaces on AA 2024-T3 were generated. All surfaces used for CLSM were polished to a mirror image surface finish with Buehler 0.05  $\mu\text{m}$  diamond suspension when used as bare surfaces or before CCC was carried out. The samples were then rinsed with tap water after the polishing process.

CCC was performed in-house using a solution containing 0.025 M  $\text{Na}_2\text{Cr}_2\text{O}_7$ , 0.024 M NaF, 0.015 M  $\text{K}_3\text{Fe}(\text{CN})_6$ , and  $\text{HNO}_3$  (added until desired pH of 1.2-2.2) after conventional cleaning procedures.<sup>42-44</sup>

Intermetallics were coupled and placed in close proximity to a large disk of AA 2024-T3 (roughly 1:100 area ratio) in a specially designed carousel during alkaline cleaning, desmutting, and conversion coating to simulate their galvanic coupling to AA 2024-T3 during treatment of a heterogeneous alloy surface. Thus, the intermetallic phases experienced not only similar electrochemical potential when galvanically coupled to AA 2024-T3, but CCC either by direct deposition or by precipitation, were physically possible. AA 2024-T3 samples were degreased, alkaline cleaned, desmutted, and then conversion coated. Others were only degreased and are referred to as untreated. The alkaline cleaning solution was 0.21 M  $\text{Na}_2\text{CO}_3$  and 0.23 M  $\text{Na}_3\text{PO}_4$  (pH 13). The desmutting solution was 50% (by volume)  $\text{HNO}_3$ . All electrodes used for electrochemical experiments were wet ground with 600 grit SiC paper before CCC or when used as untreated samples with the exception of AA 2024-T3, which was used in the as-received condition after cleaning the sample. Au and Cr electrodes were used in the untreated form only after a 600-grit SiC surface finish. Salt spray testing was performed according to ASTM B117 specifications for chromate conversion coated AA 2024-T3<sup>45</sup> by an outside laboratory to verify corrosion inhibition. They were found to be at least equal in quality to commercial products. All CCC specimens tested electrochemically were between 48-120 h old before electrochemical testing was conducted. The presence of  $\text{Cr}^{6+}$  in CCC on AA 2024-T3 of this age was verified for all treatments using X-ray absorption near-edge spectroscopy (XANES) as reported elsewhere.<sup>4,46</sup> A pre-edge peak at 5.994 keV indicated the presence of Cr(VI) in the tetrahedral coordinated state. The adsorption edge measured above 6.065 keV was used to identify the total chromate content. On visual inspection, all intermetallic compounds had a clearly visible layer of CCC on them.

OCP exposures of 2 h followed by potentiodynamic polarization experiments (at 1 mV/s) were performed in quiescent 0.1 M  $\text{Na}_2\text{SO}_4$  + 0.005 M NaCl (pH 6) at ambient temperature, on stationary and rotating disc electrodes (RDE), in three-electrode cells that were open to lab air. This environment is an analogue too low chloride-high anion solutions found in the lap-slice joints of an aircraft.<sup>47</sup> The 2 h period produced limited Cr(VI) concentrations in the bulk solution.<sup>24,48</sup> Sodium sulfate has minimal complicating effects, for instance, it only reduced the total Cr and Cr(VI) peaks by about 13% over 800 h on AA 2024-T3 treated with Alodine 1200.<sup>46</sup> Rotation speeds of 500, 2000, and 4000 rpm were used in the RDE experiments. The electrolytes were air sparged in addition to being open to lab air. In other experiments, 0.0038 M  $\text{H}_2\text{CrO}_4$  + 0.0062 M  $\text{Na}_2\text{CrO}_4$  was added to 0.1 M  $\text{Na}_2\text{SO}_4$  + 0.005 M NaCl (pH 6) to mimic Cr(VI) leaching. Net cathodic current densities ( $i_{\text{Net}} = i_{\text{cath}} - i_{\text{an}}$ ) were recorded, as this is the pertinent current density (cd) during galvanic coupling. Mass transport limiting cd ( $i_l$ ) were determined from mass transport limited regions on cathodic  $E$ -log  $i$  curves. Regions where  $i_{\text{cath}}$  was independent of  $E_{\text{applied}}$  were not always observed for Al. In these cases, the HER and proximity to OCP were avoided.

### Results

**Intermetallic bulk and surface compositions.**—Energy dispersive X-ray (EDX) analyses results from castings of Al-Cu, Al-Cu-Mg, and Al-Cu-Mn-Fe intermetallic compounds show that the electrodes consisted of large regions with compositions consistent with the  $\text{Al}_2\text{Cu}$ ,  $\text{Al}_2\text{CuMg}$ , and  $\text{Al}_{20}\text{Cu}_2(\text{MnFe})_3$  phases, respectively. XRD also confirmed the presence of these phases. Table I lists bulk compositions expressed as atomic fractions. The Al-Cu intermetallic has been analyzed in more detail elsewhere.<sup>49</sup> The surface compositions after wet grinding (and drying under a jet of warm air) obtained from AES are reported in Table II and also expressed as atomic fraction. They match the bulk compound stoichiometry and suggest that wet grinding did not significantly alter surface compositions

<sup>a</sup> XANES was conducted at the NSLS at BNL.

**Table I.** Bulk compositions of the intermetallic compound castings from energy dispersive X-ray analyses.

Intermetallic	Al	Atomic composition (%)				
		Mg	Zn	Cu	Mn	Fe
Al-Cu-Mn-Fe	71.43	-	-	7.14	10.71	10.71
Al-Cu-Mg	49.28	26.06	-	24.66	-	-
Al-Cu	66.69	-	-	33.31	-	-

except for the presence of oxygen from oxidation. The Al-Cu-Mn-Fe intermetallic was slightly richer in iron after grinding.

**Anodic and cathodic corrosion kinetics on untreated electrodes in 0.1 M Na<sub>2</sub>SO<sub>4</sub> + 0.005 M NaCl.**—Figures 2a and b illustrate the overall  $E$ -log  $i$  behavior on stationary electrodes of nonconversion coated AA 2024-T3, Al, Cu, and the Al-Cu, Al-Cu-Mg, and Al-Cu-Mn-Fe intermetallics in 0.1 M Na<sub>2</sub>SO<sub>4</sub> + 0.005 M NaCl after a 2 h exposure at OCP. The OCPs of Cu, the Al-Cu, and the Al-Cu-Mn-Fe intermetallics are more positive than that of AA 2024-T3 (horizontal line) and far more positive than those of the Al-Cu-Mg intermetallic compound and Al. The Al-Cu-Mg intermetallic is not passive at OCP and exhibits a high dissolution rate upon anodic polarization. Figure 2b shows that the Al-Cu-Mn-Fe intermetallic is passive near the OCP of AA 2024-T3 but undergoes pitting at potentials above it. AA 2024-T3 pits at its OCP and large pits have been observed in its matrix.<sup>48</sup> Cathodic kinetics were enhanced on all Cu-containing materials and AA 2024-T3 compared to high purity Al (Fig. 2a) as noted by Prior and Kier for Al containing Fe and Cu.<sup>5</sup> A large peak in cathodic current density on Cu was due to the cathodic reduction of the copper oxide. Otherwise, the principal cathodic reactions near the OCP of AA 2024-T3 are the ORR and HER at more negative potentials. It can be inferred from the data that the exchange current densities for the HER are much lower on high purity Al than on the Cu-containing materials. The exchange current density for the HER is so low<sup>50</sup> on Al that mass transport-limited ORR dominates the high purity Al electrode at potentials as negative as  $-1.5$  V<sub>SCE</sub>. HER does not occur in a pH 6 electrolyte, at standard temperature (25°C) and atmospheric pressure near the OCP of AA 2024-T3 (ca.  $-0.5$  V<sub>SCE</sub>). Therefore, mass transport limited O<sub>2</sub> reduction is one of the cathodic reactions of greatest interest when studying open circuit corrosion of this alloy either with or without CCC in near neutral chloride solutions. Clearly, this reaction occurs at higher rates on Cu-bearing phases compared to high purity Al, which exhibits additional rate limitations besides O<sub>2</sub> transport in solution. At issue is the effect of CCC on the ORR electrochemistry of micrometer sized intermetallics embedded in AA 2024-T3. The mechanism of enhancement on AA 2024-T3 likely relates to enhanced limiting current density on an array of microelectrode-sized intermetallics embedded in an Al matrix.

**Chromate conversion coated electrodes.**—SEM images of the surface of the in-house CCC on AA 2024-T3 from earlier work<sup>48</sup> revealed that they had a mud-crack appearance. This appearance might be a result of the dehydration of the coating during the drying process.

Figure 3a shows an SEM photo of a 3 min chromate conversion coated AA 2024-T3. Figure 3b shows a 2-D CLSM reflected light intensity map of a 3 min CCC AA 2024-T3 surface, while Fig. 3c shows a CLSM 3-D surface topographical maps of this surface. All

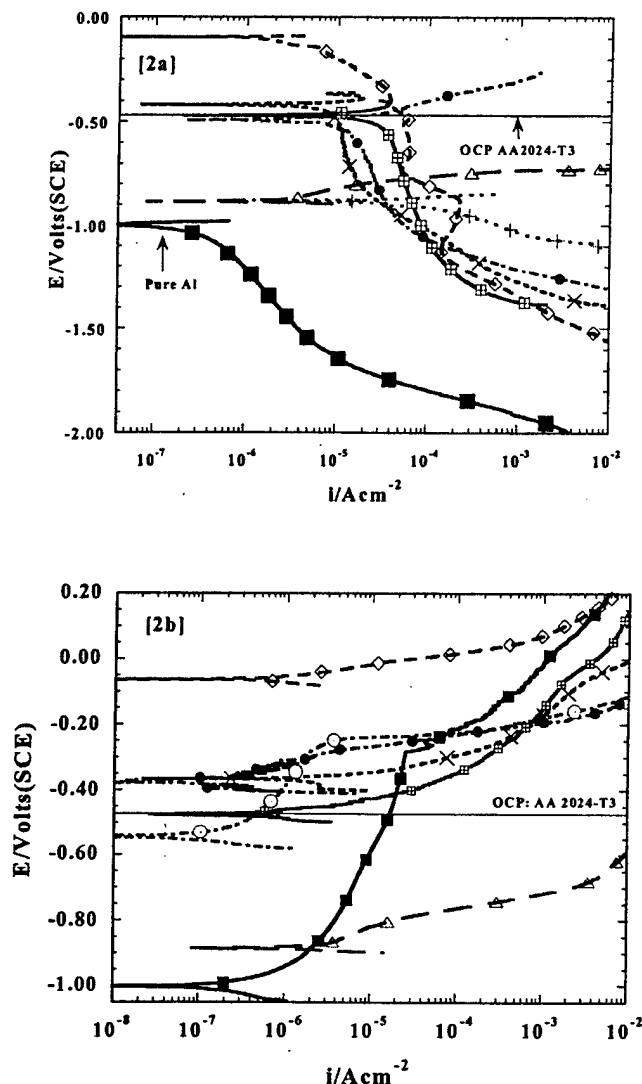


**Figure 2.** The cathodic (a, top) and anodic (b, bottom)  $E$ -log  $i$  behavior of stationary electrodes of AA 2024-T3 (□); Al (■); Cu (◇); Al-Cu (×); Al-Cu-Mg (△) (anodic); Al-Cu-Mn-Fe (●); and Al-Cu-Mn-Fe (de-aerated) (○) in 0.1 M Na<sub>2</sub>SO<sub>4</sub> + 0.005 M NaCl.

coatings were between 48-120 h old at the time microscopy was performed. Figure 3a shows that some intermetallic compounds have been removed from the surface of the metal and the area they previously occupied has been coated. Intermetallic compound dissolution was found to occur during the alkaline cleaning stage.<sup>48</sup> These particles would have either completely dissolved (e.g., if of Al-Cu-Mg type which are anodic to the Al matrix<sup>1</sup>) or would have fallen out of the hole if the Al matrix around it had dissolved away by cathodic trenching if of the Al-Cu or Al-Cu-Mn-Fe type which are cathodic to the Al matrix.<sup>49</sup> Topographical scans across some other surface features in Fig. 3b show that the area around some of the particles had corroded away as shown by the deep gullies sur-

**Table II.** Surface compositions from Auger electron spectroscopy (AES) analyses of the Al-Cu-Mg and Al-Cu-Mn-Fe intermetallic compound electrodes after wet grinding using 600 grit SiC paper.

Intermetallic	Sputter time (s)	Atomic composition (atom %)				
		Al	Cu	Mg	Mn	Fe
Al-Cu-Mg	150	34.13	17.65	15.45	-	32.76
Al-Cu-Mn-Fe	120	54.26	6.18	-	8.66	14.87

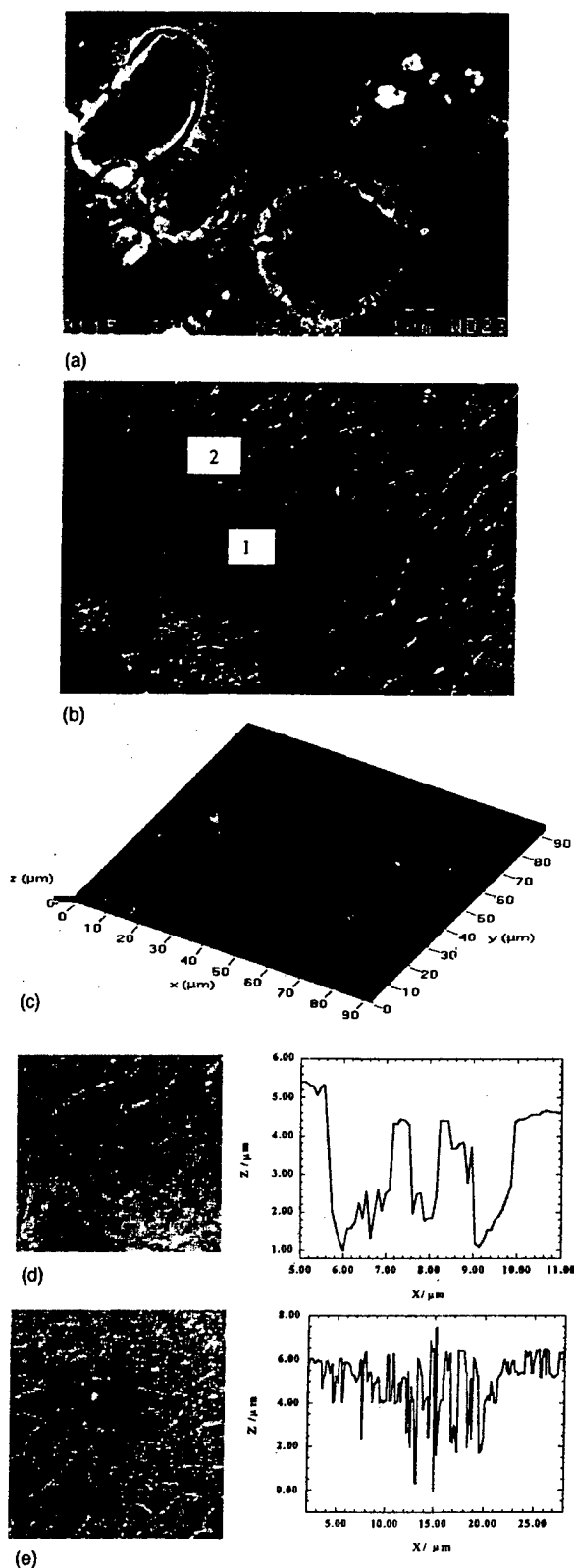


**Figure 3.** AA 2024-T3 surface with a 3 min CCC surface showing the photo of an (a) SEM image, (b) reflected light map from a CSLM image, and (c) the 3-D topographical image from a CSLM. Figure d and e show reflected light maps (left) and line topographical scans (right) of the surface features numbered 1 and 2, respectively, in b. The surfaces were finished with 0.05  $\mu\text{m}$  diamond suspension except for a which was used in the as-received condition. The magnification of b is (100 $\times$  objective lens). The entire width (from left to right) of b is 92  $\mu\text{m}$ .

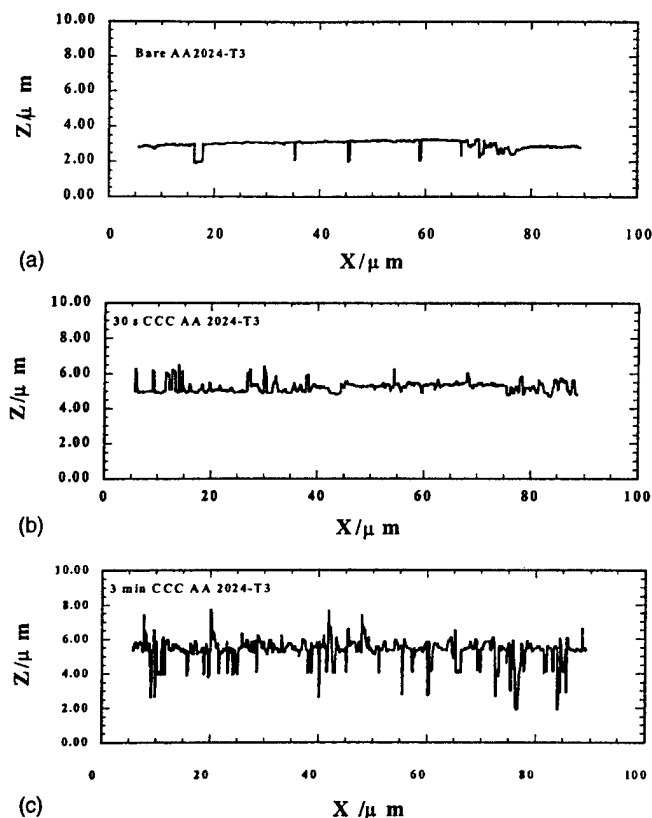


**Figure 4.** Cross-sectional surface topographical profiles (from CSLM) of (a) bare, (b) 30 s, and (c) 3 min CCC surfaces. Surfaces were finished with 0.05  $\mu\text{m}$  diamond suspension prior to CCC process.

rounding an elevated plateau or set of broad spikes (Fig. 3d). This suggests that such particles might have been cathodic to the Al matrix, hence the dissolution of the area surrounding the particle by cathodic trenching.<sup>51</sup> It is expected that the particles that remained on the surface were coated during the CCC process albeit with difficulty. However, synthesized intermetallic ingots were successfully coated in our laboratory and some others have also been successfully coated.<sup>15</sup> Figure 3e shows the topographical line scan across another surface feature showing features consistent with uneven dissolution. In this case, it appears that the particle had partially dissolved away, and some CCC may also have been deposited on top of the partially dissolved area. There does not seem to be any distinct dissolution around the edge of this particle as was observed in Fig. 3d.

Surface depth profiles of the surfaces of bare (untreated), 30 s and 3 min CCC surfaces were taken with CLSM are shown in Fig. 4a, b, and c, respectively. Care was taken to avoid possible sites of any intermetallics or other surface inclusions. It can be seen that the surfaces of the CCCs are not smooth, but are covered with pores and/or the cracks that are visible under the SEM. The topographical profiles of the imaged areas showed that the pore and crack depths on the 30 s CCC are about 1  $\mu\text{m}$  deep while those on the 3 min CCC are about 2-4  $\mu\text{m}$  deep. Since pore and crack depths tended to increase with coating time, this suggests that the thickness of the CCC increases with coating time. Other authors have reported CCCs thicknesses of between 0.1 and 1.0  $\mu\text{m}$  although no coating time was mentioned.<sup>52</sup> The increase in the number of pores and cracks per unit area with coating time suggested that the surface of the CCC became rougher with coating time.

However, due to the depth-of-field limitations on the CLSM, it is uncertain whether the depths of the pores observed in these figures (Fig. 4b and c) represent the total depth of the pores and cracks. Also, it could not be determined from CLSM whether these pores

and cracks actually penetrate the entire thickness of the coatings, or just partially.

The summary of the times until failure<sup>b</sup> from the salt spray test appears in other published work.<sup>48</sup> Both the 30 and 3 min (180 s) in-house CCC AA 2024-T3 passed the salt spray test (ASTM B-117)<sup>45,48</sup> as specified by MIL-C-81706 and MIL-C-5541E.<sup>53</sup> These results show that the in-house chromate conversion coating performed as well as commercially applied Alodine 1200<sup>c</sup> and better than the Alodine 1200 coating applied in our laboratory. This result is significant because it indicates that the CCC used and discussed in the remainder of this study was at least equal in quality to the commercial product.

XANES absorbance pre-edge peaks at 5.994 KeV on chromate conversion coated AA 2024-T3 between 48 and 120 h old (Fig. 5a), show evidence of  $\text{Cr}^{6+}$  in the CCC investigated here. Figure 5b shows both the pre- and adsorption-edge Cr peaks. Figure 5c shows that the amount of  $\text{Cr}^{6+}$  and total Cr (depicted by the pre-edge and adsorption-edge peaks, respectively) in the CCC increases with coating time and, hence, thickness of the CCC.

*Cathodic kinetics on untreated stationary electrodes as a function of the extent of prior corrosion.*—Experiments to measure the net cathodic kinetics on untreated samples in chromate-free solutions were performed on stationary AA 2024-T3 electrodes as a function of extent of prior corrosion damage.

Prior corrosion damage was controlled by either varying time at OCP or by applying anodic charge immediately prior to cathodic scans. It was found that the net  $i_1$  of ORR increased as the anodic charge applied to AA 2024-T3 (to cause pitting) increased (Fig. 6a). The OCP also became more negative as applied charge increased (Fig. 6b). The net cathodic kinetics of the Al-Cu-Mg intermetallic also increased as the extent of corrosion increased.<sup>39</sup> Experiments carried out on AA 2024-T3 in 0.1 M  $\text{Na}_2\text{SO}_4$  after a 2 h exposure at OCP compared with 0.1 M  $\text{Na}_2\text{SO}_4$  + 0.005 M NaCl also showed that the  $i_1$  for ORR decreased in the sulfate solution compared to the sulfate/chloride solution. AA 2024-T3 is not expected to pit in 0.1 M  $\text{Na}_2\text{SO}_4$  due to the absence of chloride ions in solution.<sup>48</sup> The OCP of AA 2024-T3 in 0.1 M  $\text{Na}_2\text{SO}_4$  + 0.005 M NaCl is close to its pitting potential (Fig. 2b). The greater net cathodic kinetics after 2 h at OCP observed in the 0.1 M  $\text{Na}_2\text{SO}_4$  + 0.005 M NaCl solution, corresponded with open circuit corrosion of AA 2024-T3. Therefore greater net cathodic kinetics in 0.1 M  $\text{Na}_2\text{SO}_4$  + 0.005 M NaCl can be attributed at least in part to prior open circuit corrosion. It is therefore important to consider prior corrosion of a metal since it alters the cathodic ORR and HER kinetics by increasing the electrode area (through roughening), formation of pits that alter surface pH, and increasing the extent to which the surface is possibly enriched with Cu during corrosion.<sup>54</sup>

*Cathodic kinetics on CCC stationary electrodes in 0.1 M  $\text{Na}_2\text{SO}_4$  + 0.005 M NaCl.*—In this study, we seek to assess whether or not CCC directly suppresses cathodic kinetics of the intermetallic compounds and AA 2024-T3, or indirectly through anodic inhibition. Figure 7 presents a comparison of OCPs of untreated surfaces in 0.1 M  $\text{Na}_2\text{SO}_4$  + 0.005 M NaCl to those after CCC treatment (CCC while galvanically coupled to AA 2024-T3) on stationary electrodes in a plot that depicts differences in OCP as departures from the diagonal line. The OCPs of chromate conversion coated Al, AA 2024-T3, 99.999% Cu, and the intermetallics Al-Cu and Al-Cu-Mg were not changed significantly. The OCP of the Al-Cu-

<sup>b</sup> MIL-C-4451E (Qualification): Failure is said to have occurred if five or more corrosion pits are found on the test panel after 168 h of ASTM B117 salt spray test. MIL-C-81706 (Quality conformance): Failure is said to have occurred if any visual evidence of corrosion is found on the test panel after 168 h of ASTM B117 salt spray test.

<sup>c</sup> Trade name of commercial chromate conversion coating manufactured by Henkel Corporation (formerly Parker Amchem).

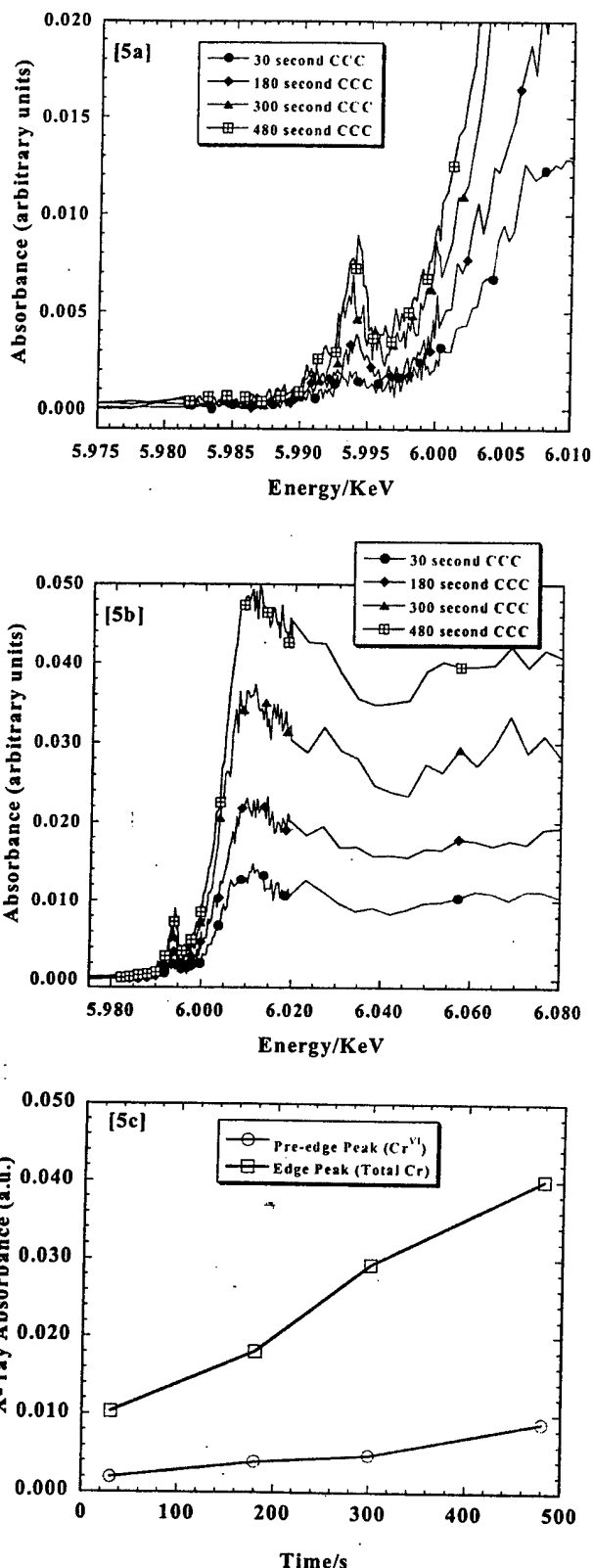
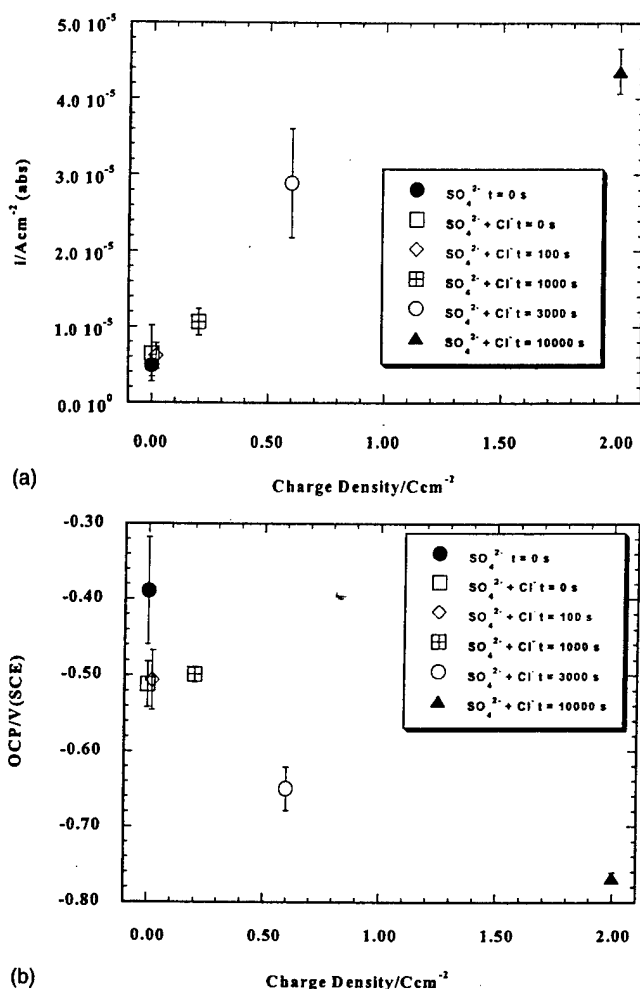


Figure 5. XANES pre-edge peak at (a) 5.994 keV and (b) adsorption-edge peaks after chromate conversion coatings of 30, 180, 300, and 480 s on AA 2024-T3 showing evidence of  $\text{Cr}^{6+}$  and total Cr in the CCC, respectively. The height of the X-ray adsorption pre-edge peak (representing amount of  $\text{Cr}^{6+}$  present) and that of the adsorption-edge peak taken above 6.065 keV (representing total amount of Cr present) as a function of coating time (c).

Mn-Fe intermetallic was lowered when a 5 min chromate conversion coating was applied (Fig. 7). It was lowered to a greater degree



**Figure 6.** Apparent cathodic reaction rate on an AA 2024-T3 stationary electrode (at  $-0.75 V_{SCE}$ ) as (a) a function of prior anodic charge density, and open circuit potential (OCP) on an AA 2024-T3 stationary electrode, (b) as a function of prior anodic charge density.  $t$  indicates time for which  $i$  of  $200 \mu A cm^{-2}$  was applied. There was no prior exposure at OCP. Electrolyte:  $0.1 M Na_2SO_4 + 0.005 M NaCl$ , or  $0.1 M Na_2SO_4$ . Error bars are at a 95% confidence level.

on the untreated intermetallic compound analogue in the presence of  $0.01 M$  chromate in the electrolyte.<sup>48</sup> The OCPs of the other intermetallic compounds and AA 2043-T3 were not reduced by 5 min CCC (Fig. 7). However, OCP information alone is insufficient to predict galvanic couple behavior. Figure 8a shows the cumulative probability plot for pitting ( $E_{pit}$ ) for untreated and 5 min CCC AA 2024-T3 in  $0.1 M Na_2SO_4 + 0.005 M NaCl$ , along with untreated AA 2024-T3 in  $0.1 M Na_2SO_4 + 0.005 M NaCl + 0.0062 M Na_2CrO_4 + 0.0038 M H_2CrO_4$ . The key result is that either chromate or CCC raises  $E_{pit}$  above OCP. (More detailed explanations for the results presented in Fig. 8f were published in Ref. 48.) CCC suppresses OCP [and post-OCP (pitting, general dissolution)] corrosion in the presence of  $Cl^-$  as shown on AA 2024-T3 in Fig. 8a and b, as does soluble chromate.<sup>d</sup> On AA 2024-T3, the extent of OCP and post-OCP corrosion suppression by chromate at pH 6 is not as potent as that of 5 min CCC at higher potentials (Fig. 8a and b).

<sup>d</sup> The extent of corrosion suppression in the presence of soluble chromate ( $0.01 M$ ) was found to be pH dependent.<sup>48</sup>  $0.01 M$  chromate additions to the  $SO_4^{2-}/Cl^-$  electrolyte mixture was found to be more potent at suppressing pitting at pH 8 compared with at pH 6.<sup>48</sup> This was thought to be due to the specification of the chromate species in the electrolyte.<sup>55</sup>

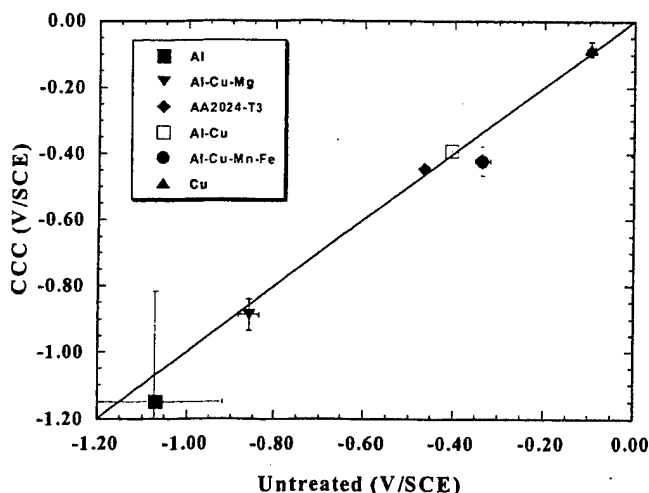


**Figure 7.** Open circuit potentials on stationary electrode after 2 h. Data shows untreated 99.998% Al, Al-Cu-Mg, AA 2024-T3, Al-Cu, Al-Cu-Mn-Fe, and 99.999% Cu compared with those of their 5 min CCC counterparts in  $0.1 M Na_2SO_4 + 0.005 M NaCl$  (pH 6). Similar results were obtained with 3 min CCC.

CCC (and soluble  $0.01 M$  chromate additions to solution) did lower the net cathodic kinetics on AA 2024-T3 and the Al-Cu intermetallic (Fig. 8c and d). Net cathodic kinetics on the Al-Cu-Mn-Fe intermetallic are also lowered when 5 min CCC was applied compared to the untreated analogue, and are even lower in the presence of  $0.01 M$  chromate compared with the 5 min CCC treated analogue (Fig. 8e). Earlier work also suggested (and is further supported here) that one observed effect of CCC and chromate on net cathodic kinetics on the Al-Cu-Mn-Fe intermetallics is at least partially due to the suppression of OCP corrosion much in the same fashion as on AA 2024-T3.<sup>39</sup> This was confirmed when elimination of  $Cl^-$  from solution produced the same apparent cathodic inhibition effect as seen when chromate was present in the  $SO_4^{2-}/Cl^-$  mixture on Al-Cu-Mn-Fe.<sup>39</sup> In contrast (with AA 2024-T3), the degree of suppression of net cathodic kinetics on the Al-Cu-Mn-Fe intermetallic compound seems to be more potent in the presence of chromate in solution compared with 5 min CCC in the  $SO_4^{2-}/Cl^-$  electrolyte mixture (Fig. 8e). This might suggest that the intermetallic compounds are not well coated. The same observation was made on the Al-Cu compound although these effects were not as pronounced as on the Al-Cu-Mn-Fe intermetallic compound. The notion of the lower degree of protection given by CCC compared with soluble chromate on intermetallic compounds is also further substantiated by the degree of anodic protection provided to the Al-Cu-Mg intermetallic compound by soluble chromate compared with 5 min CCC (Fig. 8f). More protection is given by soluble chromate as indicated by the lower net anodic current density. However, both soluble chromate and 5 min CCC reduced anodic dissolution of the Al-Cu-Mg intermetallic compound and, therefore, diminished the possibility of formation of a porous electrode surface, which would enhance the net cathodic rates (Fig. 8f). The key result is that  $CrO_4^{2-}$  and to a lesser extent CCC suppresses anodic dissolution of the Al-Cu-Mg intermetallic, and pitting of AA 2024-T3 and to a less extent the Al-Cu-Mn-Fe intermetallic, and that apparent cathodic kinetics were subsequently decreased. However, some of the apparent cathodic inhibition could be reproduced by elimination of  $Cl^-$ . Nevertheless, it cannot be completely ruled out that a portion of the reduction in net cathodic reaction rates might be due to other factors other than suppression of OCP corrosion.

*E-log i behavior of net limiting current density for ORR under mass transport controlled conditions.*—Figures 9a and b show representative  $E-log i$  plots of untreated and 3 min CCC Cu, Al, and the



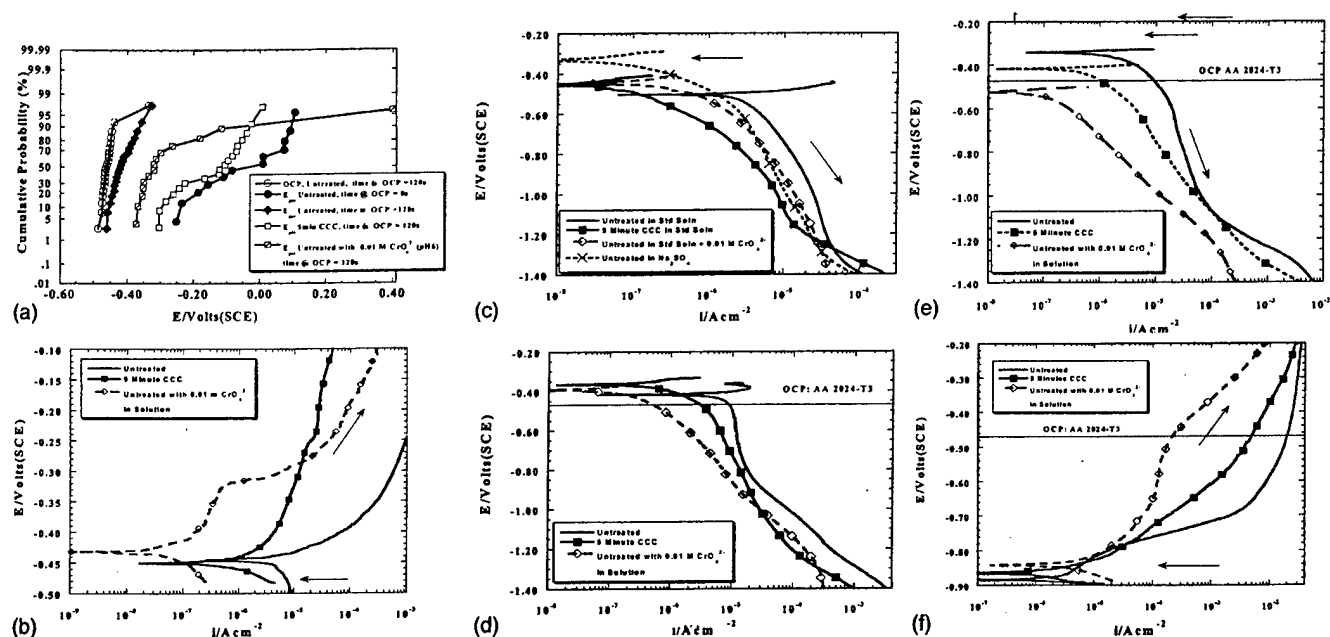


**Figure 8.** The cumulative probability plot for  $E_{pit}$  for untreated (with waiting time at OCP of 0 and 120 s), and 5 min CCC AA 2024-T3 in 0.1 M  $\text{Na}_2\text{SO}_4$  + 0.005 M NaCl, and untreated AA 2024-T3 in 0.1 M  $\text{Na}_2\text{SO}_4$  + 0.005 M NaCl + 0.0062 M  $\text{Na}_2\text{CrO}_4$  + 0.0038 M  $\text{H}_2\text{CrO}_4$  (a). The  $E$ -log  $i$  behavior of AA 2024-T3, anodic (b), AA 2024-T3, (c) cathodic, and (d) Al-Cu, (e) Al-Cu-Mn-Fe, and (f) Al-Cu-Mg intermetallics in 0.1 M  $\text{Na}_2\text{SO}_4$  + 0.005 M NaCl while untreated (bare), with 5 min CCC, and untreated with 0.0062 M  $\text{Na}_2\text{CrO}_4$  + 0.0038 M  $\text{H}_2\text{CrO}_4$  in solution.

Al-Cu-Mn-Fe intermetallic at an electrode rotation speed of 500 rpm [ $\omega^{0.5} = 7.24 \text{ (rad s}^{-1})^{0.5}$ ]. These materials represent the extremes of cathodic behavior seen in Fig. 2. Mass transport limited regimes for ORR could be selected, albeit at different potentials. Figure 10 shows the ORR mass transport limiting current density ( $i_l$ ) vs.  $\omega^{0.5}$ . A comparison of  $i_l$  in 0.1 M  $\text{Na}_2\text{SO}_4$  + 0.005 M NaCl between untreated and 3 min CCC is shown for Cu, Al-Cu-Mn-Fe, and Al, after a 2 h exposure at OCP in Fig. 10a. The mass transport limited  $\text{O}_2$  reduction current density data for the untreated Cu and the Al-Cu-Mn-Fe intermetallic almost match the ORR results predicted by the Levich equation (assuming  $n = 4$ ) for this cathodic reaction on an ideal electronic conductor with respect to angular velocity (rotation rate).<sup>56</sup> The  $i_l$  is lower on the chromate conversion coated Cu, and the Al-Cu-Mn-Fe intermetallic. It is higher on coated Al compared with untreated Al.  $i_l$  after CCC also does not obey the Levich equation. However, the relative order of the rates of the ORR kinetics are preserved on the chromate conversion coated samples (i.e., ORR rate on Cu > Al-Cu-Mn-Fe > Al). The ORR of high purity Al is much lower than predicted from mass transport of  $\text{O}_2$  in solution. The kinetics on Al are almost independent of angular velocity and do not obey the Levich equation, which is theoretically independent of electrode material for an electronic conductor with no electron or  $\text{O}_2$  transport limiting interfacial film.<sup>49</sup> This implies an additional rate limitation for Al which is likely to be the insulating

$\text{Al}_2\text{O}_3$  oxide film which limits the electron transfer reaction (ETR).<sup>f</sup> Figure 10b compares results from untreated samples in 0.1 M  $\text{Na}_2\text{SO}_4$  + 0.005 M NaCl + 0.0038 M  $\text{H}_2\text{CrO}_4$  + 0.0062 M  $\text{Na}_2\text{CrO}_4$ , to those from 3 min CCC in 0.1 M  $\text{Na}_2\text{SO}_4$  + 0.005 M NaCl.  $i_l$  is lower on the chromate conversion coated Cu but higher on the Al-Cu-Mn-Fe intermetallic (albeit very slightly) and Al compared with the untreated samples in the chromate containing solution (Fig. 10b). Results from stationary electrodes<sup>48</sup> did not show a difference in the  $i_l$  for the ORR between untreated (with and without chromate in solution), and chromate conversion coated samples in 0.1 M  $\text{Na}_2\text{SO}_4$  + 0.005 M NaCl. Extrapolation of the  $i_l$  vs.  $\omega^{0.5}$  data to 0 rpm showed that the data converges for all treatments within a statistical scatter band. Hence, high rotation at 500 rpm is a useful diagnostic condition to study whether surface treatments provide cathodic inhibition because differences between reaction rates limited by mass transport through the aqueous phase and those limited by other factors are magnified.

### Discussion

The positive OCP of AA 2024-T3 relative to that of Al (Fig. 2 and 7) is a consequence of the presence of the Cu-bearing intermetallic phases in the alloy, replated Cu, as well as Cu in the solid solution in the face centered cubic (fcc) Al phase. The role the intermetallic compounds play in the various galvanic couples is, therefore, very important especially during the initial phase of corrosion. The effect of CCC on these phases is, consequently, also of interest. The little or no change in the OCP of Cu, and the Al-Cu and Al-Cu-Mg intermetallics after CCC suggests that CCC does not alter their influence on AA 2024-T3 corrosion while embedded in the matrix. The slight reduction in the OCP of the intermetallic Al-Cu-Mn-Fe suggests that some alteration might be expected in the couples formed between this phase and the alloy matrix.  $E$ -log  $i$

<sup>e</sup> Note that the intermetallics, Cu and Al used in these RDE experiments are nominally homogeneous electrodes. In this case, the study of the effect of CCC as an ETR, diffusion, or kinetic barrier can be satisfactorily isolated and studied, separate from the effect of enhanced mass transfer at microelectrode-like areas.<sup>57-58</sup> However, in the case for instance of stationary AA 2024-T3 electrode where the apparent limiting cathodic current density may be dominated by reactions on the intermetallic compounds and replated Cu, the distribution and spacing of these microcathodic sites relative to the diffusion boundary layer dimensions would then be important. In such a situation, it would be expected that the hemispherical boundary layer ( $\delta$ ) generated over these micro-regions would increase  $i_l$  provided the radius of the intermetallics ( $r$ ) is much smaller than  $\delta$ .<sup>57-58</sup> If  $\delta$  is much smaller than  $r$ , or the spacing between these intermetallics over a sufficient area is much smaller than  $r$ , the boundary layer would approximate to a planar rather than hemispherical behavior.

<sup>f</sup> An alternative suggestion is that  $i_{l(\text{net})} = i_{l(\text{true})} - i_{l(\text{anodic})}$ , such that cathodic erosion suppresses  $i_{l(\text{net})}$ . However, studies on Al with different oxide thickness support the claim that the oxide reduces  $i_l$  because  $i_l$  is lowered when Al oxides were thicker. Moreover, studies of Al cathodic kinetics suggest that cathodic corrosion rates should be negligible under conditions of this study.<sup>59-61</sup>

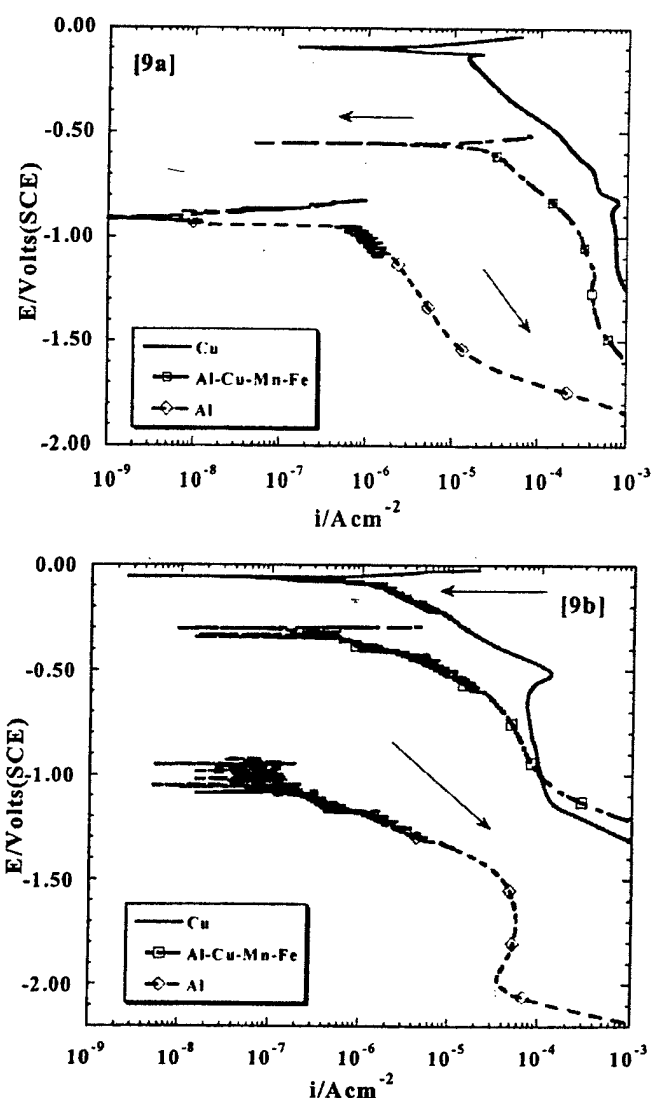


Figure 9.  $E$ -log  $i$  behavior of untreated (a) and 3 min CCC (b) Cu, Al-Cu-Mn-Fe intermetallic, and Al in 0.1 M  $\text{Na}_2\text{SO}_4$  + 0.005 M NaCl at 500 rpm ( $\omega^{0.5} = 7.24 \text{ (rad s}^{-1})^{0.5}$ ).

data for AA 2024-T3, and the intermetallics (Fig. 8), including data shown in Fig. 6 suggest that prior corrosion increases net cathodic kinetics. Figure 8d to f shows that 5 min CCC and the addition of soluble chromate (0.01 M) to the electrolyte (0.1 M  $\text{Na}_2\text{SO}_4$  + 0.005 M NaCl) have the effect of reducing the effects of prior corrosion. Net cathodic kinetics are lowered compared with the untreated analogue in 0.1 M  $\text{Na}_2\text{SO}_4$  + 0.005 M NaCl. At issue is whether the inhibition of cathodic kinetics is strictly due to minimization of OCP corrosion or results from other causes. The  $i_1$  vs.  $\omega^{0.5}$  data of 3 min CCC in 0.1 M  $\text{Na}_2\text{SO}_4$  + 0.005 M NaCl compared with the untreated analogue in the same electrolyte suggests that CCC could also act as a barrier to the ETR since higher angular velocities do not seem to increase the  $i_1$  (Fig. 10). This is not all together surprising since  $\text{Al}_2\text{O}_3$  is a known barrier to the ETR,<sup>5</sup> and  $\text{Cr}_2\text{O}_3$  covered Cr also experienced reduced cathodic kinetics in spite of it being a fairly conductive oxide (Fig. 11a). Indeed, prior studies have found that the rate of electron transfer between electrochemically passivated Cr and several redox couples decreased exponentially with passive film thickness between 5-25 Å.<sup>62</sup> The pores and cracks observed in the CCC might also act as a barrier to en-

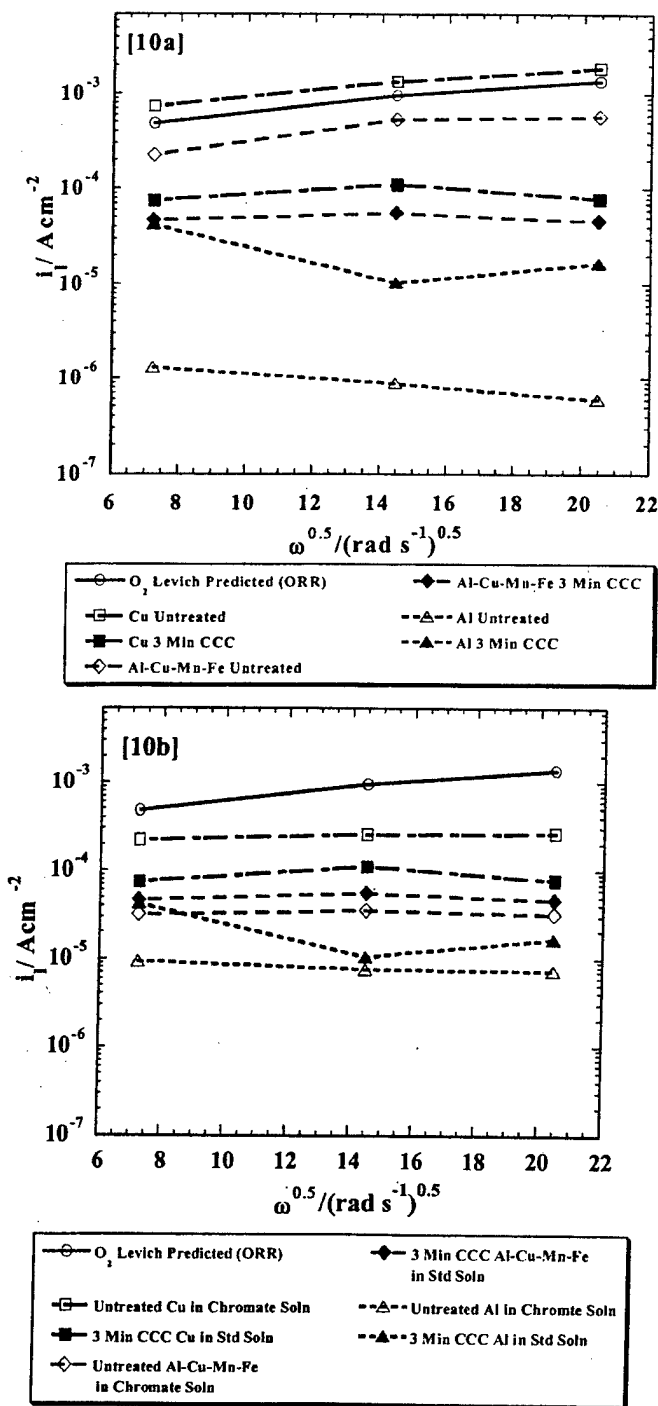
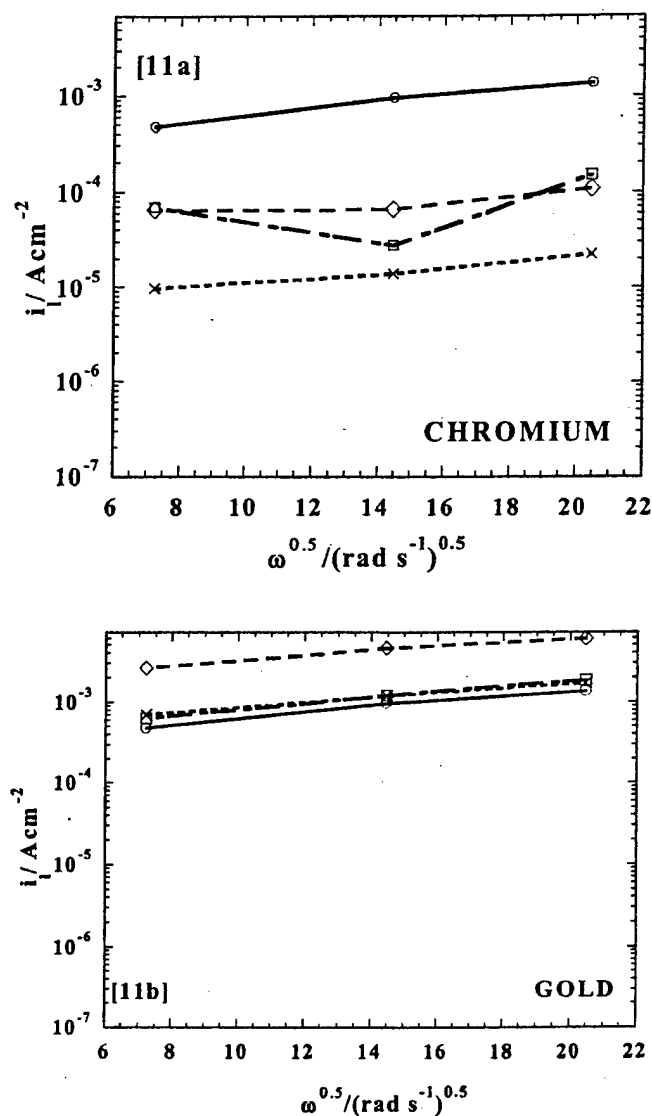


Figure 10. (a) Oxygen reduction limiting current density ( $i_1$ ) from rotating disk electrodes comparing untreated and 3 min CCC (a) Cu, Al-Cu-Mn-Fe intermetallic, and Al in 0.1 M  $\text{Na}_2\text{SO}_4$  + 0.005 M NaCl (standard solution). (b) Results from untreated samples in 0.1 M  $\text{Na}_2\text{SO}_4$  + 0.005 M NaCl + 0.0038 M  $\text{H}_2\text{CrO}_4$  + 0.0062 M  $\text{Na}_2\text{CrO}_4$  (chromate solution) compared to those from 3 min CCC in standard solution. Levich prediction at concentration of 6 ppm ( $1.88 \times 10^{-4}$  M) dissolved  $\text{O}_2$ .

hanced  $\text{O}_2$  transport to the surface of the metal generated by the stirring action of the electrode at high rotation rates.

XANES (Fig. 5) showed that  $\text{Cr}^{6+}$  is not only present in the CCC, but that the quantity of  $\text{Cr}^{6+}$  present increases with coating time. This is consistent with the findings of other authors who have described CCC as a reservoir for  $\text{Cr}^{6+}$  ions.<sup>9</sup> Earlier work<sup>39</sup> showed



**Figure 11.** Oxygen reduction limiting current density ( $i_l$ ) from rotating disk electrodes for (a) Cr and (b) Au in 0.1 M  $\text{Na}_2\text{SO}_4$  + 0.005 M NaCl,  $\square$ ; 0.1 M  $\text{Na}_2\text{SO}_4$  + 0.005 M NaCl + 0.0038 M  $\text{H}_2\text{CrO}_4$  + 0.0062 M  $\text{Na}_2\text{CrO}_4$ ,  $\diamond$ ; and in 0.1 M  $\text{Na}_2\text{SO}_4$  + 0.005 M NaCl after a 2 h pretreatment in 0.1 M  $\text{Na}_2\text{SO}_4$  + 0.005 M NaCl + 0.0038 M  $\text{H}_2\text{CrO}_4$  + 0.0062 M  $\text{Na}_2\text{CrO}_4$ ,  $\times$ . Levich prediction,  $\circ$ , at a concentration of 6 ppm ( $1.88 \times 10^{-4}$  M) dissolved  $\text{O}_2$ .

that competitive adsorption between chromate and  $\text{O}_2$  may cause fewer sites to be available for  $\text{O}_2$  reduction thereby resulting in a reduction in net cathodic kinetics albeit at more positive potentials not typical of the OCP of AA 2024-T3. From all of the above, it is quite apparent that the CCC system is a very complicated one with regard to the inhibition of mass transport limited ORR kinetics.

Four mechanisms for inhibition of mass transport limited ORR kinetics on CCC electrodes are therefore possible: (i) anodic inhibition, and a subsequent effect on cathodic kinetics through reduction in surface roughness, (ii) formation of a relatively poorly conducting phase that serves as a barrier to ETR, (iii) a physical barrier that diminishes  $\text{O}_2$  mass transport (because the expected reduction in  $\text{O}_2$  diffusion boundary layer due to electrode rotation does not penetrate into the coating's pores and cracks), and (iv) chromate ion blockage of electrode surface by competitive adsorption with  $\text{O}_2$  reduction sites.

**CCC as a corrosion (anodic) inhibitor.**—Prior corrosion damage in chromate-free solutions (before cathodic polarization) increases the net cathodic kinetics on a metal surface (Fig. 6). The degree to which the net cathodic kinetics are affected depends on the extent of prior corrosion damage. The OCP of AA 2024-T3 is close to the pitting potential due to the presence of  $\text{Cl}^-$  in the electrolyte (Fig. 8a). This results in pitting corrosion at OCP (Fig. 8a). Both CCC and soluble chromate (0.01 M) inhibit anodic (and hence OCP) corrosion on AA 2024-T3 and the Al-Cu-Mg intermetallic phase (Fig. 8a, b, and f), and is expected to also inhibit any OCP corrosion that might occur on the Al-Cu and Al-Cu-Mn-Fe intermetallics. This is consistent with the findings in earlier work.<sup>39,48</sup> CCC offers better inhibition of large matrix pit formation on the AA 2024-T3 matrix compared anodic inhibition on the Al-Cu-Mg intermetallic (Fig. 8a, b, and f). This gives credence to the notion that most intermetallic compounds found in AA 2024-T3 resist CCC formation and as a result generally possess poorer coatings compared with the rest of the Al matrix.<sup>15</sup> As a result, CCCs given minimal leaching of  $\text{Cr}^{6+}$  are by themselves not as effective as soluble chromate in offering corrosion protection on intermetallic compounds. However, Fig. 8b shows that CCC still offers some protection and, net cathodic kinetics are lowered compared to the untreated surfaces in 0.1 M  $\text{Na}_2\text{SO}_4$  + 0.005 M NaCl.

The mechanism by which CCCs are able to arrest corrosion is still unclear. Suggestions have been made that this might be connected to the  $\text{Cr}^{6+}$  ions, which these coatings carry in the pores and cracks.<sup>9,24,63</sup> However, experiments aimed at showing the release rate of  $\text{Cr}^{6+}$  ions from CCCs over a period of time showed that the amount of  $\text{Cr}^{6+}$  ions leached out into solution might not be enough to account for the extent of corrosion inhibition effected by these CCCs.<sup>24,48</sup> An alternative mechanism is that most of the chromate ions remain within the pores and cracks of the CCC where the small amounts of  $\text{Cr}^{6+}$  and slower ionic mobilities would be mitigated by the relatively shorter distances the ions have to travel to where they were needed to arrest corrosion.<sup>48</sup> However, authors such as Halada *et al.*<sup>15</sup> have indeed found very little  $\text{Cr}^{6+}$  ions in the CCC on Al-Cu-Mg intermetallics, which means less  $\text{Cr}^{6+}$  is available to arrest corrosion on chromate converted coated intermetallic compounds.  $\text{Cr}^{6+}$  reduction to  $\text{Cr}_2\text{O}_3$  could provide barrier corrosion protection of the intermetallic compounds. The vital result is brought about by CCCs and that this could account for some of the reduction in net cathodic reaction rate.

**CCC as a relatively poorly conducting phase that serves as a barrier to ETR.**—ORR studies on high purity Cr with a  $\text{Cr}_2\text{O}_3$  oxide address whether the presence of hydrated  $\text{Cr}_2\text{O}_3$  in the CCC reduces mass transport limited ORR kinetics (Fig. 11a). Pure Cr serves as a model for an intermetallic compound surface covered with  $\text{Cr}_2\text{O}_3$  (from the CCC process). The predicted value of  $i_l$  from the Levich equation is far higher than experimental data from Cr in 0.1 M  $\text{Na}_2\text{SO}_4$  + 0.005 M NaCl. When contrasted with the behavior of an ideal electronic conductor like Au (Fig. 11b), which has no oxide film, nor corrodes at OCP, the data suggests that formation of even the relatively conductive  $\text{Cr}_2\text{O}_3$  limited ETR. This is consistent with other studies of Cr.<sup>62</sup> Recall that the CCC is composed of a mixture of  $\text{Al}_2\text{O}_3$ , which does not support ETR easily,<sup>5</sup> and a hydrated chromium oxide (Eq. 1). All these taken together suggest that CCCs may act as an electronic barrier to ETR and, hence, might contribute to the reduction of the net ORR kinetics as observed in Fig. 10. This has been observed elsewhere where soluble chromate inhibited ORR kinetics on brass.<sup>64</sup>

The CCC did reduce the rate of the ORR on the intermetallic phase and Cu (Fig. 10a). However, the rates on Al increased. This is not surprising since the rate determining step on Al is not mass transport of  $\text{O}_2$  to the Al surface but likely the rate of the (ETR) across the  $\text{Al}_2\text{O}_3$  oxide film because it is either semiconducting or thin enough to allow tunneling.<sup>5</sup> The increase in the rate of the net cathodic current density on CCC Al surfaces may be due to the

modifications or destruction of the Al oxide film during the CCC process, specifically, the thinning by dissolution of the  $\text{Al}_2\text{O}_3$  oxide film by HF. The reasons for the reduction in the rate of the ORR on the intermetallics and Cu are more complicated. There is a difficulty in separating the contribution of the CCC as a physical barrier which hinders the hydrodynamically assisted transport of  $\text{O}_2$  due to rotation of the electrode, from its role as an electron transfer barrier, and from the contribution of chromate held within the pores of the CCC that can serve as an anodic inhibitor.

In experiments aimed at separating the intrinsic effects (*i.e.*, direct effects on ORR) from extrinsic effects (*e.g.*, reduction of OCP corrosion, oxide film alterations), RDE experiments were performed on gold (Au) electrodes. Au was chosen because it did not corrode at OCP, nor form an oxide film which could be altered by chromate as does even Pt.<sup>65</sup> On Au, the highest apparent ORR occurred when chromate was present in solution (Fig. 11b). This was most likely due to the additive effects of the ORR rate and the reduction of  $\text{Cr}^{6+}$  to  $\text{Cr}^{3+}$ . However, there was no effect on ORR when Au was pre-treated (immersed at OCP for 2 h) in chromate containing solution ( $0.1 \text{ M Na}_2\text{SO}_4 + 0.005 \text{ M NaCl} + 0.0038 \text{ M H}_2\text{CrO}_4 + 0.0062 \text{ M Na}_2\text{CrO}_4$ ) before cathodic polarization in nonchromate solution ( $0.1 \text{ M Na}_2\text{SO}_4 + 0.005 \text{ M NaCl}$ ) (Fig. 11b). The OCP of Au was below the reversible potential associated with  $\text{Cr}^{6+}$  to  $\text{Cr}^{3+}$  reduction suggesting that a Cr(III) deposit could have existed.

The role of the CCC solely as a barrier to ETR that reduces net cathodic kinetics on AA 2024-T3 is still not fully understood. A comparison of the ORR rate on 3-min CCC surfaces in  $0.1 \text{ M Na}_2\text{SO}_4 + 0.005 \text{ M NaCl}$  to untreated surfaces in the presence of chromate in solution (Fig. 10b) might suggest that the resistive electronic barrier role is not appreciable at least on the Al-Cu-Mn-Fe intermetallic and Al, since the net cathodic reaction rates on the chromate conversion coated surfaces are higher than without CCC. Therefore, while CCC tends to increase the deposit (coating) thickness by the production or formation of hydrated chromium oxides, the same process may actually decrease the ETR barrier by the possible dissolution of  $\text{Al}_2\text{O}_3$  by  $\text{F}^-$  contained in the coating solution.

**CCC as a physical barrier that diminishes  $\text{O}_2$  mass transport.**—The lack of any effect of  $\omega^{0.5}$  on  $i_1$  (Fig. 10) might also be partially attributed to the lack of penetration of  $\text{O}_2$  into the pores and cracks of the CCC during stirring assuming that  $\text{O}_2$  reduction occurs either at the metal/coating interface or at the base of pores in the CCC. The porous coating would control the “effective” boundary layer thickness at high stirring rates. This is similar to what is seen for ORR on metals in sea water with calcareous deposits.<sup>66</sup> Thus,  $\text{O}_2$  reduction is hampered and limited by the pores and cracks lengths in the CCC, which limit reduction in boundary layer thickness. While it could be argued that the “ETR barrier effect” of the CCC could also account for this observation, the role of the CCC as a barrier to hydrodynamically aided diffusive transport of  $\text{O}_2$  to the surface below CCC cannot be ruled out. The surfaces of CCCs are very rough and grow rougher as coating time increases (Fig. 4). According to CLSM imaging (Fig. 4), some of the pores and cracks in a 3 min CCC could be as deep as  $4 \mu\text{m}$ . Obviously, even under stirring generated by the rotation of the electrode, the rate at which  $\text{O}_2$  will diffuse to the openings of these cracks and pores will be different from the rate at which  $\text{O}_2$  will penetrate them. These pores and cracks could behave like barriers to diffusion of  $\text{O}_2$ . This is expected to have the effect of slowing down the rate of the ORR.

The expression for calculating the diffusion boundary layer thickness at the surface of a rotating disk electrode constructed of a perfect electronic conductor is given by<sup>67</sup>

$$\delta_{\text{sol}} = 1.61 D_{\text{sol}}^{1/3} \omega^{-1/2} \nu^{1/6} \quad [2]$$

where  $\delta_{\text{sol}}$  is the diffusion boundary layer thickness,  $D$  is the  $\text{O}_2$  diffusion coefficient,  $\omega$  is the angular velocity, and  $\nu$  is the kinematic viscosity.

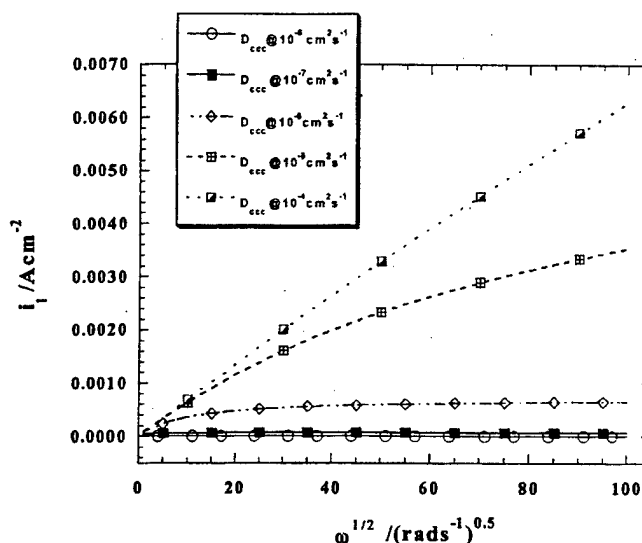


Figure 12.  $i_l$  as a function of  $\omega^{0.5}$  (square root of angular velocity) corrected for the contribution of the chromate conversion coating according to Eq. 5.  $D_{\text{ccc}}$  was varied between  $10^{-4}$  and  $10^{-8} \text{ cm}^2 \text{ s}^{-1}$ .  $\chi_{\text{ccc}}$  was taken to be  $1 \mu\text{m}$ .

matic viscosity. Rotation rates of 500, 2000, and 4000 rpm, which were employed in this work, translate to angular velocities of 52.36, 209.44, and 418.88  $\text{rad s}^{-1}$ , respectively. These angular velocities will give a diffusion boundary layer thickness of 28.6, 14.0, and  $10 \mu\text{m}$ , respectively (where  $D$  is  $1.9 \times 10^{-5} \text{ cm}^2 \text{ s}^{-1}$  and  $\nu$  is  $1.0 \times 10^{-2} \text{ cm}^2 \text{ s}^{-1}$ ). For mass transport limited ORR, the limiting current density is given by the expression

$$i_l = \frac{n F D C_{\text{bulk}}}{\delta_{\text{sol}}} \quad [3]$$

where  $\delta_{\text{sol}}$  is the  $\text{O}_2$  diffusion boundary layer thickness,  $D$  is the  $\text{O}_2$  diffusion coefficient,  $n$  is the number of electrons transferred to reduce 1 mol of  $\text{O}_2$ ,  $F$  is the Faraday constant, and  $C$  is the bulk solution concentration of  $\text{O}_2$ . If the coupled transport of  $\text{O}_2$  through the CCC out of the base of CCC pores is taken into consideration, Eq. 3 becomes<sup>68</sup>

$$i_l = \frac{n F C_{\text{bulk}}}{(\delta_{\text{sol}}/D_{\text{sol}}) + (\chi_{\text{ccc}}/D_{\text{ccc}})} \quad [4]$$

Here  $\delta_{\text{sol}}$  is the diffusion boundary layer thickness at the solution/CCC interface that is affected by stirring;  $D_{\text{sol}}$  and  $D_{\text{ccc}}$  are the diffusion coefficient of  $\text{O}_2$  in the solution and through the porous CCC serving as an interlayer, respectively. It is reasonable to assume that  $D_{\text{sol}} \gg D_{\text{ccc}}$ .  $\chi_{\text{ccc}}$  is the length of the porous layer of the CCC that is not affected by stirring,  $F$  is the Faraday constant and  $C$  is the bulk solution concentration of  $\text{O}_2$ . Substituting  $\delta_{\text{sol}}$  in Eq. 4 with the expression in Eq. 2 gives Eq. 5. The effect that a CCC has on the  $i_l$  of ORR kinetics is described by the set of curves in Fig. 12 based on Eq. 5

$$i_l = n F C_{\text{bulk}} \left( \frac{1}{(1.61 D_{\text{sol}}^{1/3} \nu^{1/6} / D_{\text{sol}} \omega^{1/2}) + (\chi_{\text{ccc}} / D_{\text{ccc}})} \right) \quad [5]$$

For the set of curves generated in Fig. 12,  $n = 4$ ,  $F = 96,500 \text{ A s}$ ,  $C_{\text{bulk}} = 1.875 \times 10^{-7} \text{ mol cm}^{-3}$ ,  $\nu = 1.0 \times 10^{-2} \text{ cm}^2 \text{ s}^{-1}$ ,  $D_{\text{sol}} = 1.9 \times 10^{-5} \text{ cm}^2 \text{ s}^{-1}$ ,  $\chi_{\text{ccc}}$  was taken as  $0.0001 \text{ cm}$ , and  $D_{\text{ccc}}$

<sup>68</sup> The full derivation of Eq. 4 can be found in Ref. 68.

was varied between  $10^{-4}$  to  $10^{-8}$   $\text{cm}^2 \text{s}^{-1}$ . The possibility of attaining a  $D_{\text{CCC}}$  value of  $10^{-4}$   $\text{cm}^2 \text{s}^{-1}$  is unlikely. However, for modeling purposes, this value was included to describe the circumstance under which Levich predictions were realized by nullifying the contribution of the CCC ( $\chi_{\text{CCC}}/D_{\text{CCC}}$ ). It is seen from Fig. 12 that even at a CCC thickness of 1  $\mu\text{m}$  (0.0001 cm), a chromate conversion coated surface would suppress ORR rates below Levich predictions and  $i_1$  would be weakly dependent on  $\omega^{0.5}$  as observed experimentally. Thus, high RDE rotation, which lowers  $\delta_{\text{sol}}$ , has no effect on  $D_{\text{CCC}}$  or  $\chi_{\text{CCC}}$ . The behavior of coated electrodes in Fig. 10 can be explained in part with the behavior of the curves in Fig. 12. The implication is that corrosion of micrometer scale intermetallic compounds embedded in the Al-matrix would not support cathodic reactions of the massive transport limited  $i_1 \propto 1/r$ , where  $r$  is the radius of the intermetallic compound. This analysis considers no effect of CCCs on  $n$ , or the effect on the  $\text{O}_2$  reduction reaction mechanism. Comparison of Fig. 10 to Fig. 12 suggests that some other inhibiting factor is still operative.

**CCC as a source of chromate ions, which block electrode surface reduction sites by competitive adsorption with  $\text{O}_2$ .**—Prior work showed some evidence of competitive adsorption for reduction sites between  $\text{O}_2$  and chromate species such as  $\text{CrO}_4^{2-}$  and  $\text{Cr}_2\text{O}_7^{2-}$  in 0.1 M  $\text{Na}_2\text{SO}_4 + 0.005 \text{ M NaCl} + 0.0062 \text{ M Na}_2\text{CrO}_4 + 0.0038 \text{ M H}_2\text{CrO}_4$ , albeit at potentials not typical of the OCP of corroding AA 2024-T3.<sup>39</sup> These experiments indicated that the ORR when under charge transfer and mixed charge transfer-mass transport-controlled conditions on Au and Cu electrodes deviated from ideal ORR behavior in the electrolyte.<sup>39</sup> The ORR kinetic behavior of these electronic conductors was described by a modified Langmuir adsorption isotherm, which satisfactorily described a situation where anionic chromate species blocked  $\text{O}_2$  adsorption sites on the metal surfaces unless potentials become negative. Chromate reduction would also block sites at cathodic potentials if the reaction products, once formed by reduction, limited ORR below its theoretical mass transport limited controlled limit. Nevertheless, since the rate of ORR on CCC Al surfaces are higher than on pure Al (Fig. 10), these effects did not seem to be strong factors on CCC surfaces of Al-based materials, but could be operative on Cu-bearing materials.

### Conclusions

1. Net cathodic mass transport limited ORR kinetics are enhanced on intermetallics and bulk Cu compared to pure Al in 0.1 M  $\text{Na}_2\text{SO}_4 + 0.005 \text{ M NaCl}$ . Reaction rates are close to the predictions of the Levich Equation.

2. ORR kinetics on Al-Cu-Mn-Fe and bulk Cu are still higher (compared to pure Al) in the presence of CCC over the observed range of disk rotation rates, but do not follow the predictions of the Levich equation. This could be partially explained by the role of the CCC as a diffusive barrier.

3. The decrease in ORR kinetics observed on chromate conversion coated RDE of Cu-bearing electrodes: Cu and Al-Cu-Mn-Fe. This was also at least partly due to the suppression of prior corrosion at OCP. The role(s) of the CCC as a barrier to ETR or as an  $\text{O}_2$  reduction site blocker are complicated by an inability to separate all the variables.

4. ORR kinetics on Cr fall below predictions of the Levich equation. Thus, the thin  $\text{Cr}_2\text{O}_3$  oxide limits electron transfer. However, reduction of the rates of ORR due to  $\text{Cr}_2\text{O}_3$  formation on chromate conversion coated Al-rich surfaces may be offset by speculated  $\text{Al}_2\text{O}_3$  alteration or destruction on Al-based materials.

### Acknowledgments

Funding from Air Force Office of Scientific Research (Major Paul Trulove, Program Manager, grant no. F49620-96-1-0178) is gratefully acknowledged. Intermetallics were supplied of the Aluminum Company of America (ALCOA). The CESE gratefully acknowledges on-going support of EG&G Instruments and Scribner

Associates, Inc. Dr. Oliver Schneider is thanked for his assistance with the CLSM.  $\text{Cr}^{6+}$  (content) measurements of the chromate conversion coating of AA 2024-T3 panels were carried out by H. S. Isaacs and C. S. Jeffcoat at BNL and supported by DOE contract no. DE-AC02-98CH10886. C. S. Jeffcoat was supported by Air Force Office of Scientific Research, contract no. F49620-96-1-0479.

The University of Virginia assisted in meeting the publication costs of this article.

### References

- G. S. Chen, M. Gao, and R. P. Wei, *Corrosion*, **52**, 8 (1996).
- R. G. Buchheit, R. P. Grant, P. F. Hlava, B. McKenzie, and G. L. Zender, *J. Electrochem. Soc.*, **144**, 2621 (1997).
- G. S. Chen, C.-M. Liao, K.-C. Wan, M. Gao, and R. P. Wei, ASTM STP 1298, W. A. Van Der Sluis, R. S. Piascik, R. Zawierucha, Editors, p. 18, ASTM, Philadelphia, PA (1997).
- J. R. Scully, T. O. Knight, R. G. Buchheit, and D. E. Peebles, *Corros. Sci.*, **35**, 185 (1993).
- M. J. Pryor and D. S. Keir, *J. Electrochem. Soc.*, **102**, 241C (1955).
- R. G. Buchheit, *J. Electrochem. Soc.*, **142**, 3994 (1995).
- P. L. Hagans and C. M. Haas, in *ASM Handbook*, 10th ed., Vol. 5, p. 405, ASM International, Materials Park, OH (1994).
- Z. A. Foroulis and M. J. Thubrikar, *J. Electrochem. Soc.*, **122**, 1296 (1975).
- P. L. Hagans and C. M. Haas, *Surf. Interface Anal.*, **21**, 65 (1994).
- N. J. Newhard, Jr., *Met. Finish.*, **70**, 49 (1972).
- A. E. Hughes, R. J. Taylor, and B. R. W. Hinton, *Surf. Interface Anal.*, **25**, 223 (1997).
- F. W. Lytle, R. B. Gregor, G. L. Bibbins, K. Y. Blohowiak, R. E. Smith, and G. D. Tuss, *Corros. Sci.*, **37**, 349 (1995).
- Z. Yu, H. Ni, G. Zhang, Y. Wang, S. Dong, and G. Zhao, *Appl. Surf. Sci.*, **62**, 217 (1992).
- N. J. Newhard, Jr., *Met. Finish.*, **70**, 66 (1972).
- G. P. Halada, C. R. Clayton, M. J. Vasquez, J. R. Kearns, M. W. Kendig, S. L. Jeanjaquet, G. G. Peterson, G. S. McCarthy, and G. L. Carr, in *Proceedings of the Symposium on Critical Factors in Localized Corrosion III*, PV 98-17, p. 139, The Electrochemical Society Proceedings Series, Pennington, NJ (1999).
- J. R. Waldrop and W. M. Kendig, *J. Electrochem. Soc.*, **145**, L11 (1998).
- L. Xia and L. McCreery, *J. Electrochem. Soc.*, **146**, 3696 (1999).
- W. R. McGovern, P. Schmutz, R. G. Buchheit, and R. L. McCreery, *J. Electrochem. Soc.*, **147**, 4494 (2000).
- J. S. Wainright, O. J. Murphy, and M. R. Antonio, *Corros. Sci.*, **33**, 281 (1992).
- L. Xia and L. McCreery, *J. Electrochem. Soc.*, **145**, 3083 (1998).
- K. Asami, M. Oki, G. E. Thompson, G. C. Woods, and V. Ashworth, *Electrochim. Acta*, **32**, 337 (1987).
- M. W. Kendig, A. J. Davenport, and H. S. Isaacs, *Corros. Sci.*, **34**, 41 (1993).
- T. Drozda and E. Maleczki, *J. Radioanal. Nucl. Chem. Lett.*, **95**, 339 (1985).
- J. Zhao, G. Frankel, and R. L. McCreery, *J. Electrochem. Soc.*, **145**, 2258 (1998).
- H. A. Katzman, G. M. Malouf, R. Bauer, and G. W. Stupian, *Appl. Surf. Sci.*, **2**, 416 (1979).
- J. A. Richardson and G. C. Wood, *J. Electrochem. Soc.*, **120**, 193 (1973).
- H. Bohni and H. H. Uhlig, *J. Electrochem. Soc.*, **116**, 906 (1969).
- S. Matsuda and H. H. Uhlig, *J. Electrochem. Soc.*, **111**, 156 (1964).
- G. B. Hatch, in *Corrosion Inhibitors*, C. C. Nathan, Editor, p. 126, NACE, Houston, TX (1973).
- C. S. Jeffcoat, H. S. Isaacs, J. Hawkins, and G. E. Thompson, Abstract 234, The Electrochemical Society Meeting Abstracts, Vol. 98-2, Boston, MA, Nov. 1-6, 1998.
- S. T. Pride, J. R. Scully, and J. L. Hudson, *J. Electrochem. Soc.*, **141**, 3028 (1994).
- F. Hunkeler and H. Bohni, *Corrosion*, **37**, 645 (1981).
- A. Sehgal, D. Lu, and G. S. Frankel, *J. Electrochem. Soc.*, **145**, 2834 (1998).
- G. M. Brown, K. Shimizu, K. Kobayahi, G. E. Thompson, and G. C. Wood, *Corros. Sci.*, **33**, 1371 (1992).
- G. M. Brown, K. Shimizu, K. Kobayahi, G. E. Thompson, and G. C. Wood, *Corros. Sci.*, **33**, 1045 (1992).
- M. Kendig and S. Jeanjaquet, Abstract 228, The Electrochemical Society Meeting Abstracts, Vol. 98-2, Boston, MA, Nov. 1-6, 1998.
- E. Akiyama and G. S. Frankel, *J. Electrochem. Soc.*, **146**, 4095 (1999).
- A. Sehgal, G. S. Frankel, B. Zoofan, and S. Rokhlin, *J. Electrochem. Soc.*, **147**, 140 (2000).
- G. O. Ilevbare and J. R. Scully, *Corrosion*, To be published.
- C. Blanc, B. Lavelle, and G. Mankowski, *Corros. Sci.*, **39**, 495 (1997).
- R. P. Wei, C.-M. Liao, and M. Gao, *Metall. Trans. A*, **29A**, 1153 (1998).
- Metals Handbook*, Vol. 2, 8th ed., p. 628, ASM International, Materials Park, OH (1964).
- Military Standard MIL-STD-1503B (USAF), p. 7 (Nov 1989).
- M. F. Stevenson, Jr., in *ASM Handbook*, Vol. 5, 10th ed., p. 482, ASM International, Metals Park, OH (1994).
- Annual Book of ASTM Standards*, section 6, Vol. 06.01, p. 1, ASTM, Philadelphia, PA (1992).
- C. S. Jeffcoat, H. S. Isaacs, A. J. Aldykiewicz, Jr., and M. P. Ryan, *J. Electrochem. Soc.*, **147**, 540 (2000).

# Inhibition of Pitting Corrosion on Aluminum Alloy 2024-T3: Effect of Soluble Chromate Additions vs Chromate Conversion Coating

G.O. Ilevbare, J.R. Scully, J. Yuan, and R.G. Kelly\*

## ABSTRACT

Pitting potentials ( $E_{pit}$ ) of aluminum alloy (AA) 2024-T3 (UNS A92024) were improved with additions of 0.01 M sodium chromate ( $\text{Na}_2\text{CrO}_4$ , pH 8) and 0.0062 M  $\text{Na}_2\text{CrO}_4$  + 0.0038 M chromic acid ( $\text{H}_2\text{CrO}_4$ , pH 6) additions to 0.1 M sodium sulfate ( $\text{Na}_2\text{SO}_4$ ) + 0.005 M sodium chloride ( $\text{NaCl}$ , pH 6) after 2-h periods at open-circuit potential (OCP). Chromate conversion coatings (CCC) on AA 2024-T3 also improved  $E_{pit}$  in 0.1 M  $\text{Na}_2\text{SO}_4$  + 0.005 M  $\text{NaCl}$ . However, CCC did not improve the  $E_{pit}$  determined in fast potentiodynamic scans without periods at OCP. These tests were designed to minimize chromate leaching and long-range transport of chromate. The OCP of CCC AA 2024-T3,  $\text{Al}_2\text{Cu}$ ,  $\text{Al}_2\text{CuMg}$ , 99.999% Cu, and 99.998% Al were not changed significantly in 0.1 M  $\text{Na}_2\text{SO}_4$  + 0.005 M  $\text{NaCl}$ . Moreover, the OCP of AA 2024-T3,  $\text{Al}_2\text{Cu}$ ,  $\text{Al}_2\text{CuMg}$ , and 99.999% Cu were not changed significantly in 0.1 M  $\text{Na}_2\text{SO}_4$  + 0.005 M  $\text{NaCl}$  with the addition of 0.01 M soluble chromate at pH 6 and pH 8. The mass transport limiting current density for  $\text{O}_2$  reduction also was not altered significantly by CCC or soluble chromate additions. Consequently, if the AA 2024-T3 matrix were polarized locally to the measured OCP of the intermetallics or replated copper, inhibition of stable pitting on AA 2024-T3 is more likely to result from suppressed pit stabilization (in 0.1 M  $\text{Na}_2\text{SO}_4$  + 0.005 M  $\text{NaCl}$  with the addition of chromate at pH 6 or pH 8, or with CCC) than from eliminating two aspects associated with the potency of local galvanic couples (e.g., OCP of cathode sites and their oxygen reduction reaction kinetics [ORR]).

**KEY WORDS:** aluminum alloy, chromate conversion coatings, copper, intermetallics, open-circuit potential, oxygen reduction reaction kinetics, pitting potential

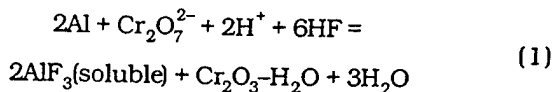
## INTRODUCTION

Al-based, precipitation age-hardened alloys containing Cu and Fe are particularly prone to localized corrosion such as pitting and/or alkaline attack either at constituent particles or caused by replated Cu.<sup>1-6</sup> It is well known that chromate conversion coating (CCC) and anodization of Al precipitation age-hardened alloys improve corrosion resistance, particularly in salt spray testing.<sup>7-10</sup> Therefore, improvements in the salt spray corrosion performance of such surface-treated alloys at open circuit suggest that either one or more of the four stages of localized corrosion at the anode site (i.e., nucleation, stabilization, growth, and repassivation) or the properties of the most active cathode sites (e.g., intermetallic phases and replated Cu) are altered by the presence of the CCC. The present work provides preliminary insight into the effects of CCC on pitting and intermetallic electrochemistry when  $\text{Cr}^{6+}$  is available within the CCC, and when it is leached into the solution in the form of soluble  $\text{Cr}^{6+}$ .<sup>11-14</sup> Chromate is highly soluble in water and is an extremely effective solution phase corrosion inhibitor, particularly for localized corrosion,<sup>15-18</sup> but exact mechanisms of inhibition are subject to debate.

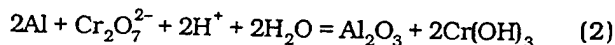
The CCC process on Al in a dichromate solution containing sodium fluoride (NaF) involves the following overall electrochemical reactions:<sup>12-14</sup>

Submitted for publication March 1999; in revised form, October 1999.

\* Center for Electrochemical Science and Engineering, Department of Materials Science and Engineering, University of Virginia, Charlottesville, VA 22903-2442.



If only a small amount of HF is present, then aluminum oxide ( $\text{Al}_2\text{O}_3$ ) is formed as well and the overall reaction is:



Thus, CCC consist of a mixture of regions of chromium (III) hydroxide ( $\text{Cr}(\text{OH})_3$ ) at sites where chromate was reduced along with regions of  $\text{Al}_2\text{O}_3$ .  $\text{Cr}^{6+}$  and  $\text{Cr}^{3+}$  may exist within the CCC in several specific forms.<sup>19-21</sup> Generally, it is believed that reduction of  $\text{Cr}^{6+}$  to  $\text{Cr}^{3+}$  in the form of hydrated chromium oxide is incomplete and that CCC typically contain 9% to 60%  $\text{Cr}^{6+}$  chromate.<sup>11-13,22</sup> Aging of coatings affects the apparent amount of  $\text{Cr}^{6+}$  present and the amount subsequently available to be leached.<sup>23-24</sup>

Exact mechanisms by which chromate or CCC inhibits metallic corrosion remain unclear and may differ in solutions of different halide/anion ratios, temperatures,<sup>25-27</sup> and pit sizes.<sup>17,28</sup> Anodic inhibition of small Al pits in dilute chloride may be observed in sodium chloride (NaCl) solutions containing soluble chromate additions,<sup>17</sup> but is not always observed.<sup>29</sup> Anodic inhibition of pits at high chloride/chromate ratios apparently is not seen.<sup>23,29</sup> Apparent cathodic inhibition of intermetallics has been reported but is subject to further investigation.<sup>29-30</sup>

In the present study, the influence of  $\text{Cr}^{6+}$  present within a CCC was compared and contrasted to the role of soluble  $\text{Cr}^{6+}$  added in solution on the initiation and stabilization of micrometer-sized pits; the open-circuit potentials (OCP) of intermetallics that enable galvanic coupling; and  $\text{O}_2$  reduction diffusion-limited current densities. Open-circuit pitting in Al-Cu and Al-Cu-Mg alloys often is observed to occur in the matrix adjacent to intermetallic particles because of local galvanic coupling.<sup>3-6,31-33</sup> At issue is whether chromate affects pit sites or alters the galvanic driving force of local corrosion on AA 2024-T3 (UNS A92024)<sup>(1)</sup>. In this study, soluble chromate was found to inhibit pit sites formed in potentiodynamic scans and affected the OCP of Al and  $\text{Al}_{20}\text{Cu}_2(\text{MnFe})_3$ , but did not affect the OCP of other tested intermetallics. CCC were found to inhibit open-circuit pitting but did not affect the OCP of the intermetallics with the exception of  $\text{Al}_{20}\text{Cu}_2(\text{MnFe})_3$ .

## EXPERIMENTAL PROCEDURES

Studies were conducted on 1.5-mm thick AA 2024-T3 sheets with the composition (wt%): 4.5% Cu,

1.30% Mg, 0.62% Mn, 0.18% Fe, 0.10% Zn, 0.093% Si, 0.018% Ti, 0.012% Ga, 0.011% V, 0.009% Cr, 0.008% Ni, 0.005% Zr, 0.003% Pb, 0.0006% Sc, < 0.002% Bi, < 0.0005% Co, < 0.0005% Ge, and bal. Al.

Other materials studied were Al-4% Cu, 99.998% Al,  $\text{Al}_2\text{Cu}$ ,  $\text{Al}_2\text{CuMg}$ , 99.999% Cu, and  $\text{Al}_{20}\text{Cu}_2(\text{MnFe})_3$ . Al-4% Cu was solution heat-treated (SHT) at 535°C for 1 h and quenched in water. Two scanning electron microscopy-energy dispersive spectroscopy (SEM-EDS) studies on AA 2024-T3 of similar composition indicated that the predominant micrometer-sized intermetallic phases detected were of the Al-Cu-Mg and Al-Cu-Fe-Mn type<sup>5-6,31-32</sup> with a lesser amount of the Al-Fe-Cu.<sup>6</sup> The  $\text{Al}_{12}\text{Si}(\text{MnFe})_3$  phase was not detected, possibly as a result of low Si contents.<sup>5</sup> Precipitate phases studied were  $\text{Al}_2\text{Cu}$  and S- $\text{Al}_2\text{CuMg}$ . Constituent particles of interest were  $\text{Al}_7\text{Cu}_2\text{Fe}$  and  $\text{Al}_{20}\text{Cu}_2(\text{MnFe})_3$ . The constituent particle  $\text{Al}_{12}\text{Si}(\text{MnFe})_3$  and common dispersoids in AA 2024-T3 ( $\text{Al}_6\text{Mn}$ ,  $\text{Al}_{20}\text{Cu}_2\text{Mn}_3$ ) were not investigated. Estimations from Al-Cu-Mg ternary phase equilibria at 430°C, where micrometer-sized  $\text{Al}_2\text{CuMg}$  second phases might remain undissolved, indicated that the weight fraction of  $\text{Al}_2\text{CuMg}$  (S phase) present was 5.13%, and the weight fraction of  $\text{Al}_2\text{Cu}$  ( $\theta$  phase) present was 4.55% in equilibrium with an Al-rich solid solution. However, if 3% Cu depletion occurs (i.e., falls by 3%) by partitioning of Cu to other Mn or Fe-rich constituents formed during solidification,<sup>34</sup> then the equilibrium weight fraction of S becomes 2.61% and that of  $\theta$  drops to 0.47%. This was consistent with one study that did not find  $\theta$  microconstituents.<sup>6</sup> Presented results concentrated on synthesized  $\text{Al}_2\text{Cu}$ ,  $\text{Al}_2\text{CuMg}$ , and  $\text{Al}_{20}\text{Cu}_2(\text{MnFe})_3$  electrodes that were mechanically ground with silicon carbide (SiC) paper. X-ray diffraction results on these castings indicated that these selected synthesized electrodes consisted predominantly of the aforementioned intermetallic phases. Moreover, a range of electrode sizes (0.0009  $\text{cm}^2$  to 0.185  $\text{cm}^2$ ) and metallographic techniques were used in attempt to isolate regions consisting of a single phase for study. The  $\text{Al}_7\text{Cu}_2\text{Fe}$  phase was not synthesized successfully and is not reported further.

CCC was performed in-house using solutions containing 0.025 M sodium dichromate ( $\text{Na}_2\text{Cr}_2\text{O}_7$ ), 0.024 M NaF, 0.015 M potassium hexacyano ferrate III ( $\text{K}_3\text{Fe}(\text{CN})_6$ ), and nitric acid ( $\text{HNO}_3$ , added until desired pH was attained). The pH of the solution was 1.2 to 2.2. CCC was conducted after conventional cleaning procedures.<sup>35-37</sup> Coating times of 30, 180, 300, and 480 s were investigated. Intermetallics were coupled to AA 2024-T3 during alkaline cleaning, desmutting, and conversion coating. Intermetallics were wet-ground to a 600-grit finish, alkaline cleaned, and desmuted before CCC. Intermetallics, not CCC, were wet-ground to a 600-grit finish before

<sup>(1)</sup> UNS numbers are listed in *Metals and Alloys in the Unified Numbering System*, published by the Society of Automotive Engineers (SAE) and cosponsored by ASTM.



experimentation. AA 2024-T3 samples were degreased, alkaline cleaned, desmutted, and conversion coated. Others were degreased only and are referred to as untreated. CCC was compared to sulfuric acid ( $\text{H}_2\text{SO}_4$ ) anodization. The alkaline cleaning solution contained 0.21 M sodium carbonate ( $\text{Na}_2\text{CO}_3$ ) and 0.23 M sodium phosphate ( $\text{Na}_3\text{PO}_4$ , pH 13) while the desmutting solution was 50% (by volume)  $\text{HNO}_3$ . The AA 2024-T3 sheets used for anodization were degreased prior to anodization. Anodization was carried out galvanostatically at a current density of  $0.015 \text{ A/cm}^2$  for 30 min in 20% (by wt)  $\text{H}_2\text{SO}_4$ .<sup>37</sup> The thickness of anodized film was estimated to be  $\sim 15 \mu\text{m}$  to  $20 \mu\text{m}$ <sup>37</sup> vs  $0.1 \mu\text{m}$  to  $1.0 \mu\text{m}$  for CCC.<sup>38</sup> Sheets also were coated with commercially supplied Alodine 1200<sup>†</sup> (Parker Amchem [now Henkel Corporation]) for 30 s and 180 s. Salt spray testing was performed according to ASTM B117 specifications for CCC AA 2024-T3 by an outside laboratory to verify corrosion inhibition.<sup>39</sup> All electrochemical testing was conducted on specimens between 48 h to 120 h old, and the presence of  $\text{Cr}^{6+}$  in CCC of this age was verified for all treatments using x-ray absorption spectroscopy (XAS).<sup>(2)</sup>

OCP and potentiodynamic polarization measurements were utilized to investigate pitting. It is now commonly accepted that the conventional pitting potential is a measure of stabilization of micropits that may have formed at potentials below the pitting potential.<sup>17,40</sup> Pitting potentials were determined using the criterion that pitting would have occurred by the time the anodic current density of the specimen reached  $3 \times 10^{-5} \text{ A/cm}^2$ , and hence, this apparent current density criterion was taken to be the pitting threshold for the various systems.<sup>17,32,41-43</sup> At this current density, enough anodic charge would have been passed so that pitting potentials reflected pit stabilization of pits large enough to include the matrix and not solely dissolution of a small region of S phase or metastable pitting. Cumulative probability plots were constructed using procedures reported elsewhere.<sup>44</sup>

Two measures were taken to decouple and distinguish possible effects of time-dependent chromate leaching and long-range chromate transport from the possible effects of a thick conversion coating or oxide barrier that might hinder  $\text{Cl}^-$  ion ingress and penetration. Large volume/electrode surface area cells ( $> 250 \text{ cm}^3$  per  $1 \text{ cm}^2$  of electrode surface area with a solution depth of 9 cm), short times at OCP, and moderately fast scan rates ( $1 \text{ mV/s}$ ) were used to limit test duration. This allowed the investigation of pit initiation and stabilization ( $E_{\text{pit}}$ ), decoupled from

the influence of significant chromate leaching. These experiments were completed in  $< 10^3 \text{ s}$ . Separate OCP pitting experiments were conducted in small volume cells ( $< 2 \text{ cm}^3$  per  $\sim 1 \text{ cm}^2$  of electrode surface area, solution depth of 1.2 cm to 1.5 cm) over  $10^6 \text{ s}$ .<sup>(3)</sup> A remotely located saturated calomel electrode (SCE) was used to detect potential fluctuations. The data acquisition rate was 1 Hz. The goal of these long-term OCP experiments was to create conditions under which leached chromates from CCC might be present in sufficient concentrations to affect potential transients associated with formation and growth of small pits not driven potentiostatically. These tests were conducted in 0.05 M NaCl exposed to lab air such that the OCP was near, but below,  $E_{\text{pit}}$ .

Chromate leaching experiments were conducted on commercial PA1200s (Alodine 1200s coating) and in-house chromate-coated samples by exposing samples to small volumes of deionized water for  $> 3,000 \text{ h}$ . Surface area/solution volume ratios of  $2:1 \text{ cm}^2/\text{mL}$  and  $116:9 \text{ cm}^2/\text{mL}$  (actual volume) were used for the PA1200s and in-house chromate samples, respectively. Aliquots of 0.1 mL were removed periodically for analysis. Aliquots were not returned to the cell after analyses. The volume of the cell solution was maintained by the addition of high-purity water. The aliquots were analyzed using capillary electrophoresis (CE) on Quanta 4000<sup>†</sup> system (Waters Co.). Fused-silica capillaries of  $75 \mu\text{m}$  inner diameter (ID) and 60 cm length were used.

The CE electrolyte used was 25 mM phosphate buffer (12.5 mM potassium dihydrogen phosphate [ $\text{KH}_2\text{PO}_4$ ] + 12.5 mM disodium hydrogen phosphate [ $\text{Na}_2\text{HPO}_4$ ] + 1 mM osmotic flow modifier in the hydroxide form [OFM-OH]), which was adjusted to pH 8 before use. The OFM-OH was prepared by passing 10 mM tetradecyl-trimethyl-ammonium bromide solution through an anion-exchange resin (Bio-Rad AG 1-X2<sup>†</sup>) that previously had been rinsed several times with 0.1 sodium hydroxide (NaOH) and high-purity water. Sample aliquots were separated in the capillary by imposition of a constant migration current of 50  $\mu\text{A}$ . Hydrostatic injection was used with a sampling time of 30 s and a height of 10 cm. Ultra-violet (UV) absorption measurements at 185 nm (using a mercury lamp) were used for the detection of chromate.

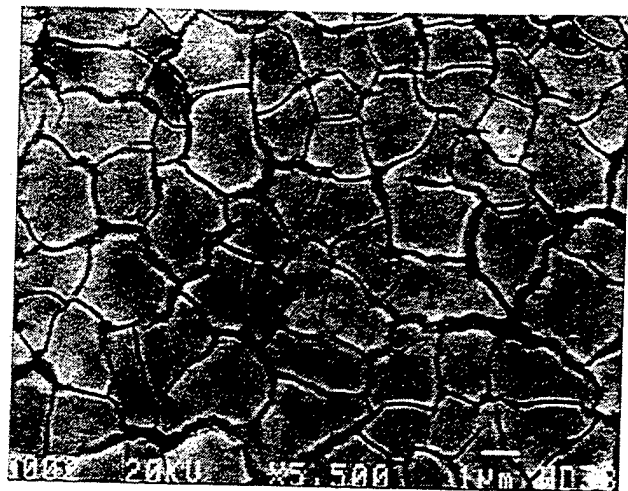
Polarization experiments were performed in quiescent 0.1 M sodium sulfate ( $\text{Na}_2\text{SO}_4$ ) + 0.005 M NaCl (pH 6), which was selected based on characterization of corrosive environments found in the lap joints of aircraft.<sup>45</sup> In these joints, many other anions often exceeded the concentration of  $\text{Cl}^-$ . This environment is more realistic for aging aircraft than more concentrated NaCl solution (e.g., 0.1 M to 1.0 M NaCl) and provides an environment where effects of inhibiting treatments on OCP and  $E_{\text{pit}}$  can be seen independently.  $E_{\text{pit}}$  is lowered significantly as a function of

<sup>†</sup> Trade name.

<sup>(2)</sup> XAS was conducted at National Synchrotron Light Source (NSLS) at Brookhaven National Laboratory (BNL).

<sup>(3)</sup> Cathodic scans on Pt in this cell indicated negligible effect of 1.2 cm depth and small volume on  $\text{O}_2$  reduction limiting current density or Pt OCP.





(a)



(b)



(c)

**FIGURE 1.** (a) Mud-crack morphology of the CCC (3-min CCC on AA 2024-T3). (b) 180-s CCC AA 2024-T3 showing the interior for pits formed during the cleaning (alkaline cleaning and desmutting) process. It clearly shows that the interior of the pits are coated. (c) Even at 30 s of coating, mud-crack morphology is still clearly visible inside this pit.

Cl<sup>-</sup>. OCP above  $E_{pit}$  could not be achieved on AA 2024-T3 in concentrated NaCl because of the nonpolarizability of active anodic pit reactions at and above  $E_{pit}$ , where the number of pits, pit size, and growth kinetics of pits increased rapidly with applied potential. This behavior would obscure observation of separate effects of treatment on OCP and  $E_{pit}$  in a polarization scan. In other experiments, 0.01 M sodium chromate ( $Na_2CrO_4$ ) was added to 0.1 M  $Na_2SO_4$  + 0.005 M NaCl to provide soluble chromate. At pH 6, the composition of the electrolyte was 0.1 M  $Na_2SO_4$  + 0.005 M NaCl + 0.0062 M  $Na_2CrO_4$  + 0.0038 M chromic acid ( $H_2CrO_4$ ). At pH 6, the chromate species existed in solution as a mixture of  $H_2CrO_4$  (ca., 50%), dichromate ( $Cr_2O_7^{2-}$  [ca., 30%]), and  $H_2CrO_4$  (ca., 20%). The composition of the electrolyte at pH 8 was 0.1 M  $Na_2SO_4$  + 0.005 M NaCl + 0.01 M  $Na_2CrO_4$ . At this pH, chromate ( $CrO_4^{2-}$ ) was the predominant species in solution (ca., 96%).<sup>46-47</sup>

## RESULTS

### Salt Spray Testing of CCC vs Untreated AA 2024-T3

Secondary electron microscopy images of the surface of the in-house CCC on AA 2024-T3 with a coating time of 180 s revealed a mud-crack appearance (Figure 1[a]). This appearance might have been a result of the dehydration of the coating during the drying process. Transmission electron micrographs of ultramicrotomed sections of aluminum substrates with CCC by other authors revealed similar appearances in their coatings.<sup>48-49</sup> Figures 1(b) (coating time: 180 s) and (c) (coating time: 30 s) show the presence of pits on the surface of the CCC AA 2024-T3. Photos of other secondary electron microscopy images taken right after the desmutting process (just before CCC was applied) revealed that these pits already were present at this stage. As can be seen from these images, the interior of the pits was covered completely by the CCC even after a coating time of 30 s.

The summary of the times until failure from the salt spray test appears in Figure 2.<sup>(4)</sup> The 30-s and 180-s in-house CCC AA 2024-T3 passed salt spray test (ASTM B-117)<sup>39</sup> as specified by MIL-C-81706 and MIL-C-5541E,<sup>50</sup> with the exception of the sheets coated in-house with Alodine 1200 for 30 s (A30). These results also showed that the in-house CCC performed as well as Alodine 1200 prepared commercially and better than the Alodine 1200 coating prepared in the laboratory. This result was significant because it indicated that the CCC used and

<sup>(4)</sup> MIL-C-445 1E (qualification): Failure is said to have occurred if five or more corrosion pits are found on the test panel after 168 h of ASTM B 117 salt spray test.

MIL-C-81706 (quality conformance): Failure is said to have occurred if any visual evidence of corrosion is found on the test panel after 168 h of ASTM B 117 salt spray test.

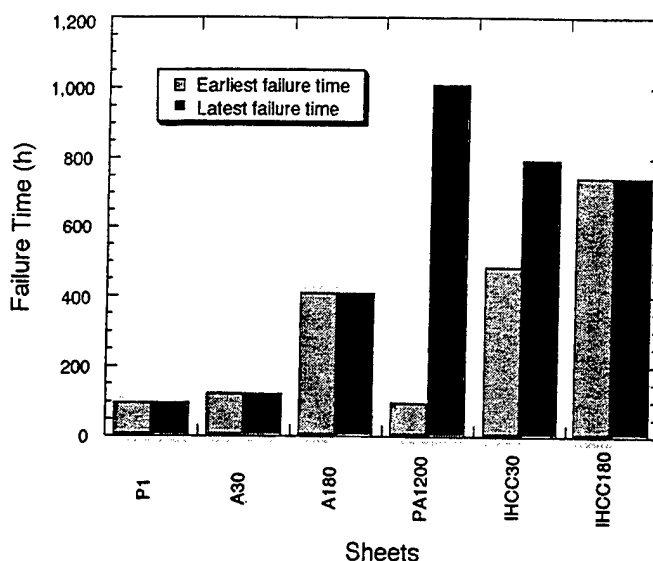
discussed was at least equal in quality to the commercial product. Thicker CCC (longer treatments) were found to contain more  $\text{Cr}^{6+}$  in XAS studies.

Figure 3 shows an optical micrograph comparison of the in-house CCC with a coating time of 180 s after exposure to salt spray for 744 h to the untreated case exposed for 95.5 h. Extensive corrosion damage occurred on this uncoated specimen. Secondary electron microscopy images revealed the presence of small pits ( $\mu\text{m}$ -sized) on the CCC specimen compared to large pits on the untreated specimen (Figure 4). These corrosion pits were easily distinguishable from those already existing on the metal as they all exceeded  $10\ \mu\text{m}$  in width or diameter. Those introduced during the cleaning process generally did not exceed  $10\ \mu\text{m}$ . The principal result of the salt spray testing was that the CCC prepared and utilized in subsequent electrochemical testing were equal or superior to commercial products.

### Chromate Leaching from CCC

#### AA 2024-T3 Exposed in Small Volume Cells

Leaching of soluble  $\text{CrO}_4^{2-}$  was observed from commercially and in-house prepared CCC after soaking in high-purity water. A typical electropherogram of one of the aliquots is shown in Figure 5, with an aliquot removed at zero time. The time dependence of the  $\text{CrO}_4^{2-}$  concentrations in Figure 6 indicates that the leaching rates of soluble  $\text{CrO}_4^{2-}$  for both samples were very close,  $\sim 0.076\ \text{ng}/\text{cm}^2\text{-h}$  and independent of the solution volume for soaking. These results can be used to estimate the  $\text{CrO}_4^{2-}$  concentrations that would develop under conditions where a thin water



**FIGURE 2.** Summary of salt spray test (ASTM B117) on AA 2024-T3. Notation: P1 = specimens were degreased, alkaline cleaned, and desmutted; A30 = coated in-house with Alodine 1200 for 30 s; A180 = in-house with Alodine 1200 for 180 s; PA1200 = coated by a commercial vendor for unknown coating time with Alodine 1200; IHCC30 = in-house CCC recipe for 30 s; IHCC180 = in-house CCC recipe for 180 s.

film exists on the surface, as would be the case in salt spray testing and atmospheric exposures. A first approximation of the water volume present can be made based upon the atmospheric corrosion literature.<sup>51-52</sup> Under high-humidity conditions,  $\sim 2\ \text{nL}/\text{cm}^2$  of water is present at  $30^\circ\text{C}$ .<sup>51</sup> Assuming that the  $\text{CrO}_4^{2-}$  leaching rate observed in the current tests can

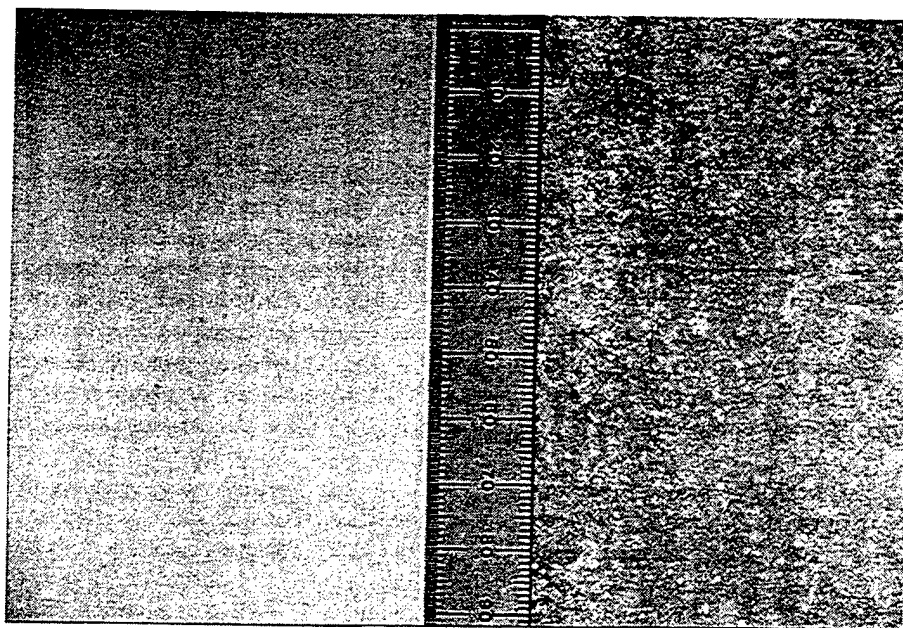
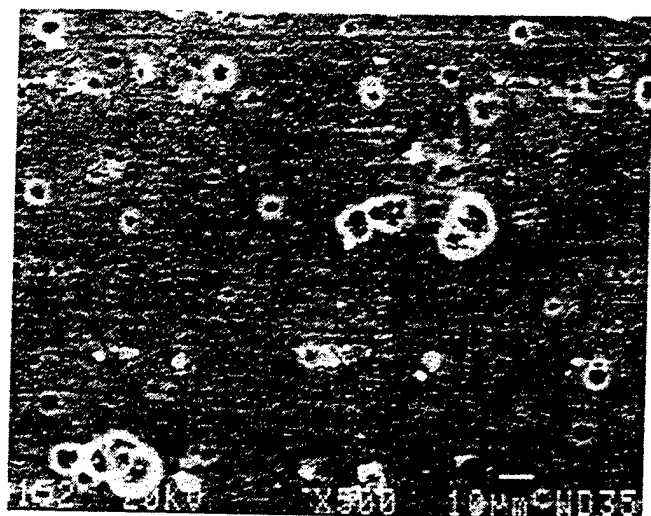
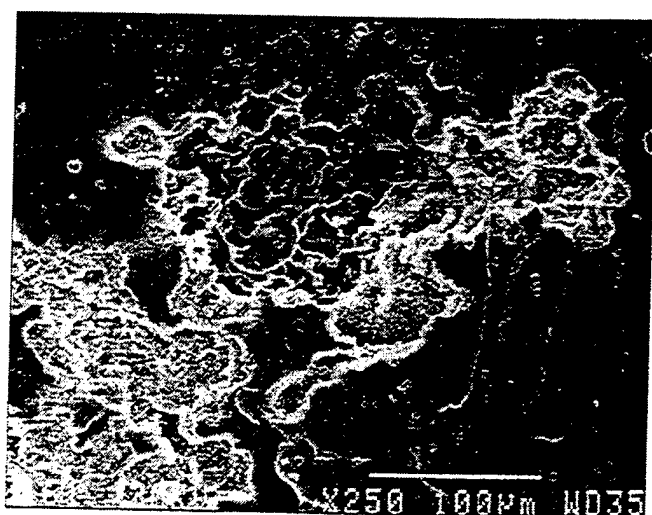


**FIGURE 3.** Comparative results of salt spray testing. Left: in-house 180-s conversion coating (IHCC180) after 744 h. Right: degreased/alkaline cleaned/desmut treatment (P1) after 95.5 h.



(a)



(b)

**FIGURE 4.** Surface of AA 2024-T3 with: (a) 3-min CCC after 744 h of salt spray. The pits caused by corrosion during salt spray test are those that are  $> 10 \mu\text{m}$  in diameter. No pits formed by the cleaning process reached dimensions of  $10 \mu\text{m}$ . The three pits meeting that criterion in this photo appear to have developed from several sites close together. (b) No CCC after 95.5 h of salt spray. Extensive corrosion damage occurred within this very large pit. It is clear that destruction is more extensive than on the CCC sample (Figure 4a).

be related to thin water film conditions, the  $\text{CrO}_4^{2-}$  concentration on the surface exposed to high humidity would accumulate at a rate of  $1 \text{ mM/h}$ . Thus, after 10 h, a chromate concentration of  $10 \text{ mM}$  would be expected.

These leaching results also can be used to approximate the concentration of chromate that would have been present in the bulk solution during the potentiodynamic and long-term open-circuit testing. In the fast potentiodynamic scans, a solution volume of  $250 \text{ mL}$  was present and the test lasted  $10^3 \text{ s}$ . Applying the same assumptions as above led to a maximum chromate concentration of  $9.4 \times 10^{-13} \text{ M}$

released into the  $0.005\text{-M NaCl} + 0.1\text{-M Na}_2\text{SO}_4$  solution during a fast scan. This was a very small concentration of chromate available in solution relative to that incorporated in the CCC. When the samples were held at OCP for  $7,200 \text{ s}$  before fast scans lasting  $10^3 \text{ s}$ , the total concentration of chromate that would have leached out into solution in  $8,200 \text{ s}$  would be  $7.71 \times 10^{-12} \text{ M}$ . In open-circuit testing in small volume cells, similar calculations predicted a chromate concentration of  $4.2 \times 10^{-7} \text{ M}$  normalized to the total solution volume after 10 days immersion. The exact size of the  $\text{Cr}^{6+}$  reservoir was not determined.

### *Pit Initiation and Stabilization Decoupled from Chromate Leaching and Under Conditions Simulating Leaching*

Figure 7 illustrates  $E\text{-log } i$  behavior, indicating a clear breakdown potential that enabled determination of  $E_{\text{pit}}$ . The question concerning the benefits of soluble chromate additions compared to the benefits of  $\text{Cr}^{6+}$  contained in the CCC on pit initiation and stabilization could be ascertained by their effects on  $E_{\text{pit}}$ . Figure 8(a) shows  $E_{\text{pit}}$  of untreated AA 2024-T3 in  $0.1 \text{ M Na}_2\text{SO}_4 + 0.005 \text{ M NaCl}$  in comparison to its OCP. It was seen clearly that  $E_{\text{pit}}$  decreased after a 2-h wait at OCP to a median value just  $20 \text{ mV}$  above the OCP. Figure 8(b) compares results from untreated samples to those of untreated AA 2024-T3 in  $0.1 \text{ M Na}_2\text{SO}_4 + 0.005 \text{ M NaCl}$  with the addition of  $0.01 \text{ M}$  total soluble chromate at two pH levels. Here, the total chromate concentration was selected to exceed the  $\text{NaCl}$  concentration. When added as  $\text{Na}_2\text{CrO}_4$  (pH 8),  $0.01 \text{ M}$  total soluble chromate was particularly potent in raising  $E_{\text{pit}}$ . The pH of a  $\text{NaCl}$  solution without chromate has a negligible effect on  $E_{\text{pit}}$  of Al.<sup>53-54</sup> Soluble chromate did raise  $E_{\text{pit}}$  significantly. Other studies indicate that chromate also reduces pit growth and metastable pit initiation rates on Al.<sup>17,55</sup> Since metastable pits grow to form stable pits, any effect of chromate on metastable pitting also likely would contribute to the elevation in  $E_{\text{pit}}$ . The elevation in  $E_{\text{pit}}$  obtained in the scan for the  $\text{H}_2\text{SO}_4$ -anodized material has been suggested to be caused by increased incubation times enabled by the thick oxide layer serving as a barrier to  $[\text{Cl}^-]$  ingress.<sup>54</sup>

Figure 8(c) compares these results to CCC AA 2024-T3 in  $0.1 \text{ M Na}_2\text{SO}_4 + 0.005 \text{ M NaCl}$ . Here, it was seen that a statistically significant elevation in  $E_{\text{pit}}$  was achieved for CCC AA 2024-T3 after 2 h exposure. Interestingly, the enhancement in  $E_{\text{pit}}$  after 2 h at OCP was much more significant for the 3-min CCC treatment compared to the 30-s CCC treatment. To separate further the effect of any  $\text{Cr}^{6+}$  leached from the coating, a separate set of experiments were conducted. Here, the electrolyte in the cell exposing the 3-min CCC was replaced after the 2-h exposure at OCP with fresh, chromate-free solution before the

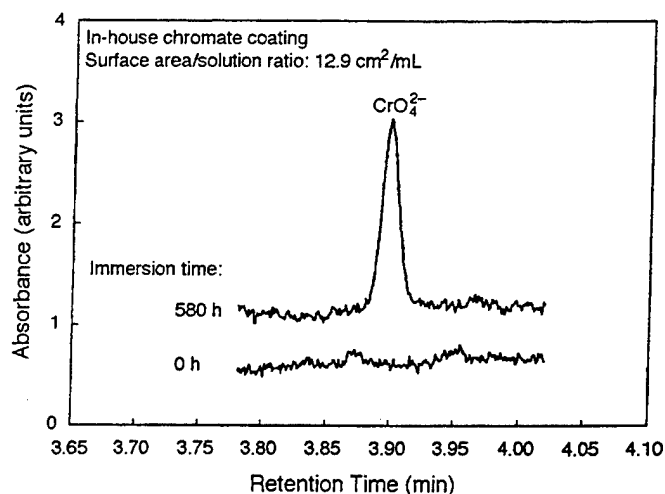


FIGURE 5. Typical electropherograms of aliquots removed from chromate leaching experiments.

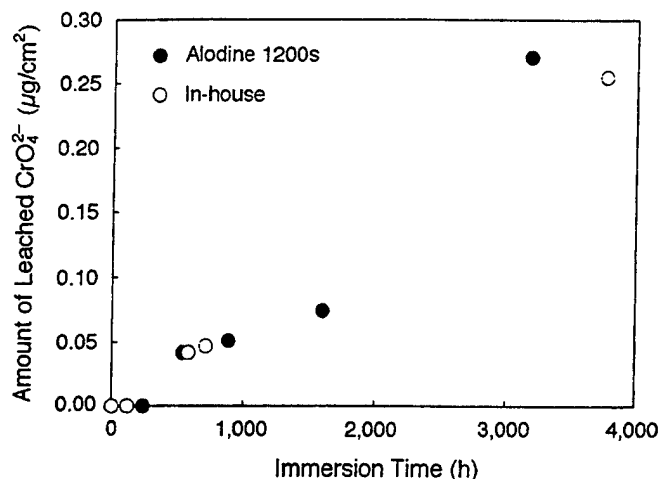


FIGURE 6. Time dependence of chromate leaching. Cumulative amount of chromate increased approximately linearly with time for the Alodine 1200 and the in-house CCC.

anodic polarization scan began. The significant enhancement of  $E_{\text{pit}}$  with conversion coating was still maintained in spite of the use of fresh electrolyte for the polarization (Figure 8[c]). The reason for the lower  $E_{\text{pit}}$  values recorded when compared to the set where fresh solution was not used for the polarization scan phase is not understood fully. In contrast, CCC coatings containing  $\text{Cr}^{6+}$  did not raise  $E_{\text{pit}}$  in fast scans after a 0-h wait at OCP. These scans were designed to minimize chromate leaching as well as the time available for chromate transport.

Key results are that the  $E_{\text{pit}}$  of CCC AA 2024-T3 increased with immersion time at OCP and conversion coating time. Soluble chromate is known to enhance  $E_{\text{pit}}$  of Al,<sup>16</sup> and this also was confirmed. Few studies report results for CCC specimens that unambiguously separate effects of the coating itself from  $\text{Cr}^{6+}$  leached into solution. Experiments in fresh solution suggested some role of the coating itself or  $\text{Cr}^{6+}$  within the coating.

### OCP and Oxygen Reduction Kinetics on Intermetallics Compared to Al and Cu

An example of OCP behavior as a function of time in 0.1 M  $\text{Na}_2\text{SO}_4 + 0.005$  M NaCl is shown for Cu, Al, AA 2024-T3, Al-4% Cu, and the intermetallics in Figure 9(a). Examples selected were representative of the typical behavior of each material. There was virtually no effect of electrode surface area on OCP. The OCP of  $\text{Al}_2\text{CuMg}$  started near  $-1.1 V_{\text{SCE}}$  and shifted in the positive direction toward  $-0.8 V_{\text{SCE}}$ . Dealloying of S- $\text{Al}_2\text{CuMg}$  has been reported.<sup>6</sup> It is reasonable to hypothesize that Cu enrichment raises the OCP of this phase during exposure. The OCP of  $\text{Al}_2\text{Cu}$  and  $\text{Al}_{20}\text{Cu}_2(\text{MnFe})_3$  shifted from  $\sim -0.37 V_{\text{SCE}}$  and  $-0.5 V_{\text{SCE}}$ , respectively, to  $\sim -0.4$  and  $-0.35 V_{\text{SCE}}$ , respectively, then remained steady over time. It was seen that Al-Cu and Al-Cu-Fe-Mn intermetallic

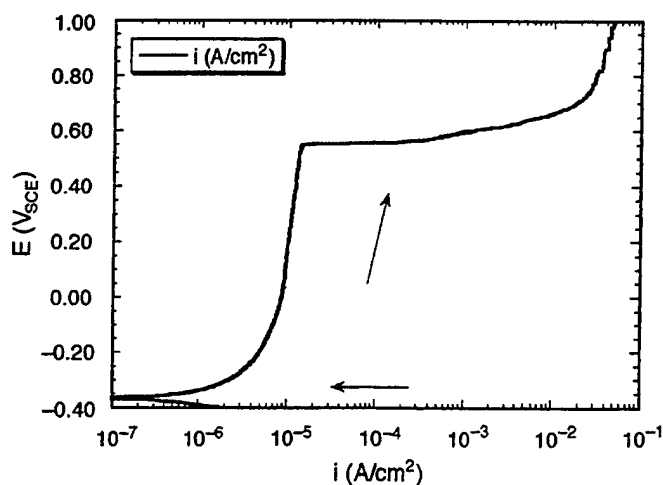
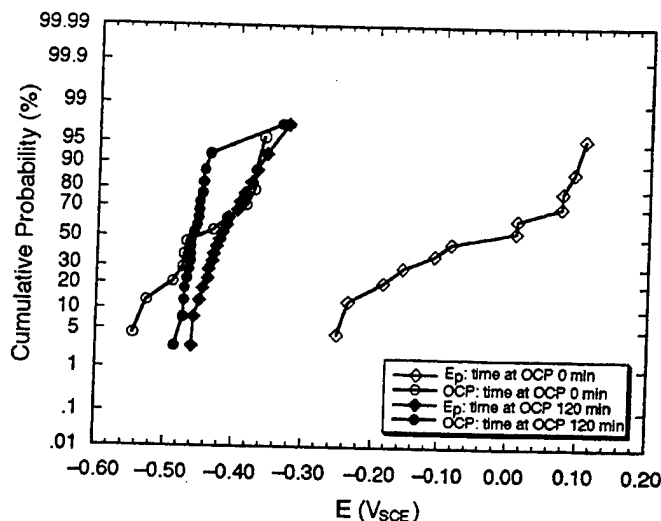


FIGURE 7. AA 2024-T3 in 0.1 M  $\text{Na}_2\text{SO}_4 + 0.005$  M NaCl + 0.01 M  $\text{Na}_2\text{CrO}_4$ . The figure illustrates  $E$ -log  $i$  behavior indicating clear breakdown potential that enabled determination of  $E_{\text{pit}}$ .  $E_{\text{pit}}$  was taken as the potential where the current density of  $3 \times 10^{-5} \text{ A/cm}^2$  was attained. Sample was used in as-received condition after degreasing.

phases and Cu representing replated Cu provided a galvanic potential driving force for the corrosion of AA 2024-T3 and S- $\text{Al}_2\text{CuMg}$ .

The OCP behavior of SHT Al-4% Cu was studied. It simulated the matrix of AA 2024-T3 without the intermetallics present (Figure 9). The OCP of Al-4% Cu was lower than those of Cu,  $\text{Al}_2\text{Cu}$ ,  $\text{Al}_{20}\text{Cu}_2(\text{MnFe})_3$ , and AA 2024-T3, but higher than that of pure Al in 0.1 M  $\text{Na}_2\text{SO}_4 + 0.005$  M NaCl (Figure 9[a]). The OCP of SHT Al-4% Cu also remained lower than those of Cu and the Cu-containing intermetallics in the presence of soluble chromate (Figures 9[b] and [c]).

Cathodic polarization curves (not shown) also revealed that the rate of cathodic kinetics on Al and Al-4% Cu were reduced significantly compared to those on Cu,  $\text{Al}_2\text{Cu}$ ,  $\text{Al}_{20}\text{Cu}_2(\text{MnFe})_3$ , and AA 2024-T3.



**FIGURE 8. (a)** Cumulative probability of the OCP and  $E_{pit}$  for untreated AA 2024-T3 in 0.1 M  $\text{Na}_2\text{SO}_4$  + 0.005 M NaCl. This figure shows the effect of the 2-h wait period at OCP on the  $E_{pit}$ . All  $E_{pit}$  were measured from polarization curves. Sweep rate was 1 mV/s. Diagram key: (○) OCP after 0 min for untreated AA2024-T3 in 0.1 M  $\text{Na}_2\text{SO}_4$  + 0.005 M NaCl; (●) OCP after 120 min for untreated AA 2024-T3 in 0.1 M  $\text{Na}_2\text{SO}_4$  + 0.005 M NaCl; (◊)  $E_{pit}$  after 0 min for untreated AA 2024-T3 in 0.1 M  $\text{Na}_2\text{SO}_4$  + 0.005 M NaCl; (◐)  $E_{pit}$  after 120 min for untreated AA2024-T3 in 0.1 M  $\text{Na}_2\text{SO}_4$  + 0.005 M NaCl.

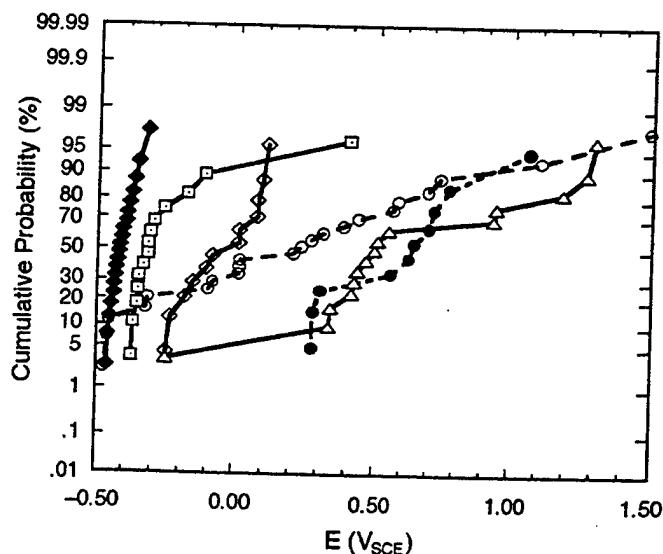


**FIGURE 8. (b)** Cumulative probability plot of  $E_{pit}$  for untreated and anodized AA 2024-T3 in 0.1 M  $\text{Na}_2\text{SO}_4$  + 0.005 M NaCl (pH 6), untreated AA 2024-T3 in 0.1 M  $\text{Na}_2\text{SO}_4$  + 0.005 M NaCl + 0.0062 M  $\text{Na}_2\text{CrO}_4$  + 0.0038 M  $\text{H}_2\text{CrO}_4$  (pH 6), and untreated AA 2024-T3 in 0.1 M  $\text{Na}_2\text{SO}_4$  + 0.005 M NaCl + 0.01 M  $\text{Na}_2\text{CrO}_4$  (pH 8). Sweep rate was 1 mV/s. Diagram key: (○)  $E_{pit}$  for untreated AA 2024-T3, rest time at OCP = 0 min; (●)  $E_{pit}$  for untreated AA 2024-T3, rest time at OCP = 120 min; (○) untreated AA 2024-T3 in 0.1 M  $\text{Na}_2\text{SO}_4$  + 0.005 M NaCl + 0.01 M  $\text{Na}_2\text{CrO}_4$  (pH 8), rest time at OCP = 0 min; (●) untreated AA 2024-T3 in 0.1 M  $\text{Na}_2\text{SO}_4$  + 0.005 M NaCl + 0.01 M  $\text{Na}_2\text{CrO}_4$  (pH 8), rest time at OCP = 120 min; (◻) untreated AA 2024-T3 in 0.1 M  $\text{Na}_2\text{SO}_4$  + 0.005 M NaCl + 0.0062 M  $\text{Na}_2\text{CrO}_4$  + 0.0038 M  $\text{H}_2\text{CrO}_4$  (pH 6), rest time at OCP = 0 min; (△) anodized AA 2024-T3 in 0.1 M  $\text{Na}_2\text{SO}_4$  + 0.005 M NaCl (pH 6), rest time at OCP = 120 min.

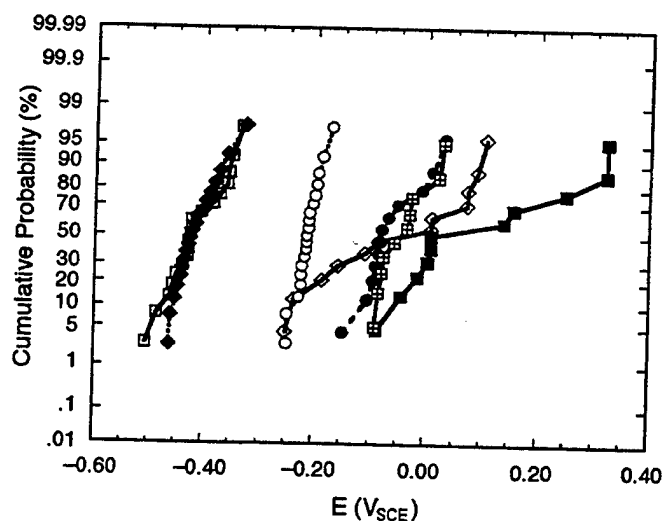


**FIGURE 8. (c)** Cumulative probability plot of  $E_{pit}$  for untreated and 30-s and 180-s CCC AA 2024-T3 in 0.1 M  $\text{Na}_2\text{SO}_4$  + 0.005 M NaCl (pH 6). This figure also shows the effect of the 2-h wait period at OCP on the pitting potential. Sweep rate was 1 mV/s. Diagram key: (○) untreated AA 2024-T3, rest time at OCP = 0 min; (●) untreated AA 2024-T3, rest time at OCP = 120 min; (○) 30-s CCC AA 2024-T3, rest time at OCP = 0 min; (●) 30-s CCC AA 2024-T3, rest time at OCP = 120 min; (◻) 3-min CCC AA 2024-T3, rest time at OCP = 0 min; (◼) 3-min CCC AA 2024-T3, rest time at OCP = 120 min; (◼) 3-min CCC AA 2024-T3, rest time at OCP = 120 min with fresh solution used during the polarization scan.

These results support the suggestion that the OCP of AA 2024-T3 is raised significantly by the presence of  $\text{Al}_2\text{Cu}$  and  $\text{Al}_{20}\text{Cu}_2(\text{MnFe})_3$  phases in its matrix, which had a higher OCP and supported the oxygen reduction reaction (ORR) kinetics at enhanced rates.

Figure 9(b) shows OCP results in 0.1 M  $\text{Na}_2\text{SO}_4$  + 0.005 M NaCl + 0.01 M  $\text{Na}_2\text{CrO}_4$  (pH 8). Figure 9(c) shows OCP results in 0.1 M  $\text{Na}_2\text{SO}_4$  + 0.005 M NaCl + 0.0062 M  $\text{Na}_2\text{CrO}_4$  + 0.0038 M  $\text{H}_2\text{CrO}_4$  (pH 6), while Figure 9(d) shows OCP results after a 5-min CCC treatment in 0.1 M  $\text{Na}_2\text{SO}_4$  + 0.005 M NaCl. A summary of the OCP after 2 h is shown in Table 1. The OCP are compared to results from the literature in Table 2. Good agreement is seen with the literature.<sup>56-60</sup>

Figures 10 and 11 present a comparison of OCP in 0.1 M  $\text{Na}_2\text{SO}_4$  + 0.005 M NaCl to those after CCC treatment<sup>(5)</sup> or after the addition of chromate in a plot that depicts differences in OCP as departures from the diagonal line. Measurements close to the line indicated little difference in OCP. The OCP of AA 2024-T3,  $\text{Al}_2\text{Cu}$ ,  $\text{Al}_2\text{CuMg}$ , and 99.999% Cu were unaltered, while that of 99.998% Al was raised only when chromate was added to 0.1 M  $\text{Na}_2\text{SO}_4$  + 0.005 M NaCl and adjusted to pH 6. Moreover, the OCP of CCC AA 2024-T3,  $\text{Al}_2\text{Cu}$ ,  $\text{Al}_2\text{CuMg}$ , and 99.999% Cu were not changed significantly. Unlike

<sup>(5)</sup> CCC while galvanically coupled to AA 2024-T3.

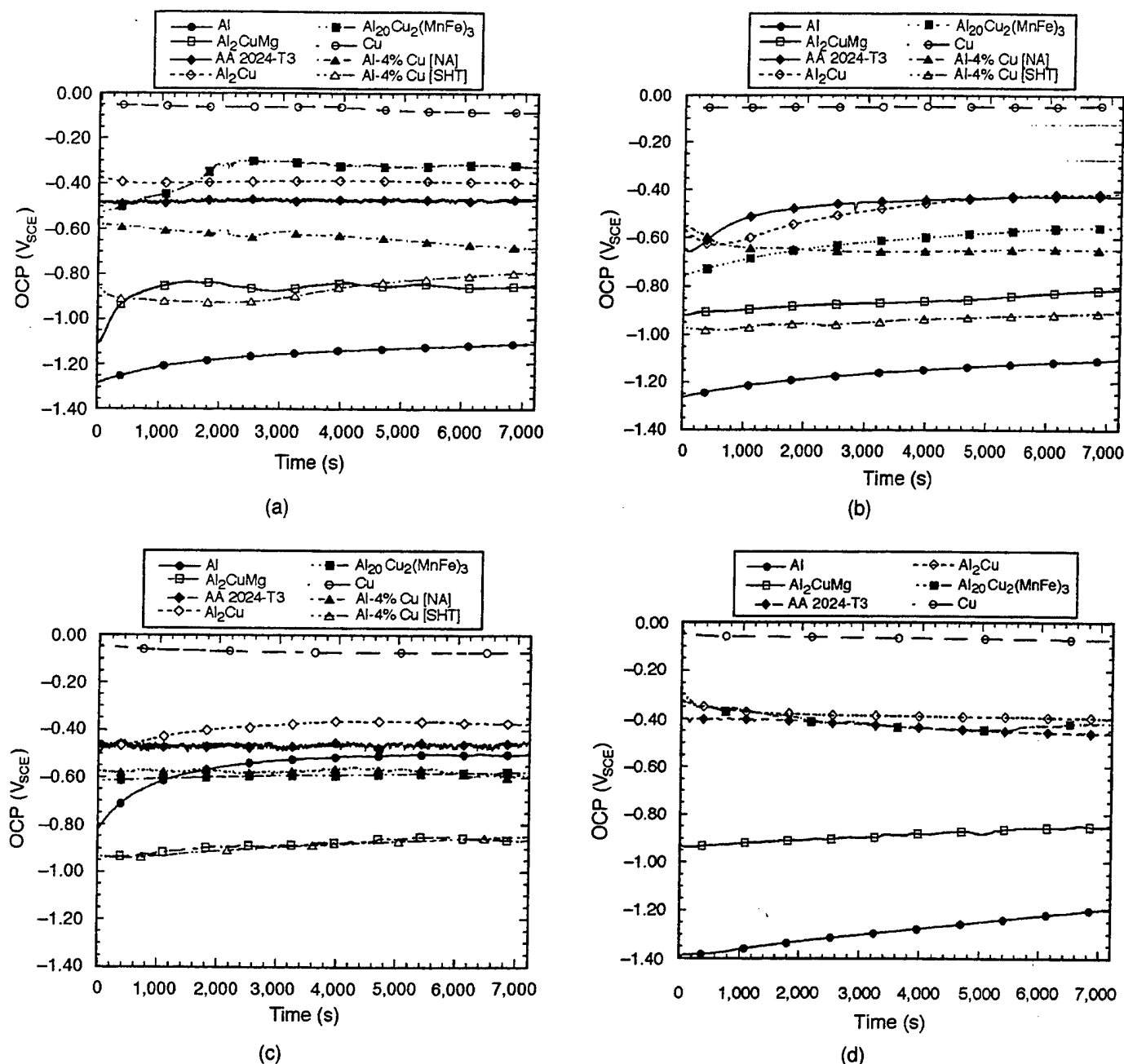


**FIGURE 9.** (a) First 2 h of OCP of Al (99.998%), Cu (99.999%), AA 2024-T3, Al-4% Cu, Al<sub>2</sub>Cu, Al<sub>20</sub>Cu<sub>2</sub>(MnFe)<sub>3</sub>, and Al<sub>2</sub>CuMg (Surfaces of the materials were finished by wet-grinding with 600-grit SiC paper except AA 2024-T3, which was used in an as-received condition.) in: (a) 0.1 M Na<sub>2</sub>SO<sub>4</sub> + 0.005 M NaCl (pH 6); (b) 0.1 M Na<sub>2</sub>SO<sub>4</sub> + 0.005 M NaCl + 0.01 M Na<sub>2</sub>CrO<sub>4</sub> (pH 8); (c) 0.1 M Na<sub>2</sub>SO<sub>4</sub> + 0.005 M NaCl + 0.0062 M Na<sub>2</sub>CrO<sub>4</sub> + 0.0038 M H<sub>2</sub>CrO<sub>4</sub> (pH 6); and (d) 5-min CCC surfaces in 0.1 M Na<sub>2</sub>SO<sub>4</sub> + 0.005 M NaCl (pH 6). Only the surfaces of Al<sub>2</sub>Cu, Al<sub>20</sub>Cu<sub>2</sub>(MnFe)<sub>3</sub>, and Al<sub>2</sub>CuMg were finished by wet-grinding with 600-grit SiC paper. All others were used in the as-received condition. (NA = naturally aged; SHT = solution heat-treated)

the result in soluble chromate at pH 6, the OCP of 99.998% Al was not raised by CCC when measured in 0.1 M Na<sub>2</sub>SO<sub>4</sub> + 0.005 M NaCl. Only the OCP of Al<sub>20</sub>Cu<sub>2</sub>(MnFe)<sub>3</sub> was lowered when chromate conversion coated in the pH 6 and pH 8 chromate-containing solutions.

<sup>(6)</sup> Soluble chromate pretreatment for 2 h at OCP minimized the cathodic reduction of Cr<sup>6+</sup> in solution as an additional cathodic reaction during ORR.

Finally, the diffusion-limited current density associated with O<sub>2</sub> reduction on stationary electrodes was not altered by CCC or soluble chromate pretreatment (Table 3).<sup>(6)</sup> Faster ORR rates were still observed on the intermetallic phases and Cu compared to Al and Al-4% Cu.

The key result was that some of the factors (e.g., differences in OCP and enhanced cathodic O<sub>2</sub> kinetics) that promote galvanic corrosion between Al-Cu

TABLE 1

OCP of AA 2024-T3, SHT Al-4% Cu,  $\text{Al}_2\text{Cu}$ ,  $\text{Al}_{20}\text{Cu}_2(\text{MnFe})_3$ ,  $\text{Al}_2\text{CuMg}$ , Al, and Cu in 0.1 M  $\text{Na}_2\text{SO}_4$  + 0.005 M NaCl, 0.1 M  $\text{Na}_2\text{SO}_4$  + 0.005 M NaCl + 0.01 M  $\text{Na}_2\text{CrO}_4$  (pH 8), 0.1 M  $\text{Na}_2\text{SO}_4$  + 0.005 M NaCl + 0.0062 M  $\text{Na}_2\text{CrO}_4$  + 0.0038 M  $\text{H}_2\text{CrO}_4$  (pH 6). OCP of CCC Treated Versions in 0.1 M  $\text{Na}_2\text{SO}_4$  + 0.005 M NaCl are Shown. Immersion for 2 h Before OCP was Recorded. All Error Values are at a 95% Confidence Level.

Electrolytes	AA 2024-T3	$\text{Al}_2\text{Cu}$	$\text{Al}_{20}\text{Cu}_2(\text{MnFe})_3$	$\text{Al}_2\text{CuMg}$	Al	Cu	Al-4% Cu (SHT <sup>(A)</sup> )
Std. Soln. <sup>(B)</sup> (pH 6)	-0.466 ± 0.01	-0.406 ± 0.014	-0.336 ± 0.017	-0.859 ± 0.024	-1.070 ± 0.151	-0.097 ± 0.009	-0.792
Std. Soln. + 0.01 M $\text{Na}_2\text{CrO}_4$ (pH 8)	-0.388 ± 0.066	-0.394 ± 0.044	-0.567 ± 0.041	-0.824 ± 0.024	-1.110 ± 0.060	-0.081 ± 0.029	-0.908
Std. Soln. + 0.0062 M $\text{Na}_2\text{CrO}_4$ + 0.0038 M $\text{H}_2\text{CrO}_4$ (pH 6)	-0.418 ± 0.076	-0.363 ± 0.102	-0.505 ± 0.103	-0.841 ± 0.003	-0.585 ± 0.177	-0.071 ± 0.015	-0.850
CCC <sup>(C)</sup> in. Std. Soln. (pH 6)	-0.447 ± 0.011	-0.392 ± 0.014	-0.423 ± 0.044	-0.887 ± 0.047	-1.150 ± 0.333	-0.083 ± 0.022	—

<sup>(A)</sup> SHT = solution heat-treated.

<sup>(B)</sup> Std. Soln. (standard solution) = 0.1 M  $\text{Na}_2\text{SO}_4$  + 0.005 M NaCl.

<sup>(C)</sup> CCC time is 5 min.

TABLE 2  
Comparison of Some OCP

Intermetallic	Environment	Mean OCP ( $V_{\text{SCE}}$ )	Source
$\theta\text{-Al}_2\text{Cu}$	0.1 M $\text{Na}_2\text{SO}_4$ + 0.005 M NaCl (Unde-aerated)	-0.406	This study
$\theta\text{-Al}_2\text{Cu}$	0.91 M NaCl + 0.09 M $\text{H}_2\text{O}_2$ (Unde-aerated)	-0.440	Reference 56
$\theta\text{-Al}_2\text{Cu}$	Sulfate solution vs pH ( $\text{N}_2$ sparged)	-0.450 to -1.100	Reference 57
S- $\text{Al}_2\text{CuMg}$	0.1 M $\text{Na}_2\text{SO}_4$ + 0.005 M NaCl (Unde-aerated)	-0.859	This study
S- $\text{Al}_2\text{CuMg}$	1.0 M NaCl (Unde-aerated)	-0.890	Reference 58
S- $\text{Al}_2\text{CuMg}$	0.5 M NaCl ( $\text{N}_2$ sparged)	-0.920	Reference 59
S- $\text{Al}_2\text{CuMg}$	0.91 M NaCl + 0.09 M $\text{H}_2\text{O}_2$ (Unde-aerated)	-0.910	Reference 60

intermetallics and the AA 2024-T3 matrix and active S- $\text{Al}_2\text{CuMg}$  phase were not changed by soluble chromate or CCC. The OCP of the Al-Cu-Mn-Fe intermetallics however was lowered slightly, and this would be expected to suppress galvanic driving force.

#### Comparison of Intermetallic OCP to $E_{\text{pit}}$

The OCP of an intermetallic in each solution was compared to the cumulative probability of achieving a given  $E_{\text{pit}}$  on AA 2024-T3. Soluble chromate and

CCC immersed in solution for 2 h were shown to shift the cumulative probability of pit stabilization to more positive potentials. Consequently, the galvanic coupling of the Al-rich matrix of AA 2024-T3 to replated Cu or Cu-rich intermetallics resulted in a reduced risk of pitting (Figure 12). A more significant benefit was obtained from the positive shift in  $E_{\text{pit}}$  than from any lowering of the OCP of any intermetallic or AA 2024-T3 itself. In fact, because chromate is an oxidizer, the mean OCP of 99.998% Al was raised.

Only the OCP of  $\text{Al}_{20}\text{Cu}_2(\text{MnFe})_3$  was lowered upon chromate additions.

### OCP Fluctuations on AA 2024-T3

Small volume/high surface area cells were used to examine the open-circuit behavior of CCC samples to examine the benefits of chromate incorporation and leaching under less severe applied voltages than with potential scans. Under quiescent conditions (as-prepared electrolyte), 0.05 M NaCl was used to ensure pitting at the OCP. The OCP of untreated AA 2024-T3 steadily decreased and fell below  $-0.9 V_{\text{SCE}}$  after 39,600 s (11 h). This fall in OCP was caused by pitting corrosion on the metal surface under open-circuit conditions. The transient of the first 9 h is shown in Figure 13(a). After  $1.08 \times 10^6$  s (300 h) of immersion, the OCP rose to between  $-0.4 V_{\text{SCE}}$  and  $-0.6 V_{\text{SCE}}$  and remained between these potentials for the remaining  $1.728 \times 10^5$  s (84 h) of the experiment. Relatively large pits (mm dimensions) were observed on these samples after the experiment.

In contrast, all CCC specimens exhibited the behavior shown by the 180-s in-house CCC sample (Figure 13[b]). They showed recurring periods of transient potential drops that lasted as long as 1,000 s and fell by as much as 30 mV before they recovered to the previous potential. These OCP fluctuations may have been associated with pits that eventually repassivated.<sup>55,61</sup> This interpretation was supported by visual analysis of the surfaces at the end of the test. Numerous pits and general discoloration (as a result of corrosion products) were observed on the untreated AA 2024-T3, whereas only a few small pits were observed on the CCC AA 2024-T3 (Figure 14).

## DISCUSSION

### Chromate Leaching and Transport

Results of the salt spray test (Figures 2 and 3) agree with the findings of other authors that CCC improves corrosion resistance.<sup>7-10</sup> OCP monitoring of CCC AA 2024-T3 immersed in 0.05 M NaCl in small volume cells showed potential fluctuations suggesting metastable pitting and repassivation (Figure 13). In these tests, local microstructural heterogeneities created local galvanic couples responsible for corrosion.<sup>1-6,32,43,62-63</sup> The observation that CCC AA 2024-T3 exhibited reduced corrosion in a salt spray test and promoted pit stifling in small volume cells did not prove whether chromate is an anodic or cathodic inhibitor. Because the anode and cathode sites were local to the freely corroding material (i.e., in close spatial proximity to each other), either mechanism of inhibition could have operated to suppress corrosion in these tests and could have been responsible for potential transients indicative of repassivation. Cathodic limitations to pit growth in Al-Cu alloys have been proposed owing to the poor ability of pure Al to

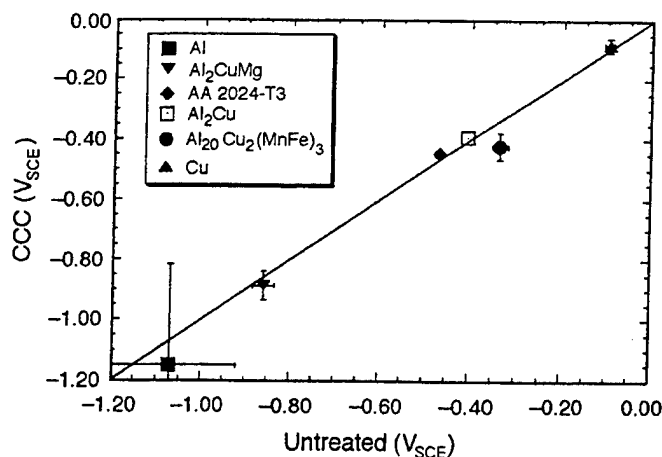


FIGURE 10. OCP untreated 99.998% Al,  $\text{Al}_2\text{CuMg}$ , AA 2024-T3,  $\text{Al}_2\text{Cu}$ ,  $\text{Al}_{20}\text{Cu}_2(\text{MnFe})_3$ , and 99.999% Cu compared with those of their 5-min CCC counterparts in 0.1 M  $\text{Na}_2\text{SO}_4$  + 0.005 M NaCl (pH 6) after 2 h.

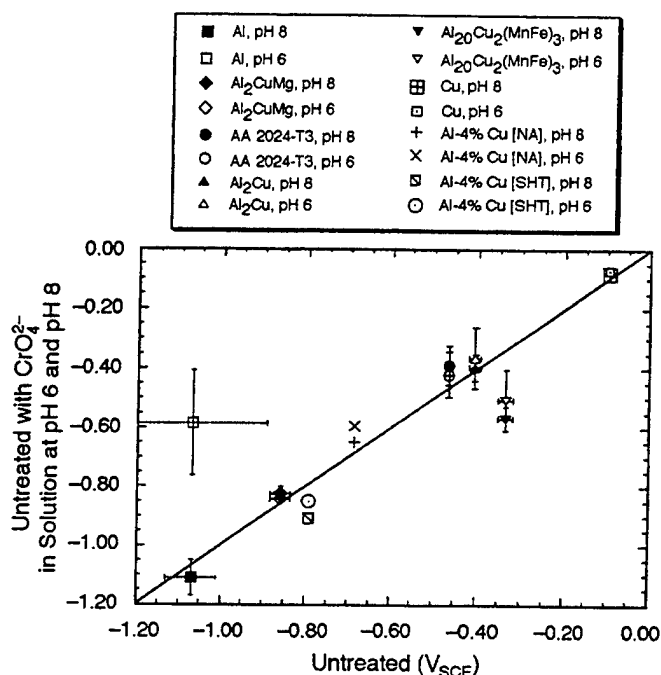


FIGURE 11. OCP (after 2 h) of untreated 99.998% Al,  $\text{Al}_2\text{CuMg}$ , AA 2024-T3, Al-4% Cu,  $\text{Al}_2\text{Cu}$ ,  $\text{Al}_{20}\text{Cu}_2(\text{MnFe})_3$ , and 99.999% Cu in 0.1 M  $\text{Na}_2\text{SO}_4$  + 0.005 M NaCl (pH 6) compared with their OCP in 0.1 M  $\text{Na}_2\text{SO}_4$  + 0.005 M NaCl + 0.01 M  $\text{Na}_2\text{CrO}_4$  (pH 8) and 0.1 M  $\text{Na}_2\text{SO}_4$  + 0.005 M NaCl + 0.0062 M  $\text{Na}_2\text{CrO}_4$  + 0.0038 M  $\text{H}_2\text{CrO}_4$  (pH 6).

support cathodic electron transfer reactions (ETR) and the small surface area fraction of intermetallic particles.<sup>64</sup>

In all studies involving potentiodynamic scans, the potentiostat was the counter electrode and supplied cathodic reactions, and any role of microstructure in supporting cathodic reactions was minimized. Pitting potentials on AA 2024-T3 were raised in this study with soluble  $\text{Cr}^{6+}$  additions in



TABLE 3

*Cathodic Current Densities at  $-0.75 V_{SCE}$  for Untreated and 5-min CCC AA 2024-T3 Samples in 0.1 M  $Na_2SO_4$  + 0.005 M NaCl (Std. Soln.), Untreated Samples in 0.1 M  $Na_2SO_4$  + 0.005 M NaCl + 0.0062 M  $Na_2CrO_4$  + 0.0038 M  $H_2CrO_4$  (pH 6) and Untreated in 0.1 M  $Na_2SO_4$  + 0.005 M NaCl + 0.01 M  $Na_2CrO_4$  (pH 8). It also includes data for untreated AA 2024-T3 and  $Al_2Cu$  in 0.1 M  $Na_2SO_4$  (pH 6) and 0.1 M  $Na_2SO_4$  + 0.0062 M  $Na_2CrO_4$  + 0.0038 M  $H_2CrO_4$  (pH 6) for comparison. All error values are at a 95% confidence level. All Values were Measured from Polarization Curves Taken After Holding at OCP for 2 h. [x] is the Number of Repeats.*

Intermetallic/ Alloy/Metal	Current Density Untreated in Std. Soln. (A/cm <sup>2</sup> )	Current Density 5-min CCC in Std. Soln. (A/cm <sup>2</sup> )	Current Density in 0.1 M $Na_2SO_4$ (A/cm <sup>2</sup> )	Current Density in 0.1 M $Na_2SO_4$ after Pretreatment at OCP for 2 h in 0.1 M $Na_2SO_4$ + 0.01 M $CrO_4^{2-}$ (A) (pH 6) (A/cm <sup>2</sup> )
Al <sup>(B)</sup>	0.1E <sup>-6</sup> to 1E <sup>-6</sup>	—	—	—
AA 2024-T3	5.363E <sup>-6</sup> ± 1.125E <sup>-6</sup> [11]	3.067E <sup>-6</sup> ± 1.125E <sup>-6</sup> [11]	2.960E <sup>-6</sup> ± 1.706E <sup>-6</sup> [6]	3.439E <sup>-6</sup> ± 3.080E <sup>-6</sup> [2]
$Al_2Cu$	16.450E <sup>-6</sup> ± 5.789E <sup>-6</sup> [8]	30.130E <sup>-6</sup> ± 317.100E <sup>-6</sup> [2]	60.790E <sup>-6</sup> ± 24.940E <sup>-6</sup> [6]	7.942E <sup>-6</sup> ± 8.390E <sup>-6</sup> [4]
$Al_{20}Cu_2(MnFe)_3$	15.250E <sup>-6</sup> ± 4.661E <sup>-6</sup> [12]	21.420E <sup>-6</sup> ± 10.470E <sup>-6</sup> [7]	—	—
Cu	66.260E <sup>-6</sup> ± 17.220E <sup>-6</sup>	—	—	—
Al-4% Cu <sup>(C)</sup> (SHT) <sup>(D)</sup>	0.547E <sup>-6</sup> [1]	—	—	—

Intermetallic/ Alloy/Metal	Current Density with $CrO_4^{2-}$ (pH 6) in Std. Soln. (A/cm <sup>2</sup> )	Current Density with $CrO_4^{2-}$ (pH 8) in Std. Soln. (A/cm <sup>2</sup> )
Al <sup>(B)</sup>	—	—
AA 2024-T3	4.276E <sup>-6</sup> ± 1.046E <sup>-6</sup> [5]	2.435E <sup>-6</sup> ± 0.945E <sup>-6</sup> [8]
$Al_2Cu$	11.400E <sup>-6</sup> ± 8.571E <sup>-6</sup> [6]	18.560E <sup>-6</sup> ± 10.550E <sup>-6</sup> [11]
$Al_{20}Cu_2(MnFe)_3$	2.832E <sup>-6</sup> ± 4.006E <sup>-6</sup> [6]	5.727E <sup>-6</sup> ± 4.408E <sup>-6</sup> [8]
Cu	18.300E <sup>-6</sup> ± 8.254E <sup>-6</sup> [8]	29.59E <sup>-6</sup> ± 4.071E <sup>-6</sup> [9]
Al-4% Cu <sup>(C)</sup> (SHT) <sup>(D)</sup>	0.377E <sup>-6</sup> [1]	0.222E <sup>-6</sup> [1]

<sup>(A)</sup> Measurements in sulfate avoid open-circuit pitting that affects cathodic ORR kinetics. Measurements after exposure to  $Cr^{6+}$  in solution were conducted in 0.1 M  $Na_2SO_4$  to minimize  $Cr^{6+}$  reduction as an additional cathodic reaction besides ORR.

<sup>(B)</sup> Cathodic current density of Al measured at  $-1.30V_{SCE}$ .

<sup>(C)</sup> Cathodic current density of Al-4% Cu measured at  $-1.00 V_{SCE}$ .

<sup>(D)</sup> SHT = solution heat-treated.

solution or with CCC after 2 h of exposure at OCP (Figures 8[b] and [c]). Considering that soluble  $Cr^{6+}$  release from CCC was detected in this and other studies<sup>24,65</sup> and reduction products of chromate were detected at pits formed in a novel cell that enabled transport of  $Cr^{6+}$  from CCC AA 2024-T3 to untreated 2024-T3,<sup>24</sup> it is suggested that  $Cr^{6+}$  is transported to pit sites in the bulk solution after it is leached from

the conversion coating. Collectively, these results suggested that transport of chromate to anodic pit sites represented one form of anodic inhibition. Indeed, anodic inhibition has been implicated in several studies.<sup>24,66</sup> However, from the present studies, the amount of chromate that would have leached out of the CCC into solution in the 8,200 s (7,200 s at OCP and 1,000 s for potential scan) that these

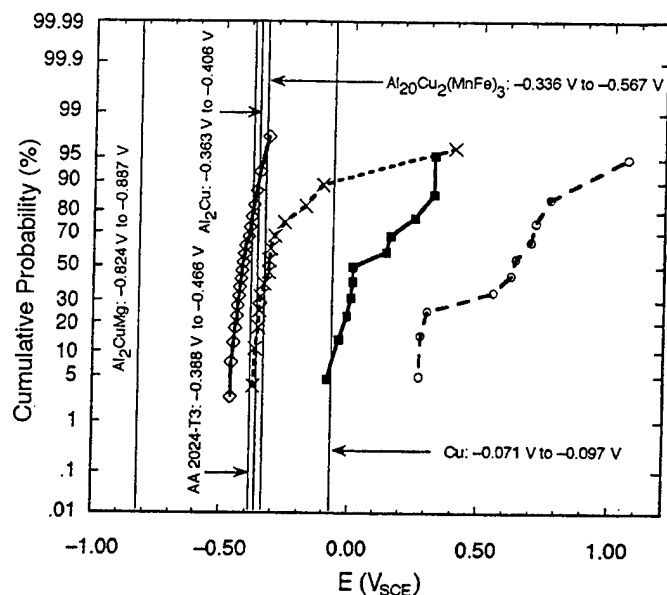
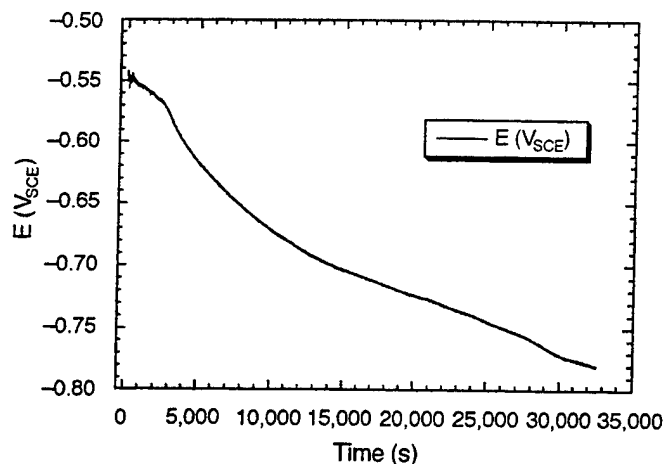


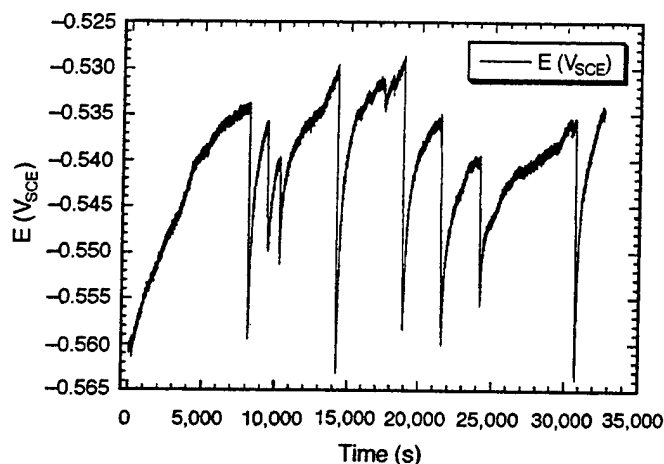
**FIGURE 12.** OCP of intermetallics compared with the cumulative probability of achieving the  $E_{pit}$  for 3-min CCC AA 2024-T3 in 0.1 M  $\text{Na}_2\text{SO}_4$  + 0.005 M NaCl (pH 6), and untreated AA 2024-T3 in 0.1 M  $\text{Na}_2\text{SO}_4$  + 0.005 M NaCl, 0.1 M  $\text{Na}_2\text{SO}_4$  + 0.005 M NaCl + 0.01 M  $\text{Na}_2\text{CrO}_4$  (pH 8), and 0.1 M  $\text{Na}_2\text{SO}_4$  + 0.005 M NaCl + 0.0062 M  $\text{Na}_2\text{CrO}_4$  + 0.0038 M  $\text{H}_2\text{CrO}_4$  (pH 6). There was a 2-h wait at OCP in all experiments. The vertical lines are the OCP indicated at the highest values attained amongst the four conditions listed above for each of the intermetallics, AA 2024-T3 and Cu. Refer to Table 1 for full results. Diagram key: (○)  $E_{pit}$  for untreated AA 2024-T3 in 0.1 M  $\text{Na}_2\text{SO}_4$  + 0.005 M NaCl; (■)  $E_{pit}$  for 3-min CCC AA 2024-T3 in 0.1 M  $\text{Na}_2\text{SO}_4$  + 0.005 M NaCl; (□)  $E_{pit}$  for untreated AA 2024-T3 in 0.1 M  $\text{Na}_2\text{SO}_4$  + 0.005 M NaCl + 0.01 M  $\text{Na}_2\text{CrO}_4$  (pH 8); (×)  $E_{pit}$  for untreated AA 2024-T3 in 0.1 M  $\text{Na}_2\text{SO}_4$  + 0.005 M NaCl + 0.0062 M  $\text{Na}_2\text{CrO}_4$  + 0.0038 M  $\text{H}_2\text{CrO}_4$  (pH 6).

experiments took ( $7.71 \times 10^{-12}$  M) was not enough to cause such improvements as observed. Therefore, a simple leaching + healing (by transport of  $\text{Cr}^{6+}$  to the pit sites) mechanism is not adequate to explain fully these observations. Also, this mechanism might be inadequate to explain the improvements observed during the spray test,<sup>39</sup> since the test prescribes a continuous salt spray with run off or condensed water. In this case, any chromate that leached out of the CCC was likely to be lost as the liquid phase drips off the metal surface.

A suggestion as to how CCC was able to improve pitting corrosion in these experiments is that a considerable amount of the  $\text{Cr}^{6+}$  incorporated in the conversion coating was not leached out but stayed in the coating. Only a small quantity of solution will exist within pores of the CCC at any given period of time in salt spray, which would result in concentration of the remaining  $\text{Cr}^{6+}$  within the CCC. An explanation for the observed improvement in  $E_{pit}$  after a 2-h wait at OCP might be explained by the need for time to allow the dry CCC (Figure 1) to rehydrate and alter the state of the  $\text{Cr}^{6+}$  species at local sites within the CCC.<sup>20</sup>



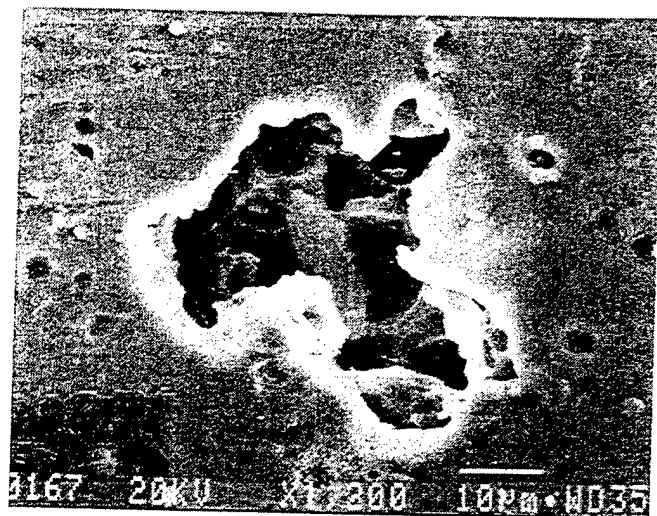
(a)



(b)

**FIGURE 13.** OCP of untreated AA 2024-T3 in 0.05 M NaCl (pH 6) showing the first 32,400 s (9 h) of immersion (a) and 180 s in-house CCC AA 2024-T3 after 691,200 s (192 h) of immersion (b). The lowest potential ever observed with the CCC was  $-0.649 \text{ V}_{\text{SCE}}$ . Notice the OCP fluctuations in the CCC sample.

Apparently,  $\text{Cr}^{6+}$  already released into aqueous solution is supplied easily to pit sites.  $\text{Cr}^{6+}$  incorporated in CCC, but not yet released in solution, apparently is supplied to remote pit sites with more difficulty. More research is required to explore the exact mechanisms of  $\text{Cr}^{6+}$  transport in conversion coatings. However, it is clear that the ionic mobility of  $\text{Cr}^{6+}$  present in a polymer of covalently bonded  $\text{Cr}^{3+}$  in aluminum hydroxide ( $\text{Al}(\text{OH})_3$ ) might be lower than its mobility in an aqueous solution in the form of  $\text{Cr}_2\text{O}_7^{2-}$ ,  $\text{HCrO}_4^-$ , or  $\text{CrO}_4^{2-}$ .<sup>20</sup> For instance, mobility of  $\text{CrO}_4^{2-}$  in an aqueous solution is  $8.81 \times 10^{-4} \text{ cm}^2 \text{ V}^{-1} \text{ s}^{-1}$ , while that of  $\text{Cr}^{3+}$  in chromium (III) oxide ( $\text{Cr}_2\text{O}_3$ ) is less than  $10^{-10} \text{ cm}^2 \text{ V}^{-1} \text{ s}^{-1}$  when estimated from extrapolating high-temperature diffusivity data of  $\text{Cr}^{3+}$  in  $\text{Cr}_2\text{O}_3$ .<sup>67-68</sup> It would be reasonable to assert that chromate present in the CCC is physically closer to pit sites such that slower transport rates could be overcome by shorter transport distances. Recall Fig-



(a)



(b)

**FIGURE 14.** Pit formed on the surface of AA 2024-T3 after > 300 h in the small volume cell with: (a) 3-min CCC. Electrolyte was 0.05 M NaCl (pH 6). The pit is small compared with that in Figure 14(b). (b) No CCC. Electrolyte was 0.05 M NaCl (pH 6). This pit measured ~ 0.1 cm across. This demonstrates the protective ability of CCC on AA 2024-T3 in this electrolyte when compared with Figure 14(a).

ures 1(b) and (c) illustrating CCC directly within pits formed during alkaline treatment or desmutting. However, numerous investigators have commented on the porosity of CCC,<sup>48-49</sup> suggesting that  $\text{Cr}^{6+}$  transport would be required to protect porous sites of low initial  $\text{Cr}^{6+}$  coverage as well as scratches, etc. Moreover, the high deposition current density reported for CCC (e.g., 3 mA/cm<sup>2</sup>) is likely to result in a conversion coating that is neither compact nor free of imperfections.<sup>69</sup>

The reasons for the higher  $E_{\text{pit}}$  values for AA 2024-T3 in 0.1 M  $\text{Na}_2\text{SO}_4$  + 0.005 M NaCl + 0.01 M  $\text{Na}_2\text{CrO}_4$  (pH 8) compared with 0.1 M  $\text{Na}_2\text{SO}_4$  + 0.005 M NaCl + 0.0062 M  $\text{Na}_2\text{CrO}_4$  + 0.0038 M

$\text{H}_2\text{CrO}_4$  (pH 6), even though the total chromate concentrations in the solutions were equal, is not fully understood. However, one explanation is that the types and amounts of  $\text{Cr}^{6+}$  species present in solution differ. According to the calculations made by Kendig, et al., 30% of the total chromate concentration at pH 6 is  $\text{Cr}_2\text{O}_7^{2-}$ .<sup>46</sup> At pH 8, 96% of the chromate is present as  $\text{CrO}_4^{2-}$ . Hence, concentration of exact  $\text{Cr}^{6+}$  species differs.

### *Creation of Local Galvanic Couples with Intermetallics*

Pitting corrosion in precipitation age-hardened Al alloys often is observed to occur adjacent to cathodic intermetallic phases (e.g., coarse constituents or precipitate phases)<sup>1-3</sup> or replated Cu often released from corroding S-Al<sub>2</sub>CuMg.<sup>6</sup> Two other schools of thought exist. One suggests that pitting occurs by selective particle dissolution when particles are active.<sup>3-6,31-33</sup> The other proposes local alkaline attack of the Al matrix by more noble particles. Both are a result of galvanic couples. The alkaline attack theory lacks consistency with experimental data since high-solution flow rates should eliminate any attack. This is not observed. Moreover, the pit theory is supported by the removal of [Cl<sup>-</sup>] where upon attack is suppressed. Studies that seek to rationalize the observation of open-circuit pitting in the Al alloy matrix, especially when adjacent to intermetallics have benefited from a comparison of  $E_{\text{pit}}$  to the OCP of the most noble intermetallic present.<sup>3-4,58</sup> These comparisons are based on the premise that the most positive galvanic couple potential that the matrix can achieve is that of the most cathodic intermetallic phase or component. Clearly, current and potential distribution mapping is required to specify the exact potential of the matrix at any distance from an intermetallic phase. However, the measured overall OCP of AA 2024-T3 (Figure 9) was similar to that of some of the Cu-containing intermetallics, suggesting that these phases govern the overall OCP of the alloy and that at some locations, the matrix may achieve this potential. This notion was supported by the lower OCP of Al-4% Cu (which simulated the matrix of AA 2024-T3 without the intermetallics) when compared to that of AA 2024-T3. If the OCP was near or at the pitting potential of the matrix in the selected test solution, then the likelihood of matrix pitting next to the intermetallic particle was greater. Corrosion adjacent to  $\theta$ -Al<sub>2</sub>Cu phases<sup>3</sup> and Al-Cu-Mn-Fe precipitates<sup>5</sup> was observed, and this would be expected based on the OCP data of Figure 9. Therefore, a comparison of pitting potentials to intermetallic OCP is justified.

The data suggest that Cu-bearing intermetallics such as Al<sub>2</sub>Cu and Al<sub>20</sub>Cu<sub>2</sub>(MnFe)<sub>3</sub> all had OCP in 0.1 M  $\text{Na}_2\text{SO}_4$  + 0.005 M NaCl that could induce pitting (Table 1 and Figures 10 through 12). However,

Cu replating is the most detrimental cathode site using this line of reasoning (Figure 12). Cu replating is almost always observed during processing of AA 2024-T3.<sup>11,70</sup> The question is whether CCC or soluble chromate additions decrease OCP, and therefore, increase the potential difference between the OCP of these materials and  $E_{\text{pit}}$  of the matrix. Comparison of AA 2024-T3 pitting potentials to the OCP of intermetallics and Cu with and without chromate as well as CCC is warranted to see whether they are altered by chromate or CCC. If pitting potentials remain unchanged and the OCP are shifted to more negative values and their cathodic kinetics are suppressed, then cathodic inhibition would be implicated. Alternatively, if OCP and cathodic reduction reaction kinetics remain the same and pitting potentials are raised by soluble chromate, then inhibition of anodic kinetics would be implicated.

CCC and soluble chromate (at the levels investigated in 0.1 M  $\text{Na}_2\text{SO}_4$  + 0.005 M NaCl) were not found to eliminate the galvanic couple caused by local microstructural heterogeneities in the solution tested (Figures 9 through 11). Another factor besides OCP in galvanic coupling is the ability of cathodes to support cathodic reactions at enhanced rates. Analysis of cathodic polarization curves of the intermetallics and AA 2024-T3 in the various solutions of study revealed only slight (if any) changes in the cathodic kinetics when untreated samples in 0.1 M  $\text{Na}_2\text{SO}_4$  + 0.005 M NaCl were compared with the untreated samples in 0.1 M  $\text{Na}_2\text{SO}_4$  or in 0.1 M  $\text{Na}_2\text{SO}_4$  after a 2-h pretreatment in 0.1 M  $\text{Na}_2\text{SO}_4$  + 0.0062 M  $\text{Na}_2\text{CrO}_4$  + 0.0038 M  $\text{H}_2\text{CrO}_4$ . Little difference was seen between CCC samples and untreated samples in 0.1 M  $\text{Na}_2\text{SO}_4$  + 0.005 M NaCl. Some of the findings are presented in Table 3 and show that no significant statistical differences were observed in the  $\text{O}_2$  reduction current density of these stationary electrodes taken at  $-0.75 V_{\text{SCE}}$ .<sup>(7)</sup> A reduction in the cathodic kinetics would have occurred if cathodic inhibition were in effect on these samples. Some intermetallics do not deposit CCC easily and form much less CCC compared with the alloy matrix.<sup>69</sup> The key result was that cathodic inhibition of ORR on intermetallics was not seen. However, one other indirect benefit of chromate that did not figure directly into this line of reasoning is the passivation of the S phase by chromate.<sup>30,71</sup> Such passivation significantly reduced Cu replating, which would be of enormous benefit to pitting resistance as shown.

## CONCLUSIONS

- ❖ Soluble chromate ( $\text{Na}_2\text{CrO}_4$ ) at a concentration of 0.01 M (pH 8) substantially inhibited pitting by rais-

ing  $E_{\text{pit}}$  of AA 2024-T3 in potentiodynamic scans conducted in 0.1 M  $\text{Na}_2\text{SO}_4$  + 0.005 M NaCl.

- ❖ Soluble chromate (0.0062 M  $\text{Na}_2\text{CrO}_4$  + 0.0038 M  $\text{H}_2\text{CrO}_4$ ) at a concentration of 0.01 M at pH 6 slightly raised  $E_{\text{pit}}$  in potential scans in 0.1 M  $\text{Na}_2\text{SO}_4$  + 0.005 M NaCl.

- ❖ Soluble chromate (as 0.0062 M  $\text{Na}_2\text{CrO}_4$  + 0.0038 M  $\text{H}_2\text{CrO}_4$ , pH 6, and 0.01 M  $\text{CrO}_4^{2-}$ , pH 8) lowered the OCP of  $\text{Al}_{20}\text{Cu}_2(\text{MnFe})_3$ . The OCP of this phase also was lowered slightly when CCC was applied.

- ❖ Pitting potentials of AA 2024-T3 were raised by 48-h to 120-h lab air aged CCC after 2 h at OCP in 0.1 M  $\text{Na}_2\text{SO}_4$  + 0.005 M NaCl. In contrast, 48-h to 120-h lab air aged CCC on AA 2024-T3 did not raise  $E_{\text{pit}}$  when polarization scans were conducted immediately after immersion. Benefits of the 2-h immersion at OCP were preserved when fresh test solution was used for polarization scans to eliminate the presence of  $\text{Cr}^{6+}$  in solution.

- ❖ Two important factors (OCP of cathode sites and ORR) influencing the driving force for local galvanic couples created by Cu and  $\text{Al}_2\text{Cu}$  in AA 2024-T3 were not eliminated by CCC or soluble chromate at pH 6 or pH 8 in 0.1 M  $\text{Na}_2\text{SO}_4$  + 0.005 M NaCl solutions. Evidence for this was the similarity of OCP on Cu,  $\text{Al}_2\text{Cu}$ , and AA 2024-T3 and persistently enhanced cathodic current density data on Al-Fe-Mn-Cu and Al-Cu intermetallics and Cu at  $-0.75 V_{\text{SCE}}$  dominated by  $\text{O}_2$  reduction.

## ACKNOWLEDGMENTS

Funding from the Air Force Office of Scientific Research (Major H. DeLong, Program Manager, grant no. F49620-96-1-0178) is acknowledged. Intermetallics were supplied by Aluminum Company of America (ALCOA), Inc., PA. The salt spray test was conducted by G. Nitowski of ALCOA, PA. EG&G Instruments, Inc. and Scribner Associates are acknowledged for support of electrochemical instrumentation and software in CESE at the University of Virginia.

## REFERENCES

1. R.B. Mears, R.H. Brown, *Ind. Eng. Chem.* 33 (1941): p. 1.001.
2. Y.V.V.R.S. Murty, T.Z. Kattamis, O.F. Devereux, R. Ambat, E.S. Dwarakadasa, *Met. Trans.* 4 (1973): p. 2,575.
3. J.R. Scully, D.E. Peebles, D. Frear, A.D. Romig, C.R. Hills, *Metall. Mater. Trans. A*, 23A (1992): p. 2,641.
4. I.L. Muller, J.R. Galvele, *Corros. Sci.* 17 (1977): p. 179.
5. G.S. Chen, M. Gao, R.P. Wei, *Corrosion* 52 (1996): p. 8.
6. R.G. Buchheit, R.P. Grant, P.F. Hlava, B. McKenzie, G.L. Zender, *J. Electrochem. Soc.* 144 (1997): p. 2,621.
7. P.L. Hagans, C.M. Haas, *ASM Handbook*, vol. 5, 10th ed. (Metals Park, OH: ASM Int., 1994), p. 405.
8. N.J. Newhard Jr., *Met. Finish.* 7 (1972): p. 49.
9. S. Springs, K. Woods, *Met. Finish.* 6 (1981): p. 49.
10. K.A. Korinek, *Metals Handbook*, vol. 13, 9th ed. (Metals Park, OH: ASM Int., 1987), p. 389.
11. P.L. Hagans, C.M. Haas, *Surf. Interface Anal.* 21 (1994): p. 65.
12. K. Asami, M. Oki, G.E. Thompson, G.C. Woods, V. Ashworth, *Electrochim. Acta* 32 (1987): p. 337.
13. M.W. Kendig, A.J. Davenport, H.S. Isaacs, *Corros. Sci.* 34 (1993): p. 41.

<sup>(7)</sup>  $\text{O}_2$  reduction was under mass transport control on Cu-bearing intermetallics at  $-0.75 V_{\text{SCE}}$ .

14. H.A. Katzman, G.M. Malouf, R. Bauer, G.W. Stupian, *Appl. Surf. Sci.* 2 (1979): p. 416.
15. J.A. Richardson, G.C. Wood, *J. Electrochem. Soc.* 120 (1973): p. 193.
16. H. Bohni, H.H. Uhlig, *J. Electrochem. Soc.* 116 (1969): p. 906.
17. S.T. Pride, J.R. Scully, J.L. Hudson, *J. Electrochem. Soc.* 141 (1994): p. 3,028.
18. R.P. Frankenthal, *Corros. Sci.* 7 (1967): p. 61.
19. J.S. Wainright, O.J. Murphy, M.R. Antonio, *Corros. Sci.* 33 (1992): p. 281.
20. L. Xia, L. McCreery, *J. Electrochem. Soc.* 145 (1998): p. 3,083.
21. F.W. Lytle, R.B. Gregor, G.L. Bibbins, K.Y. Blohowiak, R.E. Smith, G.D. Tuss, *Corros. Sci.* 37 (1995): p. 349.
22. T. Drozda, E. Maleczki, *J. Radioanal. Nucl. Chem. Lett.* 95 (1985): p. 339.
23. A.E. Hughes, R.J. Taylor, B.R. Hinton, *Surf. Interface Anal.* 25 (1997): p. 223.
24. J. Zhao, G. Frankel, R.L. McCreery, *J. Electrochem. Soc.* 145 (1998): p. 2,258.
25. S. Matsuda, H.H. Uhlig, *J. Electrochem. Soc.* 111 (1964): p. 156.
26. G.B. Hatch, *Corrosion Inhibitors*, ed. C.C. Nathan (Houston TX: NACE, 1973), p. 126.
27. C.S. Jeffcoat, H.S. Isaacs, J. Hawkins, G.E. Thompson, "The Effect of Chromate Concentration on the Repassivation of Corroding Aluminum," 194th Meeting of the Electrochemical Society, held Nov. 1-6, abstract no. 234, vol. 98-2 (New Jersey: Electrochemical Society [ECS], 1998).
28. F. Hunkeler, H. Bohni, *Corrosion* 37 (1981): p. 645.
29. A. Sehgal, D. Lu, G.S. Frankel, *J. Electrochem. Soc.* 145 (1998): p. 2,834.
30. M. Kendig, S. Jeanjaquet, "Inhibition of Electrochemical Reactions on Cu-Rich Aluminum Intermetallics," 194th Meeting of the Electrochemical Society, abstract no. 228, vol. 98-2, held Nov. 1-6 (New Jersey: ECS 1998).
31. G.S. Chen, C.-M. Liao, K.-C. Wan, M. Gao, R.P. Wei, "Effects of Environment on the Initiation Crack Growth," ASTM STP 1298, eds. W.A. Van Der Sluys, R.S. Piascik, R. Zawierucha (West Conshohocken, PA: ASTM, 1997), p. 18.
32. C. Blanc, B. Lavelle, G. Mankowski, *Corros. Sci.* 39 (1997): p. 495.
33. R.P. Wei, C.-M. Liao, M. Gao, *Met. Trans. A* 29A (1998): p. 1,153.
34. E.A. Starke, University of Virginia, correspondence to J.R. Scully, July, 1997.
35. T. Lyman, ed., *Metals Handbook*, vol. 2, 8th ed. (Metals Park, OH: ASM Int., 1964), p. 628.
36. Military Standard, MIL-STD-1503B (United States Air Force [USAF]), "Preparation of Aluminum Alloys for Surface Treatments and Inorganic Coatings" (Information Handling Service, Department of Defense, 1989), p. 7.
37. M.F. Stevenson Jr., *ASM Handbook*, vol. 5, 10th ed. (Metals Park, OH: ASM Int., 1994), p. 482.
38. K.A. Korinek, *Metals Handbook*, vol. 13, 9th ed. (Metals Park, OH: ASM Int., 1987), p. 392.
39. Annual Book of ASTM Standards, section 6, vol. 06.01 (West Conshohocken, PA: ASTM, 1992), p. 1.
40. P.C. Pistorius, G.T. Burstein, *Phil. Trans. R. Soc. Lond., A* 341 (1992): p. 531.
41. A. Broli, H. Holtan, *Corros. Sci.* 13 (1973): p. 237.
42. W. Zhang, S. Smialowska, G.S. Frankel, "Influence of Cr<sup>6+</sup> Concentration and pH on Polarization Curves of AA 2024-T3," Multidisciplinary University Research Initiative (MURI) Report by G. S. Frankel (Columbus, OH: Fontana Corrosion Center, The Ohio State University, 1998), p. 51.
43. M. Kendig, M. Cunningham, S. Jeanjaquet, D. Hardwick, *J. Electrochem. Soc.* 144 (1997): p. 3,721.
44. T. Shibata, T. Takeyama, *Corrosion* 33 (1977): p. 243.
45. M.E. Inman, R.G. Kelly, S.A. Willard, R.S. Piascik, "Coordinated Metallographic, Chemical, and Electrochemical Analyses of Fuselage Lap Splice Corrosion," Proc. of the Aircraft Structure Integrity Program (ASIP) Conference, Atlanta, November 1996.
46. M.W. Kendig, R. McCreery, J. Ramsey, "Spaciation of Oxo-Chromium (VI) Anions and the Corrosion Inhibition of Al Alloys," abstract no. 530, vol. 99-2, 196th Meeting of the Electrochemical Society, held October 17-22 (Pennington, NJ: ECS, 1999).
47. M. Pourbaix, *Atlas of Electrochemical Equilibria in Aqueous Solutions*, 2nd ed. (Houston TX: NACE, 1974).
48. G.M. Brown, K. Shimizu, K. Kobayahi, G.E. Thompson, G.C. Wood, *Corros. Sci.* 33 (1992): p. 1,371.
49. G.M. Brown, K. Shimizu, K. Kobayahi, G.E. Thompson, G.C. Wood, *Corros. Sci.* 33 (1992): p. 1,045.
50. P.L. Hagens, "Alternatives to Chromium for Metal Finishing," National Center for Manufacturing Sciences (NCMS) report 0273RE95 (Ann Arbor, MI: NCMS, 1995).
51. J.F. Dante, R.G. Kelly, *J. Electrochem. Soc.* 140 (1993): p. 1,890.
52. S.P. Sharma, *J. Electrochem. Soc.* 127 (1980): p. 21.
53. H. Bohni, H.H. Uhlig, *Corros. Sci.* 9 (1969): p. 353.
54. Z. Foroulis, M.J. Thubrikar, *J. Electrochem. Soc.* 122 (1975): p. 1,296.
55. S.T. Pride, J.R. Scully, J.L. Hudson, "Electrochemical Noise Measurements for Corrosion Applications," ASTM STP 1277, J.R. Kearns, J.R. Scully, P.R. Roberge, D.L. Reichert, J.L. Dawson, eds. (West Conshohocken, PA: ASTM, 1996), p. 307.
56. R.H. Brown, W.L. Fink, M.S. Hunter, *Trans. AIME* 143 (1941): p. 115.
57. B. Mazurkiewicz, A. Piotrowski, *Corros. Sci.* 23 (1983): p. 697.
58. K. Urushino, K. Sugimoto, *Corros. Sci.* 19 (1979): p. 225.
59. R.G. Buchheit, *J. Electrochem. Soc.* 142 (1995): p. 3,994.
60. W.W. Binger, E.H. Hollingsworth, D.O. Sprowls, *Aluminum*, ed. K.R. Van Horn (Metals Park, OH: ASM Int., 1967), p. 209.
61. P.C. Pistorius, "Electrochemical Noise Measurements for Corrosion Applications," ASTM STP 1277, eds. J.R. Kearns, J.R. Scully, P.R. Roberge, D.L. Reichert, J.L. Dawson (West Conshohocken, PA: ASTM, 1996), p. 343.
62. M.S. Hunter, G.R. Frank Jr., D.L. Robinson, "Mechanism of Corrosion of 2024 Alloy as Revealed by Electron Microscopy," Proc. Int. Cong. on Metallic Corrosion (Houston TX: NACE, 1963), p. 102.
63. J.R. Scully, T.O. Knight, R.G. Buchheit, D.E. Peebles, *Corros. Sci.* 35 (1993): p. 185.
64. M.J. Pryor, D.S. Keir, *J. Electrochem. Soc.* 102 (1955): p. 241C.
65. J. Wan, G.E. Thompson, K. Lu, C.J.E. Smith, *Physica B*, 208/209 (1995): p. 511.
66. D. Gilroy, P.J. Eddowes, I.M. Dalrymple, I. Azkarate, V. Madina, F. Seco, A. del Barrio, J. Parkes, M. Byrne, E.M. Almeida, M. Maia, D. Pereira, F.L. Bentes, *Met. Finish.* 10 (1996): p. 26.
67. W.D. Kingery, H.K. Bowen, D.R. Uhlmann, *Introduction to Ceramics* (New York, NY: John Wiley, 1976), p. 240.
68. D.R. Lide, ed., *CRC Handbook of Chemistry and Physics* (Boca Raton: CRC Press, 1990).
69. J.R. Waldrop, M.W. Kendig, *J. Electrochem. Soc.* 145 (1998): p. L11.
70. N. Dimitrov, J.A. Maan, K. Sieradski, *J. Electrochem. Soc.* 146 (1999): p. 98.
71. G.O. Ilievbare, J. Yuan, R.G. Kelly, J.R. Scully, "Inhibition of Corrosion on Chromate Conversion Coated AA 2024-T3: Behavior of Intermetallic Compounds," abstract no. 111, vol. 98-1, 193rd Meeting of the Electrochemical Society, held May 3-8, (Pennington, NJ: ECS, 1998).

# Mass-Transport-Limited Oxygen Reduction Reaction on AA2024-T3 and Selected Intermetallic Compounds in Chromate-Containing Solutions

G.O. Ilevbare and J.R. Scully\*

## ABSTRACT

Oxygen reduction reaction (ORR) kinetics were investigated on synthesized Al-Cu, Al-Cu-Mg, and Al-Cu-Fe-Mn intermetallic phases and compared to AA2024-T3 (UNS A92024), as well as high-purity Al, Cu, and Au. These tests were conducted in 0.1 M sodium sulfate ( $\text{Na}_2\text{SO}_4$ ) with and without either 0.005 M sodium chloride ( $\text{NaCl}$ , pH 6), 0.01 M sodium chromate ( $\text{Na}_2\text{CrO}_4$ , pH 8), or 0.0062 M  $\text{Na}_2\text{CrO}_4$  + 0.0038 M chromic acid ( $\text{H}_2\text{CrO}_4$ , pH 6) additions using stationary and rotating disk electrodes. Mass-transport-rate-controlled ORR were near theoretical values on all Cu-bearing materials and Au in 0.1 M  $\text{Na}_2\text{SO}_4$  with and without 0.005 M  $\text{NaCl}$ . Theoretical limiting current densities (CD) were not achieved in the mass-transport-controlled regime on Al because of the rate limitation of electron transfer through its oxide film. Four effects of chromate additions on such cathodic reaction rates were identified as follows:

- Little intrinsic effect of chromate pretreatment on mass-transport-controlled ORR on high-purity Cu, Cu-containing Al-based intermetallics, and Au electrodes in the absence of open-circuit corrosion. Charge transfer-controlled and mixed-controlled ORR are lowered possibly by the blocking of  $\text{O}_2$  adsorption sites by chromate anions.
- Decreased net cathodic kinetics on AA2024-T3 as a function of the degree to which chromate suppressed open-circuit pitting corrosion prior to cathodic polarization.
- Increased net cathodic kinetics on high-purity Al.

— Decreased ORR kinetics on S-Al<sub>2</sub>CuMg as a result of minimization of Al(Mg) dissolution and, subsequently, minimization of the formation of a high, Cu-rich surface. Comments are made regarding the influence of each of these phenomena on open-circuit pitting of AA2024-T3.

**KEY WORDS:** AA2024, aluminum, chromate, copper, gold, intermetallic compounds, mass-transport rates, oxide films, oxygen reduction reaction kinetics, sodium chloride

## INTRODUCTION

Aluminum-based precipitation age-hardened alloys containing Cu and Fe are particularly prone to localized corrosion such as pitting often induced by local galvanic cells formed by Cu- and Fe-containing intermetallic phases or replated Cu.<sup>1-6</sup> In AA2024-T3 (UNS A92024),<sup>(1)</sup> pit initiation sites include Al-Cu-Mg particles,<sup>1</sup> the periphery of Cu-enriched Al-Cu-Mg particles that have been dealloyed of Al and Mg,<sup>2</sup> and the matrix adjacent to Al-Cu-Fe-Mn particles.<sup>3</sup> In fact, coalesced pit sites that promote fatigue initiation often are formed near constituent particles.<sup>3</sup> It is well known that chromate conversion coating (CCC) and anodization of Al precipitation age-hardened alloys improve localized corrosion resistance, particularly in chloride salt spray testing.<sup>1-2,7-8</sup> Improvements in the localized corrosion performance of such surface-treated alloys suggests that either one or more of the four stages of localized corrosion at the anode site (i.e., nucleation, stabilization, growth, and repassivation) or the properties of cathode sites (e.g., cathodic intermetallic phases and replated Cu) are altered by the presence of the CCC. This paper pro-

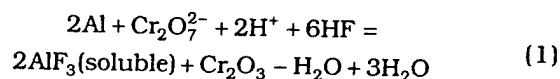
Submitted for publication April 2000; in revised form, September 2000.

\* Center for Electrochemical Science and Engineering, Department of Materials Science and Engineering, University of Virginia, Charlottesville, VA 22904-4745.

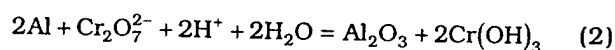
<sup>(1)</sup> UNS numbers are listed in *Metals and Alloys in the Unified Numbering System*, published by the Society of Automotive Engineers (SAE) and cosponsored by ASTM.

vides preliminary insight into the role of reported leaching of Cr(VI)<sup>9-14</sup> as a possible means of altering the cathodic electrochemistry of active anodic or cathodic intermetallic phases. Chromate is highly soluble in water and is an extremely effective solution phase corrosion inhibitor, particularly for localized corrosion.<sup>13-18</sup> Effects of chromate on the corrosion electrochemistry of intermetallics that create galvanic cells in Al-based precipitation age-hardened alloys is at present uncertain.

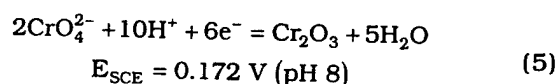
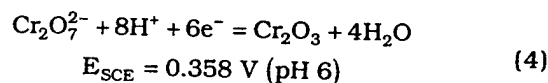
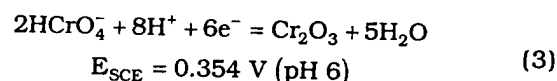
The CCC process on Al in a dichromate solution containing sodium fluoride (NaF) involves the following overall electrochemical reaction:



If only a small amount of hydrofluoric acid (HF) is present, then aluminum oxide ( $\text{Al}_2\text{O}_3$ ) is formed as well, and the overall reaction is:



Thus, CCC consist of a mixture of regions of chromium hydroxide ( $\text{Cr}(\text{OH})_3$ ) at sites where chromate was reduced along with regions of  $\text{Al}_2\text{O}_3$ . Thus, Al oxidation is required to form CCC, and it is reasonable to expect that these reactions are also thermodynamically and chemically possible on Cu-containing intermetallic phases that include a significant concentration of Al.  $\text{Cr}^{6+}$  and  $\text{Cr}^{3+}$  may exist within the CCC in several specific forms.<sup>19-21</sup> It is generally believed that reduction of  $\text{Cr}^{6+}$  to  $\text{Cr}^{3+}$  in the form of hydrated chromium oxide is incomplete and that CCC typically contain 9% to 60%  $\text{Cr}^{6+}$  chromate.<sup>11-13,22</sup> Aging of the coatings affects the amount of  $\text{Cr}^{6+}$  present and the amount subsequently available to be leached out.<sup>23-24</sup>  $\text{Cr}^{6+}$  can be reduced to  $\text{Cr}^{3+}$  by a number of reactions. If the formation of chromium oxide ( $\text{Cr}_2\text{O}_3$ ) at pH 6 and pH 8 is considered:



These potentials are negligibly affected by the formation of  $\text{Cr}(\text{OH})_3$  instead of  $\text{Cr}_2\text{O}_3$ . Hence, chromate is an oxidizer when added to near-neutral solutions. Moreover, these reaction products are thermody-

namically possible over the potential range near the open-circuit potential (OCP) of AA2024-T3 in near-neutral pH chloride solutions (e.g.,  $-0.5 \text{ V}$  vs saturated calomel electrode [SCE] to  $-0.6 \text{ V}_{\text{SCE}}$ ) and will occur concurrently with  $\text{O}_2$  reduction (e.g.,  $0.635 \text{ V}_{\text{SCE}}$ ) and  $\text{H}_2\text{O}$  reduction (e.g.,  $-0.595 \text{ V}_{\text{SCE}}$ ).

Exact mechanisms by which chromate or its reaction products inhibit metallic corrosion remain unclear and may differ in solutions of different halide/anion ratios, temperatures,<sup>25-27</sup> and pit sizes.<sup>17,28</sup> Anodic inhibition of small Al pits in dilute chloride may be observed in sodium chloride (NaCl) solutions containing soluble chromate additions<sup>17</sup> but is not always observed.<sup>29</sup> Anodic inhibition of pits at high chloride/chromate ratios is not seen.<sup>28-29</sup> Apparent cathodic inhibition of intermetallics has been reported but is subject to further investigation.<sup>29-30</sup> One issue is whether these reaction products alter the cathodic kinetics, in what is normally the mass-transport-limited oxygen reduction reaction (ORR) regime by lowering the rate of electron transfer through Al-Cr-rich oxides.

In this study, effects of soluble chromate additions on ORR rates were addressed to ascertain whether chromate additions can intrinsically alter net cathodic reaction rates so as to minimize the ability of local heterogeneities to form potent galvanic couples on AA2024-T3.

## EXPERIMENTAL PROCEDURES

Studies were conducted on mill-finished surfaces of 1.5-mm thick AA2024-T3 sheets with the following composition (wt%): 4.5% Cu, 1.30% Mg, 0.62% Mn, 0.18% Fe, 0.10% Zn, 0.093% Si, 0.018% Ti, 0.012% Ga, 0.011% V, 0.009% Cr, 0.008% Ni, 0.005% Zr, 0.003% Pb, 0.0006% Sc, < 0.002% Bi, < 0.0005% Co, < 0.0005% Ge, and bal. Al. Scanning electron microscopy/energy-dispersive spectroscopy (SEM/EDS) studies indicate Al-Cu-Mg and Al-Cu-Mn-Fe constituents on these surfaces. Other materials studied were 99.998% Al,  $\text{Al}_2\text{Cu}$ ,  $\text{Al}_2\text{CuMg}$ , 99.999% Cu, 99.9985% Au, and  $\text{Al}_{20}\text{Cu}_2(\text{MnFe})_3$ . Two SEM/EDS studies on AA2024-T3 of similar composition indicated that the predominant micrometer-sized intermetallic phases detected were of the Al-Cu-Mg and Al-Cu-Fe-Mn type,<sup>1-3,31-32</sup> with a lesser amount of the Al-Fe-Cu phase.<sup>2</sup> This is consistent with one study that did not find  $\theta$  microconstituents<sup>2</sup> and Al-Cu-Mg phase equilibria.<sup>33</sup> The  $\text{Al}_{12}\text{Si}(\text{MnFe})_3$  phase was not detected, possibly because of low Si contents.<sup>1</sup> Precipitate phases studied here were  $\text{Al}_2\text{Cu}$  and  $\text{Al}_2\text{CuMg}$ . Constituent particles of interest were  $\text{Al}_7\text{Cu}_2\text{Fe}$  and  $\text{Al}_{20}\text{Cu}_2(\text{MnFe})_3$ . The  $\text{Al}_7\text{Cu}_2\text{Fe}$  phase was not successfully synthesized and is not reported further. The common dispersoids in AA2024-T3 ( $\text{Al}_6\text{Mn}$ ,  $\text{Al}_{20}\text{Cu}_2\text{Mn}_3$ ) were not investigated here. This study concentrates on synthesized  $\text{Al}_2\text{Cu}$ ,  $\text{Al}_2\text{CuMg}$ ,

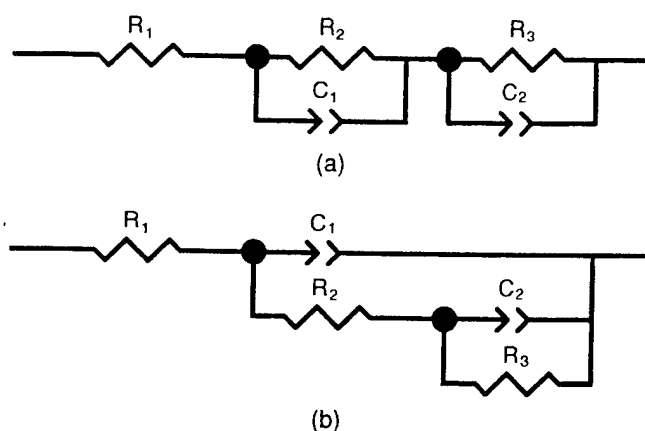


**FIGURE 1.** Two possible models for equivalent circuits representing a porous or defective anodic film.  $R_1$  is resistance of the electrolyte.  $R_2$  and  $R_3$  could represent the resistance of the porous layer and the resistance of either the barrier layer or charge transfer.  $C_1$  and  $C_2$  are constant phase elements and would represent the pores in the film barrier layer or interfacial capacitance within the pores. Both circuit models yield identical circuit parameters.

and  $\text{Al}_{20}\text{Cu}_2(\text{MnFe})_3$  intermetallic castings. X-ray diffraction results on these castings indicated that selected synthesized electrodes consisted predominantly of the aforementioned desired intermetallic phases. Moreover, a range of electrode sizes ( $0.0009 \text{ cm}^2$  to  $0.185 \text{ cm}^2$ ) and metallographic-masking techniques were used to attempt to isolate regions consisting of a single phase for study. All electrodes were wet-ground to a 600-grit surface finish with silicon carbide (SiC) paper.

Auger electron spectroscopy (AES) was conducted with a Perkin-Elmer 560 ESCA/SAM<sup>†</sup> system at a chamber pressure of  $\sim 10^{-10}$  torr. It was equipped with a channel electron multiplier detector. AES spectra were taken with an electron gun voltage of 3 keV at a resolution of 0.6%. Depth profiles were generated with Ar-sputtering at a beam voltage of 3 kV, in the raster mode, at a pressure (in the ion gun) between 10 mPa and 20 mPa.

OCP exposures followed by potentiodynamic polarization experiments were performed in quiescent 0.1 M sodium sulfate ( $\text{Na}_2\text{SO}_4$ ) + 0.005 M NaCl (pH 6) at ambient temperature, on stationary electrodes, in a three-electrode cell that was open to lab air. Details are discussed elsewhere.<sup>34</sup> This environment was based on measurements of corrosive environments found in the lap-splice joints of aircraft.<sup>22</sup> In other experiments, 0.01 M sodium chromate ( $\text{Na}_2\text{CrO}_4$ ) was added to 0.1 M  $\text{Na}_2\text{SO}_4$  + 0.005 M NaCl (final pH was 8) to mimic Cr(VI) leaching. The same experiments were repeated in 0.1 M  $\text{Na}_2\text{SO}_4$  + 0.005 M NaCl + 0.0068 M  $\text{Na}_2\text{CrO}_4$  + 0.0038 M chromic acid ( $\text{H}_2\text{CrO}_4$ ) (pH 6). In rotating disc electrode (RDE) experiments, cathodic potential scans at a sweep rate of 1 mV/s

were performed after a 2-h exposure at OCP in 0.1 M  $\text{Na}_2\text{SO}_4$  + 0.005 M NaCl (pH 6) at rotation speeds of 500, 2,000, and 4,000 rpm. Cathodic scans at these rotation speeds also were carried out in 0.1 M  $\text{Na}_2\text{SO}_4$  + 0.005 M NaCl (pH 6) after a 2-h pretreatment at OCP in 0.1 M  $\text{Na}_2\text{SO}_4$  + 0.005 M NaCl + 0.0068 M  $\text{Na}_2\text{CrO}_4$  + 0.0038 M  $\text{H}_2\text{CrO}_4$  (pH 6). These electrodes were rinsed with deionized, distilled water before the cathodic scans. All electrolytes were air-sparged. The mass-transport-limiting current density ( $i_l$ ) was calculated from mass-transport-limited regions on cathodic E-logi curves. In the case of Al, where clear regions were not observed, the hydrogen evolution reaction (HER) and OCP portions of the curves were avoided in estimating the ORR limiting current density. Electrochemical impedance spectroscopy (EIS) experiments were conducted at the OCP on  $\text{Al}_2\text{CuMg}$  and  $\text{Al}_{20}\text{Cu}_2(\text{MnFe})_3$  after various exposure times at OCP. In other experiments, EIS data was collected on Al at OCP after potentiostatic polarization for various periods of time at potentials between  $-0.5 V_{\text{SCE}}$  and  $1.5 V_{\text{SCE}}$ . Spectra were collected from between 0.01 Hz and 100 kHz at 10 points/decade. Nonlinear least square (NLLS) fitting was used to calculate the impedance parameters using the circuit model in Figure 1(a). Original fits to EIS data were performed using the model shown in Figures 1(a) and (b) as well as others. The model in Figure 1(a) was better for earlier in the exposure time before pores developed, while the model in Figure 1(b) was better (more physically realistic) for latter times when pores developed. The models in Figures 1(a) and (b) produced the same values for the circuit parameters, which are consistently used throughout.

## RESULTS

### Intermetallic Bulk Composition and Surface Composition

Results presented here concentrate on synthesized  $\text{Al}_2\text{Cu}$ ,  $\text{Al}_2\text{CuMg}$ , and  $\text{Al}_{20}\text{Cu}_2(\text{MnFe})_3$  intermetallics.  $\text{Al}_2\text{Cu}$  has been analyzed in more detail elsewhere.<sup>35</sup> Compositions of the castings are given in wt% and atomic fraction in Table 1. The surface compositions after wet-grinding with SiC paper to 600 grit (and drying under a jet of warm air) obtained from AES are reported in Table 2. Surface compositions match the compound stoichiometry used throughout this paper.  $\text{Al}_{20}\text{Cu}_2(\text{MnFe})_3$  was slightly richer in Fe after wet-grinding. Mn substitution for Fe can lead to grains of variable Mn/Fe ratios, which was observed.

### Anodic and Cathodic Corrosion Kinetics in 0.1 M $\text{Na}_2\text{SO}_4$ + 0.005 M NaCl

Figures 2(a) and (b) illustrate the overall E-logi behavior of stationary electrodes of AA2024-T3, Al, Cu,  $\text{Al}_2\text{Cu}$ ,  $\text{Al}_2\text{CuMg}$ , and  $\text{Al}_{20}\text{Cu}_2(\text{MnFe})_3$  in 0.1 M

<sup>†</sup> Trade name.



$\text{Na}_2\text{SO}_4 + 0.005 \text{ M NaCl}$  after a 2-h exposure at OCP. Several features are notable. These include the high OCP of Cu,  $\text{Al}_2\text{Cu}$ , and  $\text{Al}_{20}\text{Cu}_2(\text{MnFe})_3$ . The OCP of these electrodes were more positive than that of AA2024-T3 (indicated with the horizontal line) and far more positive than  $\text{Al}_2\text{CuMg}$  and high-purity Al. However, they were below potentials for chromate reduction listed earlier. Previous studies of Cu and  $\text{Al}_2\text{Cu}$  in borate-containing buffers<sup>4</sup> indicate similar positive OCP over a range of pH. It should be noted that OCP were positive on Cu and  $\text{Al}_2\text{Cu}$ , starting at the time of exposure, and did not drift positive with time (Figure 3). The OCP of  $\text{Al}_{20}\text{Cu}_2(\text{MnFe})_3$  drifted positive with time. The synthesized  $\text{Al}_2\text{CuMg}$  phase had an OCP after 2 h of near  $-0.85 \text{ V}_{\text{SCE}}$ , which is consistent with the literature.<sup>36-38</sup> The OCP of  $\text{Al}_2\text{CuMg}$  started near  $-1.1 \text{ V}_{\text{SCE}}$ , shifted toward  $-0.8 \text{ V}_{\text{SCE}}$ , and then stabilized after  $\approx 1,000 \text{ s}$  (Figure 3). Moreover,  $\text{Al}_2\text{CuMg}$  was not spontaneously passive and exhibited dissolution upon anodic polarization.  $\text{Al}_{20}\text{Cu}_2(\text{MnFe})_3$  was initially passive near the OCP of AA2024-T3 (Figure 2(c)), while  $\text{Al}_2\text{CuMg}$  actively corroded. Impedance data at the OCP on  $\text{Al}_{20}\text{Cu}_2(\text{MnFe})_3$  and  $\text{Al}_2\text{CuMg}$  (Figure 4) showed increases in the values of constant phase elements (CPE)  $C_1$  and  $C_2$  and decreases in the CPE exponent,  $n$ ,<sup>(2)</sup> with exposure time. These suggest that the surfaces became porous and that the porous surface areas of both intermetallics increased with time of immersion at OCP between 0 and 10 h. These results were consistent with polarization data presented for  $\text{Al}_2\text{CuMg}$  phase in Figure 2(b). For  $\text{Al}_{20}\text{Cu}_2(\text{MnFe})_3$ , however, the increase in values of  $C_1$  and  $C_2$  with time at OCP might suggest either that the passivity of  $\text{Al}_{20}\text{Cu}_2(\text{MnFe})_3$  was not stable over long periods of time or that the limited potential range of the passive region made it prone to localized dissolution at OCP when small shifts in potential occur during long immersion times. The values of impedance modulus ( $|Z|$ ) fell with time between 0 h and 10 h for both intermetallic compounds.  $|Z|$  for  $\text{Al}_{20}\text{Cu}_2(\text{MnFe})_3$  was higher than for  $\text{Al}_2\text{CuMg}$ , suggesting that  $\text{Al}_{20}\text{Cu}_2(\text{MnFe})_3$  was less prone to active dissolution at OCP than  $\text{Al}_2\text{CuMg}$ .  $\text{Al}_2\text{Cu}$  had an OCP near its  $E_{\text{pit}}$  but was passive. This was confirmed in identical tests performed in  $0.1 \text{ M Na}_2\text{SO}_4$ .

Net cathodic kinetics were enhanced on all Cu-containing materials as well as AA2024-T3 (Figure 2(a)) compared with Al.<sup>(3)</sup> A peak in cathodic current density on Cu was caused by the cathodic reduction of the copper oxide (CuO). Otherwise, the principal cathodic reactions were the ORR and HER at more negative potentials. It is clear that the exchange cur-

<sup>(2)</sup> See Appendix.

<sup>(3)</sup> Net cathodic kinetics are given by  $i_{\text{net}} = i_{\text{cath}} - i_{\text{an}}$  in cases where cathodic corrosion produces  $i_{\text{an}}$ .  $i_{\text{net}}$  is the current density that may be supplied during galvanic coupling. Hereafter, this is called the net cathodic reaction rate normalized by original geometric electrode area.

**TABLE 1**  
Weight and Atomic Percentages  
of the Intermetallics Castings

Phases	Al	Mg	Zn	Cu	Mn	Fe
Elemental Composition (wt%)						
$\text{Al}_{20}\text{Cu}_2(\text{MnFe})_3$	54.01	—	—	12.72	16.50	16.77
$\text{Al}_2\text{CuMg}$	38.05	17.14	—	44.81	—	—
$\text{Al}_2\text{Cu}$	45.96	—	—	54.04	—	—
Atomic Composition (%)						
$\text{Al}_{20}\text{Cu}_2(\text{MnFe})_3$	71.43	—	—	7.14	10.71	10.71
$\text{Al}_2\text{CuMg}$	49.28	26.06	—	24.66	—	—
$\text{Al}_2\text{Cu}$	66.69	—	—	33.31	—	—

**TABLE 2**  
AES Analyses of the Surface Compositions  
of the Intermetallic Compounds  
( $\text{Al}_2\text{CuMg}$  and  $\text{Al}_{20}\text{Cu}_2(\text{MnFe})_3$ ) Tested

Sputter Time (s)	Atomic Composition of Al <sub>2</sub> CuMg (at%)				
	Al	Cu	Mg	O	
150	34.13	17.65	15.45	32.76	
Sputter Time (s)	Atomic Composition of Al <sub>20</sub> Cu <sub>2</sub> (MnFe) <sub>3</sub> (at%)				
	Al	Cu	Mn	Fe	O
120	54.26	6.18	8.66	14.87	16.03

rent density for the HER was much lower on Al than the Cu-containing materials. In fact, the exchange current density for the HER is so low<sup>39</sup> on Al that mass-transport-limited ORR dominates the high-purity Al electrode at potentials as low as  $-1.5 \text{ V}_{\text{SCE}}$ . The mass-transport-limited ORR (dominant from  $-0.5 \text{ V}$  to  $-1.0 \text{ V}$  on  $\text{Al}_2\text{Cu}$  and  $\text{Al}_{20}\text{Cu}_2(\text{MnFe})_3$ ) was clearly faster on the Cu-bearing materials compared to pure Al, as noted by Pryor and Keir.<sup>5</sup> Note that net cathodic kinetics were particularly enhanced on  $\text{Al}_2\text{CuMg}$  compared to the other materials, even high-purity Cu. The origins of this behavior are discussed below. Mass-transport-limited  $\text{O}_2$  reduction is one of the cathodic reactions of greatest interest when studying open-circuit corrosion of AA2024-T3 either with or without the chromate inhibitor. At issue is the effect of soluble chromate on this reaction.

Figure 5(a) shows the net cathodic E-log*i* behavior of pure Cu, Al, and  $\text{Al}_{20}\text{Cu}_2(\text{MnFe})_3$  in  $0.1 \text{ M Na}_2\text{SO}_4 + 0.005 \text{ M NaCl}$  at an electrode rotation speed of 500 rpm ( $\omega^{0.5} = 7.24 \text{ [rad/s]}^{0.5}$ ). Oxygen reduction  $i_1$  data from rotating disk electrodes in  $0.1 \text{ M Na}_2\text{SO}_4 + 0.005 \text{ M NaCl}$  are shown for pure Cu,  $\text{Al}_{20}\text{Cu}_2(\text{MnFe})_3$ , and pure Al in scans conducted after a 2-h exposure at OCP (Figure 5b). The  $i_1$  data for the Cu and  $\text{Al}_{20}\text{Cu}_2(\text{MnFe})_3$  almost match those results predicted from the Levich equation with respect to angular velocity (rotation rate).<sup>40</sup> The  $i_1$  on Al was much lower than predicted from mass transport of  $\text{O}_2$  in solution. The kinetics were almost independent of

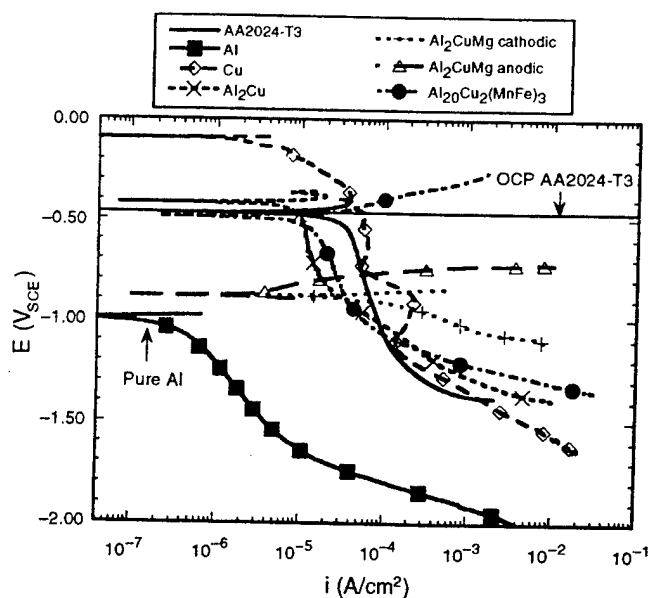


FIGURE 2(a). The cathodic E-logi behavior of stationary electrodes of AA2024-T3, Al, Cu,  $\theta$ -Al<sub>2</sub>Cu, S-Al<sub>2</sub>CuMg, and Al<sub>20</sub>Cu<sub>2</sub>(MnFe)<sub>3</sub> in 0.1 M Na<sub>2</sub>SO<sub>4</sub> + 0.005 M NaCl under ambient aeration. (Ohmically corrected).

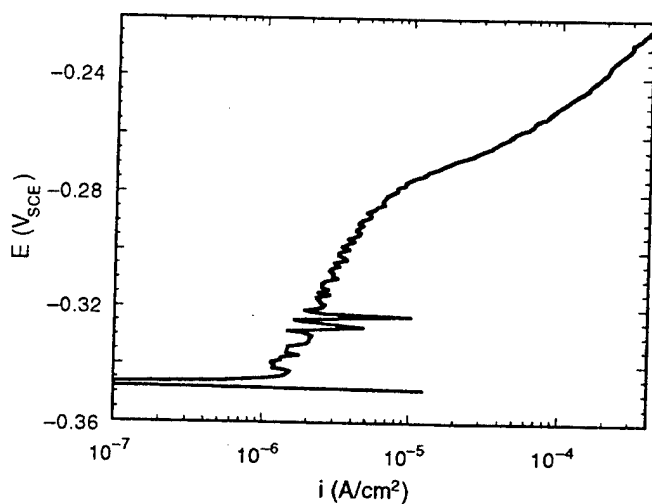


FIGURE 2(c). The anodic E-logi behavior of Al<sub>20</sub>Cu<sub>2</sub>(MnFe)<sub>3</sub> near the OCP in 0.1 M Na<sub>2</sub>SO<sub>4</sub> + 0.005 M NaCl under ambient aeration.

angular velocity and did not obey the Levich equation, which is theoretically independent of electrode material. This implies an additional rate limitation for Al, or a high rate of corrosion on Al at cathodic potentials. However, Figures 6(a) and (b) show that the kinetics of ORR decreased on Al with increasing oxide thickness, suggesting control by electron transfer through the oxide (Discussion). A critical unresolved issue is whether chromate could reduce the cathodic ORR kinetics on the intermetallics or

<sup>(4)</sup> Pitting potential was the potential at which a current density of  $3.0 \times 10^{-5}$  A/cm<sup>2</sup> was attained by the sample. For further details, see an earlier work.<sup>34</sup>

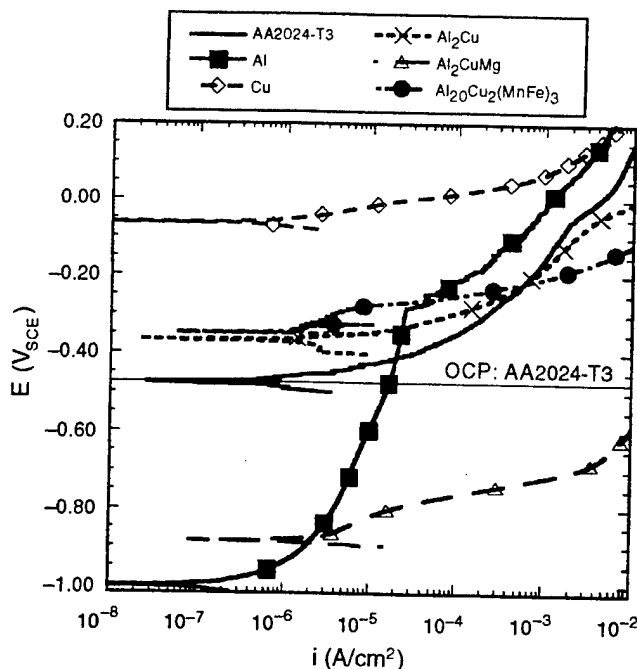


FIGURE 2(b). The anodic E-logi behavior of stationary electrodes of AA2024-T3, Al, Cu,  $\theta$ -Al<sub>2</sub>Cu, S-Al<sub>2</sub>CuMg, and Al<sub>20</sub>Cu<sub>2</sub>(MnFe)<sub>3</sub> in 0.1 M Na<sub>2</sub>SO<sub>4</sub> + 0.005 M NaCl under ambient aeration.

on replated Cu, represented in this study by the Cu electrode.

### Cathodic Kinetics in Chromate-Free Solutions as a Function of the Extent of Prior Corrosion

Cathodic kinetics experiments in chromate-free solutions were performed on stationary AA2024-T3 electrodes as a function of extent of prior corrosion damage. Extent of prior corrosion damage was controlled by either varying time at OCP or applying indicated levels of anodic charge immediately prior to cathodic scans. Figure 7(a) shows representative E-logi behavior of AA2024-T3 in 0.1 M Na<sub>2</sub>SO<sub>4</sub> and 0.1 M Na<sub>2</sub>SO<sub>4</sub> + 0.005 M NaCl after a 2-h hold at OCP. The OCP in 0.1 M Na<sub>2</sub>SO<sub>4</sub> + 0.005 M NaCl was close to the pitting potential (Figure 7(b)).<sup>(4)</sup> AA2024-T3 was not expected to pit in 0.1 M Na<sub>2</sub>SO<sub>4</sub> because of the absence of chloride ions in solution.

Greater net cathodic kinetics after 2 h at OCP shown in 0.1 M Na<sub>2</sub>SO<sub>4</sub> + 0.005 M NaCl were consistent with open-circuit corrosion occurring on AA2024-T3 in this electrolyte (Figure 7[a]). The  $i_1$  (taken at  $-0.75$  V<sub>SCE</sub>) for ORR in 0.1 M Na<sub>2</sub>SO<sub>4</sub> was  $2.96 \times 10^{-6} \pm 1.706 \times 10^{-6}$  A/cm<sup>2</sup>, while in 0.1 M Na<sub>2</sub>SO<sub>4</sub> + 0.005 M NaCl it was  $7.594 \times 10^{-6} \pm 0.906 \times 10^{-6}$  A/cm<sup>2</sup> (error values are reported at a 95% confidence level). This shows a slight statistically significant decrease in  $i_1$  for ORR in noncorrosive sulfate solution compared with the sulfate + NaCl solution (Figure 7[a]). Net cathodic reaction kinetics observed on polarization, after application of an anodic charge

to cause pitting on AA2024-T3, increased as the anodic charge applied increased (Figure 8[a]).<sup>(5)</sup> The OCP measured after the application of these anodic charges also became more negative as applied charge increased (Figure 8[b]).

The net cathodic kinetics of  $\text{Al}_2\text{CuMg}$  also increased as the extent of corrosion that had occurred increased. This is evident in Figure 9(a), which compares the net cathodic E-log*i* behavior of  $\text{Al}_2\text{CuMg}$  after 60 s at OCP with the behavior after 60 min at  $-0.6 V_{\text{SCE}}$  (near the OCP of AA2024-T3) in 0.1 M  $\text{Na}_2\text{SO}_4 + 0.005 \text{ M NaCl}$ . At  $-0.6 V_{\text{SCE}}$ ,  $\text{Al}_2\text{CuMg}$  was experiencing severe dissolution and likely dealloying (Figure 2). Figure 9(a) shows that the kinetics of the ORR and HER increased on  $\text{Al}_2\text{CuMg}$  with the amount of anodic charge passed. Raw impedance data and circuit model parameters show the values of  $C_1$  on  $\text{Al}_2\text{CuMg}$  after 60 s at OCP and at  $-0.6 V_{\text{SCE}}$  for 60 min to be  $15.86 \Omega^{-1} \text{ s}^n/\text{cm}^2$  and  $59.06 \Omega^{-1} \text{ s}^n/\text{cm}^2$ , respectively (normalized for area, with  $n = 0.92$  and  $0.79$ , respectively).<sup>(6)</sup> The increase in the value of  $C_1$  most likely indicates an increase of surface area between the two cases. The impedance of  $\text{Al}_2\text{CuMg}$  after 60 s at OCP was higher than after 60 min at  $-0.6 V_{\text{SCE}}$  ( $|Z|$  at 10 Hz =  $59.06 \Omega\text{-cm}^2$  after 60 s at OCP vs  $15.86 \Omega\text{-cm}^2$  after 60 min at  $-0.6 V_{\text{SCE}}$ , respectively). Together, these changes support the notion that net cathodic kinetics (ORR and HER) normalized by original surface area are enhanced on  $\text{Al}_2\text{CuMg}$  with the amount of anodic charge passed. Figure 9(b) shows porous electrode formation on  $\text{Al}_2\text{CuMg}$  in 0.1 M  $\text{Na}_2\text{SO}_4 + 0.005 \text{ M NaCl}$ . The key result here is that prior corrosion alters net cathodic ORR and HER reduction kinetics by increasing electrode area (through roughening), forming pits that alter surface pH, and increasing the extent to which the surface is enriched in replated Cu during corrosion.<sup>(4)</sup>

### Cathodic Kinetics After Exposure in Chromate-Containing Solutions When Chromate Inhibitor Suppresses Corrosion at OCP

The goal of this study was to assess whether or not chromate directly suppresses cathodic kinetics on intermetallics versus indirectly through anodic inhibition. However, prior open-circuit corrosion affects net cathodic kinetics as clearly shown above. Attempts to study cathodic reaction kinetics in chromate-containing solutions that contain chloride are complicated by any effect that chromate might have on the suppression of open-circuit corrosion. This is

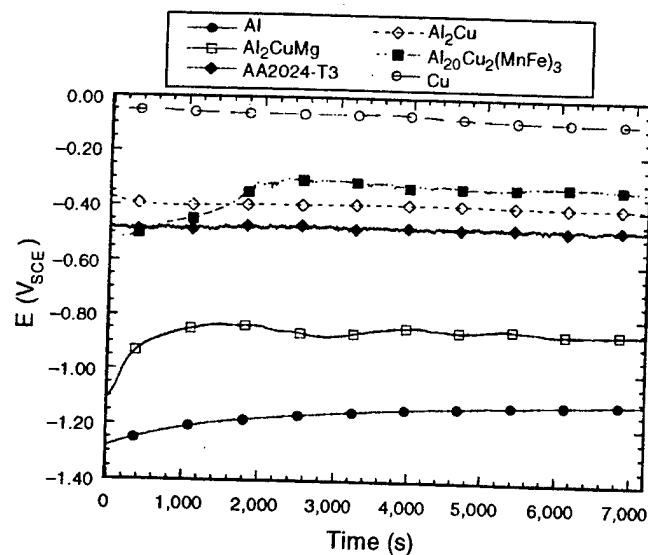


FIGURE 3. First 2 h of OCP of Al (99.998%), Cu (99.999%), AA2024-T3,  $\text{Al}_2\text{Cu}$ ,  $\text{Al}_{20}\text{Cu}_2(\text{MnFe})_3$ , and  $\text{Al}_2\text{CuMg}$  stationary electrodes in 0.1 M  $\text{Na}_2\text{SO}_4 + 0.005 \text{ M NaCl}$  (pH 6).

illustrated by anodic polarization of  $\text{Al}_2\text{CuMg}$  with and without chromate (Figure 10[a]). Chromate passivated the  $\text{Al}_2\text{CuMg}$  phase. Further evidence is provided by the EIS data showing  $|Z|$  at 10 Hz vs time (Figure 10[b]).  $|Z|$  was much higher over time when chromate was present in solution. In the absence of chromate, however,  $|Z|$  was much lower and the shape of the resulting EIS spectra can be modeled according to porous electrode theory.<sup>(42-46)</sup>  $C_1$  and  $C_2$  values were consistently lower when chromate was present in solution and  $n$  was higher, indicating an oxide. This suggests that the increase in surface area at OCP (which is probably caused by the development of porosity on the electrode surface) is not as severe in the presence of chromate (Figure 10[c]). Chromate is shown to significantly lower the corrosion rate of the  $\text{Al}_2\text{CuMg}$  phase and, therefore, diminish the possibility of forming a porous electrode surface, which has been clearly shown to enhance net cathodic reaction rates (Figures 7 through 9). Impedance measurements from  $\text{Al}_{20}\text{Cu}_2(\text{MnFe})_3$  also show improvements in passivity caused by chromate (Figure 11).

Suppression of OCP corrosion also is shown for AA2024-T3, which forms pits near its OCP without chromate (Figure 7[b]), but does not undergo stable pitting at OCP in chromate-bearing solutions as a result of the elevation of  $E_{\text{pit}}$  above OCP (Figure 12). In each case, OCP corrosion was suppressed by soluble chromate additions and net cathodic kinetics were altered.

### Cathodic Kinetics After Exposure to Chromate Inhibitor

An accurate assessment of the role of chromate on net cathodic kinetics requires that prior OCP cor-

<sup>(5)</sup> It is recognized that net cathodic kinetics at  $-0.75 V_{\text{SCE}}$  after corrosion could represent a mixture of ORR and HER as a result of the acidic pH shift. However, experiments in sulfate are dominated by mass-transport-limited ORR at  $-0.75 V_{\text{SCE}}$ . Other complexities related to the effect of sulfate (e.g., Cu-sulfate complex chemistry) have not been explored in the present work.

<sup>(6)</sup>  $n$  is a frequency-independent parameter, as defined in the Appendix.

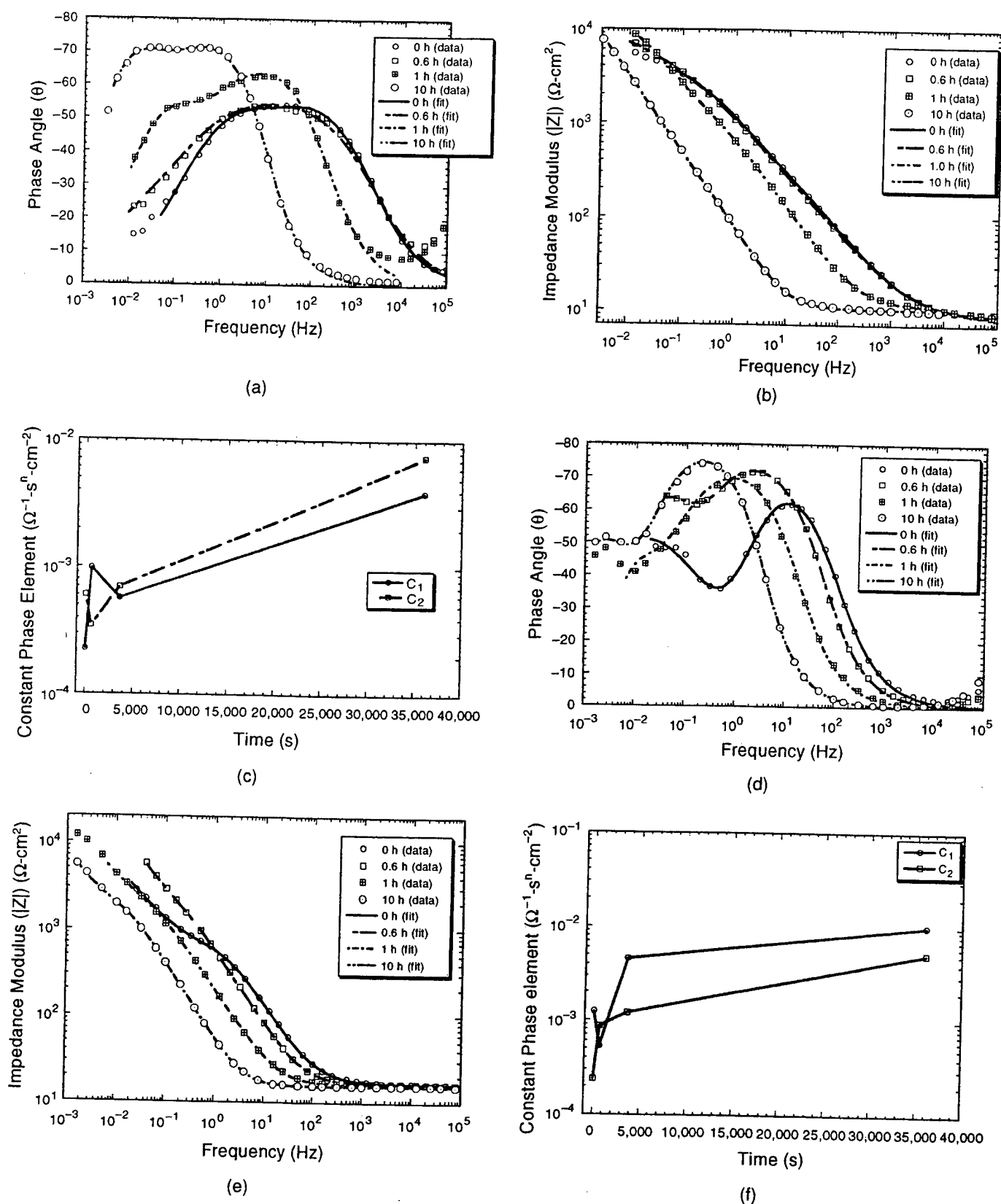


**FIGURE 4.** An  $\text{Al}_{20}\text{Cu}_2(\text{MnFe})_3$  stationary electrode in  $0.1 \text{ M Na}_2\text{SO}_4 + 0.005 \text{ M NaCl}$  (pH 6), after various exposure times at OCP: (a) phase angle vs frequency, (b) impedance modulus  $|Z|$  vs frequency, and (c) CPE ( $\Omega^{-1} \text{ s}^n/\text{cm}^2$ ) vs time ( $n$  for  $C_1 = 0.67$  to  $0.92$ ; for  $C_2 = 0.64$  to  $0.81$ ). Also, shown as an  $\text{Al}_2\text{CuMg}$  stationary electrode  $0.1 \text{ M Na}_2\text{SO}_4 + 0.005 \text{ M NaCl}$  (pH 6) after various exposure times at OCP: (d) phase angle vs frequency, (e)  $|Z|$  vs frequency, and (f) CPE ( $\Omega^{-1} \text{ s}^n/\text{cm}^2$ ) vs time ( $n$  for  $C_1 = 0.70$  to  $0.98$ ; for  $C_2 = 0.84$  to  $0.98$ ).

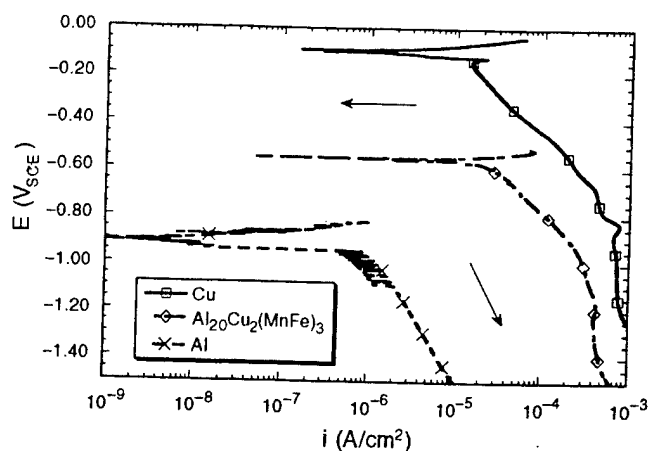


FIGURE 5(a). Cathodic  $E$ -log  $i$  behavior of pure Cu, Al, and  $\text{Al}_{20}\text{Cu}_2(\text{MnFe})_3$  in 0.1 M  $\text{Na}_2\text{SO}_4$  + 0.005 M NaCl at ambient aeration and electrode rotation speed of 500 rpm ( $\omega^{0.5} = 7.24$ ).

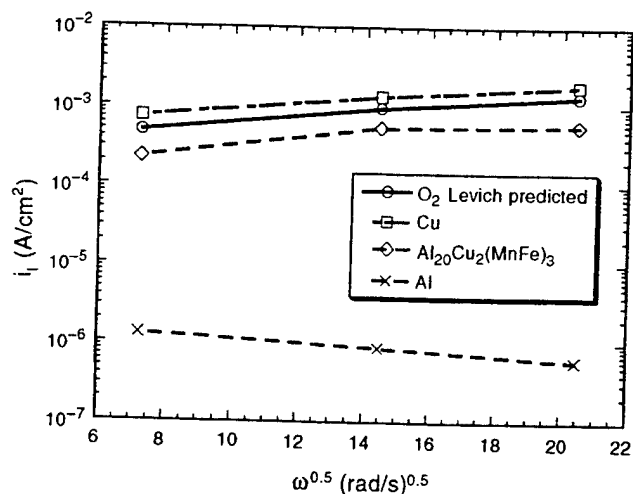


FIGURE 5(b). Oxygen reduction limiting current density ( $i_l$ ) data from rotating disk electrodes for pure Cu,  $\text{Al}_{20}\text{Cu}_2(\text{MnFe})_3$ , and pure Al in 0.1 M  $\text{Na}_2\text{SO}_4$  + 0.005 M NaCl at ambient aeration. Levich prediction at concentration of 6 ppm ( $1.88 \times 10^{-4}$  M) dissolved  $\text{O}_2$ .

rosion damage be minimized so that surface area and composition changes are minimized. A second complication in discovering the effects of chromate on ORR is that chromate-containing solutions provide a second cathodic reactant ( $\text{Cr}^{6+}$ ) that will be reduced, in addition to oxygen, over the potential range of interest for mass-transport-controlled  $\text{O}_2$  reduction. The third complication is the thickening of the oxide film on the metal or intermetallic by the chromate oxidizer. To sort out these effects, materials that do not corrode or otherwise pit as readily at OCP and do not grow thicker passive films are required. Tests also must be conducted after chromate pretreatment to minimize  $\text{Cr}^{6+}$  reduction.

In rotating disc electrode experiments, Cu and  $\text{Al}_{20}\text{Cu}_2(\text{MnFe})_3$  were tested in both chromate-bearing solutions and after 2 h exposure in chromate-bearing solutions (immediate transfer to 0.1 M  $\text{Na}_2\text{SO}_4$  +

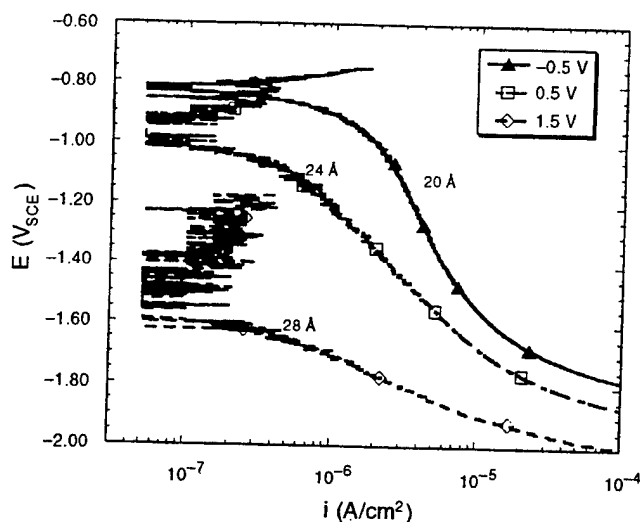


FIGURE 6(a). Polarization curves of pure Al after holding potentiostatically at -0.5, 0.5, and 1.5  $V_{\text{SCE}}$  in 0.1 M  $\text{Na}_2\text{SO}_4$  (pH 6) to grow barrier oxide film.

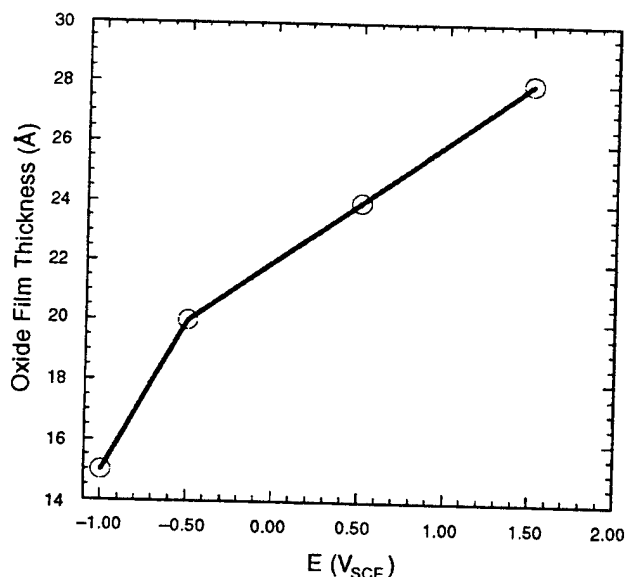


FIGURE 6(b). Calculated film thickness (from impedance measurements assuming a dielectric constant of 10 and a parallel plate capacitor model) as a function of applied potential of pure Al after potentiostatic holds at -1.0, -0.5, 0.5, and 1.5  $V_{\text{SCE}}$ , and for pure Al exposed to 0.1 M  $\text{Na}_2\text{SO}_4$  (pH 6).

0.005 M NaCl after rinsing in deionized, distilled water). Cathodic ORR kinetics (Figures 13[a] and [b]) after chromate pretreatment were altered on Cu, which registered a reduction in cathodic kinetics. They were not reduced on  $\text{Al}_{20}\text{Cu}_2(\text{MnFe})_3$ . ORR kinetics also were reduced on Cu and  $\text{Al}_{20}\text{Cu}_2(\text{MnFe})_3$  in RDE measurements made in chromate-containing solutions after 2 h of pretreatment at OCP in these solutions (Figures 14[a] and [b]). The results are striking in that net charge-transfer-controlled ORR rates were reduced but mass transport ORR rates were not reduced to the low ORR rates seen on Al.

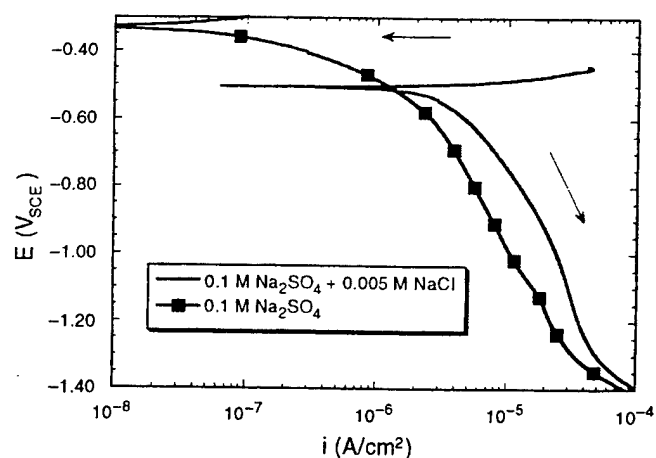


FIGURE 7(a). Representative  $E$ -log $i$  behavior of AA2024-T3 on stationary electrodes in 0.1 M  $\text{Na}_2\text{SO}_4$  and 0.1 M  $\text{Na}_2\text{SO}_4$  + 0.005 M NaCl after a 2-h exposure at OCP.

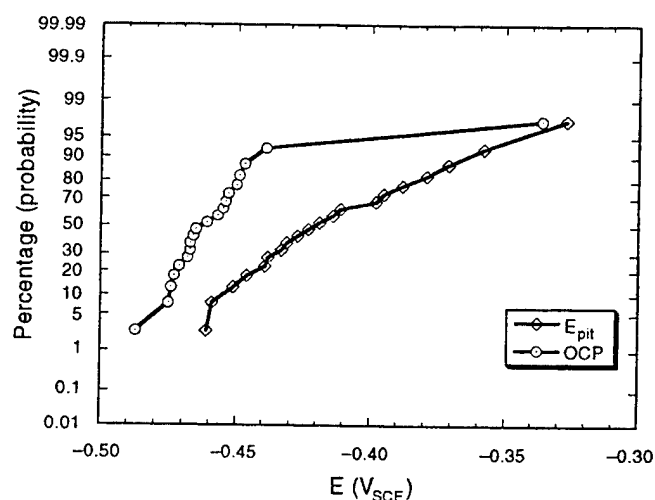


FIGURE 7(b). Cumulative probability plot of the OCP and  $E_{\text{pit}}$  of AA2024-T3 in 0.1 M  $\text{Na}_2\text{SO}_4$  + 0.005 M NaCl after a 2-h exposure at OCP.

Reductions in ORR were thought to originate from the ability of chromate to alter the surface of the electrodes (compared to when chromate was absent [Figure 5]). This is thought to have occurred either by preventing corrosion at OCP, by changing the oxide composition by  $\text{Cr(VI)}$  reduction, or by thickening the oxide film on the metal to such an extent that the kinetics no longer strictly obeyed the Levich equation.

However, an additional mechanism is that  $\text{CrO}_4^{2-}$  and  $\text{SO}_4^{2-}$  anions block surface sites associated with  $\text{O}_2$  adsorption.<sup>(7)</sup> To investigate this theory, a metal that neither would corrode at OCP nor had an oxide film that could be thickened by the oxidizing effect of chromate had to be examined. Pure gold (Au)

<sup>(7)</sup> Albeit at potentials where  $\text{Cr(VI)}$  could be reduced to  $\text{Cr}_2\text{O}_3$  after adsorption.

(99.9985%) was chosen. Figure 15 shows that pretreatment in solutions containing chromate does not alter the mass-transport-limited ORR cathodic kinetics on Au. However, charge-transfer-controlled ORR kinetics were reduced. Further, mass-transport-controlled cathodic kinetics in the presence of chromate were enhanced compared with when chromate was absent. This was caused by a combination of the ORR and the chromate reduction reaction (from  $\text{Cr}^{6+}$  to  $\text{Cr}^{3+}$ ) when chromate was in solution. The total mass-transport-limiting current density on Au in the presence of chromate in Figure 15 can be represented as follows:  $i_{\text{total}} = i_{\text{O}_2} + i_{\text{[CrVI to CrIII]}}$ .  $i_{\text{O}_2}$  is the limiting current density for the ORR, while  $i_{\text{[CrVI to CrIII]}}$  represents that for the reduction of  $\text{Cr}^{6+}$  to  $\text{Cr}^{3+}$ .

Additional tests were carried out in the halide-free sulfate solutions on stationary electrodes of AA2024-T3,  $\text{Al}_{20}\text{Cu}_2(\text{MnFe})_3$ , and  $\text{Al}_2\text{Cu}$  with and without a 2-h chromate pretreatment to eliminate the effects of corrosion on net ORR kinetics. No alterations of net cathodic kinetics were seen after pretreatment in chromate when compared to noncorrosive 0.1 M  $\text{Na}_2\text{SO}_4$  (Figure 16). Cr peaks were detected in x-ray photoelectron spectroscopy (XPS) measurements on AA2024-T3 after such exposures in other studies.<sup>24</sup> This is similar to the behavior of AA2024-T3 (Figure 7[a]), where removal of  $\text{Cl}^-$  reduced net cathodic kinetics. Enhanced ORR and HER kinetics were observed on AA2024-T3 in 0.1 M  $\text{Na}_2\text{SO}_4$  + 0.005 M NaCl, but Figures 2[b] and 7[b] indicate that pitting is possible at OCP. Chromate present at 0.01 M concentrations did reduce net cathodic ORR reaction rates. However, part of the reduction seen in NaCl-bearing solutions can, in part, be attributed to minimization of OCP corrosion such as pitting.

One key finding of this section is that mass-transport-limited ORR kinetics on Cu-bearing materials were not reduced to levels of pure Al by chromate pretreatment. Limited changes in mass-transport-controlled ORR kinetics can be seen when corrosion damage is minimized prior to cathodic polarization, and oxide film thickening (or other alterations) resulting from the oxidizing effect of chromate are accounted for (as seen on Au). However, charge-transfer-controlled ORR kinetics are reduced even on noncorroding electrodes such as Au.

## DISCUSSION

### Enhancement in Cathodic Kinetics on Al-Cu-X Intermetallics

A reduction in the rate of cathodic kinetics will undoubtedly result in a reduced rate of corrosion on the metal, as expressed by the following equation:

$$I_{\text{corr}} = i_{\text{an}} A_{\text{an}}(E_{\text{corr}}) = i_{\text{ca}} A_{\text{ca}}(E_{\text{corr}}) \quad (6)$$

where  $I_{\text{corr}}$  is the corrosion current,  $i_{\text{an}}$  and  $i_{\text{ca}}$  are the net anodic and cathodic current densities, respectively, at  $E_{\text{corr}}$  (corrosion potential), and  $A_{\text{an}}$  and  $A_{\text{ca}}$  are the anodic and cathodic reaction areas at  $E_{\text{corr}}$ , respectively.

Recall that ORR is an important cathodic reaction near the OCP of AA2024-T3 ( $-0.5 V_{\text{SCE}}$  to  $-0.6 V_{\text{SCE}}$ ) in near-neutral aerated solutions. Pryor and Keir attributed the lower  $O_2$  reduction reaction rate on commercial-purity Al to an additional possible rate limiting or slow step, besides solution phase  $O_2$  transport, consisting of electron transfer through the insulating Al-oxide formed on Al electrodes.<sup>(8)</sup> Evidence supporting control of ORR by oxide properties is the fact that net cathodic reaction rates for Al are a function of prior anodic polarization potential (below the pitting potential) and, therefore,  $Al_2O_3 \cdot nH_2O$  oxide thickness (Figure 6). The electrical current density describing the flow of electrons through the oxide to support ORR at the oxide/solution interface will clearly be a function of the voltage field strength across the oxide and its conductivity, but the exact relationship is unknown. An alternative explanation is that  $i_{\text{I(Net)}} = i_{\text{I(true)}} - i_{\text{an}}$ , where  $i_{\text{an}}$  represents the dissolution rate of Al under cathodic polarization. However, a correction of  $i_{\text{I(Net)}}$  by a passive current density ranging from  $10^{-5} A/cm^2$  to  $10^{-6} A/cm^2$  would not account for  $i_{\text{I(true)}}$  values as high as  $10^{-4} A/cm^2$  seen on Cu (Figure 2). Moreover, oxide thickness is shown to reduce net cathodic reaction rates on Al (Figure 6), suggesting that electron transfer limits the mass-transport-limiting current density on Al rather than cathodic corrosion.

If the cathodic  $O_2$  reduction reaction is considered to be under mixed charge transfer-mass transfer control, the following expression is obtained on a homogeneous electrode with a term included to describe the additional rate limitation by electron transfer through the oxide:

$$\frac{1}{i_{\text{ca}}} = \frac{1}{i_{\text{ct}}} + \frac{1}{i_1} + \frac{1}{i_{\text{el}}} \quad (7)$$

Here,  $i_{\text{ca}}$  is the overall  $O_2$  reduction current density,  $i_{\text{ct}}$  describes  $O_2$  reduction under charge transfer control,  $i_1$  describes the mass-transport-limiting current density, and  $i_{\text{el}}$  represents the electrical current density describing the flow of electrons through the oxide to support ORR at the oxide/solution interface. Clearly,  $i_{\text{ca}}$  rate will be described by the lowest of the three current densities given in Equation (7). In the case of one-dimensional transport of  $O_2$  to a homogeneous planar electrode,  $i_1$  is given by this expression:

<sup>(8)</sup> The present discussion considers only a homogeneous electrode and does not yet consider micron-scale disc electrodes embedded in an insulating plate.

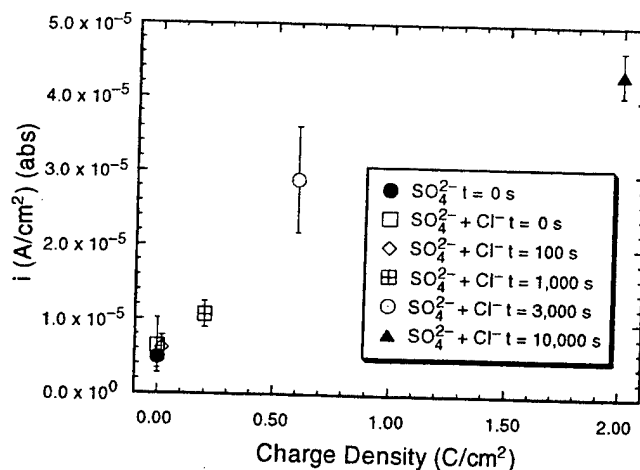


FIGURE 8(a). Apparent cathodic reaction rate on an AA2024-T3 stationary electrode (at  $-0.75 V_{\text{SCE}}$ ) as a function of prior anodic charge density.  $t$  indicates time for which  $i$  of  $200 \mu A/cm^2$  was applied. There was no prior exposure at OCP. Electrolyte:  $0.1 M Na_2SO_4 + 0.005 M NaCl$  and  $0.1 M Na_2SO_4$ . Error bars are at a 95% confidence level. abs (vertical axis) = absolute.

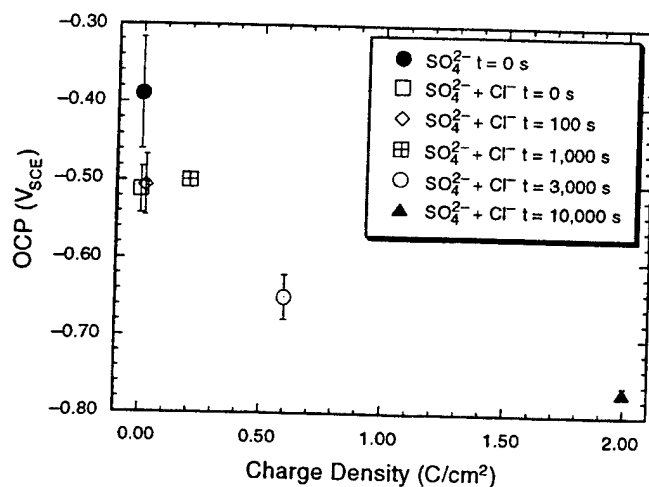


FIGURE 8(b). OCP on an AA2024-T3 stationary electrode as a function of prior anodic charge density. Electrolyte:  $0.1 M Na_2SO_4 + 0.005 M NaCl$  and  $0.1 M Na_2SO_4$ .  $t$  indicates time for which  $i$  of  $200 \mu A/cm^2$  was applied. There was no prior exposure at OCP.

$$i_{O_2} = \frac{nFD_{O_2}C_{O_2}}{\delta_{O_2}} \quad (8)$$

where  $F$  is the Faraday constant,  $D_{O_2}$  is the diffusion coefficient of  $O_2$ ,  $C_{O_2}$  is the bulk solution concentration of  $O_2$ , and  $\delta_{O_2}$  is the thickness of the diffusion boundary layer at the electrode surface. The failure of oxide-covered Al to follow Equation (8) indicates that the rate-controlling step for  $O_2$  reduction on Al is not the aqueous phase transport of  $O_2$  across a concentration gradient in solution. Instead, something else controls reduction such as the supply of electrons through the insulating oxide to support ca-

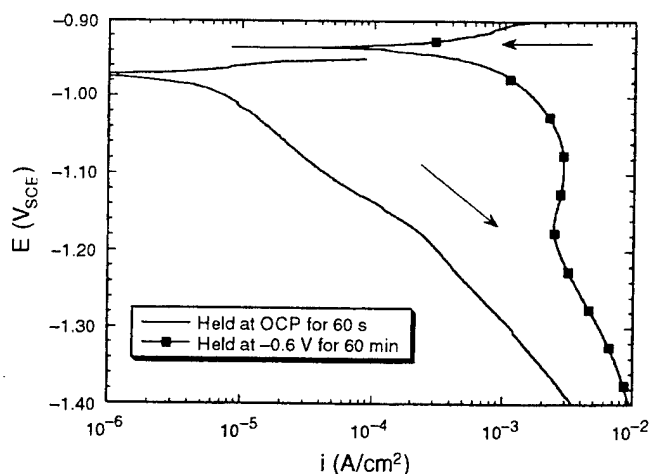


FIGURE 9(a). *E*-log *i* behavior of an  $\text{Al}_2\text{CuMg}$  stationary electrode in  $0.1 \text{ M Na}_2\text{SO}_4 + 0.005 \text{ M NaCl}$  (pH 6) after 60 s at OCP compared with after 60 min at  $-0.6 \text{ V}_{\text{SCE}}$ . At  $-0.6 \text{ V}_{\text{SCE}}$ ,  $\text{Al}_2\text{CuMg}$  corrodes extensively (Figure 2).



FIGURE 9(b). Porous electrode formation on  $\text{Al}_2\text{CuMg}$  in  $0.1 \text{ M Na}_2\text{SO}_4 + 0.005 \text{ M NaCl}$ .

thodic electronic transfer reactions. In RDE experiments, the Levich equation is given by the following equation:

$$I_l = i_l A_{\text{ORR}} = 0.62 \ln A_{\text{ORR}} F C_{\text{O}_2} D_{\text{O}_2}^{0.67} \nu^{-0.167} \omega^{0.5} \quad (9)$$

where  $i_l$  is the limiting current density,  $A_{\text{ORR}}$  is the electrode area that can support ORR,  $\nu$  is the kinematic viscosity, and  $\omega$  is the angular velocity of the electrode area. In the ideal case of metallic conductors, the ORR  $i_l$  depends on  $A_{\text{ORR}}$ , bulk oxygen concentration ( $C_{\text{bulk}}$ ),  $D_{\text{O}_2}$ , and the square root of the angular velocity ( $\omega^{0.5}$ ) of the rotating disk. An overall expression for the net cathodic current density  $i_{\text{ca}}$  (described by Equation [7]) with parallel hydrogen evolution can be given by Equation (10), neglecting  $i_{\text{et}}$ :

<sup>(9)</sup> Alkaline production would contribute to oxide thinning, which is an alternative mechanism.

<sup>(10)</sup> Even if conductivity is due to electron tunneling.

$$i_{\text{ca}} = \frac{i_0 i_{\text{O}_2 / \text{OH}^-} \exp \left[ \frac{2.3(E_{\text{int}} - E_{\text{eq O}_2 / \text{OH}^-})}{b_c} \right]}{i_l + i_{\text{O}_2 / \text{OH}^-} \exp \left[ \frac{-2.3(E_{\text{int}} - E_{\text{eq O}_2 / \text{OH}^-})}{b_c} \right]} + i_{\text{O}_2 / \text{H}_2} \exp \left[ \frac{-2.3(E_{\text{int}} - E_{\text{eq H}_2\text{O} / \text{H}_2})}{b_c} \right] \quad (10)$$

where  $i_0$  is the exchange current density,  $E_{\text{int}}$  and  $E_{\text{eq}}$  are the interfacial and equilibrium potentials, respectively,  $b_c$  is the Tafel slope, and  $i_l$  and  $i_{\text{ca}}$  have been previously defined. This represents the total cathodic current density for ORR and HER on homogeneous solid metallic phases that are electronic conductors with fast electronic conduction (e.g., bare metals). This equation provides a good description for the behavior of Cu (Figure 5[a]) and Au.

Clearly,  $i_{\text{et}}$  is negligible for Cu-bearing intermetallics, presumably because the oxide is either very thin<sup>(9)</sup> or very ionically or electronically conductive. Consequently,  $i_{\text{ca}}$  is determined by the Levich equation in the mass-transport-limiting region. Scully, et al., attributed the enhancement of cathodic reactions on  $\text{Al}_2\text{Cu}$  to the presence of Cu clusters in the insulating Al oxide of  $\theta\text{-Al}_2\text{Cu}$ .<sup>35</sup> These clusters were embedded in the Al oxide over intermetallics and could enhance cathodic electron transfer reactions. Streblow, Scully, Buchheit, and coworkers have all detected Cu clusters in a hydrated Al oxide and corrosion products formed over Al-Cu alloys,  $\text{Al}_2\text{Cu}$  and  $\text{Al}_2\text{CuMg}$ .<sup>2,35,47-48</sup> The Cu clusters apparently alter the conductivity of the oxide film over the intermetallic phase. If present in sufficient quantity to provide an effective short circuit path<sup>(10)</sup> through insulating Al-oxide, then electron transfer is not a rate limitation. These Cu clusters apparently provide sufficient electronic conductivity to remove  $i_{\text{et}}$  in Equation (7) as a rate limitation in these intermetallics. Note that the likely additional effect of Cu on the exchange current density or Tafel slope for ORR shown above will not have an effect on  $i_l$ .

It is interesting to note that an abrupt transition is observed from the poor cathodic behavior of high-purity Al to fast kinetics on Al-Cu and Al-Cu-Mn-Fe intermetallics (Figure 2[a]), even though they may be covered with an Al-rich oxide.<sup>35</sup> However, this oxide likely contains Cu clusters or other defects.<sup>31,35</sup> Conductivity has been modeled in granular materials consisting of an insulator-conductor composite such as W- $\text{Al}_2\text{O}_3$  and Pt- $\text{Al}_2\text{O}_3$ .<sup>49-51</sup> In these models, a critical volume fraction of the conducting phase  $x_c$  provides the short circuit path for easy electrical conduction. At  $x > x_c$ , conduction was attributed to simple metallic transport in the network of the metallic phase. At  $x < x_c$ , electrical conductance was attributed to quantum mechanic tunneling. For  $\text{Al}_2\text{Cu}$  or



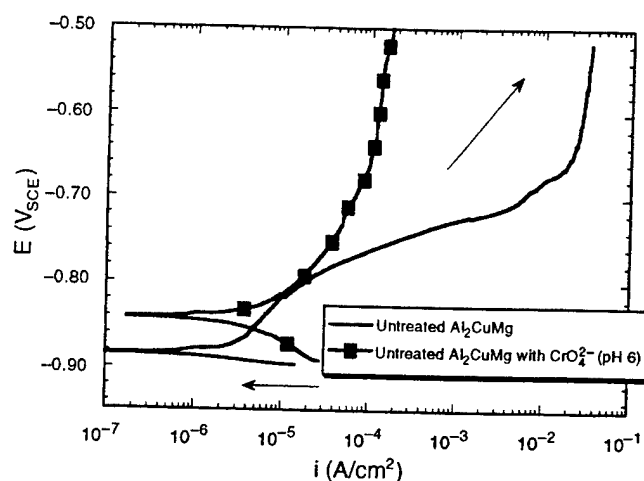


FIGURE 10(a). *E-log i* behavior of an  $\text{Al}_2\text{CuMg}$  stationary electrode in  $0.1 \text{ M Na}_2\text{SO}_4 + 0.005 \text{ M NaCl}$  (pH 6) and  $0.1 \text{ M Na}_2\text{SO}_4 + 0.005 \text{ M NaCl} + 0.0062 \text{ M Na}_2\text{CrO}_4 + 0.0038 \text{ M H}_2\text{CrO}_4$  (pH 6).

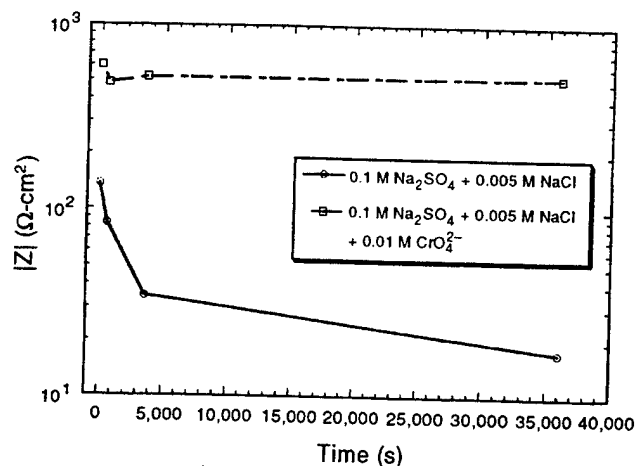


FIGURE 10(b). Impedance modulus,  $|Z|$ , at 10 Hz as a function of time on an  $\text{Al}_2\text{CuMg}$  stationary electrode in  $0.1 \text{ M Na}_2\text{SO}_4 + 0.005 \text{ M NaCl}$  (pH 6) compared to  $0.1 \text{ M Na}_2\text{SO}_4 + 0.005 \text{ M NaCl} + 0.0062 \text{ M Na}_2\text{CrO}_4 + 0.0038 \text{ M H}_2\text{CrO}_4$  (pH 6).

$\text{Al}_2\text{CuMg}$  examined here,  $x$  is unknown. However,  $x_c$  values of 0.47 to 0.54 have been observed for  $\text{W-Al}_2\text{O}_3$ .<sup>49-51</sup> Above this value, an increase of 8 orders of magnitude in oxide-metal composite conductivity was seen. The effect would be that  $i_{cl}$  would no longer limit ORR rates and mass transport of  $\text{O}_2$  in solution would be the sole rate-determining factor for  $i_l$ . Indeed, intermetallics such as  $\text{Al}_{20}\text{Cu}_2(\text{MnFe})_3$  behave almost the same as Cu and Au.

#### Apparent vs Intrinsic Inhibition of $\text{O}_2$ Reduction by Chromate

At issue is whether or not chromate intrinsically or apparently inhibits the reduction of  $\text{O}_2$ . Intrinsic inhibition occurs at constant pH, electrode area, electrode composition, etc. Apparent inhibition represents reduced net kinetics caused by changes in these factors. It has been shown that either pitting or general corrosion of AA2024-T3 and some intermetallics occurs near OCP in the presence of Cl<sup>-</sup> (Figure 7). The presence of chromate in solution serves to inhibit these anodic reactions at OCP and/or to raise the pitting potential above the OCP (Figures 10, 11, and 16). A reduction in net cathodic kinetics ( $i_{ca}$ ) is, subsequently, observed in corrosive chloride-containing solutions where chromate inhibits OCP corrosion and  $\text{Al}_2\text{CuMg}$  phase dealloying. Also, as the degree of corrosion damage accelerated by anodic polarization increases in AA2024-T3, the OCP falls and the net cathodic current density increases (Figure 8). The observed cathodic kinetics of  $\text{Al}_2\text{CuMg}$  also has been shown to be enhanced after extensive corrosion damage has occurred, leading to formation of a porous, high-surface-area electrode (Figure 9). These substantiate the concept that prior OCP corrosion alters subsequent net cathodic kinetics in NaCl-bearing solution.

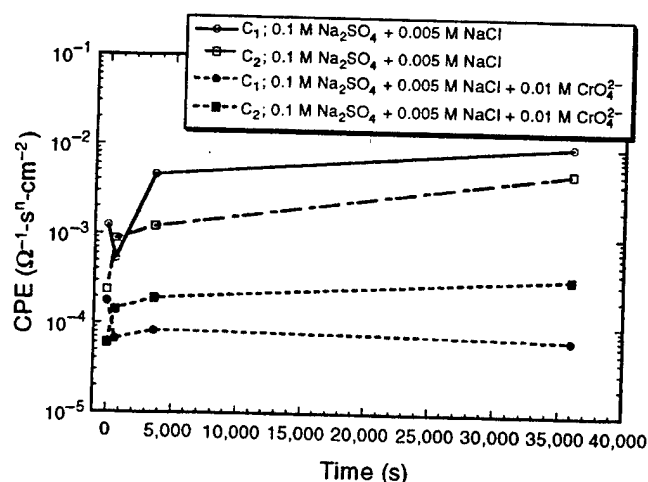


FIGURE 10(c). CPE  $C_1$  and  $C_2$ , as a function of time, on an  $\text{Al}_2\text{CuMg}$  stationary electrode in  $0.1 \text{ M Na}_2\text{SO}_4 + 0.005 \text{ M NaCl}$  (pH 6) compared to  $0.1 \text{ M Na}_2\text{SO}_4 + 0.005 \text{ M NaCl} + 0.0062 \text{ M Na}_2\text{CrO}_4 + 0.0038 \text{ M H}_2\text{CrO}_4$  (pH 6). Range of CPE exponent values without chromate in solution for  $C_1$  and  $C_2$  were 0.70 to 0.98 and 0.84 to 0.98, respectively. Range of CPE exponent values with chromate in solution for  $C_1$  and  $C_2$  were 0.63 to 0.73 and 0.84 to 0.89, respectively.

At least two types of apparent alterations of net cathodic kinetics are produced by chromate: minimizing dissolution and possible porous surface area development on the  $\text{Al}_2\text{CuMg}$  phase and suppression of OCP pitting of AA2024-T3, Al-Cu, and Al-Cu-Mn-Fe intermetallics. A third is the possible action of chromate as an oxidizer that thickens oxide films on Cu and  $\text{Al}_{20}\text{Cu}_2(\text{MnFe})_3$ , as suggested by EIS (Figure 11). This would reduce net cathodic kinetics as observed in the comparison of Figure 5 to Figures 13 and 14. Chromate has even been reported to thicken oxides on Pt.<sup>52-53</sup> The reasons why increases in net cathodic kinetics are observed after chromate treat-

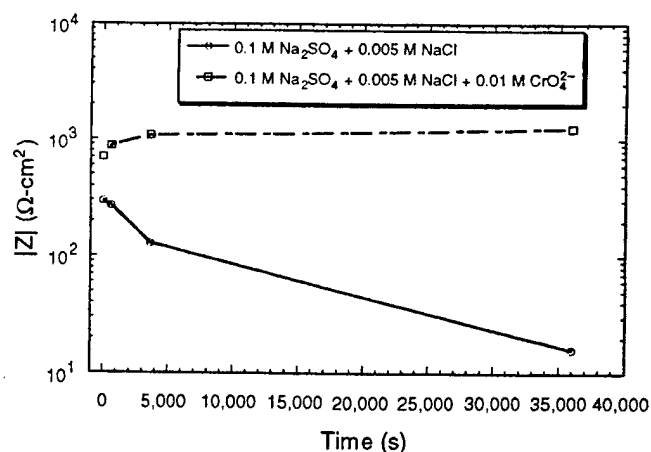


FIGURE 11(a). Impedance modulus,  $|Z|$ , at 10 Hz as a function of time on an  $\text{Al}_{20}\text{Cu}_2(\text{MnFe})_3$  stationary electrode in 0.1 M  $\text{Na}_2\text{SO}_4$  + 0.005 M NaCl (pH 6) compared to 0.1 M  $\text{Na}_2\text{SO}_4$  + 0.005 M NaCl + 0.0062 M  $\text{Na}_2\text{CrO}_4$  + 0.0038 M  $\text{H}_2\text{CrO}_4$  (pH 6).

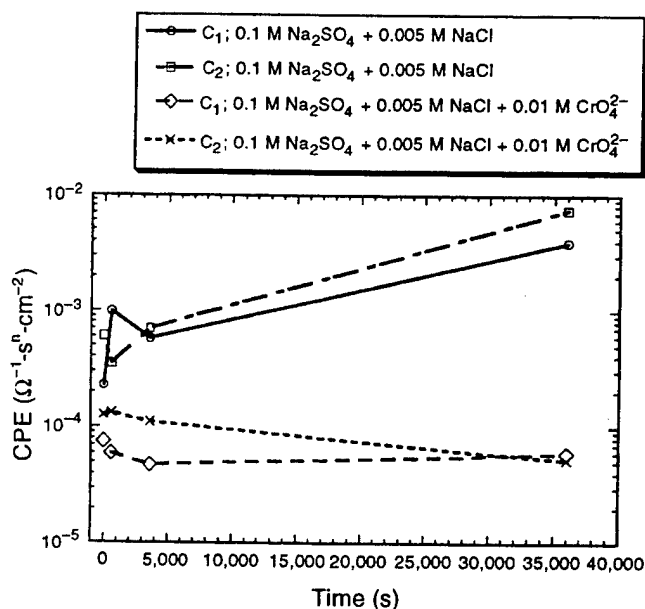


FIGURE 11(b). CPE  $C_1$  and  $C_2$ , as a function of time, on an  $\text{Al}_{20}\text{Cu}_2(\text{MnFe})_3$  stationary electrode in 0.1 M  $\text{Na}_2\text{SO}_4$  + 0.005 M NaCl (pH 6) compared to 0.1 M  $\text{Na}_2\text{SO}_4$  + 0.005 M NaCl + 0.0062 M  $\text{Na}_2\text{CrO}_4$  + 0.0038 M  $\text{H}_2\text{CrO}_4$  (pH 6). Range of CPE exponent values without chromate in solution for  $C_1$  and  $C_2$  were 0.65 to 0.92 and 0.64 to 0.81, respectively. Range of CPE exponent values with chromate in solution for  $C_1$  and  $C_2$  were 0.80 to 0.84 and 0.74 to 0.78, respectively.

ment of Al compared to a decrease for Cu and  $\text{Al}_{20}\text{Cu}_2(\text{MnFe})_3$  also might lie in the relative contributions of the chromate reduction reaction to the net cathodic kinetics of these different metals. The rate of cathodic ORR kinetics on Al is much lower (2 to 3 orders of magnitude lower) than Cu and  $\text{Al}_{20}\text{Cu}_2(\text{MnFe})_3$  (Figure 5). Therefore, any small contribution to the net cathodic current density  $i_{\text{ca}}$  by the reduction of chromate would be much more signifi-

cant on Al than on Cu or  $\text{Al}_{20}\text{Cu}_2(\text{MnFe})_3$  and much more easily observed. The conductivity of the Al oxide film also might have been altered by the presence of chromate. Moreover, although Cu and  $\text{Al}_{20}\text{Cu}_2(\text{MnFe})_3$  are relatively passive at OCP, their breakdown potentials (Figure 2[b]) are close to their OCP. It is therefore not unreasonable that, on occasion, corrosion occurs on Cu and  $\text{Al}_{20}\text{Cu}_2(\text{MnFe})_3$  at OCP (these were tested when not galvanically coupled to AA2024-T3 as they would be in the matrix of AA2024-T3). When passivity breakdown occurs, net cathodic kinetics will be slightly more enhanced as demonstrated. The presence of chromate would undoubtedly serve to decrease the cathodic current density by suppressing corrosion.

The use of Au allowed for the elimination of the aforementioned factors and enabled measurement of the effect of chromate only on the rate of mass-transport-limited ORR rates (Figure 15). Here, it was shown that chromate pretreatment did not affect the mass-transport-limited ORR rates. Furthermore, the presence of chromate in solution increased  $i_{\text{ca}}$  in the mass transport region as a result of the additive effects of the ORR and the chromate reduction reaction ( $\text{Cr}^{6+}$  to  $\text{Cr}^{3+}$ ). The rate of reduction of Cr(VI) to Cr(III) is relatively fast on Au,<sup>52-54</sup> and its reduction products are not specifically adsorbed on its surface. However, reduced mixed or charge-transfer-controlled ORR rates are observed on Au and Cu. This suggests that  $\text{CrO}_4^{2-}$  and other anions could block  $\text{O}_2$  adsorption sites and, thus, provide a mechanism for "intrinsic" inhibition of ORR.

#### Anion Competitive Adsorption Model for ORR Suppression

Figures 17(a) and (b) for Au and Cu clearly indicate that the ORR under charge transfer and mixed charge transfer mass-transport-controlled conditions deviate from the ideal ORR behavior described by Equation (10) when  $\text{SO}_4^{2-}$  and  $\text{Cl}^-$  are present in the electrolyte. The deviation of charge-transfer-controlled behavior from ideal theoretical kinetics is even greater with the presence of chromate (in this case, at pH 6, a mixture of chromate species consisting of  $\text{HCrO}_4^-$ ,  $\text{CrO}_4^{2-}$ , and  $\text{CrO}_2^{2-}$  as a result of the speciation of chromate<sup>55</sup>). However, as the cathodic potential is reduced further, the kinetics of ORR reach the expected result for mass-transport-limited ORR even with  $\text{SO}_4^{2-}$ ,  $\text{Cl}^-$ , and the chromate species present in solution. Results on Au in particular require another role for the chromate species to produce ORR suppression, besides its effect on OCP corrosion rates. This is because metal dissolution and surface area changes do not occur on Au. One possible explanation is that competitive adsorption of  $\text{SO}_4^{2-}$ ,  $\text{Cl}^-$ , and the chromate species block  $\text{O}_2$  adsorption sites. Another possibility is that  $\text{Cr}_2\text{O}_3$  and  $\text{Cr}(\text{OH})_3$  surface formation hinder ORR.<sup>56</sup> Although  $\text{CrO}_4^{2-}$  might be

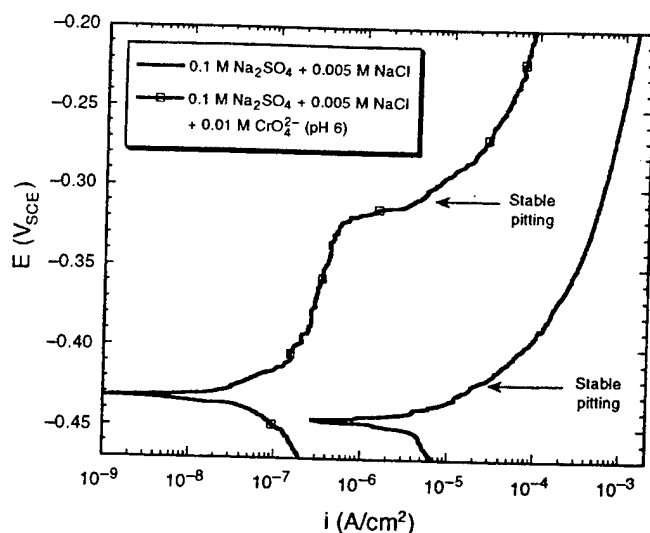


FIGURE 12(a). *E-log i* behavior of an AA2024-T3 stationary electrode in 0.1 M Na<sub>2</sub>SO<sub>4</sub> + 0.005 M NaCl (pH 6) and 0.1 M Na<sub>2</sub>SO<sub>4</sub> + 0.005 M NaCl + 0.0062 M Na<sub>2</sub>CrO<sub>4</sub> + 0.0038 M H<sub>2</sub>CrO<sub>4</sub> (pH 6) showing stable pitting.

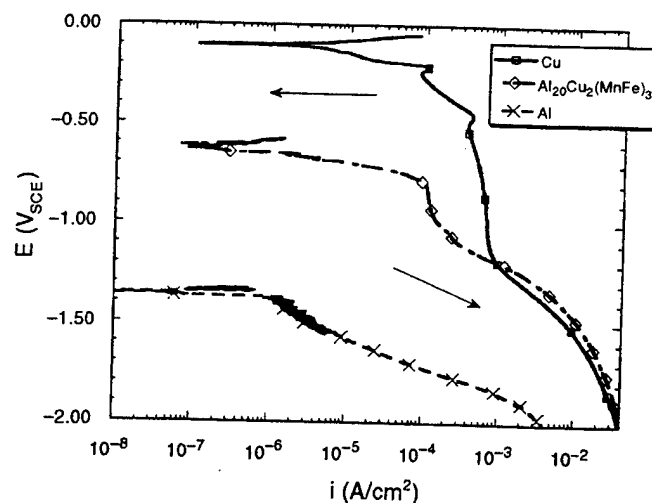


FIGURE 13(a). Cathodic *E-log i* behavior of pure Cu, Al, and Al<sub>20</sub>Cu<sub>2</sub>(MnFe)<sub>3</sub> in 0.1 M Na<sub>2</sub>SO<sub>4</sub> + 0.005 M NaCl (pH 6) at electrode rotation speed of 500 rpm ( $\omega^{0.5} = 7.24$ ) after a 2-h pretreatment in 0.1 M Na<sub>2</sub>SO<sub>4</sub> + 0.005 M NaCl + 0.0062 M Na<sub>2</sub>CrO<sub>4</sub> + 0.0038 M H<sub>2</sub>CrO<sub>4</sub> (pH 6) at OCP. All electrolytes were at ambient aeration.

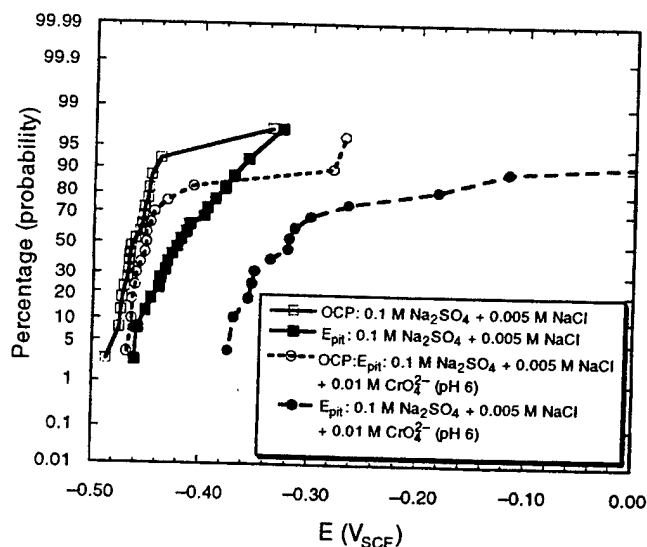


FIGURE 12(b). Cumulative probability plot of OCP and  $E_{pit}$  of an AA2024-T3 stationary electrode in 0.1 M Na<sub>2</sub>SO<sub>4</sub> + 0.005 M NaCl (pH 6) and of  $E_{pit}$  in 0.1 M Na<sub>2</sub>SO<sub>4</sub> + 0.005 M NaCl + 0.0062 M Na<sub>2</sub>CrO<sub>4</sub> + 0.0038 M H<sub>2</sub>CrO<sub>4</sub> (pH 6) showing a clear separation between OCP and  $E_{pit}$  with chromate in solution.

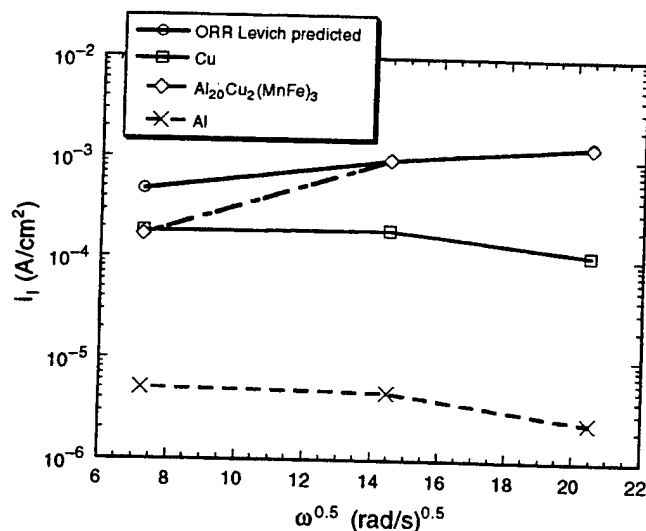
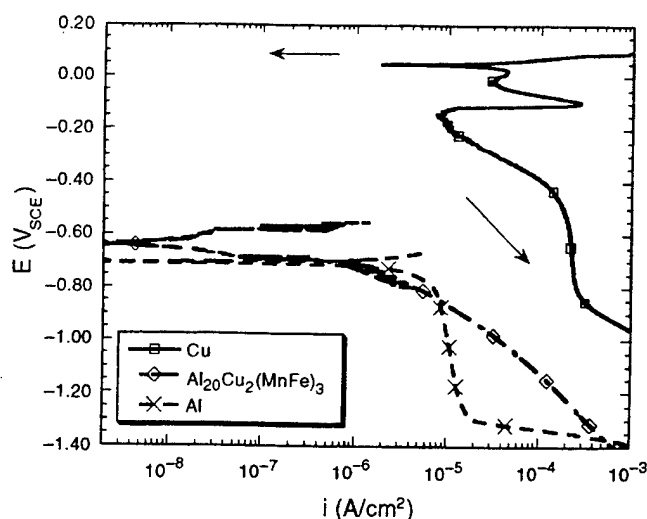


FIGURE 13(b). Oxygen reduction limiting current density ( $i_l$ ) data from rotating disk electrodes for pure Cu and Al, and Al<sub>20</sub>Cu<sub>2</sub>(MnFe)<sub>3</sub> in 0.1 M Na<sub>2</sub>SO<sub>4</sub> + 0.005 M NaCl (pH 6) after a 2-h pretreatment in 0.1 M Na<sub>2</sub>SO<sub>4</sub> + 0.005 M NaCl + 0.0062 M Na<sub>2</sub>CrO<sub>4</sub> + 0.0038 M H<sub>2</sub>CrO<sub>4</sub> (pH 6). All electrolytes were at ambient aeration.

expected to be reduced immediately to Cr(III) at such cathodic potentials below the Cr(VI) redox potential (Equations [3] through [5]), radiotracer measurements on Fe show that CrO<sub>4</sub><sup>2-</sup> adsorption is a precursor to Cr<sub>2</sub>O<sub>3</sub> and Cr(OH)<sub>3</sub> formation.<sup>57-58</sup> Hence, if SO<sub>4</sub><sup>2-</sup> and Cl<sup>-</sup> block surface sites, then the adsorption and subsequent reduction of the chromate species is hindered. This claim is supported by experimental evidence because Cr(VI)-Cr(III) reduction rates on Au never reached their predicted ideal mass-transport-limited cathodic current densities. This is likely

caused by blocking of reduction sites by SO<sub>4</sub><sup>2-</sup> and Cl<sup>-</sup>. However, chromate, SO<sub>4</sub><sup>2-</sup>, and Cl<sup>-</sup> anions could become desorbed at negative potentials because of unfavorable electrostatic forces where these forces repel the anions, as many classical electrocapillary studies indicate.<sup>59-60</sup> Any remaining chromate species adsorption that persists at negative potentials must derive from nonelectrostatic or chemical interactions. Therefore, competitively adsorbed anions could block ORR sites, except at very negative potentials. A somewhat analogous argument has been made for anodic



**FIGURE 14(a).** Cathodic  $E$ -log  $i$  behavior of pure Cu and Al, and  $\text{Al}_{20}\text{Cu}_2(\text{MnFe})_3$ , in  $0.1 \text{ M Na}_2\text{SO}_4 + 0.005 \text{ M NaCl} + 0.0062 \text{ M Na}_2\text{CrO}_4 + 0.0038 \text{ M H}_2\text{CrO}_4$  (pH 6) at ambient aeration and an electrode rotation speed of  $500 \text{ rpm}$  ( $\omega^{0.5} = 7.24$ ).

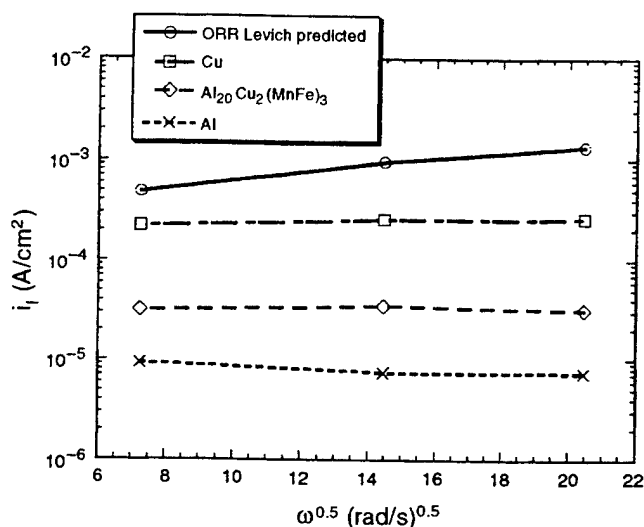


**FIGURE 14(b).** Oxygen reduction limiting current density ( $i_l$ ) data from rotating disk electrodes for pure Cu and Al and  $\text{Al}_{20}\text{Cu}_2(\text{MnFe})_3$  in  $0.1 \text{ M Na}_2\text{SO}_4 + 0.005 \text{ M NaCl} + 0.0062 \text{ M Na}_2\text{CrO}_4 + 0.0038 \text{ M H}_2\text{CrO}_4$  (pH 6) at ambient aeration. Levich prediction at concentration of  $6 \text{ ppm}$  ( $1.88 \times 10^{-4} \text{ M}$ ) dissolved  $\text{O}_2$ .

inhibition by  $\text{CrO}_4^{2-}$  where competitive adsorption between chromate and  $\text{Cl}^-$  impedes the ability to form a passive film.<sup>25,61-62</sup> Streblow and Titze have utilized a potential-dependent Langmuir isotherm to describe the role of competitive adsorption between competitive aggressive and inhibitive anions (e.g.,  $\text{SO}_4^{2-}$ ,  $\text{Cl}^-$ ,  $\text{CrO}_4^{2-}$ ) on anodic dissolution.<sup>62</sup> A similar treatment was used here to model the way in which adsorbed anions could block oxygen reduction sites as a function of heat of adsorption, concentration, and applied potentials. The general form of such an adsorption isotherm is as follows:

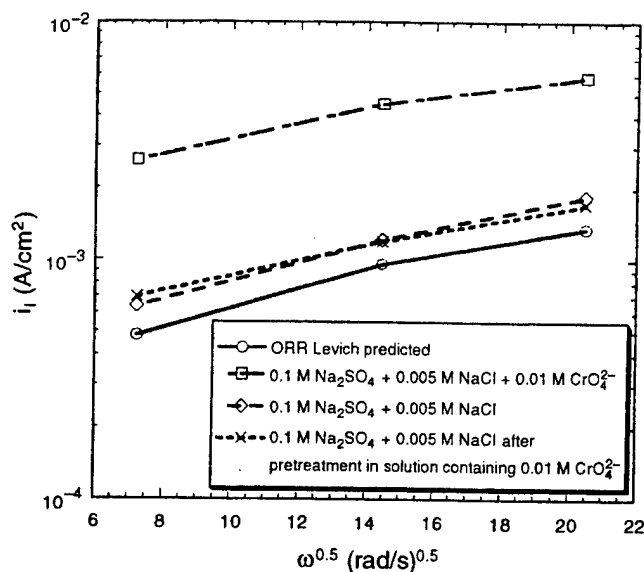


**FIGURE 15.** Oxygen reduction limiting current density ( $i_l$ ) from rotating disk electrodes of pure Au in  $0.1 \text{ M Na}_2\text{SO}_4 + 0.005 \text{ M NaCl}$  (pH 6),  $0.1 \text{ M Na}_2\text{SO}_4 + 0.005 \text{ M NaCl}$  (pH 6) after a 2-h pretreatment in  $0.1 \text{ M Na}_2\text{SO}_4 + 0.005 \text{ M NaCl} + 0.0062 \text{ M Na}_2\text{CrO}_4 + 0.0038 \text{ M H}_2\text{CrO}_4$  (pH 6), and in  $0.1 \text{ M Na}_2\text{SO}_4 + 0.005 \text{ M NaCl} + 0.0062 \text{ M Na}_2\text{CrO}_4 + 0.0038 \text{ M H}_2\text{CrO}_4$  (pH 6). Levich prediction at concentration of  $6 \text{ ppm}$  ( $1.88 \times 10^{-4} \text{ M}$ ) dissolved  $\text{O}_2$ . All electrolytes were at ambient aeration.

$$\frac{\theta_{\text{Anions}}}{1 - \theta_{\text{Anions}}} = kC_{\text{Anions}} \exp\left(\frac{-\Delta H_{\text{ads}}}{RT}\right) \exp\left(\frac{EF}{RT}\right) \quad (11)$$

where  $\Delta H_{\text{ads}}$  is the heat of adsorption of a particular species,  $E$  is the electrochemical potential, and other terms have their usual meanings. Here, the electrochemically active electrode area for ORR would be reduced according to the following relationship:

$$A_{\text{ORR}} = A_{\text{electrode}}(1 - \theta_{\text{Anions}}) \quad (12)$$

A chromate adsorption isotherm has been developed for Fe as a function of chromate concentration.<sup>61</sup> It was found to obey the Temkin isotherm.<sup>61</sup> Unfortunately, the exact mathematical description of a chromate adsorption isotherm in terms of applied potential is unclear for the materials used in this study (i.e.,  $k$  and  $\Delta H_{\text{ads}}$  are unknown).  $\theta_{\text{Anions}}$  was varied according to a modified version of Equation (11) (Equation (13)), which produces modification of  $A_{\text{ORR}}$  according to Equation (12).  $A_{\text{ORR}}$  is used in Equation (10) and affects both  $i_{\text{ct}}$  and  $i_l$ . Equation (10) then was used to develop the family of  $E$ -log  $i$  curves indicated in Figure 17 for a range of hypothetical values:

$$\frac{\theta_{\text{Anions}}}{1 - \theta_{\text{Anions}}} = kC_{\text{Anions}} \exp\left(\frac{(E - E_o)F}{RT}\right) \quad (13)$$

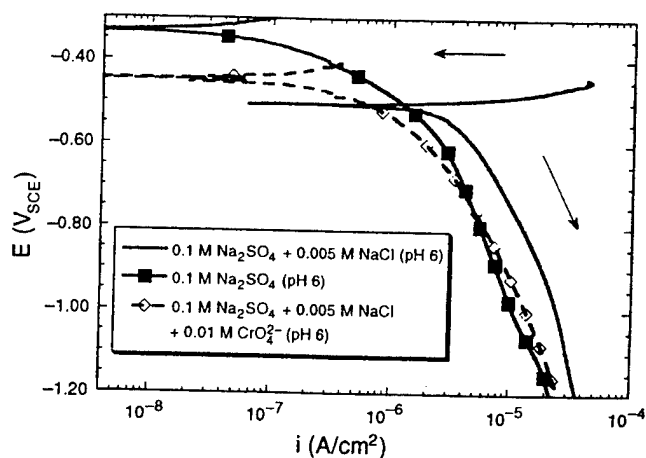


FIGURE 16(a). *E*-log *i* behavior of an AA2024-T3 stationary electrode in 0.1 M Na<sub>2</sub>SO<sub>4</sub> + 0.005 M NaCl (pH 6), 0.1 M Na<sub>2</sub>SO<sub>4</sub> (pH 6) and 0.1 M Na<sub>2</sub>SO<sub>4</sub> + 0.005 M NaCl + 0.0062 M Na<sub>2</sub>CrO<sub>4</sub> + 0.0038 M H<sub>2</sub>CrO<sub>4</sub> (pH 6) after a 2-h exposure at OCP.

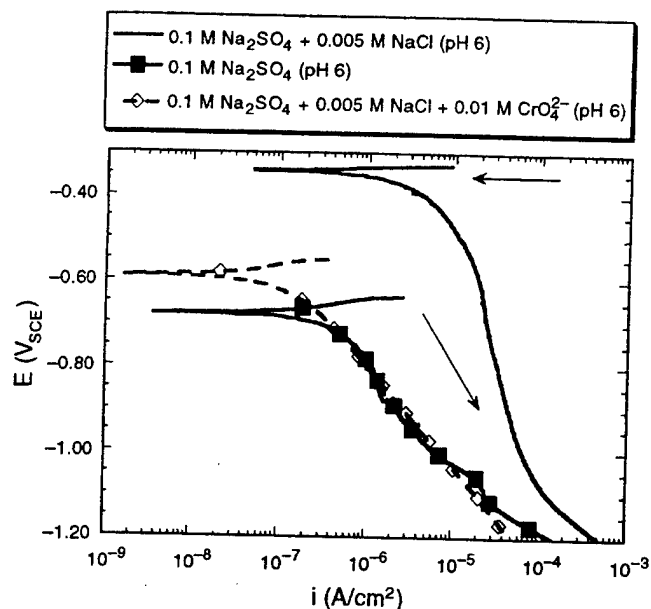


FIGURE 16(b). *E*-log *i* behavior of an Al<sub>20</sub>Cu<sub>2</sub>(MnFe)<sub>3</sub> stationary electrode in 0.1 M Na<sub>2</sub>SO<sub>4</sub> + 0.005 M NaCl (pH 6), 0.1 M Na<sub>2</sub>SO<sub>4</sub>, and 0.1 M Na<sub>2</sub>SO<sub>4</sub> + 0.005 M NaCl + 0.0062 M Na<sub>2</sub>CrO<sub>4</sub> + 0.0038 M H<sub>2</sub>CrO<sub>4</sub> (pH 6) after a 2-h exposure at OCP.

where  $1/D = \epsilon$  and  $\epsilon$  is the potency term accounting for strength of attraction.  $E$  and  $E_0$  are the applied electrochemical potential and the assumed potential where the coverage is 0.5.  $F$  is the Faraday constant,  $R$  is the molar gas constant,  $T$  is temperature,  $C_{\text{Anions}}$  is the bulk solution concentration of anions, and  $k$  is an unknown Langmuir constant.  $kC_{\text{Anions}}$  was taken to be 1. For the cathodic kinetics modeled here, all anion adsorption was assumed to cease at very negative potentials consistent with electrocapillary curve behavior where the surface's excess of anions vanishes at cathodic potentials. The result produced the set of cathodic *E*-log *i* curves indicated in Figure 17. These ORR kinetics indeed mimic the behavior observed on Au and Cu. These results do not identify the exact parameters associated with Equations (11) through (13), but such hypothesized blockage of ORR sites by anions is certainly consistent with the experimental data. Although the data modeled in Figure 17 include only SO<sub>4</sub><sup>2-</sup> and Cl<sup>-</sup> anions, the presence of chromate anions in solution is expected to contribute further to the deviation of charge-transfer-controlled behavior from ideal theoretical kinetics. This is vividly seen for Cu in Figure 14.

Unfortunately, according to this model, suppression of the ORR by chromate chemisorption would not necessarily be operative at very negative potentials typical of the OCP of corroding AA2024-T3. Chromate reduction could block sites at cathodic potentials if its reaction products, once formed by reduction, limited ORR below its theoretical mass-transport-controlled limit. However, such a benefit is not seen on Al, as already has been discussed. Specifically, suppression of the ORR reaction by rate-limiting electron transmission across the oxide film is the dominant rate-limiting factor that lowers ORR rates on Al. Apparently, any O<sub>2</sub> adsorption site blockage by anions is more than offset by the role of chro-

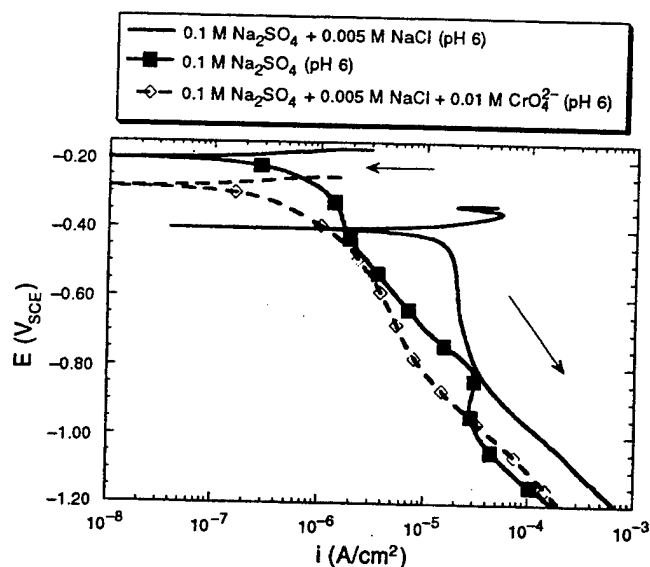
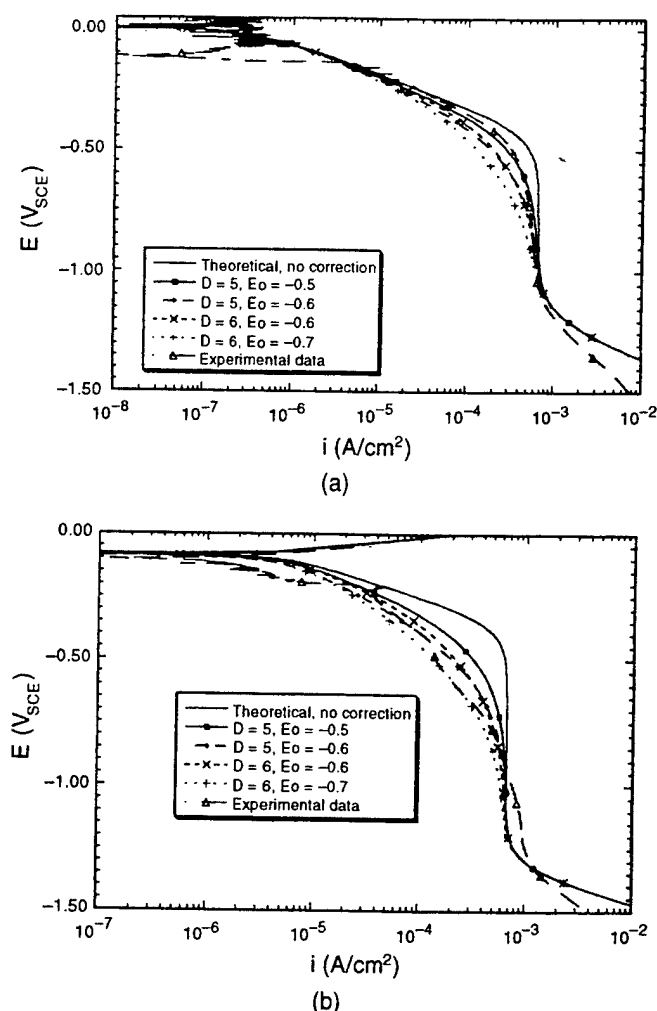


FIGURE 16(c). *E*-log *i* behavior of an Al<sub>2</sub>Cu stationary electrode in 0.1 M Na<sub>2</sub>SO<sub>4</sub> + 0.005 M NaCl (pH 6), 0.1 M Na<sub>2</sub>SO<sub>4</sub>, and 0.1 M Na<sub>2</sub>SO<sub>4</sub> + 0.005 M NaCl + 0.0062 M Na<sub>2</sub>CrO<sub>4</sub> + 0.0038 M H<sub>2</sub>CrO<sub>4</sub> (pH 6) after a 2-h exposure at OCP.

mate or its reduction products in modifying oxide thickness, conductivity, or supply of another cathodic reactant. In fact, the dominant effect of chromate ions on Al is actually to raise  $i_{\text{ca}}$  (Figure 6). The key point is that blockage of ORR sites by chromate anions is consistent with experimental data for Cu and Au. However, it is not seen at negative potentials, nor appears to be the dominant effect on Al-based materials.



**FIGURE 17.**  $i$ , corrected for exponential coverage effects for (a) Au and (b) Cu in 0.1 M  $\text{Na}_2\text{SO}_4$  + 0.005 M NaCl at 500 rpm ( $\omega^{0.5} = 7.24 \text{ rad/s}$ ).  $E_0$  is the potential at which adsorbed inhibitor coverage is 0.5, and  $1/D = \epsilon$ , which is a potency factor accounting for strength of attraction (added to Equation [13]). At no correction:  $D = 1$ .

### Open-Circuit Corrosion of AA2024-T3

A key question concerns the role of reduction in cathodic kinetics on microgalvanic coupling if it is brought about by chromate-induced reduction of OCP dissolution. Another important question is whether this phenomenon inhibits open-circuit corrosion even if mass-transport  $\text{O}_2$  reduction kinetics are not altered. Clearly, chromate inhibits corrosion of  $\text{Al}_2\text{CuMg}$ , which reduces the possible formation of a porous Cu-rich phase and Cu replating (Figure 10).<sup>2</sup> Therefore, minimization of Cu release through passivation of  $\text{Al}_2\text{CuMg}$  would lower cathodic reaction rates. Similarly, chromate suppresses AA2024-T3 pitting, which minimizes the release of Cu from Al-Cu solid solution (Figure 12). In turn, both of these limit subsequent net cathodic reaction rates by minimizing Cu replating, surface area increase,<sup>5</sup> acidic or alkaline pH shifts, etc. Any Cu replated on AA2024-

T3 surfaces during corrosion (e.g., during alkaline treatment or corrosion in  $\text{Cl}^-$ )<sup>41</sup> would raise cathodic reaction rates when such deposited Cu is negatively polarized to the OCP of AA2024-T3 (Figure 2). However, to fully separate the effects of soluble chromate inhibitors on anodic vs cathodic reactions, experiments must be conducted using electrodes that separate anodes from cathodes. Studies containing anodes and cathodes on the same surface are complicated by these multiple influences of chromate.

### CONCLUSIONS

- ❖ Mass-transport-limited ORR rates are enhanced on intermetallics and bulk Cu compared to pure Al in 0.1 M  $\text{Na}_2\text{SO}_4$  + 0.005 M NaCl.
- ❖ Net ORR rates on intermetallics and bulk Cu compared to pure Al are still enhanced in the presence of chromate or after pretreatment in chromate over the range of disk rotation rates.
- ❖ Prior (e.g., at OCP) corrosion alters net cathodic reaction rates in the mass-transport-limited oxygen reduction regime by increasing electrode area through surface roughening, pit formation, and the extent to which the surface is covered by replated Cu.
- ❖ Chromate at 0.01 M concentration levels inhibits OCP corrosion and, in turn, decreases net cathodic reaction rates on AA2024-T3.
- ❖ Chromate at 0.01 M concentration levels lowers the active dissolution rate/passivates  $\text{Al}_2\text{CuMg}$ . Net cathodic reaction rates are subsequently inhibited.
- ❖ Reduction in net mass-transport-limited ORR reaction rates were observed after pretreatment in chromate at 0.01 M concentration levels on Cu, but not on  $\text{Al}_{20}\text{Cu}_2(\text{MnFe})_3$ . Mass-transport-limited ORR rates on  $\text{Al}_{20}\text{Cu}_2(\text{MnFe})_3$  were inhibited by the addition of 0.01 M chromate in 0.1 M  $\text{Na}_2\text{SO}_4$  + 0.005 M NaCl.
- ❖ Mass-transport-controlled ORR cathodic kinetics on stationary electrodes of AA2024-T3 in 0.1 M  $\text{Na}_2\text{SO}_4$  were not reduced by chromate. Net ORR rates were reduced in sulfate, or sulfate + chromate compared with NaCl + sulfate where prior corrosion occurred.
- ❖ Charge-transfer-controlled ORR rates were reduced on Cu and Au. This may have been caused by adsorption of chromate anions that blocked  $\text{O}_2$  reduction sites. However, such potential-dependent adsorption was suppressed at cathodic potentials, possibly by electrostatic anion repulsion.

### ACKNOWLEDGMENTS

Funding from Air Force Office of Scientific Research (H. DeLong and P. Truelove, Program Managers, Grant no. F49620-96-1-0178) is gratefully acknowledged. Intermetallics were supplied by the Aluminum Company of America (ALCOA). The CESE gratefully acknowledges ongoing support of Perkin

Elmer Instruments and Scribner Associates, Inc. Helpful discussions with M.W. Kendig and R.L. McCreery are gratefully acknowledged. C.F. Quarmby is acknowledged for assisting in E-logi modeling of some of the data.

## APPENDIX

Capacitance values can be defined in an indirect way. The impedance function  $Z$  of constant phase element (CPE) is given by the following:<sup>63-64</sup>

$$Z_{\text{CPE}} = \frac{1}{Y_0} (j\omega)^n \quad (\text{A-1})$$

where  $\omega$  is the angular velocity (rad/s), and  $n$  and  $Y_0$  are frequency-independent parameters. When  $n = 1$ , the CPE is an ideal capacitor (C) and  $Y_0 = C$ .  $n = 0.5$  typically represents diffusional impedance. When  $n = 0$ , the CPE becomes a pure resistor and  $R$  (resistance) is equal to  $1/Y_0$ . The CPE parameter plotted on the vertical axes of Figures 4(c), 4(f), 10(c), and 11(b) is therefore  $Y_0$ . In this study, CPE was used to express data because  $n < 1$  but  $n > 0.5$ . For a given frequency, the relationship between the real and the imaginary part of impedance of the CPE ( $Z_{\text{CPE}}$ ) and the fitted capacitance ( $Z_c$ ) is:<sup>63-64</sup>

$$j \operatorname{Im}(Z_{\text{CPE}}) = Z_c \quad (\text{A-2})$$

therefore:

$$j \operatorname{Im}\left(\frac{1}{Y_0} (j\omega)^{-n}\right) = \frac{1}{j\omega C} \quad (\text{A-3})$$

where  $C$  denotes the resulting capacitance. Equation (A-3) can be written as a function of  $(j\omega)^{-n}$ :<sup>63-64</sup>

$$(j\omega)^{-n} = \omega^{-n} \left[ \cos\left(-n \frac{\pi}{2}\right) + j \sin\left(-n \frac{\pi}{2}\right) \right] \quad (\text{A-4})$$

Therefore, at the frequency where the phase angle is at maximum, the capacitance  $C$  can be given by:<sup>63-64</sup>

$$C = Y_0 \omega^{n-1} / \sin\left(n \frac{\pi}{2}\right) \quad (\text{A-5})$$

## REFERENCES

- G.S. Chen, M. Gao, R.P. Wei, *Corrosion* 52, 1 (1996): p. 8.
- R.G. Buchheit, R.P. Grant, P.F. Hlava, B. Mckenzie, G.L. Zender, *J. Electrochem. Soc.* 144 (1997): p. 2,621.
- G.S. Chen, C.-M. Liao, K.-C. Wan, M. Gao, R.P. Wei, "Pitting Corrosion and Fatigue Crack Nucleation," in *Effects of the Environment on the Initiation of Crack Growth* ASTM STP 1298, W.A. Van Der Sluys, R.S. Piascik, R. Zawierucha, eds. (West Conshohocken, PA: ASTM, 1997), p. 18.
- J.R. Scully, T.O. Knight, R.G. Buchheit, D.E. Peebles, *Corros. Sci.* 35 (1993): p. 185.
- M.J. Pryor, D.S. Keir, *J. Electrochem. Soc.* 102, 10 (1955): p. 241C.
- R.G. Buchheit, *J. Electrochem. Soc.* 142 (1995): p. 3,994.
- P.L. Hagans, C.M. Haas, "Chromate Conversion Coatings," in *ASM Handbook*, 10th ed., vol. 5 (West Conshohocken, PA: ASTM, 1994), p. 405.
- Z.A. Foroulis, M.J. Thubrikar, *J. Electrochem. Soc.* 122 (1975): p. 1,296.
- S. Springs, K. Woods, *Met. Finish.* 6 (1981): p. 49.
- K.A. Korinek, "Chromate Conversion Coatings," in *Metals Handbook*, 9th ed., vol. 13 (West Conshohocken, PA: ASTM, 1987), p. 392.
- P.L. Hagans, C.M. Haas, *Surf. Interface Anal.* 21 (1994): p. 65.
- K. Asami, M. Oki, G.E. Thompson, G.C. Woods, V. Ashworth, *Electrochim. Acta* 32 (1987): p. 337.
- M.W. Kendig, A.J. Davenport, H.S. Isaacs, *Corros. Sci.* 34 (1993): p. 41.
- H.A. Katzman, G.M. Malouf, R. Bauer, G.W. Stupian, *Appl. Surf. Sci.* 2 (1979): p. 416.
- J.A. Richardson, G.C. Wood, *J. Electrochem. Soc.* 120 (1973): p. 193.
- H. Bohni, H.H. Uhlig, *J. Electrochem. Soc.* 116 (1969): p. 906.
- S.T. Pride, J.R. Scully, J.L. Hudson, *J. Electrochem. Soc.* 141 (1994): p. 3,028.
- R.P. Frankenthal, *Corros. Sci.* 7 (1967): p. 61.
- J.S. Wainright, O.J. Murphy, M.R. Antonio, *Corros. Sci.* 33 (1992): p. 281.
- L. Xia, L. McCreery, *J. Electrochem. Soc.* 145 (1998): p. 3,083.
- F.W. Lytle, R.B. Gregor, G.L. Bibbins, K.Y. Blohowiak, R.E. Smith, G.D. Tuss, *Corros. Sci.* 37 (1995): p. 349.
- M.E. Inman, R.G. Kelly, S.A. Willard, R.S. Piascik, "Coordinated Metallographic, Chemical, and Electrochemical Analyses of Fuselage Lap Splice Corrosion," *Proc. of the ASIP Conference*, held in Atlanta, November 1996 (Dayton, OH: U.S. Air Force, 1996).
- A.E. Hughes, R.J. Taylor, B.R. Hinton, *Surf. Interface Anal.* 25 (1997): p. 223.
- J. Zhao, G. Frankel, R.L. McCreery, *J. Electrochem. Soc.* 145 (1998): p. 2,258.
- S. Matsuda, H.H. Uhlig, *J. Electrochem. Soc.* 111 (1964): p. 156.
- G.B. Hatch, *Corrosion Inhibitors*, C.C. Nathan, ed. (Houston, TX: NACE International, 1973), p. 126.
- C.S. Jeffcoat, H.S. Isaacs, J. Hawkins, G.E. Thompson, "The Effect of Chromate Concentration on the Repassivation of Corroding Aluminum," *ECS Meeting Abstract no. 234* (Pennington, NJ: Electrochemical Society [ECS], 1998).
- F. Hunkeler, H. Bohni, *Corrosion* 37 (1981): p. 645.
- A. Sehgal, D. Lu, G.S. Frankel, *J. Electrochem. Soc.* 145 (1998): p. 2,834.
- M. Kendig, S. Jeanjaquet, *ECS Meeting Abstract no. 228* (Pennington, NJ: ECS, 1998).
- C. Blanc, B. Lavelle, G. Mankowski, *Corros. Sci.* 39 (1997): p. 495.
- R.P. Wei, C.-M. Liao, M. Gao, *Met. Trans. A* 29A (1998): p. 1,153.
- Metals Handbook*, vol. 2, 8th ed. (Materials Park, OH: ASM International, 1964), p. 628.
- G.O. Ilevbare, J.R. Scully, J. Yuan, R.G. Kelly, *Corrosion* 56 (2000): p. 227.
- J.R. Scully, D.E. Peebles, D. Frear, A.D. Romig, C.R. Hills, *Metall. Mater. Trans. A* 23A (1992): p. 2,641.
- K. Urushino, K. Sugimoto, *Corros. Sci.* 19 (1979): p. 225.
- R.G. Buchheit, L.P. Montes, M.A. Martinez, J. Michael, P.F. Hlava, *J. Electrochem. Soc.* 146 (1999): p. 4,424.
- W.W. Binger, E.H. Hollingsworth, D.O. Sprowls, *Aluminum*, K.R. Van Horn, ed. (Materials Park, OH: ASM International, 1967), p. 209.
- M. Pourbaix, *Atlas of Electrochemical Equilibria in Aqueous Solution*, 2nd ed. (Houston, TX: NACE, 1974), p. 168.
- A.J. Bard, L.R. Faulkner, *Electrochemical Methods Fundamentals and Applications* (New York, NY: John Wiley, 1980), p. 284.
- N. Dimitrov, J.A. Mann, K. Sieradzki, *J. Electrochem. Soc.* 146 (1999): p. 89.
- R. deLevie, in *Advances in Electrochemistry and Electrochemical Engineering*, P. Delahay, ed., vol. 6 (New York, NY: Interscience, 1967), p. 329.

43. R. deLevie, *Electrochim. Acta* 8 (1963): p. 751.
44. R. deLevie, *Electrochim. Acta* 9 (1964): p. 1,231.
45. J.P. Candy, P. Fouilloux, M. Keddam, H. Takenouti, *Electrochim. Acta* 9 (1981): p. 1,029.
46. H. Keiser, K.D. Beccu, M.A. Gutjahr, *Electrochim. Acta* 21 (1976): p. 539.
47. H.H. Strehlow, C.J. Doherty, *J. Electrochem. Soc.* 125 (1978): p. 30.
48. H.H. Strehlow, C.M. Melliar-Smith, W.M. Augustyniak, *J. Electrochem. Soc.* 125 (1978): p. 915.
49. B. Abeles, P. Sheng, M.D. Coutts, Y. Arie, *Adv. Phys.* 24 (1975): p. 407.
50. J.V. Mantese, W.A. Curtin, W.W. Webb, *Phys. Rev. B* 33 (1986): p. 7,897.
51. B. Abeles, H.L. Pinch, J.I. Gittleman, *Phys. Rev. Lett.* 35 (1975): p. 247.
52. K. Niki, N. Tanaka, A. Yamada, E. Itabashi, W.H. Hartford, *Encyclopedia of Electrochemistry of the Elements*, vol. 9, part B, ed. A.J. Bard (New York, NY: Marcel Dekker, Inc., 1986), p. 255.
53. F. Baumann, I. Sham, *Anal. Chem.* 29 (1957): p. 303.
54. F. Baumann, I. Sham, *J. Am. Chem. Soc.* 78 (1956): p. 5,550.
55. M. Kendig, R. McCreery, J. Ramsey, L. Xia, "Speciation of Oxo-Chromium (VI) Anions and the Corrosion Inhibition of Al Alloys," in *Passivity in Localized Corrosion: Int. Symp. in Honor of Professor Norio Sato*, R.G. Kelly, B. MacDougall, M. Seo, H. Takahashi, PV 99-27 (Pennington, NJ: ECS, 1999), p. 239.
56. G.O. Ilevbare, C.S. Jeffcoate, J.R. Scully, "Mass Transport Limited Oxygen Reduction Kinetics on Chromate Conversion Coated Al-Cu-, Al-Cu-Mg, and Al-Cu-Mn-Fe Intermetallic Compounds," in *Passivity in Localized Corrosion: Int. Symp. in Honor of Professor Norio Sato*, R.G. Kelly, B. MacDougall, M. Seo, H. Takahashi, PV 99-27 (Pennington, NJ: ECS, 1999), p. 269.
57. N. Hackerman, R.A. Powers, *J. Phys. Chem.* 57 (1953): p. 139.
58. E.S. Ivanov, N.G. Kluychnikov, *Prot. Met., Engl. Transl.* 5 (1969): p. 476.
59. D.C. Grahame, *Chem. Rev.* 41 (1947): p. 441.
60. D.C. Grahame, Soderberg, *J. Chem. Phys.* 22 (1954): p. 449.
61. E. McCafferty, *J. Electrochem. Soc.* 137 (1990): p. 3,731.
62. H.H. Strehlow, B. Titze, *Corros. Sci.* 17 (1979): p. 461.
63. E.P.M. Van Westing, G.M. Ferrari, J.H.W. De Wit, *Corros. Sci.* 34 (1993): p. 1,511.
64. S.F. Mertens, C. Xhoffer, B.C. De Cooman, E. Tenimernan, *Corrosion* 53 (1997): p. 381.

## CORROSION RESEARCH CALENDAR

*CORROSION* is a technical research journal devoted to furthering the knowledge of corrosion science and engineering. Within that context, *CORROSION* accepts notices of calls for papers and upcoming research grants, meetings, symposia, and conferences. All pertinent information, including the date, time, location, and sponsor of an event should be sent as far in advance as possible to: Angela Jarrell, Managing Editor, *CORROSION*, 1440 South Creek Drive, Houston, TX 77084-4906. Notices that are not accompanied by the contributor's name, daytime telephone number, and complete address will not be considered for publication.

### 2001

- February 18-20 — 2001 A Coatings Odyssey, 25th Biennial Western Coatings Society Symposium — Anaheim, CA;** Contact Henry Kirsch, 562/942-1833.
- \* February 21-23 — Army Corrosion Summit — Tampa, FL;** Contact Claire Lesinski, Phone: 727/549-7013; E-mail: lesinski@cfc.com.
- February 21-25 — 2nd International Exhibition and Conference on Concrete — Mumbai, India;** Contact Gajanan M. Sabnis, Phone: 202/806-6580; E-mail: gms@sabnis.com.
- \* February 26-28 — NACE Northern Area Western Conference — Anchorage, AK;** Contact John Daley, 907/343-0268.
- \* March 11-16 — CORROSION/2001 — Houston, TX;** Contact NACE, 281/228-6200.
- April 16-20 — 4th Latin American Biodeterioration and Biodegradation Symposium—4 LABS — Buenos Aires, Argentina;** Contact Blanca Rosales, Phone: +54 11 4709 3621; Fax: +54 11 47093210; E-mail: brosales@citefa.gov.ar.
- \* May 1-3 — Western States Corrosion Seminar — Pomona, CA;** Contact John Fisk, 909/392-5452.
- \* Sponsored or cosponsored by NACE International.**
- \* May 8-9 — Symposium on Outdoor and Indoor Corrosion — Phoenix, AZ;** Contact Dorothy Fitzpatrick, 610/832-9677.
- June 10-14 — 7th European Conference on Advanced Materials and Processes — Rimini, Italy;** Contact Organizing Secretariat, Associazione Italiana di Metallurgia (AIM), Phone: +39 02 7602 1132; Fax: +39 02 7602 0551.
- \* June 17-20 — 5th International Symposium on Superalloys 718, 625, 706 and Derivatives — Pittsburgh, PA;** Contact Marlene Karl, Phone: 724/776-9000, ext. 232; Fax: 724/776-3770; E-mail: karl@tms.org.
- June 17-21 — American Water Works Association Annual Conference and Exposition — Washington, DC;** Contact AWWA, 303/347-6160.
- June 17-22 — 5th Electrochemical Impedance Spectroscopy Symposium — Marilleva, Trento, Italy;** Contact Pier Luigi Bonora, Phone: +39 0461 882428; Fax: +39 0461 881977; E-mail: Pierluigi.Bonora@ing.unitn.it.
- July 16-20 — 2001 U.S. Navy and Industry Corrosion Technology Information Exchange and Exhibits — Louisville, KY;** Contact Don Hileman, Phone: 502/364-5231; Fax: 502/364-5354; E-mail: hilemande@nswcl.navy.mil.
- \* August 5-9 — 10th International Conference on Environmental Degradation of Materials in Nuclear Power Systems—Water Reactors — Lake Tahoe, NV;** Contact NACE, 281/228-6200.
- \* August 21-24 — 10th International Symposium on Corrosion in the Pulp and Paper Industry — Helsinki, Finland;** Contact Tero Hakkarainen, Phone: +358 9 456 5410; Fax: +358 9 456 7002; E-mail: tero.hakkarainen@vtt.fi.
- \* August 26-29 — NACE Northern Area Eastern Conference — Halifax, NS, Canada;** Contact Don Marchand, Phone: 902/883-2220; Fax: 902/758-3622.
- \* September 9-14 — NACE Fall Committee Week — Phoenix, AZ;** Contact NACE, 281/228-6200.
- September 16-21 — International Conference on Hydrogen Effects on Material Behavior and Corrosion Deformation Interaction — Moran, WY;** Contact Gary Was, Phone: 734/763-4675; Fax: 734/763-4540; E-mail: gsw@umich.edu.
- \* September 18-20 — NACE UK Section Joint Conference with ICORR — Edinburgh, Scotland;** Contact Institute of Corrosion, Phone: +44(0) 1525 851771; Fax: +44(0) 1525 376690; E-mail: admin@icorr.demon.co.uk.



# PASSIVITY AND LOCALIZED CORROSION

*An International Symposium in Honor of Professor Norio Sato*

## Editors

M. Seo  
Hokkaido University  
Sapporo, Japan

B. MacDougall  
National Research Council of Canada  
Ottawa, Canada

H. Takahashi  
Hokkaido University  
Sapporo, Japan

R. G. Kelly  
University of Virginia  
Charlottesville, Virginia, USA



CORROSION DIVISION

Proceedings Volume 99-27



THE ELECTROCHEMICAL SOCIETY, INC.,  
65 South Main St., Pennington, NJ 08534-2839, USA

# MASS TRANSPORT LIMITED OXYGEN REDUCTION KINETICS ON CHROMATE CONVERSION COATED Al-Cu, Al-Cu-Mg AND Al-Cu-Mn-Fe INTERMETALLIC COMPOUNDS.

†G.O. Ilevbare, \*C. S. Jeffcoat and †J.R. Scully  
 †Center For Electrochemical Science and Engineering, Department of Materials Science and Engineering, University of Virginia, Charlottesville, VA 22903-2442.  
 • Fontana Corrosion Center, The Ohio State University, Columbus, OH 43210

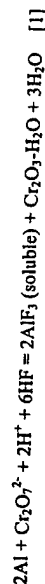
## ABSTRACT

Mass transport limited oxygen reduction reaction (ORR) kinetics were investigated on bulk synthesized analogues of Al-Cu, Al-Cu-Mg, and Al-Cu-Fe-Mn intermetallic phases with and without chromate conversion coating (CCC) in 0.1 M Na<sub>2</sub>SO<sub>4</sub> + 0.005 M NaCl (pH 6). The results were compared to AA 2024-T3 and high purity Al, Cu, Cr and Au. Cathodic ORR mass transport limiting current densities (c.d.) of Al-based materials are lower than the theoretical predictions in the mass transport controlled regime of ideal electronic conductors. This suggests a second rate limiting effect in the case of Al-based materials. CCC inhibits open circuit corrosion which affects cathodic kinetics but its role as an enhanced barrier to electron transfer remains unclear.

## INTRODUCTION

Aluminum-based precipitation age hardened alloys containing Cu and Fe are prone to localized corrosion such as pitting. Pitting and alkaline attack are often induced by local galvanic cells formed by Cu- and Fe-containing intermetallics or replated Cu (1-6). In AA 2024-T3 pit initiation sites include Al-Cu-Mg particles (1), the periphery of Cu-enriched Al-Cu-Mg particles that have been dealloyed of Al and Mg (2), and the matrix adjacent to Al-Cu-Fe-Mn particles (1). Both chromate conversion coating (CCC) and anodization of these alloys improve localized corrosion resistance, particularly in chloride salt spray testing (7, 8). This suggests that either one or more of the four stages of localized corrosion at the anodic site (*i.e.*, nucleation, stabilization, growth, and repassivation) or the properties of sites that support fast cathodic reactions (*e.g.*, cathodic intermetallic phases and replated Cu) are altered by the presence of the CCC.

The CCC process on Al in a dichromate solution containing NaF involves the following overall electrochemical reaction.



Al<sub>2</sub>O<sub>3</sub> is dissolved by fluoride. This is generally regarded as desirable since it facilitates the formation of CCC. Thus, CCCs consist of a mixture of regions of Cr(OH)<sub>3</sub> at sites where chromate is reduced with regions of Al<sub>2</sub>O<sub>3</sub>. Al oxidation is required to form CCCs. It is

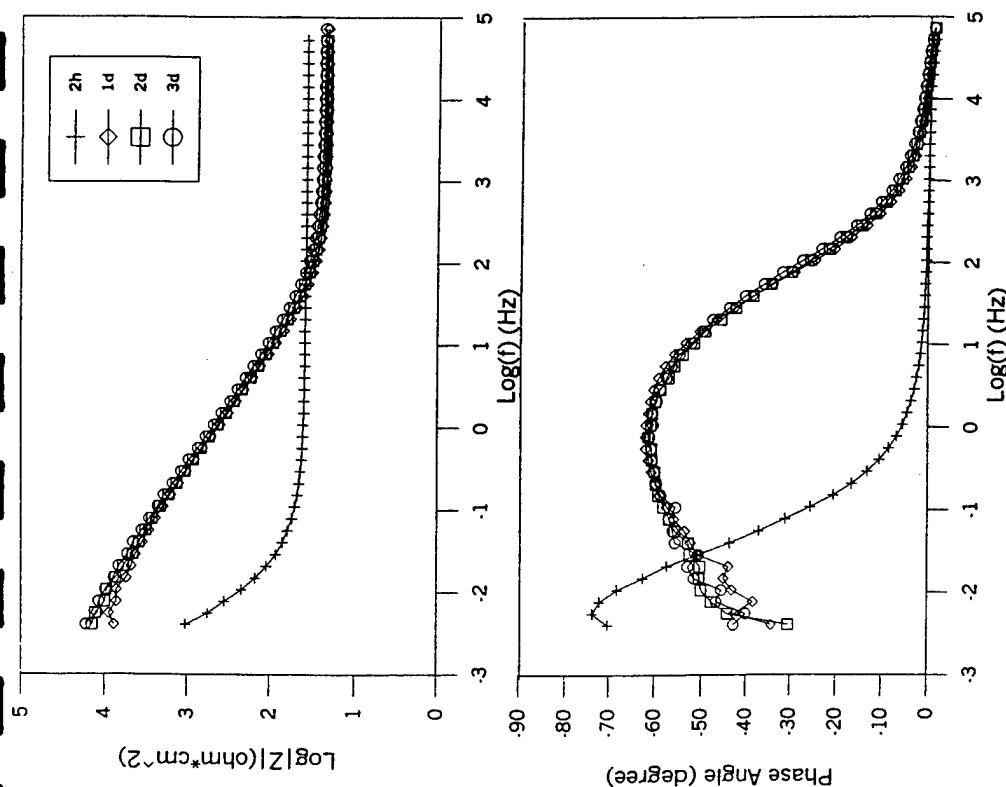


Fig. 5. Bode plots for cerated 1020 steel in 5 w/o NH<sub>3</sub> + 0.2 w/o NaOH at 100°C as a function of exposure time.

expected that Al oxidation is also thermodynamically possible on Cu-containing intermetallic phases that include a significant concentration of Al.  $\text{Cr}^{6+}$  and  $\text{Cr}^{3+}$  may exist within the CCC in several specific forms (9-11). The reduction of  $\text{Cr}^{6+}$  to  $\text{Cr}^{3+}$  in the form of hydrated chromium oxide is often incomplete and CCCs typically contain 9-60%  $\text{Cr}^{6+}$  chromate (12-15). Aging of the coatings affects the amount of  $\text{Cr}^{6+}$  present and, hence, the amount available to be leached out (16, 17).

Chromate is an extremely effective solution phase corrosion inhibitor for localized corrosion (14, 18-20). The mechanisms by which chromate or its reaction products inhibit metallic corrosion may differ in solutions of different halide/anion ratios, temperatures (21-23) and pit sizes (24-26). The role of the CCC as a physical barrier to anodic dissolution, and its effects on the electrochemistry of intermetallics that create galvanic cells in Al-based precipitation age hardened alloys are not certain. For instance, deposited layers have been found to contain pores (27, 28). Apparent cathodic inhibition of ORR on intermetallics has been reported in chromate solution but is subject to further investigation (26, 29). This paper provides preliminary insight into the role of CCCs both as an electron transfer reaction (ETR) barrier, and as a reservoir for leached  $\text{Cr(VI)}$  (12-14, 18). Both factors may alter the cathodic electrochemistry of relevant intermetallic phases. At issue is whether these reaction products along with the physical presence of the CCC alter cathodic kinetics, in what is normally the mass transport limited ORR regime on electronic conducting phases. In this study, we address whether CCCs can intrinsically alter cathodic reaction rates so as to minimize the ability of local heterogeneities to form potent galvanic couples on AA 2024-T3.

## MATERIALS AND PROCEDURES

Studies were conducted on 1.5 mm thick AA 2024-T3 sheets with the composition (major elements): Cu 4.5%, Mg 1.30%, Mn 0.62%, Fe 0.18%, Zn 0.10%, Si 0.093%, (in wt. %), balance Al. Other materials studied were polycrystalline 99.998% Al, 99.999% Cu, 99.9985% Au, 99.7% Cr,  $\text{Al}_2\text{Cu}$ ,  $\text{Al}_2\text{CuMg}$ , and  $\text{Al}_{10}\text{Cu}_2(\text{MnFe})_3$  (the latter 3 being intermetallic phases found as precipitates or constituent particles in AA 2024-T3). X-ray diffraction (XRD) showed that the castings consisted predominantly of the desired intermetallic phases. CCC was performed in-house using solutions containing 0.025 M  $\text{Na}_2\text{Cr}_2\text{O}_7$ , 0.024 M NaF, 0.015 M  $\text{K}_3\text{Fe(CN)}_6$  and  $\text{HNO}_3$  (added until desired pH of 1.2-2.2) after conventional cleaning procedures (30-32). Intermetallics were coupled to AA 2024-T3 during alkaline cleaning, desmutting and conversion coating to simulate their galvanic coupling to AA 2024-T3 during treatment. AA 2024-T3 samples were degreased, alkaline cleaned, desmuted and then conversion coated. Others were only degreased and are referred to as untreated. The alkaline cleaning solution was 0.21 M  $\text{Na}_2\text{CO}_3$  and 0.23 M  $\text{Na}_3\text{PO}_4$  (pH 13). The desmutting solution was 50% (by vol.)  $\text{HNO}_3$ . All electrodes were wet ground with 600 grit SiC paper before CCC or when used as untreated samples with the exception of AA 2024-T3. The thickness of the CCC (33) was estimated to be between 0.1 and 1.0  $\mu\text{m}$ . Salt spray testing was performed according to ASTM B117 specifications for chromate conversion coated AA 2024-T3 (34) by an outside laboratory to verify corrosion inhibition. They were found to be at least equal in quality to commercial products. All CCC specimens were between 48-120 h old before electrochemical testing was conducted. The presence of  $\text{Cr}^{6+}$  in CCC of this age was verified for all treatments using X-ray absorption spectroscopy (XAS)\*. Auger Electron Spectroscopy (AES) was used to carry out surface composition analyses with a Perkin-Elmer

\* XAS was conducted at the NSLS at BNL

560 ESCA/SAM system at a chamber pressure of about  $10^{-10}$  Torr. The AES system was equipped with an electron multiplier detector and a cylindrical mirror analyser. AES spectra were taken with an electron gun voltage of 3 keV at a resolution of 0.6%. Depth profiles were generated with Ar-sputtering at a beam voltage of 3 kV, in the raster mode, at a pressure (in the ion gun) of between 10 and 20 mPa.

Open circuit potential (OCP) exposures of 2 hours followed by potentiodynamic polarization experiments (at 1 mV/s) were performed in quiescent 0.1 M  $\text{Na}_2\text{SO}_4$  + 0.005 M NaCl (pH 6) at ambient temperature, on stationary and rotating disc electrodes (RDE), in 3-electrode cells that were open to lab air. This environment was an analogue to low chloride-high anion solutions based on measurements of corrosive environments found in the lap-splice joints of aircrafts (35). Rotation speeds of 500, 2000, and 4000 rpm were used in RDE experiments. The electrolytes were air sparged in addition to being open to lab air. Mass transport limiting c.d. (i) were determined from mass transport limited regions on cathodic E-log i curves. Regions where  $i_{\text{lim}}$  was independent of  $E_{\text{applied}}$  were not always observed for Al. In these cases, the hydrogen evolution reaction (HER) and proximity to OCP were avoided. In other experiments, 0.0038 M  $\text{H}_2\text{C}_2\text{O}_4$  + 0.0062 M  $\text{Na}_2\text{CrO}_4$  was added to 0.1 M  $\text{Na}_2\text{SO}_4$  + 0.005 M NaCl (pH 6) to mimic  $\text{Cr(VI)}$  leaching.

## RESULTS

### Intermetallic bulk and surface compositions

Energy dispersive x-ray analyses results from castings of  $\text{Al}_2\text{Cu}$ ,  $\text{Al}_2\text{CuMg}$ , and  $\text{Al}_{10}\text{Cu}_2(\text{MnFe})_3$  show that the electrodes consisted predominantly of the desired intermetallic compositions. XRD confirmed the presence of the desired phases. Table I lists bulk compositions.  $\text{Al}_2\text{Cu}$  has been analyzed in more detail elsewhere (36). The surface compositions after wet grinding obtained from AES are reported in Table II. They match the bulk compound stoichiometry and suggest that wet grinding did not significantly alter composition except for the presence of oxygen from oxidation and contamination.  $\text{Al}_{10}\text{Cu}_2(\text{MnFe})_3$  was slightly richer in iron after grinding.

### Anodic and cathodic corrosion kinetics on untreated electrodes in 0.1 M $\text{Na}_2\text{SO}_4$ + 0.005 M NaCl

Figures 1a and 1b illustrate the overall E-logi behavior on stationary electrodes of AA 2024-T3, Al, Cu,  $\text{Al}_2\text{Cu}$ ,  $\text{Al}_2\text{CuMg}$ , and  $\text{Al}_{10}\text{Cu}_2(\text{MnFe})_3$  in 0.1 M  $\text{Na}_2\text{SO}_4$  + 0.005 M NaCl after a 2 hour exposure at OCP. The OCP of Cu,  $\text{Al}_2\text{Cu}$ , and  $\text{Al}_{10}\text{Cu}_2(\text{MnFe})_3$  are more positive than that of AA 2024-T3 (horizontal line) and far more positive than those of  $\text{Al}_2\text{CuMg}$  and Al.  $\text{Al}_2\text{CuMg}$  is not passive at OCP and exhibits a high dissolution rate upon anodic polarization. Figure 1b shows that  $\text{Al}_{10}\text{Cu}_2(\text{MnFe})_3$  is passive near the OCP of AA 2024-T3 but undergoes pitting at potentials above it. Passivity of  $\text{Al}_{10}\text{Cu}_2(\text{MnFe})_3$  and  $\text{Al}_2\text{Cu}$  at OCP were confirmed by both EIS and deaeration of solutions. Therefore,  $\text{Al}_{10}\text{Cu}_2(\text{MnFe})_3$  and  $\text{Al}_2\text{Cu}$  have OCPs near their  $E_{\text{pit}}$  but are passive. AA 2024-T3 pits at its OCP and large pits have been observed in its matrix. Cathodic kinetics were enhanced on all Cu-containing materials and AA 2024-T3 compared to pure Al (Figure 1a) as noted by Prior and Kier (5).

A peak in cathodic current density on Cu was due to the cathodic reduction of the copper oxide. Otherwise, the principal cathodic reactions near the OCP of AA 2024-T3 are the oxygen reduction reaction (ORR) and hydrogen evolution reaction (HER) at more negative potentials ( $< -0.6$  V<sub>SCE</sub>). The exchange current density for the ORR and HER are much lower on Al than the Cu-containing materials. The exchange current density for the HER is so low (37) on Al that mass transport limited ORR dominates the high purity Al electrode at potentials as negative as  $-1.5$  V<sub>SCE</sub>. HER does not occur in a pH 6 electrolyte, at standard temperature (25°C) and pressure near the OCP of AA 2024-T3 (ca.  $-0.5$  V<sub>SCE</sub>). Therefore, mass transport limited O<sub>2</sub> reduction is one of the cathodic reactions of greatest interest when studying open circuit corrosion of this alloy either with or without CCC in near neutral chloride solutions. Clearly, this reaction occurs at higher rates on Cu-bearing phases compared to high purity Al. At issue is the effect of CCC on the ORR electrochemistry of intermetallics embedded in AA 2024-T3.

#### Chromate conversion coated electrodes

XAS absorbance pre-edge peaks on chromate conversion coated AA 2024-T3 (Figure 2a) show evidence of Cr<sup>6+</sup> in the CCC. Figure 2b shows that the amount of Cr<sup>6+</sup> and total Cr (depicted by the pre-edge and edge peaks respectively) in the CCC increases with coating time and, hence, thickness of the CCC. Figure 3 presents a comparison of OCPs in 0.1 M Na<sub>2</sub>SO<sub>4</sub> + 0.005 M NaCl to those after CCC treatment<sup>8</sup> on stationary electrodes in a plot that depicts differences in OCP as departures from the diagonal line. The OCPs of chromate conversion coated Al, AA 2024-T3, Al<sub>2</sub>Cu, Al<sub>2</sub>CuMg and 99.999% Cu were not changed significantly. Only the OCP of Al<sub>2</sub>Cu<sub>2</sub>(MnFe)<sub>3</sub> was lowered when chromate conversion coated. The key result is that one of the factors (*i.e.*, differences in OCPs) that promotes galvanic corrosion between Al-Cu intermetallics and the AA 2024-T3 matrix and the active Al<sub>2</sub>CuMg phase is not changed by CCC. The OCP of the Al-Cu-Mn-Fe intermetallic was, however, slightly lowered and this would be expected to suppress the galvanic driving force.

#### Cathodic kinetics on untreated and CCC electrodes as a function of the extent of prior corrosion

Cathodic kinetics on untreated samples in *chromate-free* solutions were performed on stationary AA 2024-T3 electrodes as a function of extent of prior corrosion damage. Prior corrosion damage was controlled by either varying time at OCP or by applying anodic charge immediately prior to cathodic scans. It was found that *i*<sub>c</sub> of ORR increased as the anodic charge applied to AA 2024-T3 (to cause pitting) increased. The OCP also became more negative as applied charge increased. The cathodic kinetics of Al<sub>2</sub>CuMg also increased as the extent of corrosion that had occurred increased. Experiments carried out on AA 2024-T3 in 0.1 M Na<sub>2</sub>SO<sub>4</sub> after a 2 hour exposure at OCP compared with 0.1 M Na<sub>2</sub>SO<sub>4</sub> + 0.005 M NaCl also showed that the *i*<sub>c</sub> for ORR decreased in the sulfate solution compared with the sulfate/chloride solution. The OCP of AA 2024-T3 in 0.1 M Na<sub>2</sub>SO<sub>4</sub> + 0.005 M NaCl is close to its pitting potential (Figure 1b). AA 2024-T3 is not expected to pit in 0.1 M Na<sub>2</sub>SO<sub>4</sub> due to the absence of chloride ions in solution. Therefore the greater cathodic kinetics in

<sup>8</sup> CCC while galvanically coupled to AA 2024-T3.

0.1 M Na<sub>2</sub>SO<sub>4</sub> + 0.005 M NaCl can be attributed at least in part to prior open circuit corrosion. CCC suppresses OCP corrosion as shown on AA 2024-T3 (Figure 4).

Figures 5a and 5b show representative E-log*i* plots of untreated and 3 minute CCC Cu<sub>2</sub>Al<sub>2</sub>Cu<sub>2</sub>(MnFe)<sub>3</sub> and Al at electrode rotation speed of 500 rpm ( $\omega^{0.5} = 7.24$  (rad s<sup>1/2</sup>)). These materials represent the extremes of cathodic behavior seen in Figure 1. Mass transport regimes for ORR could be selected, albeit at different potentials. Figure 6 shows the ORR mass transport limiting current density (*i*<sub>l</sub>) vs.  $\omega^{0.5}$ . A comparison of *i*<sub>l</sub> in 0.1 M Na<sub>2</sub>SO<sub>4</sub> + 0.005 M NaCl between untreated and 3 minute CCC are shown for Cu<sub>2</sub>Al<sub>2</sub>Cu<sub>2</sub>(MnFe)<sub>3</sub> and Al after a 2 hour exposure at OCP in Figure 6a.

The mass transport limited O<sub>2</sub> reduction current density data for the Cu and Al<sub>2</sub>Cu<sub>2</sub>(MnFe)<sub>3</sub> almost match the ORR results predicted by the Levich Equation for an ideal electronic conductor with respect to angular velocity (rotation rate) (38). The Al data is much lower than predicted from mass transport of O<sub>2</sub> in solution. The kinetics are almost independent of angular velocity and do not obey the Levich Equation, which is theoretically limiting interface (36). This implies an additional rate limitation for Al which is likely to be the insulating Al<sub>2</sub>O<sub>3</sub> oxide film which limits ETR. The *i*<sub>l</sub> is lower on chromate conversion coated Cu and Al<sub>2</sub>Cu<sub>2</sub>(MnFe)<sub>3</sub> and higher on Al compared with the untreated samples. *i*<sub>l</sub> after CCC do not also obey the Levich Equation. However, the relative order of the rates of the ORR kinetics are preserved (*i.e.*, ORR rate on Cu > Al<sub>2</sub>Cu<sub>2</sub>(MnFe)<sub>3</sub> > Al) on the chromate conversion coated samples. *i*<sub>l</sub> is lower on the chromate conversion coated Cu but higher on Al<sub>2</sub>Cu<sub>2</sub>(MnFe)<sub>3</sub> (albeit very slightly) and Al compared with the untreated samples in the chromate containing solution (Figure 6b). Results from stationary electrodes (39) did not show a difference in *i*<sub>l</sub> of the ORR between untreated (with and without chromate in solution), and chromate conversion coated samples in 0.1 M Na<sub>2</sub>SO<sub>4</sub> + 0.005 M NaCl. Extrapolation of the *i*<sub>l</sub> vs.  $\omega^{0.5}$  data to 0 rpm showed that the data converges for all treatments within a statistical scatter band.

## DISCUSSION

In galvanic couples on corroding AA 2024-T3, the most dangerous specie is replated Cu because of its high OCP and rate of ORR compared with the AA 2024-T3 matrix which predominantly contains Al (Figure 1). The positive OCP of AA 2024-T3 (Figures 1 and 3) is a consequence of the presence of the Cu-bearing phases in the alloy, as well as Cu in the solid solution in the f.c.c. (face centered cubic) Al phase. The role the intermetallics play in the various galvanic couples is therefore very important. The effect of CCC on these phases is of interest.

The little or no change in the OCP of Cu, Al<sub>2</sub>Cu and Al<sub>2</sub>CuMg after CCC suggests that CCC does not alter the potential driving force on AA 2024-T3. The slight reduction in the OCP of Al<sub>2</sub>Cu<sub>2</sub>(MnFe)<sub>3</sub> suggests that some alteration might be expected in the couples formed between this phase and the alloy matrix. Three mechanisms for inhibition of mass transport limited ORR kinetics on CCC electrodes are possible: a) a physical barrier that diminishes O<sub>2</sub> mass transport because stirring does not penetrate into the coating pores b) a barrier to ETR and c) anodic inhibition. Results of ORR studies on Cr with a Cr<sub>2</sub>O<sub>3</sub> oxide addresses whether the presence of Cr<sub>2</sub>O<sub>3</sub> reduces mass transport limited ORR kinetics. The predicted value from the Levich Equation is far higher than experimental data. This suggests

that conductive  $\text{Cr}_2\text{O}_3$  limited ETR compared to an ideal electronic conductor. Recall that the CCC is composed of a mixture of  $\text{Al}_2\text{O}_3$  which does not support ETR easily, and a hydrated chromium oxide. Figures 2 and 3 show that  $\text{Cr}^{6+}$  is not only present in the CCC but that the quantity of  $\text{Cr}^{6+}$  present increases with coating time. This means that consideration must be given to the effect of the CCC not only as an electron transfer barrier, but also as a reservoir for the storage of  $\text{Cr}^{6+}$  species that play a role in anodic reaction inhibition. From this (Figure 4) and some of our other work to be published elsewhere (39), it is known that CCC improves the pitting potential ( $E_{\text{pit}}$ ) on AA 2024-T3 in 0.1 M  $\text{Na}_2\text{SO}_4 + 0.005 \text{ M NaCl}$  after a 2 h exposure at OCP. This means that prior corrosion at OCP is reduced. The cathodic reaction rate is also reduced as a result.

Figure 6a shows that CCC did reduce the rate of the ORR on all the intermetallic phases and Cu. The rates on Al increased. This is not surprising since the rate determining step on Al is not mass transport of  $\text{O}_2$  to the Al surface but the rate of the ETR across the  $\text{Al}_2\text{O}_3$  oxide film (5). The increase in the rate of the ETR on CCC Al surfaces may be due to the modifications in the oxide film during the CCC process, specifically, the thinning and dissolution of the  $\text{Al}_2\text{O}_3$  oxide film by the presence of HF. The reasons for the reduction in the rate of the ORR on the intermetallics and Cu are more complicated. There is a difficulty in separating the contribution of the CCC as a physical or electron transfer barrier from the contribution of chromate held within the pores of the CCC that can serve as an anodic inhibitor.

In experiments aimed at separating the intrinsic (i.e., direct effects on ORR) from extrinsic (e.g., reduction of OCP corrosion, oxide film alterations) effects, RDE experiments were performed on gold (Au) electrodes. Au is an ideal electronic conductor. Au was chosen because it did not corrode at OCP nor have an oxide film which could be altered by chromate as does even Pt (40). On Au, the highest ORR occurred when chromate was present in solution (Figure 7a). This was likely due to the additive effects of the ORR rate and the reduction of  $\text{Cr}^{6+}$  to  $\text{Cr}^{3+}$ . However, there was no effect on ORR when Au was pretreated in chromate containing solution before cathodic polarization. This suggests that chromate has little or no intrinsic effect on ORR. The role of the CCC solely as a physical barrier to ETR that reduces the cathodic kinetics is still unclear. A comparison of the ORR rate on 3 minute CCC surfaces in 0.1 M  $\text{Na}_2\text{SO}_4 + 0.005 \text{ M NaCl}$  to untreated surfaces in the presence of chromate in solution (Figure 6b) might suggest that the barrier role is not appreciable at least on  $\text{Al}_2\text{O}_3(\text{MnFe})_3$  and Al since the cathodic reaction rates on the chromate conversion coated surfaces are higher. At least two types of extrinsic alterations of apparent cathodic kinetics are produced by CCC: a) the minimizing dissolution and porous Cu electrode formation on the Al-Cu-Mg phase, which lessens Cu surface enrichment and sponge formation and b) the reduction of OCP pitting of AA 2024-T3, Al-Cu as well as Al-Cu-Mn-Fe intermetallics.  $\text{Cr}_2\text{O}_3$  inhibits ETR but destruction of  $\text{Al}_2\text{O}_3$  by fluoride may enhance ETR. Therefore, the role of the CCC as a physical or ETR barrier that inhibits cathodic kinetics is still inconclusive.

## CONCLUSIONS

1. Cathodic mass transport limited ORR kinetics are enhanced on intermetallics and bulk Cu compared to pure Al in 0.1 M  $\text{Na}_2\text{SO}_4 + 0.005 \text{ M NaCl}$ . They are close to the predictions of the Levich Equation.

2. ORR kinetics on intermetallics and bulk Cu are still enhanced (compared to pure Al) in the presence of CCC over the range of disk rotation rates, but do not follow the predictions of the Levich Equation.
3. The OCPs of AA 2024-T3, Al, Cu,  $\text{Al}_2\text{CuMg}$  and  $\text{Al}_3\text{Cu}$  were not altered by CCC.
4. A decrease in ORR kinetics is observed on chromate conversion coated RDE. This was at least partly due to the suppression of prior corrosion at OCP.

## ACKNOWLEDGEMENTS

Funding from Air Force Office of Scientific Research (Major Hugh DeLong, Program Manager, Grant No. F49620-96-1-0178) is gratefully acknowledged. Intermetallics were supplied of the Aluminum Company of America (ALCOA). The CESE gratefully acknowledges on-going support of EG&G instruments and Scribner Associates, Inc.

## REFERENCES

1. G.S. Chen, M. Gao, R.P. Wei, *Corrosion*, **52**, 8 (1996).
2. R.G. Buchheit, R.P. Grant, P.F. Hlava, B. McKenzie, G.L. Zender, *J. Electrochem. Soc.*, **144**, 2621 (1997).
3. G.S. Chen, C.-M. Liao, K.-C. Wan, M. Gao, R.P. Wei, ASTM STP 1298, W.A. Van Der Sluys, R.S. Piascik, R. Zawierucha, Eds., p.18, ASTM (1997).
4. J.R. Scully, T.O. Knight, R.G. Buchheit, D.E. Peebles, *Corros. Sci.*, **35**, 185 (1993).
5. M.J. Pryor, D.S. Keir, *J. Electrochem. Soc.*, **140**, 241C (1993).
6. R.G. Buchheit, *J. Electrochem. Soc.*, **142**, 241C (1995).
7. P.L. Hagans and C.M. Haas, in *ASM Handbook 10<sup>a</sup> ed.*, Vol. 5, pp. 405, ASM International Ohio, (1994).
8. Z.A. Foroulis and M.J. Thubrikar, *J. Electrochem. Soc.*, **122**, 1296 (1975).
9. J.S. Weinright, O.J. Murphy, M.R. Antonio, *Corros. Sci.*, **33**, 281 (1992).
10. L. Xia, L. McCreery, *J. Electrochem. Soc.*, **145**, 3083 (1998).
11. F.W. Lytle, R.B. Gregor, G.L. Bibbins, K.Y. Blohowiak, R.E. Smith, G.D. Tuss, *Corros. Sci.*, **37**, 349 (1995).
12. P.L. Hagans, C.M. Haas, *Surface and Interface Analysis*, **21**, 65 (1994).
13. K. Asami, M. Oki, G.E. Thompson, G.C. Woods, and V. Ashworth, *Electrochimica Acta*, **32**, 337 (1987).
14. M.W. Kendig, A.J. Davenport and H.S. Isaacs, *Corros. Sci.*, **34**, 41 (1993).
15. T. Drozda and E. Malecki, *J. Radioanal Nucl Chem Lett.*, **95**, 339 (1985).
16. A.E. Hughes, R.J. Taylor, B.R. Hinton, *Surface and Interface Analysis*, **25**, 223 (1997).
17. J. Zhao, G. Frankel, R.L. McCreery, *J. Electrochem. Soc.*, **145**, 2258 (1998).
18. H.A. Katzman, G.M. Malouf, R. Bauer and G.W. Stupian, *Applications of Surface Science*, **2**, 416 (1979).
19. J.A. Richardson and G.C. Wood, *J. Electrochem. Soc.*, **120**, 193 (1973).
20. H. Bohni and H.H. Uhlig, *J. Electrochem. Soc.*, **116**, 906 (1969).
21. S. Matsuda, H.H. Uhlig, *J. Electrochem. Soc.*, **111**, 156 (1964).
22. G.B. Hatch, in *Corrosion Inhibitors*, Ed. by C.C. Nathan, p. 126, NACE (1973).
23. C.S. Jeffcoat, H.S. Isaacs, J. Hawkins, G.E. Thompson, ECS Meeting Abstract #234, Nov, (1998).
24. S.T. Pride, J.R. Scully and J.L. Hudson, *J. Electrochem. Soc.*, **141**, 3028 (1994).
25. F. Hunkeler, H. Bohni, *Corrosion*, **37**, 645 (1981).

26. A. Sehgal, D. Lu, G.S. Frankel, *J. Electrochem. Soc.*, **145**, 2834 (1998).  
 27. G.M. Brown, K. Shimizu, K. Kobayashi, G.E. Thompson, G.C. Wood, *Corros. Sci.*, **33**, 1371 (1992).  
 28. G.M. Brown, K. Shimizu, K. Kobayashi, G.E. Thompson, G.C. Wood, *Corros. Sci.*, **33**, 1045 (1992).  
 29. M. Kendig, S. Jeanjaquet, ECS Meeting Abstract #228, Nov. (1998).  
 30. *Metals Handbook* vol. 2, 8<sup>th</sup> ed., p. 628, ASM International Metals Park, OH (1964).  
 31. Military Standard MIL-STD-1503B (USAF), Preparation of Aluminum Alloys for Surface Treatments and Inorganic Coatings, p. 7, November 1989.  
 32. M. F. Stevenson Jr. in *ASM Handbook* vol. 5, 10<sup>th</sup> ed., p. 482, ASM International Metals Park, OH (1994).  
 33. K. A. Korinek in *Metals Handbook* vol. 13, 9<sup>th</sup> ed., p. 392, ASM International Metals Park, OH (1987).  
 34. *Annual Book of ASTM Standards*, Section 6, vol. 06.01, p. 1, ASTM Philadelphia PA (1992).  
 35. M. E. Inman, R. G. Kelly, S. A. Willard, and R. S. Pisciotti, "Coordinated Metallographic, Chemical and Electrochemical Analyses of Fuselage Lap Splice Corrosion", Proc. of the ASIP Conference, Atlanta, November 1996.  
 36. J.R. Scully, D.E. Peebles, D. Frear, A.D. Romig, C.R. Hills, *Metallurgical and Materials Transactions A*, **23A**, 2641 (1992).  
 37. M. Pourbaix, *Atlas of Electrochemical Equilibria in Aqueous Solution* 2<sup>nd</sup> ed. NACE Houston, TX (1974).  
 38. A. J. Bard and L. R. Faulkner, in *Electrochemical Methods Fundamentals and Applications*, p.284, John Wiley New York (1980).  
 39. G.O. Ilevbare, J.R. Scully, J.Yuan and R.G. Kelly to be published (in Print) in *Corrosion Journal*.  
 40. K. Niki, N. Tanaka, A. Yamada, E. Itabashi and W. H. Hartford, in *Encyclopedia of Electrochemistry of the Elements*, Volume IX part B, Ed. by A. J. Bard, p.255, Marcel Dekker, Inc., New York (1986).

Table I. Bulk compositions of the intermetallics castings from energy dispersive x-ray analyses.

Phases	Atomic Composition (%)					
	Al	Mg	Zn	Cu	Mn	Fe
Al <sub>2</sub> Cu <sub>2</sub> (MnFe) <sub>3</sub>	71.43	-	-	7.14	10.71	10.71
Al <sub>2</sub> CuMg	49.28	26.06	-	24.66	-	-
Al <sub>2</sub> Cu	66.69	-	-	33.31	-	-

Table II. Surface compositions from Auger electron spectroscopy (AES) analyses of Al<sub>2</sub>CuMg and Al<sub>2</sub>Cu<sub>2</sub>(MnFe)<sub>3</sub> electrodes after wet grinding using 600 grit SiC paper.

Phase	Sputter Time (s)	Atomic Composition of (at.%)				
		Al	Cu	Mg	Mn	O
Al <sub>2</sub> CuMg	150	34.13	17.65	15.45	-	32.76
Al <sub>2</sub> Cu <sub>2</sub> (MnFe) <sub>3</sub>	120	54.26	6.18	-	8.66	14.87
						16.03

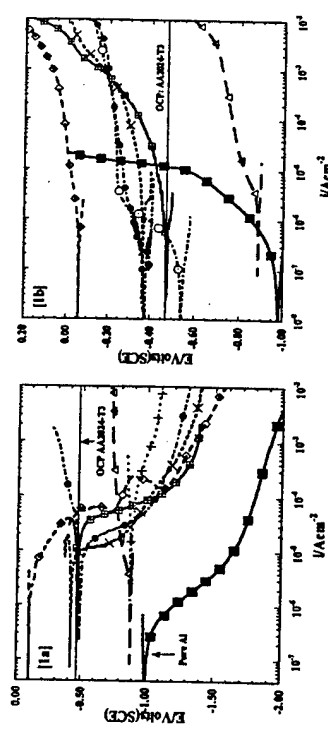


Figure 1. The cathodic (1a) and anodic (1b) E-log i behavior of stationary electrodes of AA 2024-T3: Al, Cu, Al<sub>2</sub>Cu, Al<sub>2</sub>CuMg + (cathodic), Δ (anodic), Al<sub>20</sub>Cu<sub>2</sub>(MnFe)<sub>3</sub> and Al<sub>20</sub>Cu<sub>2</sub>(MnFe)<sub>3</sub> (degraded) in 0.1 M Na<sub>2</sub>SO<sub>4</sub> + 0.005 M NaCl.

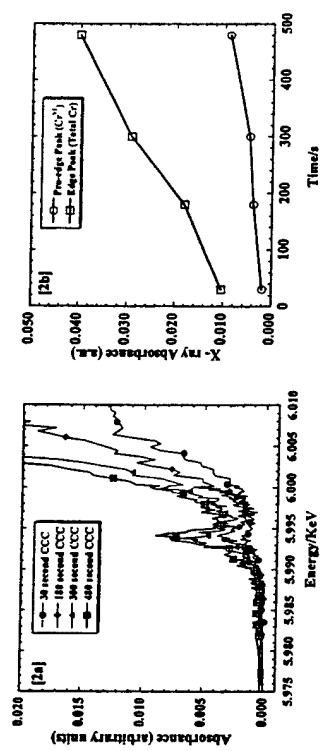


Figure 2. XAS pre-edge peak at 5.994 keV after chromate conversion coatings of 30, 180, 300 and 480 seconds on AA2024-T3 showing evidence of Cr<sup>6+</sup> in the CCC (2a). The height of the x-ray absorption pre-edge peak (representing amount of Cr<sup>6+</sup> present) and that of the edge peak (representing total amount of Cr present) as a function of coating time (2b).

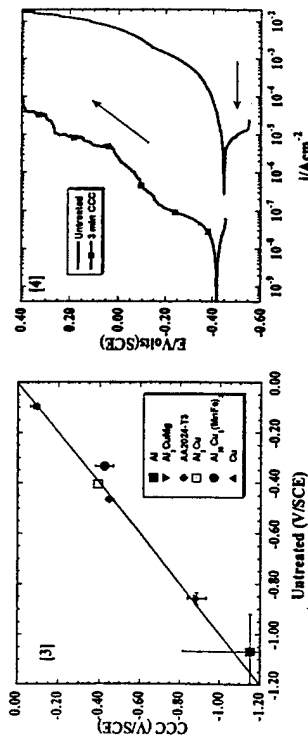


Figure 3 (Left). Stationary electrode open circuit potentials after 2 hours on untreated 99.998% Al, Al<sub>3</sub>CuMg, AA 2024-T3, Al<sub>3</sub>Cu, Al<sub>3</sub>Cu<sub>2</sub>(MnFe), and 99.999% Cu compared with those of their 5 minute CCC counterparts in 0.1 M Na<sub>2</sub>SO<sub>4</sub> + 0.005 M NaCl (pH 6). Similar results were obtained with 3 minute CCC. Figure 4 (Right). E-logi behavior of untreated and 3 minute CCC AA 2024-T3 in 0.1 M Na<sub>2</sub>SO<sub>4</sub> + 0.005 M NaCl after 2 hour exposure at OCP.

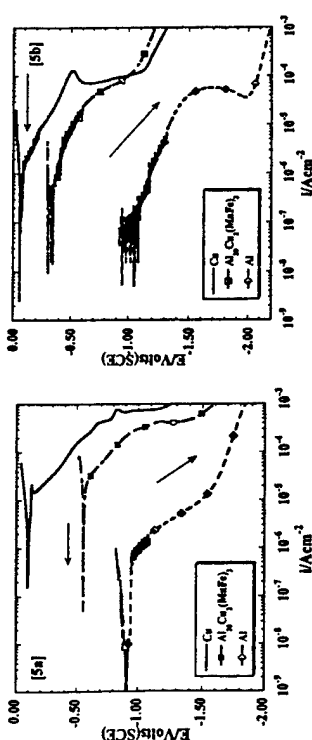


Figure 5. E-logi behavior of untreated (5a) and 3 minute CCC (5b) Cu, Al<sub>3</sub>Cu<sub>2</sub>(MnFe)<sub>3</sub> and Al in 0.1 M Na<sub>2</sub>SO<sub>4</sub> + 0.005 M NaCl at 500 rpm ( $\omega^{0.5} = 7.24 \text{ (rad s}^{-1})^{0.5}$ ).

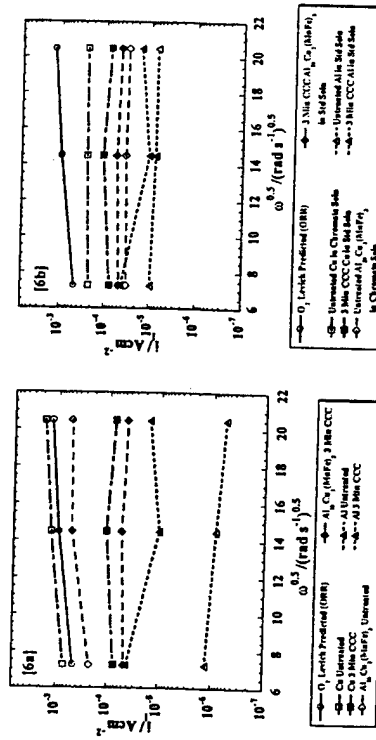


Figure 6. Oxygen reduction limiting current density (ii) from rotating disk electrodes comparing untreated and 3 minute CCC (6a) Cu, Al<sub>3</sub>Cu<sub>2</sub>(MnFe)<sub>3</sub>, and Al in 0.1 M Na<sub>2</sub>SO<sub>4</sub> + 0.005 M NaCl (Std Soln.). 6b compares results from untreated samples in 0.1 M Na<sub>2</sub>SO<sub>4</sub> + 0.005 M NaCl + 0.0038 M H<sub>2</sub>CrO<sub>4</sub> + 0.0062 M Na<sub>2</sub>CrO<sub>4</sub> (Chromate Soln.) to those with 3 minute CCC in Std. Soln. Levich prediction at concentration of 6 ppm ( $1.88 \times 10^{-4} \text{ M}$ ) dissolved O<sub>2</sub>.

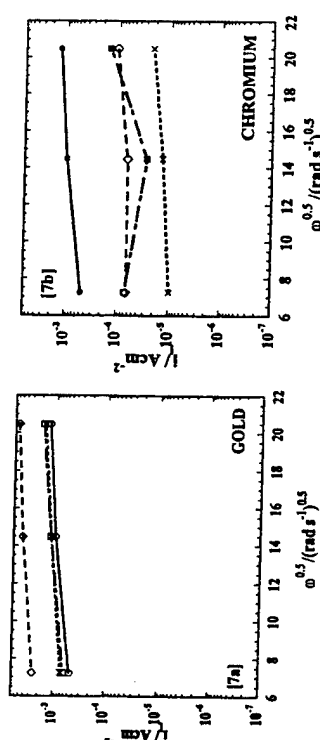


Figure 7. Oxygen reduction limiting current density (ii) from rotating disk electrodes for Au (7a) and Cr (7b) in 0.1 M Na<sub>2</sub>SO<sub>4</sub> + 0.005 M NaCl, 0.1 M Na<sub>2</sub>SO<sub>4</sub> + 0.005 M NaCl + 0.0038 M H<sub>2</sub>CrO<sub>4</sub> + 0.0062 M Na<sub>2</sub>CrO<sub>4</sub>, and in 0.1 M Na<sub>2</sub>SO<sub>4</sub> + 0.005 M NaCl after a 2 hour pretreatment in 0.1 M Na<sub>2</sub>SO<sub>4</sub> + 0.005 M NaCl + 0.0038 M H<sub>2</sub>CrO<sub>4</sub> + 0.0062 M Na<sub>2</sub>CrO<sub>4</sub>. X, Levich prediction, O<sub>2</sub> at a concentration of 6 ppm ( $1.88 \times 10^{-4} \text{ M}$ ) dissolved O<sub>2</sub>.

# CORROSION AND CORROSION PREVENTION OF LOW DENSITY METALS AND ALLOYS

*Proceedings of the International Symposium*

## Editors

B. A. Shaw  
Penn State University  
University Park, Pennsylvania, USA

R. G. Buchheit  
Ohio State University  
Columbus, Ohio, USA

J. P. Moran  
Aluminum Company of America  
Alcoa Center, Pennsylvania, USA



CORROSION DIVISION

Proceedings Volume 2000-23



THE ELECTROCHEMICAL SOCIETY, INC.  
65 South Main St., Pennington, NJ 08534-2839, USA



## REFERENCES

1. M. W. Kendig, A. J. Davenport, and H. S. Isaacs, *Corr. Sci.*, **34**, 41 (1993).
2. F. W. Lytle, R. B. Gregor, G. L. Bibbins, K. Y. Blohowiak, R. E. Smith, and G. D. Tuss, *Corr. Sci.*, **37**, 349 (1995).
3. H. Bohni and H. Uhlir, *J. Electrochem. Soc.*, **116**, 906 (1969).
4. S. T. Pride, J. R. Scully and J. L. Hudson, *J. Electrochem. Soc.*, **141**, 3028 (1994).
5. F. Hunkeler and H. Bohni, *Corrosion*, **37**, 645 (1981).
6. H. A. Katzman, G. M. Malouf, R. Bauer, and G. W. Stupian, *Appl. Surf. Sci.*, **2**, 416 (1979).
7. J. Zhao, G. Frankel, and R. L. McCreery, *J. Electrochem. Soc.*, **145**, 2258 (1998).
8. L. Xia, E. Akiyama, G. Frankel, R. L. McCreery, *J. Electrochem. Soc.*, **147**, 2556-2562 (2000).
9. J. D. Ramsey and R. L. McCreery, *J. Electrochem. Soc.*, **146** (11), 4076 (1999).
10. J. D. Ramsey, L. Xia, M. W. Kendig, and R. L. McCreery, *Corros. Sci.*, Submitted.
11. L. Xia and R. L. McCreery, *J. Electrochem. Soc.*, **145**, 3083 (1998).
12. W. R. McGovern, P. Schmutz, R. G. Buchheit, R. L. McCreery, *J. Electrochem. Soc.*, **147**, 4494-4501 (2000).

## IN-SITU CONFOCAL LASER SCANNING MICROSCOPY SURFACE METROLOGY STUDIES OF CORROSION ON AA 2024-T3

O. Schneider, G. O. Ilevbare, R.G. Kelly, J.R. Scully  
Center for Electrochemical Science and Engineering, Department of Materials Science and Engineering, University of Virginia, Charlottesville, VA 22904-4745

## ABSTRACT

Galvanic corrosion at Al-Cu, Al-Cu-Mg, and Al-Cu-Fe-Mn intermetallic phases was investigated and compared on bare and epoxy-coated, polished surfaces of AA2024-T3. Exposures were conducted in 0.1 M Na<sub>2</sub>SO<sub>4</sub> + 0.005 M NaCl (pH 6), 0.1 M Na<sub>2</sub>SO<sub>4</sub> + 0.005 M NaCl + 0.0001 M NaOH (pH 10), 0.1 M Na<sub>2</sub>SO<sub>4</sub> + 0.005 M Cl<sup>-</sup> (as AlCl<sub>3</sub>) (pH 3) and 0.5 M NaCl (pH 6). The results showed similar morphology of attack at each type of intermetallic compound on the bare surfaces in all three electrolytes investigated, as well as under coated surfaces in 0.5 M NaCl. These results suggest that the morphology and mechanism of the initial stages of local attack may be similar in all these systems.

## INTRODUCTION

Aluminum-based precipitation age hardened alloys containing Cu and Fe are prone to localized corrosion such as pitting induced by galvanic interactions between Cu-rich intermetallics compounds and the Al-alloy matrix. These local galvanic cells, which induce pitting and alkaline attack, are often formed by Cu- and Fe-containing intermetallics or replated Cu (1-13). In AA 2024-T3, pit initiation sites include Al-Cu-Mg particles (1, 2, 7, 11-13), the periphery of Cu-enriched Al-Cu-Mg particles that have been dealloyed of Al and Mg (2), and the matrix adjacent to Al-Cu and Al-Cu-Fe-Mn particles (1, 8, 11, 10). Of these intermetallics, the Al-Cu-Mg type is the most active. It is anodic to the Al-matrix and generally dissolves leaving a fine Cu-sponge (resulting from the de-alloying of both Al and Mg). Thus, with time it now becomes cathodic to the matrix (1, 2, 12, 13). Under certain conditions, some authors have observed rings of redeposited Cu around these Al-Cu-Mg precipitates (14). As much as 60% of the intermetallics on the surface of an AA 2024-T3 sample could be the Al-Cu-Mg type (2, 15). The Al-Cu, and Al-Cu-Mn-Fe types of intermetallic compounds are positive (serve as cathodic sites) relative to the Al-matrix (16). As a result, Cu<sup>2+</sup> ions dissolved in solution can be reduced on these particles (1). The generation of OH<sup>-</sup> ions at these particles due to the reduction of oxygen leads to alkaline attack of the Al adjacent to these particles, resulting in a trench-like attack morphology, which often forms a perimeter around the particle (8, 11, 17, 18). In addition, pitting can occur in the matrix in halide containing solutions (16).

This work focuses on the comparison of the attack morphology of localized corrosion on AA 2024-T3 at these intermetallic compounds with various electrolyte/surface treatment combinations. One goal is to ascertain whether or not the same morphology of attack seen on a bare (uncoated) surface containing native oxides occurs in a similar manner underneath an organic coating. Also of interest is the effect of bulk solution pH and chloride concentration

on the attack morphologies at intermetallic particles, especially when considering under-film corrosion, where occluded chemistries are formed. Epoxy-coated AA 2024-T3 samples usually corrode in 0.5 M NaCl at sites associated with blister formation (19). The occluded solutions are known to have high chloride concentrations and low pH (19). On large areas, blister formation takes place within a few days for a 10  $\mu$ m thick coating. The results reported here are the preliminary findings in this work with bare and epoxy-coated surfaces.

## EXPERIMENTAL PROCEDURES

Studies were conducted on 1.5 mm thick AA 2024-T3 sheets (from Kaiser) with the composition (major elements): Cu 4.5%, Mg 1.30%, Mn 0.62%, Fe 0.18%, Zn 0.10%, Si 0.093%, (in wt %), balance Al. AA 2024-T3 panels were cut from 90 x 120 cm sheets to squares of about 2.5 x 2.5 cm. One face of the panels was abraded with SiC paper (from 180 up to 1200 grit), and then polished with 1  $\mu$ m diamond suspension (Buehler). A thickness of about 0.1-0.3 mm of the sample was removed during the grinding and polishing processes. Some of the samples were coated with an organic coating. The applied epoxy polyamide coating is typical for aircraft primers. It was prepared by mixing equal weights of Epon Resin 1001-CX-75 with Epi-Cure 3115 Curing agent X73 (Fatty acid-polyethylenepolyamine based polyamide mixture), and adding 5% Butylcellosolve. Coating was done on a spin-coater. The samples were cured in a desiccator at ambient pressure for at least two weeks. The coating thickness was determined to be approximately 10  $\mu$ m.

SEM-EDS (Scanning Electron Microscopy-Energy Dispersive X-Ray Spectroscopy) studies were conducted on bare (polished) AA 2024-T3 samples to identify and analyze the intermetallic particles on the surface with a Jeol 840 SEM coupled to a Kevex EDS system at a voltage of 20 KV. Secondary Electron Images (SEI) were generated in all cases. In order to monitor the topography changes in-situ while performing electrochemical experiments, a flat electrochemical cell was constructed and mounted on the x,y,z-stage of the Confocal Laser Scanning Microscope (CLSM). The samples were then transferred to the cell where the specific features identified under the SEM were first identified under CLSM (without electrolyte) with a 100x immersion objective lens, and then studied in-situ under electrolyte immersion. In a few samples, SEM-EDS was also performed after the immersion experiment. The reference electrode was an Ag/AgCl microelectrode. Under immersion conditions, changes in surface morphology were monitored with time, and the open circuit potential (OCP) monitored in parallel for some samples, and measured periodically for others. 0.5 M NaCl (pH 6) was chosen as an example of a very corrosive environment. A solution containing 0.005 M NaCl + 0.1 M Na<sub>2</sub>SO<sub>4</sub> (pH 6)\* was chosen for its lower corrosivity. It produces differences between OCP and the pitting potential ( $E_{pi}$ ) in AA 2024-T3 (16). However, some galvanically induced pitting corrosion is still observed in this electrolyte because of the close proximity of OCP to pitting potential associated with the Al-matrix (16). This composition (0.005 M NaCl + 0.1 M Na<sub>2</sub>SO<sub>4</sub> (pH 6)) has a Cl<sup>-</sup> concentration ([Cl<sup>-</sup>]), which closely matches the [Cl<sup>-</sup>] found in aircraft lap-splice joints (20, 21), and has been used in previous studies (16,22). However, the electrolyte composition in aircraft lap-splice joints is more complicated (20). To examine the influence of the pH, 0.1 M Na<sub>2</sub>SO<sub>4</sub> + 0.005 M NaCl + 0.0001 M NaOH (pH 10, "alkaline solution"), and 0.1 M Na<sub>2</sub>SO<sub>4</sub> + 0.005 M Cl<sup>-</sup> (as 0.00167 M AlCl<sub>3</sub>) adjusted to pH 3 with H<sub>2</sub>SO<sub>4</sub> ("acidic solution") were also used.

\* This is referred to as standard solution.

Confocal Laser Scanning Microscopy (CLSM) was carried out on a Zeiss model LSM 510 microscope. Imaging was performed with an argon laser (488 nm wavelength). The z-scanning stage moved the sample surface stepwise (0.6  $\mu$ m step height) through the focal plane. At each z-position, the sample was scanned in the x-y direction. A three dimensional surface topography and 2D microscopic images with infinite depth of focus could be calculated (contact-free) from the images recorded at each z-step. Data for surface roughness, surface profiles and pit depths could also be obtained. This method has recently been applied to corrosion studies on AA2024-T3 (8, 9, 23).

## RESULTS

### SEM-EDS studies

SEM-EDS results of bare polished samples of AA 2024-T3 showed the presence of Al-Cu, Al-Cu-Mg and Al-Cu-Mn-Fe type intermetallic compounds. These intermetallic compounds were formed as constituent particles at high temperatures. Al-Cu-Mg intermetallic particles were usually spherical while Al-Cu and Al-Cu-Mn-Fe intermetallics had blocky angular features (Figure 1a and 1b). Clustering of distinct Al-Cu and Al-Cu-Mn-Fe particles was especially observed.

Results from EDS analyses of the intermetallic particles on AA 2024-T3 prior to electrolyte exposure are presented in Table 1. Differences in apparent composition were observed amongst particles with the same elemental constituents. The composition of some of the intermetallic particles were consistent with the stoichiometry of the most common intermetallics in AA 2024-T3, namely:  $\theta$ -Al<sub>2</sub>Cu,  $\delta$ -Al<sub>3</sub>CuMg and Al<sub>30</sub>Cu<sub>2</sub>(MnFe). Others were not. Si was detected in some of the spectra. The Si might have come from the SiC paper used in the grinding process or may have resided in the alloy. EDS showed that some intermetallic particles contained distinct regions with differing composition. Regions containing an Al-Cu-Mg composition occurred next to regions, which predominantly contained an Al-Cu composition (Particles 5 in Table 1, and Figures 1a and 1b).

### Galvanic corrosion behavior of bare AA 2024-T3

Corrosion studies on bare AA 2024-T3 in the four different solutions described above were performed with CLSM. The observed galvanic corrosion morphological features associated with micron scale constituent particles could be divided into four different categories: (i) particles which corroded themselves, (ii) particles which caused trenching in the adjacent matrix, (iii) particles which did not corrode at all during the time of immersion and (iv) pitting near intermetallic compounds.

Particles identified with EDX as Al-Cu-Mg particles started to corrode immediately after exposure to standard solution. The corrosion behavior of the particle in Figure 1a composed of regions of Al-Cu-Mg and Al-Cu is shown in Figure 1c after 2 h immersion. The Al-Cu-Mg phase corroded, whereas the Al-Cu-phase did not. Figures 1d-1f show the corrosion of the particle from Figure 1b at selected times. After 13 minutes, the Al-Mg-Cu phase already showed corrosion at the surface. After 40 minutes, corrosion attack had occurred on the

entire Al-Cu-Mg surface and had expanded into the matrix. The other sections of the constituent particle remained with slight indications of trenching in the matrix. After 110 minutes, other sites had developed corrosion pits within the matrix.

Many small pits developed either on the matrix or at small intermetallic particles on the AA2024-T3 samples within minutes of exposure to 0.5 M NaCl. Several large particles also showed localized corrosion attack on them, even in standard solution. One particle (hexagonal shape, ~10 µm diameter (not shown)) started corroding at a spot in the middle. The corrosion expanded and covered the whole particle within a few hours, followed by the attack of the surrounding matrix. Another particle showed pit formation at one edge and dissolution progressed through the rest of the particle (also not shown). In that case the attack of the matrix started before the particle completely corroded.

Figures 2a-2c show the formation of four pits on an intermetallic exposed to 0.5 M NaCl, of which three merged together. Two of these pits initiated at the interface with the matrix, and the other two on the particle, itself. The surrounding matrix exhibited pit formation, as well.

Figures 2d-2f show particle corrosion starting at several locations along the interface with the matrix as well as pit formation in the upper left area, which initiated at a smaller particle and grew to a much larger size. Concerning the large intermetallic compound, the total area (particle + corroded) remained fairly constant during the exposure time. This means that the particle corroded out, whereas the matrix itself was only slightly attacked, if at all in the vicinity of this large intermetallic compound. Otherwise the total area would have increased with time.

Samples exhibited trenching around particles in all electrolytes. An example from standard solution is given in Figures 3a and 3b. Both pictures show the same particle surrounded by a trench 2.5 µm wide. The particle itself has not been affected by corrosion at all after 1 day of exposure and even still shows the polishing lines. The depth of the trench is about 3 µm. It was observed in standard solution that large-sized indentations<sup>b</sup> made on a sample (~30 µm diameter), in which severe corrosion of the matrix took place, prevented trenching at all nearby particles. These nearby particles were of both Al-Cu and Al-Cu-Mn-Fe types. The particles that showed trenching had rather high Cu-concentrations (Table 2), with virtually no Mn or Fe suggesting they were Al-Cu. Indeed, several particles where no trenching occurred were identified as Al-Cu-Fe-Mn. In some cases, the matrix around some Al-Cu particles remained unattacked even though these were close to others which were attacked. In other cases on samples exposed to the pH 3 and pH 10 solutions, the matrix surrounding all the particles in entire clusters (especially the large ones above ~5 µm in diameter) was attacked. Other particle clusters where no trenching occurred were also observed on the same sample. In general, the acidic solution did not inhibit trenching compared with the alkaline solution.

In several cases, a combination of cathodic trenching and anodic dissolution was observed on the same particle. This is shown in Figures 3c-3e for the acidic solution. Within two hours, corrosion ended on some parts of the particle agglomerate, whereas other parts formed narrow trenches with time.

<sup>b</sup> Micro-hole put onto the metal surface that acted as an identification marker for surface features during microscopy.

Before immersion, the entire epoxy coated sample was masked off with another coating (XP2000 by Pyramid Plastics), except for a 2 x 2 mm exposure window. Because of the reduced at-risk area, it took more than 2 weeks of exposure for a blister to form. OCP were in the range of -0.24 V to -0.27 V (SCE) during the second week of immersion. Figure 4a shows the intermetallic particles at a selected area after 2 weeks of immersion. Some of them had partially corroded during the surface preparation procedures (before the epoxy coating was applied). These features showed no additional corrosion during the two weeks of immersion. Figure 4b shows the same area 2 days later. Notably, a blister had formed. The OCP decreased to about -0.8 V (SCE). Several intermetallics were now more severely corroded. It was determined by visual inspection under CLSM that Cu redeposition and corrosion product deposition had taken place, but the area covered by Cu deposition and corrosion products (~6700 µm<sup>2</sup>) was smaller than the area of coating delamination (~8700 µm<sup>2</sup>). The Cu deposited (dark area) with the outer area of the deposit close to the leading edge of the delamination front. A halo with little deposited material formed around some of the corrosion pits. By this time, the blister was 100 µm in diameter. Figure 4c shows a three-dimensional profile of the delaminated coating over the blister taken one day later, showing a diameter of 160 µm and a height of 25 µm.

Cathodic trenching also appeared to occur under the conditions present in a blister. Figures 5a-5f show corrosion progressing from an intermetallic particle. At an early stage of exposure, a ring-like structure could be observed around this intermetallic. However, this caused no corrosion. The lines visible in Figure 5a can be attributed to the delamination of the coating (moving from left to right). The particle had been reached by the delamination front but showed no corrosion at this stage. Once the coating over the particle was fully delaminated, trenching and attack of the matrix around the particle started (Figure 5b). With time, several corrosion features in the matrix grew together (Figure 5c). Once the particle became completely engulfed by the blister, it was attacked and dissolved (Figure 5d). Further, the matrix between this particle and particles nearby corroded and the sites interconnected (Figure 5d-5f).

## DISCUSSION

The shapes of the intermetallic phases found by SEM are consistent with the findings of other authors (7-9, 13, 15, 24-26). The variations in the chemical compositions of the different phases (Table 1) could be due to a number of reasons: (i) the interaction volume of the SEM-EDS beam may possibly be greater than the volume of the intermetallics, resulting in signals also being collected from the Al-matrix; (ii) selective dissolution during wet grinding; or (iii) an indication of more than one phase (transitional phases) of these intermetallics being present on the metal surface. The increased Cu-content found after corrosion might be due to Cu replating or dealloying of other constituents.

The SEM-EDX observation of Al-Cu-Mg and Al-Cu phases adjacent to one other is confirmed by the findings of other authors who reported the occurrence of different intermetallic phases in very close proximity to one another (27). This proximity caused a

<sup>c</sup> It is possible that formation of one constituent particle can serve as a nucleation site for the next one.

selective dissolution of the Al-Cu-Mg phase, whereas the Al-Cu phase remained unattacked for a long time (Figure 1). It is also possible that the proximity of the nobler area (or a nobler particle in close proximity to an Al-Cu-Mg particle) even accelerates the corrosion of the Al-Cu-Mg by serving as cathodic site. The corrosion of the matrix in the vicinity of this particle can be explained by the formation of sufficiently aggressive solution to promote attack the Al-matrix. The reason for the initiation of corrosion (filiform-like) several  $\mu\text{m}$  below the original site of Al-Cu-Mg dissolution is unknown at this point (Figure 1f). The filiform-like corrosion (Figure 1d) might have initiated at other defects in the matrix.

Several factors might contribute to the localized attacks on the large-sized intermetallic particles. The observed differences in local composition within the same particle (which have also been observed by other authors (25)) might be a reason. This compositional variation might lead to a galvanic couple within a particle, and initiate pitting on the particle, or dissolution beginning at the interface to the matrix (Figure 2, Figures 3c-3e). The pitting of the particle as well as the matrix in Figure 2b might suggest the presence of small defects with a size close to the resolution of the microscope ( $< 500 \text{ nm}$ ), which act as initiation sites. These may be Al-Cu-Mg particles.

Cathodic trenching has been extensively discussed in the literature (1, 3, 8, 10, 11, 17, 18). In the present work, it was found that the susceptibility to trenching is not the same for all particles (Table 2). The data in Table 2 suggested that Al-Cu particles trench faster than Al-Cu-Mn-Fe in standard solution. Although differences in susceptibility to trenching of particles cathodic to the Al-matrix were also observed in the alkaline and acidic solutions, post-corrosion analyses are yet to be carried out to confirm whether the Al-Cu particles were more susceptible to trenching than the Al-Cu-Mn-Fe ones in these solutions. Clearly, further investigation is still required in this area as selective trenching of particles could be limited only to certain specific conditions under which the tests were carried out. Trenching might depend not only on the exact particle composition, and the intermetallic compound crystal plane exposed, but also on the micro-structural and compositional details of the corrosion processes in the matrix close to each type of intermetallic. For instance, extensive recrystallization of small grains next to the constituents particles could change corrosion properties of the matrix. It is possible that acidic concentration fields oppose alkaline trenching. However, observations of trenching in the acidic electrolyte argue against this.

It is believed (28), that the area surrounding the delaminated area associated with coating blisters fulfills the function of the cathode for blisters, at least on steel. This theory leads to the question of whether the corrosion morphology is similar to that on bare samples, or if, for example, no cathodic trenching can be observed within the blister because the cathodic sites exists elsewhere. It is also unclear how the initiation of a blister takes place on AA 2024-T3. The results presented above do not allow for any statement about the mechanism of blister initiation to be made. It can be speculated that blister formation started at an intermetallic compound showing the most extensive corrosion at that time, which was the closest to the blister center. The corrosion pattern shown in Figure 5 suggests that cathodic trenching might occur, at least for a short time in blisters. This suggests that part of the cathodic reaction is carried by that intermetallic particle at that time, and that anodic and cathodic processes still can take place close together in a blister environment. However, it must be pointed out that this particle was very close to the delamination front, and corrosion of the particle itself cannot be completely ruled out even at the stage shown in Figure 5b. Further studies are therefore required to show if this behavior is general or limited to the growth edge of the blister. Once the particle is fully exposed to the acidic solution known to be present in blisters (19), it dissolves. Corrosion does not take place symmetrically around the particles,

but there seems to be a preference for the interconnection of corroded areas.

## CONCLUSIONS

1. Variations in composition were observed amongst particles with the same elemental constituents.
2. The composition of some of the intermetallic particles were consistent with the stoichiometry of the most common intermetallics in AA 2024-T3, namely:  $\theta\text{-Al}_2\text{Cu}$ ,  $\text{S-Al}_2\text{CuMg}$  and  $\text{Al}_{12}\text{Cu}_2(\text{MnFe})$ .
3. EDS showed that some agglomerated intermetallic particles contained more than one phase. This led to different rates and morphologies of corrosion attack within one agglomerated particle.
4. The Al-Cu-Mg particles were the most active in all the electrolytes investigated on the bare polished samples.
5. Corrosion within some intermetallic particles was localized.
6. All Al-Cu and Al-Cu-Mn-Fe particles do not have the same propensity to promote trenching of the Al-matrix. This was observed in  $0.1 \text{ M Na}_2\text{SO}_4 + 0.005 \text{ M NaCl}$  (pH 6),  $0.1 \text{ M Na}_2\text{SO}_4 + 0.005 \text{ M NaCl} + 0.0001 \text{ M NaOH}$  (pH 10) and  $0.1 \text{ M Na}_2\text{SO}_4 + 0.005 \text{ M Cl}^-$  (as  $\text{AlCl}_3$ ) (pH 3).
7. The morphology of initial stages of corrosion attack at the micro-scale at the intermetallic compounds on bare AA 2024-T3 is the same in all the electrolytes investigated.
8. Preliminary indications are that pitting in the matrix or at small matrix particles is more evident in  $0.5 \text{ M NaCl}$  than in other solutions used.
9. Indications of trenching of the Al-matrix around intermetallic compounds was observed in coating blisters formed under organic coatings in  $0.5 \text{ M NaCl}$  solutions.

## ACKNOWLEDGEMENTS

The authors gratefully acknowledge the AFOSR for the financial support of the project under contract number F49620-96-1-0178, with Major Paul Trulove as program director. Perkin Elmer Instruments and Scribner Associates, Inc. are thanked for continuing support of electrochemical instrumentation and software in CESE.

## REFERENCES

1. G.S. Chen, M. Gao, R.P. Wei, *Corrosion*, **52**, 8 (1996).
2. R.G. Buchheit, R.P. Grant, P.F. Hlava, B. McKenzie, G.L. Zender, *J. Electrochem. Soc.*, **144**, 2621 (1997).
3. G.S. Chen, C.-M. Liao, K.-C. Wan, M. Gao, R.P. Wei, *ASTM STP 1298*, W.A. Van Der Sloys, R.S. Piascik, R. Zawierucha, Eds., p.18, ASTM (1997).
4. J.R. Scully, T.O. Knight, R.G. Buchheit, D.E. Peebles, *Corros. Sci.*, **35**, 185 (1993).
5. M.J. Pryor, D.S. Keir, *J. Electrochem. Soc.*, **102**, 241C (1955).
6. R.G. Buchheit, *J. Electrochem. Soc.*, **142**, 3994 (1995).
7. M. Buehler, J. Kerimo, F. Guillaume and W.H. Smyrl, *J. Electrochem. Soc.*, **147**, 3691 (2000).

8. M.A. Alodan and W.H. Smyrl, *J. Electrochem. Soc.*, **144**, L282 (1997).
9. M.A. Alodan and W.H. Smyrl, *J. Electrochem. Soc.*, **145**, 1571 (1998).
10. P. Schmutz and G.S. Frankel, *J. Electrochem. Soc.*, **145**, 2295 (1998).
11. T. Suter and R.C. Alkire, in *Critical factors in Localized Corrosion III*, Electrochemical Society Proceedings 98-17 p.118 (1999).
12. R.G. Buchheit, L.P. Montez, M.A. Martinez, J. Micheal and P.F. Hlava, *J. Electrochem. Soc.*, **146**, 4424 (1999).
13. V. Guillaumin and G. Mankowski, *Corros. Sci.*, **41**, 421 (1999).
14. N. Dimitrov, J.A. Mann and K. Sieradzki, *J. Electrochem. Soc.*, **146**, 98 (1999).
15. C. Blanc, B. Lavelle and G. Mankowski, *Corros. Sci.*, **39**, 495 (1997).
16. G.O. Ilievbare, J.R. Scully, J. Yuan and R.G. Kelly, *Corrosion*, **56**, 227 (2000).
17. M. Buchler, T. Walari and W.H. Smyrl, *Corros. Sci.*, **42**, 1661 (2000).
18. J.O. Park, C.H. Paik, Y.H. Huang and R.C. Alkire, *J. Electrochem. Soc.*, **146**, 517 (1999).
19. A.M. Mienisch, J. Yuan, R.G. Kelly and S.R. Taylor, *J. Electrochem. Soc.*, **146**, 4449 (1999).
20. K.S. Lewis, M.Sc. Thesis, University of Virginia, 1999.
21. M.E. Inman, R. G. Kelly, S. A. Willard, and R. S. Piascik, "Coordinated Metallographic, Chemical and Electrochemical Analyses of Fuselage Lap Splice Corrosion", Proc. of the ASIP Conference, Atlanta, November 1996.
22. R.G. Kelly, O. Schneider and J. Yuan, ECS Meeting Abstract Vol. 99-1, Abstract #81, May, (1998).
23. F. Guillaume, L.F. Darfias-Mejias, M. Buchler and W.H. Smyrl, in *Critical factors in Localized Corrosion III*, Electrochemical Society Proceedings 98-17 p.155 (1999).
24. G.P. Halada, C.R. Clayton, M.J. Vasquez, J.R. Kearns, M.W. Kendig, S. L. Jeanjaquet, G.G. Peterson, G.S. McCarthy and G.L. Carr, in *Critical factors in Localized Corrosion III*, Electrochemical Society Proceedings 98-17 p.139 (1999).
25. T.J.R. Leclère, A.J. Davenport, J. Deakin, D. Raikes and R.C. Newman, in *Critical factors in Localized Corrosion III*, Electrochemical Society Proceedings 98-17 p.130 (1999).
26. P. Schmutz and G.S. Frankel, *J. Electrochem. Soc.*, **145**, 2285 (1998).
27. P. Campestri, E.P.M. van Westing, H.W. van Rooijen and J.H.W. de Wit, *Corrosion Science*, **42**, 1853 (2000).
28. T. Nguyen, J.B. Hubbard and J.M. Pommersheim, *J. Coating Tech.*, **68**, 45 (1996)

Table 1. EDS analyses (in At. %) of intermetallic particles before exposure to electrolyte.

Particle	Al	Cu	Mg	Mn	Fe
1	64.0	26.5	9.5	0.0	0.0
2	96.7	2.0	1.0	0.1	0.2
3	73.6	26.2	0.0	0.2	0.0
4	80.32	19.1	0.3	0.14	0.14
5-1	62.48	20.8	16.5	0.14	0.08
5-2	81.0	17.9	0.7	0.1	0.3
6	74.7	12.4	0.0	3.7	9.2
7	83.1	8.7	6.1	0.1	0.0
8	85.8	5.2	0.2	3.5	5.3
9	88.3	3.7	0.3	3.0	4.7
10	97.1	2.4	0.3	0.2	0.0

Table 2. EDS analyses (in At. %) of intermetallic particles after exposure to electrolyte.

Particle	Al	Cu	Mg	Mn	Fe	Corrosion
A	51.4	48.3	0.0	0.2	0.1	Trenched
B	64.8	34.8	0.0	0.2	0.2	Trenched
C	86.7	12.9	0.0	0.3	0.1	Trenched
D	77.6	8.7	0.0	5.1	8.6	No trench
E	80.2	7.3	0.0	5.2	7.3	No trench
F	76.1	8.6	0.0	5.3	9.8	No trench
G	71.5	28.0	0.0	0.0	0.5	No trench
H	77.4	21.8	0.0	0.3	0.5	Trenched
I	84.9	4.4	0.0	6.3	4.4	No trench
J	72.1	25.2	2.4	0.2	0.1	Trenched
K	75.9	7.6	0.0	6.4	10.1	No trench
L	95.6	3.1	0.5	0.4	0.4	Trenched
M	32.7	66.5	0.0	0.5	0.3	Trenched
N	65.4	34.6	0.0	0.0	0.0	Trenched
O	95.9	2.7	0.7	0.7	0.0	Dark part Close to N
P	85.3	14.7	0.0	0.0	0.0	Trenched

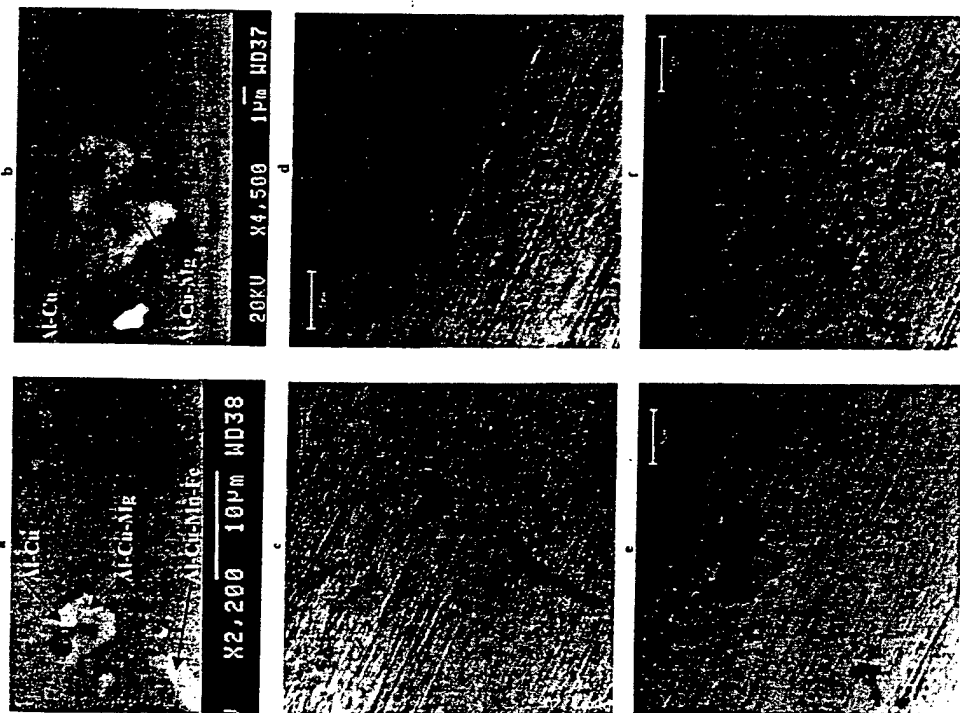


Figure 1: Selective Al-Cu-Mg corrosion on bare AA2024-T3: (1a, 1b) Secondary electron SEM image of particles showing Al-Cu phase in the middle and Al-Cu at the top (1a) CLSM image of the particle front (1a) after 2 h immersion in standard solution (d-f) CLSM of the particle from (1b) during immersion in standard solution (immersion times 13 (1d), 40 (1e), and 110 min (1f)).

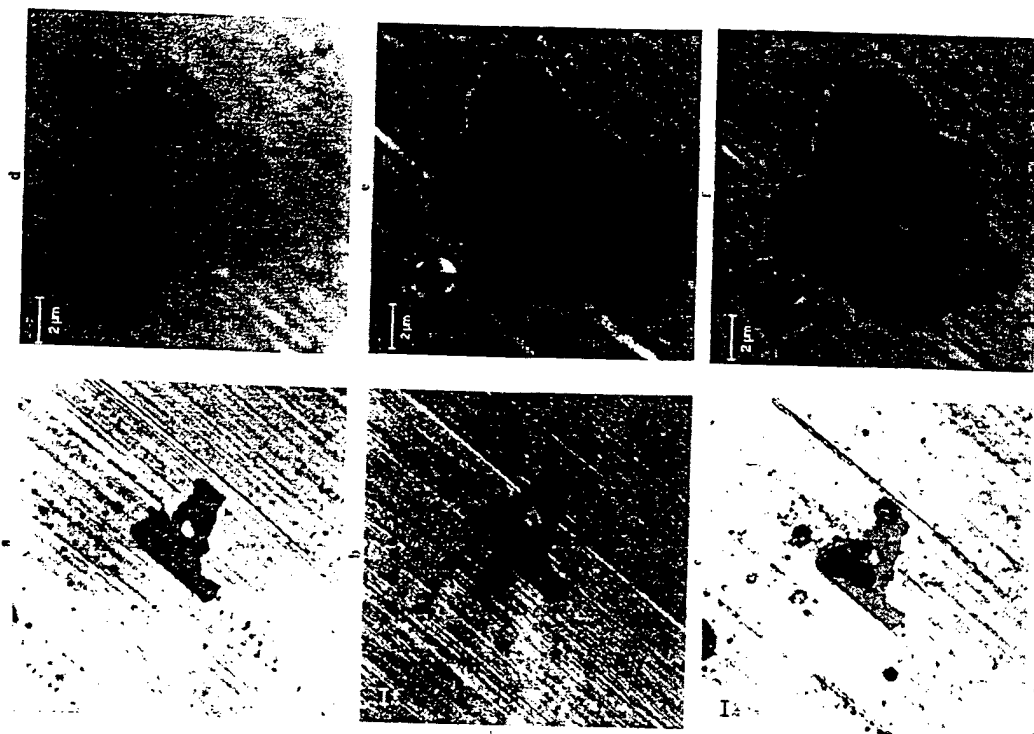
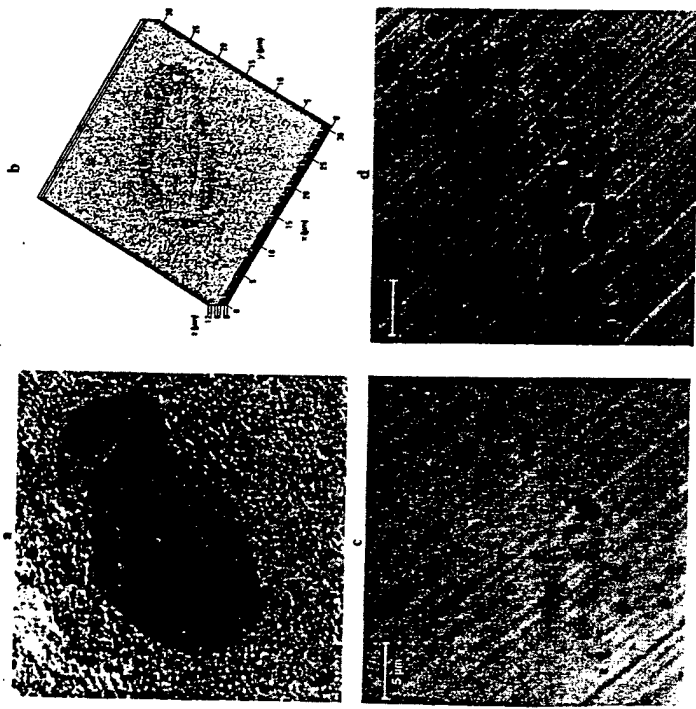
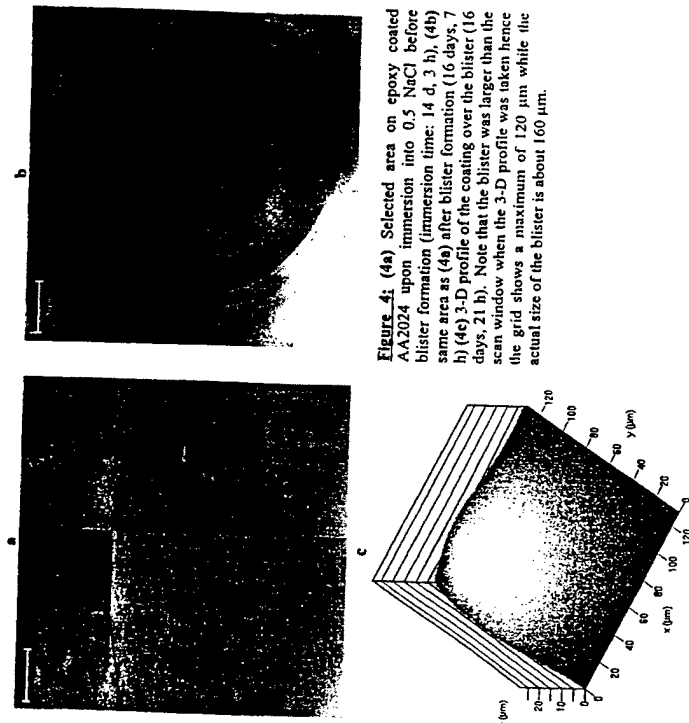


Figure 2: (2a-c) Localized attack on intermetallic particle in 0.5 M NaCl (bar: 2  $\mu$ m, i.t: 0 (2g), 50 (2h), and 97 min (2i)); (2d-f) dissolution of intermetallic in 0.5 M NaCl starting at the interface to the matrix (bar: 2  $\mu$ m, i.t: 0 (2j), 22 (2k), and 65 min (2l)). The growth of pits at small particles in the matrix is also seen.



**Figure 2:** (3a, 3b) Cathodic trenching in standard solution (bar: 2  $\mu\text{m}$ , immersion times: 1 day); (3c) Cluster of intermetallic inclusions on bare AA2024-T3, exposed to pH 3 0.1 M  $\text{Na}_2\text{SO}_4$  + 0.005  $\text{Cl}^-$  (bar: 5  $\mu\text{m}$ , immersion times: 0 (3c), 110 (3d), 280 min (3e))



**Figure 4:** (4a) Selected area on epoxy coated AA2024 upon immersion into 0.5  $\text{NaCl}$  before blister formation (immersion time: 14 d, 3 h); (4b) same area as (4a) after blister formation (16 days, 7 h); (4c) 3-D profile of the coating over the blister (16 days, 21 h). Note that the blister was larger than the scan window when the 3-D profile was taken hence the grid shows a maximum of 120  $\mu\text{m}$  while the actual size of the blister is about 160  $\mu\text{m}$ .

M. J. Vasquez, G. P. Halada, C. R. Clayton,  
Department of Materials Science and Engineering  
State University of New York at Stony Brook  
Stony Brook, New York 11794-2275

J. P. Longtin  
Department Mechanical Engineering  
State University of New York at Stony Brook  
Stony Brook, New York 11794-2300

# ABSTRACT

This paper discusses the influence of the structure of Chromate Conversion Coatings (CCC) formed on AA2024-T3 and on intermetallic compounds (IMCs) constituents of AA2024-T3 as a function of aging. Extended X-ray Absorption Fine Structure (EXAFS), X-ray Absorption Near Edge Structure (XANES) and contact angle measurements were used to monitor the structural changes and surface hydrophobicity respectively of the CCC with time. It was observed that the different IMCs have little effect on the structural changes that occur in the CCC, though in all cases, a slight decrease in the Cr(VI) to Cr(III) ratio occurred during the first 24 hours following coating. EXAFS data appeared to indicate an increase in ordering in the CCC structure with time.

# INTRODUCTION

The structure and composition of commercial Chromate Conversion Coating (CCC) have been studied in detail by a few groups over the past five years [1-6] but not systematically as a function of time. The adherence of paint to a CCC improves significantly as the CCC is allowed to "age" for 24 hours before applying the paint. Recent investigations have considered some of the effects of aging on CCC composition and morphology for an alloy such as AA2024-T3 [3,5-6]. Opinions vary on the commercial significance of CCC aging. It has been stated that it is not desirable in commercial practice to paint a CCC that is more than two days old [3]. Korinek [1] observed that during 24 hours of aging the CCC became hydrophobic and less soluble in nitric acid, this he attributed to lower Cr(VI) to Cr(III) concentration ratios. Hatanaka, et al., [2] attributed the observed deterioration of adhesion properties and corrosion resistance of a conversion coating to dehydration and microcrack formation. "Aging," in

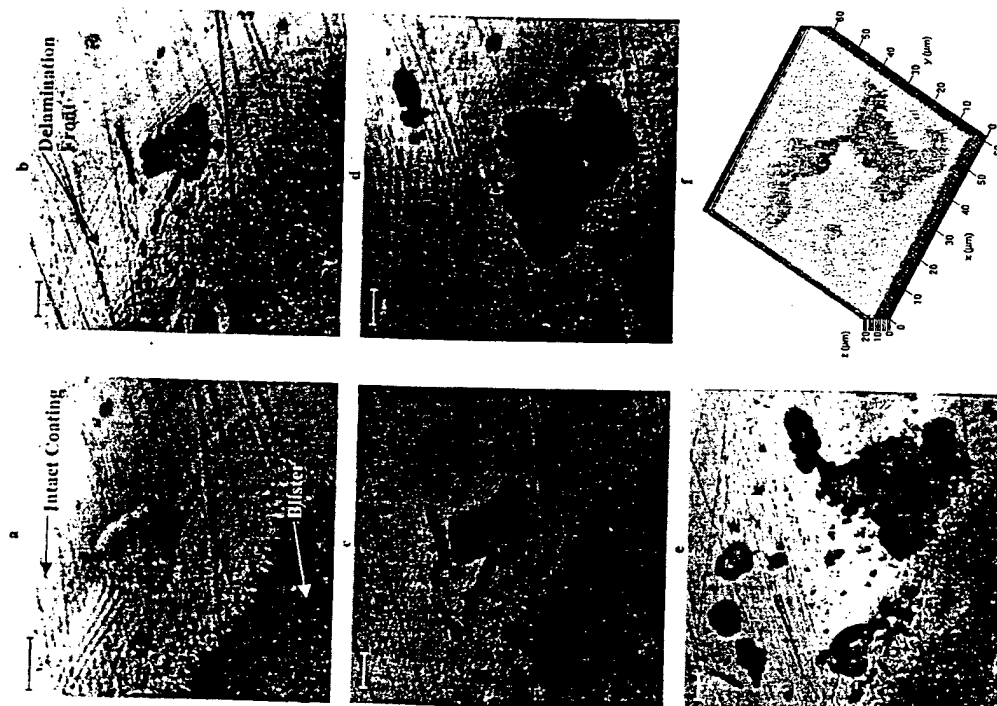


Figure 3: Under-film corrosion around a particle upon blister growth (all bars: 5  $\mu$ m). (5a) Delamination fringe at particle (16 d 21 h). (5b) Cathodic trenching, matrix corrosion (17 d, 6 h). (5c) Coalescence of corroded areas (17 d, 10 h). (5d) Particle and matrix in between the previously attacked areas dissolved (18 d 3 h). (5e) Connection with next particle (zoomed out, 18 d 10 h). (5f) Connection to three particles from (5e) (19 d, 10 h).



## Phenomenology of Localized Coating Failure on AA1100-H14

J. M. Williams\*, O.M. Schneider<sup>#</sup>, R.G. Kelly<sup>#</sup>

\*Luna Innovations, Inc.

701 Charlton Ave, Charlottesville, VA 22903

<sup>#</sup>Department of Materials Science and Engineering, University of Virginia  
116 Engineer's Way, Charlottesville, VA 22904

### Abstract

The global potential and the local potential associated with the intermetallic particles (IMCs) of the alloy combined to control blister initiation. Upon immersion in NaCl solutions, epoxy-coated panels experienced an increase in the OCP to near or above the mean pitting potential (due to solution uptake and oxygen transport through the coating) followed by a subsequent decrease in OCP (due to local passive layer breakdown by  $\text{Cl}^-$  at the bare metal surface), which coincided with observations of active blisters. Galvanic effects between the Al matrix and IMCs, known to contribute to the localized corrosion of bare Al alloys, were found to contribute to underfilm corrosion of AA1100-H14. The effect of varying chloride concentrations revealed a process that competed with potential control for blister initiation: water uptake by the coating. At low  $\text{Cl}^-$  concentrations, the degree of open circuit pitting was the controlling parameter for blister initiation whereas at high  $\text{Cl}^-$  concentrations water uptake dominated. Blister growth occurs on AA1100-H14 by way of anodic undermining, where a thin layer of Al matrix is dissolved underneath the organic coating causing detachment of the coating from the substrate. All blisters behaved as net anodes in the early stages of life. A fast shift to dominant cathodic activity occurred on AA1100-H14 if iron oxide deposited inside the blister.

### Key words

Organic coatings, AA 1100-H14, blisters

### Introduction

Blistering is usually one of the first signs of insufficient protection of organic coatings against corrosion. Blisters are local regions where adherence between the coating and the substrate has been lost, so that solution may accumulate and corrosion may begin. The mechanism of blister growth depends on the type of electrochemical activity occurring inside the blister, *i.e.*, whether the blister shows anodic or cathodic activity. The modes of blister growth corresponding to cathodic or anodic activity are very different and operate under specific conditions.

Cathodic blistering occurs as a result of the production of an alkaline environment underneath the coating due to the cathodic reaction. The prerequisite for the development of cathodic blisters is that the substrate is capable of supporting a cathodic reaction, which in the case of neutral or alkaline environments is oxygen reduction. The loss of adhesion associated with corroding coated steel under cathodic conditions is known as cathodic delamination. It can occur either in the presence or in the absence of an applied potential. The major driving force for cathodic delamination in air is the reduction of oxygen, which produces hydroxyl ions and

reaction intermediates<sup>1-3</sup>. The products of oxygen reduction are believed to be a destructive agent to the coating/substrate bond as the pH is high in the regions where the cathodic reaction is taking place. The value of the pH at the delamination front depends on the rate of reaction, shape of the delamination front, and the rate of hydroxyl ion diffusion away from the delamination front<sup>4</sup>.

Growth occurs by a progression of delamination from the central anodic site; the detached regions of coating eventually swell with occluded blister solution as the blister takes shape. Separation of anodes and cathodes occurs because of differences in oxygen permeability at these sites so that a potential gradient exists between them, acting as a driving force for cathodic delamination. Therefore, the delamination front (cathode) is usually represented by positive potentials while the delaminated region (anode) is represented by negative potentials. pH values between 10 and 12 have been reported at the delamination front<sup>4</sup>. Koehler concluded that delamination was due to saponification of the coating in his studies on polybutadiene-coated steel<sup>5</sup>. Saponification is the hydrolysis of esters in the presence of strong soluble bases. Anodic undermining represents a class of corrosion underneath an organic coating where the major separation process is anodic dissolution of the substrate under the coating. A thin layer of the substrate is selectively dissolved so that the organic coating becomes detached from the surface. Figure 7 shows the anodic undermining mechanism<sup>6</sup>.

Aluminum is particularly susceptible to anodic undermining; it can also occur on coated steel under applied anodic potentials<sup>4,7</sup>. Anodic undermining bears a close relationship to pitting, although it tends to occur preferentially to pitting. The mechanism is activated by the presence of chloride, and it tends to prevent pit development in areas where pitting would normally be expected (*i.e.*, where the cathode is located). For this reason, significant corrosion damage is usually not observed at the cathodes in anodic undermining experiments<sup>7</sup>. The corrosion associated with anodic undermining occurs at a low rate initially. Growth occurs by way of a progressively advancing mode of crevice corrosion where the crevice, or anode, exists at the bare metal interface underneath freshly detached coating.

Anodic undermining is not as widely addressed in the literature as cathodic delamination. Galvanic effects and principles of crevice corrosion have been accepted as providing a suitable explanation for the undermining mechanism.

## Experimental Procedures

A five-step cleaning protocol was used to degrease alloy samples cut into 7.6 cm by 7.6 cm panels prior to the coating procedure. Panel thickness was approximately 1.13 mm (44.5 mils). Panel surfaces and edges were scrubbed with a sponge soaked in Alconox® and deionized water. A rinse with 18 MΩ-cm Milli-Q water (from a Millipore Milli-Q™ system) followed, and each panel was dried with forced air. Panels were then cleaned with sequentially in isopropanol and hexane. The clear epoxy coating mixture used for all experiments was a 1:1:0.1 ratio of three components: resin, curing agent, and solvent. The resin was a bisphenol A-epichlorohydrin based epoxy solution manufactured by Shell with product name "Epon(R) Resin 1001-CX-75." The resin contained 16.3% methyl isobutyl ketone and 8.7% xylene with a remaining balance of the Epon resin. The second component of the coating mixture was 70% (by weight) fatty acid-polyethylene polyamine based polyamide curing agent with both high molecular weight and high viscosity and 30% xylene (by weight). The curing agent was also manufactured by Shell with product name "Epi-cure(R) 3115." In addition, the coating formulation contained butylcellosolve (ethylene glycol + monobutyl ether) acting as a solvent for increased viscosity.

Coating application consisted of a 25 second spin-coating procedure conducted at two different speeds. Each panel was centered on the spinning chuck of the KW4a spincoater (manufactured by Chemat Technology) and held in place by vacuum. Using the 10 mL syringe, approximately 1 mL of coating was released onto the center of the panel while sitting on the chuck. The spincoater spun at 8,000 rpm for 10 seconds followed by a 15 second spin at maximum speed of 10,000 rpm. In some cases, the vacuum was unable to hold panels to the chuck; such panels were damaged and immediately discarded. One spincoating sequence was usually enough to uniformly coat each panel. If necessary, the same spincoating sequence was run a second time to ensure uniform application. Following coating application, panels were allowed to cure inside a drying chamber containing Drierite® for a period of at least one week before immersion. Dry coating thickness averaged 10  $\mu\text{m}$  over five readings with values ranging from 2  $\mu\text{m}$  to 22  $\mu\text{m}$ . The data were obtained with a PosiTector® Series 6000-NOS2 coating thickness gauge.

Water uptake of the epoxy coating was studied using freestanding thin films of the same coating formulation described above. Glass substrates were spincoated with the coating. After a two-week curing period inside a dessicator, the films were wetted with 18 M $\Omega$ -cm Milli-Q and cut along the edges with a scalpel blade. Using the blade, the intact coating was carefully detached from the glass substrate and allowed to dry in an evacuated dessicator. The freestanding film experiments used a three-electrode setup to run alternating OCP and EIS measurements in NaCl solutions of the following concentrations: 0.02M, 0.2M, 0.5M, and 2M.

## Results

### *Blister Initiation*

Blisters were grown on epoxy-coated substrates immersed in varying  $\text{Cl}^-$  concentrations under ambient conditions. Blister initiation times varied from five days to 2-3 months after initial exposure. Figure 22 shows AA1100-H14 blister initiation times versus immersion solution chloride concentration.

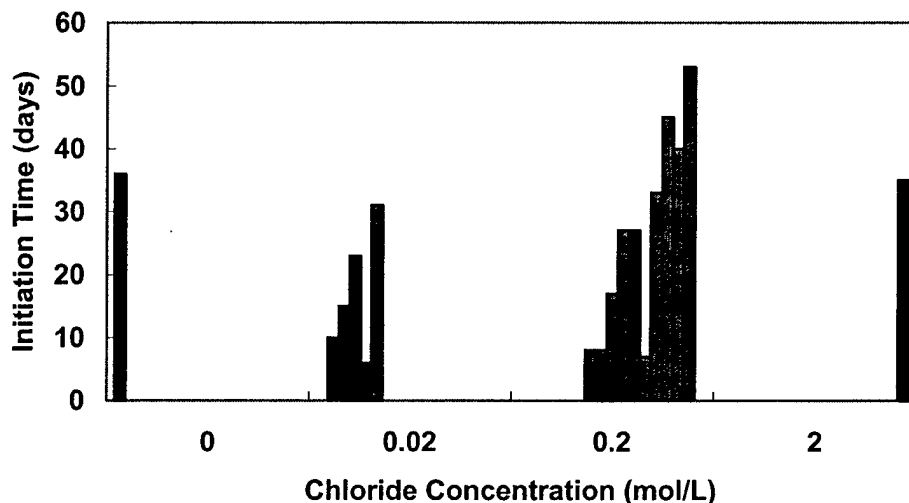


Figure 1. Blister initiation time vs.  $\text{Cl}^-$  concentration. The gray bars corresponding to 0M and 0.02M  $\text{Cl}^-$  represent blister initiation in 0.2M NaCl after an initial exposure to more dilute NaCl solutions.

More blisters formed in 0.2M NaCl than in any other immersion solution for coated AA1100-H14. Figure 23 shows the number of total blisters formed on each AA1100-H14 panel. As observed with the initiation time, the percentage of AA1100-H14 panels immersed in each NaCl solution that formed blisters showed a maximum at 0.2M as shown in Figure 24.

Of the twelve-coated AA1100-H14 samples seeded with 1M NaCl salt islands, only two blisters initiated at a salt island site. The initiation time of these particular blisters did not differ significantly from the initiation times of non-island blisters.

#### *Blister Growth Rates*

Blister diameters were measured with the aid of a digital microscope camera at different points during blister life. Similar growth rates occurred for blisters grown in 0.02M and 0.2M NaCl immersion solutions. The AA1100-H14 blisters grown in 2M grew laterally very slowly, if at all. Figure 26 shows lateral growth rates for blisters in mm/day for times after which blisters were visually detected.

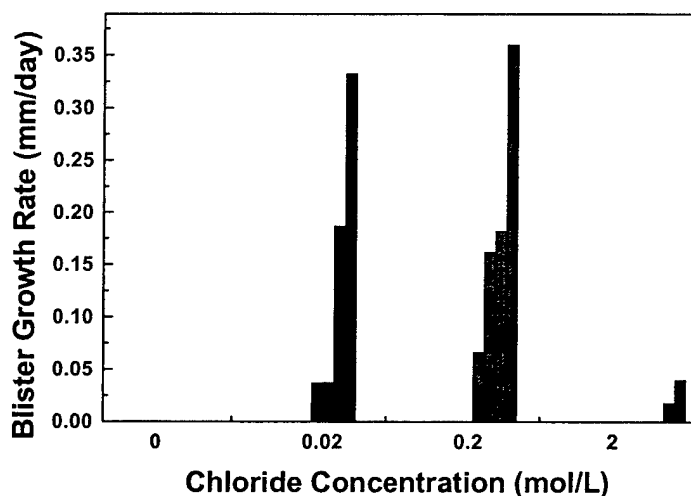


Figure 2. Lateral growth rates for different AA1100-H14 blisters in each immersion solution.

#### *Physical Observations*

AA1100-H14 blisters tended to be hemispherical in shape with circular growth. Blister formation was limited to one or two on each panel. The internal blister color ranged from milky white to no color. Gas bubbles were readily seen through the coating, as was corrosion product accumulation. Some blisters showed a defined circle of corrosion product at the center surrounded by concentric rings of more product. Infrequently, a dark reddish-brown center, later determined to contain Fe, appeared inside blisters, surrounded by corrosion product accumulation. Figure 29 shows photos of characteristic AA1100-H14 blister features.

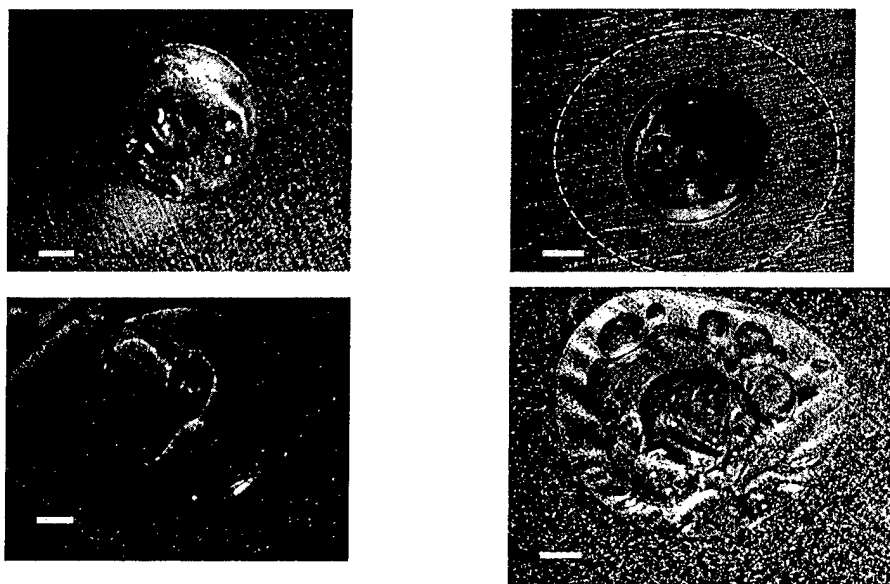


Figure 3. Digital photographs of characteristic AA1100-H14 blister features (neutral pH). (a) Colorless, hemispherical blister grown in 0.2M NaCl. (b) Active blister with delamination front highlighted by dashed line (0.2M NaCl). (c) 0.02M NaCl blister showing corrosion product rings near the center. (d) Large gas bubbles are easily seen through the coating of a blister grown in 0.2M NaCl.

#### *Open Circuit Potential Behavior*

Daily OCP measurements show some variation during the course of blister life. In some cases, a sharp decrease in OCP on the order of 150–200 mV accompanied blister formation. This distinct OCP decrease was not always seen, for instance, in the case of Cell 4 and Cell 6 blisters (see Figure 31 below) grown in 0.2M NaCl. However, OCP data for other 0.2M NaCl (and other Cl<sup>-</sup> concentrations) blisters do show the distinct decrease. Metastable events were often seen during daily OCP measurements both before and after the appearance of a blister. Figures 31 - 33 show daily global OCP fluctuations as active blisters initiate and grow.

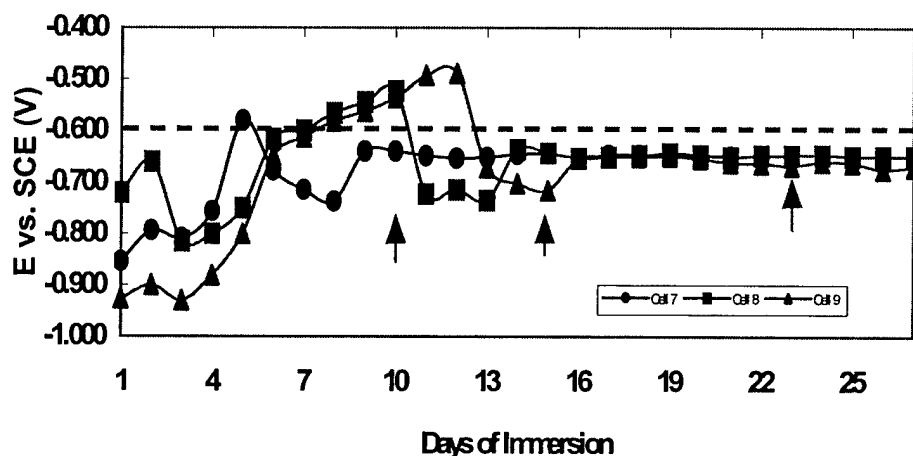


Figure 4. Daily open circuit potentials for 0.02M NaCl blisters showing distinct OCP decrease upon blister formation. Arrows indicate the day a blister was visible, and the dashed line indicates the pitting potential for AA1100-H14 in 0.02M NaCl.

### *Anodic Activity inside AA1100-H14 Blisters*

AA1100-H14 blisters showed dominant anodic activity inside blister areas (represented by a blue color). AA1100-H14 blisters tended to show anodic activity. The area surrounding these blisters underneath the organic coating showed anodic activity, cathodic activity, or a combination of both. Figure 44(a) shows surrounding cathodic activity (represented by negative potentials in this scan) as does Figure 44(b).

### *Cathodic Activity inside AA1100-H14 Blisters*

Cathodic activity was detected inside AA1100-H14 blisters that had a reddish-brown color located at their centers. Such blisters would show dominating cathodic activity with the surrounding areas outside of the blister containing some anodic activity underneath the epoxy coating. Figure 45 shows example photographs and SRET scans. Note that the surrounding area of the blister in Figure 45(b) denoted by anodic activity may be an exaggerated representation of the potential differences between the substrate and probe due to the height of the blister during signal conditioning.

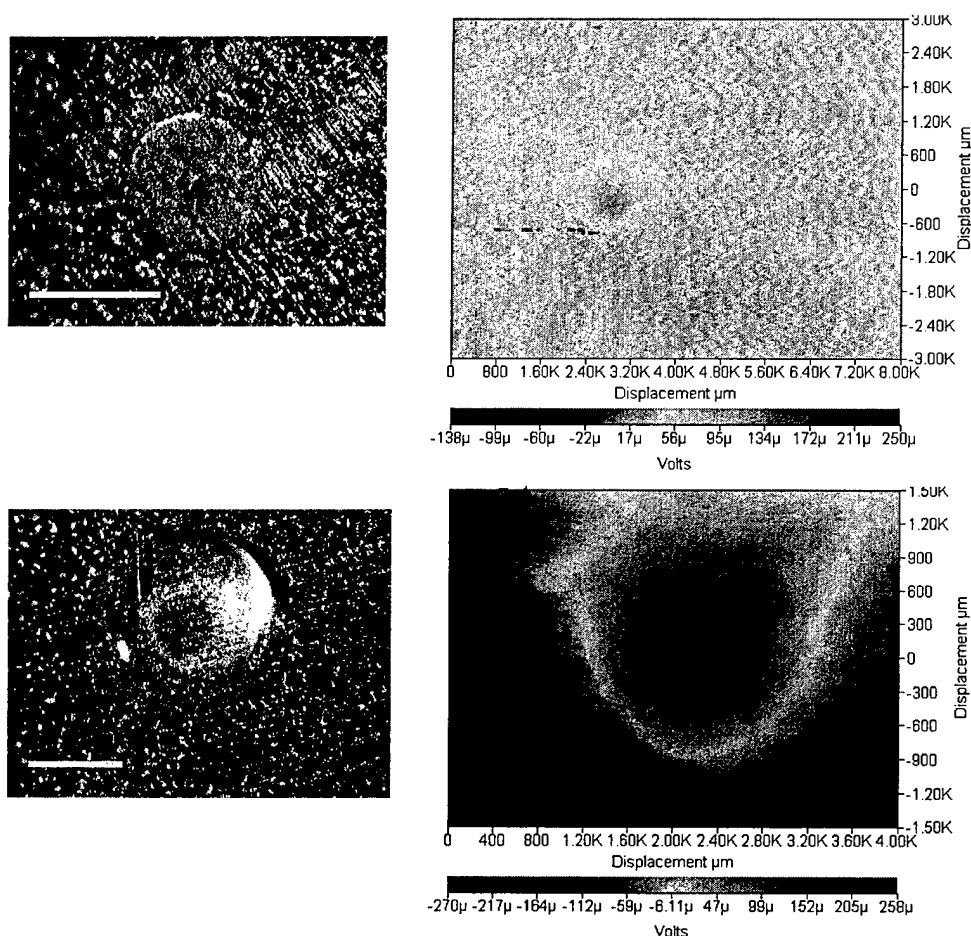


Figure 5. SRET scans and corresponding photographs of active AA1100-H14 blisters showing cathodic activity; photos taken same day as the scans (0.2M NaCl). (a) A dark brown deposit at the blister center causes the blister to exhibit positive electrochemical activity. (b) Scan showing a cathodic AA1100-H14 blister containing a dark center. The sharp line in scans (a) and (b) occurring at 600 μm (x-direction) is an artifact of the software.

### *Blister Corrosion Morphology*

Large salt deposits were found inside AA1100-H14 blisters in all NaCl concentrations. The most common form of corrosion attack found inside AA1100-H14 blisters grown in 0.02M and 0.2M NaCl was shallow pitting. SEM images of the characteristic shallow pitting are seen in Figure 49(a-b). CLSM images, as seen in Figure 49(c-d), allowed determination of the size and depth of AA1100-H14 pits. The average pit depth was 10  $\mu\text{m}$  while average pit width was 20  $\mu\text{m}$ . These shallow pits were highly hemispherical in nature and often littered with constituent particles. EDX indicated that AA1100-H14 constituent particles mainly consisted of elemental Al (75+ wt%), Si (5+ wt%), and Fe (less than 10 wt%) in varying concentrations. Other elements included Cu (less than 5 wt%), Zn (less than 2 wt%), Na, and Cl. Shallow pitting was also found in 2M NaCl blisters.

A large density of shallow pitting was usually found at the blister center; however, pitting was found throughout the expanse of the blister area reaching all the way to blister edges. The symmetrical nature of the pitting found in AA1100-H14 blisters suggested a possible correlation to metallurgical features of the alloy, i.e., subgrain structure. As seen in Figure 50, average feature sizes between an expanse of shallow pitting and the subgrain structure of polished AA1100-H14 are not related. The subgrain structure of AA1100-H14 is approximately three times the size of shallow pitting inside blisters.

For AA1100-H14 blisters containing corrosion product rings, the largest density of shallow pitting was again found at the blister center. Lower densities of pits were located in each section of the product rings. Figure 51 shows a series of CLSM images of a blister grown in 0.02M NaCl containing corrosion product rings near its center. Average pit depths are approximately 10  $\mu\text{m}$  or less.

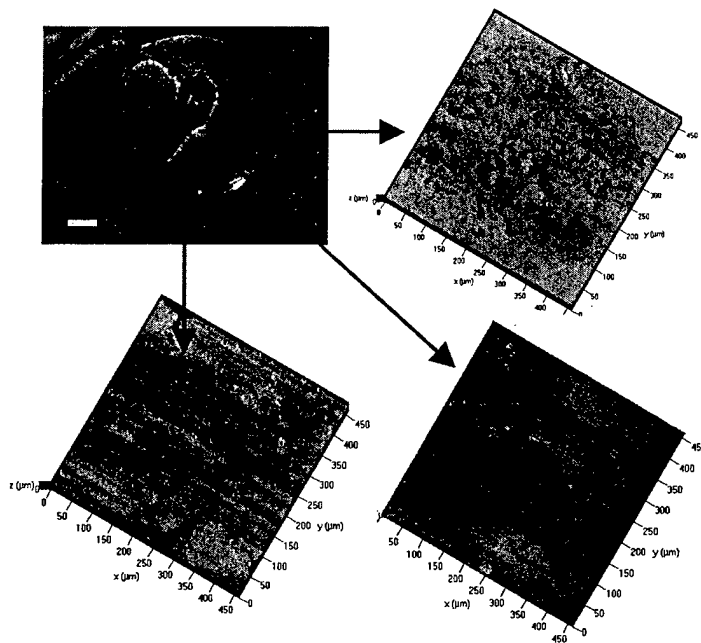


Figure 6. Digital photograph (a) and CLSM images (200x) of a three-week-old blister grown in 0.02M NaCl with corrosion product rings. (b) CLSM image of blister center showing the highest density of shallow pitting. (c) CLSM image of area between outer ring and center and (d) CLSM image of pitting at the corrosion product outer ring. The lesser density of pitting beyond the blister center is evident. Average pit depth is less than 10  $\mu\text{m}$ .

### Freestanding Thin Films and Coating Capacitance Behavior

Coating capacitance values,  $C_{\text{coat}}$ , were obtained through equivalent circuit model fits of impedance spectra of freestanding thin epoxy films. Assuming that capacitance changes are proportional to permittivity changes, the percentage of water uptake by the epoxy coating can be calculated directly from coating capacitance changes using the following equation<sup>8</sup>:

$$\Phi = (\text{Log}C_t/C_0)/\text{log}\epsilon_{\text{water}}$$

where  $C_t$  is the coating capacitance at time  $t$ ,  $C_0$  is the capacitance at the start of the experiment (linearly extrapolated from  $C_t(t)$  for  $t \rightarrow 0$ ) and  $\epsilon_{\text{water}}$  is the dielectric constant of pure water ( $\sim 80$  at  $25^\circ\text{C}$ ). The distribution of water is assumed to be random and uniform throughout the coating. From the coating capacitance data, diffusion coefficients at each  $\text{Cl}^-$  concentration were calculated assuming a continuous model where each layer of thickness of the coating contributes to the overall film capacitance<sup>9</sup>. The calculated diffusion coefficients for water through freestanding epoxy coatings decreased from  $6.43 \times 10^{-11} \text{ cm}^2/\text{s}$  to  $3.92 \times 10^{-12} \text{ cm}^2/\text{s}$  for concentrations from  $0.02 \text{ M}$  to  $2 \text{ M}$  for an assumed coating thickness of  $10 \mu\text{m} \pm 3 \mu\text{m}$  error. The percentage of water uptake by the epoxy coating is shown in Figure 64, calculated from the Figure 63  $C_{\text{coat}}$  values. Note the highest percentage of water uptake occurred in films exposed to the more dilute  $0.02\text{M}$   $\text{NaCl}$  immersion solution. This fact is also reflected in the highest  $C_{\text{coat}}$  values of Figure 63.

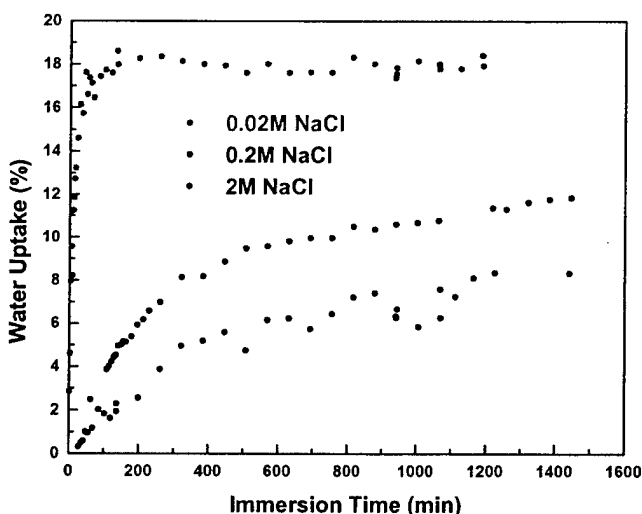


Figure 7. Percentage of water uptake by freestanding epoxy films determined using  $C_{\text{coat}}$  values. Films exposed to the lowest  $\text{Cl}^-$  concentrations exhibited the highest percentage of water uptake.

### Discussion

The blister framework presented here considers substrate heterogeneities and their contribution to the initiation and development of blisters. Constituent particles and intermetallic compounds are known to produce widespread micro-galvanic activity in uncoated Al-Cu alloys. The critical role of copper, known to largely influence the corrosion properties of Al-Cu alloys in general, is likely to control and manipulate underfilm corrosion as well. It is suspected that the micro-galvanic activity at and below the substrate surface affects how the coating degrades and the resulting corrosion morphology associated with this degradation. This framework attempts to relate blister formation and growth to the microscopic electrochemical environment resulting



from substrate heterogeneities. From there, the framework expands to show the relationship between the substrate and the macroscopic environment that develops as a consequence of microscopic galvanic activity.

### *Blister Initiation*

Blister initiation cannot occur without the formation of pathways through the coating that allow ion transport from the solution environment to the bare metal surface, whether through inherent pores within the coatings and/or other defects. The sources of these pathways or their formation as a result of water uptake, for example, are not addressed in this work. The assumption has been made, relative to this framework, that corrosion precludes blister formation so that the swelling of the coating due to osmotic pressure is a consequence of pitting phenomena underneath the coating.

Blister initiation on Al-Cu alloys appears to be potential-controlled. Blister initiation times decreased to only one or two days on AA1100-H14 as a result of potentiostatic holds at more noble potentials (higher than  $E_{\text{pit}}$ ), like those of the approximate open circuit potential of AA2024-T3. These reduced initiation times compared to those seen on AA2024-T3 under OCP conditions. Most of the AA1100-H14 coated samples that initiated blisters under OCP conditions did so with a simultaneous decrease in the open circuit potential. An initial increase in the global open circuit potential is mainly due to the uptake of water by the epoxy film and an increased cathodic reaction rate (ORR requires water as a reactant). The coated panel surrounding the tiny corrosion anode at the bottom of a pore or defect acts as a large cathode due to the ability of oxygen to permeate the film; as a consequence, the cathode-to-anode area increases. An increased cathodic reaction rate also causes an increase in the passive dissolution rate so that the potential has to increase to support the reaction, per mixed potential theory. In some cases, the global OCP measured for the first several days on coated AA1100-H14 rose above the measured pitting potential, as in Figure 32, so that stable pits were initiated prior to the appearance of a blister; however, blisters also initiated without the global OCP necessarily ever rising above  $E_{\text{pit}}$ . Metastable transients were observed in the measured global OCP frequently, both before and after the appearance of an active blister. These observations suggest that metastable pits may have been capable of causing blister formation below  $E_{\text{pit}}$ .

Another consideration is the alloy's tendency to pit at or near open circuit, most likely due to local clusters of Cu and Fe impurities. Any local increase in the potential of the Al matrix above  $E_{\text{pit}}$  (for the appropriate  $\text{Cl}^-$  concentration) near a Cu or Fe-containing particle can cause stable pitting due to the Cu and Fe-rich particles' tendency to enhance cathodic kinetics<sup>10</sup>. Therefore, local matrix potential increases in AA1100-H14 could be enough to induce pitting without a global OCP increase above  $E_{\text{pit}}$ .

The issue of whether the subsequent potential decrease is a consequence of blister formation or vice versa is entangled in the pitting kinetics on the alloy. Destabilization of the passive film occurs at local sites on the Al matrix upon chloride migration to the bare metal-solution interface. Following mixed potential theory, locally higher current densities at the bare metal sites where the passive layer has broken down cause a subsequent potential decrease, reducing the rate of anodic dissolution and accelerating the ORR. The new dissolution rate is still higher than the passive dissolution rate of the alloy, so that pitting damage is more severe than it was before the passive layer was destroyed. An accelerated ORR can lead to enhanced delamination at cathodic sites and promote blister formation.

Pit stability on Al is dependent on changes in the local pit environment, mainly local pH and  $\text{Cl}^-$  concentration<sup>11</sup>. Occluded chemistries developed inside initiating blisters may be the key to continued pit stability on AA1100-H14 so that localized passive layer breakdown and the subsequent potential decrease depend solely on the support of the local blister environment. This explanation is not likely due to the induction time needed to develop an appropriate occluded solution to support stable pitting.

It is likely that blister formation is a consequence of the potential decrease occurring as a result of pitting; this is evidenced by the first observation of blisters at the "bottom" of a global OCP decrease, as seen in Figures 32 and 33. Blister initiation on AA1100-H14 is controlled by potential with the assistance of water uptake and oxygen transport through the coating, both of which are discussed in the next section.

Results of the freestanding thin film experiments were in agreement with results obtained in the literature<sup>12-14</sup>. The main finding was that water uptake decreased with increasing chloride concentration. With this result, it was expected that the most dilute of the tested immersion solutions, 0.02M NaCl, would show the greatest degree of blistering, and the most concentrated solution, 2M NaCl would show the least amount; however, the intermediate concentration of 0.2M NaCl was found to be the most aggressive chloride concentration by far for coated AA1100-H14. More blisters initiated at this  $\text{Cl}^-$  concentration than in any of the other tested immersion solutions. Refer to Figures 23 and 24. Coated AA1100-H14 panels immersed in high purity Milli-Q water did not initiate blisters, likely due to the lack of chloride ions available to instigate pitting. The fact that the mid-range chloride concentration immersion solution displayed the highest degrees of blistering implies that there are two competing processes in blister initiation.

Just as the results presented in this work suggest that blister initiation is controlled by potential, solution environment factors such as water uptake and oxygen availability become competing factors for blister formation at specific ranges of  $\text{Cl}^-$  concentration. Potential differences, namely between the OCP and  $E_{\text{pit}}$ , control blister initiation at lower  $\text{Cl}^-$  concentrations while water uptake and oxygen transport direct blister formation at the higher chloride concentrations.

#### *Resulting Surface Anode/Cathode Development*

As mentioned previously, blister formation probably originates at a corroding IMC, which has been suggested to later become the center of the blister. Common phases found in AA1100-H14 include  $\text{FeAl}_3$  and  $\text{Fe}_3\text{SiAl}_{12}$ . Fe, presumably in the form of iron oxides, was found to deposit at the center of some AA1100-H14 blisters. Blisters with Fe deposits exhibited cathodic activity as determined through SRET experiments. When describing blistering on steel due to paint defects, Funke reported observations of a brown spot located at the center of the blister, later determined to be simple rust by chemical analysis<sup>15</sup>. These blisters tended to be cathodic in nature, and Funke attributed a membrane of hydrated iron oxides covering the defect whose metallic base was corroding to furthering blister growth due to osmotic pressure effects. Anodic polarization at the bottom of the pore occurs once the area is depleted in oxygen due to blockage by semipermeable corrosion products. Circular cathodic regions develop around the anodic pore, setting up conditions for cathodic delamination discussed earlier for coated steel.

IMC corrosion of Fe-containing particles in AA1100-H14 and the formation of iron oxide precipitates on the substrate at the center of the blister alter the electrochemical activity inside AA1100-H14 blisters. The entire blister area becomes cathodic, and the development of the

cathodic region throughout the blister occurs according to the cathodic delamination scenario posed for coated steel. Note that anodic activity that might be occurring underneath the iron oxide precipitate would not be detected during the SRET scan.

#### *Blister Growth Mechanism – Anodic Undermining vs. Cathodic Delamination*

There are three possible mechanisms that can support blister growth on epoxy-coated AA1100-H14: (1) cathodic delamination, (2) anodic undermining, and (3) corrosion product wedging. Corrosion product wedging, which is heavy accumulation of product at the substrate/coating interface that forces coating detachment by mechanical force, has not been mentioned in this work previously. Evidence exists for and against both cathodic delamination and anodic undermining and will be discussed below.

Corrosion product wedging has been eliminated from consideration for three reasons. First, corrosion product accumulation usually occurred homogeneously throughout the blister area and tended to be of uniform thickness. Blisters that contained concentric rings and circles of product only at blister centers without heavy accumulation elsewhere continued to grow without product buildup near blister edges. Second, deeper pitting would be expected underneath corrosion product near blister edges due to crevice effects. SEM and CLSM examination did not reveal increased pit depth near blister edges. Evidence of episodic growth would be characterized by deep pitting patterns at the edges of each product ring; however, CLSM studies indicated reduced pitting within the ring areas compared to the blister center. Third, a time factor would be required between growth spurts for adequate buildup of corrosion product to promote the wedge effect. Lateral blister growth rates tended to be linear for AA1100-H14 with no evidence of an incubation period prior to growth for corrosion product accumulation.

#### *Anode/Cathode Development*

SRET data indicated that the majority of blisters grown on epoxy-coated AA1100-H14 showed purely anodic behavior with cathodic activity distributed outside of the blister underneath the coating. Only the few AA1100-H14 blisters with iron oxide deposits at their centers exhibited cathodic activity.

Potentials representing anodic activity were spread out through the entire expanse of the blister, all the way out to blister edges. Corrosion damage also extended to the edges of blisters. This implies that anodic undermining is the main mechanism of blister growth for AA1100-H14. AA1100-H14 susceptibility to anodic undermining was indicated by the potentiostatic hold experiments at the approximate open circuit potential of AA2024-T3 where blister growth was promoted by anodic polarization. The poor dry adhesion exhibited by AA1100-H14 eases anodic undermining by facilitating the progression of coating detachment from the substrate upon metal dissolution. A random distribution of adhesion throughout a coated substrate rationalizes random blister locations, in the absence of substrate heterogeneities.

Locally delaminated sites may act as local cathodes outside of the blister that support anodic undermining inside the blister. Recall that the locally delaminated sites were areas of small delamination where corrosion products collected, and no corrosion damage was detected inside these features; however, local delamination was only observed at chloride concentrations of 0.2M and above. For the 0.02M NaCl case, the cathodic reaction may be distributed over the unblistered substrate immediately adjacent to the active blister without discrete local cathodes developing due to the decreased concentration of aggressive anion. SRET experiments over

areas of local delamination were unable to detect any significant cathodic activity at these sites. It is assumed that these sites acted as cathodes due to the heavy accumulation of corrosion product with no appreciable corrosion damage (with the exception of crevice corrosion along the edges). The mechanism of delamination at these particular sites is unclear at this time. The effect of IR drop has also not been clarified with respect to the distance between potentially cathodic delaminated sites and the anodic blister. Locally delaminated sites were located across the expanse of each coated panel, and IR drop would become a problem the farther away these cathodic sites were from the anodic blister.

The possibility of cathodic delamination on AA1100-H14 may exist for cathodic AA1100-H14 blisters containing iron oxide deposits. As described above, the development of the cathodic region throughout the Fe-containing blister appears to occur according to the cathodic delamination scenario posed for coated steel. Deep pits greater than the typical shallow 10  $\mu\text{m}$  depth for AA1100-H14 were observed underneath the iron deposits, providing the anodic center to support surrounding cathodic activity. Decreased pitting was detected radiating out from the central Fe deposit, supporting a central anode inside cathodic blisters.

#### *Local Electrochemical and Chemical Blister Development*

AA1100-H14 blisters tend to show either complete anodic or complete cathodic activity; SRET data did not indicate anode/cathode separation within each blister. Local OCP measurements taken with microelectrodes inside individual blisters, although weak in volume, provide some information regarding the galvanic nature of active blisters with the unblistered substrate and suggest whether a blister would be expected show either anodic or cathodic activity. Table 16 compares global OCP values at the time of blister initiation with the local internal blister OCP and pH obtained prior to sampling. The 0.2M NaCl measurements reflect blisters with Fe-containing deposits at their centers.

Galvanic coupling between the blisters initiated in 0.02M NaCl and their respective substrates outside of the blister indicate that the unblistered substrate would be more active than the blister, with the blister serving as a net cathode. CE data reveals a few interesting points. Chloride was detected in concentrations greater than the bulk for both blisters, suggesting increased anion migration into the blister to compensate for amplified corrosion activity; detected  $\text{Al}^{3+}$  concentrations were 0.03M ( $-0.510V_{\text{SCE}}$ ) and  $8 \times 10^{-4}\text{M}$  ( $-0.560V_{\text{SCE}}$ ). The latter aluminum cation concentration was the lowest  $\text{Al}^{3+}$  concentration detected and indicates little corrosion activity inside the blister. Reduced metal dissolution inside a growing blister suggests cathodic activity and would rationalize the high measured local OCP for the  $-0.560V_{\text{SCE}}$  blister. The 0.02M NaCl local OCP measurements reflect early attempts at microelectrodes and blister sampling, and caution should be used when making conclusions about the local electrochemistry and chemistry of these blisters based on potentially large errors.

All of the 0.2M NaCl local OCP data reflects blisters containing iron (oxide) deposits and would be expected to behave as cathodes. pH values obtained for the blisters denoted by \* support the local OCP measurements and the concept of cathodic blisters. Local OCP values were nobler than the potential of the unblistered substrate, and the high pH values (especially a value of 10) are consistent with cathodic activity. Low pH values inside blisters reflect high anodic dissolution rates. The differences in pH values may be reflective of the driving force for galvanic activity indicated by the potential differences between the blisters and the unblistered substrates. For example, a larger driving force for coupling exists ( $\sim 44\text{ mV}$ ) for the high pH blister. The local OCP of  $-0.807V_{\text{SCE}}$  is also consistent with cathodic activity.

The last value corresponding to 0.2M NaCl,  $-0.963V_{SCE}$  indicates that the outside of the blister is nobler than the blister area, despite the tendency for Fe-containing blisters to exhibit cathodic activity; however, the unblistered substrate and blister OCPs are separated by only 5 mV. A slightly higher chloride and aluminum concentration detected in the 0.2M NaCl blister with a local OCP of  $-0.963V_{SCE}$  provides little information with respect to the apparent anodic behavior of the blister.

It is likely that corrosion activity had been stifled for the blister represented by the first set of local OCP and pH values for 2M NaCl blisters. Local measurements were conducted over 200 days after blister initiation. pH values of 5 to 8 imply reduced amounts of  $Al^{3+}$  due to the low solubility of  $Al(OH)_3$  in this pH range. CE data was available for the blister with a pH of 5.3, which was the youngest blister initiated at the time of local measurement. Chloride and aluminum were detected in relatively high concentrations compared to other blisters, 0.3M and 0.06M, respectively so that a correlation between local OCP, pH, and chemistry cannot be made with this set of data. The local OCP does indicate that the blister was anodic compared to the rest of the unblistered substrate, which would be expected, based on the deep pitting morphology seen inside the blister area upon examination.

It should be noted that acetate was detected in some AA1100-H14 blisters. Acetate is not a component of the electrolytic solutions used in CE testing; thus, the organic acid likely originates from the epoxy coating itself. Acetone as a cleaning agent has been proposed to account for the presence of acetate in a variety of circumstances<sup>16</sup>, but acetate was detected in AA1100-H14 blisters even though acetone was not used in the alloy's cleaning procedure. The presence of acetate in occluded blister solutions may be an indication of coating degradation, although possible sources in the coating formulation are unknown at this time.

### *Resulting Corrosion Morphology*

The typical corrosion morphology for 0.02M and 0.2M NaCl blisters was shallow pitting that was, in general, uniformly distributed throughout the blister area. One contribution to such morphology is the poor dry adhesion as shown through POTS. With low adhesion between the epoxy coating and the AA1100-H14 substrate, it would be expected that blister growth laterally would be enhanced due to decreased forces that must be overcome in order for the coating to detach from the substrate. In this manner, lateral growth of corrosion pits that develop underneath the detached coating is facilitated since their formation relies on the geometry of the occluded site inside a blister, which is also not constrained by high adhesion. On AA1100-H14, pitting then would be expected to be wide and shallow because large pit depths are not required to compensate for the inability to grow outward.

AA1100-H14 corrosion morphology can also be explained by growth due to anodic undermining, which bears a close relationship to pitting. A short incubation time would be necessary to allow sufficient metal dissolution to cause coating detachment. In this manner, blister growth would be largely irregular during the early stages of anodic undermining. In other words, a perfectly circular region of delaminated coating around an active blister at its periphery would be rare. Light microscope and CLSM studies have indicated that regions of the coating detach in individual round sections, such as those described in local delamination. See Figure 54(b). Individual delaminated areas resemble small bubbles in the organic coating. Small pockets of occluded solution in each small delamination set up appropriate conditions for pitting and can cause pit shapes consistent with the detached region geometry. These observations suggest that episodic growth in AA1100-H14 blisters may result from individual delaminated

pockets in the coating that later coalesce into a larger, round delamination front, such as the one seen in Figure 29(b) and Figure 44(b). Note that anodic activity was detected throughout both the swollen part of the blister in Figure 44(b) as well as in the delamination front, providing further evidence for anodic undermining.

General corrosion attack on the order of 2-3  $\mu\text{m}$  was observed inside AA1100-H14 blisters that had been exposed to deaerated conditions. No appreciable blister growth was measured during the deaeration period; however, it has been suggested that reduced corrosion rates were supported during deaeration by the HER due to precipitation formation. The light general corrosion attack is consistent with metal dissolution that leads to anodic undermining, providing further evidence for the alloy's capacity for anodic undermining. Hemispherical pitting of the morphology usually seen under ambient conditions was also observed in the deaerated blister area, having likely occurred both before and after deaeration. Blister growth was not supported during deaeration by way of anodic undermining because the anodic dissolution rates were lowered significantly by the decrease in potential associated with elimination of the ORR.

## Conclusions

Blister initiation is controlled by potential and the chloride concentration of the bulk solution for AA1100-H14. Upon immersion, the coated alloys experience global increases in the OCP (to near or above  $E_{\text{pit}}$ ) associated with water uptake and oxygen transport through the coating and an increasing cathode-to-anode ratio. This potential increase is followed by a potential decrease associated with local sites of passive layer breakdown and pitting upon which simultaneous blister formation occurs. The tendency for single blister initiation on AA1100-H14 is related to the cathodic protection afforded by the subsequent potential decrease and the decreased local electrochemistry due to low particle density.

Blister growth appears to occur on AA1100-H14 by way of anodic undermining supported by results from SRET, dry adhesion tests, corrosion morphology in the blister area, local delamination morphology, blister initiation in sulfate + chloride electrolyte, and local blister environment characterization. The possibility of cathodic delamination as a mechanism for coated Al alloy blister growth has not been completely eliminated, although most of the results presented in this work better support anodic undermining. All blisters behave as net anodes in the early stages of life. A fast shift to dominant cathodic activity occurs on AA1100-H14 if iron oxide deposits inside the blister. The epoxy coating detaches in a series of small areas of delamination that coalesce prior to new blister growth spurts. The formation and function of locally delaminated sites outside of active blisters is unclear at this time.

The effect of varying chloride concentrations revealed a competing process with potential control: water uptake by the coating. Slower water uptake occurs at high  $\text{Cl}^-$  concentrations (*i.e.*, 2M NaCl) reducing the amount of reactant water available for the cathodic reaction and decreasing the transport medium for cations to the coating/substrate interface to maintain electroneutrality.

## Acknowledgements

The financial support of AFOSR (Paul Trulove) is gratefully acknowledged.

## References

1. Leidheiser, H. J. and Kendig, M. W., *Corrosion*, **32**, 69-76 (1976).

2. Dickie, R. A. and Smith, A. G., *Chemtech*, **10**, 31-35 (1980).
3. Leng, A., Streckel, H., Hofmann, K. and Stratmann, M., *Corrosion Science*, **41**, 599-620 (1999).
4. Leidheiser, H. J., *Corrosion*, **38**, 374-383 (1982).
5. Koehler, E. L., *Corrosion*, **40**, 5-8 (1984).
6. de Jong, H. F. and Moonen, W. A. J., *Aluminum*, **62**, 511-516 (1986).
7. Koehler, E. L., in *Localized Corrosion*, ed. R. W. Staehle, NACE, Houston, (1974).
8. Brasher, D. M. and Kingsbury, A. H., *Journal of Applied Chemistry*, **4**, 62 (1954).
9. Bellucci, F. and Nicodemo, L., *Corrosion*, **49**, 235-247 (1993).
10. Scully, J. C., Peebles, D. E., Romig, J. A. D., Frear, D. R. and Hills, C. R., *Met. Trans. A*, **23A**, 2641 (1992).
11. Frankel, G. S., *Journal of the Electrochemical Society*, **145**, 2186-2198 (1998).
12. Kittelberger, W. W. and Elm, A. C., *Industrial and Engineering Chemistry*, **38**, 695-699 (1946).
13. Leidheiser, H. J. and Wang, W., *Journal of Coatings Technology*, **53**, 77-84 (1981).
14. Brasher, D. M. and Nurse, T. J., *Journal of Applied Chemistry*, **9**, 96-106 (1959).
15. Funke, W., *Progress in Organic Coatings*, **9**, 29-46 (1981).
16. Kagwade, S. V., Clayton, C. R., Du, M. L. and Chiang, F. P., in *The Electrochemical Society Proceedings Series Proceedings of the Symposium on Surface Oxide Films*, J. A. Bardwell, p., The Electrochemical Society Proceedings Series, (1996).